Atmospheric Turbulence Characterisation Using Scintillation Detection and Ranging

---

A thesis submitted in partial fulfilment of the
requirements for the Degree of Doctor of Philosophy in Astronomy
at the University of Canterbury

by

Judy L. Mohr

Department of Physics and Astronomy
University of Canterbury
November 24, 2009

Abstract

Astronomical images taken by ground-based telescopes are subject to aberrations induced by the Earth's atmosphere. Adaptive optics (AO) provides a real-time solution to compensate for aberrated wavefronts. The University of Canterbury would like to install an AO system on the 1-m McLellan telescope at Mount John University Observatory (MJUO). The research presented in this thesis is the first step towards this goal.

To design an effective AO system it is important to understand the characteristics of the optical turbulence present at a site. Scintillation detection and ranging (SCIDAR) is a remote sensing method capable of measuring the refractive index structure constant, $C_N^2(h)$, and the wind velocity profile, $V(h)$. The dominant near ground turbulence (NGT) at MJUO required the use of both pupil-plane and generalised SCIDAR.

A purpose-built SCIDAR system was designed and constructed at low cost, using primarily off-the-shelf components. UC-SCIDAR saw first light at MJUO in 2003, and has since undergone several revisions. The current version employs two channels for simultaneous pupil-plane and generalised SCIDAR measurements, and is very portable. Through the use of a different mounting plate the system could be easily placed onto any telescope.

$C_N^2(h)$ profiling utilised standard analysis techniques. $V(h)$ profiling using data from a 1-m telescope is not common, and existing analysis techniques were extended to provide meaningful $V(h)$ profiles, via the use of partial triplet analysis.

$C_N^2(h)$ profiling between 2005 and 2007 indicate strong NGT and a weak turbulent layer located at 12 – 14 km above sea level, associated with the tropopause region. During calm weather conditions, an additional layer was detected at 6 – 7 km above sea level. $V(h)$ profiles suggest that the tropopause layer velocity is nominally 12 – 30 m/s, and that NGT velocities range from 2 m/s to over 20 m/s, dependent on weather. Little seasonal variation was detected in either $C_N^2(h)$ or $V(h)$ profiles. The average coherence length, r_0, was found to be 12 ± 5 cm and 7 ± 1 cm for pupil-plane and generalised measurements respectively, for a wavelength of 589 nm. The average isoplanatic angle, θ_0, was 1.5 ± 0.5 arcseconds and 1.1 ± 0.4 arcseconds for pupil-plane and generalised profiles respectively. No seasonal trends could be established in the measurements for the Greenwood frequency, f_G, due to gaps present in the $V(h)$ profiles obtained.

A modified Hufnagel-Valley (HV) model was developed to describe the $C_N^2(h)$ profiles at MJUO. The estimated r_0 from the model is 6 cm for a wavelength of 589 nm, corresponding to an uncompensated angular resolution, θ_{res}, of 2.5 arcseconds. θ_0 is 0.9 arcseconds. A series of $V(h)$ models were developed, based on the Greenwood wind model

with an additional Gaussian peak located at low altitudes, to encompass the various $V(h)$ profiles seen at MJUO. Using the modified HV model for $C_N^2(h)$ profiles and the suggested model for $V(h)$ profiles in the presence of moderate ground wind speeds, f_G is estimated at 79 Hz. The Tyler frequency, f_T, is estimated at 11 Hz.

Due to financial considerations, it is suggested that the initial AO design for MJUO focuses on the correction of tip/tilt only, utilising self-guiding, as it is unlikely that any suitable guide stars would be sufficiently close to the science object. The low f_T suggests that an AO system with a bandwidth in the order of 60 Hz would be adequate for tip/tilt correction.

Acknowledgements

I would like to acknowledge all the assistance that I have received over the years.

Thank you to Assoc. Prof. Peter Cottrell (Department of Physics & Astronomy) for support and supervision. It was you that planted the idea of adaptive optics into my head in the first place, so you only have yourself to blame.

Thank you to Dr Rachel Johnston (ARANZ Scanning Ltd., formerly Department of Electrical & Computer Engineering) for all your help with SCIDAR theory and the initial algorithms used in analysis and simulation. Without your help I would have spent decades trying to get things working.

Thank you to Graeme Kershaw (Department of Physics & Astronomy) for all your work in building the custom mounting components for UC-SCIDAR. Thank you for all the mechanical drawings you provided.

Thank you to C. Clare Worley (Department of Physics & Astronomy) for collecting the data during 2005 while I was on maternity leave. A large portion of my research used this data and without it I wouldn't have a thesis.

Thank you to Steve Weddell (Department of Electrical & Computer Engineering) for your assistance with the V2006 system and the loan of the cameras used in V2007 system.

Thank you to Philipp Hof (Department of Electrical & Computer Engineering) for the development of the trigger board system that was used in the V2006 system. It is unfortunate that the V2006 system failed for other reasons.

A big thank you to all the staff at Mount John University Observatory with special mention of the following:

Thank you to Alan Gilmore (Mount John University Observatory) for all the knowledge that you have passed on to me about how skies move. You have an amazing wealth of knowledge and I feel fortunate that you were willing to share some of it with me.

Thank you Nigel Frost (Mount John University Observatory) for your assistance in mounting UC-SCIDAR at MJUO and the late night repairs when the dome failed.

Thank you to Gijs Hovens for your assistance with CAD models of the telescope which helped me to understand how the telescope moved so I could get my direction calculations correct. You also helped me in a big way with editing. You have gone well beyond the call of a husband.

Thank you to Bea Hovens for providing funding to attend the SPIE conference in September of 2008 and for looking after my family while I was overseas.

Thank you to Dr Richard Lane (Applied Research Associates NZ Ltd., formerly

Department of Electrical & Computer Engineering) for the help you provided in the beginning with the acquisition of equipment needed for the development of UC-SCIDAR.

Last but not least, thank you to my handsome little man and my beautiful baby girl for reminding me everyday why I am doing this in the first place.

Contents

List of Figures

List of Tables

List of Abbreviations and Symbols

Abbreviations:

AO	adaptive optics
DM	deformable mirror
FSM	fast steering mirror
HV	Hufnagel-Valley ($C_N^2(h)$ model)
MJUO	Mount John University Observatory
NGT	near ground turbulence
RA-Dec	Right Ascension/Declination
RMS	root-mean-square
SCIDAR	scintillation detection and ranging
UT	Universal Time

Symbols:

A	telescope azimuth angle (radians, degrees)
a	telescope altitude angle (radians, degrees)
a, b	coefficients of the peak strength in $C_B(\rho, \phi, \Delta t)$
α	coefficent related to Δm
α Cen	α Centauri
α Cru	α Crucis
β	corrected wind direction from North (degrees)
b_{m}	measured wind direction (degrees)
b_ϕ	measured wind direction with respect to the telescope aperture (degrees)
$C_B(\rho, \phi, \Delta t)$	spatio-temporal scintillation covariance of a binary star system
$C_{B,\parallel}$, $C_{B,\perp}$	extracted parallel and perpendicular slice from $C_B(\rho, \phi, 0)$
$C_N^2(h)$	refractive index structure constant ($\mathrm{m}^{-2/3}$)
$C_S(\rho, \phi, \Delta t)$	spatio-temporal scintillation covariance of a single star
$C_T^2(h)$	temperature structure constant
D_{EP}	diameter of entrance pupil

D_{T}	diameter of telescope aperture (m)
d	defocus distance (km)
d_{sub}	diameter of sub-aperture (m)
Δh	altitude spatial sampling (m/pix)
Δm	binary star system magnitude difference
Δr	spatial sampling across the aperture (m/pix)
Δt	time delay (seconds)
Δv	velocity sampling (m/s.pix)
δ	declination (degrees)
ε_β	estimate error in β resulting from telescope motion
ε_C	error on the $C_N^2(h)$ estimate
ε_S	error on the slice fit
$\varepsilon_{\lvert\vec{v}\rvert}$	estimate error in $\lvert V(h)\rvert$ resulting from telescope motion
$F/\#$	F-number
f_E	effective focal length
f_G	Greenwood frequency (Hz)
f_{g}	focal length of generalised field lens
f_{p}	focal length of pupil-plane field lens
f_{T}	focal length of the telescope (m)
f_T	Tyler frequency (Hz)
γ	regularisation parameter
H, HA	hour angle (hours)
h, h_L, h_i	altitude (km)
$h_{\max}$	maximum detectable altitude (km)
k	wavenumber (m^{-1})
λ	wavelength (m)
$m(\rho)$	measurment signal
n_{pix}	number of pixels
φ	surface latitude position (radians, degrees)
ϕ	binary star system angular separation (arcseconds)
ρ	spatial position (x, y, z) (m)
r_0	turbulent coherence length (m)
S, $S(\rho)$	extracted 1D slice from $C_B(\rho, \phi, 0)$
$s(\rho)$	scintillation signal
σ	statistical standard deviation
σ^2	statistical variance
$T(\rho, h)$	inversion kernel matrix

τ_0	turbulence coherence time (seconds)
θ_0	isoplanatic angle (radians, arcseconds)
θ Eri	θ Eridanus
$\theta_{\rm res}$	angular resolution (radians, arcseconds)
υ Car	υ Carina
$V(h)$	wind velocity profile (m/s)
$\|V(h)\|$	measured wind speed (m/s)
$V_{\rm max}(h)$	maximum detectable velocity (m/s)
(x, y, z)	cartesian coordinates
z	propagation distance (m)
ζ	zenith angle (radians, degrees)

Chapter 1

Introduction

One of the major problems in imaging through the Earth's atmosphere is the distortion of images caused by atmospheric turbulence. Optically the atmosphere can be thought of as a group of lenses of varying size and refractive index that continually change because the atmosphere is in a constant state of motion, both spatially and temporally. The effect of the Earth's atmosphere on starlight can be visualised by thinking of the incoming wavefront as a flat sheet of paper. Atmospheric turbulence reduces the wavefront to a crumpled piece of paper and as a consequence distorts the resulting image.

As a planar wavefront encounters a turbulent layer, phase variations are induced. Over large propagation distances these phase variations are seen as large amplitude variations known as *scintillation*. Scintillation is due to the variations that occur in the refractive index along the line of sight, resulting from variations in local air temperature, local air pressure and, to a lesser extent, the local humidity (*Roddier*, 1981). Rapid scintillation reduces spatial resolution and severely hinders the ability to detect faint objects. An ideal diffraction-limited image (Figure 1.1(a)) is reduced to a speckled image for short exposures (Figure 1.1(b)).

The aim of image processing, post or real-time, is to take the crumpled wavefront and flatten it to approximate the incoming planar wavefront, to obtain higher spatial resolution in the corrected images. Adaptive optics (AO) provides a real-time solution for the compensation of aberrations present in the incident wavefront. This is achieved by means of a closed-loop system that utilises deformable optics. Accurate measurements and models of atmospheric turbulence are an essential tool in the design of an AO system (*Northcott*, 1999). Knowledge of the refractive index structure constant, $C_N^2(h)$, which is related to the turbulence strength, and knowledge of the wind velocity, $V(h)$, are needed for AO system design (*Avila et al.*, 2001).

This thesis aims to characterise the optical turbulence above one site in particular: Mount John University Observatory.

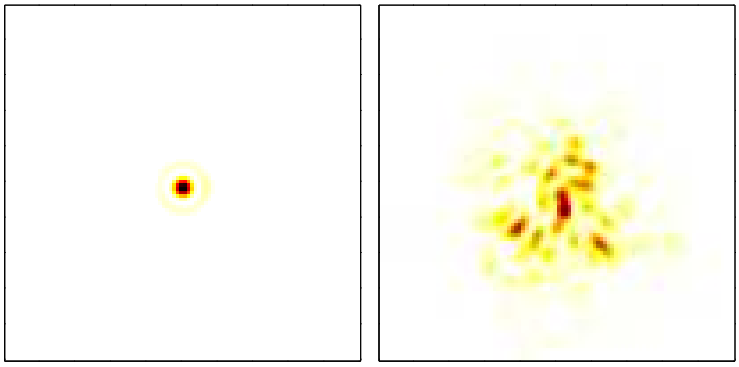

(a) (b)

Figure 1.1: The effect of atmospheric turbulence. (a) The diffraction-limited image of a star where no distortions are induced by the atmosphere. (b) The real situation where a speckle pattern is seen in the short exposure image due to the aberrations induced by the atmosphere.

1.1 Mount John University Observatory

The Mount John University Observatory (MJUO), located at Tekapo, New Zealand, is used for astronomical research and is operated by the University of Canterbury. The research telescopes on the site include two 60-cm reflectors (the 60-cm Optical Craftsmen Telescope and the 60-cm Boller & Chivens Telescope), a 1-m reflector (the 1-m McLellan Telescope) and a 1.8-m telescope (MOATel), which is dedicated to the MOA project.* Figure 1.2 shows an aerial view of MJUO taken in 2005.

The 1-m McLellan telescope is used for a variety of different astronomical research and is known to experience bad seeing by observers. Angular resolution is typically in the order of 2 arcseconds† but this can deteriorate to the point that a star system such as α Crucis (α Cru), which has an angular separation of 4 arcseconds, cannot be resolved into its components. It is desired to install an AO system on the 1-m telescope to improve photometric imaging with the CCD photometer head and to improve light throughput into the HERCULES échelle spectrograph currently installed on the 1-m telescope. The research discussed in this thesis is the initial step towards achieving this goal.

The telescopes used during this research at MJUO were the 1-m McLellan and 60-cm Boller & Chivens telescopes, and are shown in Figure 1.3.

*The MOA project searches for microlensing events caused by the gravitational field of a massive object (the lens) bending of light rays. It is a collaborative project run by Massey University, the University of Auckland, the University of Canterbury and Victoria University of Wellington in New Zealand, along with Nagoya University in Japan.

†Pers. comm. Alan Gilmore, Mount John University Observatory.

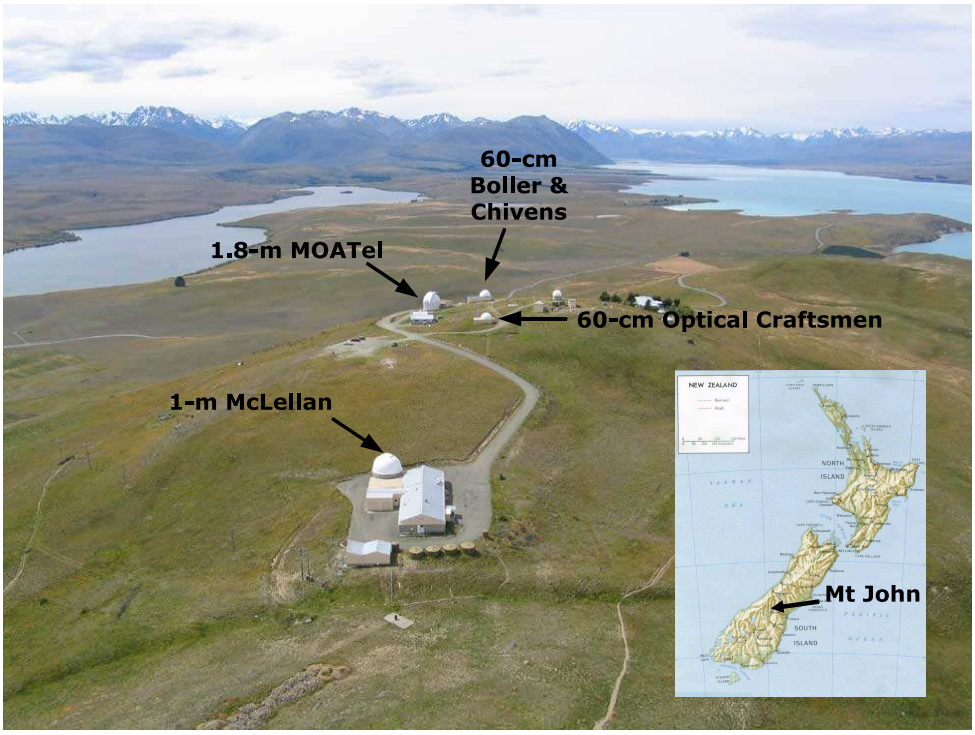

Figure 1.2: Aerial view of Mount John University Observatory. Photo of site provided by Alan Gilmore.

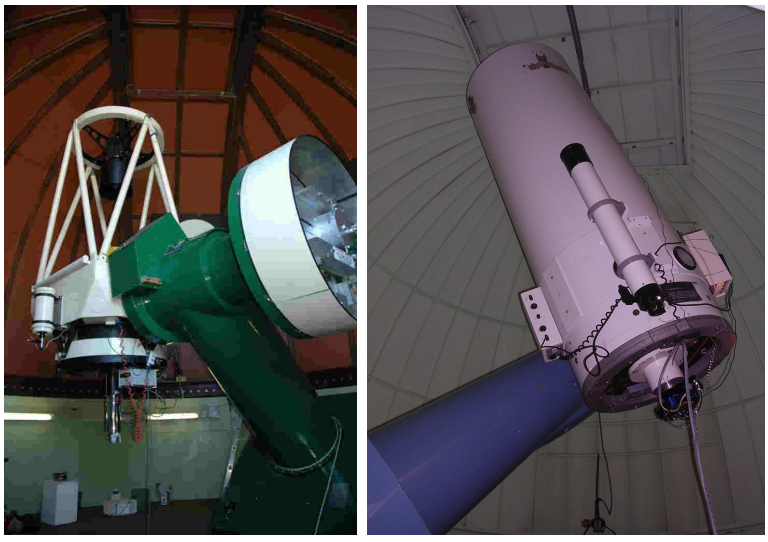

(a) 1-m McLellan (b) 60-cm Boller & Chivens

Figure 1.3: Telescopes used during this research at MJUO. Photos provided by Alan Gilmore.

1.2 A Turbulent Atmosphere

The Earth's atmosphere extends to several hundred kilometres above the Earth's surface and is made up of four main temperature zones: troposphere, stratosphere, mesosphere and the thermosphere. The transition regions between these four temperature zones are known as the tropopause, stratopause and mesopause respectively.

The troposphere is the first layer beginning at ground level and extends to 7 km at the poles and 17 km at the equator, with variations due to local weather conditions (*Sturman and Tapper*, 1996). The troposphere experiences a large amount of vertical mixing due to solar heating of the Earth's surface. It has a maximum air temperature near the surface of the Earth, which is on average 15°C, decreasing to approximately -60°C at its upper region (*Andrews*, 2004). Because the troposphere contains more than 80% of the atmospheric mass (*Sturman and Tapper*, 1996), the majority of optical turbulence found in the atmosphere occurs in this layer, with small amounts of optical turbulence extending to higher altitudes. The temperature variations that give rise to optical turbulence are considered to be significant only in the troposphere (*Hardy*, 1998). Typically optical turbulence is greatest near ground level and decreases exponentially with increasing altitude with the exception of peaks that occur due to wind shear (*Hardy*, 1998).

The tropopause marks the transition zone from the troposphere to the stratosphere. The thickness of the tropopause varies with latitude and season because of differing surface heats. It lies at an average altitude of approximately 11 km in mid-latitudes regions such as New Zealand (*Sturman and Tapper*, 1996). Seasonal variations can significantly change the height of the the tropopause. In New Zealand, the tropopause may lie 2 – 4 km higher during summer than during winter (*Sturman and Tapper*, 1996). At the tropopause there is often a peak in optical turbulence due to wind shear (*Hardy*, 1998). Above the tropopause there is a rapid decrease in turbulence. The effects of optical turbulence become insignificant at altitudes above 25 km (*Hardy*, 1998).

Figure 1.4 indicates the approximate temperature profile present in the atmosphere with increasing altitude, extending up to 25 km.

1.2.1 Describing Atmospheric Turbulence

When considering *optical turbulence*, one traditionally discusses the refractive index fluctuations experienced (*Andrews*, 2004). Many volumes have been written about the effects of atmospheric turbulence on the incident wavefront, such as *Roddier* (1981) and *Roggemann et al.* (1997).

Optical turbulence requires both the presence of turbulent air structures and back-

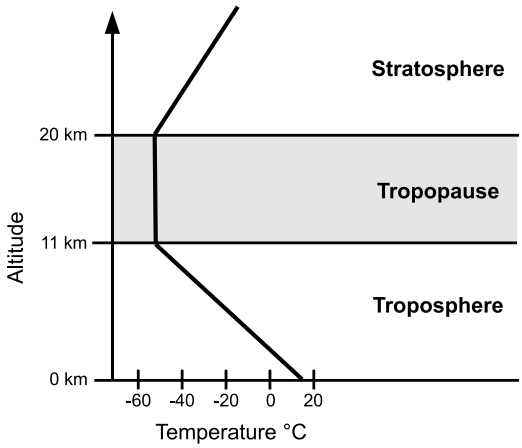

Figure 1.4: Vertical structure of the atmosphere.

ground temperature gradients (*Jumper et al.*, 2007). As the potential temperature gradients tend towards zero in a mixing region of the atmosphere then the optical turbulence also tends toward zero.

The *refractive index structure function*, $D_N(\rho)$, provides a useful function for characterising optical turbulence and arises from the analysis of the optical transfer function (*Roggemann et al.*, 1997). It is the square of the difference of two random processes and is defined as (*Roggemann et al.*, 1997)

$$D_N(\rho) = \langle |N(\rho') - N(\rho' - \rho)|^2 \rangle, \tag{1-1}$$

where $N(\rho')$ is the refractive index of the atmosphere at a spatial position ρ'. $\langle\rangle$ denotes the ensemble average.

Assuming Kolmogorov turbulence, the structure function takes on a 2/3 law dependence on ρ (*Roddier*, 1981),

$$D_N(\rho) = C_N^2 \rho^{2/3}, \tag{1-2}$$

where C_N^2 is the *refractive index structure constant*, a measure of the turbulence strength. In practice C_N^2 is not constant as it varies with geographical location, altitude and time.

Roddier (1981) suggests that turbulence is concentrated into thin layers with typical thicknesses of 100 – 200 m where C_N^2 increases by more than one order of magnitude above its background level. Below 4 km above sea level, the local terrain plays an important role, forcing air movement in particular directions (*Sturman and Tapper*, 1996). The behaviour of turbulence above 4 km is almost independent of location. Typically the turbulence is strongest near ground level, reaches a minimum around 6 – 9 km, then slightly increases

to a secondary maximum near the tropopause and decreases again in the stratosphere. As C_N^2 is highly dependent on altitude, it is better described as a function of altitude h. $C_N^2(h)$ provides a measure of a turbulent layer's contribution to the induced aberrations.

A useful parameter for characterising the resolution of an imaging system is *Fried's parameter* or the *turbulence coherence length*, r_0 (*Fried*, 1966). r_0 describes the telescope diameter for which nearly diffraction-limited resolution can be obtained if there is no attempt to compensate for atmospheric turbulence. It is defined as (*Tyson*, 1991)

$$r_0 = \left[0.423k^2 \sec(\zeta) \int C_N^2(h)dh\right]^{-3/5}, \tag{1-3}$$

where $k = 2\pi/\lambda$ is the wavenumber for a given wavelength λ and ζ is the zenith angle. r_0 is widely used to describe a variety of atmospheric phenomenon.

Another useful parameter for characterising the effects of atmospheric turbulence is the *isoplanatic angle*, θ_0. This defines the maximum angular separation between two object for which turbulence induced distortions are essentially identical (*Klückers et al.*, 1998). θ_0 is defined as (*Parenti and Sasiela*, 1994)

$$\theta_0 = \left[2.91k^2 \sec^{8/3}(\zeta) \int C_N^2(h)h^{5/3}dh\right]^{-3/5}. \tag{1-4}$$

Unlike r_0, θ_0 is dependent on $h^{5/3}$ indicating that weak high altitude layers have a significant impact on θ_0.

Atmospheric turbulence is in a constant state of motion. The *Greenwood frequency*, f_G, describes the rate at which the turbulence structure above a site changes with time. It is defined as (*Tyson and Frazier*, 2004)

$$f_G = 0.255 \left[k^2 \sec\zeta \int C_N^2(h)V(h)^{5/3}dh\right]^{3/5}, \tag{1-5}$$

where $V(h)$ is the average wind velocity as a function of altitude h. f_G determines how quickly an AO system is required to respond to adequately compensate for the aberrations induced by atmospheric turbulence.

A closely related parameter to f_G is the *turbulence coherence time*, τ_0, which is defined as (*Klückers et al.*, 1998)

$$\tau_0 = \left[2.91k^2 \sec\zeta \int C_N^2(h)V(h)^{5/3}dh\right]^{-3/5}. \tag{1-6}$$

τ_0 can be related to f_G by

$$\tau_0 = \frac{0.134}{f_G}. \tag{1-7}$$

1.3 Measuring Atmospheric Turbulence

There are five different contributing zones to atmospheric turbulence (*Roddier*, 1981). *Dome* and *mirror seeing* refer to the turbulence resulting from turbulence eddies inside the dome and telescope respectively. *Surface layer* turbulence results from the temperature variations between air inside and outside the dome. *Boundary layer* turbulence tends to extend to 10s of metres above the dome and *free atmosphere* turbulence lies above this. Turbulence in the first four zones can be measured with sensors located near to the ground, but the measurement of free atmosphere turbulence is more complicated.

Existing turbulence profiling systems were available at the time this project commenced, however budget constraints did not permit for long term observations using these systems. A low-cost purpose built system was needed. A brief overview of the various turbulence detection techniques is presented here.

The oldest methods of measuring the structure of the atmosphere are *in situ* techniques (*Hoinka*, 1997). Temperature and pressure probes are used in conjunction with wind velocity meters to measure the local properties of atmosphere. Optical turbulence properties are inferred from the temperature structure constant, $C_T^2(h)$. Assuming Kolmogorov turbulence, the refractive index structure constant, $C_N^2(h)$, can be related to $C_T^2(h)$ by (*Avila*, 2002)

$$C_N^2(h) = \left[\frac{8 \times 10^{-6} P}{T^2}\right] C_T^2(h), \tag{1-8}$$

where P and T are the local pressure and temperature respectively.

Sensors placed on towers allow for continuous measurements of a particular point, however the height of a tower is limited and hence measurements are restricted to low altitudes only. Airborne sensors, by means of a balloon or aircraft, do allow for measurements in the free atmosphere, however they do not provide measurements sufficiently continuous in time (*Azouit and Vernin*, 1980). Instead they provide a snap-shot of the conditions as they pass through a given region of the atmosphere. The cost associated with airborne sensors inhibit the ability to collect more than a few profiles in a given night (*Avila*, 2002). Remote sensing technologies provide the ability to measure atmosphere properties over a range of altitudes simultaneously.

Measurements of image motion are more commonly used to estimate r_0. A *differential image motion monitor* (DIMM) utilises an aperture mask containing two or more apertures overlaid on a larger one (*Tokovinin*, 2002). The variance of the differential image

motion between the sub-images is calculated and compared to the theoretical variances based on Kolmogorov turbulence to provide an estimate of r_0 (*Avila*, 2002). Estimates of temporal parameters is limited as wind speed profiles must be obtained from external measurements (*Tokovinin et al.*, 2008).

Recently *Tokovinin et al.* (2008) proposed a new technique (and instrument) based on DIMM that was capable of measuring the atmospheric coherence time, τ_0. The technique, termed *fast defocus* (FADE), utilises a single defocussed telescope aperture image with a central obscuration. A series of short exposure images are acquired at a frame rate of 500 Hz or greater, from which the radius of the image ring is estimated. From the defocussed images r_0 and τ_0 are estimated.

FADE and DIMM give an indication of the integral properties of $C_N^2(h)$, but do not provide the altitude distribution of $C_N^2(h)$, which is vital in the determination of the isoplanatic angle, θ_0.

Light detection and ranging (LIDAR) systems operate on the same principle as DIMM, but use a laser beacon as a reference source which can be targeted at altitudes ranging from 250 m to 15 km (*Gimmestad et al.*, 2007). In a LIDAR system, portions of the atmosphere are not profiled due to the finite altitude of the beacon. In addition the costs associated with laser systems are typically well outside the budget of small observatories.

Sound detection and ranging (SODAR) instruments detect back-scatter due to irregularities in thermal turbulence of the scale size $\lambda/2$ where λ is the wavelength of the SODAR measurements (*Avila*, 2002). The $C_N^2(h)$ profiles are obtained from the measured $C_T^2(h)$ profiles. SODAR systems tend to be highly portable, however they have a limited range due to the attenuations that result from humidity factors (*Vernin et al.*, 1990) and contamination from external sources (*Eaton*, 2005). High altitude turbulence extending into the tropopause region may not be detectable using SODAR.

A *multi-aperture scintillation sensor* (MASS) uses scintillation from a single star captured by an aperture masked on a small telescope (8 – 15 cm) (*Tokovinin et al.*, 2005). Any phase variations induced by atmospheric turbulence are weak and must propagate large distances to produce measurable scintillation, as scintillation is proportional to $h^{5/6}$ (*Roddier*, 1981). As such, MASS measurements are blind to near ground turbulence (NGT) (*Tokovinin et al.*, 2005). Attempts have been made to extend MASS to generalised measurements, however generalised MASS resulted in an overestimate of angular resolution which was attributed to telescope tracking errors and diffraction effects on the aperture edge (*Kornilov et al.*, 2003). MASS measurements are considered reliable in weak turbulence, however in strong scintillation MASS is known to overestimate angular resolution in the free atmosphere (*Tokovinin et al.*, 2005).

The technique known as *shadow band ranging* (SHABAR) uses scintillation from an extended source such as the sun, moon or planets to measure the turbulence structure extending up to 500 m above the ground at a high altitude resolution (*Tokovinin*, 2007). The angular diameter of an extended light source effectively averages scintillation resulting from high-altitude turbulent layers, making SHABAR suitable for the detection of NGT only. Originally SHABAR was developed for use with the sun (*Beckers*, 2001), but has since been expanded for use with the moon (termed a lunar scintillometer, or LuSci) (*Tokovinin*, 2007) to characterise the boundary layer present at various sites (*Hickson and Lanzetta*, 2004; *Thomas-Osip et al.*, 2008; *Tokovinin*, 2007).

Slope detection and ranging (SLODAR) measures the local wavefront tilt using a wavefront sensor, typically a Shack-Hartmann (SH) sensor, to estimate turbulence profiles (*Wilson*, 2002). As light from a binary star system is typically used, the angular separation, ϕ, must be appropriate to ensure that both companions are within the field of view of the lens system and the resulting sub-aperture images are sufficiently separated in the image plane (*Wang et al.*, 2008). During the design of a SLODAR system it is desirable to obtain spot images for each sub-aperture that are diffraction-limited, such that $d_{\text{sub}}/r_0 \approx 1$, where d_{sub} is the sub-aperture size measured in the same plane as r_0. When this thesis research commenced, a lenslet array with a standard surface coating was in the order of US$2000. The acquisition of a suitable SH lenslet array was not financially feasible.

Scintillation detection and ranging (SCIDAR) measures stellar scintillation as seen by the aperture of the telescope to infer characteristics about the atmospheric turbulence above a site (*Fuchs et al.*, 1998; *Avila et al.*, 2001). A sequence of short exposure images, conjugate to the telescope aperture, are taken. From these images a covariance image is found from which $C_N^2(h)$ and $V(h)$ profiles can be determined. SCIDAR traditionally computes the spatio-temporal correlation of short exposure images of the scintillation patterns produced by binary stars. Pupil-plane SCIDAR places the measurement plane at the telescope aperture. This enables a clear picture of optical turbulence in the free atmosphere to be obtained, because pupil-plane SCIDAR is insensitive to any NGT. By using a simple lens change, the measurement plane can be shifted to a virtual plane located below the telescope. This increases the propagation distance such that scintillation caused by NGT can also be measured. This version of SCIDAR is known as *generalised* SCIDAR (*Klückers et al.*, 1998).

The use of SCIDAR allows for the full $C_N^2(h)$ and $V(h)$ profiles to be obtained. The lenses associated are reasonably cheap. It was therefore decided to use a SCIDAR system where costs could be kept to a minimum by using primarily off-the-shelf components.

1.3.1 SCIDAR Systems

When using a binary star system, the angular separation, ϕ, has a strong influence on the altitude range used for measurements. A narrow ϕ provides for the ability to detect full atmospheric profiles, whereas a wide ϕ will result in the detection of low altitude turbulence only. The use of wide binaries has been used in the system dubbed *low layer SCIDAR* (LOLAS) (*Avila et al.*, 2008). LOLAS is based on generalised SCIDAR and was designed for use with a 40-cm Meade telescope. With $\phi = 70$ arcseconds the maximum altitude seen with LOLAS is approximately 1200 m.

Systems that measure profiles that extend to the free atmosphere include Cute-SCIDAR, which is mounted on the 1-m Jacobus Kepteyn Telescope in La Palma (*Hoegemann et al.*, 2004), and the instrument developed by Nice University, which has been used on the 1.5-m and 2.1-m telescopes at Observatorio Astronómico Nacional de San Pedro Mártir in Mexico (*Avila et al.*, 2006) and on the 2.2-m telescope on Mauna Kea (*Tokovinin et al.*, 2005). These systems utilise primarily generalised SCIDAR measurements.

Scintillation is considered a weak observable and as such it is assumed that free atmosphere profiling using binary star SCIDAR requires a telescope with a diameter of 1 m or larger (*Tokovinin*, 2007). In addition the number of suitably bright binary star systems is limited. This has led to the development of SCIDAR using single stars.

Single star SCIDAR (SSS) has been implemented in two different ways. *Coburn et al.* (2005) proposed a system that used a CCD on a movable stage such that the position of the measurement plane could be moved. By moving the measurement plane to an altitude above the telescope where optical turbulence existed then in theory the scintillation resulting from the layer would not be detectable. By scanning through the atmosphere searching for a null in scintillation the altitude structure of turbulence could be found. Although the full profile could be ascertained, the scanning approach requires multiple measurement planes to be employed. In the presence of strong NGT, the strength of the NGT may hinder the ability to detect a null in the scintillation and high altitude turbulent layers could be masked.

An alternative SSS approach is to compute the temporal covariance for scintillation images from a single star using a static measurement plane (*Habib et al.*, 2006). With increasing time delay between successive frames the position of the covariance peaks are separated depending on the wind speed associated with the given layers. When the peaks are sufficiently separated then the individual layer strengths can be determined in conjunction with the layer's wind speed. For this approach to be successful multiple temporal covariances need to be computed using different values of the time delay between consecutive frames, Δt. Layers with a high wind speed may not be detectable at multiple Δt. In addition, the wind velocity associated with different layers may be similar and

hence the covariance peaks may not separate sufficiently. Gaps may exist in the resulting $C_N^2(h)$ and $V(h)$ profiles.

The system designed for use at MJUO utilises binary star SCIDAR, with the intention of acquiring $C_N^2(h)$ and $V(h)$ profiles for use in the design of an AO system.

1.4 Adaptive Optics

Real-time compensation of turbulence induced aberrations in astronomical images using AO requires the use of a wavefront sensor, a correction device, a system controller and a guiding system (*Tyson*, 1991). The specific components used and their arrangement will depend on the level of compensation targeted. Figure 1.5 shows the typical configuration for use with an astronomical telescope, where aberrations are compensated for prior to image aperture using a closed-loop system.

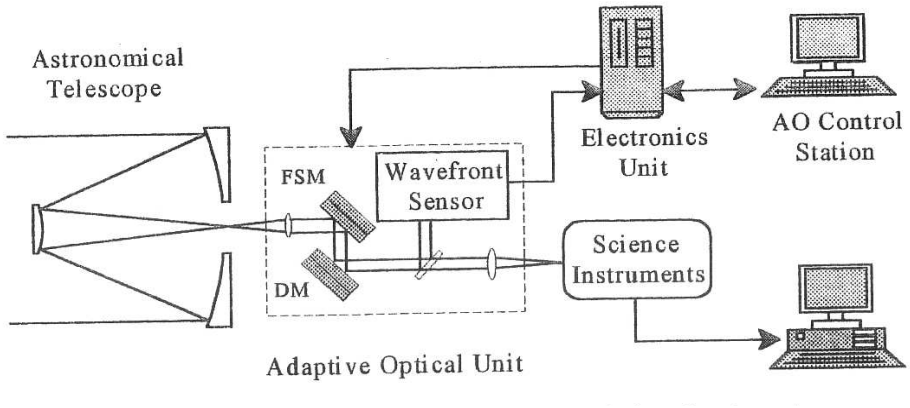

Figure 1.5: A generic AO system for use with an astronomical telescope and a natural guide star. An AO system will consist of a wavefront sensor, a compensation device in the form of a deformable mirror (DM) and/or fast steering mirror (FSM), and a control system. Reprinted from *Hardy* (1998).

The wavefront sensor images the wavefront and produces an electrical input signal that provides an estimate of the aberrations present in the incident light. Many different sensor configurations are available. In general, the resolution of the wavefront reconstruction is dependent on the size of the sub-apertures used. The smaller the sub-apertures, the finer the sampling.

Short exposure astronomical images consist of a speckled pattern where the centroid moves randomly. Variations in centroid position are usually corrected by using a fast steering mirror (FSM), also known as a tip/tilt mirror. Tip/tilt compensation

can be incorporated into a system for the compensation of higher order aberrations or implemented as a separate system.

High order aberrations that lead to the speckled image appearance can be compensated for using a deformable mirror (DM). The level of high order compensation achieved depends on the DM design. The exact compensation of wavefront aberrations requires very high spatial sampling which is impossible to implement, resulting in a residual fitting error.

An AO system must utilise some form of guiding system to determine the atmospheric turbulence present at the time. The guide object can be the science object being observed or an external source, such as a nearby star located in close proximity to the science object or a laser source. It is unlikely that MJUO will utilise a laser guide star due to the costs associated with such a system and hence no further detail is provided here. A more detailed discussion on the use of laser guide stars in AO can be found in *Hardy* (1998).

The control computer uses the information from the wavefront sensor to control the FSM and the DM in order to compensate for the distortions in the wavefront. The incoming wavefront is *reconstructed* by the control computer.

The performance of an AO system is reliant on the speed of the control computer and the efficiency of its calculations. Processing requirements for an AO system are quite complex and depend on (*Tyson*, 2000):

- atmospheric conditions,
- the size and site of the telescope,
- the direction of the observed object and the wavelength of observation,
- the number of channels of correction to be controlled,
- the brightness of the guide object.

AO systems typically have bandwidths in the range of 10 to 1000 Hz and are located after the telescope pupil (*Beckers*, 1993).

1.5 Thesis Organisation

This thesis is organised into the following chapters:

- Chapter 2 discusses the basic theory of optics and the mathematical treatment of characterising atmospheric turbulence. Also discussed is the phenomenon known as scintillation and how SCIDAR uses scintillation captured from a binary star system to determine $C_N^2(h)$ and $V(h)$ profiles.

- Chapter 3 presents the system design for the SCIDAR instrument developed during the course of this research.
- The practical implementation of determining $C_N^2(h)$ profiles from SCIDAR data is detailed in Chapter 4.
- The determination of $V(h)$ profiles is detailed in Chapter 5.
- Chapter 6 discusses the measurements taken at MJUO during the course of this research.
- Chapter 7 discusses the trends found in the SCIDAR data and presents a set of $C_N^2(h)$ and $V(h)$ models that could be used to begin the development of an AO system at MJUO.
- Chapter 8 contains a preliminary assessment of the AO design parameters for MJUO and makes recommendations as to how the development of such a system should proceed.
- Chapter 9 summarises the main conclusions and suggests areas of further research for the SCIDAR instrument developed, the methods used to extract $C_N^2(h)$ and $V(h)$ profiles, and the data and models presented.

Chapter 2

Imaging Through Turbulence

To develop an instrument that can effectively measure atmospheric turbulence it is important to have an understanding of certain aspects of the field of optics and the effects of turbulence on an incident wavefront.

Optics can be divided into three main areas; geometrical optics, physical optics and quantum optics. The concepts of geometrical optics are available in any standard physics text, such as *Halliday and Resnick* (1988), and will not be discussed further here. Physical or Fourier optics provides a more in-depth analysis of light propagation, while quantum optics describes the quantum nature of light and is outside the scope of this research.

Section 2.1 introduces the concepts of apertures and diffraction. Section 2.2 introduces polynomials commonly used to describe turbulence induced aberrations and the effects abberations have on the resolution of a system. Section 2.3 discusses mathematical models that are commonly used to describe $C_N^2(h)$ and $V(h)$ profiles, while section 2.4 discusses the theory behind the technique used to measure $C_N^2(h)$ and $V(h)$ profiles.

2.1 Using an Aperture

The amount of light from a given source is limited when using an aperture. The aperture can be part of one of the optics in the system or a separate component. The entrance pupil and the exit pupil are the images of the aperture in object and image space respectively. In the schematic shown in Figure 2.1 the position of the entrance pupil and the aperture coincide. For a telescope this is commonly the case.

The *F-number* gives an indication about the number of photons that will be collected in an area specified by the image size. It is based on the effective focal length of the imaging system, f_E, and the diameter of the entrance pupil, D_{EP}, and is defined as (*Greivenkamp*, 2004)

$$F/\# = \frac{f_E}{D_{EP}}. \tag{2-1}$$

The F-number is typically referred to as the *speed of the imaging system* as it is gives an indication of the exposure time required (*Halliday and Resnick*, 1988). A smaller F-

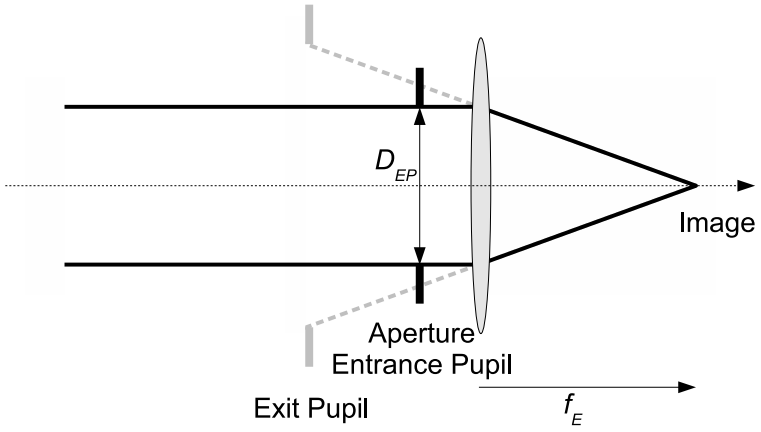

Figure 2.1: Schematic of the aperture and pupil positions. The amount of light in a system is limited by the aperture. The entrance and exit pupils are images of the aperture in object and image space respectively. In this example the position of the entrance pupil and the aperture coincide.

number for a given f_E means that D_{EP} is larger allowing more light through the system, requiring shorter exposure times. A system with a small F-number is said to be a *fast* imaging system.

The *depth of focus* (DOF) describes the amount that the image position can be shifted from the nominal position before the resulting image blurs, and the image diameter exceeds the blur diameter criterion specified by $D_{\Delta i}$ (*Greivenkamp*, 2004). If the maximum allowable image offset was Δi and the image diameter at Δi was $D_{\Delta i}$ then

$$\text{DOF} = \pm\Delta i \approx \pm\frac{D_{\Delta i} f_E}{D_{EP}} = \pm D_{\Delta i} F/\#. \tag{2-2}$$

A schematic of the DOF is shown in Figure 2.2.

The *field of view* (FOV) describes the maximum angular size of an object as seen from the entrance pupil. For telescopes, where science objects are extremely distant (*Greivenkamp*, 2004),

$$\text{FOV} \approx 2\theta_{1/2} \approx \frac{2h_i}{f_E}, \tag{2-3}$$

where $\theta_{1/2}$ is half the angular size of the stellar field, h_i is half of the image size seen in the image plane and f_E is the effective focal length of the telescope. Figure 2.3 shows a schematic of the field of view.

2.1.1 Diffraction

> "Diffraction is the bending of a wave as it passes through a gap or around the edge of a barrier." (*Howison*, 1992)

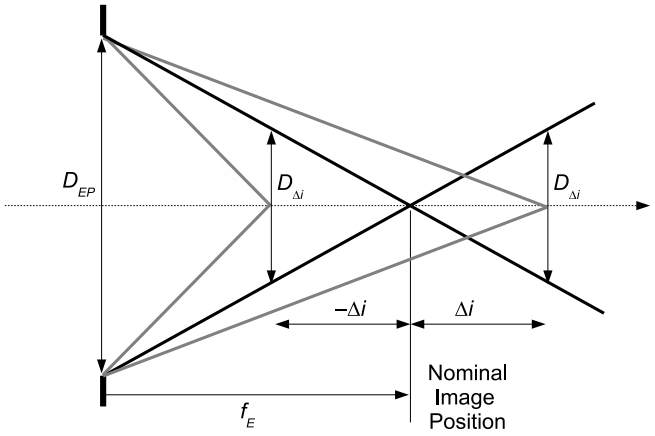

Figure 2.2: Depth of focus estimation. An image can form between $-\Delta i$ and Δi before an image blurs excessively. The diameter of the image $D_{\Delta i}$ can be related to the F-number of the system $F/\# = f_E/D_{EP}$.

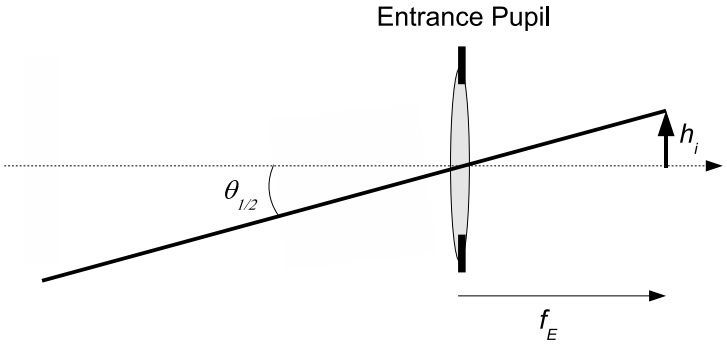

Figure 2.3: Determination of field of view. An image of size $2h_i$ will represent a stellar field that has an angular size of $2\theta_{1/2}$.

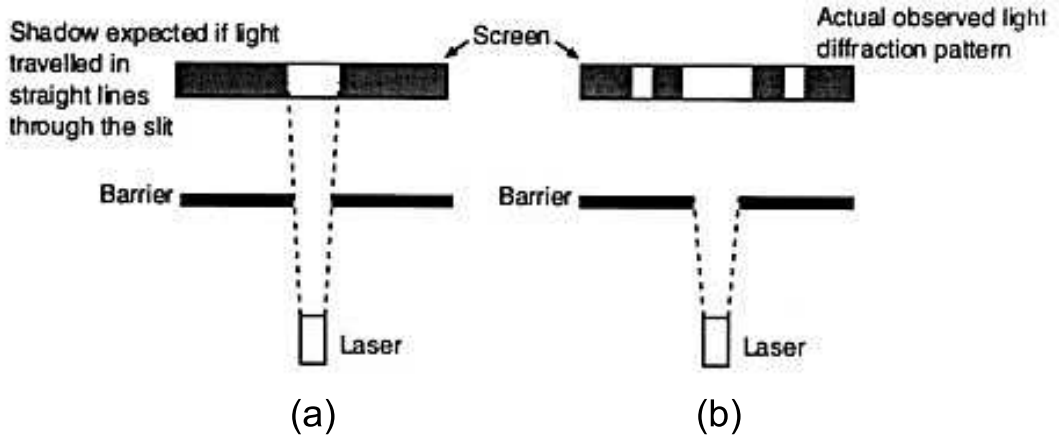

Figure 2.4: The propagation of light through a thin slit. Geometrical optics suggest that shadows form on the screen except the area where light travels in a straight line. In reality dark and light fringes are seen forming a diffraction pattern. Reprinted from *Howison* (1992).

Consider an ideal monochromatic wavefront observed through a thin slit. Using the geometrical optics model, light travels in a straight line and hence shadows would form on a screen except for a small area corresponding to the thin slit, shown in Figure 2.4(a). In reality a pattern of light and dark fringes are observed, as shown in Figure 2.4(b).

In a system with a circular, aperture the diffraction pattern seen is a bright central spot surrounded by a set of concentric circles which progressively get weaker (Figure 2.5(a)). The diffraction-limited image from a circular aperture of diameter D_{EP} has an intensity function of (*Longhurst*, 1973)

$$I(\mathbf{P}) = \left(\frac{2J_1(\omega)}{\omega} \right)^2 \tag{2-4}$$

where $I(\mathbf{P})$ is the intensity at point $\mathbf{P}$ in the observation plane, $J_1(w)$ is a first order Bessel function and

$$\omega = \frac{\pi}{\lambda} \frac{D_{EP}}{z} \sqrt{x^2 + y^2} \tag{2-5}$$

for a given wavelength λ at a distance z from the aperture plane. (x, y) describe the corresponding point in the aperture plane. Equation (2-4) is also known as the *Airy disc function* and is shown in Figure 2.5.

If the image plane was located at $z = f_E$ from the entrance pupil, then

$$\omega = \frac{\pi}{\lambda F/\#} \sqrt{x^2 + y^2}. \tag{2-6}$$

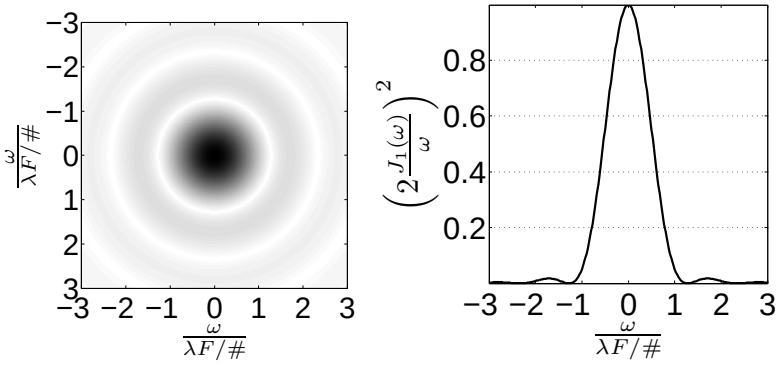

(a) 2D Airy disc (b) 1D Airy disc

Figure 2.5: The Airy disc function.

Table 2.1: Position of the successive maxima and minima of an Airy disc.

	$\frac{\omega}{\lambda F/\#}$	$\left(\frac{2J_1(\omega)}{\omega}\right)^2$
Central maximum	0	1
First minimum	1.22	0
First maximum	1.64	0.0175
Second minimum	2.24	0
Second maximum	2.66	0.0042
Third minimum	3.24	0
Third maximum	3.7	0.0016
Fourth minimum	4.24	0

Table 2.1 indicates the positions of the first few maximum and minimum points.

The resolution limit of an imaging system is determined by its ability to distinguish between two neighbouring points (*Longhurst*, 1973). If two objects are close together the resulting diffraction patterns would overlap. The objects are said to be resolvable if the centre of one Airy disc falls on the first minimum of the other. From Table 2.1 the minimum resolvable distance, d_{res}, would be

$$d_{\text{res}} = 1.22\lambda F/\#. \tag{2-7}$$

The minimum angular resolution, θ_{res}, is found by dividing d_{res} by the effective focal length, such that

$$\theta_{\text{res}} = 1.22\frac{\lambda}{D_{EP}} \tag{2-8}$$

Equation (2-8) is known as the *Rayleigh criterion* (*Halliday and Resnick*, 1988).

2.2 Turbulence Induced Aberrations

The departure of the wavefront from the ideal is not only due to diffraction, but also due to aberrations. Atmospheric turbulence makes a significant contribution to the wavefront aberrations.

In the field of adaptive optics, wavefront aberrations are commonly described mathematically using a set of Zernike polynomials. Zernike polynomials are defined over a unit circle and are orthogonal over it. They are typically defined in polar coordinates, (r, θ), and given radial symmetry. Using the scheme presented by *Noll* (1976), they are defined as

$$Z_{\text{even}j}(r,\theta) = \sqrt{n+1}R_n^m(r)\sqrt{2}\cos(m\theta),\ m \neq 0 \quad (2\text{-}9)$$

$$Z_{\text{odd}j}(r,\theta) = \sqrt{n+1}R_n^m(r)\sqrt{2}\sin(m\theta),\ m \neq 0 \quad (2\text{-}10)$$

$$Z_j(r,\theta) = \sqrt{n+1}R_n^0(r),\ m = 0, \quad (2\text{-}11)$$

where

$$R_n^m(r) = \sum_{s=0}^{(n-m)/2} \frac{(-1)^s(n-s)!}{s![(n+m)/2-s]![(n-m)/2-s]!} r^{n-2s}. \quad (2\text{-}12)$$

The values of n and m are positive integers that satisfy $m \leq n$ and $n - m =$ even. The index j is a mode ordering number and is a function of n and m. The first eight modes of Zernike polynomials are shown in Figure 2.6.

Zernike polynomials are commonly used to describe the residual phase error resulting from uncompensated modes of abberations. *Noll* (1976) calculated the residual phase errors for the first few modes based on the ratio of the telescope diameter D_{T} to the coherence length r_0. Table 2.2 shows the residual phase errors associated with the compensation of the first eight Zernike modes.

Figure 2.7 shows how the residual phase error varies with the number of modes corrected for varying values of r_0 given a 1-m telescope. Compensating for the low-order aberration modes produces the most significant results. Compensating for higher order aberrations, i.e. 10 modes versus 15 modes, has substantially less effect. For higher-mode correction the curve is asymptotic where the curve can be approximated by (*Noll*, 1976)

$$\sigma^2_{(fit=n_{\text{Zern}})} = 0.2944 n_{\text{Zern}}^{-\sqrt{3}/2} \left(D_{\text{T}}/r_0\right)^{5/3}. \quad (2\text{-}13)$$

where n_{Zern} is the number of low order Zernike modes corrected.

If the Z_2 and Z_3 modes of aberrations (tip and tilt) were corrected perfectly then

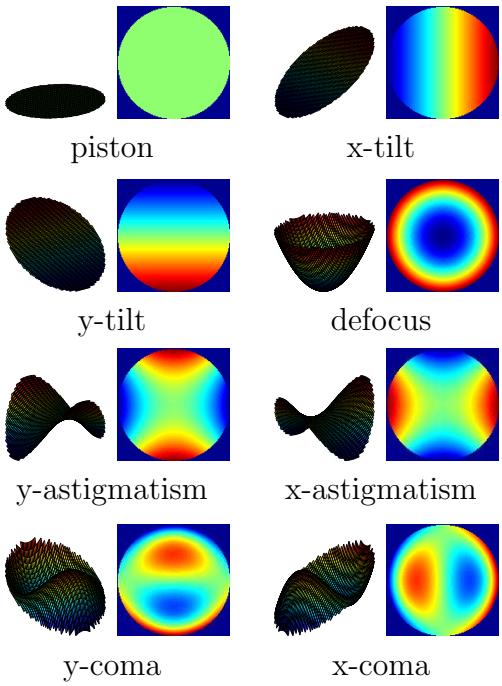

Figure 2.6: The first eight modes of Zernike polynomials.

Table 2.2: Residual phase error and aberration functions for the first eight modes of Zernike polynomials.

Zernike Mode	Aberration Function	Aberration Type	Residual Error[a] (rad^2)
Z_1	1	piston	$1.030(D_\mathrm{T}/r_o)^{5/3}$
Z_2	$r\cos(\theta)$	tip	$0.582(D_\mathrm{T}/r_o)^{5/3}$
Z_3	$r\sin(\theta)$	tilt	$0.134(D_\mathrm{T}/r_o)^{5/3}$
Z_4	$\sqrt{3}(2r^2-1)$	defocus	$0.111(D_\mathrm{T}/r_o)^{5/3}$
Z_5	$\sqrt{6}r^2\sin(2\theta)$	astigmatism	$0.0880(D_\mathrm{T}/r_o)^{5/3}$
Z_6	$\sqrt{6}r^2\cos(2\theta)$	astigmatism	$0.0648(D_\mathrm{T}/r_o)^{5/3}$
Z_7	$\sqrt{8}(3r^2-2)r\sin(\theta)$	coma	$0.0587(D_\mathrm{T}/r_o)^{5/3}$
Z_8	$\sqrt{8}(3r^2-2)r\cos(\theta)$	coma	$0.0525(D_\mathrm{T}/r_o)^{5/3}$

[a] (*Noll*, 1976)

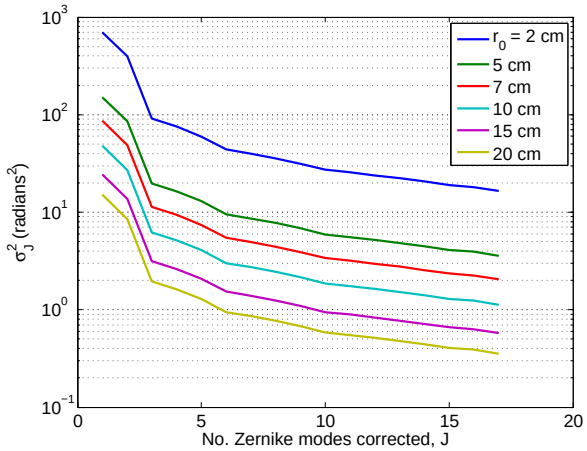

Figure 2.7: The effect of the number of aberration modes corrected on the residual error as defined by *Noll* (1976).

the residual error would be $0.134(D_\mathrm{T}/r_0)^{5/3}$. These two modes contain 87% of the energy present in an aberrated wavefront (*Noll*, 1976). Without full compensation of these low-order modes, correction of higher-order modes would not produce any significant improvement in image quality, especially in the longer exposure images that are typically used in astronomical imaging. X-tilt and Y-tilt, along with varying levels of coma, result in motion of the image's centre.

Figure 2.8 shows the effect of increasing D_T/r_0 on short and long exposure images. For $D_\mathrm{T}/r_0 \approx 1$ the short-exposure image (Figure 2.8(a)) is close to diffraction-limited and nearly all the image degradation seen for long exposures (Figure 2.8(e)) is due to image motion (*Hardy*, 1998). As D_T/r_0 increases, the effects of image motion lessen and the diameter of the long-exposure images approach that of the short-exposure images. The long exposures can be described by an Airy disc. Aberrations induced by the atmosphere result in a spreading of the central peak (Figures 2.8(f), 2.8(g) and 2.8(h)) which also results in a weaker peak intensity (Figure 2.9). As such the minimum angular resolution θ_res found using equation (2-8) is no longer valid. Instead θ_res is now specified by

$$\theta_\mathrm{res} = 1.22\frac{\lambda}{r_0}, \tag{2-14}$$

where r_0 is the turbulence coherence length (refer to equation (1-3), page 6).

2.3 Modelling $C_N^2(h)$ and $V(h)$

Optical turbulence is highly irregular, where turbulence strengths can vary by an order of magnitude around a mean value (*Hardy*, 1998). Commonly used models represent a

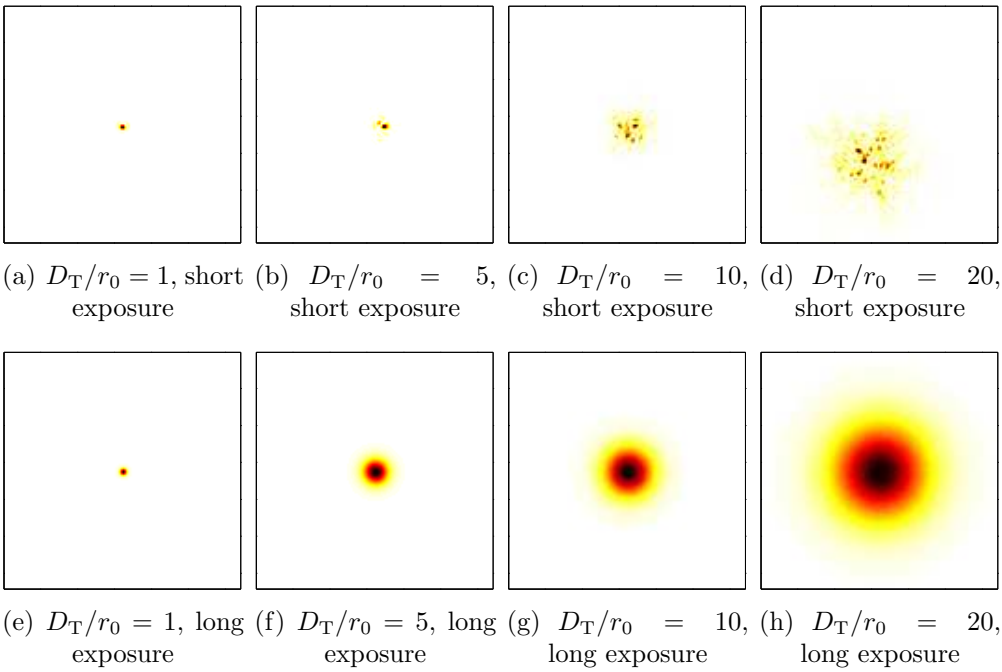

(a) $D_T/r_0 = 1$, short exposure (b) $D_T/r_0 = 5$, short exposure (c) $D_T/r_0 = 10$, short exposure (d) $D_T/r_0 = 20$, short exposure

(e) $D_T/r_0 = 1$, long exposure (f) $D_T/r_0 = 5$, long exposure (g) $D_T/r_0 = 10$, long exposure (h) $D_T/r_0 = 20$, long exposure

Figure 2.8: The effect of increasing D_T/r_0 on short- and long-exposures. For $D_T/r_0 = 1$ images are diffraction-limited.

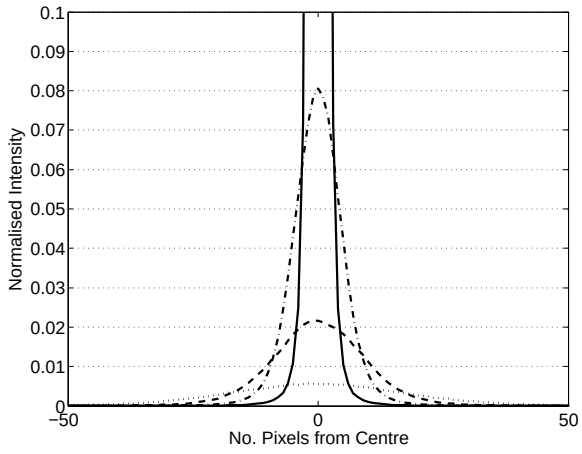

Figure 2.9: Intensity functions of long-exposure images with increasing D_T/r_0. (—) $D_T/r_0 = 1$. $(- \cdot -)$ $D_T/r_0 = 5$. (- -) $D_T/r_0 = 10$. $(\cdots)$ $D_T/r_0 = 20$. Intensities have been normalised to the peak intensity for $D_T/r_0 = 1$.

mean profile of $C_N^2(h)$ measurements taken over extended periods of time.

The Hufnagel-Valley (HV) model is commonly used to describe turbulence at an astronomical site (*Tyson and Frazier*, 2004). It consists of three components:

- an exponentially decreasing $C_N^2(h)$ through the troposphere,
- a peak at approximately 10 km above ground corresponding to a tropopause layer, and
- a strong surface layer.

The HV model has the form of (*Andrews*, 2004)

$$\begin{aligned} C_N^2(h) &= 2.7 \times 10^{-16} \exp\left(\frac{-h}{1500}\right) \\ &\quad +5.94 \times 10^{-53} h^{10} \left(\frac{w}{27}\right)^2 \exp\left(\frac{-h}{1000}\right) \\ &\quad +A \exp\left(\frac{-h}{100}\right), \end{aligned} \tag{2-15}$$

where h is the altitude above ground, $A = C_N^2(0)$ is the ground level value of $C_N^2(h)$, and w is the root-mean-square wind speed given by (*Hardy*, 1998)

$$w = \left[\left(\frac{1}{15 \times 10^3}\right) \int_{5\times10^3}^{20\times10^3} V(h)^2 dh\right]^{1/2}, \tag{2-16}$$

where $V(h)$ is the wind speed profile. It should be noted that the limits of integration are chosen to such that w is a measure of the wind speed in the free atmosphere. Wind flows below 5 km above sea level are subject to local terrain and ground structures (*Sturman and Tapper*, 1996). The Southern Alps extend up to approximately 4 km above sea level. Above 25 km above sea level, the effects of optical turbulence becomes insignificant (*Hardy*, 1998). However some will dispute that this limit is in fact as low as 20 km above sea level (*Andrews*, 2004; *Klückers et al.*, 1998; *Tyson and Frazier*, 2004). Hence an upper limit of 20 km is imposed on w.

The parameters w and A in equation (2-15) are adjusted to obtain the conditions for a given site. The HV 5-7 model has parameters set such that $r_0 = 5$ cm and $\theta_0 = 7$ μrad (1.44 arcseconds) for a wavelength $\lambda = 500$ nm at $\zeta = 0°$. Under these conditions $A = 1.7 \times 10^{-14}$ and $w = 21$ m/s. Figure 2.10 shows the HV 5-7 $C_N^2(h)$ model.

The HV model only reflects turbulent layers located near-ground and at the tropopause. At many sites around the world additional layers have been detected at low- to mid-troposphere altitudes (*Avila et al.*, 2004; *Fuensalida et al.*, 2004; *Prieur et al.*, 2001;

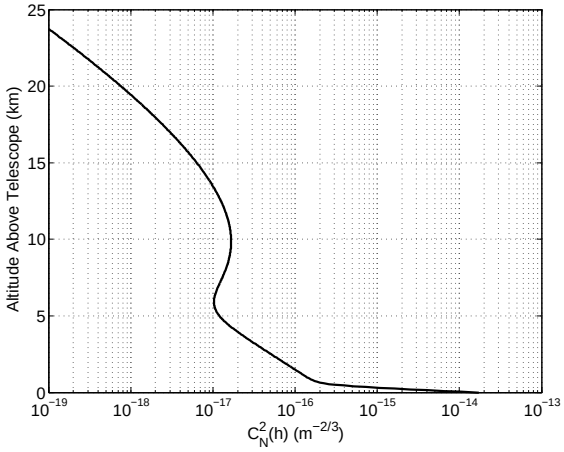

Figure 2.10: The Hufnagel-Valley (HV) 5-7 $C_N^2(h)$ model. This is a HV model with parameters set such that $r_0 = 5$ cm and $\theta_0 = 7$ μrad (1.44 arcseconds) for a wavelength $\lambda = 500$ nm and a zenith angle $\zeta = 0°$.

Wang et al., 2008). The HV model can be extended to incorporate these additional layers by using (*Hardy*, 1998)

$$\begin{aligned} C_N^2(h) &= A\exp\left(-\frac{h}{H_A}\right) + B\exp\left(-\frac{h}{H_B}\right) \\ &\quad + Ch^{10}\exp\left(-\frac{h}{H_C}\right) + D\exp\left(-\frac{(h-H_D)^2}{2d^2}\right), \end{aligned} \tag{2-17}$$

where A is the turbulence coefficient for near-ground (i.e. $C_N^2(0)$) and H_A is the height for its $1/e$ decay, B and H_B are similarly defined for turbulence in the troposphere, and C and H_C are related to the turbulence peak located at the tropopause. The fourth term in equation (2-17) can be used to define one or more isolated layers where D and H_D define the strength and height of the layer and d specifies the layer thickness. When expressed in this form, the coefficients of the HV 5-7 model are: $A = 1.7 \times 10^{-14}$, $H_A = 100$ m, $B = 2.7 \times 10^{-16}$, $H_B = 1500$ m, $C = 3.59 \times 10^{-53}$, $H_C = 1000$ m, and $D = 0$.

A Gaussian model, developed by Greenwood, can be used for the atmospheric wind profile such that (*Tyson and Frazier*, 2004)

$$V(h) = V(0) + V(H_T)\exp\left[-\left(\frac{h\cos\zeta - H_T}{L_T}\right)^2\right] \times \left[\sin^2\beta + \cos^2\beta\cos^2\zeta\right]^{1/2}, \tag{2-18}$$

where $V(0)$ is the wind velocity at ground level, $V(H_T)$ is the velocity at the tropopause located at an altitude H_T, L_T is the thickness of the tropopause layer and β is the wind direction relative to the telescope azimuth. The Bufton model is a specific Greenwood model where $V(0) = 5$ m/s and $V(H_T) = 30$ m/s with $H_T = 9.4$ km and $L_T = 4.8$ km for

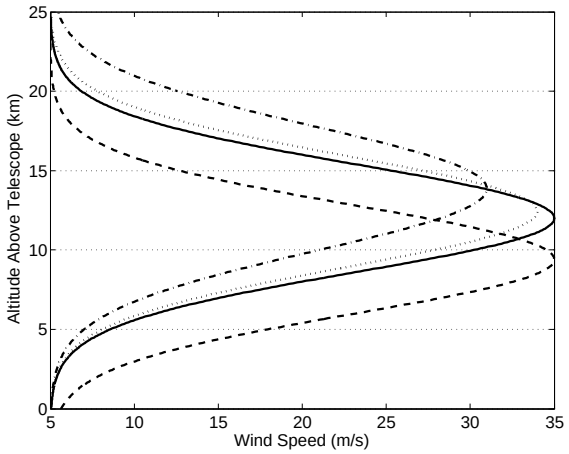

Figure 2.11: Greenwood wind velocity model. (—) $V(0) = 5$ m/s, $V(H_T) = 30$ m/s, $H_T = 12$ km, $L_T = 4.8$ km, $\zeta = 0°$ and $\beta = 0°$; $(\cdots)$ $\zeta = 15°$; $(- \cdot -)$ $\zeta = 30°$; (- -) Bufton.

$\zeta = 0°$ and $\beta = 0°$. Figure 2.11 shows the Greenwood wind model for various parameters.

2.4 Scintillation

Scintillation arises from the propagation of phase variations induced by atmospheric turbulence over large distances. The level of scintillation is given by the *scintillation index*, σ_I^2, which is defined as the variance of the intensity fluctuations (*Roddier*, 1981)

$$\sigma_I^2 = 2.25k^{7/6} \sec^{11/6} \zeta \int_0^\infty C_N^2(h) h^{5/6} dh. \tag{2-19}$$

Scintillation resulting from a layer close to ground will have a weak scintillation index. Therefore the perceived level of variation in intensity will be reduced and the size of scintillation patches will be small (Figure 2.12(a)). As the propagation distance increases (Figures 2.12(b), 2.12(c) and 2.12(d)) the scintillation index increases, as does the perceived size of scintillation patches. From equation (2-19) the strength of scintillation is proportional to $h^{5/6}$. For a layer with a given $C_N^2(h)$ and wavelength, increasing the propagation distance will increase the variations detected in light intensity across a given region. It is this relationship that forms the basis behind SCIDAR, which is the method used for measuring atmospheric turbulence during this research.

2.4.1 Using Scintillation to Measure Atmospheric Turbulence

SCIDAR uses the spatio-temporal covariance functions of scintillation images to infer the characteristics of the atmospheric turbulence at a site. A sequence of short exposure images conjugate to the telescope aperture are taken. From these images a covariance

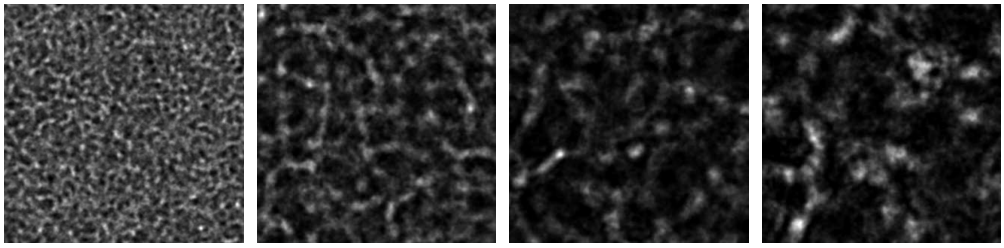

(a) $h = 1$ km, $\sigma_I^2 = 0.11$ (b) $h = 5$ km, $\sigma_I^2 = 0.42$ (c) $h = 10$ km, $\sigma_I^2 = 0.74$ (d) $h = 20$ km, $\sigma_I^2 = 1.32$

Figure 2.12: Scintillation index σ_I^2 increases with propagation distance. $r_0 = 10$ cm, $\lambda = 589$ nm, $\zeta = 0$ radians.

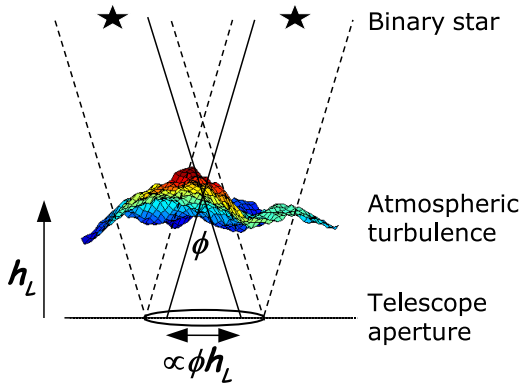

Figure 2.13: The concept of pupil-plane binary star SCIDAR. Light from each star passes through the same turbulent region forming identical scintillation patterns separated by a distance proportional to the angular separation of the binary star system ϕ and the height of the turbulent layer above the measurement plane h_L.

image is found from which $C_N^2(h)$ and $V(h)$ profiles can be determined (*Klückers et al.*, 1998).

SCIDAR measurements are typically taken using a binary star system, as shown in Figure 2.13. Light from each star passes through the same region of a turbulent layer forming identical, but separated, scintillation patterns. The distance between the two scintillation patterns is directly proportional to the angular separation of the binary star system, ϕ, and the height of the turbulent layer, h_L.

In the traditional form of SCIDAR (known as *pupil-plane* or *classical* SCIDAR) stellar scintillation patterns are measured at the telescope pupil. Any phase variations induced by atmospheric turbulence are very weak and must propagate large distances to produce measurable scintillation (refer to equation (2-19)). Therefore any scintillation

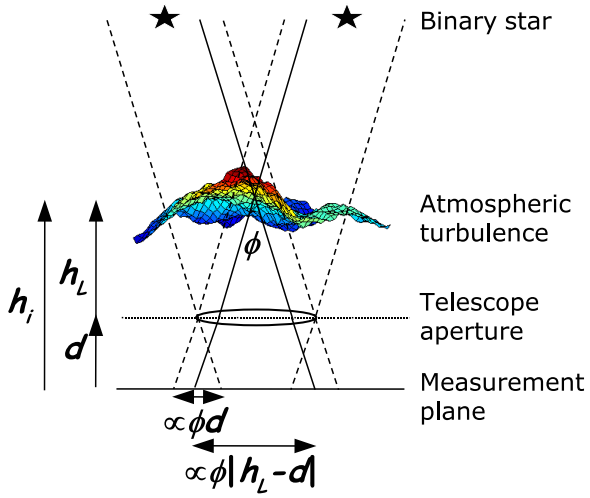

Figure 2.14: The concept of generalised binary star SCIDAR. Scintillation patterns from each star are separated by a distance proportional to the binary star separation ϕ and the height of the turbulent layer above the measurement plane $h_i = |h_L - d|$. Due to sign conventions d is negative.

resulting from near-ground turbulence (NGT) is not readily detectable. Using a simple lens change the measurement plane is shifted to a virtual plane located below the telescope. This increases the propagation distance such that scintillation from NGT can be adequately measured. This version of SCIDAR is known as *generalised* SCIDAR (*Klückers et al.*, 1998).

In generalised SCIDAR, as in pupil-plane SCIDAR, light from each star passes through the same region of a turbulent layer forming identical scintillation patterns where the distance between the two patterns is proportional to ϕ and the total propagation distance of the wavefront, $h_i = |h_L - d|$ (Figure 2.14). d is the distance to the virtual measurement plane below the telescope, termed the *defocus distance*. Due to sign conventions detailed in Appendix A, d is negative. The resulting aperture images from each star are defocussed and separated by an amount proportional to ϕ and d. Figure 2.15 shows a typical pupil-plane and generalised SCIDAR scintillation image.

Figure 2.16 shows the usual lens configurations for both pupil-plane and generalised SCIDAR. For pupil-plane SCIDAR (Figure 2.16(a)), the telescope aperture is imaged onto a CCD by a field lens L_p (*Klückers et al.*, 1998). The focal length of L_p, f_p, is chosen to provide a spatial sampling across the telescope aperture $\Delta r \approx 0.01$ m/pix. If the distance between L_p and the telescope aperture, p_p, is sufficiently large then the image plane at i_p from L_p is located at approximately f_p behind the fields lens. To achieve a focussed image then L_p is placed approximately f_T away from the telescope primary mirror L_T, where f_T is the effective focal length of the telescope.

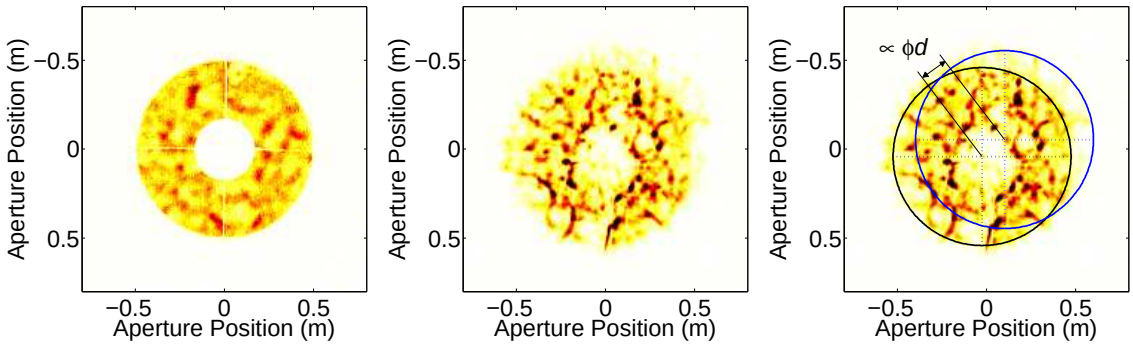

(a) Pupil-plane frame (b) Generalised frame (c) Annotated generalised frame

Figure 2.15: Typical scintillation images from pupil-plane and generalised SCIDAR. Images contain two aperture images that are separated by a distance proportional to the angular stellar separation, ϕ, and the defocus distance, d. For pupil-plane data d is zero and hence the images overlap completely.

For generalised SCIDAR (Figure 2.16(b)), the field lens L_{g} is placed in the same location as L_{p}. If the position of the image plane is unchanged, then L_{T} acts like another lens, imaging a measurement plane at a distance d below the aperture plane. Assuming that the focal length of the L_{g}, f_{g}, is less than f_{p}, the distance behind L_{g} to the image plane $i_{\mathrm{g}} \approx f_{\mathrm{p}}$ and $p_{\mathrm{p}} \approx f_{\mathrm{T}}$ then

$$d \approx \frac{-f_{\mathrm{T}}^2 \left(f_{\mathrm{g}} - f_{\mathrm{p}}\right) - f_{\mathrm{T}} f_{\mathrm{g}} f_{\mathrm{p}}}{f_{\mathrm{g}} f_{\mathrm{p}}}. \tag{2-20}$$

For full derivation of equation (2-20) see Appendix B.

The majority of SCIDAR measurements at MJUO were taken with the 1-m McLellan telescope operating at a $F/13.5$ focal ratio. For a pupil-plane SCIDAR lens with a focal length 12.7 mm and a generalised SCIDAR lens with a focal length 10 mm, the ideal defocus distance d is 3.9 km below the telescope.

Regardless whether pupil-plane or generalised SCIDAR is employed the techniques used to determine both $C_N^2(h)$ and $V(h)$ profiles are similar.

The determination of $C_N^2(h)$ and $V(h)$ profiles from scintillation images require the spatio-temporal covariance of scintillation patterns from a binary star system, $C_B(\rho, \phi, \Delta t)$. $C_B(\rho, \phi, \Delta t)$ describes a series of triplets where each triplet corresponds to a different turbulent layer consisting of a central peak with two weaker secondary peaks. If the exposure time is sufficiently short and the acquisition frame rate is sufficiently fast then Taylor's hypothesis suggests that turbulent structures move without deformation (*Caccia*

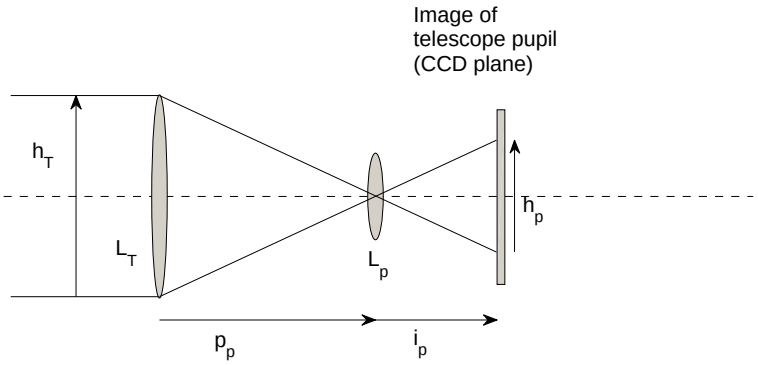

(a) Pupil-plane Lens Placement

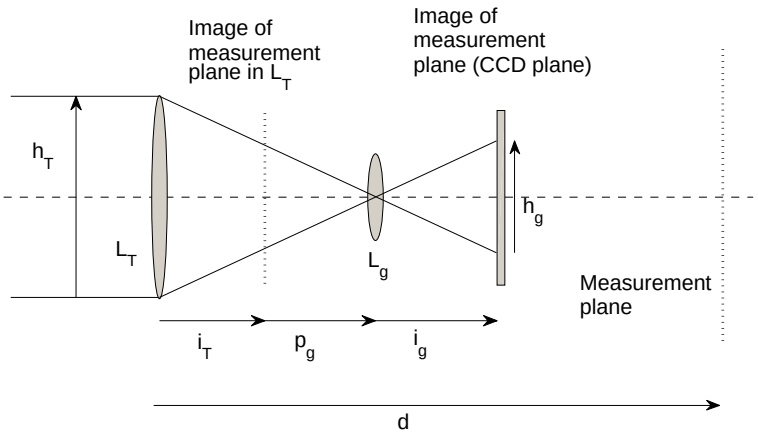

(b) Generalised Lens Placement

Figure 2.16: Optical layout for pupil-plane and generalised SCIDAR. In pupil-plane SCIDAR the telescope mirror, $L_{\rm T}$, is imaged by the field lens, $L_{\rm p}$, onto the CCD plane. For generalised SCIDAR, $L_{\rm p}$ is replace by $L_{\rm g}$. In this case, $L_{\rm T}$ acts like another lens. The combination of $L_{\rm T}$ and $L_{\rm g}$ image a measurement plane located at d below the telescope onto the CCD plane. Image is based on Fig. 2 in *Klückers et al.* (1998).

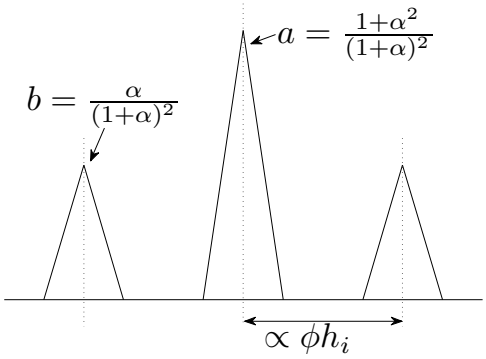

Figure 2.17: Schematic of a binary star system covariance triplet profile from a single layer of turbulence. The distance between the central peak and secondary peak is proportional to the binary star system separation, ϕ, and the height of the layer above the measurement plane, h_i. $\alpha = 10^{-0.4\Delta m}$, where Δm is the magnitude difference between the binary star system components.

et al., 1987; *Roddier*, 1981). Therefore $C_B(\rho, \phi, \Delta t)$ can be written as (*Avila et al.*, 2001)

$$C_B(\rho, \phi, \Delta t) = \sum_{i=1}^{n} aC_S(\rho - v) + b\left[C_S(\rho - v - \phi h_i) + C_S(\rho - v + \phi h_i)\right], \tag{2-21}$$

where ρ is the radial coordinate in the direction of the binary star system, Δt is the time delay between successive scintillation frames and $v = V(h_i)\Delta t$ for a given layer with velocity $V(h_i)$ at height h_i. The coefficients a and b are given by (*Avila et al.*, 2001)

$$a = \frac{1+\alpha^2}{(1+\alpha)^2}, b = \frac{\alpha}{(1+\alpha)^2}, \alpha = 10^{-0.4\Delta m}, \tag{2-22}$$

where Δm is the magnitude difference between the binary star system companions. Note that the expression for α is derived from the definition of apparent stellar magnitude verses the light intensity received at the instrument for the visual spectrum where α is the ratio of light intensity received from the binary star companions.

Each triplet in the series has a central peak that corresponds to the equivalent covariance of a single star for a given layer, $C_S(\rho, \Delta t)$, scaled by a. The two secondary peaks correspond to $C_S(\rho, \Delta t)$ scaled by b and are offset from the central peak by a distance proportional to ϕh_i (Figure 2.17).

$C_S(\rho, 0)$ is the 2D Fourier transform of the power spectrum of the scintillation fluctuations, $W(f)$, seen at the measurement plane. $W(f)$ is given by (*Roddier*, 1981)

$$W(f) = 0.039k^2 f^{-11/3} \int_0^\infty C_N^2(h) \sin^2(\pi \lambda h f^2) dh \tag{2-23}$$

where λ is the wavelength and $k = 2\pi/\lambda$. For an aperture with circular symmetry, as in the case of a telescope, then (*Goodman*, 2005)

$$C_S(\rho, 0) = 2\pi \int_0^\infty W(f) f J_0(2\pi\rho f) df, \tag{2-24}$$

where J_0 is a zeroth order Bessel function of the first kind. Let

$$K(\rho, h) = 0.245k^2 \int_0^\infty f^{-8/3} \sin^2(\pi\lambda h f^2) J_0(2\pi\rho f) df, \tag{2-25}$$

which is the theoretical spatial covariance function of a single star produced by a layer at height h where $\int C_N^2(h)dh = 1$ and assuming Kolmogorov turbulence (*Avila et al.*, 1997). Then from equations (2-23), (2-24) and (2-25)

$$C_S(\rho, 0) = \int_0^\infty K(\rho, h) C_N^2(h) dh. \tag{2-26}$$

When $\Delta t = 0$, equations (2-21) and (2-26), allow the use of binary star system covariances to estimate $C_N^2(h)$ profiles. This is discussed in more detail in Chapter 4.

If a layer at height h_i was moving at a velocity $V(h_i)$ then the scintillation pattern produced at the ground would move with the same $V(h_i)$. Assuming Taylor's hypothesis (i.e. spatio-temporal sampling is such that turbulent elements move without distortion) then two scintillations patterns, produced by a single star, separated by Δt are physically separated by $V(h_i)\Delta t$ (*Caccia et al.*, 1987). Hence

$$C'_S(\rho, \Delta t) = C'_S(\rho - V(h_i)\Delta t). \tag{2-27}$$

Taylor's hypothesis also suggests that the peak strength at $\Delta t = 0$ remains unchanged for $\Delta t > 0$, such that

$$C'_S(V(h_i)\Delta t) = C'_S(0, 0). \tag{2-28}$$

Hence the spatio-temporal covariance function given by equation (2-21) describes a series of triplets where each triplet has been shifted from a null position (defined by $\Delta t = 0$) by $V(h_i)\Delta t$.

Figure 2.18 shows a schematic for the determination of wind velocities from scintillation spatio-temporal covariances. If Δr is the spatial sampling applied across the aperture then the shift seen in the triplet pattern for $\Delta t > 0$ is directly proportional to $\Delta r/\Delta t$. The magnitude of the shift is directly related to the wind speed, and the direction of the shift b_ϕ can be related to the direction of the wind, provided that information about the telescope's orientation with respect to the ground is available. The determination of $V(h)$

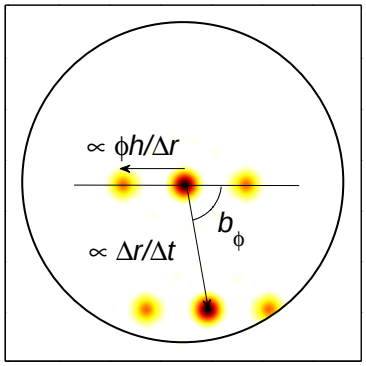

Figure 2.18: Determination of wind velocity from scintillation spatio-temporal covariances. The maximum detectable velocity depends on multiple factors, including the time delay, Δt, between frames, spatial sampling across the aperture, Δr, the altitude of the layer, h, the angular separation of the binary companions, ϕ, and the measured direction of the shifted triplet, b_ϕ, with respect to the direction of the binary. Triplets shown correspond to $\Delta t = 0$ (i.e. auto-covariance) and the triplet from the cross-covariance between frames taken Δt apart.

profiles from spatio-temporal covariances is discussed in more detail in Chapter 5.

2.4.2 Altitude Sampling of SCIDAR

Consider the geometry defined in Figure 2.19. If the height of the layer above the measurement plane was h_L then

$$h_L = \frac{r_L}{\phi}, \tag{2-29}$$

for very small ϕ, where r_L is the measured distance between the two identical scintillation patches in the aperture plane. If a spatial sampling of Δr is used and r_L is divided into n_{pix} pixels then

$$h_L = \frac{n_{\text{pix}}\Delta r}{\phi}. \tag{2-30}$$

If Δh is the altitude sampling such that h_L is also divided into n_{pix} pixels then

$$\Delta h = \frac{\Delta r}{\phi}. \tag{2-31}$$

This can be expanded to incorporate zenith angle, ζ, such that (*Klückers et al.*, 1998)

$$\Delta h = \frac{\Delta r}{\phi \sec \zeta}. \tag{2-32}$$

For $\Delta r = 0.01$ m/pix and $\phi = 4$ arcseconds, $\Delta h \approx 500$ m at zenith.

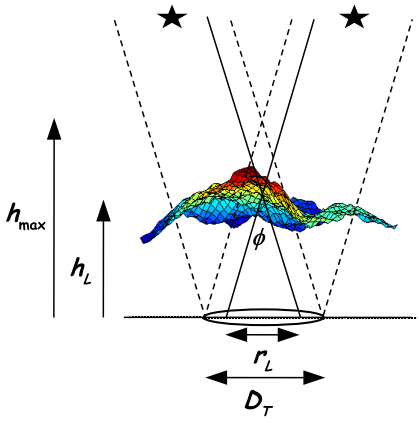

Figure 2.19: Geometry for altitude sampling in SCIDAR.

Similarly, if two identical scintillation patterns are located at either edge of the aperture and hence at a distance D_{T}, then the height associated is defined as (*Klückers et al.*, 1998)

$$h_{\max} \approx \frac{D_{\mathrm{T}}}{\phi}. \tag{2-33}$$

The value $h_{\max}$ defines the maximum detectable height for SCIDAR measurements taken with a telescope of diameter D_{T}. The separation between any scintillation patterns resulting from layers located above $h_{\max}$ will be too large to be appropriately sampled and hence no corresponding covariance triplet pattern will exist. This results in a null measurement for layers above $h_{\max}$.

For adequate profiling $h_{\max}$ should be greater than the altitude for which optical turbulence is assumed to be negligible. For pupil-plane SCIDAR this is assumed to be 20 km (*Klückers et al.*, 1998). For generalised SCIDAR, $h_{\max} \geq 20km + |d|$.

2.5 The SCIDAR System and Analysis Techniques

Chapter 3 contains a full description of the purpose-built SCIDAR instrument, whereas further details on the extraction of $C_N^2(h)$ and $V(h)$ profiles are discussed in Chapters 4 and 5 respectively. Chapter 6 presents the $C_N^2(h)$ and $V(h)$ profiles obtained for MJUO.

Chapter 3

An Instrument to Collect Scintillation Data

This chapter discusses the development of the purpose-built instrument. The system developed during the course of this research to measure the atmospheric turbulence present at MJUO contained significant levels of noise, primarily resulting from the CCD cameras used. There were several different camera models used throughout the system development, each with its own noise characteristics.

Sections 3.1 through 3.4 outline the historical development of the SCIDAR system, where the issues surrounding the noise characteristics of the CCD cameras is addressed in the relevant sections. Section 3.5 outlines the operating parameters for the latest version of the SCIDAR system.

3.1 Early UC-SCIDAR

Development of a University of Canterbury SCIDAR system (UC-SCIDAR) began in 2003 (*Johnston et al.*, 2004, 2005; *Mohr et al.*, 2006, 2008). The goal was to design a low cost system that could be used to profile the optical turbulence above MJUO, while providing the flexibility to change system components to enable different experiments to be conducted. Two imaging channels were incorporated so simultaneous measurements could be collected and the results compared directly.

UC-SCIDAR saw first light on the 1-m McLellan telescope at MJUO in late 2003, at an approximate cost of US$4000. To keep costs to a minimum the system design utilised primarily off-the-shelf components. The system has since evolved through several iterations.

It was decided to employ a 300x400 mm mountable breadboard system to allow for ease of mounting on the telescope and relatively quick change of component positions if needed. Although different cameras and lenses have been used throughout the years, the mountable breadboard concept is still used today and will most likely continue to be used.

The breadboard was mounted using standard angle brackets purchased from Thorlabs. The angle brackets are attached to an aluminium plate drilled specifically for

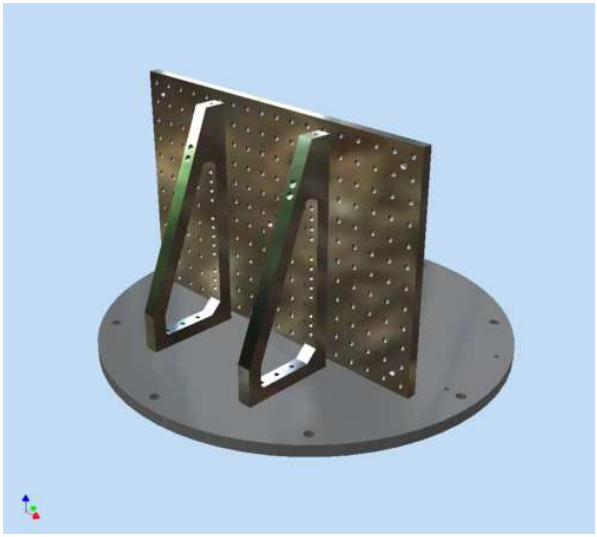

Figure 3.1: The UC-SCIDAR breadboard is mounted onto the telescope using off-the-shelf angle brackets and a custom aluminium plate. Image provided by Graeme Kershaw, Department of Physics & Astronomy.

mounting on the 1-m telescope (Figure 3.1). By changing the mounting plate the system will fit onto any telescope. (See Appendix C for the construction drawing for the mounting plate for MJUO.)

The system consists of two channels each with its own CCD camera and lenses. The light from the telescope was split into the two channels using a 1 inch cube beamsplitter made from BK7 glass with coatings for visual wavelengths (400 – 700 nm) which provided a 50/50 intensity split (Thorlabs BS013). This permitted for direct comparison between the two channels as minimal differences existed between the two channels.

Initially the two channel system was intended to compare two different optical remote sensing techniques: generalised SCIDAR and *slope detection and ranging* (SLODAR). SLODAR works on a similar principal to SCIDAR, but instead of scintillation images, each star will produce a group of spots formed by a Shack-Hartmann (SH) lenslet array (*Wilson*, 2002). To properly sample turbulent motion with a SH lenslet array, the size of the lenslets must be chosen such that $d_{\rm sub}/r_0 \approx 1$, where $d_{\rm sub}$ is the sub-aperture size in the plane of r_0. If $d_{\rm sub}/r_0 > 1$ the resulting spots will have large motions associated and/or speckling of the spots may occur making it difficult to identify corresponding spot images from frame-to-frame. With the cost associated with a SH lenslet array at the time ($\geq$US\$2000), the University of Canterbury was unable to acquire an appropriate SH lenslet array within the budget constraints for the project and hence the idea of using SLODAR was abandoned.

Prior measurements taken at MJUO in April 1999 by Imperial College indicated that the strong near ground turbulence (NGT) was masking turbulence found at higher

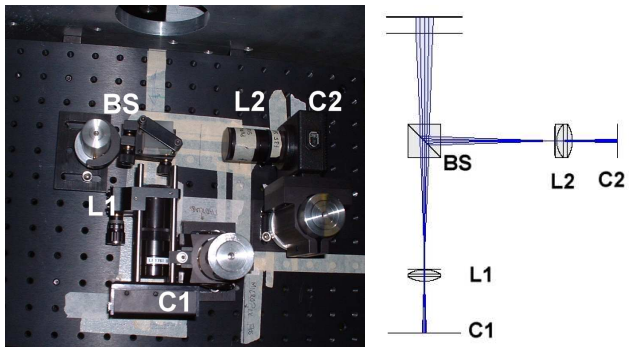

(a) Physical Layout (b) Optical Layout

Figure 3.2: Physical and optical layout of the UC-SCIDAR instrument in 2004.

altitudes (*Johnston and Lane*, 1999; *Johnston et al.*, 2002). As such both pupil-plane and generalised SCIDAR would be needed to adequately profile the site. The two channel system design provided an ideal platform for simultaneous pupil-plane and generalised SCIDAR measurements.

Figure 3.2 shows the physical and optical layout of UC-SCIDAR used in 2004. The light from the telescope was split into the two channels with a 50/50 intensity split cube beamsplitter (BS). The straight path, used for pupil-plane SCIDAR, consisted of a field lens (L1), mounted in a z-translation stage to allow for fine adjustment, and a Thorlabs DC111 camera (C1). The side path, used for generalised SCIDAR, consisted of a field lens (L2) which was mounted a focal length of L1 from the CCD of a Micropix M640 camera (C2).

Both the Micropix M640 and Thorlabs DC111 cameras are firewire (IEEE-1394) cameras containing a Sony ICX084AL CCD sensor. The sensor is a 640x480 chip with 7.4 μm square pixels. At full resolution, both cameras operate at up to 30 Hz, with exposure times ranging from 0.1 ms to 64 s. During capture the cameras can be synchronised through software to ensure that each path is imaged simultaneously. The cameras were typically operated at maximum gain with exposures in the order of 1 ms and with a frame rate of 30 Hz. As the data from each channel was analysed separately the precise synchronisation between channels was not necessary. However it did ensure that the data sets concerned were imaging the same turbulent structure.

For pupil-plane SCIDAR measurements a 35-mm focal length achromat was selected for L1. For the 1-m telescope operating at a focal ratio of $F/13.5$, the resulting image utilised 73% of the CCD with each pixel representing 2.85 mm of the primary mirror. For generalised SCIDAR, a 25.4-mm focal length bi-convex lens was used to virtually propagate the scintillation to 1.95 km below the telescope.

Johnston et al. (2004) described the system design used at the time with preliminary

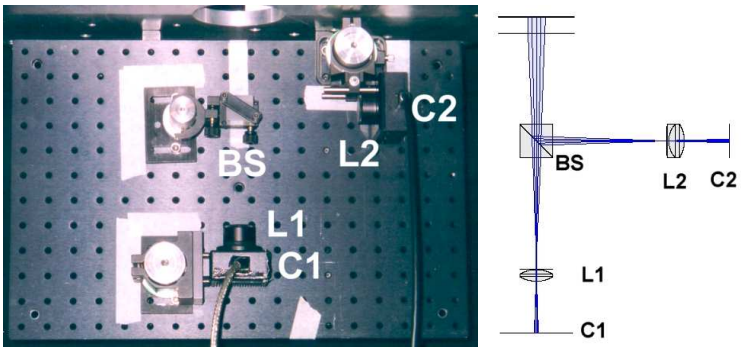

(a) Physical Layout (b) Optical Layout

Figure 3.3: Physical and optical layout of the UC-SCIDAR instrument during late 2004 – 2005.

results. The UC-SCIDAR instrument was not optimised for the low light levels typical of an astronomical setting. The high background noise of the cameras prevented the extraction of sufficient signal for conclusive results. As such the system was redesigned with different lenses to allow more light to fall onto a smaller area of the chip.

3.2 UC-SCIDAR V2005

Due to alignment issues that resulted from the early UC-SCIDAR design, the cameras used for C1 and C2 were swapped. Figure 3.3 shows the physical and optical layout of UC-SCIDAR that was used from late 2004. C2 (the Thorlabs DC111 camera) was mounted on a z-translation stage to allow for fine adjustment of its positioning. The positions of L1 and L2 were fixed with respect to the corresponding camera CCD.

In 2005, the pupil-plane SCIDAR lens (L1) was replaced with a 12.7-mm focal length achromat. The shorter focal length meant that for the 1-m telescope at $F/13.5$ only 26.5% of the CCD was utilised with a spatial sampling, Δr, of 0.008 m/pix. The generalised SCIDAR lens (L2) was replaced with a 10-mm focal length achromat resulting in an ideal defocus distance of $\sim$ 3.9 km below the telescope. The larger spatial sampling allowed for shorter exposures times to be used on bright binaries that were optimally positioned in the Southern skies during winter months. Figure 3.4 shows typical pupil-plane and generalised scintillation images captured by the system used in 2005 (henceforth termed UC-SCIDAR V2005).

An observational campaign for assessing seasonal changes in turbulence at MJUO was undertaken by Clare Worley as part of her ASTR480 project (*Worley*, 2005). Measurements were taken on a monthly basis from February through to September. Due to time constraints only a small amount of the data collected was analysed at the time. However the work provided useful parameters to optimise the collection process and assess whether

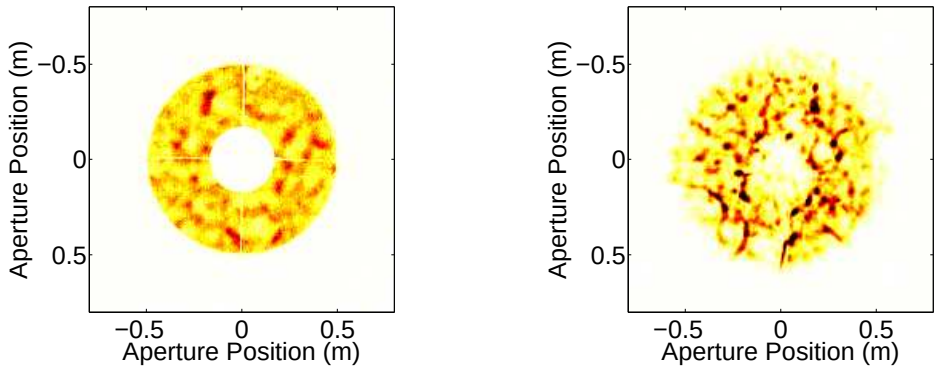

(a) Pupil-plane SCIDAR (b) Generalised SCIDAR

Figure 3.4: Typical frames from (a) pupil-plane and (b) generalised SCIDAR data taken using UC-SCIDAR V2005.

any particular run would provide a reliable estimate of the structure of turbulence. Part of this work was presented in November 2005 at the Image and Vision Computing Conference (IVCNZ'05) (*Johnston et al.*, 2005). A significant portion of the results presented in this thesis used data taken during 2005.

3.2.1 Camera Noise Characteristics

For the configuration used in UC-SCIDAR V2005, a spatial sampling, Δr, of 0.008 m/pix was typically used, with a frame rate of 30Hz. As such, an ideal pupil-plane SCIDAR image would be spread across 127 pixels. Due to the nature of a generalised SCIDAR image, the majority of an image taken using a binary star system with $\phi = 13$ arcseconds would be spread across 200 pixels in the widest direction. To decrease processing time, a window of 256x256 centred around the image centroid was used for analysis. For consistency during noise removal, dark frames were sampled using the same window patch of the CCD. The following discussion uses the 256x256 windowed data.

The cameras used in UC-SCIDAR V2005 had a high level of electron noise associated with dark current. Table 3.1 tabulates the average number of photons detected per pixel over 1000 frames for both cameras used with an exposure time of 1 ms and maximum gain. For dark frames, both cameras exhibit similar characteristics with approximately 2.5 photons per pixel detected (standard deviation $\sigma \approx 0.3$). When looking at images taken from neighbouring sky similar statistics are found. It was decided to use dark frames in noise removal processing, as not every run had corresponding sky frames collected and the noise statistics indicated that the level of dark current detected would have a greater effect on the noise floor of the pupil-plane and generalised SCIDAR images than the noise from the neighbouring sky.

Consider a single pupil-plane and generalised SCIDAR frame from a typical obser-

Table 3.1: The average number of photons per pixel for the cameras used in UC-SCIDAR V2005 with an exposure time of 1 ms and maximum gain.

	Dark Frames		Neighbouring Sky	
	mean	σ	mean	σ
Micropix M640	2.50	0.31	2.52	0.31
Thorlabs DC111	2.48	0.33	2.49	0.33

vation run using UC-SCIDAR V2005 (shown in Figure 3.5). For data collected using the Micropix M640 (typically pupil-plane SCIDAR measurements), a significant amount of the data has frequencies less than 20 Hz (Figure 3.5(c)). For data collected using the Thorlabs DC111 (typically generalised SCIDAR measurements) a significant amount of the data is less than 40 Hz (Figure 3.5(f)). For both cameras a strong peak appears at approximately 47 – 49 Hz. Upon closer examination of an averaged dark frame from both cameras (Figure 3.6), where the ensemble consists of 1000 frames, the peak seen is associated with noise. As noise of this frequency is present in both cameras it is believed that it is associated with the proximity of the power supply for the cameras to the cable connections to the computer. However it can removed from the data by way of a narrow band-pass filter.

The filter being used in the analysis of V2005 data is a twentieth order Butterworth band-pass filter design to remove only the identified frequencies. Figure 3.7 shows the scintillation frames and their corresponding frequency content after filtering has been applied for the data used in Figure 3.5. Note that the target frequency has been effectively removed while keeping relevant data intact.

Consider run #30 taken in June 2005. This run was collected using α Centauri (α Cen)* with an exposure time of 1 ms on both imaging channels. Figure 3.8 shows data from the pupil-plane SCIDAR measurements. Data from the generalised SCIDAR measurements are shown in Figure 3.9.

The $C_N^2(h)$ profiles obtained for pupil-plane data (Figure 3.8(c)) and for generalised data (Figure 3.9(c)) clearly indicate a turbulent layer at 11 – 12 km above sea level and a strong layer near ground level.†

Due to the amount of noise present in the extracted pupil-plane data (Figure 3.8(b)), the resulting $C_N^2(h)$ profile contains additional noise spikes. Using a regularisation parameter of 0.15 during pupil-plane analysis the coherence length, r_0 is estimated to be 24 cm, however error on the calculated r_0 is nearly 100% due to the level of noise present in the extracted data slice. However when filtering is applied to each individual frame

*$\phi = 10.2$ arcseconds, $\Delta m = 1.36$ (Source: 2005 Almanac)

†Mount John University Observatory is at an elevation of 1048 m above sea level.

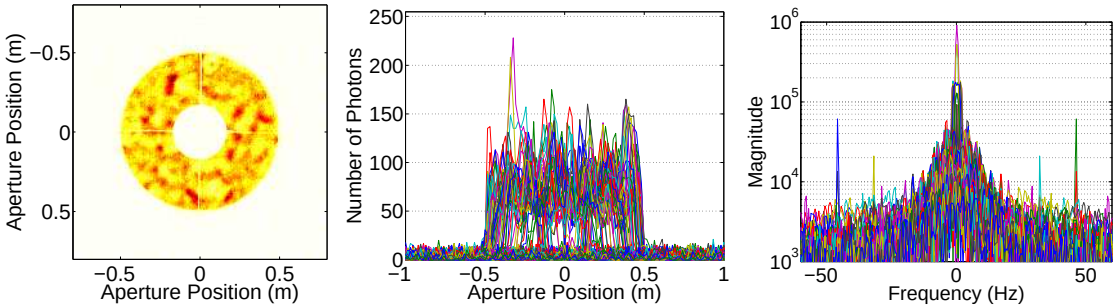

(a) Micropix M640 Image (b) Number of photons in (a) (c) Frequency content of (a)

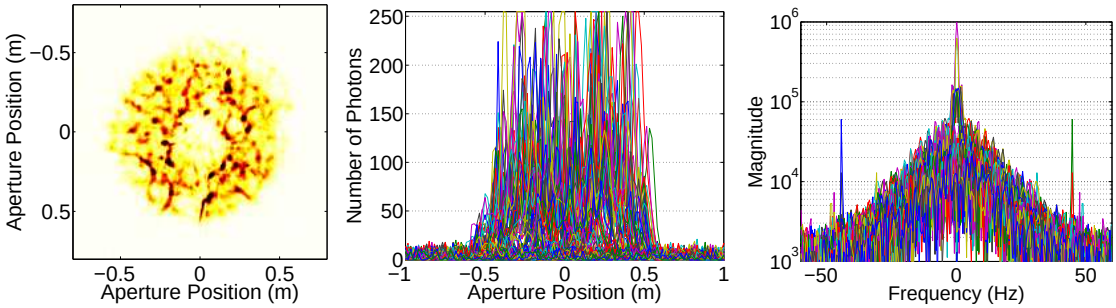

(d) Thorlabs DC111 Image (e) Number of photons in (d) (f) Frequency content of (d)

Figure 3.5: The frequency content of typical images captured by UC-SCIDAR V2005. The strong peak at approximately 47 – 49 Hz in both cameras can be attributed to readout noise. Data captured at a frame rate of 30 Hz.

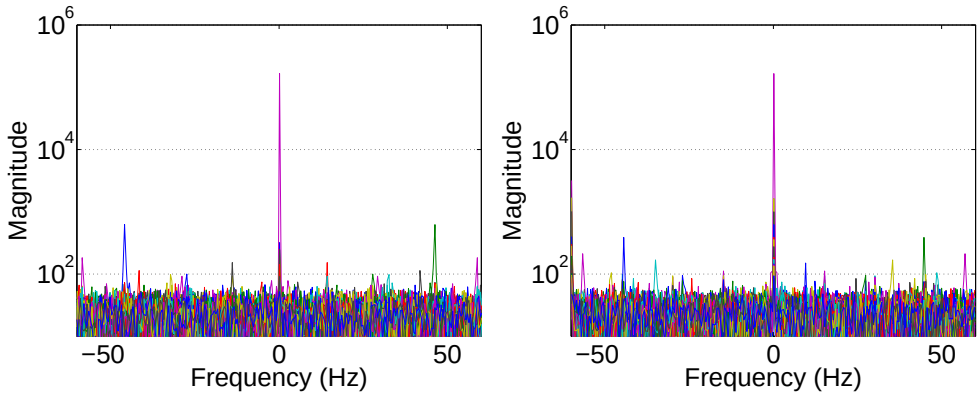

(a) Micropix M640 (b) Thorlabs DC111

Figure 3.6: The average frequency content of 1000 dark frames captured by the V2005 system taken at an exposure of 1 ms. Data captured at a frame rate of 30 Hz.

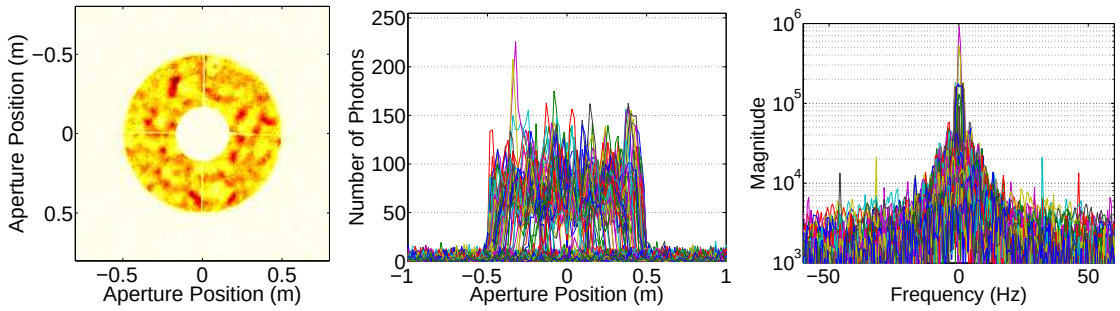

(a) Micropix M640 Image (b) Number of photons in (a) (c) Frequency content of (a)

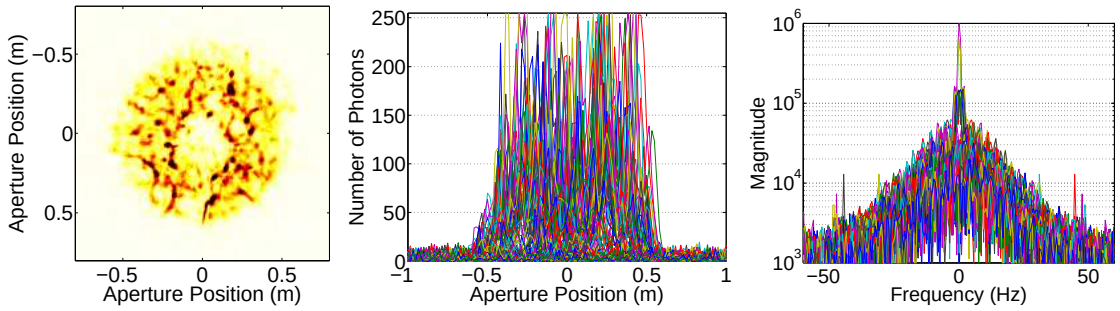

(d) Thorlabs DC111 Image (e) Number of photons in (d) (f) Frequency content of (d)

Figure 3.7: The frequency content of the data used in Figure 3.5 after a band-pass filter removing only the signal that is at 47 – 49 Hz has been applied. Data captured at a frame rate of 30 Hz.

before its use in the determination of the covariance, termed *pre-filtering*, there is a clear improvement in pupil-plane SCIDAR data (Figures 3.8(d)–(f)) with the noise level dropping, resulting in data peaks becoming more readily detectable (Figure 3.8(d)). The resulting r_0 estimate using the same level of regularisation becomes 23 ± 5 cm. When filtering is applied after the covariance has been determined, termed *post-filtering*, similar improvements are seen in pupil-plane SCIDAR data (Figures 3.8(g)–(i)), the estimate for r_0 becomes 22 ± 5 cm. (Full details on slice extraction, $C_N^2(h)$ determination and errors are presented in Chapter 4.)

In generalised data (Figure 3.9) the covariance strength of the near ground layer dominates the profile and is nearly 100 times stronger than the background noise. Hence filtering data has little influence over the resulting $C_N^2(h)$ profile and the resulting r_0 estimate, which was 6.7 ± 0.7 cm for all three cases when using a regularisation parameter of 0.05. Although this shows that for generalised data filtering is not required, for consistency of analysis filtering was applied to data collected from both channels of the V2005 system.

Pre-filtering is considered good-practice, however post-filtering can also be applied in its place, reducing the need to re-process data that has been processed without the filtering applied.

In the above analysis, identical processing parameters were applied for all three cases.

3.3 UC-SCIDAR V2006

Information about the wind velocity profile, $V(h)$, is required to determine how quickly turbulence changes above a site and hence how quickly an AO system is required to respond. This can be obtained from SCIDAR data (*Klückers et al.*, 1998) if sequential frames are captured at a sufficient frame rate.

UC-SCIDAR V2005 utilised a fixed frame rate of 30 Hz, although individual frames can be obtained with an exposure time of 1 ms. For a star with $\phi = 10$ arcseconds the maximum velocity detectable using UC-SCIDAR V2005 is approximately 15 m/s, where a full covariance triplet pattern can be seen for a layer at 10 km above the observatory regardless of the direction of the wind with respect to telescope orientation. Based on the Bufton wind model, described in Chapter 2, a layer at 10 km can be expected to have a wind speed of 30 m/s. To adequately measure the $V(h)$ profile above MJUO, the time delay between successive frames would need to be in the order of 17 ms. (The maximum wind velocity based on the system design is discussed further in Chapter 5.)

As part of the collaborative efforts between the Department of Physics & Astronomy and Department of Electrical & Computer Engineering, an external triggering device was developed that would utilise cameras already available in the research group. The trigger system was designed to sequentially trigger the cameras such that image pairs could be captured with a known time delay Δt. Each observation run would produce two pupil-plane or generalised SCIDAR $C_N^2(h)$ profiles and a single $V(h)$ profile taken from a cross-correlation between sequential images from the two different channels.

As the Thorlabs DC111 camera used in the UC-SCIDAR V2005 system did not have an external trigger facility, both cameras were replaced with Micropix M1024 CCD cameras. These cameras (using a Sony ICX204AL chip) have a 1024x768 grid of 4.65 μm square pixels and a maximum frame rate of 15 Hz. However the field lenses remained unchanged.

During field testing, the new system did not perform as expected. The CCD readout from both cameras was jumbled (Figure 3.10). Due to the random nature of the jumbled images, an insufficient number of image pairs could be collected to make the system viable. It is believed that the increased number of pixels in each camera and the operation of the trigger system was overtaxing the computer processor being used. Due to the number of undesirable factors in the system, the trigger system was abandoned, and cameras with a faster frame rate were used.

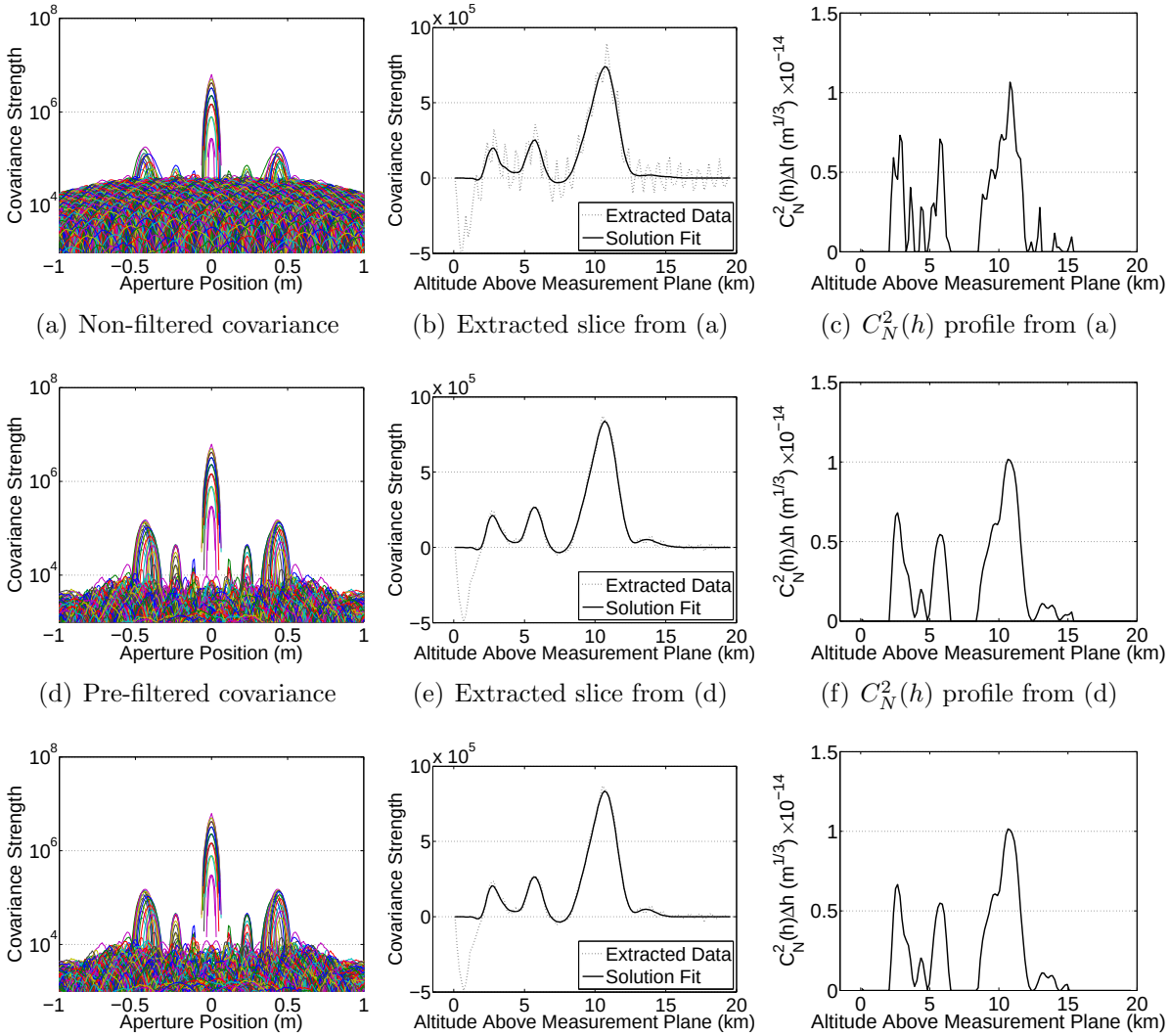

(a) Non-filtered covariance (b) Extracted slice from (a) (c) $C_N^2(h)$ profile from (a)

(d) Pre-filtered covariance (e) Extracted slice from (d) (f) $C_N^2(h)$ profile from (d)

(g) Post-filtered covariance (h) Extracted slice from (g) (i) $C_N^2(h)$ profile from (g)

Figure 3.8: Covariance and $C_N^2(h)$ profiles obtained using the Micropix M640 from UC-SCIDAR V2005. ((a) – (c)) Without filtering the resulting r_0 estimate is 24 cm with nearly 100% due to the noise in the extracted slice. ((d) – (f)) Using pre-filtering. $r_0 = 23 \pm 5cm$ ((g) – (i)) Using post-filtering. $r_0 = 22 \pm 5cm$. Regularisation parameter used was 0.15 for all three cases.

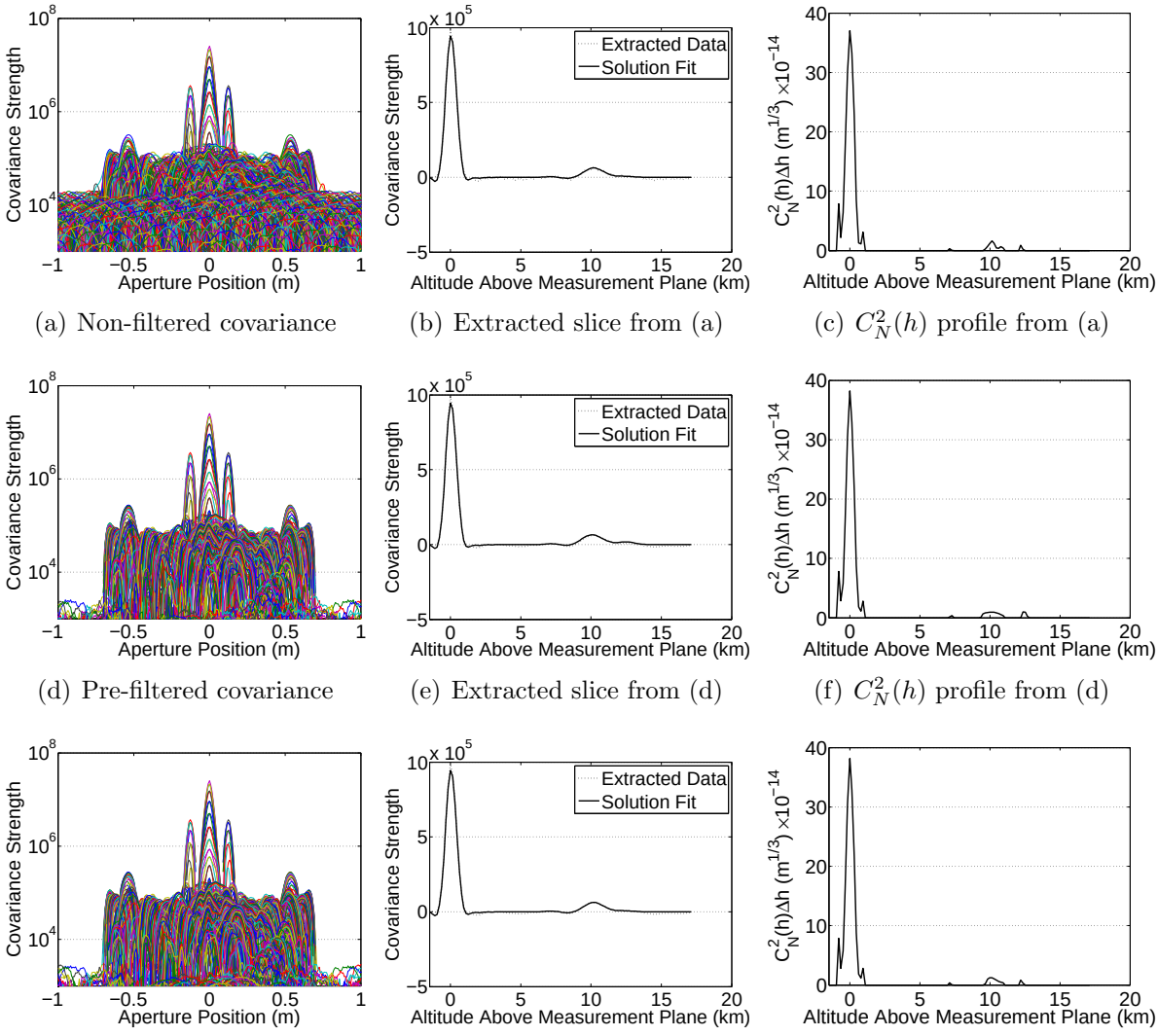

(a) Non-filtered covariance (b) Extracted slice from (a) (c) $C_N^2(h)$ profile from (a)

(d) Pre-filtered covariance (e) Extracted slice from (d) (f) $C_N^2(h)$ profile from (d)

(g) Post-filtered covariance (h) Extracted slice from (g) (i) $C_N^2(h)$ profile from (g)

Figure 3.9: Covariance and $C_N^2(h)$ profiles obtained using the Thorlabs DC111 from UC-SCIDAR V2005. ((a) – (c)) Without filtering. ((d) – (f)) Using pre-filtering. ((g) – (i)) Using post-filtering. Regularisation parameter used was 0.05 for all three cases. The estimate for r_0 was 6.7 ± 0.7 cm for all three cases.

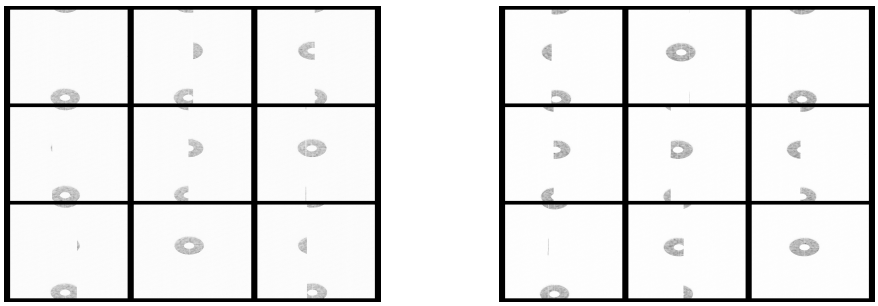

(a) (b)

Figure 3.10: The system employed during 2006 resulted in a jumbled image readout. Selected images from (a) camera C1 and (b) camera C2.

3.4 UC-SCIDAR V2007

January 2007 saw the first use of a Dragonfly Express CCD camera from Point Grey Research (PGR). This camera uses a Kodak KAI-0340DM sensor which has a 640x480 grid of 7.4 μm square pixels. At full resolution the camera has a frame rate of 120 Hz, with the potential of capturing at 200 Hz with partial scanning. Exposure times range from 20 μs to 63 s. As pixel sizes are identical to those of the V2005 system the same lenses are used in the 2007 system (henceforth termed UC-SCIDAR V2007). The Dragonfly Express CCD cameras utilise a firewire-b (IEEE-1394b) specification. As such a different acquisition system was used.

Figure 3.11 shows the physical and optical layout of UC-SCIDAR V2007. In addition to the change of cameras, it was decided to use a magnetic mount for the beamsplitter (BS). This meant that the beamsplitter could quickly be removed from the optical path and all available light could be collected with the straight path channel (C1) if deemed necessary. This proved useful during thin cloud cover and the use of faint binary star systems during capture. When operating in single camera mode (i.e. beamsplitter removed) a simple lens change (at L1) swapped C1 between pupil-plane and generalised SCIDAR.*

3.4.1 Camera Noise Characteristics

Data collected on January 24, 2007, used UC-SCIDAR V2007 operating in single camera mode with a frame rate of 100 Hz. At this frame rate, the camera had a split frame noise characteristic (Figure 3.12). Unfortunately the pixel index where the noise levels change is positioned such that a portion of the SCIDAR measurement is subject to one level of

*Removal of the beamsplitter will effect the optical path length of the system which will require the telescope focal position to be changed. Any image size differences are compensated for during the analysis the the data.

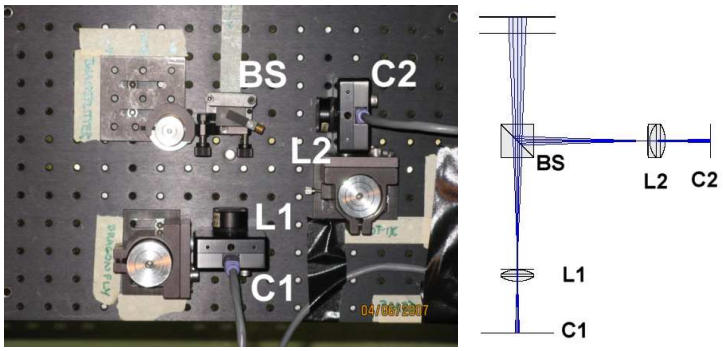

(a) Physical layout (b) Optical layout

Figure 3.11: Physical and optical layout of UC-SCIDAR V2007.

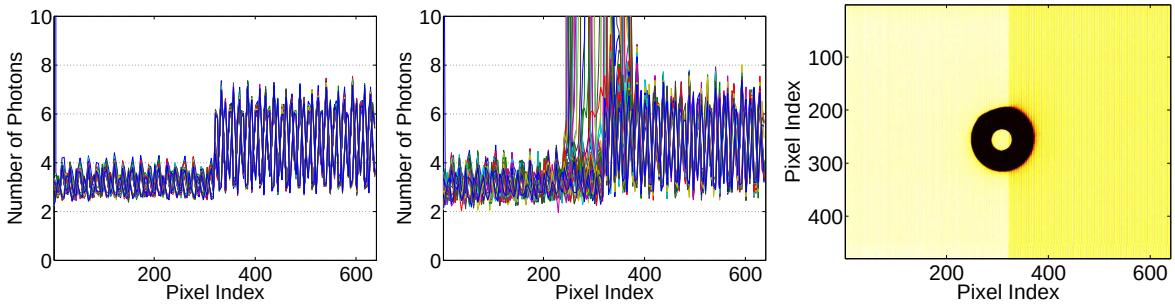

(a) Average dark frame (b) Average data frame (c) 2D average data frame

Figure 3.12: Noise characteristic of the PGR Dragonfly Express CCD operating at 100 Hz. The split level characteristics seen are positioned such that part of the SCIDAR measurement was subject to one level of dark current, and the remainder was subject to another.

dark current and the remainder is subject to another. As the position of the split change is deterministic, noise removal by way of average noise was used in the analysis of this data. Data taken after January 24, 2007, utilised a frame rate of 60 Hz, which did not have the split noise characteristic (Figure 3.13). (See Appendix D for details on noise removal by way of average noise.)

The lens configuration and pixel sizes used in the UC-SCIDAR V2007 results in the same spatial sampling as the V2005 system. As such processing on data from UC-SCIDAR V2007 is also performed on a 256x256 window. For the following discussion the data has been windowed to a 256x256 patch of the chip centred around the typical location of pupil-plane and generalised data for the respective cameras.

Table 3.1 tabulates the average number of photons detected per pixel over 1000 frames for both Dragonfly Express cameras used when operating at 60 Hz. For dark frames, both cameras exhibit similar characteristics with approximately 1.6 photons per pixel detected (standard deviation $\sigma \approx 0.1$). When looking at images taken from neigh-

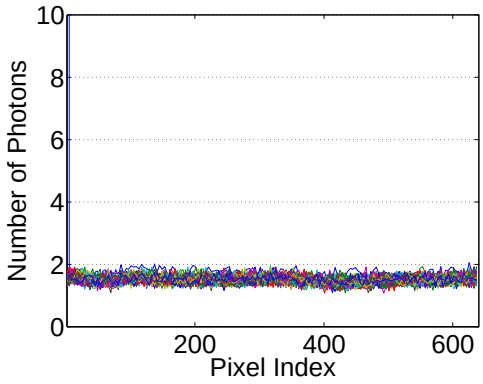

Figure 3.13: Noise characteristics of the Dragonfly Express CCD operating at 60 Hz.

Table 3.2: The average number of photons per pixel for the cameras used in UC-SCIDAR V2007 when using a frame rate of 60 Hz.

	Dark Frames		Neighbouring Sky	
	mean	σ	mean	σ
Dragonfly Express (C1)	1.525	0.084	1.534	0.084
Dragonfly Express (C2)	1.599	0.097	1.604	0.097

bouring sky similar statistics were found. This indicates that the level of dark current detected has a greater effect on the noise floor of the pupil-plane and generalised SCIDAR images. It was decided to use dark frames in the noise removal processing for similar reasons given for the V2005 system.

Through examination of the frequency content of the average dark frame from both cameras used in the V2007 system (Figure 3.14) a strong peak is seen in camera C2 (Figure 3.14(b)) at approximately 25 Hz that is not seen in C1 (Figure 3.14(a)). This is most likely related to something within the camera itself. From Figure 3.15, scintillation data from generalised SCIDAR contains frequencies of 25 Hz and hence filtering of this frequency may result in the removal of scintillation data. For the sake of data integrity it was decided to leave the data from UC-SCIDAR V2007 unfiltered during analysis for both channels.

3.5 System Operation

3.5.1 System Mounting and CCD Orientation

The UC-SCIDAR system is mounted so that the breadboard runs North to South when the telescope is at zenith. CCD cameras are mounted on the East side of the board ensuring that the firewire cables are normal to the breadboard. In the case of UC-SCIDAR V2007,

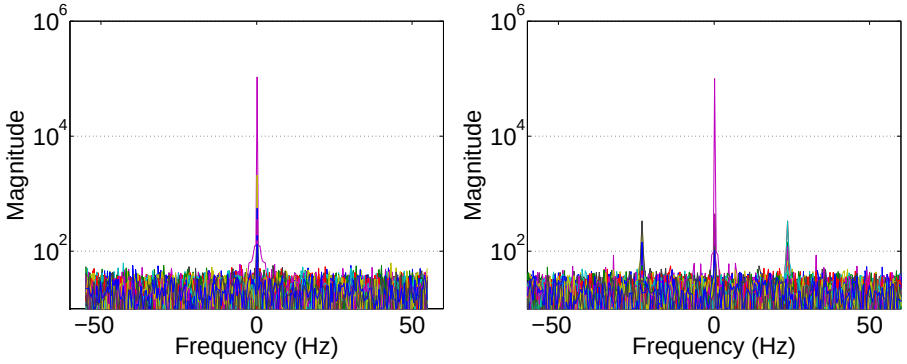

(a) Dragonfly Express (C1) (b) Dragonfly Express (C2)

Figure 3.14: The average frequency content of 1000 dark frames taken using UC-SCIDAR V2007 at an exposure of 1 ms operating at 60 Hz.

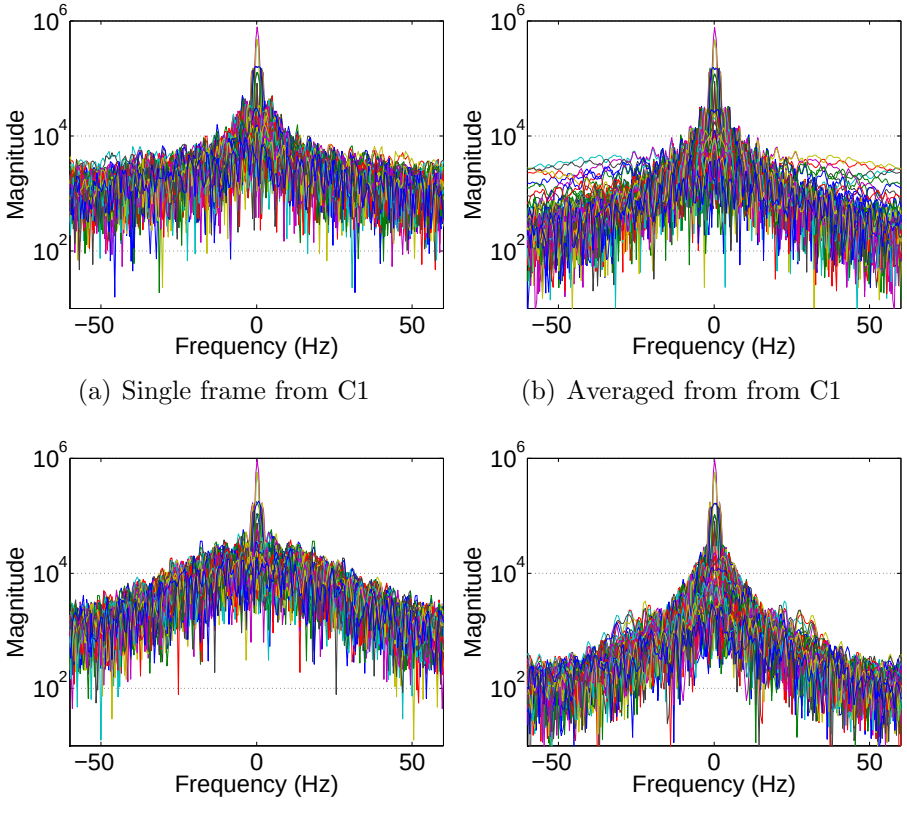

(a) Single frame from C1 (b) Averaged from from C1

(c) Single frame from C2 (d) Averaged from from C2

Figure 3.15: The frequency content of a SCIDAR data taken using UC-SCIDAR V2007 at an exposure time of 1 ms operating at 60 Hz. ((a) and (b)) Camera C1. ((c) and (d)) Camera C2.

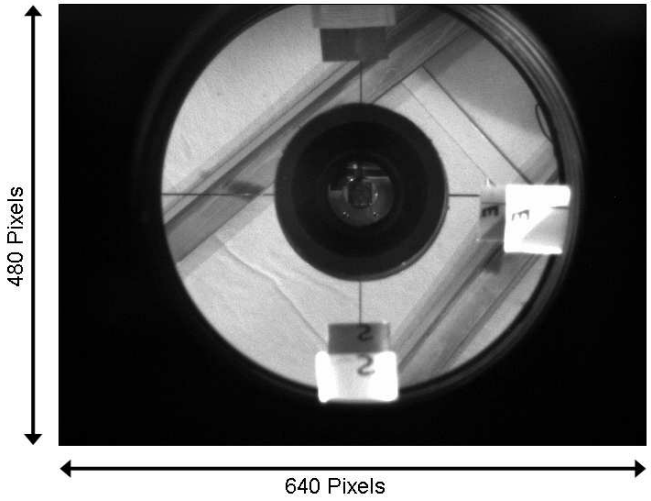

Figure 3.16: Image of primary mirror as captured by the straight path CCD camera using a multi-lens camera configuration. The orientation of the image has been modified to use standard compass coordinates. The image was captured by Steve Weddell (Department of Electrical & Computer Engineering) using UC-SCIDAR V2007 with non-SCIDAR lenses.

the longer CCD chip direction is oriented along the West/East plane at zenith. Figure 3.16 shows an image of the primary mirror as captured by the CCD camera on the straight path. Note that this image was captured using a multi-lens camera configuration which adds reflections into the optical system. The image shown has been modified accordingly.

When using the SCIDAR field lenses, the resulting images from UC-SCIDAR V2007 are oriented with respect to the primary mirror of the telescope such that the following angle corrections are required:

$$\begin{aligned} \theta_{\mathrm{C1}} &= -\theta_{\mathrm{measured}}, \\ \theta_{\mathrm{C2}} &= \theta_{\mathrm{measured}} + \frac{\pi}{2}, \end{aligned} \tag{3-1}$$

where $\theta_{\mathrm{measured}}$ is the measured angle from a specified datum and θ_{C1} and θ_{C2} are the corrected angles for cameras C1 and C2 respectively.

3.5.2 Star Selection

Due to the location of MJUO, binary stars such as α Crucis (α Cru) and α Centauri (α Cen) can be used for a large portion of the year. However in the summer months, when both α Cru and α Cen are too far from zenith, fainter stars such as θ Eridanus (θ Eri) and υ Carina (υ Car) can be used in single camera mode. The stellar parameters for stars used with UC-SCIDAR data presented in this thesis are listed in Table 3.3.

Table 3.3: Stellar parameters for stars used with UC-SCIDAR data presented in this thesis.

Star	Right Ascension	Declination	Epoch	ϕ (arcsec)	m_1	Δm	Source
α Cru	12h 27m	-63° 07'	2000	3.9	1.25	0.3	2005 Almanac
α Cen	14h 39m	-60° 51'	2000	13.3	-0.01	1.36	2000 Bright Star Catalog
			2005.5	10.2			2005 Almanac
			2006.5	9.4			2006 Almanac
			2007.5	8.7			2007 Almanac
θ Eri	02h 58.5m	-40° 17'	2002	8.4	3.20	0.92	WDS Star Catalog
υ Car	09h 47.3m	-65° 06'	2000	5.0	3.02	2.98	WDS Star Catalog

3.6 The Analysis Techniques and Measured Profiles

The techniques used to determine $C_N^2(h)$ and $V(h)$ profiles from UC-SCIDAR data are discussed in Chapters 4 and 5 respectively. The measured profiles for MJUO are presented in Chapter 6.

Chapter 4

Refractive-Index Structure Constant Extraction Techniques

SCIDAR utilises two different measurement planes. *Pupil-plane* SCIDAR acquires scintillation images at the aperture of the telescope and is useful in measuring turbulence at mid- to high-altitudes. As discussed in Chapter 2, the level of scintillation detected is a function of $h^{5/6}$, hence pupil-plane SCIDAR is insensitive to turbulence that originates near-ground. *Generalised* SCIDAR uses field lenses to virtually shift the measurement plane to a *defocus distance*, d, below the telescope. This approach makes near ground turbulence (NGT) more readily detectable.

SCIDAR uses a series of short exposure scintillation images of the aperture to calculate the 2D spatio-temporal covariance. The 2D covariance consists of a series of triplets where each triplet is associated with a different turbulent layer, as the images are typically taken using a binary star system. The profile of a triplet depends not only on the strength and height of the associated layer, but also the off-axis angle of the telescope and the parameters of the binary star.

Chapter 2 summarised how $C_N^2(h)$ profiles are found from scintillation spatio-temporal covariances theoretically. This chapter discusses the practical aspects of using scintillation images to estimate $C_N^2(h)$ profiles. Section 4.1 defines the spatial covariance function and how $C_N^2(h)$ profiles are extracted from it. Section 4.2 then discusses a means of quantifying the error on $C_N^2(h)$ estimation for use in further discussion. Section 4.3 discusses the merits of aperture normalisation and how the normalisation matrix used for generalised SCIDAR differs from that used for pupil-plane SCIDAR. Section 4.4 presents the regularisation method used in the $C_N^2(h)$ estimation from noisy scintillation data. Section 4.5 examines the accepted methodology of finding $C_N^2(h)$ profiles. This section also examines the observational parameters that affect these profiles. Sections 4.6 and 4.7 discuss the practical limitations of zenith angle and exposure times on estimated $C_N^2(h)$ profiles respectively. Finally the effects of strong NGT on estimated $C_N^2(h)$ profiles are examined in section 4.8.

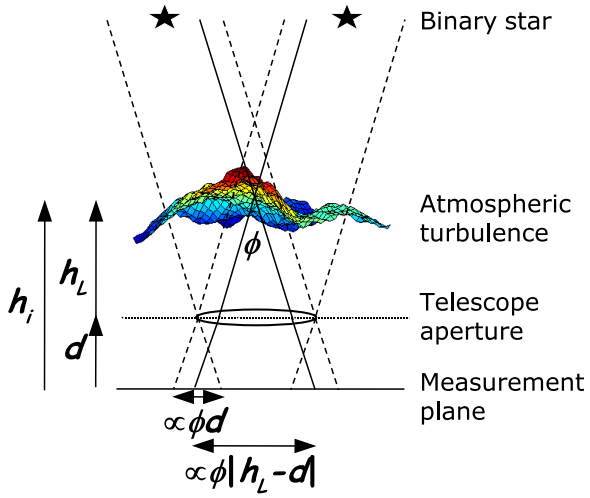

Figure 4.1: The concept of binary star SCIDAR. Light from each star passes through the same turbulent region forming identical scintillation patterns separated by a distance proportional to the binary star separation ϕ and the height of the turbulent layer above the measurement plane $h_i = |h_L - d|$. Due to sign conventions d is negative. (This figure is a reprint of Figure 2.14 on page 28.)

A chronological $C_N^2(h)$ analysis of UC-SCIDAR data is presented in Chapter 6.

4.1 Determination of Turbulence Strength

Consider a single turbulent layer located at altitude h_i above the measurement plane (Figure 4.1). Light from each stellar companion passes through the same turbulent region forming identical, but separated, scintillation patterns at the aperture. If the angular separation between the stellar companions is ϕ, then the patterns are separated by a distance proportional to ϕh_i. If a generalised measurement plane is used then $h_i = |h_L - d|$ where h_L is the altitude of the layer above the telescope aperture and d is the defocus distance to the measurement plane located below the telescope aperture. Because of sign conventions, d is negative.

$C_N^2(h)$ profiles are obtained from the spatio-temporal covariance functions of a binary star $C_B(\rho, \phi, \Delta t)$ for $\Delta t = 0$, resulting in a spatial covariance, $C_B(\rho, \phi, 0)$, which is also called the auto-covariance. $C_B(\rho, \phi, 0)$ can be written as (*Klückers et al.*, 1998; *Avila et al.*, 2001)

$$C_B(\rho, \phi, 0) = \sum_{i=1}^{n} aC_S(\rho) + b\left[C_S(\rho - \phi h_i) + C_S(\rho + \phi h_i)\right], \tag{4-1}$$

where ρ is the radial coordinate in the direction of the binary star and h_i represents the

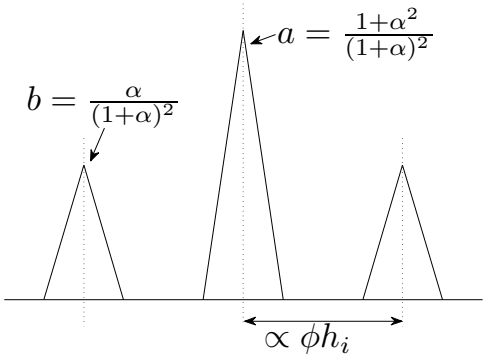

Figure 4.2: Schematic of a binary star system covariance triplet profile from a single layer of turbulence. The distance between the central peak and secondary peak is proportional to the binary star system separation, ϕ, and the height of the layer above the measurement plane, h_i. $\alpha = 10^{-0.4\Delta m}$, where Δm is the magnitude difference between the binary star system components. (This figure is a reprint of Figure 2.17 on page 31.)

height of each individual layer above the measurement plane. The coefficients a and b are given by (*Avila et al.*, 2001)

$$a = \frac{1+\alpha^2}{(1+\alpha)^2}, b = \frac{\alpha}{(1+\alpha)^2}, \alpha = 10^{-0.4\Delta m}, \tag{2-22}$$

where Δm is the magnitude difference between the binary star companions. Each layer triplet has a central peak that corresponds to the covariance of a single star for a given layer, $C_S(\rho)$, scaled by a. The two secondary peaks correspond to $C_S(\rho)$ scaled by b and are offset from the central peak by a distance proportional to ϕh_i (Figure 4.2).

$C_S(\rho, 0)$ is the 2D Fourier transform of the power spectrum of the scintillation fluctuations seen at the measurement plane. For an aperture with circular symmetry, as in the case of a telescope,

$$C_S(\rho, 0) = \int_0^\infty K(\rho, h) C_N^2(h) dh, \tag{2-26}$$

where $K(\rho, h)$, the kernel for the inverse problem, is the theoretical spatial covariance function of a single star produced by a layer at height h where $\int C_N^2(h)dh = 1$ and assuming Kolmogorov turbulence (*Avila et al.*, 1997) (refer to equation (2-25), page 32). Equations (4-1) and (2-26) allow the use of binary star covariances to estimate $C_N^2(h)$ profiles.

From equation (4-1), the position of the central peak remains unchanged, whereas the positions of the secondary peaks are dependent on the heights of the respective turbulent layers. The overall covariance strength of the central peak is the sum of all layer central peaks, and the contribution from individual layers are indistinguishable (Figure

4.3(a)). As a consequence SCIDAR measurements rarely use the primary peak and instead use the information from the secondary peaks.

The secondary peak $C_S(\rho - \phi h_i)$ contains all the information required to determine the altitude and $C_N^2(h)$ strength for a given layer. Extraction of $C_S(\rho - \phi h_i)$ from the 2D covariance is typically performed by calculating the difference between the section slices parallel and perpendicular to the direction of the binary star system, $C_{B,\parallel}$ and $C_{B,\perp}$ respectively, such that (*Tokovinin et al.*, 2005)

$$C_S(\rho - \phi h) \approx C_{B,\parallel} - C_{B,\perp}, \tag{4-2}$$

where $C_S(\rho - \phi h)$ denotes the secondary peak profile for all layers. Figure 4.3(b) shows the directions of $C_{B,\parallel}$ and $C_{B,\perp}$. The extracted slices are shown in Figure 4.3(c). When using $C_S(\rho - \phi h)$ in equation (2-26), the kernel $K(\rho, h)$ has ideal secondary peak information along the diagonal line of ρh (Figure 4.3(d)).

To simplify calculations, equation (2-26) can be expressed in matrix form (*Johnston et al.*, 2002)

$$S(\rho) = T(\rho, h) \times C_N^2(h), \tag{4-3}$$

where $S(\rho)$ is a vector containing the extracted 1D slice of the spatial covariance (i.e. $C_{B,\parallel} - C_{B,\perp}$) as measured at the measurement plane, and $T(\rho, h)$ is a matrix of ideal secondary peak covariances.

An infinite number of solutions are available for equation (4-3), so an iterative approach must be employed in its solution. Figure 4.4 indicates the main steps in determining $C_N^2(h)$ profiles from 2D spatial covariances. The various techniques used are discussed in detail in *Johnston et al.* (2000) and *Johnston et al.* (2002). The analysis as it applies to UC-SCIDAR data is continued in section 4.3.

4.2 Error on $C_N^2(h)$ Estimation

Before continuing the discussion on determining $C_N^2(h)$ profiles, it is important to understand and quantify the reliability of a $C_N^2(h)$ estimate. The error on $C_N^2(h)$ estimation can be determined by calculating the root-mean-square (RMS) error on $C_N^2(h)$. The technique was proposed by *Klückers et al.* (1998) and is discussed in more detail in *Johnston et al.* (2002). It is summarised here.

Let the solution obtained, $\widehat{C_N^2(h)}$, and the true profile, $C_N^2(h)$, be contained in the *solution plane*. Let the spatial covariance slice taken from the data, $S(\rho)$, and the corresponding covariance function obtained from $\widehat{C_N^2(h)}$, i.e. $\widehat{S(\rho)} = T(\rho, h) \times \widehat{C_N^2(h)}$, be contained in the *data plane*, as illustrated in Figure 4.5.

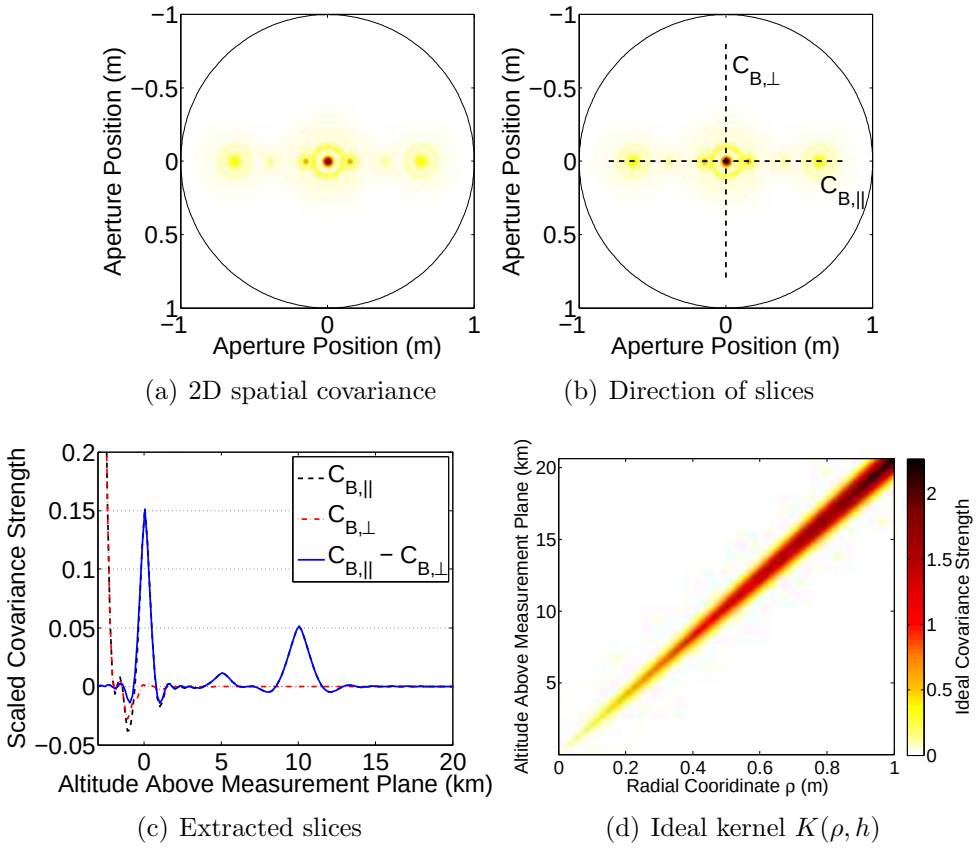

(a) 2D spatial covariance (b) Direction of slices

(c) Extracted slices (d) Ideal kernel $K(\rho, h)$

Figure 4.3: Secondary peak slice extraction. (a) The position of the central peak from all layers is overlapped such that the overall central peak is the summation of all turbulent layers. (b) To extract secondary peak information for use in $C_N^2(h)$ profiling, slices along the direction of the binary, $C_{B,\parallel}$, and perpendicular to the binary, $C_{B,\perp}$, are taken. The extracted slice $C_{B,\parallel} - C_{B,\perp}$ is shown in (c). (d) The kernel $K(\rho, h)$ needed to obtain $C_N^2(h)$ profiles contains secondary peak information along the diagonal.

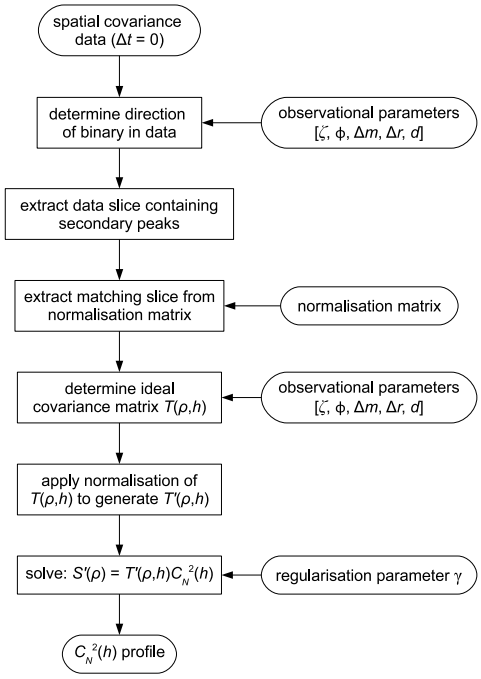

Figure 4.4: The main steps taken to determine $C_N^2(h)$ profiles using the techniques detailed in *Johnston et al.* (2000) and *Johnston et al.* (2002).

The RMS error on $C_N^2(h)$, ε_C, can be defined as

$$\varepsilon_C = \varepsilon\{C_N^2(h) - \widehat{C_N^2(h)}\} = \sqrt{\frac{(C_N^2(h) - \widehat{C_N^2(h)})^2}{(C_N^2(h))^2}}. \tag{4-4}$$

ε_C cannot be found directly because $C_N^2(h)$ is not known. It can be approximated by finding $\varepsilon_{C_P} = \varepsilon\{\widehat{C_N^2(h)} - C_N^2(h)_P\}$, where $C_N^2(h)_P$ is a perturbed version of $\widehat{C_N^2(h)}$ such that

$$C_N^2(h)_P = \widehat{C_N^2(h)} + \beta W. \tag{4-5}$$

W represents random Gaussian noise and β is a noise weighting. The value of β is set so that the RMS error on covariance, $\varepsilon_S = \varepsilon\{S(\rho) - \widehat{S(\rho)}\}$, equals the RMS error on the perturbed covariance, $\varepsilon_{S_P} = \varepsilon\{\widehat{S(\rho)} - S_P(\rho)\}$, where $S_P(\rho) = T(\rho, h) \times C_N^2(h)_P$. When this occurs ε_{C_P} is considered to be a good approximation of ε_C. ε_{C_P} allows the error on the estimation of any parameter based on $C_N^2(h)$ to be found, and it provides a quantifiable cross-check on whether the solution obtained, $\widehat{C_N^2(h)}$, is reliable.

ε_C is a comparative measure that provides information as to how well the $C_N^2(h)$ estimate reflects the data collected, where lower ε_C indicate a better fit of the $C_N^2(h)$ profile to the data. $C_N^2(h)$ estimates resulting in ε_C values approaching 1 should not be trusted as they do not reflect the raw data. However a low ε_C is not a guarantee of a

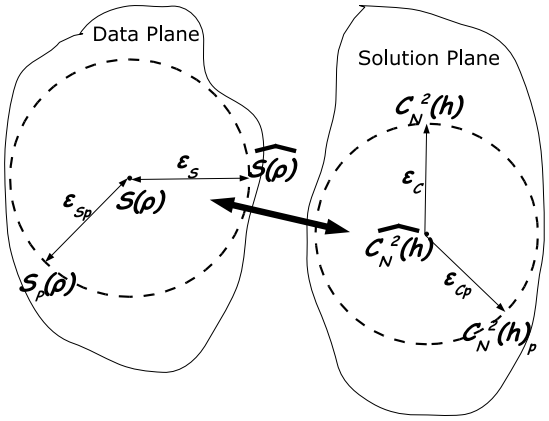

Figure 4.5: Schematic interpretation of the method for determining the error on $C_N^2(h)$ for any particular observed profile obtained. Based on Fig. 10 in *Klückers et al.* (1998).

good $C_N^2(h)$ profile. This is discussed further in section 4.4.

4.3 Aperture Normalisation

A scintillation frame from a binary star will contain two separate aperture images that overlap. Figure 4.6 shows typical scintillation frames (pupil-plane and generalised) from both simulated and UC-SCIDAR data. For a given binary star separation, ϕ, and a known defocus distance, d, the centre of the aperture images are offset relative to each other by a distance proportional to ϕd (Figures 4.6(b) and 4.6(e)). The direction of the binary determines the angle at which the aperture images are offset. For pupil-plane SCIDAR, d is zero and hence the aperture images overlap completely (Figures 4.6(c) and 4.6(f)).

The signal in the frame, $m_B(\rho, \phi)$, can be described by (*Johnston et al.*, 2002)

$$m_B(\rho,\phi) = [s(\rho) + \overline{s}(\rho)] + \alpha\,[s(\rho+\phi d) + \overline{s}(\rho+\phi d)]\,, \tag{4-6}$$

where $s(\rho)$ is the zero-mean scintillation data and $\overline{s}(\rho)$ is the mean scintillation data. α is defined by equation (2-22). If $\overline{m_B}(\rho,\phi)$ is the average signal in the frame, then the averaged spatial covariance is

$$\begin{aligned} C_B^{\otimes}(\rho,\phi) &= (m_B(\rho,\phi)\otimes m_B(\rho,\phi)) - (\overline{m_B}(\rho,\phi)\otimes\overline{m_B}(\rho,\phi)) \\ &= (m_B(\rho,\phi)\otimes m_B(\rho,\phi)) - ([\overline{s}(\rho)+\alpha\overline{s}(\rho+\phi d)]\otimes[\overline{s}(\rho)+\alpha\overline{s}(\rho+\phi d)]) \\ &= (1+\alpha^2)\,(s(\rho)\otimes s(\rho)) \\ &\quad +\alpha\,[(s(\rho)\otimes s(\rho+\phi d)) + (s(\rho)\otimes s(\rho-\phi d))]\,, \end{aligned} \tag{4-7}$$

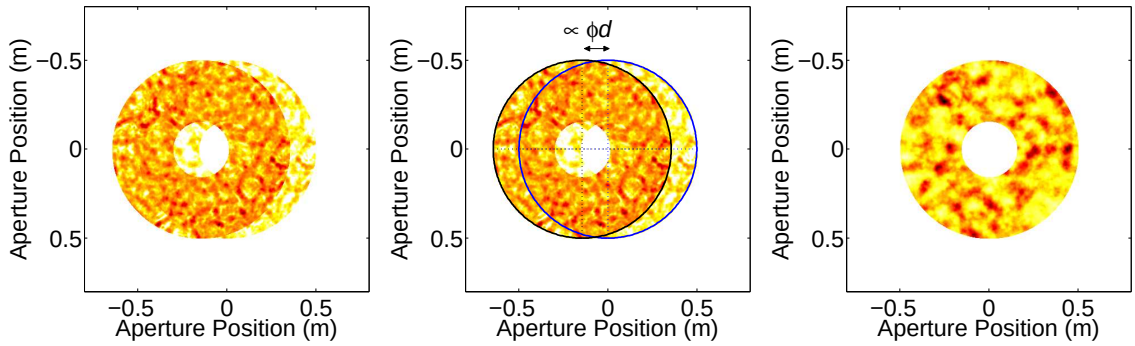

(a) Simulated generalised frame (b) Annotated simulated frame (c) Simulated pupil-plane frame

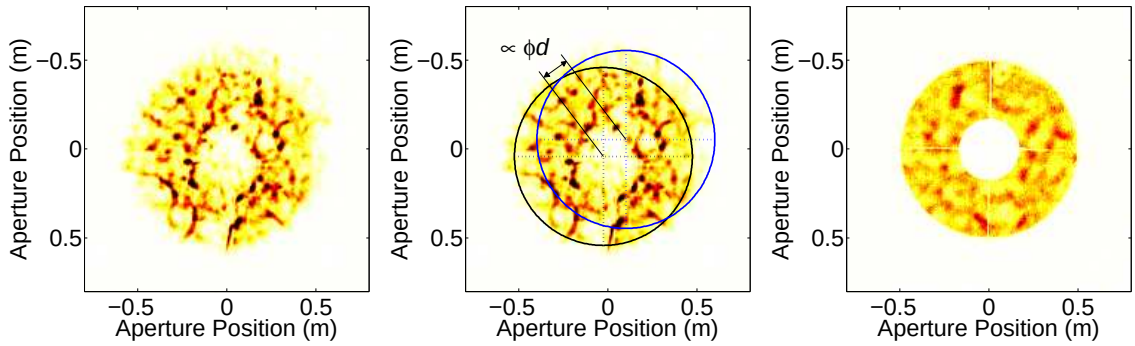

(d) UC-SCIDAR generalised frame (e) Annotated UC-SCIDAR frame (f) UC-SCIDAR pupil-plane frame

Figure 4.6: Typical scintillation frames from simulated and UC-SCIDAR data. Images contain two aperture images that are separated by a distance proportional to the angular stellar separation, ϕ, and the defocus distance, d. ((c) and (f)) For pupil-plane data d is zero and hence the images overlap completely.

where $\otimes$ denotes the convolution operator. As SCIDAR frames are subject to an aperture, $C_B^{\otimes}(\rho,\phi)$ must be normalised for aperture effects to remove any bias toward the aperture itself. This can be achieved by dividing $C_B^{\otimes}(\rho,\phi)$ by the auto-correlation of the mean signal, $(\overline{s}(\rho)+\alpha\overline{s}(\rho+\phi d))$ (*Klückers et al.*, 1998), which is

$$(1+\alpha^2)\left(\overline{s}(\rho)\otimes\overline{s}(\rho)\right)+\alpha\left[\left(\overline{s}(\rho)\otimes\overline{s}(\rho+\phi d)\right)+\left(\overline{s}(\rho)\otimes\overline{s}(\rho-\phi d)\right)\right]. \tag{4-8}$$

For pupil-plane SCIDAR,

$$\left(\overline{s}(\rho)\otimes\overline{s}(\rho)\right)=\left(\overline{s}(\rho)\otimes\overline{s}(\rho+\phi d)\right)=\left(\overline{s}(\rho)\otimes\overline{s}(\rho-\phi d)\right), \tag{4-9}$$

because d is zero. Hence the normalisation term expressed in (4-8) becomes (*Johnston et al.*, 2002)

$$(1+\alpha)^2\left(\overline{s}(\rho)\otimes\overline{s}(\rho)\right). \tag{4-10}$$

For generalised SCIDAR, the aperture images do not overlap completely. Hence the

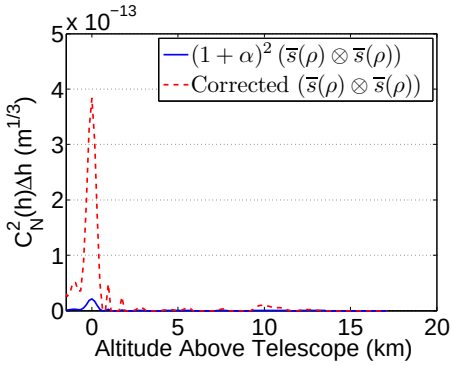

Figure 4.7: Estimated $C_N^2(h)$ profiles for generalised data from run #30 (June 2005) based on different normalisation terms. The use of $(1+\alpha)^2\,(\overline{s}(\rho)\otimes\overline{s}(\rho))$ (i.e. the term used for pupil-plane analysis) severely underestimates the turbulence strength present. The corrected normalisation term allows for the fact that the resulting aperture images from each binary companion is not fully overlapped. r_0 estimates for the profiles shown are 36 ± 4 cm and 6.4 ± 0.8 cm for the pupil-plane normalisation and the corrected normalisation respectively.

normalisation term described in equation (4-10) is not appropriate. Instead an estimate of $(\overline{s}(\rho)\otimes\overline{s}(\rho))$ is required, which can be found by deconvolving the expression in (4-8) with

$$\frac{1+\alpha^2}{\alpha}\delta(\rho) + \delta(\rho+\phi d) + \delta(\rho-\phi d), \tag{4-11}$$

where $\delta(\rho)$ describes a unit impulse (*Johnston et al.*, 2002).

Consider generalised UC-SCIDAR data from run #30 taken during June 2005. This data was collected using α Cen and was captured with an exposure time of 1 ms. The measurement plane was located approximately 3 km below the telescope. (See Appendix B for the determination of defocus distances from data.) The strength of the $C_N^2(h)$ profile is severely underestimated when using $(1+\alpha)^2\,(\overline{s}(\rho)\otimes\overline{s}(\rho))$ (i.e. the normalisation term for pupil-plane analysis) (Figure 4.7), resulting in an estimate for the coherence length, r_0, of 36 ± 4 cm. This contrasts with the simultaneous pupil-plane data, which estimates r_0 to be 21 ± 4 cm. Correcting the normalisation term in the generalised analysis by deconvolving equation (4-8) with (4-11), results in a revised r_0 estimate of 6.4 ± 0.8 cm, which is more realistic for MJUO.

4.3.1 Noise Amplification in Aperture Normalisation

The use of equation (4-3) to solve for $C_N^2(h)$ requires an aperture normalised slice. The division of $C_B^{\otimes}(\rho,\phi)$ by the normalisation term, $(\overline{s}(\rho)\otimes\overline{s}(\rho))$, can significantly amplify any noise present. Figure 4.8 shows the effect of aperture normalisation on the noise contained in an extracted slice and corresponding $C_N^2(h)$ profile for the pupil-plane UC-SCIDAR data from run #30 taken during June 2005. This data used an exposure time

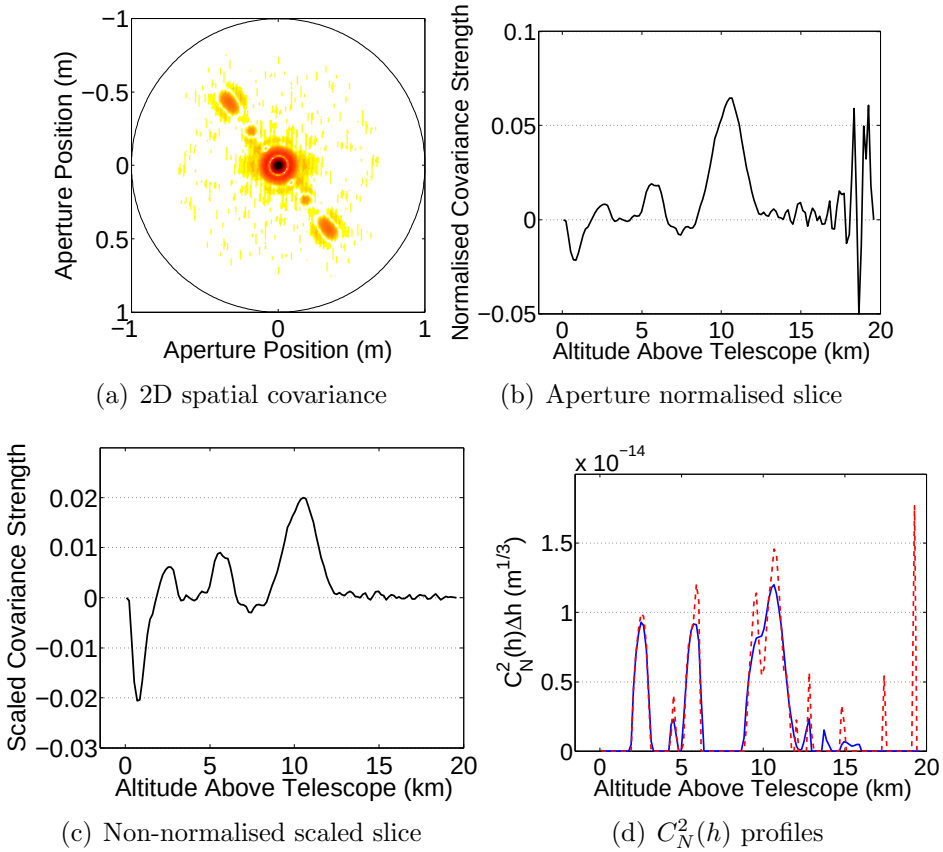

(a) 2D spatial covariance (b) Aperture normalised slice

(c) Non-normalised scaled slice (d) $C_N^2(h)$ profiles

Figure 4.8: Effects of aperture normalisation by way of division on pupil-plane UCSCIDAR data from run #30 taken during June 2005. (a) In the 2D spatial covariance background noise can be seen. (b) The noise is amplified in the aperture normalised slice, especially near the aperture edge. (c) A scaled slice that is not aperture normalised does not contain the amplified noise. (d) The $C_N^2(h)$ profile obtained using the aperture normalised slice (- - -) contains noisy spikes with an error on estimation of 1.01, whereas the $C_N^2(h)$ profile obtained using the scaled non-normalised slice (—) is smoother and the error on estimation is 0.33.

of 1 ms. In the 2D spatial covariance background noise can be seen (Figure 4.8(a)). The noise present in the extracted slice containing secondary peaks was amplified during aperture normalisation (Figure 4.8(b)), especially near the edge of the aperture, and is propagated through to the $C_N^2(h)$ estimate (Figure 4.8(d)). This is also reflected in the error on $C_N^2(h)$ estimation, ε_C, which was found to be 1.01. This level of error indicates that the $C_N^2(h)$ estimate cannot be trusted as the inversion process also fitted noise.

Instead of applying aperture normalisation to noisy data, it is possible to apply the aperture normalisation to the noise-free ideal covariance matrix kernel, such that (*Johnston et al.*, 2002)

$$S'(\rho) = T'(\rho, h) \times C_N^2(h), \tag{4-12}$$

where $S'(\rho)$ is a scaled 1D slice extracted from $C_B^{\otimes}(\rho, \phi)$ and

$$T'(\rho, h) = T(\rho, h) \left(\overline{s}(\rho) \otimes \overline{s}(\rho)\right). \tag{4-13}$$

Using the scaled non-normalised slice shown in Figure 4.8(c), along with a normalised kernel, a smoother $C_N^2(h)$ profile is obtained (Figure 4.8(d)) and ε_C drops to 0.33. This reduced level of error indicates a better estimate for $C_N^2(h)$.

In generalised data, the error generated by division noise is more problematic as there exists a smaller area of overlapped aperture images from each of the binary companions. In the normalised covariance matrix kernel, a decreased weighting is given to height values that are averaged over a smaller area corresponding to a smaller degree of aperture overlap (*Johnston et al.*, 2002). This can improve the $C_N^2(h)$ estimates and in turn the r_0 estimates.

Figure 4.9(a) shows the full generalised $C_N^2(h)$ profile for run #30, June 2005, using both a normalised slice and a normalised kernel. As with the pupil data, the normalised slice was slightly noisier. However there is no advantage in using a normalised kernel over the normalised slice. ε_C for the normalised slice was found to be 0.06 where as ε_C for the normalised kernel was 0.21. r_0 estimates were 5.6 ± 0.2 cm and 6.5 ± 0.8 cm for the normalised slice and normalised kernel respectively. The slight increase in r_0 for the normalised kernel does support the visual observation of a smoother profile, however little difference exists between the two r_0 estimates. This is due to the strength of the NGT which masks measurements from the free-atmosphere. If NGT was truncated from the slice prior to $C_N^2(h)$ determination, there is a clear advantage of using a normalised kernel over a normalised slice (Figure 4.9(b)). For the normalised slice, ε_C is 2.59 indicating that the slice used was extremely noisy and the results should not be trusted. When using a normalised kernel ε_C decreases to 0.54. This still leaves doubt as to the reliability of the measurement, but will at least provide a measurement for use in site trending.

4.4 Regularisation

There are an infinite number of solutions available for equation (4-12) and an iterative approach must be used. The technique used for the inversion algorithm follows that proposed by *Johnston et al.* (2000).

A $C_N^2(h)$ estimate can be obtained by minimizing the least-squares error function,

$$E = ||T'(\rho, h) C_N^2(h) - S'(\rho)||^2. \tag{4-14}$$

However any noise present in $S'(\rho)$ will propagate through to the $C_N^2(h)$ estimate and

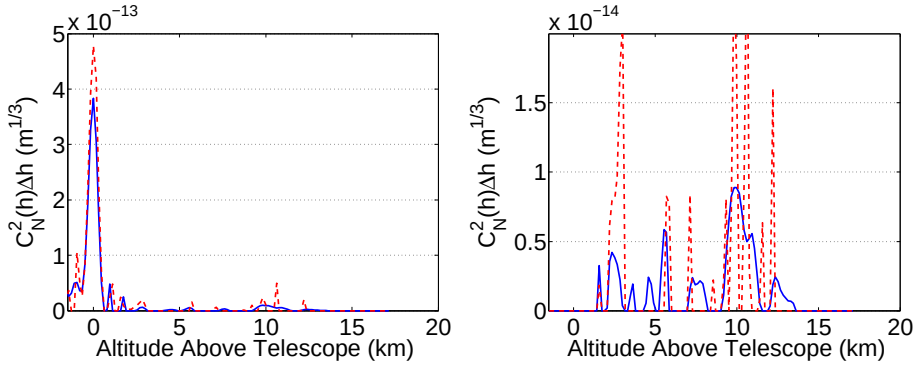

(a) Full profile (b) NGT truncated

Figure 4.9: Estimated $C_N^2(h)$ profiles for generalised UC-SCIDAR data from run #30 (June 2005) based on different normalisation points used. (a) Little benefit exists in using a normalised slice (- - -) over a normalised kernel (—) due to the strength of the NGT. (b) Truncating the slices to exclude NGT prior to $C_N^2(h)$ determination produces a very noisy result when using a normalised slice (- - -) compared to the normalised kernel (—).

can lead to unacceptably high levels of noise in the solution. A practical approach is to regularise the solution by incorporating a statement of the energy of the profile into the error function. Using Tikhonov-Miller regularisation, a minimization of the following error function is required (*Johnston et al.*, 2000),

$$E = ||T'(\rho, h)C_N^2(h) - S'(\rho)||^2 - \gamma||C_N^2(h)||^2. \tag{4-15}$$

The first term ensures the fit to the data and the second term is an assumption regarding the energy used in the regularisation of the problem. The parameter γ defines the tradeoff between the fit to the data and the requirement for a smooth $C_N^2(h)$ profile. When γ is 0, equation (4-15) reduces to equation (4-14) and the $C_N^2(h)$ estimate fits any residual noise in the data. While this will result in a small ε_C, the $C_N^2(h)$ profile will likely contain many false peaks and would not be considered representative of the true turbulent structure. When γ is 1, the emphasis is placed on the $C_N^2(h)$ estimate, hence the fit may no longer sufficiently match the actual data resulting in a large ε_C.

Consider the simultaneous UC-SCIDAR pupil-plane and generalised data used above (i.e. run #30 from June 2005). Figures 4.10 and 4.11 show the estimated $C_N^2(h)$ profiles using various values of γ. For pupil-plane data, a small γ value results in a $C_N^2(h)$ profile that is exceptionally noisy (Figures 4.11(a) and 4.10(a)). In the generalised data, the covariance strength resulting from NGT is substantially greater than any noise or other signals present (Figures 4.11(b) and 4.10(c)). This suggests that more regularisation is required for pupil-plane data than for generalised data. For γ values approaching 1, the

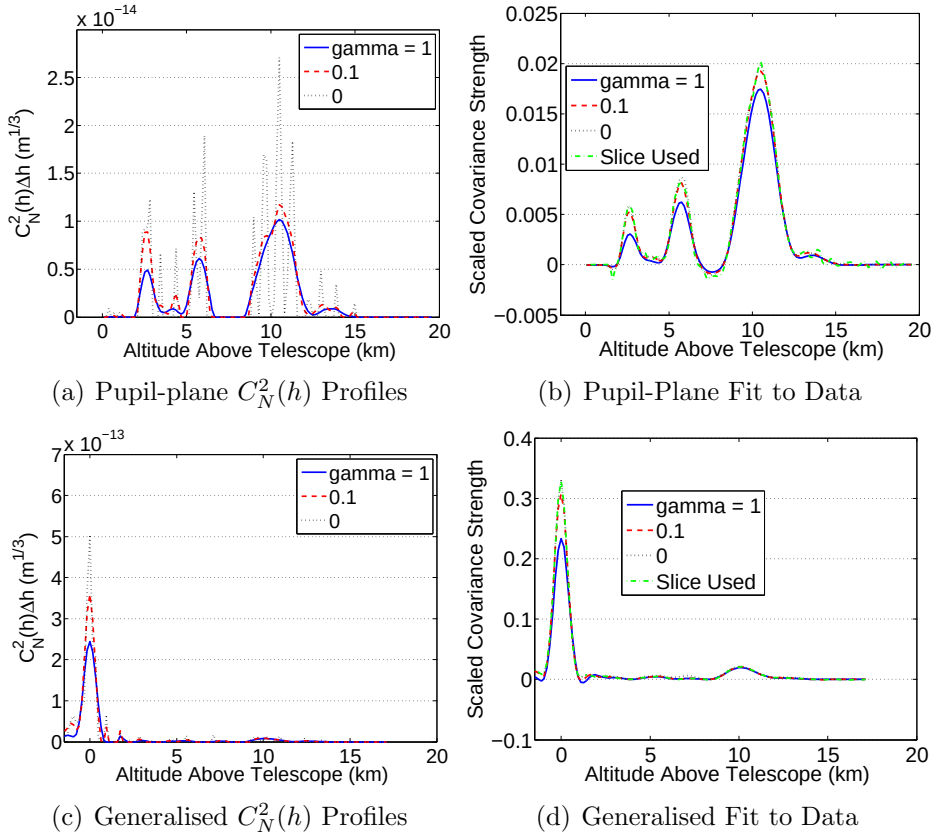

(a) Pupil-plane $C_N^2(h)$ Profiles (b) Pupil-Plane Fit to Data

(c) Generalised $C_N^2(h)$ Profiles (d) Generalised Fit to Data

Figure 4.10: Estimated $C_N^2(h)$ profile and fit to data for selected values of γ on both data channels found in run #30 from June 2005. A small γ places more emphasis on the fit to data and as a result fits residual noise. A large γ moves the solution too far from data.

estimated slice from the $C_N^2(h)$ profile (i.e. $T'(\rho, h)C_N^2(h)$) no longer sufficiently matches the actual data slice used (Figures 4.10(b) and 4.10(d)).

Figure 4.12 shows the estimated r_0 values for the profiles shown in Figures 4.10 and 4.11. Regardless of the γ value used there is little variation in r_0 for generalised data where the standard deviation, σ_{r_0}, is 1.1 cm with a mean, $\overline{r_0}$, of 5.1 cm. The error on r_0 increases with greater γ values, as more emphasis is placed on the $C_N^2(h)$ solution, which moves the results away from the data. Similar levels of variation exist in r_0 values found for pupil-plane data where $\overline{r_0} = 21.0$ cm and $\sigma_{r_0} = 0.8$ cm. For large γ, the error on the pupil-plane r_0 approaches ± 13 cm, which is unacceptable. To minimize the error on the estimate of $C_N^2(h)$, and hence r_0, γ should be restricted to 0.2 or less for pupil-plane analysis.

Unfortunately no relationship was found that correlates the selection of γ to an optimal $C_N^2(h)$ profile estimation and hence the best estimate of r_0 and other adaptive optics design parameters. However it is clear that some level of regularisation is useful in the analysis of noisy SCIDAR data. A γ value of 0.15 was selected for use in the site

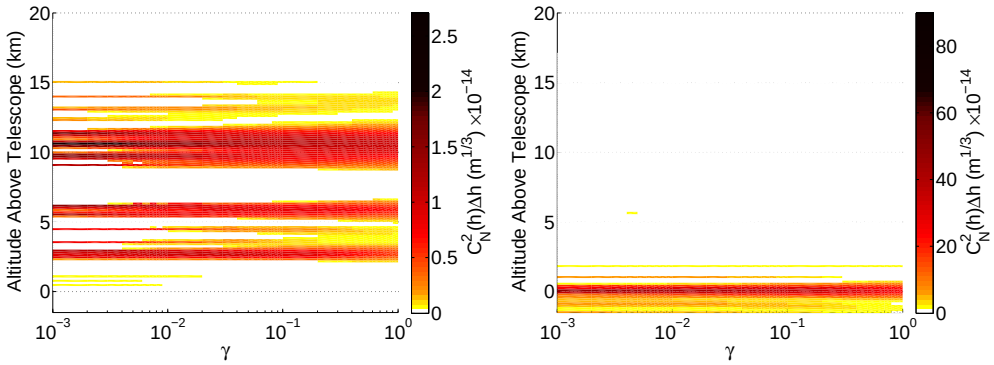

(a) Pupil-plane (b) Generalised

Figure 4.11: Estimated $C_N^2(h)$ profiles for various amounts of regularisation as defined by γ on both data channels found in run #30 from June 2005.

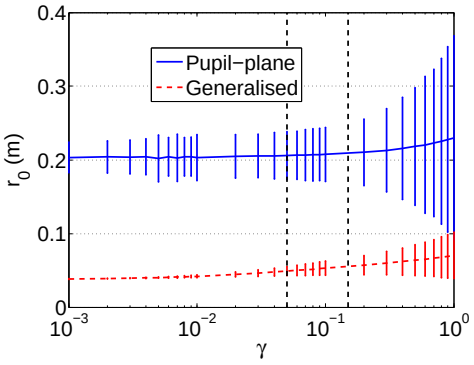

Figure 4.12: Estimated r_0 values for various values of γ on both data channels found in run #30 from June 2005. The dashed vertical lines indicate $\gamma = 0.05$ and 0.15.

trending analysis of pupil-plane data from UC-SCIDAR. This value was based on the effect of γ on $C_N^2(h)$ profiles from various runs taken throughout the SCIDAR campaign at MJUO that provided visually the best fit to the data while providing the smoothest $C_N^2(h)$ profile. As generalised data does not require as much regularisation, a γ value of 0.05 was selected.

4.5 Residual Central Peak Information

Theoretically it is possible to obtain reasonable $C_N^2(h)$ estimates using the algorithm outlined in Figure 4.4 incorporating the techniques described so far. Practically, issues arise during the secondary peak slice extraction. The extraction of the slice containing the secondary peaks, $C_S(\rho - \phi h)$, from the 2D spatial covariance is highly dependent on the ability to remove the central peak from the discretised data. The extraction using the difference between parallel and perpendicular slices (refer to equation (4-2)) does not always completely remove the central peak. This can result in the solution containing false layers at low altitudes or the strengths of existing low altitude layers being artificially inflated. There are many different factors that affect the profile of the central peak and hence the ability to properly remove it. This section examines these in more detail, using the parameters as indicated in Table 4.1, unless otherwise stated.

Table 4.1: Parameters used in simulations for the discussion of central peak profiles.

Layer strength, $\int C_N^2(h)dh$	1×10^{-14} m$^{1/3}$
Altitude above measurement plane, h	10 km
Telescope diameter, D_T	1 m
Zenith, ζ	0°
Separation, ϕ	10 arcseconds
Magnitude difference, Δm	1
Spatial sampling, Δr	1/128 m/pix
Wavelength, λ	589 nm

4.5.1 Pixelisation of Covariance Data

Each pixel across the aperture image represents a physical distance defined by the spatial sampling, Δr. Δr is determined by the field lenses used in the SCIDAR instrument, and it has a significant impact on the level of pixelisation in a 2D spatial covariance matrix. A smaller Δr will have less pixelisation which will minimise the difference between slices taken at different angles.

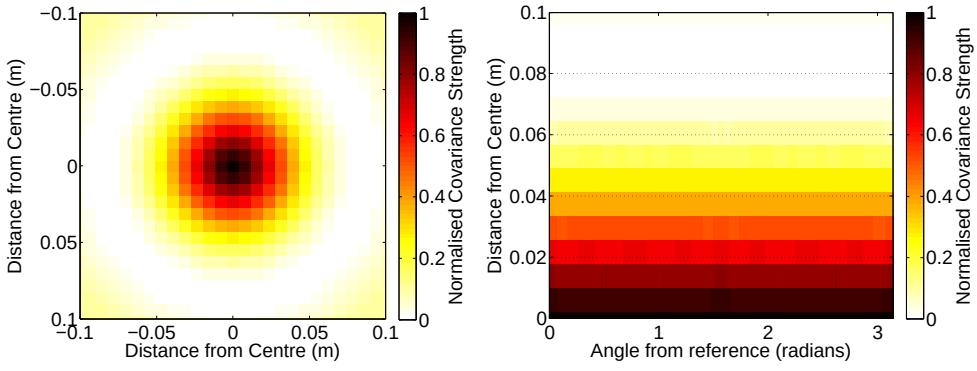

(a) 2D Covariance (b) Polar Coordinates

(c) Extracted Slice $\Delta r = 1/128$ m/pix (d) Extracted Slice $\Delta r = 1/512$ m/pix

Figure 4.13: Residual peak information will result during slice extraction due to pixelisation of a covariance profile. (a) 2D spatial covariance of a single star from a layer at 10 km above the measurement plane in cartesian coordinates and (b) polar coordinates. Covariance strengths have been normalised between zero and one. (c) For $\Delta r = 1/128$ m/pix, the maximum residual covariance strength is 0.0183. (d) For $\Delta r = 1/512$ m/pix, the maximum residual covariance strength is decreased to 0.0025.

Consider a 2D covariance containing only the central peak (i.e. single star covariance) for a layer located at 10 km above the measurement plane with covariance strength normalised between zero and one. Figure 4.13(a) shows cartesian coordinates and Figure 4.13(b) shows polar coordinates when using $\Delta r = 1/128$ m/pix. If an extracted profile of the peak at a given angle was subtracted from an extracted reference profile then a residual covariance strength is found due to pixelisation. The maximum residual strength for $\Delta r = 1/128$ m/pix is 0.0183 (Figure 4.13(c)) and could be decreased with smaller Δr (0.0025 for $\Delta r = 1/512$ m/pix, Figure 4.13(d)). When extending this pixelisation concept to full triplet profiles any residual central peak information could be interpreted as a secondary peak resulting from a strong low altitude layer, particularly when secondary peaks are located in close proximity to the central peak.

Figure 4.14 shows the extracted slices and $C_N^2(h)$ profile estimates for a simulated profile using α Cen ($\phi = 10$ arcseconds, $\Delta m = 1.3$, Epoch 2007) and α Cru ($\phi = 4$

Table 4.2: The altitude and turbulence strength of layers present in a simulated profile.

Layer Altitude (km)	$\int C_N^2(h)dh$ ($m^{1/3}$)	$r_0(\lambda = 589\text{nm})$ (cm)
0	3×10^{-12}	5.06
5	1×10^{-13}	38.95
10	3×10^{-13}	20.15
Full Profile	3.4×10^{-12}	4.69

arcseconds, $\Delta m = 0.3$, Epoch 2007). The altitudes and strengths of the layers used are tabulated in Table 4.2. For both simulations, Δr was set to 1/128 m/pix and d was -3 km below the aperture, utilising an ideal spatial covariance profile.

For α Cen (Figures 4.14(a) and 4.14(b)), the secondary peaks are spaced far enough away from the central peak such that residual covariance peaks are negligible compared to the strengths of the NGT and 10 km layers. The estimated r_0 from the profile is 4.7 ± 0.1 cm, which is the expected value for the full profile. For α Cru, the secondary peak from the NGT layer becomes merged with the central peak (Figure 4.14(c)). As a result the extracted slice contains a region affected by residual peak information due to pixelisation. This results in a false layer detected at 2 km below ground (Figure 4.14(d)). The false layer is approximately a third of the strength of the NGT layer and significantly lowers the r_0 estimate based on the profile to 3.96 ± 0.02 cm. If the $C_N^2(h)$ estimate was truncated to exclude the false layer, then the revised r_0 estimate becomes 4.69 ± 0.02 cm.

Avila et al. (2001) suggest that the non-zero values occurring near the measurement plane are due to the inversion process, which is very sensitive to noise because scintillation is proportional to $h^{5/6}$. Hence results within $\sim$ 1 km of the measurement plane could be incorrect. The above simulation supports this argument. However the non-zero values do not result from the inversion process alone, but rather from the slice extraction containing residual peak information due to pixelisation. The simplest solution is to truncate the $C_N^2(h)$ profiles obtained below a certain distance from the measurement plane. As suggested by *Avila et al.* (2001), 1 km from the measurement plane should be considered as unreliable. However in some circumstances truncating data at 1 km may not be appropriate.

For generalised SCIDAR data, $C_N^2(h)$ profile estimates could easily be truncated to exclude any layer detected below ground due to pixelisation. Any turbulence detected below ground are clearly false. However for pupil-plane data there is no clear point where data are obviously false. Turbulence that exists within the first few kilometers will be detected in pupil-plane data, albeit weakly. It is impossible to know exactly how much of the calculated $C_N^2(h)$ strength is from the true layer and how much is related to residual central peak. To decide at what height above the measurement plane the data

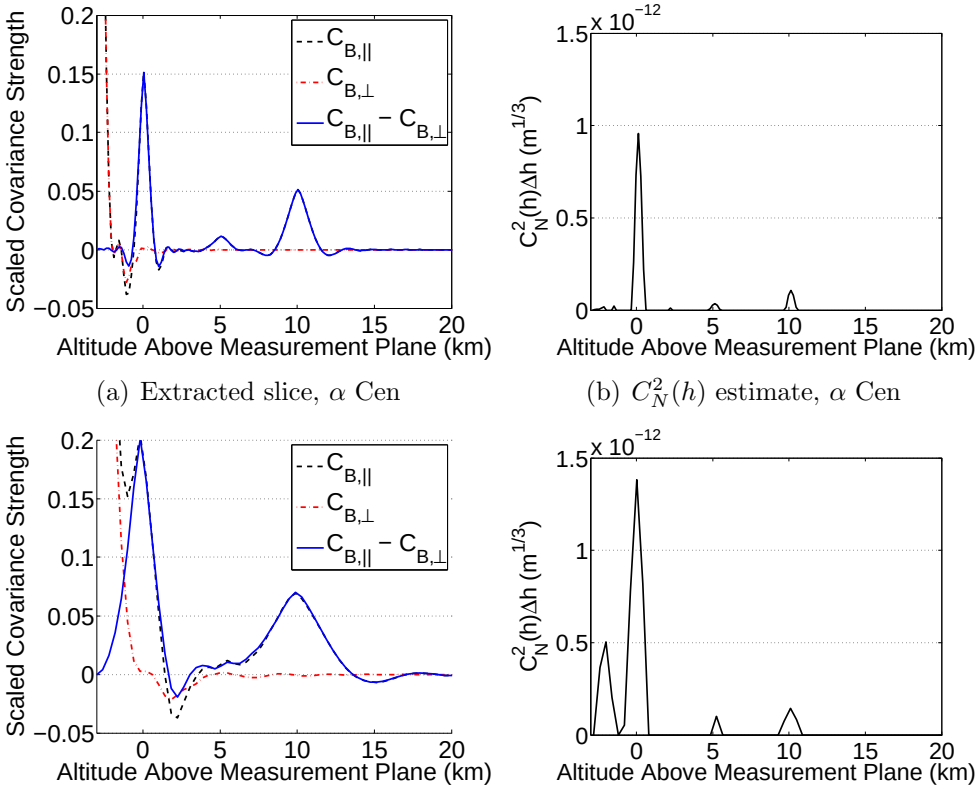

(a) Extracted slice, α Cen (b) $C_N^2(h)$ estimate, α Cen

(c) Extracted slice, α Cru (d) $C_N^2(h)$ estimate, α Cen

Figure 4.14: Extracted slices and $C_N^2(h)$ profile estimates for a simulated turbulence structure using α Cen and α Cru as the observable. (a) The profile resulting from α Cen contains secondary peaks far enough away from the central peak such that residual peak information is negligible and (b) has little effect on the $C_N^2(h)$ profile. (c) With a decreased ϕ (i.e. α Cru), the secondary peaks merge with the central peak. (d) The resulting residual peak information may result in a strong false layer detected near the measurement plane.

should be truncated, it is important to understand what other factors, besides pixelisation, influence the profile of the central peak. Parameters such as the layer altitude above the measurement plane, h, and the binary system separation, ϕ, have the greatest impact on the shape of the central peak. Other factors such as the strength of the layer, as measured by $\int C_N^2(h)dh$, and the magnitude difference between stellar companions, Δm, will have an impact on the effective removal of the central peak when multiple layers are present.

4.5.2 Altitude Sampling in Covariance Data

When multiple layers are present the lower altitude layers may have secondary peaks that blend with the central peak resulting from higher layers, demonstrated in Figure 4.14(c). The likelihood of this happening depends on the altitude sampling used, which is a function of the spatial sampling of the telescope aperture, Δr, and the binary star system separation, ϕ. From Chapter 2, the spatial altitude sampling, Δh, is defined by

$$\Delta h = \frac{\Delta r}{\phi \sec \zeta}, \tag{2-32}$$

where ζ is the angle of the telescope from zenith in radians. In addition the maximum altitude that can be measured, $h_{\max}$, is

$$h_{\max} \approx \frac{D_{\mathrm{T}}}{\phi}, \tag{2-33}$$

for a telescope with an aperture diameter of D_{T}.

For a 1-m telescope, the largest ϕ that can be used to detect a layer at 10 km above the measurement plane is 20.6 arcseconds. For $\Delta r = 1/128$ m/pix, $\Delta h \approx 81$ m/pix for measurements at zenith. However for ϕ of 2 arcseconds, $\Delta h \approx 800$ m/pix and $h_{\max} \approx 100$ km. The width of the central peak remains constant regardless of ϕ for a 10 km layer with respect to the number of pixels (Figure 4.15(a)). However when the number of pixels is related to altitude above the measurement plane, then the width of the central peak narrows with increasing ϕ, due to the relationship of Δh with ϕ (Figure 4.15(b)). For binary systems with a small separation the width of the central peak resulting from a strong high altitude layer can be wide enough to obscure any turbulent activity happening in the low- to mid-altitude range. When ϕ is 4 arcseconds (i.e. α Cru) any secondary peaks from turbulence located up to 3.5 km above the telescope could blend with the central peak from a layer located at > 10 km. When ϕ is 14 arcseconds (such as α Cen in 2003) any secondary peaks from turbulent layers located < 1 km could blend with the central peak.

Regardless of telescope angle from zenith (Figure 4.16(a)), ζ, the width of the central

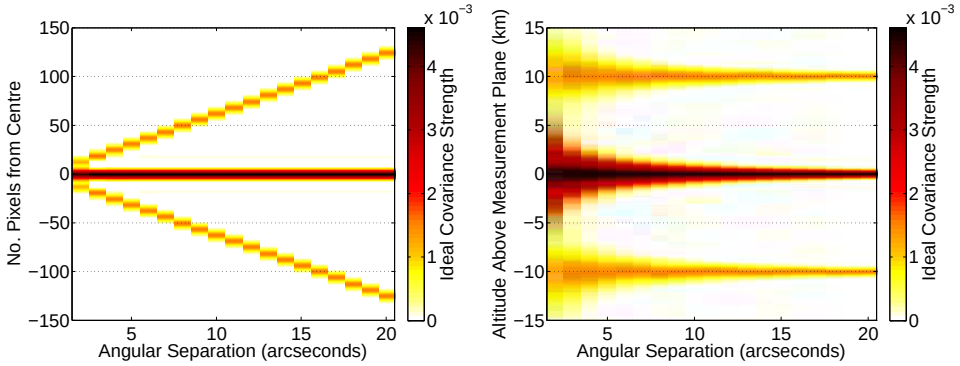

(a) Profile in no. pixels (b) Profile in altitude

Figure 4.15: The effect of angular stellar separation, ϕ, on the profile of the spatial covariance triplet. ϕ ranges from 2 to 20 arcseconds. Other simulation parameters are detailed in Table 4.1. (a) The width of the peaks is constant with respect to the number of pixels from the centre. (b) The width of peaks narrows as separation increases with respect to the altitude above the measurement plane.

peak remains constant with respect to the number of pixels. However the widths of the peaks narrow slightly with increasing ζ with respect to the altitude above the measurement plane (Figure 4.16(b)). Over the range that SCIDAR measurements are typically taken (i.e. $\leq 30°$, *García-Lorenzo and Fuensalida* (2006b)) the variation in width can be considered negligible as variation is limited to the range specified by Δh. If larger zenith angles were used then these variations should be considered.

UC-SCIDAR (V2005 and V2007) was designed to utilise $\Delta r \approx 1/127$ m/pix for a 1-m telescope with focal ratio of $F/13.5$. Slight operational variations occur due to the physical vertical position of the secondary mirror with respect to the focal plane. The position of the secondary mirror has the greatest influence on the size of generalised images, for which Δr ranged from 1/90 to 1/140 m/pix. This corresponds to a Δh range of $\sim$ 230 to $\sim$ 150 m for the simulation in Figure 4.17. The width of a central peak increases slightly with decreasing Δr, because of the number of pixels the peak occupies. However when converted to altitude above the measurement plane the variations seen in peak widths are negligible and can be attributed to the error due to pixelisation. This is due to the seen decrease in Δh.

The height of a turbulent layer, h, above the measurement plane not only affects the covariance strengths of the triplet profile but also the widths of the measured peaks. Consider scintillation captured on a 1-m telescope using the parameters in Table 4.1. With an increasing turbulent layer height for a constant layer strength both the measured covariance strength and widths of the peaks increase (Figure 4.18). Note that h does not change Δh. Hence any increase seen in the pixel width will also be seen as an increase

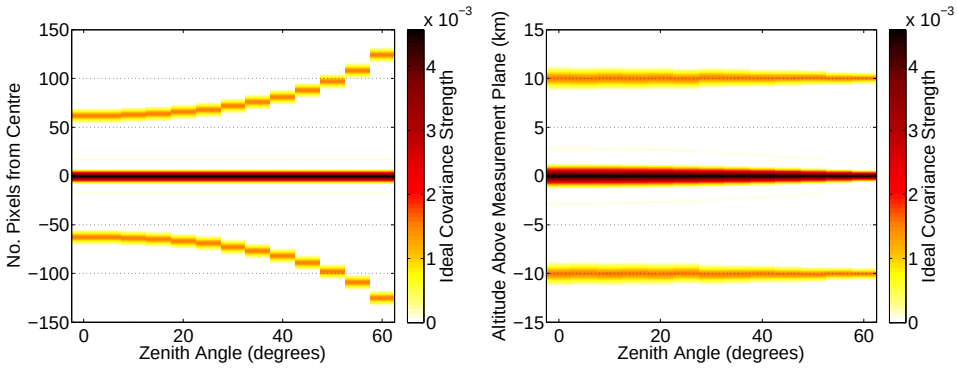

(a) Profile in no. pixels (b) Profile in altitude

Figure 4.16: The effect of telescope angle from zenith, ζ, on the profile of the spatial covariance triplet. Simulation parameters are detailed in Table 4.1. (a) The centre the width of the peaks is constant with respect to the number of pixels. (b) The peaks narrow slightly as ζ increases with respect to the altitude above the measurement plane.

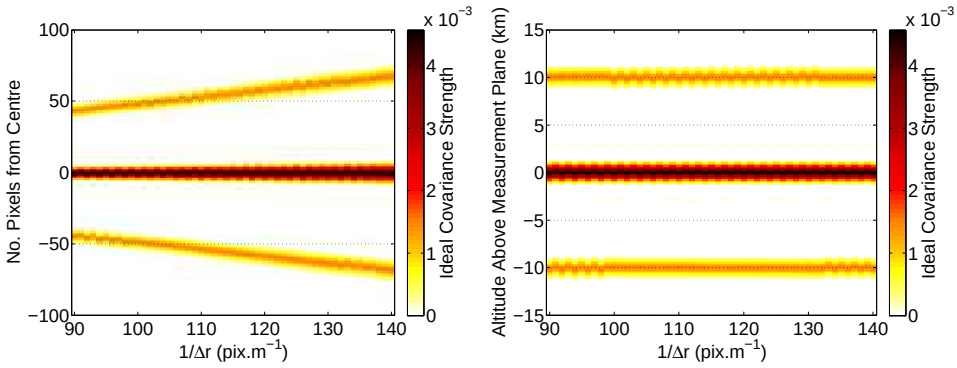

(a) Profile in no. pixels (b) Profile in altitude

Figure 4.17: The effect of spatial sampling, Δr, on the profile of the spatial covariance triplet. Simulation parameters are detailed in Table 4.1. (a) The width of the central peak widens slightly with decreasing Δr with respect to the number of pixels from the centre. (b) Variations of the peak widths are negligible with respect to the altitude above the measurement plane because of the slight widening is compensated for by the decrease in Δh.

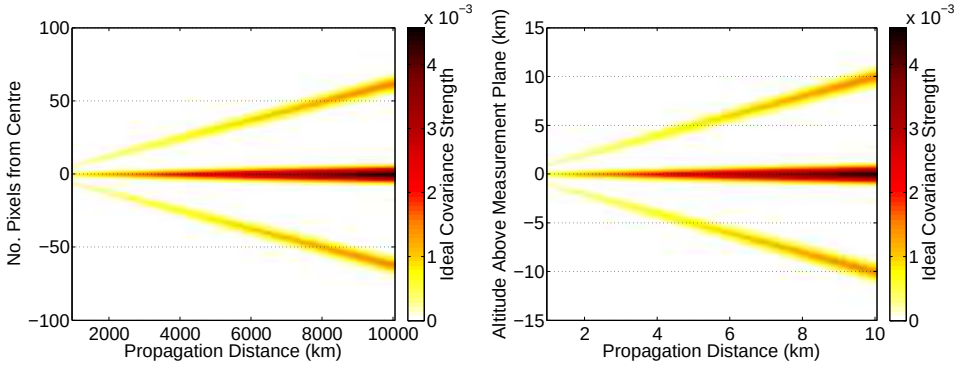

(a) Profile in no. pixels (b) Profile in altitude

Figure 4.18: Ideal triplet profiles for various turbulent layer heights, h, above the measurement plane with a constant $\int C_N^2(h)dh$. Other simulation parameters are detailed in Table 4.1. The width of the peaks increase with h. Note Δh remains constant so any increase in (a) pixel width will also be seen as an increase in (b) altitude.

in altitude width. For a fixed layer height with increasing layer strength, $\int C_N^2(h)dh$, the widths of the triplet peaks remain unchanged (Figure 4.19).

Note that the magnitude difference between binary star companions, Δm, does not impact on altitude sampling and hence the width of the profile from individual layers remains constant. Δm only impacts on the relative strengths of the peaks, as does $\int C_N^2(h)dh$. This will affect the shape of the central peak profile when multiple layers are considered.

4.5.3 Data Truncation

Data truncation will always be a trade-off between retaining valid data and filtering out false data. To ensure that there is consistency in applying data truncation one must consider how to determine where to apply truncation. Figure 4.20(a) shows an ideal central peak profile for a single layer located at 10 km above the measurement plane. The ideal profile follows an Airy disc profile with a main peak and many successive but weaker peaks. The positions of first maximum, minimum and zero point (i.e. the point where the covariance strength is zero) are indicated. Figure 4.20(b) shows how the position of these points change as the height of the turbulent layer increases. The central peak width remains constant when profiling with respect to the number of pixels from the centre for ϕ and ζ.

Ideally the point of first maximum would be used to define the level of truncation. This ensures that secondary peaks from weak low altitude layers are far enough removed from the central peak to make it unlikely residual central peak information is used in the $C_N^2(h)$ estimation. For a single layer at 10 km, the first maximum occurs at 18

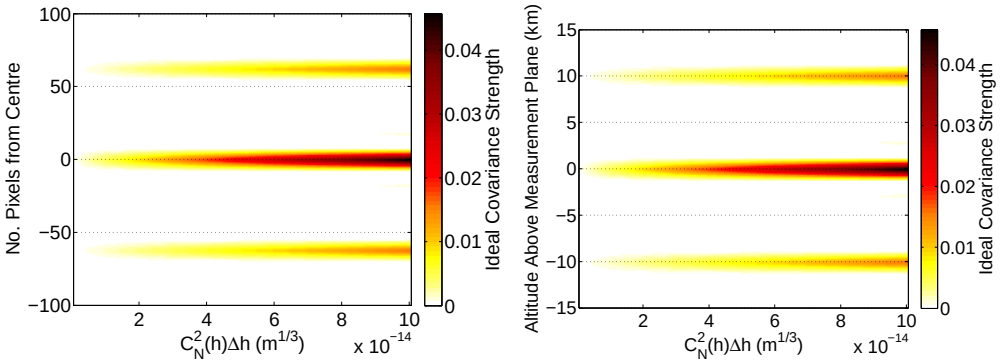

(a) Profile in no. pixels (b) Profile in altitude

Figure 4.19: Ideal triplet profiles for various turbulence strengths, $\int C_N^2(h)dh$, for a constant h above the measurement plane. Other simulation parameters are detailed in Table 4.1. The width of the central peak remains constant with respect to both (a) the number of pixels and (b) the altitude.

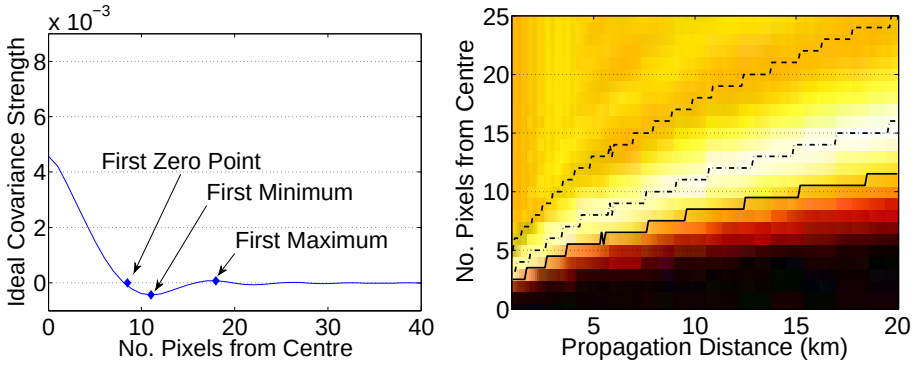

(a) Layer at 10 km (b) Various h above measurement plane

Figure 4.20: Ideal central peak profile for a single layer indicating the first maximum, minimum and zero point. (a) Layer located at 10 km above the measurement plane. (b) Various propagation distance h. Positions of (- - -) first maximum (- · - ·) first minimum and (—) zero point are indicated.

pixels from the centre pixel. When $\phi = 10$ arcseconds this equates to 2.9 km above the measurement plane. At MJUO, experience shows that truncating pupil-plane data to > 3 km would remove layers attributed to NGT and/or low weather systems. These altitudes can be successfully measured by generalised SCIDAR data. For generalised SCIDAR, a truncation of 3 km above the measurement plane would remove any falsely detected layers below ground as UC-SCIDAR was designed to utilise a defocus distance of 3.9 km below the telescope.

With decreasing ϕ, the altitude sampling, Δh, increases. For $\phi = 4$ arcseconds, 20 pixels equates to 8.0 km above the measurement plane. For UC-SCIDAR, it would not be realistic to truncate the first 8.0 km of data as experience shows that this would remove the majority of the $C_N^2(h)$ profile estimated. If one was to use the first zero point, located at 9 pixels for a 10 km layer, then a truncation of 3.6 km and 1.4 km would be required for $\phi = 4$ and 10 arcseconds respectively.

Up to this point the discussion has been based on a single layer of turbulence. A more realistic profile includes a combination of NGT and mid- to high-altitude turbulence. Figure 4.21 shows the ideal central peak profiles that equate to various layer combinations for the layers detailed in Table 4.2. The defocus distance used in simulations is 3 km. The positions of the first maximum, minimum and zero point in terms of pixels are indicated in Table 4.3. Given a Δh of 400 m and 160 m for $\phi = 4$ and 10 arcseconds respectively, the equivalent heights above the measurement plane are indicated in Table 4.4.

For a profile that uses only the 5 km and 10 km layers (i.e. a pupil-plane type profile) the first maximum, minimum and zero point occurs at 20, 12 and 9 pixels. As discussed above the use the first zero point would be preferred as this equates to 3.6 km for α Cru. However in some circumstances the first zero point occurs after the first maximum. Consider a profile which incorporates a NGT and 10 km layer. Due to the relative strengths of the central peaks of the individual layers, for α Cru the first zero point occurs at 10 pixels (4 km) where the first maximum occurs at 8 pixels (3.2 km). Hence the use of the first zero point is not suitable.

Let us examine truncation as specified by the first minimum. Consider run #15 from June 2005. This run was captured using the V2005 system on 13 June 2005 using α Cru with an exposure time of 1.5 ms. Figure 4.22 shows the pupil-plane and generalised $C_N^2(h)$ profiles obtained. When no truncation is applied to the pupil-plane data (Figure 4.22(a)) the resulting $C_N^2(h)$ profile contains strong low altitude turbulence. The estimated r_0 is 18.3 ± 0.6 cm. Truncating by the first minimum of the central peak profile removes the first 4 km of the profile (Figure 4.22(b)), increasing the estimated r_0 to 30.9 ± 1.0 cm.

Figure 4.22(c) shows the generalised $C_N^2(h)$ profile obtained without truncation with a defocus distance of -3.4 km. The profile shows layers below ground, which are clearly

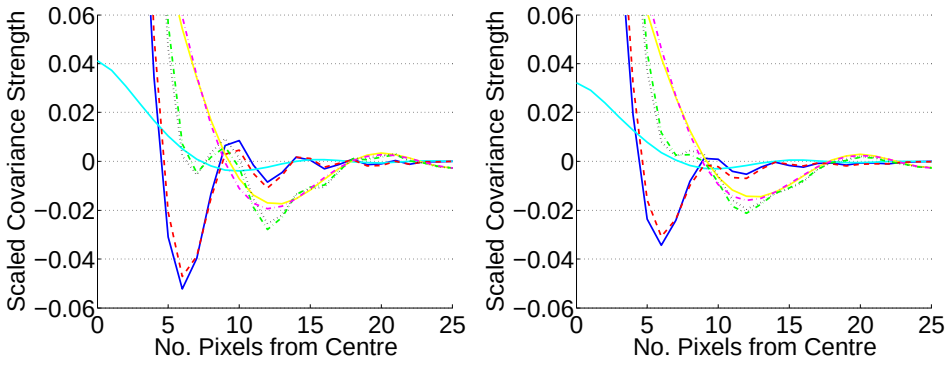

(a) α Cen (b) α Cru

Figure 4.21: Ideal perpendicular slices indicating the effects of multiple layers on the profile of the central peak. (a) Simulations using $\phi = 10$ arcseconds and $\Delta m = 1.3$. (—) NGT layer only. (—) 5 km layer only. (—) 10 km layer only. (- - -) NGT and 5 km layers. ($\cdots$) NGT and 10 km layers. (- · - ·) NGT, 5 km and 10 km layers. (- · - ·) 5 km and 10 km layers. (a) Simulations using $\phi = 4$ arcseconds and $\Delta m = 1.0$. Other simulations parameters are based on Table 4.1.

Table 4.3: Number of pixels from the centre of the central peak to the first maximum, minimum and zero point for the various curves shown in Figure 4.21.

	First Maximum		First Minimum		First Zero Point	
Layers	α Cen	α Cru	α Cen	α Cru	α Cen	α Cru
NGT only	10	9	6	6	5	5
5 km only	16	15	10	10	8	8
10 km only	20	20	13	13	9	9
NGT + 5 km	10	9	6	6	5	5
NGT + 10 km	9	8	7	7	7	10
NGT + 5 km + 10 km	9	8	7	7	7	9
5 km + 10 km	20	20	12	12	9	9

Table 4.4: Distance above the measurement plane to the first maximum, minimum and zero point for the various curves shown in Figure 4.21. Numbers shown are in km.

	First Maximum		First Minimum		First Zero Point	
Layers	α Cen	α Cru	α Cen	α Cru	α Cen	α Cru
NGT only	1.6	3.6	1.0	2.4	0.8	2.0
5 km only	2.6	6.0	1.6	4.0	1.3	3.2
10 km only	3.2	8.0	2.1	5.2	1.4	3.6
NGT + 5 km	1.6	3.6	1.0	2.4	0.8	2.0
NGT + 10 km	1.4	3.2	1.1	2.8	1.1	4.0
NGT + 5 km + 10 km	1.4	3.2	1.1	2.7	1.1	3.6
5 km + 10 km	3.2	8.0	1.9	4.8	1.4	3.6

false layers resulting from residual central peak information. Truncating by the first minimum results in the first 2.4 km of the profile being removed, removing the false peak (Figure 4.22(d)).

Although the level of truncation used in the pupil-plane analysis removed a significant portion of the low altitude $C_N^2(h)$ profile, by combining the analysis with the corresponding generalised $C_N^2(h)$ profile, the full profile can be obtained.

Unfortunately when truncation, as specified by the first minimum of the central peak profile, was applied generically across all data collected by UC-SCIDAR (V2005 and V2007), truncation resulted in a null profile or an inappropriate truncation level for generalised measurements, in a significant number of cases.

Figure 4.23 shows the $C_N^2(h)$ profiles obtained from a simultaneous pupil-plane and generalised SCIDAR run collected on 3 May 2007 (pupil-plane: run #231; generalised: run #230) using α Cen at an exposure time of 2 ms. In the pupil-plane $C_N^2(h)$ profile (Figure 4.23(a)), an exceptionally strong near ground layer is detected, resulting in an r_0 estimate of 23 ± 2 cm. Application of first minimum truncation results in the removal of the first 5 km of the profile (Figure 4.23(b)), increasing r_0 to 33 ± 3 cm.

The generalised $C_N^2(h)$ profile used a defocus distance of -2.3 km and did not result in a false peak (Figure 4.23(c)), estimating r_0 to be of 5.4 ± 0.1 cm. Defocus distance for this run was -2.3 km. Applying first minimum truncation removed everything below 3 km above the site (Figure 4.23(d)), resulting in an r_0 estimate of 32.8 ± 0.9 cm. This is clearly incorrect as all low level turbulence is removed from both pupil-plane and generalised analysis.

The above example was collected using α Cru, which from simulation is prone to near ground layer secondary peaks merging with the central peak due to the resulting Δh. Issues with truncation are not restricted to α Cru data.

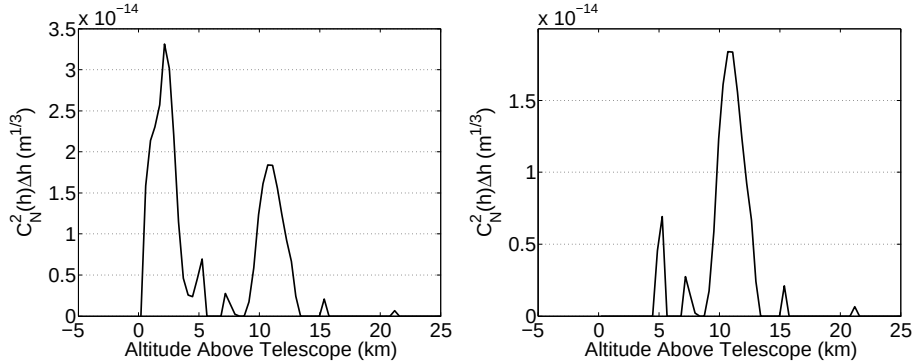

(a) Pupil-plane $C_N^2(h)$ profile without truncation

(b) Pupil-plane $C_N^2(h)$ profile with truncation

(c) Generalised $C_N^2(h)$ profile without truncation

(d) Generalised $C_N^2(h)$ profile with truncation

Figure 4.22: $C_N^2(h)$ profiles obtained from run #15 from June 2005. Data was taken using α Cru with an exposure time of 1.5 ms. If no level of truncation is applied then (a) the pupil-plane profile indicates an exceptionally strong low altitude layer and (c) the generalised profile contains a peak that is located below ground. Application of truncation to the first minimum of the central peak profile (b) removes the low altitude turbulence from the pupil-plane profile and (d) removes the false layer peak from the generalised profile. Altitudes shown are above ground.

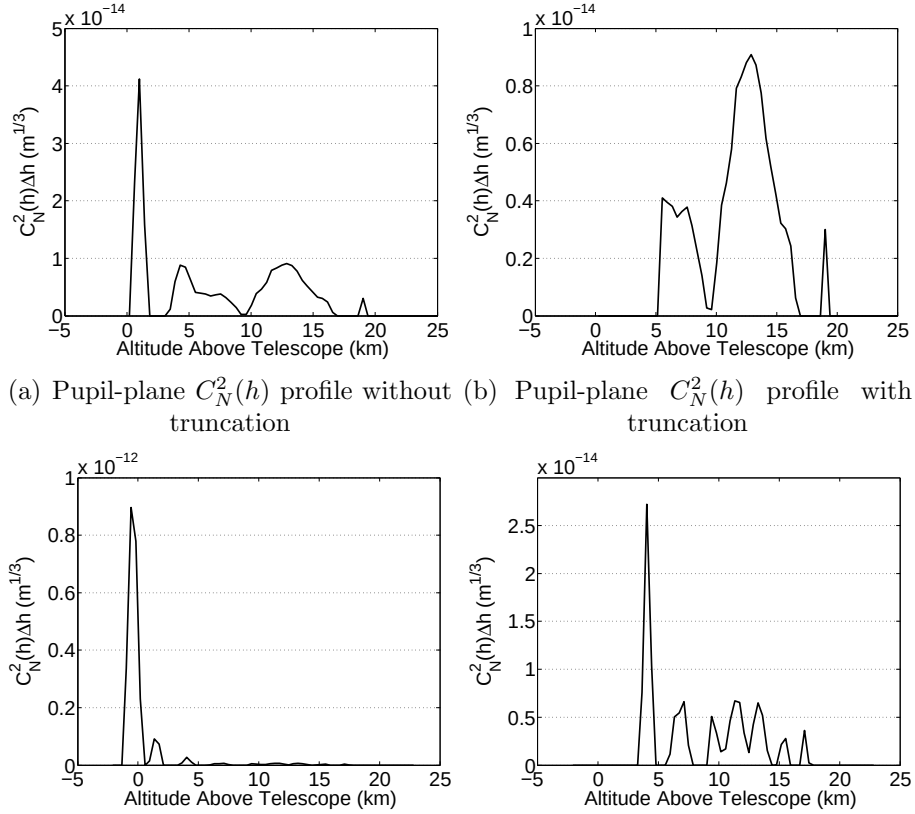

(a) Pupil-plane $C_N^2(h)$ profile without truncation

(b) Pupil-plane $C_N^2(h)$ profile with truncation

(c) Generalised $C_N^2(h)$ profile without truncation

(d) Generalised $C_N^2(h)$ profile with truncation

Figure 4.23: $C_N^2(h)$ profiles obtained from a simultaneous pupil-plane and generalised SCIDAR run from May 2007 (Pupil-plane: run #231; Generalised: run #230). Data was taken using α Cru with an exposure time of 2 ms. If no level of truncation is applied then (a) the pupil-plane profile indicates an exceptionally strong low altitude layer (b) which is removed during truncation. (c) The generalised profile in this case does not contain a peak that is located below ground, and hence no truncation is required. (d) However if truncation is applied an unacceptable proportion of the generalised $C_N^2(h)$ profile is removed. Altitudes shown are above ground.

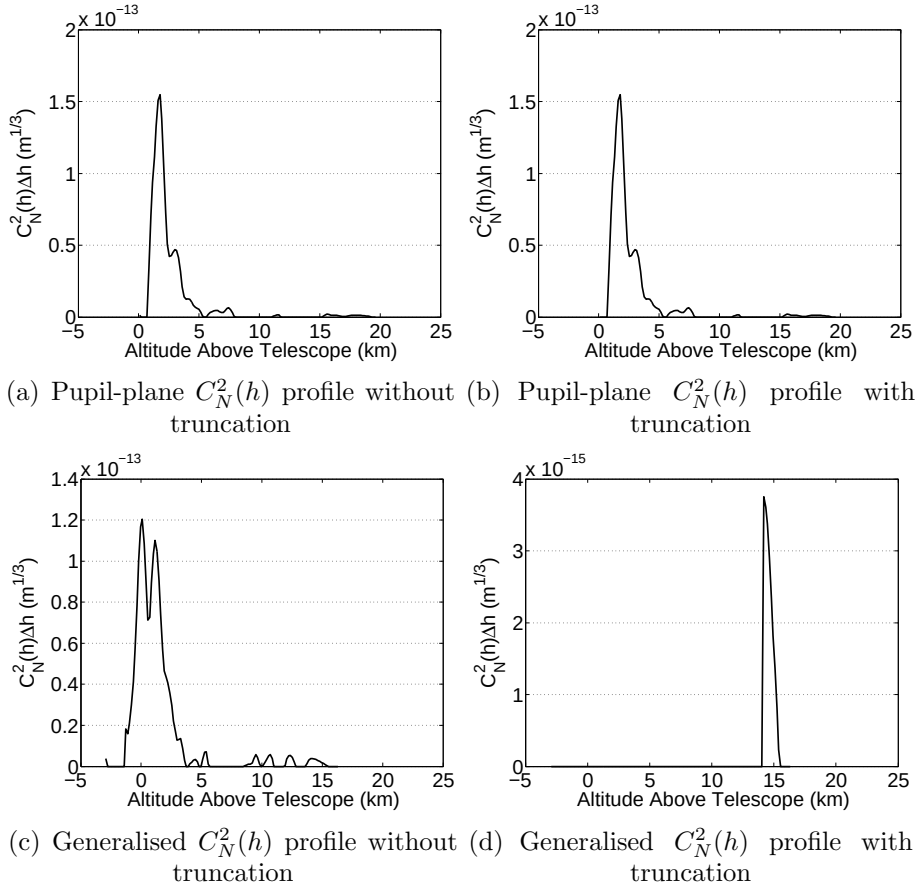

(a) Pupil-plane $C_N^2(h)$ profile without truncation

(b) Pupil-plane $C_N^2(h)$ profile with truncation

(c) Generalised $C_N^2(h)$ profile without truncation

(d) Generalised $C_N^2(h)$ profile with truncation

Figure 4.24: $C_N^2(h)$ profiles obtained from run #29 from July 2005. Data was taken using α Cen with an exposure time of 2 ms. If no level of truncation is applied then (a) the pupil-plane profile indicates an exceptionally strong low altitude layer, (b) however truncation makes no difference to the profile. (c) The generalised profile contains a split near ground peak profile. (d) If truncation is applied a profile with a weak peak at 15 km above the site is obtained. Altitudes shown are above ground.

Figure 4.24 shows the $C_N^2(h)$ profiles obtained from run #29 taken in July 2005. This data was collected using α Cen at an exposure time of 2 ms, during a period of increasing cloud cover. Pupil-plane analysis indicated strong near ground turbulence resulting in an r_0 estimate of 7 ± 2 cm. Truncation did not change the pupil-plane $C_N^2(h)$ profile. Generalised analysis resulted in a splitting of the peak located near ground, with $r_0 = 6.2 \pm 0.2$ cm. Truncation resulted in the removal of the majority of the profile leaving a single peak located at 15 km above the telescope. The estimated r_0 was 98 ± 3 cm, which is clearly incorrect as the 1-m telescope at MJUO does not achieve diffraction-limited imaging.

Due to the inconsistent results from first minimum truncation, it was decided that full profiles would be used for the purposes of trending. Generalised estimates of r_0 values were adjusted by removing any false peaks located below the telescope. For full $C_N^2(h)$

analysis of individual runs see Appendix E.

4.6 Effects of Zenith on Measurements

Stellar objects that are suitable for use with UC-SCIDAR are limited due to the magnitude of the stars required to obtain sufficient signal and the binary separation required to provide adequate altitude sampling. α Cen and α Cru have been successfully used with UC-SCIDAR for the past several years. However these stars are in prime viewing positions for only a fraction of the year. Although there are more stars available for use with the V2007 system, the noise characteristics and system design of the V2005 system limited it to the use of α Cen and α Cru data for trending purposes. Some data was collected at zenith angles, ζ, that are outside the accepted range for use in SCIDAR with $\zeta > 30°$.

During July 2005, a clear calm evening provided the opportunity for measurements to be taken over a period of approximately five hours, using α Cen. The telescope tracked α Cen through a range of ζ, starting at $\sim$20°and moving to $\sim$50°. Observational parameters and key analysis numbers for the sequence of runs taken on July 8, 2005, are summarised in Table 4.5. Each of the runs indicated used UC-SCIDAR V2005, with an exposure time of 1 ms for both cameras. For consistency, all runs were processed using the pre-filtering regime discussed in Chapter 3. A correction factor of $(\sec\zeta)$ has been applied to all error estimates with $\zeta > 30$.

Due to the increased ζ, the altitude sampling, Δh, decreases noticeably during the data sequence. As Δr is constant, being a function of the instrument setup itself, the maximum height of the SCIDAR measurements above the telescope, $h_{\max}$, also decreases. This in itself imposes a limitation on ζ. $C_N^2(h)$ models tend to include a turbulent layer in the tropopause region (*Andrews*, 2004), hence any method used to measure optical turbulence above a site should include this region. The tropopause is nominally at 11 km above sea level, and may vary up to 4 km over mid-latitude regions such as New Zealand (*Sturman and Tapper*, 1996). To ensure that the tropopause is adequately captured, $h_{\max}$ should be limited to values greater than 15km. For the data sequence in Table 4.5, pupil-plane measurements have the required range when ζ is less than 40°. ζ is limited to less than 30° for generalised measurements, where $h_{\max}$ is also restricted by the defocus distance.

Analysis of the effects of ζ on profiles obtained is limited to 14 km and 12 km above the telescope for pupil-plane and generalised measurements respectively, for the remainder of this section.

Examination of the pupil-plane $C_N^2(h)$ profiles (Figure 4.25(a)) reveals thick high-altitude layers ranging from 9 to 12 km with lower layers located at 4 km and 7 km for

Table 4.5: Observational parameters for a sequence of runs taken on July 8, 2005. All runs were taken using α Cen as an exposure time of 1ms. UT is the universal time and HA is the hour angle at the time of observation. A correction factor of $(\sec\zeta)$ has been applied to all error estimates with $\zeta > 30°$.

Run ID	UT	HA	Air Mass	ζ	Δh(m)		$h_{\max}$ (km)		ε_C (%)		$r_0(\lambda = 589\text{nm}, \zeta = 0°)$ (cm)	
				(degrees)	P	G	P	G	P	G	P (< 14km)	G (< 12km)
8	8:57	00:37	1.05	17.8	157	154	20.0	16.7	63	13	21 ± 8	9.0 ± 0.7
9	9:05	00:45	1.05	18.2	156	154	19.9	16.6	68	13	24 ± 9	8.0 ± 0.6
12	9:42	01:22	1.07	20.8	154	152	19.6	16.0	70	14	21 ± 9	8.2 ± 0.6
13	9:50	01:30	1.07	21.5	153	151	19.5	15.9	75	14	22 ± 10	8.7 ± 0.8
15	10:05	01:45	1.09	23.1	151	149	19.3	15.7	70	13	19 ± 8	8.9 ± 0.7
16	10:13	01:58	1.09	23.9	151	148	19.2	15.6	70	16	19 ± 8	8.7 ± 0.9
17	11:29	03:10	1.19	32.5	139	137	17.7	14.4	50	12	20 ± 6	7.9 ± 0.6
18	11:38	03:18	1.20	33.5	137	135	17.5	14.2	70	14	22 ± 8	7.5 ± 0.6
19	11:56	03:36	1.23	35.7	134	132	17.1	14.1	65	13	18 ± 7	7.4 ± 0.6
20	12:04	03:44	1.25	36.7	132	130	16.8	13.9	79	12	21 ± 10	7.9 ± 0.6
21	13:11	04:52	1.40	44.9	117	115	14.9	12.4	45	12	20 ± 5	5.9 ± 0.4
22	13:19	05:00	1.43	45.8	115	113	14.6	12.2	51	11	19 ± 6	7.2 ± 0.5
23	13:36	05:17	1.49	47.8	111	109	14.1	11.7	57	10	22 ± 8	6.6 ± 0.4
24	13:46	05:27	1.52	49.0	108	106	13.8	11.7	65	10	22 ± 9	6.6 ± 0.4

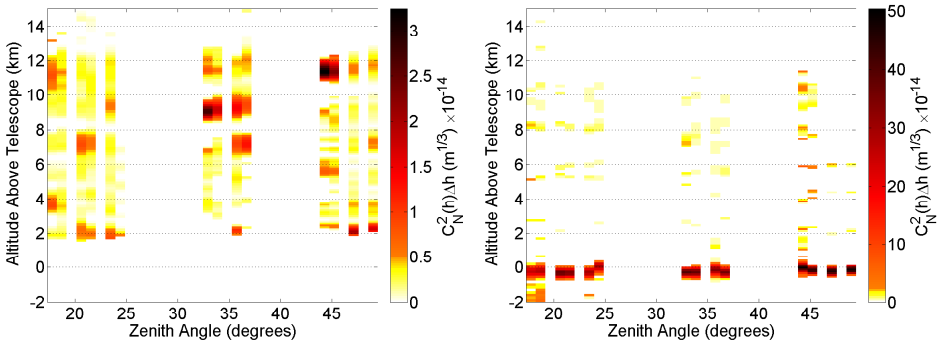

(a) Pupil plane (b) Generalised

Figure 4.25: $C_N^2(h)$ profiles for runs listed in Table 4.5.

ζ less than 30°. Lower peaks could possibly be attributed to residual information due to pixelisation. As ζ increases to ∼35°, the thick high-altitude layer is seen as two layers where a 9 km layer is strong compared to a higher layer seen at 11km. As ζ continues to increase the 9 km and 11 km layer can still be seen, where the 11 km is now the stronger of the two layers. However little other information can be determined as the profiles appear to have a significant amount of ringing noise in the profiles. There is little variation across all pupil-plane measurements with respect to r_0, and can be estimated at $\sim$ 20 cm across the data sequence for r_0 calculated with $\zeta = 0°$.

As expected, generalised $C_N^2(h)$ profiles are dominated by NGT (Figure 4.25(b)). Very little can be determined about the locations of the high altitude layers as the strengths of the layers put them at the noise levels of the profile.

An assumption is made during the SCIDAR analysis that layers move parallel to the ground. Air movement near the ground can also be in the vertical direction due to local geographical features present (*Sturman and Tapper*, 1996). SCIDAR measurements are more likely to see this vertical movement of NGT when using larger ζ. In the analysis, this is exhibited as an increase of NGT layer strength, resulting in a downward trend in the r_0 values for generalised measurements (Figure 4.26).

Data used in the analysis had a gap in time of approximately one hour between runs that used $\zeta < 30°$ and those that had $\zeta \approx 35°$. Over this time frame it is realistic to assume that turbulence profiles will change, however in the high altitude region it is unlikely to change significantly. Hence with the exception of the differences between profiles for the 9km range, this suggests that if data was part of a sequence then data with ζ up to 35° could be included in site trending, providing it is backed up by data taken at $\zeta < 30°$. If there is no supporting data taken at $\zeta < 30°$ within a short-time frame, then data in this range should be considered suspect and not included.

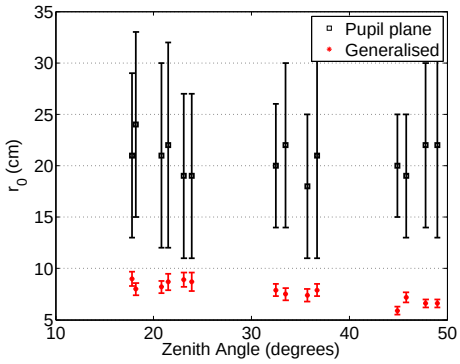

Figure 4.26: Calculated r_0 values for runs listed in Table 4.5.

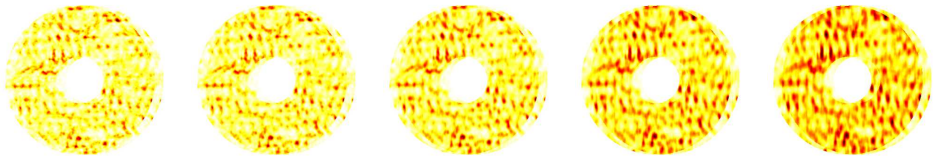

(a) 1 ms (b) 1.25 ms (c) 1.5 ms (d) 1.75 ms (e) 2 ms

Figure 4.27: Simulated scintillation images with increasing exposure time with layer velocity of 4 m/s.

4.7 Effects of Exposure Time

According to Taylor's hypothesis, turbulent structures will move without distortion assuming that the sampling rate is sufficient (*Caccia et al.*, 1987). However over a given exposure time the structures will still move. The resulting image would indicate the average scintillation seen during the exposure time, blurring the turbulence. Figure 4.27 shows this effect on simulated scintillation image where a single layer was moving with a velocity of 4 m/s. The longer the exposure time, the more blurred the image becomes. However the level of blurring is dependent on the speed of the layer. If a layer was moving with a velocity of 12 m/s (Figure 4.28), then the amount of blurring associated with increased exposures would be much worse. The blurred scintillation will result in an underestimated $C_N^2(h)$ strength for a given layer. (Details for the simulation of long exposure scintillation frames are discussed in Appendix F.)

Figure 4.29 shows the $C_N^2(h)$ profiles from a sequence of observations runs taken on 9 July 2005. For all runs, data was collected using α Cen with an altitude sampling $\Delta h \approx 150$ m for both pupil-plane and generalised measurements. From the pupil-plane analysis for an exposure of 1 ms, layers are detected at 2, 4, 6 and 10 km above sea level. The r_0 was found to be approximately 27 cm. In the generalised analysis layers are seen at ground level and at 2 km above sea level. Because the layer at 2 km is seen in both

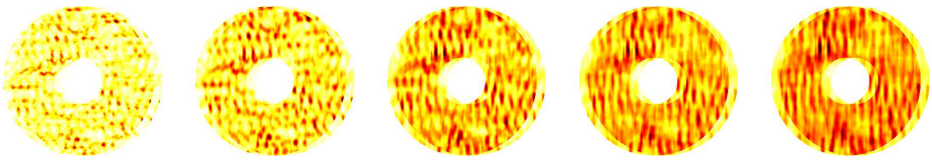

(a) 1 ms (b) 1.25 ms (c) 1.5 ms (d) 1.75 ms (e) 2 ms

Figure 4.28: Simulated scintillation images with increasing exposure time with layer velocity of 12 m/s.

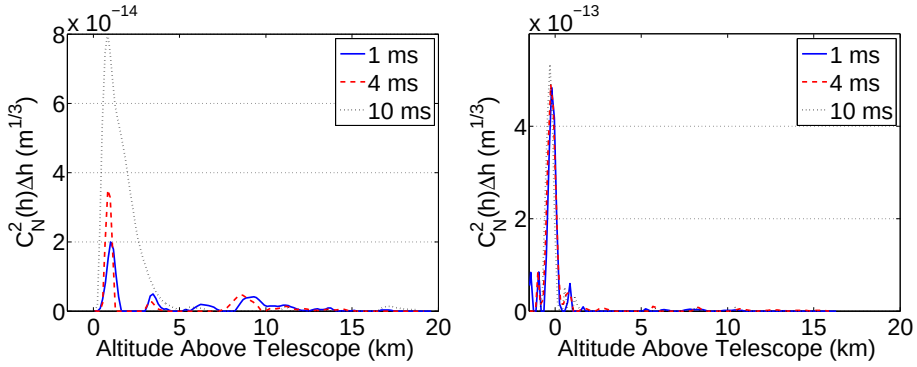

(a) Pupil-plane (b) Generalised

Figure 4.29: The effects of increasing exposure time on $C_N^2(h)$ profiles where $\Delta h \approx 150$ m. Runs shown were taken on 9 July 2005 using α Cen.

pupil-plane and generalised analysis it is highly probable that turbulence is present at this altitude. When an exposure time of 4 ms is used, layer positions in the pupil-plane analysis shift slightly, but little variation is seen in layer strengths for high altitude with the r_0 also found to be approximately 27 cm. As the exposure time continues to increase the layer at approximately 10 km disappears. In addition the profile associated with the low altitude increases dramatically. This will be associated with the blurring that occurs resulting in an increase in residual central peak information, decreasing r_0 to 10 cm. For the generalised data there is little variation that is seen with increasing exposure time, with r_0 estimated to be slightly less than 6 cm in all cases. This is because the majority of NGT is associated with the dome. Dome turbulence will have zero velocity and hence increased exposure times would not blur the resulting scintillation.

Figure 4.30 shows the $C_N^2(h)$ profiles from data collected during July 2004. Data was collected using α Cen with an altitude sampling Δh of 65 m and 80 m for pupil-plane and generalised measurements respectively. When increasing the exposure time from 2 ms to 5 ms, the measured strength for the layer located at 9 km above sea level decreases. At the same time, the strength of the 2 km peak increases. r_0 for an exposure time of 2 ms was found to be approximately 10 cm, which decreased to 9.5 cm for 5 ms. Again this will

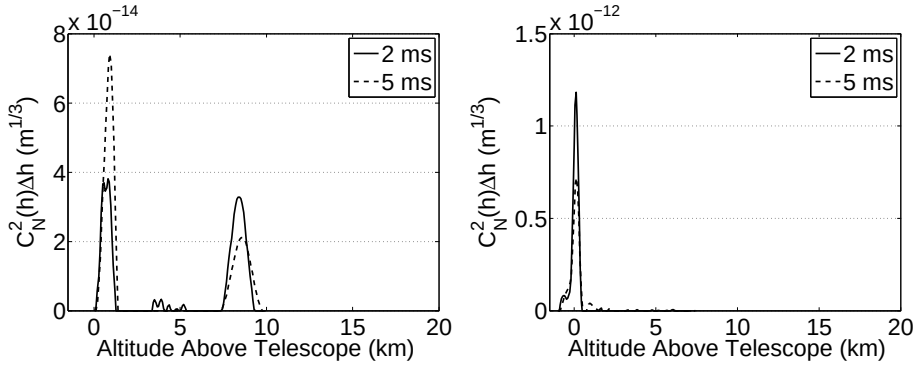

(a) Pupil-plane (b) Generalised

Figure 4.30: The effects of increasing exposure time on $C_N^2(h)$ profiles where pupil-plane $\Delta h \approx 65$ m and generalised $\Delta h \approx 80$ m. Runs shown were taken on 22 July 2004 using α Cen.

be associated with increased blurring resulting in an increase in the residual central peak information. In this case the generalised data also showed a decrease in the near-ground peak. This will be due to the finer altitude sampling used. Turbulence that is located outside of the dome will have a non-zero velocity and hence an increase in the exposure time will blur the scintillation originating from this layer. Although dome turbulence remains unblurred, the finer spatial sampling means that the system used at the time was better able to distinguish between dome turbulence and boundary-layer turbulence.

To limit the blurring effects of exposure time, it was decided to limit profiling analysis to include only those runs with an exposure time of 3.5 ms or less. This would ensure that the scintillation detected was not subject to excessive blurring for layers with a non-zero velocity.

4.8 Profiles in the Presence of Strong NGT

The r_0 estimates obtained using pupil-plane SCIDAR should always be better than that obtained using generalised SCIDAR, as pupil-plane measurements are insensitive to NGT. However when NGT is exceptionally strong, scintillation originating from NGT will still be detectable in pupil-plane measurements, resulting in pupil-plane r_0 estimates that may be less than or approximately equal to those obtained using generalised SCIDAR. This phenomenon occurred with UC-SCIDAR data in the presence of thickening cloud and/or high wind speeds at ground level, resulting in layer strengths that obscured high altitude activity.

Figure 4.31 shows the covariances and $C_N^2(h)$ profiles for run #26 taken on 7 July 2005. This run was taken using α Cru with an exposure time of 2 ms, during a period

of increasing cloud cover with low ground wind speeds. The estimated r_0 values were 5.8 ± 0.2 cm and 6.5 ± 0.1 cm for pupil-plane and generalised measurements respectively. The central peak in the pupil-plane 2D covariance (Figure 4.31(a)) is elongated in the direction of the binary. Any turbulence originating from low altitude layers will result in secondary peaks that will merge with the central peak. This can be seen in the extracted slice in the direction of the binary, $C_{B,\parallel}$, shown in Figure 4.31(c). The resulting slice used for the determination of the $C_N^2(h)$ profile, $C_{B,\parallel} - C_{B,\perp}$, most likely contains significant levels of central peak information. For generalised data, the secondary peaks associated with ground level turbulence results in secondary peaks that are sufficiently removed from the central peak (Figure 4.31(b)). Although the extracted slice used in the determination of the generalised $C_N^2(h)$ profile likely contains residual central peak information, the levels will be small compared to the strength of the NGT layer.

Figure 4.32 shows the covariances and $C_N^2(h)$ profiles from two sequential runs taken on 6 May 2007. Run #422 (UT11:36) was a pupil-plane observation using α Cen with an exposure time of 1 ms. Run #430 (UT11:56) was a generalised observation using α Cen with an exposure time of 1.5 ms. Both runs were taken during a period of increasing cloud cover with rapidly increasing ground wind speeds. The estimated r_0 values were 6.0 ± 1.0 cm and 6.1 ± 0.1 cm for pupil-plane and generalised measurements respectively. As with the above example, the central peak in the pupil-plane 2D covariance (Figure 4.32(a)) is elongated in the direction of the binary, with secondary peaks originating from low altitude turbulence merging with the central peak. For generalised data, the secondary peaks for ground level turbulence are sufficient separated from the central peak (Figure 4.32(b)).

It should be noted that the apparent change in binary direction between Figures 4.31(a) and 4.31(b) and Figures 4.32(a) and 4.32(b) is not only due to the different star used, but also the different systems used at time of acquisition.

For the purposes of trending, in the event of strong NGT where the pupil-plane estimate of r_0 is less than the generalised estimate, then generalised r_0 values are used for pupil-plane averages. This will ensure that the effects of residual peak information are minimised in the monthly averages obtained.

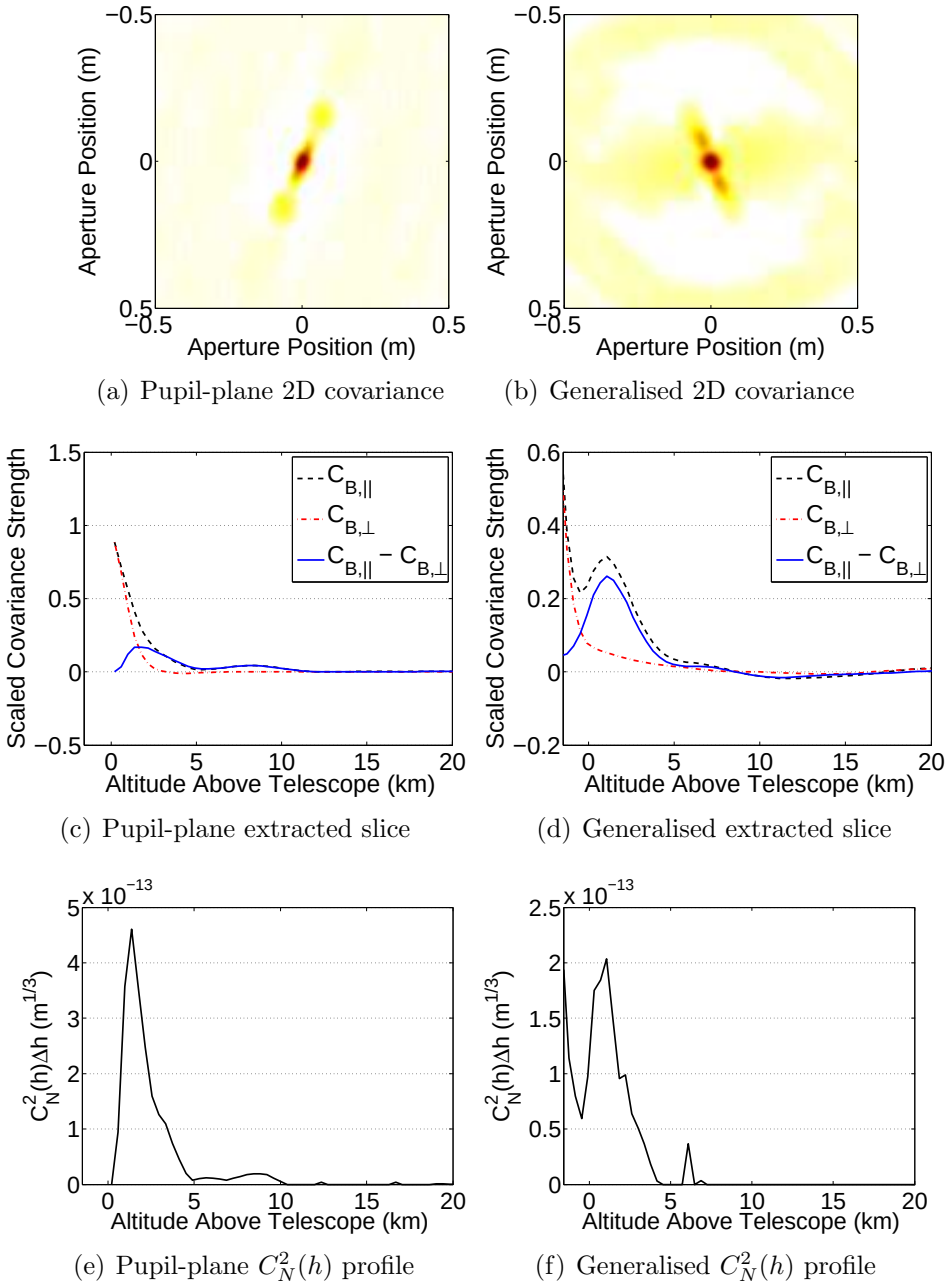

(a) Pupil-plane 2D covariance (b) Generalised 2D covariance

(c) Pupil-plane extracted slice (d) Generalised extracted slice

(e) Pupil-plane $C_N^2(h)$ profile (f) Generalised $C_N^2(h)$ profile

Figure 4.31: Covariances and $C_N^2(h)$ profiles of UC-SCIDAR data in the presence of strong NGT taken during July 2005. The elongation of the central peak seen in the pupil-plane covariance, shown in (a), could contain secondary peaks resulting from low altitude turbulence. As such the extracted slice used in the pupil-plane $C_N^2(h)$ estimate could contain significant amounts of residual peak information. For generalised data, the secondary peaks resulting from ground level turbulence are sufficiently separated from the central peak, shown in (b), reducing the level of residual central peak information. The estimated r_0 values were 5.8 ± 0.2 cm and 6.5 ± 0.1 cm for pupil-plane and generalised measurements respectively.

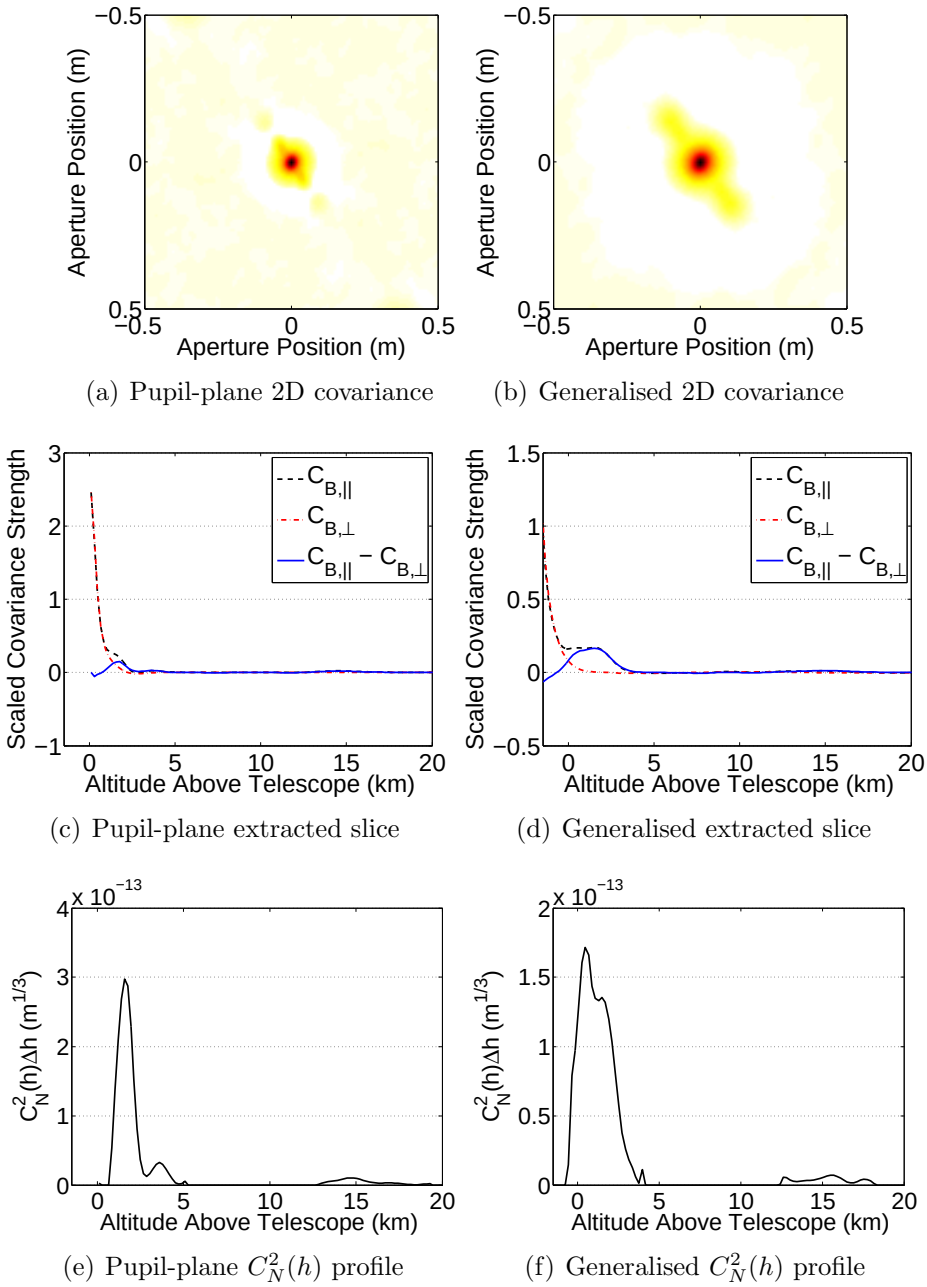

(a) Pupil-plane 2D covariance (b) Generalised 2D covariance

(c) Pupil-plane extracted slice (d) Generalised extracted slice

(e) Pupil-plane $C_N^2(h)$ profile (f) Generalised $C_N^2(h)$ profile

Figure 4.32: Covariances and $C_N^2(h)$ profiles of UC-SCIDAR data in the presence of strong NGT taken during May 2007. The estimated r_0 values were 6.0 ± 1.0 cm and 6.1 ± 0.1 cm for pupil-plane and generalised measurements respectively.

4.9 The $V(h)$ Analysis Techniques and Measured Profiles

The extraction of $V(h)$ profiles from UC-SCIDAR data is presented in Chapter 5.

Full $C_N^2(h)$ analysis for individual runs can be found in Appendix E. Site trending of $C_N^2(h)$ profiles can be found in Chapters 6 and 7.

Chapter 5

Wind Velocity Extraction Technique

While the $C_N^2(h)$ profile provides information about the required spatial sampling for wavefront sensing and the isoplanatic angle over which adequate corrections can be applied, it is the wind velocity profile, $V(h)$, that indicates how fast an adaptive optics system must respond to adequately correct for turbulence induced aberrations. Scintillation frames can be used to infer both $C_N^2(h)$ and $V(h)$ profiles, and both are required as part of an effective adaptive optics system design.

According to Taylor's hypothesis, if the sampling rate (both spatially and temporally) is fast enough then the turbulent elements move without distortion (*Caccia et al.*, 1987). Hence any correlation existing between two scintillation patterns separated in time by Δt will result from turbulent elements carried by the wind. By using the 2D covariance between two scintillation frames taken at time t and $t + n\Delta t$ for $n = 0, 1, \ldots x$, both the turbulence strength and wind velocity of a given layer can be found.

Klückers et al. (1998), *Johnston et al.* (2002) and Chapter 4 discuss in detail how to find $C_N^2(h)$ profiles from SCIDAR images. Little literature exists on finding $V(h)$ from these same images. The first results of simultaneous detection of $C_N^2(h)$ and $V(h)$ were published in *Klückers et al.* (1998). Since then, an interactive CLEAN type algorithm for $V(h)$ estimation was developed (*Avila et al.*, 2001), which in turn led to an automatic wind velocity determination method based on the CLEAN algorithm (*Prieur et al.*, 2004). A more recent $V(h)$ determination approach uses wavelet analysis (*García-Lorenzo and Fuensalida*, 2006b).

Usually SCIDAR $V(h)$ profiling uses generalised plane measurements taken on a 2-m class telescope using an intensified CCD operating at frame rates in excess of 60 Hz. This provides data that contains sufficient signal to readily identify fast and slow moving layers at various altitudes. The low SNR inherent to UC-SCIDAR, and the fact measurements at MJUO were taken primarily on a 1-m telescope at frame rates of 30 and 60 Hz using a standard CCD camera, meant that the standard techniques for $V(h)$ profiling required modification. A technique called *partial triplet analysis* was developed. The resulting algorithm was presented at the Image and Vision Computing New Zealand

(IVCNZ) 2008 Conference (*Mohr et al.*, 2008).

At MJUO, the pupil plane measurements provides better estimations of velocities for mid- to high-altitude layers because of the dominant NGT layers. Generalised measurements are necessary for determination of NGT velocity. Both are required to provided an overall $V(h)$ profile.

Chapter 2 introduced the spatio-temporal covariance function which was simplified to the spatial covariance function in Chapter 4 for use in $C_N^2(h)$ determination. This chapter discusses the steps taken to analyse spatio-temporal covariances from UC-SCIDAR data for $V(h)$ profiling. Section 5.1 expands on the spatio-temporal covariance function for $\Delta t > 0$. Section 5.2 introduces the first steps of the velocity detection algorithm (temporal covariance data conditioning) required for analysis. Section 5.3 looks at Δt limitations and the maximum detectable velocity. Section 5.4 introduces the new approach for analysing temporal SCIDAR data (i.e. partial triplet analysis) with further discussion on the effects of aperture noise. Section 5.5 looks at the remaining steps of the velocity detection algorithm, discussing data validation and proximity of data peaks. Section 5.6 expands on $V(h)$ measurements to include determination of true wind direction found from geometry and telescope motion. Section 5.6.3 discusses error on velocity estimation resulting from telescope motion. Finally, sections 5.7 and 5.8 discuss the effects of long exposures and strong NGT on velocity determination respectively.

Appendix F provides details on how the simulations were generated for this chapter.

5.1 Determination of Temporal Features

The spatial covariance function for a single star, $C_S(\rho)$, as first discussed in Chapter 2, is given by a 2D Fourier transform of the power spectrum of stellar scintillation patterns. The spatial covariance function for a binary star, $C_B(\rho, \phi, 0)$, can be expressed as

$$C_B(\rho, \phi, 0) = \sum_{i=1}^{n} aC_S(\rho) + b\left[C_S(\rho - \phi h_i) + C_S(\rho + \phi h_i)\right], \tag{4-1}$$

where ϕ is the angular separation of the two companions of the binary star. The coefficients a and b are given by

$$a = \frac{1+\alpha^2}{(1+\alpha)^2}, b = \frac{\alpha}{(1+\alpha)^2}, \alpha = 10^{-0.4\Delta m}, \tag{2-22}$$

where Δm is the magnitude difference of the binary star.

Each turbulent layer will have an associated wind velocity. Whether the velocity of a layer is detected depends on a number of factors, including the turbulence strength,

$C_N^2(h)$, of the individual layers, the position of the detected triplet in relation to other triplets and the system aperture.

If a layer at height h_i was moving at a velocity $V(h_i)$, then the scintillation pattern at the measurement plane would move with the same $V(h_i)$. Assuming Taylor's hypothesis applies, i.e. spatio-temporal sampling is such that turbulent elements move without distortion, then two scintillations patterns produced by a single star, but separated by Δt, are physically separated by $V(h_i)\Delta t$ (*Caccia et al.*, 1987). Hence

$$C'_S(\rho, \Delta t) = C'_S(\rho - V(h_i)\Delta t). \tag{2-27}$$

Taylor's hypothesis also suggests that the peak strength at $\Delta t = 0$ remains unchanged for $\Delta t > 0$, such that

$$C'_S(V(h_i)\Delta t) = C'_S(0, 0). \tag{2-28}$$

The spatial covariance function in equation (4-1) can be expanded to a spatio-temporal covariance by incorporating Taylor's hypothesis (*Avila et al.*, 2001)

$$C'_B(\rho, \phi, \Delta t) = \sum_{i=1}^{n} aC'_S(\rho - v) + b\left[C'_S(\rho - v - \phi h_i) + C'_S(\rho - v + \phi h_i)\right], \tag{5-1}$$

where $v = V(h_i)\Delta t$. C'_S will differ slightly from C_S due to the slight de-correlation of scintillation between frames (partial failure of Taylor's hypothesis) and the fluctuations of $V(h_i)$ that may exist over the integration time. This will result in a C'_S that is slightly smaller and wider than C_S. This does not alter the position of the covariance peaks relative to each other. For the purpose of further discussion, it is assumed that $C'_B(\rho, \phi, \Delta t)$ is an equal but shifted version of $C_B(\rho, \phi, 0)$.

Consider a simulated profile outlined in Table 5.1. The spatio-temporal covariance consists of a series of triplets each corresponding to the different turbulent layers. Equation (5-1) simplifies to the spatial covariance function used in $C_N^2(h)$ profiling when $\Delta t = 0$, where the central peaks for each triplet overlap (Figure 5.1(a)). Weak secondary peaks may become obscured by the strength of the overall central peak. As Δt increases, the triplets separate (Figures 5.1(b) and 5.1(c)) and the position of each triplet is shifted from the image origin by $V(h_i)\Delta t$. The strengths of the NGT and 10 km layers make the triplet associated with the 5 km layer difficult to identify even when separated. For large values of Δt (Figure 5.1(d)), the triplets associated with fast moving layers, such as the 10 km layer, are no longer detectable as the resulting shift is greater than the sampled region. For each Δt there is a maximum velocity that can be detected. This is discussed further in section 5.3.

To obtain the full $V(h)$ profile it is necessary to take temporal covariances with at

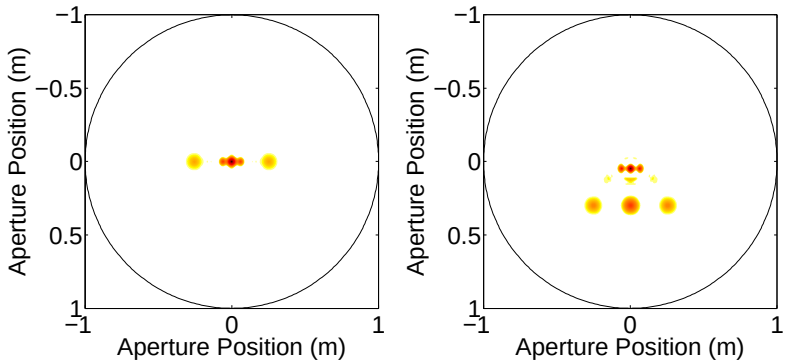

(a) $\Delta t = 0$ ms (b) $\Delta t = 1$ ms

(c) $\Delta t = 16.7$ ms (d) $\Delta t = 33.3$ ms

Figure 5.1: Effect of Δt on simulated spatio-temporal covariances. (a) The triplets are overlapped in the spatial covariance ($\Delta t = 0$). ((b) and (c)) With increasing Δt the triplets separate in accordance with $V(h_i)\Delta t$, however weak layers may be masked by stronger layers. (d) Fast moving layers will not be detectable for large Δt, as the triplet no longer appears within the aperture.

Table 5.1: The altitude, strength and velocity of layers present in a simulated profile.

Layer Altitude (km)	$\int C_N^2(h)dh$ ($m^{1/3}$)	$r_0(\lambda = 589\text{nm})$ (cm)	Wind Speed (m/s)
0	3×10^{-12}	5.06	5
5	1×10^{-13}	38.95	12
10	3×10^{-13}	20.15	30
Full Profile	3.4×10^{-12}	4.69	

least two different Δt values. Typically the time difference required to sample fast moving high altitude velocities, Δt_{high}, is in the order of 10 - 20 ms (*Klückers et al.*, 1998). The time difference required for slow moving low altitude layers, Δt_{low}, is significantly longer. Using multiple Δt in temporal SCIDAR analysis is not only necessary to capture fast moving versus slow moving layers, but also provides an added check for layers moving at similar velocities.

In the above simulated example the 5 km layer was masked by the strength of the other two layers. This phenomenon is common in real data and hence it is necessary to devise a means to detect the location of weak layers amongst strong layers. Figure 5.2 outlines the main steps used to determine wind velocity using the UC-SCIDAR algorithm. The spatio-temporal covariance data is obtained using the covariance algorithms outlined in Appendix D. Further data conditioning is then applied to the covariance data by way of aperture normalisation and thresholding for background scintillation noise. Section 5.2 addresses the data conditioning of the temporal covariance data, while the remaining steps of the algorithm are discussed in section 5.5. $V(h)$ profiles are extracted from the 2D temporal covariance by way of a user-interactive algorithm.

5.2 Data Conditioning in Temporal SCIDAR

To use spatio-temporal covariance data for $V(h)$ profiling, it is necessary to remove the bias of the covariance toward the aperture and then threshold the data with respect to the background scintillation noise. This is particularly important for data with low SNR, as in the case with data from UC-SCIDAR.

5.2.1 Aperture Normalisation in Temporal SCIDAR

Aperture effects can be normalised by dividing the covariance function of the data signal, $C_B^{\otimes}(\rho, \phi, \Delta t)$ by correlation of the average signal, $(\bar{m} - \bar{n})$, such that

$$C_B(\rho, \phi, \Delta t) = \frac{C_B^{\otimes}(\rho, \phi, \Delta t)}{C_{(\bar{m}-\bar{n})}^{\otimes}(\rho, \phi, \Delta t)}, \tag{5-2}$$

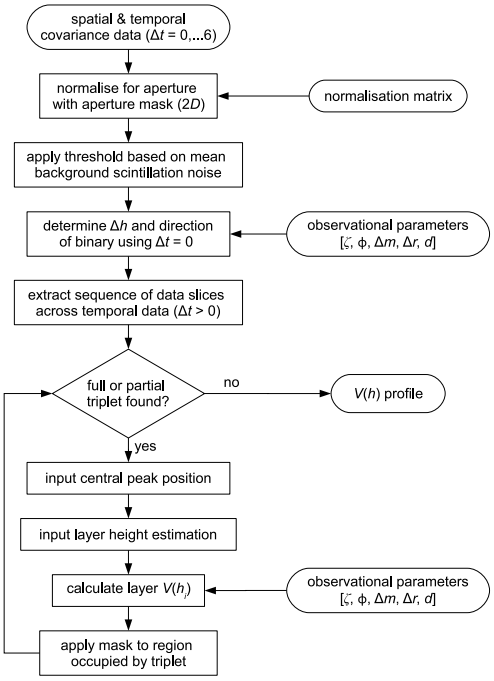

Figure 5.2: The UC-SCIDAR velocity detection algorithm used to determine $V(h)$ profiles.

where

$$C^{\otimes}_{(\bar{m}-\bar{n})}(\rho,\phi,\Delta t) = (\bar{m}(\rho,\phi,t) - \bar{n}(\rho,\phi,t)) \otimes (\bar{m}(\rho,\phi,t+\Delta t) - \bar{n}(\rho,\phi,t+\Delta t)). \quad (5\text{-}3)$$

In $C_N^2(h)$ determination, aperture normalisation is performed during the inversion because the division in equation (5-2) amplifies noise, especially near aperture edges. The division is changed to multiplication of the T-matrix in the inversion (refer to section 4.3, page 59). For temporal SCIDAR, no such modification can be made due the type of measurement. Instead it is necessary to apply an aperture mask, which removes any points that exist outside a region specified by the size and shape of the aperture.

Figure 5.3 demonstrates the effects of equation (5-2) on a simulated example for an annulus aperture. When aperture normalisation by way of division is applied to the data shown in Figures 5.3(a) and 5.3(b), any normalised data is dominated by the noise located outside the aperture region (Figures 5.3(c) and 5.3(d)). By applying a circular mask with a diameter proportional to $2D_{\mathrm{T}}$, where D_{T} is the diameter of the telescope aperture, the normalised data triplets are revealed (Figures 5.3(e) and 5.3(f)).

In the simulated example there is no benefit in applying aperture normalisation for determining velocity, as the triplet is readily identified without normalisation. However for data with low SNR, aperture normalisation can substantially aid in the detection of

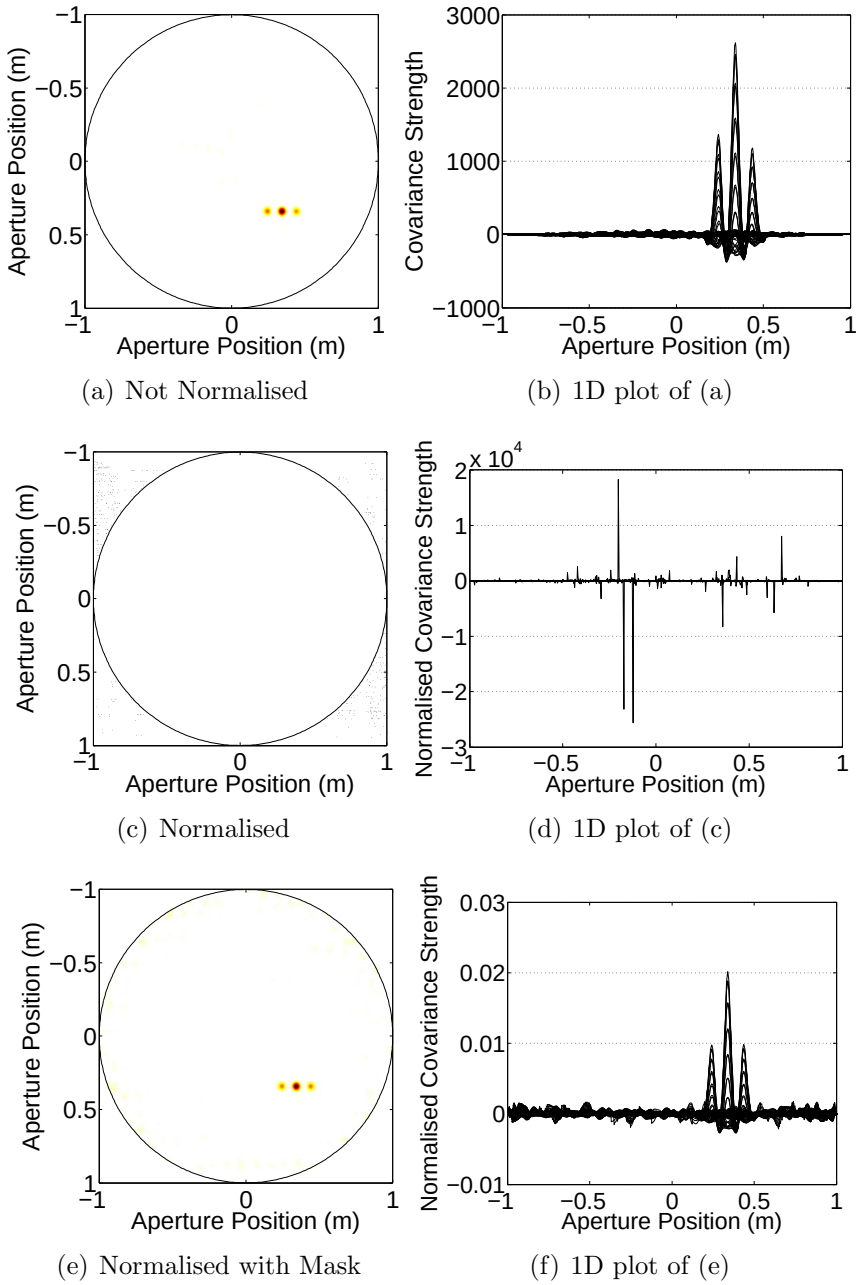

(a) Not Normalised (b) 1D plot of (a)

(c) Normalised (d) 1D plot of (c)

(e) Normalised with Mask (f) 1D plot of (e)

Figure 5.3: Normalisation for aperture effects within simulated data. ((c) and (d)) The division operator amplifies any noise located outside the aperture region , ((e) and (f)) hence it is necessary to mask data to the aperture region.

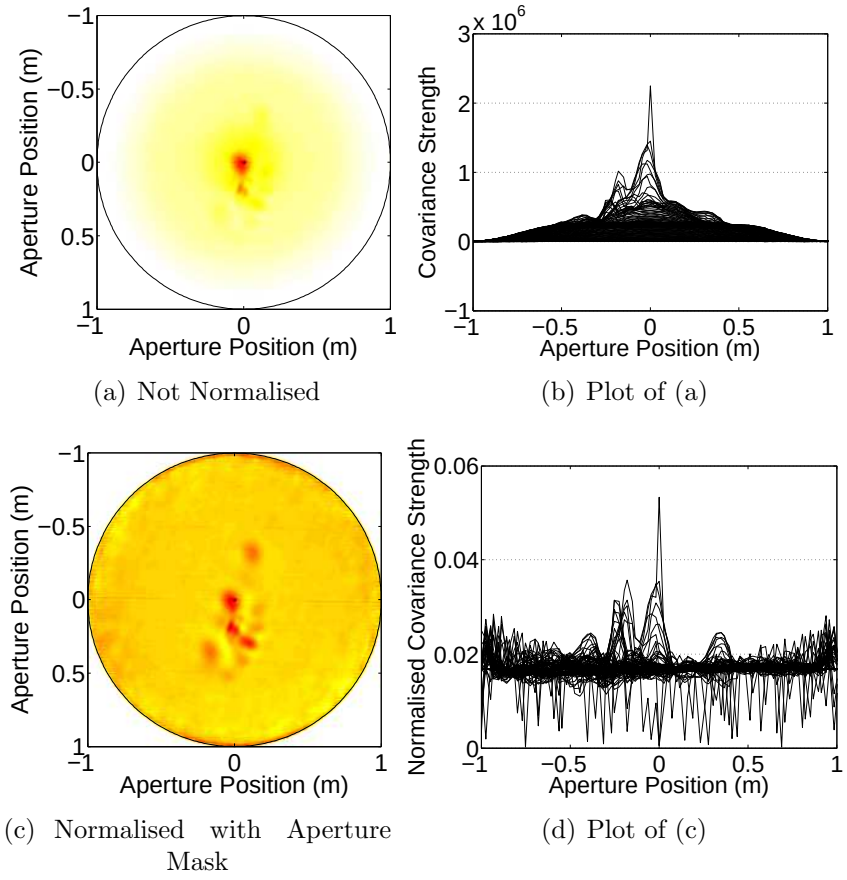

(a) Not Normalised

(b) Plot of (a)

(c) Normalised with Aperture Mask

(d) Plot of (c)

Figure 5.4: For data with low SNR (run #230, January 2007) aperture normalisation can substantially aid in the detection of triplets. ((a) and (b)) Only central peaks are detectable with secondary peaks masked. ((c) and (d)) When aperture normalisation with an aperture mask is applied secondary peaks come to the foreground.

layer triplets, and it is standard practice to remove the bias toward the aperture.

Run #230 from January 2007 contained data with low SNR (30.2). For the V2007 system the ideal SNR was at least 70, to ensure that the noise floor was low enough to minimize aperture effects. Figure 5.4 shows the the non-normalised and normalised spatio-temporal covariance for $\Delta t = 16.7$ ms. In the non-normalised covariance (Figures 5.4(a) and 5.4(b)) only the central peaks can be clearly identified and the secondary peaks are obscured by background noise. The secondary peaks come to the foreground with aperture normalisation using an aperture mask (Figures 5.4(c) and 5.4(d)). The position of peaks remain unchanged. The normalised covariance for this example still contains a significant amount of background scintillation noise.

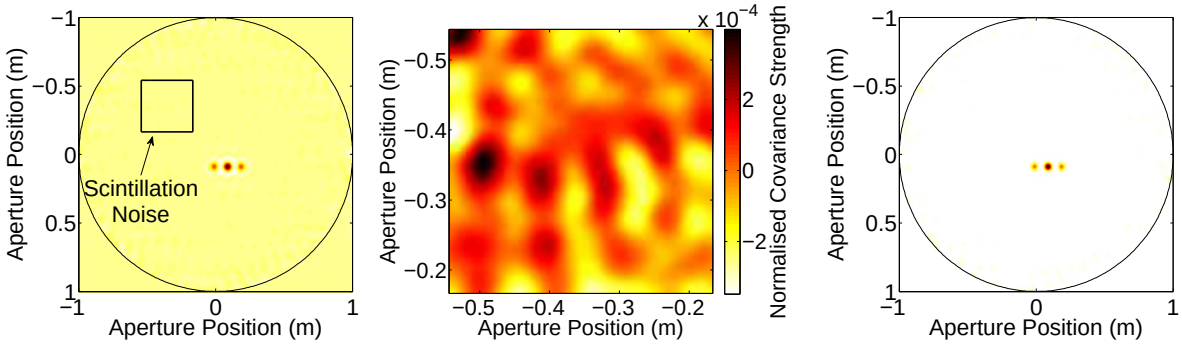

(a) Strong Triplet Detected (b) Background Scintillation Noise (c) Threshold set to mean background

Figure 5.5: Background scintillation noise in simulated data. The aperture normalised covariance strength of the background scintillation noise for the region specified in (a) is weak compared to the triplet seen. However setting a threshold based on the mean background scintillation noise may improve visual detection of weak layers.

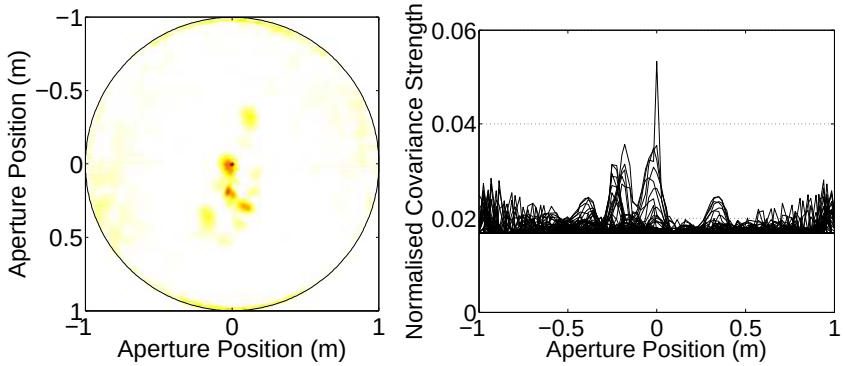

(a) Strong Triplet Detected (b) Background Scintillation Noise

Figure 5.6: Threshold based on background scintillation noise applied to data shown in Figures 5.4(c) and 5.4(d).

5.2.2 Background Scintillation Noise

Performing a temporal correlation between two frames results in the presence of a weak correlation between background scintillation noise. When the layer triplets are also weak this noise can dominate. Consider the ideal case where no dark current or ambient light noise is present. Although background scintillation noise is weak compared to the strong triplet (Figure 5.5(a)), by setting a threshold to the mean of the scintillation noise for a specified region (Figure 5.5(b)) background scintillation noise can be accounted for. This concept is applied to the data in Figures 5.4(c) and 5.4(d), which results in Figure 5.6. By applying a threshold level based on the mean background scintillation noise, data points can be more readily identified.

5.3 Maximum Detectable Velocity

There is a maximum detectable velocity that is dictated by Δt, the size of the telescope aperture, D_{T}, the altitude of the layer, h, the angular separation of the binary companions ϕ and the measured direction of the wind velocity, b_ϕ, with respect to the direction of the binary separation (Figure 5.7(a)). Let the spatial sampling across the aperture be such that each pixel represents Δr. This means that the velocity of a given layer is proportional to $\Delta r/\Delta t$ (Figure 5.7(a)) and the distance between the central peak and the secondary peaks is proportional to $\phi h/\Delta r$. Use of a full triplet pattern in the identification of moving layers provides a method of checking layer altitude and $C_N^2(h)$ strength.

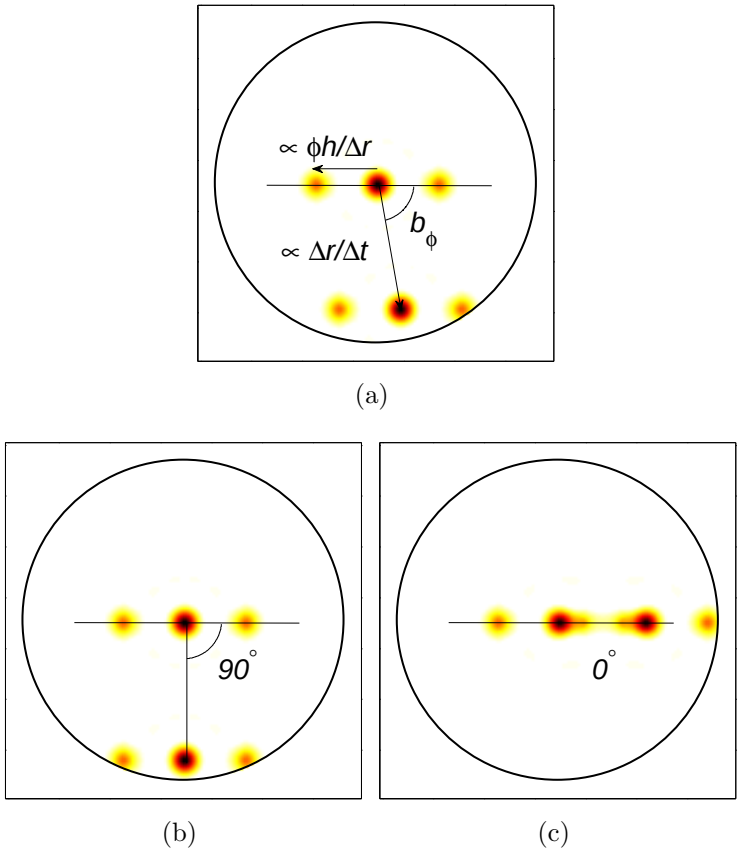

Figure 5.7: The maximum velocity detectable depends on multiple factors, including the time delay, Δt, between frames, spatial sampling across the aperture, Δr, the altitude of the layer, h, the angular separation of the binary companions, ϕ, and the measured direction of the shifted triplet, b_ϕ, with respect to the direction of the binary. Triplets shown correspond to $\Delta t = 0$ (i.e. auto-covariance) and the triplet from the cross-covariance between frames taken Δt apart for (a) $0° < b_\phi < 90°$, (b) $b_\phi = 90°$, and (c) $b_\phi = 0°$.

If $V(h)$ is the velocity of a layer at altitude h and D_{T} is the telescope diameter, then from geometry between the velocity sampling Δv $(= \Delta r/\Delta t)$ of the turbulent layer and

the spatial sampling of the telescope aperture Δr,

$$\left(\frac{D_{\mathrm{T}}}{\Delta r}\right)^2 \geq \left(\frac{V(h)\sin b_\phi}{\Delta v}\right)^2 + \left(\frac{h}{\Delta h} + \frac{V(h)\cos b_\phi}{\Delta v}\right)^2, \tag{5-4}$$

where the region of the covariance defining the aperture has a diameter of $2D_{\mathrm{T}}$. The altitude sampling, Δh, is found by (*Klückers et al.*, 1998)

$$\Delta h = \frac{\Delta r}{\phi \sec \zeta}, \tag{2-32}$$

where ζ is the zenith angle. The maximum velocity detectable, $V_{\max}(h)$, will occur when b_ϕ is 90°(Figure 5.7(b)). At this point

$$V_{\max}^2(h) \leq \frac{D_{\mathrm{T}}^2 - h^2\phi^2 \sec^2 \zeta}{\Delta t^2}. \tag{5-5}$$

The higher a layer is located, the slower the layer needs to be moving to be detected with a full triplet. When b_ϕ is 0° (Figure 5.7(c)) then

$$V_{\max}(h) \leq \frac{D_{\mathrm{T}} - h\phi \sec \zeta}{\Delta t}. \tag{5-6}$$

Δr does not appear in equations (5-5) and (5-6), because all measured values are proportional to Δr.

Equations 5-5 and 5-6 suggest that the $V_{\max}(h)$ is highly dependent on b_ϕ, ϕ, h and D_{T}. Consider the maximum velocity for a layer located at 10 km above the telescope (i.e. the region where wind velocity is at a maximum based on the Bufton wind model (*Tyson and Frazier*, 2004)). Figures 5.8(a) and 5.8(b) show the maximum detectable velocity using full triplets for this layer given a 1-m telescope. To detect a 10 km layer moving at 30 m/s in a perpendicular direction to the binary (i.e. $b_\phi = 90°$), Δt would be limited to ≤ 32.7 ms for a star with $\phi = 4$ arcseconds (the smallest separation that will produce viable generalised UC-SCIDAR results). For a star with $\phi = 14$ arcseconds (the widest separation successfully used with UC-SCIDAR), Δt reduces to ≤ 24.5 ms. If the velocity direction was in the direction of the binary (i.e. $b_\phi = 0°$) then the maximum respective Δt values become 26.9 ms and 10.7 ms. To ensure that a velocity of 30 m/s was captured on a 1-m telescope using full triplets, regardless of b_ϕ, then the minimum frame rate used should be ~ 100 Hz.

Other research groups tend to use telescopes with apertures larger than 1 m for SCIDAR measurements. Figures 5.8(c) and 5.8(d) show the maximum detectable velocity given a 2-m telescope. In this case, Δt is limited to less than 62.7 ms (~ 16 Hz) to capture

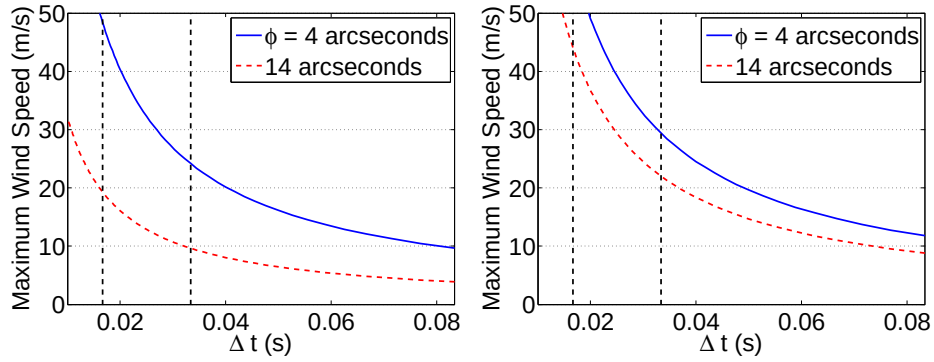

(a) $D = 1$ m; $b_\phi = 0°$ (b) $D = 1$ m; $b_\phi = 90°$

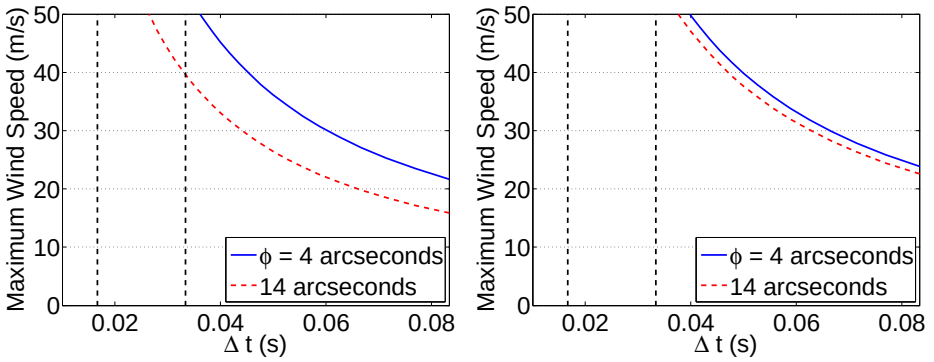

(c) $D = 2$ m; $b_\phi = 0°$ (d) $D = 2$ m; $b_\phi = 90°$

Figure 5.8: The theoretical maximum velocity detectable of a layer at 10 km above a site. The maximum Δt capable of detecting full triplets on a 1-m telescope if the wind direction with respect to the binary, b_ϕ, is 0° (a) and 90° (b) is significantly less than that for a 2-m telescope ((c) and (d)). The vertical dashed lines indicate Δt = 16.7 and 33.3 ms, respectively.

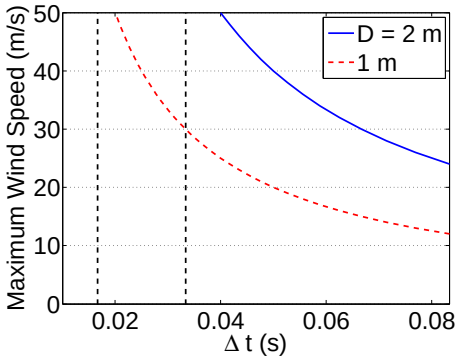

Figure 5.9: The maximum wind speed detectable using partial triplet analysis on a 1-m and a 2-m telescope. Partial triplet analysis is independent of stellar separation and wind direction, and as a result larger Δt values can be used.

a full triplet for $\phi = 4$ arcseconds and 44.0 ms ($\sim$ 23 Hz) for $\phi = 14$ arcseconds, regardless of b_ϕ .

UC-SCIDAR V2005 has a frame rate of 30 Hz, whereas V2007 has a frame rate of 60 Hz. At these frame rates the maximum detectable velocity using full triplet analysis for a 10 km layer on a 1-m telescope (Figures 5.8(a) and 5.8(b)) is shown in Table 5.2. A tropopause layer can be expected to move faster than 24 m/s, and as such 30 Hz is insufficient to detect full triplets from fast moving layers. This limits the use of V2005 data and so *partial triplet analysis* was developed to make better use of the UC-SCIDAR data available to trend $V(h)$.

Table 5.2: Maximum detectable velocity (m/s) using full triplet analysis on a 1-m telescope for a 10 km layer.

Separation ϕ (arcseconds)	4		14	
CCD Frame rate (Hz)	30	60	30	60
$b_\phi = 0°$	24	48	9.6	19
$b_\phi = 90°$	29	59	22	44

Although the full triplet profile has the added benefit that a $C_N^2(h)$ strength can be found, a partial triplet, containing the central peak and at least one secondary peak, can still be used to measure the velocity of any given layer. Assuming b_ϕ is not 90°, then equation (5-4) simplifies to

$$V(h) \leq \frac{D_{\mathrm{T}}}{\Delta t}. \tag{5-7}$$

When b_ϕ is 90°, both secondary peaks will reach the outer aperture edge at the same time. Figure 5.9 shows the frame rates required to detect a partial triplet based on equation (5-7). To detect a layer moving at 30 m/s the capture frame rate required needs to be at least 30 Hz for a 1-m telescope.

Partial triplet analysis in velocity profiling requires an understanding of how the profile of a triplet changes as it approaches the edge of the aperture.

5.4 Partial Triplet Analysis

As the scintillation pattern from a binary star shifts across the aperture fewer points will provide a correlation. This not only weakens the overall strength of the correlation peaks but changes the shape of the profile for a given aperture. If a cross-covariance was determined between a series of frames separated in time by $\Delta t = 0$ (i.e. the auto-covariance) then the covariance triplet profile would have the ideal central to secondary

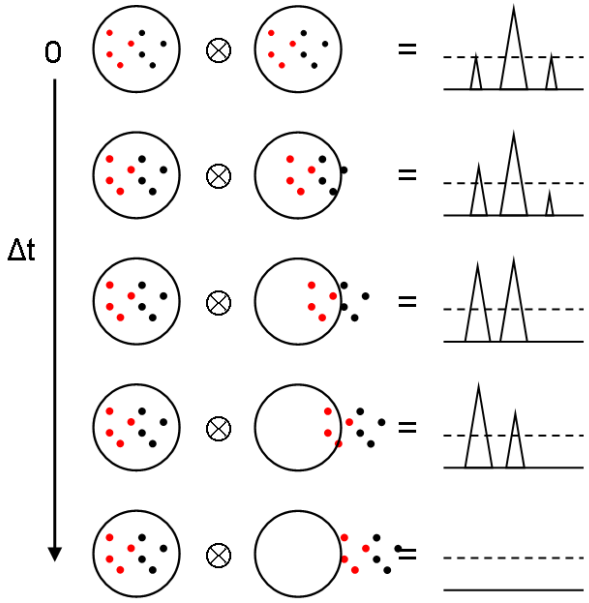

Figure 5.10: With increasing Δt the corresponding scintillation patches used in the temporal covariance analysis shift off the aperture region, changing the shape of the spatio-temporal covariance profile. The operator $\otimes$ denotes cross-correlation. Images are not to scale.

peak ratio. As Δt is increased, fewer corresponding scintillation patches are contained within the region defined by the aperture. The secondary peak closest to the aperture edge in the direction of the shift would be weakened with respect to the central peak, whereas the other secondary peak would strengthen (Figure 5.10).

Equation (5-1) assumes that the strength of both secondary peaks compared to the central peak are a constant ratio regardless of the position of the triplet relative to the aperture, namely

$$\frac{b}{a} = \frac{\alpha}{1+\alpha^2}. \tag{5-8}$$

In partial triplet analysis, where the geometry of the aperture becomes the limiting factor, this assumption is incorrect.

When Δt is large enough that the correlating scintillation seen in the frame results from only one of the stellar companions, then only two points of correlation will exist, with the peaks having similar strength. As fewer correlating points exist, the strength of the remaining secondary peak will exceed the central peak.

Figures 5.11(a) and 5.11(b) show the resulting comparative strengths of the central and secondary peaks of a simulated 5km layer moving at 12 m/s on a 1-m annulus aperture as Δt is increased between consecutive frames. In Figure 5.11(a) a gradual weakening of spot intensities due the effects of the aperture is seen. If aperture normalisation was

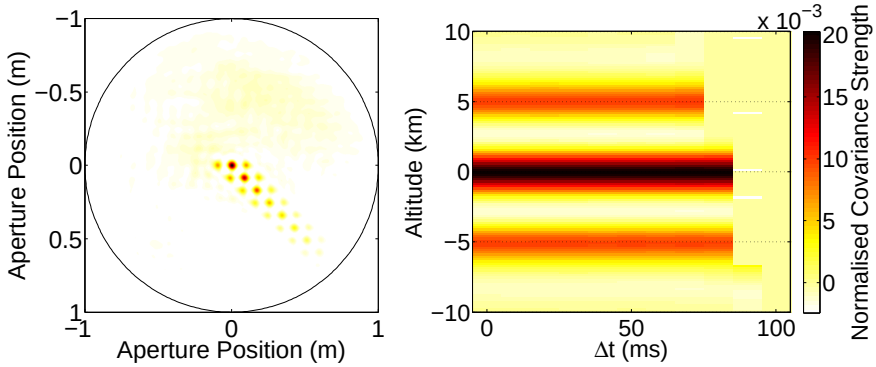

(a) Position of triplet (b) Relative strength of peaks

Figure 5.11: Simulated spatio-temporal covariance triplet for a 5 km layer approaching the edge of an annulus aperture. ((a)) As a simulated spatio-temporal covariance triplet shifts toward the edge of the aperture a gradual weakening of the spot intensities is seen, which results from the data bias toward the aperture. (b) After aperture normalisation, a full triplet could be detected for Δt up to 70 ms. Partial triplet analysis allows for Δt of 80 ms to be used.

applied, then full triplet analysis would be limited to 70 ms (Figure 5.11(b)). Partial triplet analysis allows for use of Δt up to 80 ms. The theoretical maximum Δt is 83.3 ms according to equation (5-7) which defines the point at which no correlation is detectable.

5.4.1 Partial Triplets and the Aperture

The point at which full triplets become partial triplets is aperture dependent. Consider a simulated 5km layer moving at 12 m/s with a b_ϕ of 45°. Figure 5.12 shows the expected shape of triplet profiles for scintillation images captured using circular and annulus apertures with as outer diameter of 1 m and a 1-m square aperture for a range of Δt values. For all apertures, scintillation was simulated for a binary star with separation of 4 arcseconds, Δm of 0.3 and imaging at zenith. When Δt is 50 ms, there is little variation that is seen in the triplet profile shape between the three different apertures and the ideal aperture independent profile as defined by equation 5-1 exists (Figure 5.12(a)). For larger Δt values, the profiles from the three different apertures becomes significantly different compared to the ideal profile. As expected one secondary peak weakens while the other strengthens (Figure 5.12(c)). When Δt is 80 ms (Figure 5.12(e)), one of the secondary peaks becomes obscured by noise for both the circular and the annulus apertures, while the remaining secondary peak exceeds the strength of the primary peak.

If aperture effects are taken into account (Figures 5.12(b), 5.12(d) and 5.12(f)) then the ideal triplet profile is obtained for all aperture types. Note that for $\Delta t = 80$ ms, although one of the secondary peaks is missing for both circular and annulus apertures the ideal secondary-to-central peak ratio is obtained for the remaining peaks.

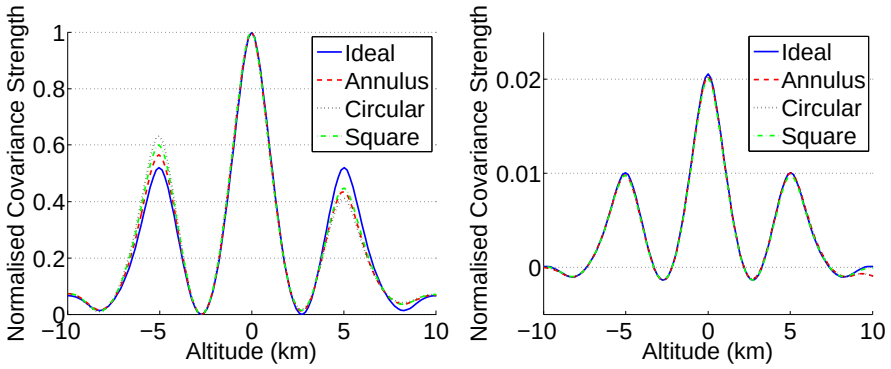

(a) $\Delta t = 50$ ms (b) $\Delta t = 50$ ms aperture normalised

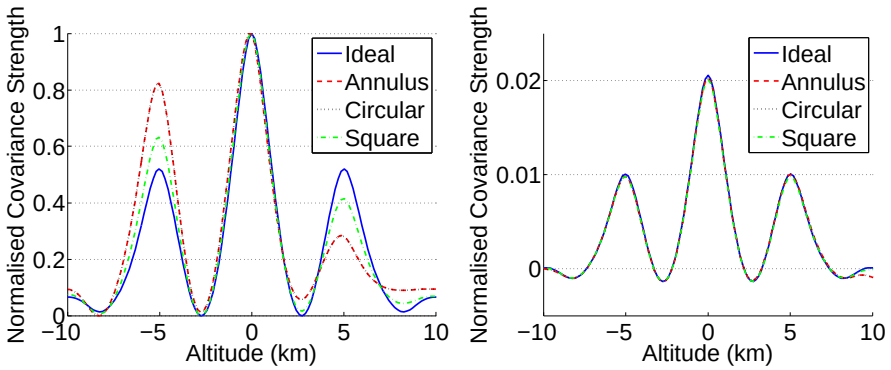

(c) $\Delta t = 70$ ms (d) $\Delta t = 70$ ms aperture normalised

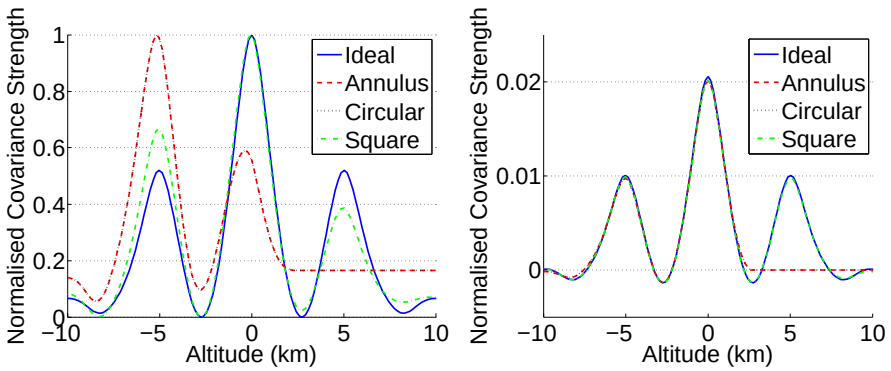

(e) $\Delta t = 80$ ms (f) $\Delta t = 80$ ms aperture normalised

Figure 5.12: Extracted slices from simulated 2D spatio-temporal covariances for a 5 km layer using various Δt. ((a) and (c)) With increasing Δt, the strength of one secondary peak decreases with respect to the central peak, whereas the other secondary peak increases. (e) When Δt is sufficiently large, one secondary peak is no longer detectable and the strength of the remaining two peaks is the same. ((b) and (d)) When covariances are aperture normalised, the ideal ratio of the secondary peak strength to the central peak strength is obtained. (f) For large Δt, only one secondary peak is visible for the annulus and circular apertures.

5.5 Velocity Detection Algorithm

Section 5.1 briefly outlined the main steps that are used in the UC-SCIDAR algorithm. The covariance data conditioning discussed in section 5.2 ensures data points are brought to the foreground making it easier to determine the location of layer triplets. This section discusses the steps taken after data conditioning and issues that surround the determination of central peak positions and layer heights for full and partial triplet analysis.

The approach used to analyse UC-SCIDAR temporal data after data conditioning is a modification of a CLEAN algorithm utilising *a priori* information about the data type to successively remove identified data points and enhance weaker data points until only noise remains. A CLEAN-based algorithm has previously been successfully applied to temporal SCIDAR data (*Prieur et al.*, 2004). To apply CLEAN to UC-SCIDAR the triplets resulting from various layers need to be appropriately modelled to successively remove them from a data set. Current models assume weak Kolmogorov turbulence with ideal triplet patterns and secondary peak strengths, with temporal sampling such that Taylor's hypothesis holds true. However the spatial and temporal sampling used in UC-SCIDAR, the aperture size of the telescope, and strong NGT present at MJUO, means that current covariance models do not adequately match profiles seen in the data.

Consider Figure 5.13, which uses the simulated profile outlined in Table 5.1. When $\Delta t = 0$, the triplets are difficult to distinguish (Figure 5.13(a)). If Δt was sufficiently large then the triplets would separate. The strengths of the NGT and 10 km layers obscure the presence of the 5 km layer (Figure 5.13(b)). If the region that the stronger triplets occupy are set to the background level (Figures 5.13(c) and 5.13(d)) then the 5km layer becomes readily detectable.

The practical implementation of the current analysis algorithm calculates a series of equally spaced slices taken along the axis of the binary, which is calculated from the spatial covariance (i.e. $\Delta t = 0$). Using identifiable full and partial triplets in the matrix of slices, the size and position of a rectangular region that fully encompasses each triplet is calculated and set to the level of the background noise. By doing this, some data will be lost. To extract the full $V(h)$ profile multiple passes through the algorithm may be required, however this simplified approach is adequate to estimate the velocity of the various layers.

Currently the position of the central peak of each triplet pattern and the height of the layer above the measurement plane is manually identified. Previous attempts at automating triplet detection (*Prieur et al.*, 2004; *García-Lorenzo and Fuensalida*, 2006a) have had limited success, and were designed to utilise full triplet analysis. Although *Prieur et al.* (2004) makes brief mention of the possibility of using a partial triplet in the

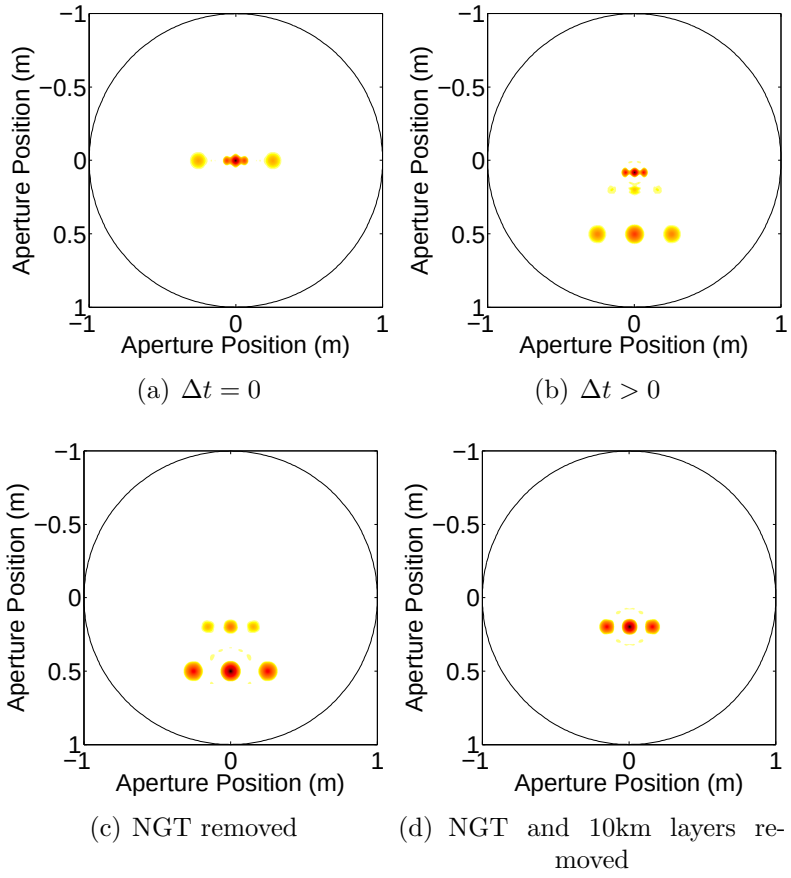

(a) $\Delta t = 0$ (b) $\Delta t > 0$

(c) NGT removed (d) NGT and 10km layers removed

Figure 5.13: Simulated 2D spatio-temporal covariance with triplets of successive strengths set to background levels. (a) Triplets are overlapped in the auto-covariance (i.e. when $\Delta t = 0$). (b) When Δt is sufficiently large the layers separate. Due to the strength of the NGT and 10 km layer, the 5 km layer is masked. ((c) and (d)) The successive removal of strong layers aids in the detection of the 5 km layer.

analysis, no elaboration is given. In addition, the automated systems are unable to detect layers with a low SNR triplet or triplets that are located in close proximity to each other. The automatic detection algorithms have similar or lesser performance to an interactive detection algorithm. As such it was decided to not automate the UC-SCIDAR algorithm at this stage.

5.5.1 Partial Triplets and Data Validation

It is beneficial to use multiple values of Δt to not only capture motion from slow and fast moving layers, but provide a check within the data itself for velocity measurements. The use of partial triplet analysis in conjunction with full triplet analysis allows for multiple Δt to be used with UC-SCIDAR data to capture the velocity of a given layer.

Figure 5.14 shows data for α Cru from run #104, June 2007, which used a generalised

measurement plane at -1.9 km below the telescope aperture. The CCD was operating with an exposure time of 2 ms and a frame rate of 60 Hz. Three different layers could be identified: a near-ground layer attributed to dome-seeing; a second near-ground layer moving at approximately 9 m/s; and a third layer found at an altitude of $\sim$ 13 km above the telescope moving at approximately 23 m/s. For the high-altitude layer the theoretical maximum Δt for full triplet analysis (equation (5-4)) is 36 ms. However a frame rate of 30 Hz (i.e. $\Delta t = 33.3$ ms) results in a triplet where one of the secondary peaks is located on the edge of the aperture and is lost in the noise. Hence partial triplet is required. From equation (5-7), Δt is limited to 43.5 ms or shorter for partial triplet analysis.

Regardless of the Δt used, the strength of the two near-ground layers mask the high altitude layer (Figure 5.14(a)). Using layer removal, the 13 km layer becomes clearly identifiable. For $\Delta t = 16.7$ ms, a full triplet is detected (Figure 5.14(b)). For $\Delta t = 33.3$ ms, a partial triplet is detected (Figure 5.14(c)). Figure 5.14(d) shows the triplet profiles for both $\Delta t = 16.7$ ms and 33.3 ms. Note that the +15 km secondary peak is missing for $\Delta t = 33.3$ ms.

Figures 5.15 and 5.16 shows data for α Cru from run #11, January 2007. This particular data set utilised a pupil-plane measurement plane. The CCD was operating at an exposure time of 1.5 ms and a frame rate of 100 Hz. Multiple layers could be identified ranging in heights from 2 km to 19 km. Two different high altitude layers could be identified at 13 and 19 km above the telescope. A combination of full and partial triplet analysis identified that these layers were moving at approximately 29 and 11 m/s respectively. Looking at the 2D spatio-temporal covariance images for $\Delta t = 0$ to 60 ms (Figure 5.15) the progression of separation can be seen. Extracted slices taken through the triplets for various Δt are shown in Figure 5.16. The 13 km layer is weak compared to the other layers seen. Due to the height and speed of the 13 km layer, the maximum Δt that can be used to detect the layer is 34 ms. Hence no triplet peaks are detected for $\Delta t > 30$ ms. The maximum Δt to detect a 19 km layer is 90.9 ms. However the de-correlation of the scintillation patches (i.e. the partial failure of Taylor's hypothesis) results in dominating background scintillation noise.

Comparison of altitudes obtained through temporal analysis with those obtained through spatial analysis provides an additional level of data validation. The $C_N^2(h)$ profile from run #150, June 2007 (Figure 5.17(a)), indicated the presence of turbulent layers at approximately 1.5, 3.5, 8 and 11.5 km above the telescope, with another possible layer at approximately 5 km. Examination of the normalised extracted slice from the spatial covariance when $\Delta t = 0$ ms taken in the direction of the binary (Figure 5.17(b)) reveals strong secondary covariance peaks associated with layers at 1.5, 3.5 and 11.5 km. As such these three layers are the most likely to be detected during temporal analysis. Additional

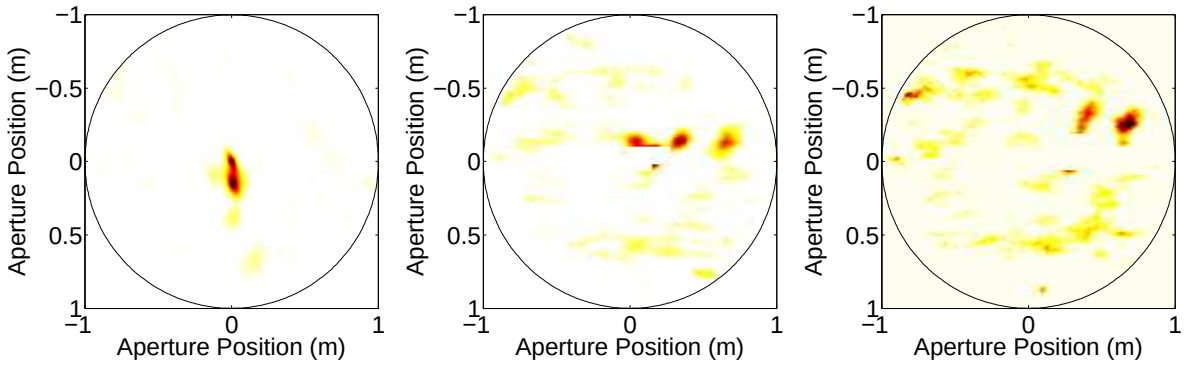

(a) $\Delta t = 16.7$ ms

(b) $\Delta t = 16.7$ ms; rotated to horizontal

(c) $\Delta t = 33.3$ ms; rotated to horizontal

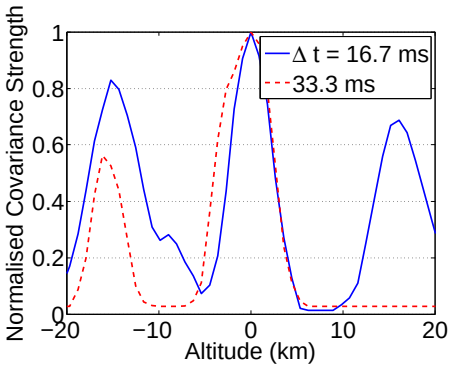

(d) Normalised slice through 12 km layer

Figure 5.14: Extracted temporal covariance triplet for multiples of Δt. Data shown is from run #104, June 2007, and used a generalised measurement plane -1.9 km below the telescope. The extracted layer was found to be at $\sim$ 15 km above the measurement plane (i.e. $\sim$ 13 km above the telescope) moving at about 23 m/s. (a) Three layers are present: two near-ground layers mask the 13 km layer. (b) When the near-ground layers have been removed, the high altitude layer is clearly identifiable. With longer Δt, partial triplet analysis is required ((c) and (d)). Note the missing secondary peak for $\Delta t = 33.3$ ms.

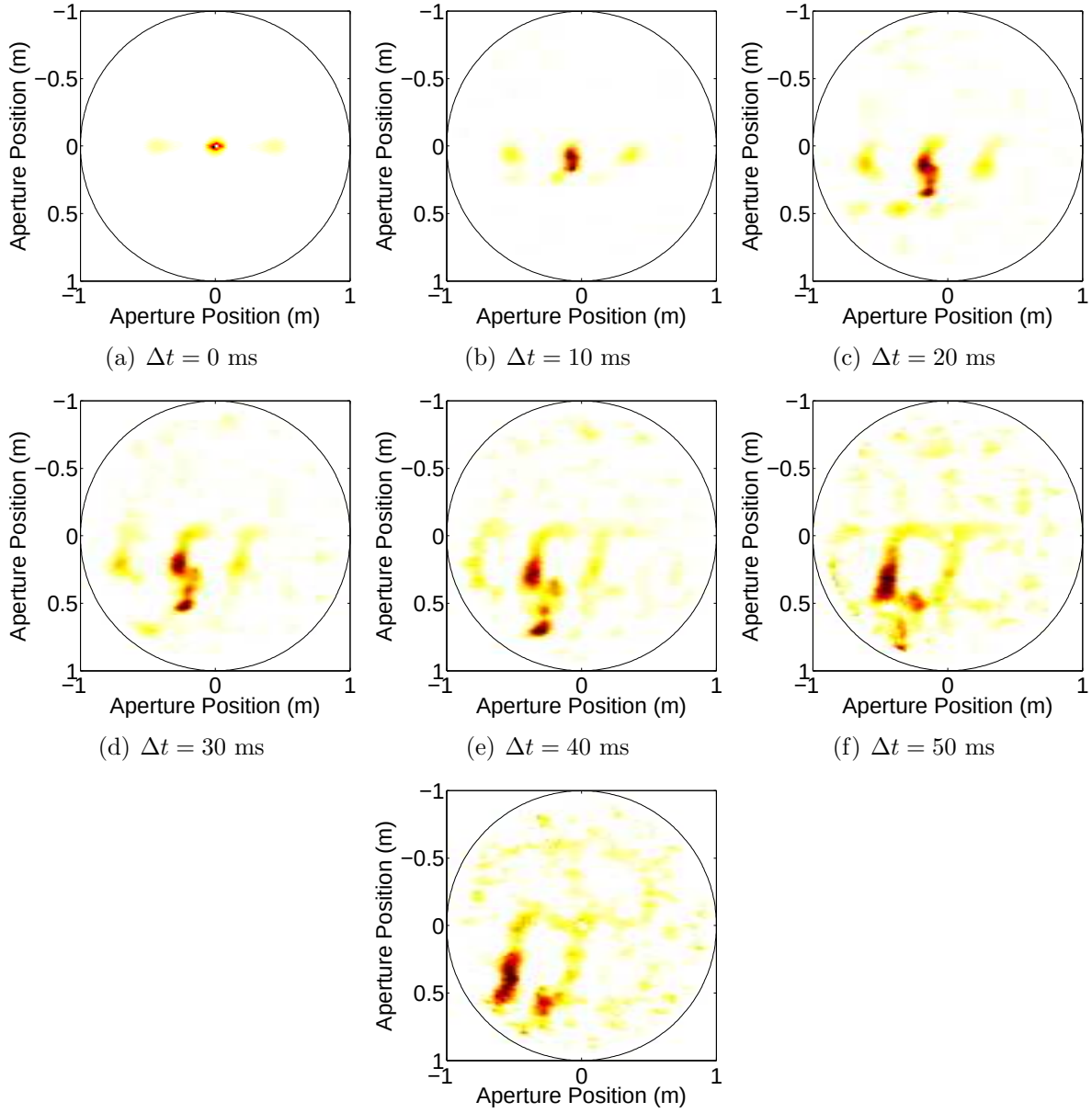

(a) $\Delta t = 0$ ms (b) $\Delta t = 10$ ms (c) $\Delta t = 20$ ms

(d) $\Delta t = 30$ ms (e) $\Delta t = 40$ ms (f) $\Delta t = 50$ ms

(g) $\Delta t = 60$ ms

Figure 5.15: 2D spatio-temporal covariances for various Δt values for run #11, January 2007.

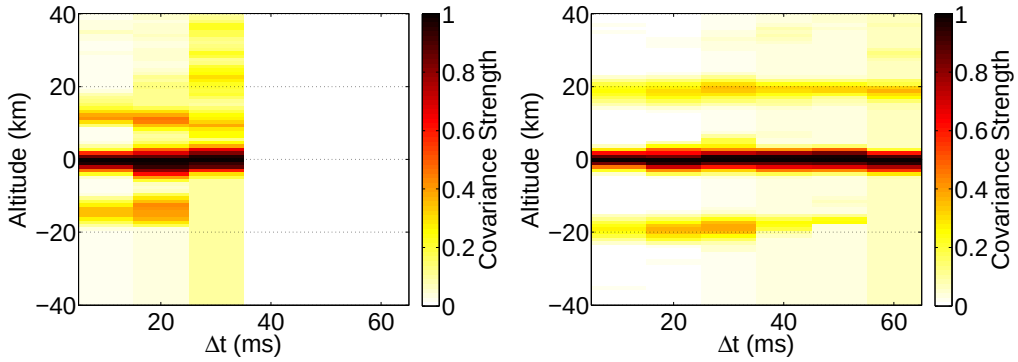

(a) 13 km layer slices (b) 19 km layer slices

Figure 5.16: Extracted slice profiles from run #11, January 2007 for various Δt values. (a) Slices through ∼13 km layer. (b) Slices through ∼19 km layer.

weak secondary covariance peaks can be seen at 5 and 8 km.

Temporal analysis for $\Delta t = 16.7$ ms (Figure 5.17(c)) resulted in layers at 1.5, 3.5, 4.5 and 11.5 km above the site travelling at 13.3, 20.7, 8.2 and 26.3 m/s respectively. However comparison with analysis for longer Δt values (Figures 5.17(d) and 5.17(e)) led to only three layers identified: 1.5, 3.5 and 11.5 km above the site travelling at 13, 20.5 and 26 m/s respectively. The 4.5 km layer detected when $\Delta t = 16.7$ ms was treated as a false data point, as it was not detected in the analysis of longer Δt. The 8 km layer detected through $C_N^2(h)$ analysis was not detected through temporal SCIDAR. It is possible that it may have had similar velocity to another stronger layer, as discussed in the next section.

5.5.2 Proximity of Peaks to Others

It is common for a peak from a given triplet to be located in close proximity to a peak from another triplet, especially for short Δt. Typically layers found to be moving at different velocities will have triplets that separate for higher values of Δt.

Consider simulated data for two layers at similar heights (4.5 and 5 km above the telescope) and travelling at similar speeds (9 and 12 m/s respectively). Figure 5.18 demonstrates how the two layers can easily be mistaken for a singular layer with a combined strength of the two layers in the $C_N^2(h)$ profile. In the spatial covariance (Figure 5.19(a)) the two layers overlap and are indistinguishable. Temporal analysis using a short Δt (e.g. 16.7 ms shown in Figure 5.19(b)) results in a blurred triplet pattern. With increasing Δt (Figures 5.19(c) and 5.19(d)) the two layers become distinguishable and separated.

Unfortunately not all triplets will separate with increasing Δt. It is possible to have two different layers that have the same wind speed. During temporal analysis of run #150 from June 2007 (Figure 5.17), a layer at ∼8km was never detected. It is possible that a

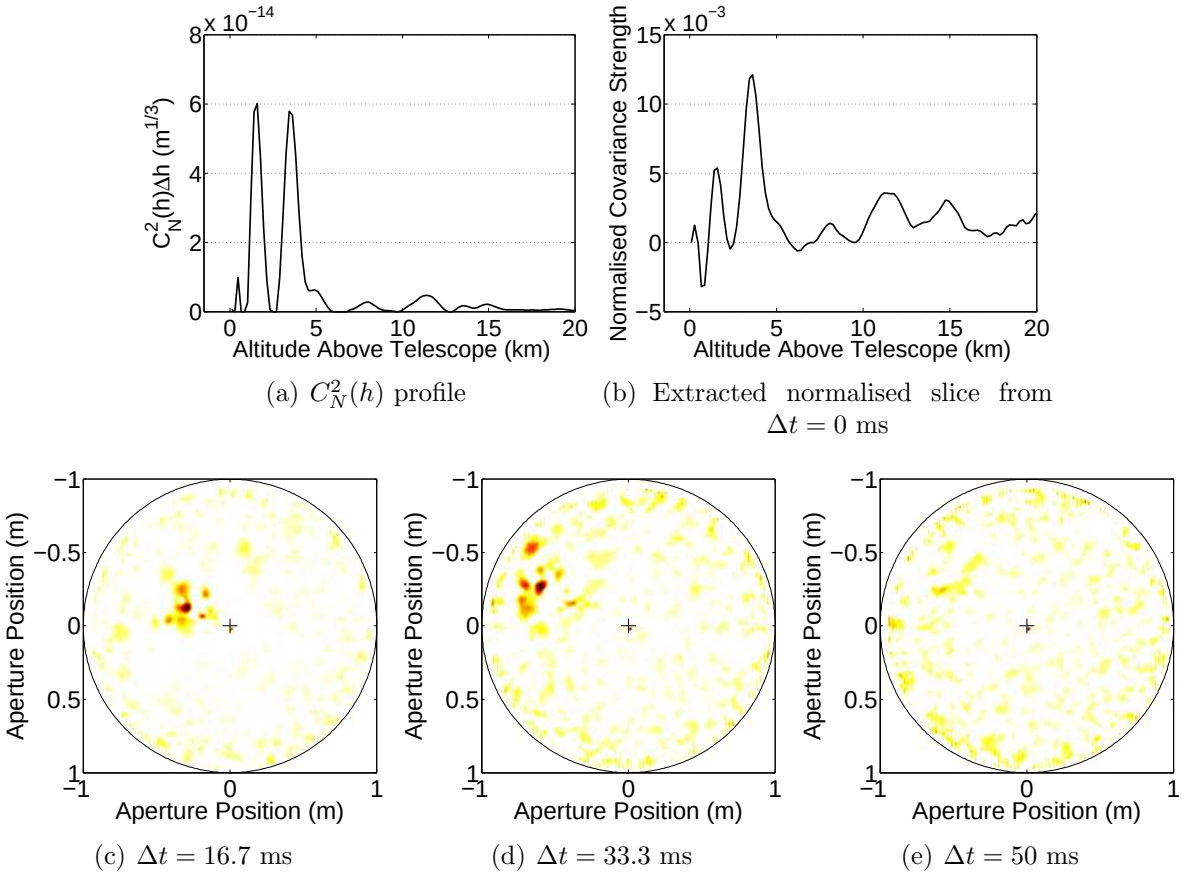

(a) $C_N^2(h)$ profile

(b) Extracted normalised slice from $\Delta t = 0$ ms

(c) $\Delta t = 16.7$ ms

(d) $\Delta t = 33.3$ ms

(e) $\Delta t = 50$ ms

Figure 5.17: Spatial and temporal analysis of run #150 from June 2007. (a) The $C_N^2(h)$ profile and (a) the extracted normalised slice from $\Delta t = 0$ reveals layers at 1.5, 3.5, 8 and 11.5 km above the telescope, with another possible layer at ~ 5 km. Comparative temporal analysis for (c) $\Delta t = 16.7$ ms, (d) 33.3 ms and (e) 50 ms, led to the identification of only three layers identified: 1.5, 3.5 and 11.5 km above the site travelling at 13, 20.5 and 26 m/s respectively.

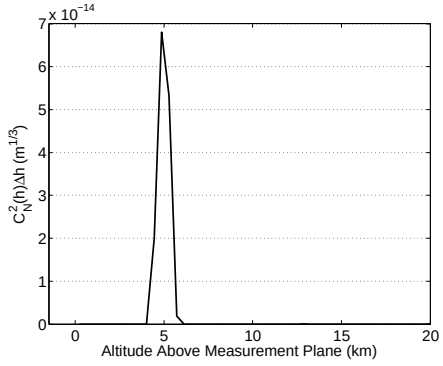

Figure 5.18: $C_N^2(h)$ profile for ideal layers located at 4.5 and 5 km and travelling at 9 and 12 m/s respectively. Simulated strength of the 5 km layer is half the strength of the 4.5 km layer. The profile can easily be interpreted as a singular layer with the combined strength of the two layers.

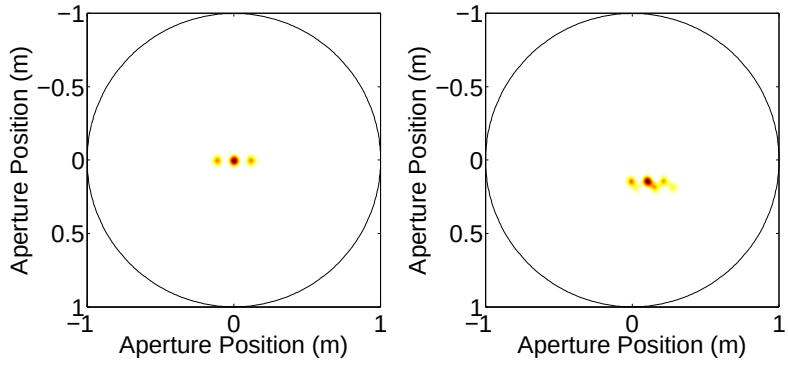

(a) $\Delta t = 0$ ms (b) 16.7 ms

(c) 33.3 ms (d) 50.0 ms

Figure 5.19: Increasing the value of Δt can separate triplets. Triplets shown are based on the ideal for a 4.5 km layer and 5 km layer travelling at 9 and 12 m/s respectively. Simulated strength of the 5 km layer is half the strength of the 4.5 km layer.

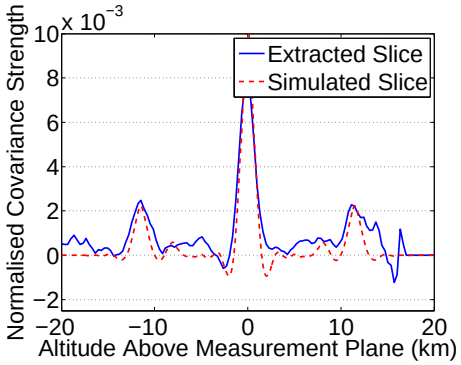

Figure 5.20: Extracted slice from run #150 from June 2007 that reveals the existence of two layers travelling at similar speeds.

layer at this height was moving at a similar speed to that of another layer. Figure 5.20 shows the extracted slice from the data point containing information about the layer at 11.5 km above the site. Through close examination there is a second set of secondary peaks present (although noisy). A simulated profile of two layers located at 8 and 11.5 km above the measurement plane where the 11.5 km layer is three times the strength of the 8 km layer (indicated by the dashed red line in Figure 5.20) has similar secondary peak strength of that of the real data. Although this is not conclusive, it does provide a possible explanation for the lack of an 8 km layer wind speed measure.

5.5.3 Dome/Telescope Turbulence and Pupil-Plane Measurements

SCIDAR measurements will always have a certain amount of optical turbulence associated with the dome and/or telescope. This turbulence will not be moving and hence will remain at the image origin of the spatio-temporal covariance for any value of Δt. At MJUO, the dome/telescope turbulence is extremely strong and for pupil-plane data this turbulence manifests itself as a point spike located at the image origin. Consider the 5 km layer found in run #250, May 2007. In the centre of the spatio-temporal covariance a correlation spike exists that can be attributed to the dome and/or telescope (Figures 5.21(a), (b) and (c)). When $\Delta t = 16.7$ ms the dome/telescope spike is located between the central peak and one of the secondary peaks and hence does not effect the overall shape of the profile. At $\Delta t = 33.3$ ms, one of the secondary peaks overlaps this spike and become artificially inflated. By the time $\Delta t = 50$ ms, the resulting covariance triplet has shifted by a sufficient amount that the spike does not affect the triplet profile in anyway.

The simplest way to remove the correlation spike associated with dome/telescope turbulence in pupil-plane data is to set a region surrounding the central pixel to the background noise level. This will bring to the foreground triplet patterns associated with

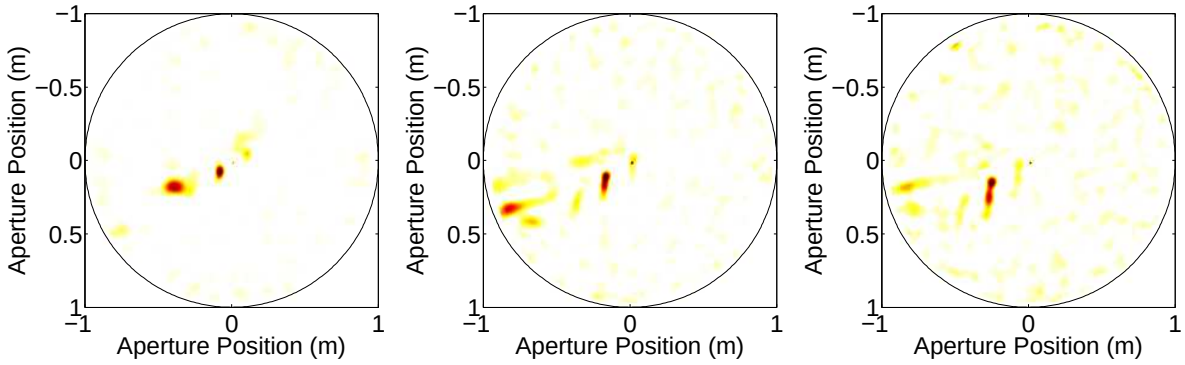

(a) $\Delta t = 16.7$ ms (b) $\Delta t = 33.3$ ms (c) $\Delta t = 50$ ms

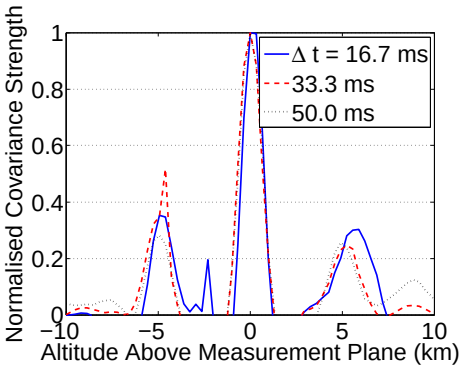

(d) Normalised Slice Through 5km Layer

Figure 5.21: Extracted temporal covariance triplet for multiple Δt. The layer extracted from run #250, May 2007, was found to be at approximately 5 km above the telescope, moving at approximately 6 m/s.

turbulent layers located above the dome. However if a peak from one of these triplet patterns overlaps the region surrounding the correlation spike, as in the case above, then data will be lost. In these instances partial triplet analysis is required.

5.6 Determining Wind Direction from SCIDAR

In characterising the rate at which turbulence changes above a site it is only the wind speed that is used, however the direction of the wind with respect to the orientation of the primary mirror will have a bearing on the error on the estimated wind speed due to projection errors. In addition, knowledge of wind direction could provide an insight that could link meteorological data to observational conditions.

This section looks at how SCIDAR measurements can be used to obtain the wind direction that is associated with each layer and the corrections that can be applied to compensate for telescope motion. This requires an understanding of how the orientation of the primary mirror changes as the telescope tracks a star.

The determination of projection errors on the estimated wind speed is discussed in section 5.6.3.

5.6.1 The Horizontal and Equatorial Coordinate Systems

The motion of the primary mirror will depend on the type of celestial coordinate system employed in the design of the telescope. Two main celestial coordinate systems are used. A *horizontal* coordinate system uses the local telescope position to define its reference frame. An *equatorial* coordinate system uses measurements based on the celestial polar axis. Full details on these coordinate systems, including how to convert between them can be found in *Roy and Clarke* (1988). A brief description, adapted from *Roy and Clarke* (1988), can be found here.

Figure 5.22 shows the celestial sphere as seen by an observer located at point **O**. Let **Z** be the direction of *zenith* and **P** be the *North celestial pole*. The *meridian* would be defined by a plane that intersects **NZSZ'** and the *horizon* defined by **NYESW**. If **OX** was the instantaneous direction of the observed object, then the angles $\angle$**YOX** (i.e. the angle above the horizon) and $\angle$**NOY** (i.e. the angle from North projected on the horizon) would be the *altitude*, a, and *azimuth*, A, respectively. Note the zenith angle, ζ, (defined by the angle $\angle$**ZOX**) is related to a by

$$a = 90^\circ - \zeta. \tag{5-9}$$

The coordinate system defined by altitude and azimuth is known as the *horizontal* (or *alt-azimuth*) coordinate system.

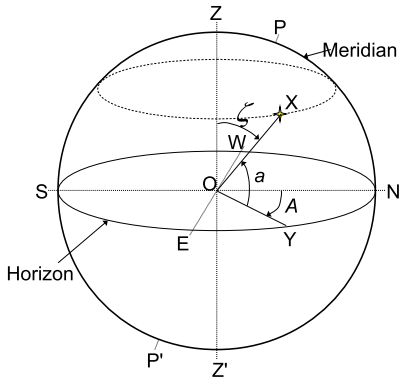

Figure 5.22: The observer's celestial sphere. Refer to text for full description. (Based on Fig. 7.2 from *Roy and Clarke* (1988).)

The horizontal coordinate system utilises a reference frame that is specific to the observer's location on the Earth's surface. However in defining the position of a celestial body it is more advantageous to use a reference frame that is related to the Earth's rotational axis.

From an observer's perspective, heavenly bodies rotate about an axis which is aligned with the Earth's rotational axis. The angle this *celestial polar axis* forms with the observer's horizon is related to the observer's latitude, φ, from the equator (Figure 5.23). For a star located at X in Figure 5.24, the *declination* of a star, δ, is the angular distance (typically defined in degrees) from the celestial equator toward the celestial pole through the star (Figure 5.24). The *hour angle*, H, is angle from the meridian through the star measured toward the west. As a star moves through the sky, H gradually increases while δ remains constant. This coordinate system is known as the *equatorial* (also called *RA-Dec*) coordinate system.

Using spherical geometry, it is possible to derive the following expressions to convert from δ and H to a and A assuming that an observer has a surface latitude of φ (*Roy and Clarke*, 1988):

$$\sin a = \sin\varphi \sin\delta + \cos\varphi \cos\delta \cos H \tag{5-10}$$

$$\cos A \cos a = \cos\varphi \sin\delta - \sin\varphi \cos\delta \cos H \tag{5-11}$$

$$\sin A \cos a = -\cos\delta \sin H \tag{5-12}$$

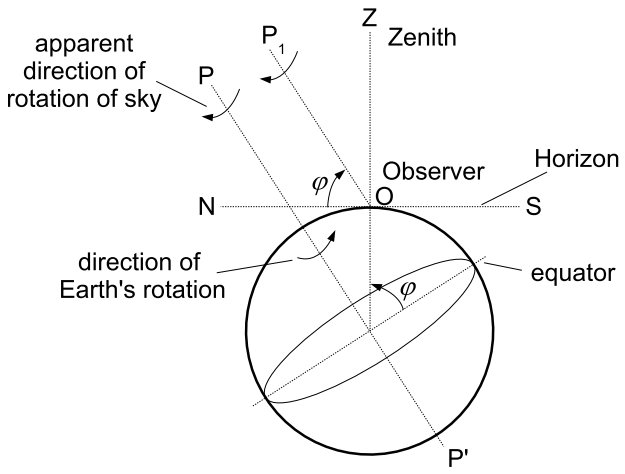

Figure 5.23: The celestial polar axis. The axis of rotation for the heavens is aligned with the Earth's rotational axis. The angle that the celestial polar axis forms with the horizon is equal to the latitude φ from the equator. (Based on Fig. 7.1 from *Roy and Clarke* (1988).)

and vice versa:

$$\sin\delta = \sin\varphi\sin a + \cos\varphi\cos a\cos A \quad (5\text{-}13)$$

$$\cos H\cos\delta = \cos\varphi\sin a - \sin\varphi\cos a\cos A \quad (5\text{-}14)$$

$$\sin H\cos\delta = -\cos a\sin A \quad (5\text{-}15)$$

5.6.2 Telescope Motion

The telescopes that were used during this research at MJUO, the 1-m McLellan and 60-cm Boller & Chivens telescopes, use an equatorial coordinate system to define their physical position. The primary mirror undergoes a 3D rotation with respect to the ground. Due to the latitude of MJUO (43°59.2′ S) the telescopes' right ascension drives (i.e. the drive that controls hour angle rotation) are not perpendicular to the ground. Instead they are oriented such that the axis of rotation is about the celestial polar axis. As the telescope tracks a star, additional rotation is applied to the primary mirror with respect to the ground such that a different edge of the primary mirror will be at the highest point (Figure 5.25). This motion is beneficial in observational astronomy where long exposures are required as the primary mirror, and hence any coupled measurement instrument, remains in a constant orientation with respect to the observed stellar field.

For SCIDAR measurements, this means that over a long period of time the orientation of the binary in the calculated spatio-temporal covariances remains constant.

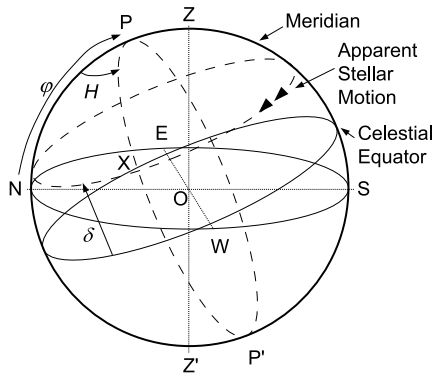

Figure 5.24: The equatorial system. Refer to text for full description. (Based on Fig. 7.3 from *Roy and Clarke* (1988).)

However a constant wind direction with respect to the ground will be seen as a rotating wind with variable magnitude in the spatio-temporal covariances.

Let XYZ be defined such that the axes are aligned with West, North and Zenith respectively (Figure 5.26). If $X_{\rm m}Y_{\rm m}Z_{\rm m}$ is the coordinate system attached to the mirror surface then the rotation of the primary mirror through a declination δ and an hour angle H for a given surface latitude φ can be described by:

$$\begin{bmatrix} x_{\rm m} \\ y_{\rm m} \\ z_{\rm m} \end{bmatrix} = \begin{bmatrix} l_{\rm x} & m_{\rm x} & n_{\rm x} \\ l_{\rm y} & m_{\rm y} & n_{\rm y} \\ l_{\rm z} & m_{\rm z} & n_{\rm z} \end{bmatrix} \times \begin{bmatrix} x \\ y \\ z \end{bmatrix}, \tag{5-16}$$

where

$$\begin{aligned} l_{\rm x} &= \cos H, \\ m_{\rm x} &= \sin\varphi \sin H, \\ n_{\rm x} &= -\cos\varphi \sin H; \end{aligned} \tag{5-17}$$

$$\begin{aligned} l_{\rm y} &= -\sin H \sin\delta, \\ m_{\rm y} &= \cos\varphi\cos\delta + \sin\varphi\cos H\sin\delta, \\ n_{\rm y} &= \sin\varphi\cos\delta - \cos\varphi\cos H\sin\delta; \end{aligned} \tag{5-18}$$

$$\begin{aligned} l_{\rm z} &= \sin H\cos\delta, \\ m_{\rm z} &= \cos\varphi\sin\delta - \sin\varphi\cos H\cos\delta, \\ n_{\rm z} &= \sin\varphi\sin\delta + \cos\varphi\cos H\cos\delta. \end{aligned} \tag{5-19}$$

Figure 5.25: Motion of the primary mirror of a RA-Dec telescope. Tracking a star from an hour angle of -3:00 to +3:00 results in multi-axes rotation. The marked mirror point is not always on the highest edge. Motions shown are based on simulation for a RA-Dec telescope at MJUO tracking α Cru.

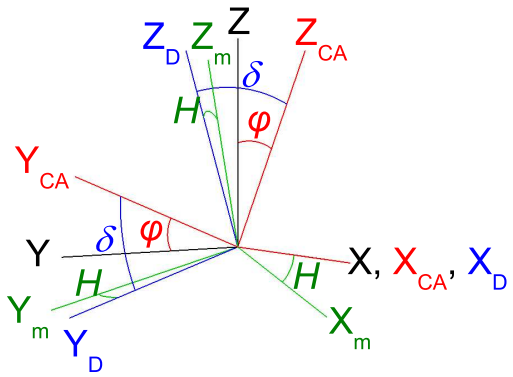

Figure 5.26: Rotation of mirror coordinate system $X_{\rm m}Y_{\rm m}Z_{\rm m}$ through a declination δ and an hour angle H for a given surface latitude φ. The angle between Z and $Z_{\rm m}$ is a function of φ, δ and H

(See Appendix G for full derivation.)

Consider wind originating from one of the four quarters (i.e. North, South, East or West). If the telescope was to track α Cru at approximately $\delta = -63°$ through an hour angle of -3 to $+3$ hrs, the projected path of the measured velocity would be that seen in Figure 5.27(a). Figure 5.27(b) shows the projected paths of winds originating from North-East, South-East, South-West and North-West. Note that these paths are not rotationally symmetric. Using this information the direction of wind for a given layer can be estimated based on the instantaneous orientation of the telescope. Look-up tables for multiple δ to estimate wind directions from data can be found in Appendix H.

Consider May 3, 2007 where α Cru was tracked through an hour angle of -2 hr to +1 hr. Figure 5.28 shows 2D spatio-temporal covariances for $\Delta t = 16.7$ ms for a selection of runs taken during the observation sequence. A layer at approximately 12 km above the telescope was identified. As the telescope tracks α Cru, the position of the triplet shifts from a South-West to a Westerly direction. Figure 5.29(a) shows the measured wind

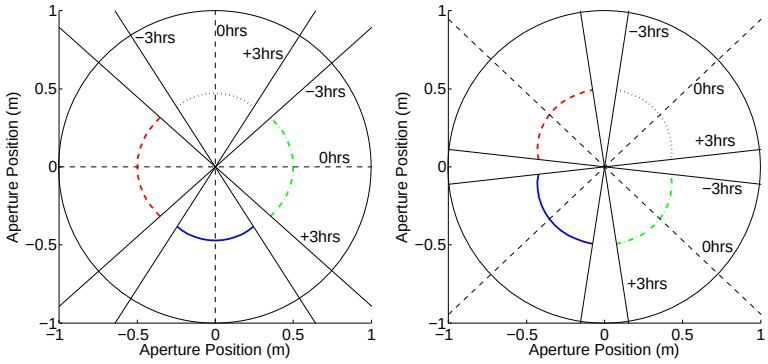

(a) (b)

Figure 5.27: Observed shift of the central peak for different wind directions while tracking through hour angle of -3 hrs to +3 hrs for a star at a declination of -63°7' (e.g. α Cru). (a) — Southerly, - - - Westerly, ··· Northerly, - · - Easterly; (b) — South-Westerly, - - - North-Westerly, ··· North-Easterly, - · - South-Easterly.

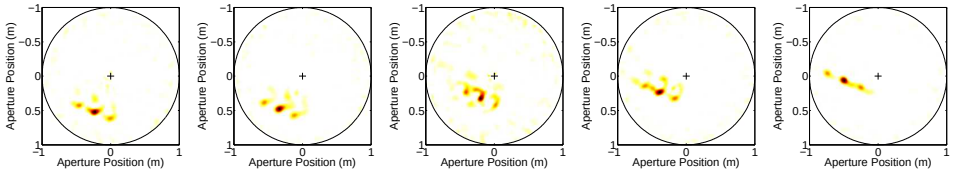

(a) UT 08:14, HA-02:07 (b) UT 08:42, HA-01:39 (c) UT 09:18, HA-01:03 (d) UT 10:46, HA+00:25 (e) UT 11:27, HA+1:05

Figure 5.28: Progression of measured velocity triplets as the telescope tracks α Cru. All runs shown were taken on May 3, 2007 using a pupil-plane field lens on the straight channel of UC-SCIDAR V2007. The dominate layer seen is 11 – 13 km above sea level. As the telescope tracks the star (from (a) to (e)) the measured wind direction shifts from the SW to the W. This translation is an effect of telescope motion.

directions for high altitude layers detected during the observation sequence. At the start of the sequence (indicated by dark blue) the measure wind direction indicates that the wind is originating from South to South-West. At the end of the sequence (indicated by light blue) the measured wind direction indicates a Westerly wind. When compensating for telescope orientation, the variations lessen considerably and the measurements indicate that wind was originating between South-West to West. This particular result is discussed further in Chapter 6.

5.6.3 Telescope Motion and Error

Astronomical observations are rarely taken with the telescope pointed at zenith. The primary mirror is almost always tilted with respect to the ground. As a projection error will exist on the estimated wind velocity.

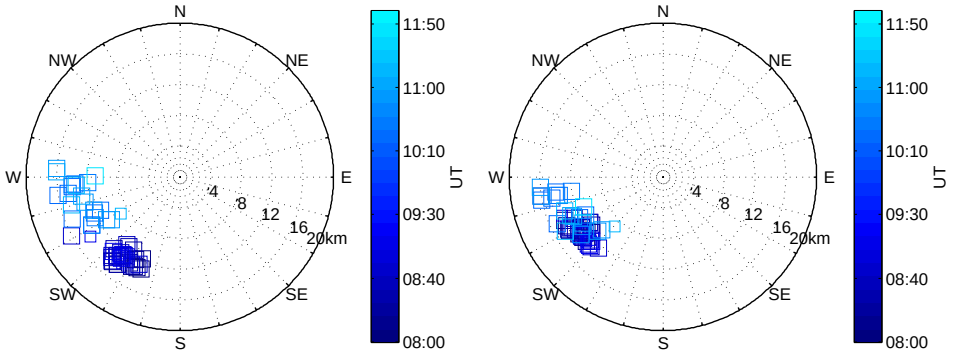

(a) Measured wind direction (b) Corrected wind direction

Figure 5.29: The effect of telescope motion on measured wind direction. Data shown is for a sequence of runs taken on May 3, 2007 tracking α Cru through an hour angle of -2 to +1.5 hours. Only high altitude layer directions are shown.

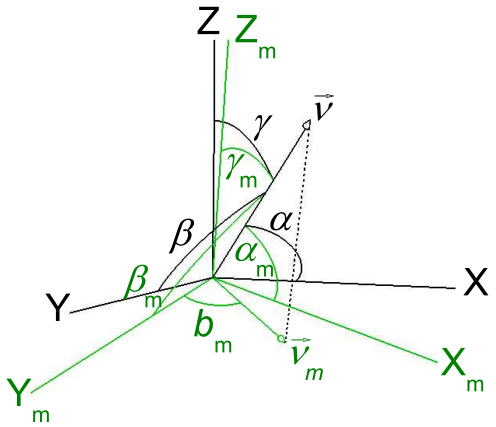

Figure 5.30: Rotation of mirror coordinate system $X_\mathrm{m}Y_\mathrm{m}Z_\mathrm{m}$ in 3D space. The vector $\vec{v}$ forms an angle α, β and γ with the X-, Y- and Z-axes respectively. The projection of $\vec{v}$ on the $X_\mathrm{m}Y_\mathrm{m}$ plane, $\vec{v}_\mathrm{m}$, forms an angle b_m with the Y_m-axis.

Let XYZ define a coordinate system such that the X-, Y- and Z-axes are aligned with West, North and the observer's zenith respectively (Figure 5.30). If $X_\mathrm{m}Y_\mathrm{m}Z_\mathrm{m}$ describes the coordinates of the primary mirror after 3D rotation, then the observed velocity, $\vec{v}_\mathrm{m}$, would be a projection of the true wind velocity, $\vec{v}$.

Consider a mirror rotating through zenith angle ζ only (i.e. rotation in declination only). If β was the angle between the vector $\vec{v}$ and the Y-axis and b_m the angle between the projection $\vec{v}_\mathrm{m}$ and the Y_m-axis, then the error in the difference between β and b_m would be given by (*García-Lorenzo and Fuensalida*, 2006b):

$$\varepsilon_\beta = (\beta - b_\mathrm{m})_\mathrm{radians} = \beta - \arccos\left(\frac{\cos\zeta\cos\beta}{\sqrt{1-\sin^2\zeta\cos^2\beta}}\right), \qquad (5\text{-}20)$$

and the ratio of the projection magnitude, $|\vec{v}_{\rm m}|$ to the true magnitude $|\vec{v}|$ would be (*García-Lorenzo and Fuensalida*, 2006b):

$$\varepsilon_{|\vec{v}|} = \frac{|\vec{v}_{\rm m}|}{|\vec{v}|} = \sqrt{1 - sin^2\zeta \cos^2\beta}. \tag{5-21}$$

Both equations (5-20) and (5-21) assume that wind travels horizontal to the ground and that the telescope is pointed at an azimuth angle, A, of $0°$(i.e. motion along the meridian). They adequately describe the error on $V(h)$ for an alt-azimuth telescope when an azimuth angle correction is applied to β such that the angle β in both equations is replaced by $(\beta - A)$. However for a RA-Dec telescope, these equations do not apply.

Let $\vec{v}$ define a vector in space determined by the direction cosines $(\cos\alpha, \cos\beta, \cos\gamma)$ in XYZ and $(\cos\alpha_{\rm m}, \cos\beta_{\rm m}, \cos\gamma_{\rm m})$ in $X_{\rm m}Y_{\rm m}Z_{\rm m}$ (Figure 5.30). Then

$$x = |\vec{v}|\cos\alpha; \quad y = |\vec{v}|\cos\beta; \quad z = |\vec{v}|\cos\gamma, \tag{5-22}$$

$$x_{\rm m} = |\vec{v}|\cos\alpha_{\rm m}; \quad y_{\rm m} = |\vec{v}|\cos\beta_{\rm m}; \quad z_{\rm m} = |\vec{v}|\cos\gamma_{\rm m}. \tag{5-23}$$

If $\vec{v_{\rm m}}$ was the projection of $\vec{v}$ onto the $X_{\rm m}Y_{\rm m}$ plane and formed an angle $b_{\rm m}$ with the $Y_{\rm m}$-axis, then

$$x_{\rm m} = |\vec{v_{\rm m}}|\sin b_{\rm m}; y_{\rm m} = |\vec{v_{\rm m}}|\cos b_{\rm m}. \tag{5-24}$$

The length of $\vec{v_{\rm m}}$ is

$$|\vec{v_{\rm m}}| = |\vec{v}|\sin\gamma_{\rm m}. \tag{5-25}$$

Assuming that the motion of all turbulent layers is confined to the XY plane (i.e. has no Z component) then

$$\begin{aligned} \sin\gamma_{\rm m}\sin b_{\rm m} &= l_{\rm x}\sin\beta + m_{\rm x}\cos\beta, \\ \sin\gamma_{\rm m}\cos b_{\rm m} &= l_{\rm y}\sin\beta + m_{\rm y}\cos\beta, \\ \cos\gamma_{\rm m} &= l_{\rm z}\sin\beta + m_{\rm z}\cos\beta. \end{aligned} \tag{5-26}$$

Note β is measured in a westerly direction from Y (i.e. negative bearing measurement) and $b_{\rm m}$ is measured westerly from $Y_{\rm m}$.

The error in the measurement direction, $\varepsilon_{\angle{\rm v}}$, has two components. One is related to the direction found in the plane specified by $X_{\rm m}Y_{\rm m}$ as measured by the CCD and the other is related to the telescope motion from Z, such that

$$\begin{aligned} \varepsilon_{\angle{\rm v}} &= \varepsilon_\beta + \varepsilon_\gamma \\ &= (\beta - b_{\rm m}) + (\gamma - \gamma_{\rm m}). \end{aligned} \tag{5-27}$$

As γ_{m} cannot be measured empirically from the CCD, focus is given to ε_β. Using the relations in equation (5-26),

$$\varepsilon_\beta = (\beta - b_{\mathrm{m}})_{\mathrm{radians}} = \beta - \arctan\left(\frac{l_{\mathrm{x}}\sin\beta + m_{\mathrm{x}}\cos\beta}{l_{\mathrm{y}}\sin\beta + m_{\mathrm{y}}\cos\beta}\right). \tag{5-28}$$

Using equations (5-26) and (5-25), the error in the velocity magnitude, $\varepsilon_{|\vec{v}|}$, is defined as

$$\varepsilon_{|\vec{v}|} = \frac{|\vec{v_{\mathrm{m}}}|}{|\vec{v}|} = \sqrt{1 - (l_{\mathrm{z}}\sin\beta + m_{\mathrm{z}}\cos\beta)^2}. \tag{5-29}$$

Figure 5.31 shows the effects of the actual wind direction β on $\varepsilon_{|\vec{v}|}$ and ε_β. The maximum error does not occur in the direction that the telescope is looking (i.e. the azimuth bearing of the object). This is due to the additional rotation seen by the primary mirror. $\varepsilon_{|\vec{v}|}$ is maximum when

$$(l_{\mathrm{z}}\sin\beta + m_{\mathrm{z}}\cos\beta)^2 = 0. \tag{5-30}$$

This occurs when:

$$\beta = n\pi \pm \arccos\left(\sqrt{\frac{l_{\mathrm{z}}^2}{l_{\mathrm{z}}^2 + m_{\mathrm{z}}^2}}\right), \tag{5-31}$$

where n is an integer and the implementation of $\pm$ will depend whether the telescope is looking westerly (i.e. positive hour angle) or easterly (i.e negative hour angle). Figure 5.32 indicates the wind directions, β, for which a true wind velocity measurement would be obtained. For declinations near zenith, the primary mirror is required to undergo greater rotations for larger hour angles and hence have larger variations in the expected β.

The velocity magnitude results presented in this thesis do not account for measurement error resulting from telescope motion, however velocity direction results do.

(See Appendix G for full derivations.)

5.7 Velocity Measurements Using Longer Exposures

The effects of increasing exposure time on scintillation images was discussed in section 4.7 (page 85). Over a given exposure time turbulent structures continue to move, blurring the scintillation images seen, depending on the speed of a given layer. For spatial analysis, this has the effect of decreasing the estimated $C_N^2(h)$ strengths of high altitude turbulence while elongating the central peak, masking secondary peaks from low altitude turbulence. For temporal analysis, longer exposures blur all the peaks associated with a given layer. Figure

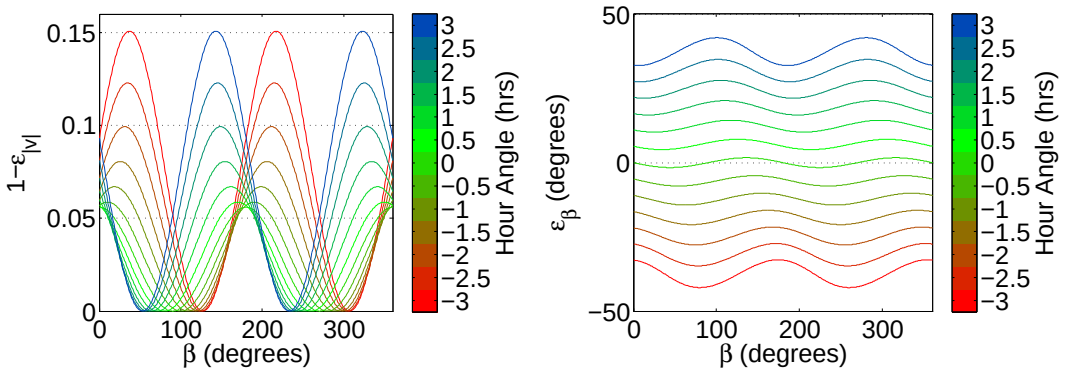

(a) Error in Wind Speed $\varepsilon_{|\vec{v}|}$ (b) Error in Wind Direction ε_β

Figure 5.31: The effect of actual wind direction, β, on the (a) error in wind speed and (b) wind direction when using an RA-Dec telescope. Values shown are for telescope at MJUO tracking of stellar object at $\delta = -63°15'$ through an hour angle of -3:00 to 3:00 depicted by the different colours.

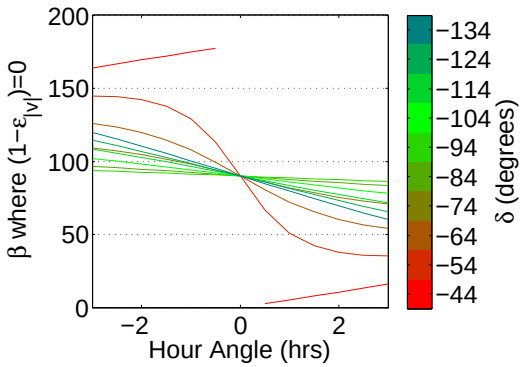

Figure 5.32: Wind directions β resulting in $(1-\varepsilon_{|\vec{v}|}) = 0$. For declinations tracks (indicated the the different colours) approach the zenith crossing the meridian the telescope mirror is require to undergo greater rotation for large hour angles. Hence larger variations can be expected in β.

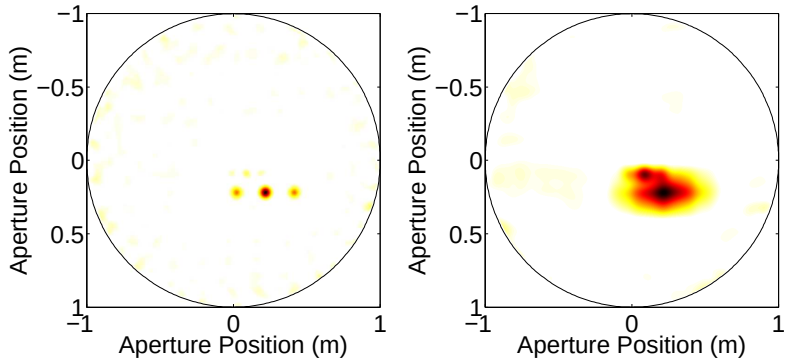

(a) Exposure time: 1 ms (b) Exposure time: 2 ms

Figure 5.33: Simulated 2D spatio-temporal covariances with increasing exposure time. Layers used were located at 5 and 10 km moving at 12 and 30 m/s respectively.

5.33 shows the effects of increased exposure time on simulated data. The simulation shown used the layer parameters indicated in Table 5.1 (page 97) with zero defocus distance. Stellar parameters were based on α Cru. Δt between consecutive frames used was 10 ms.

For an exposure time of 1 ms, all peaks associated with a given layer are well separated. The triplet pattern for the 10 km layer is very strong, masking the 5 km layer. For an exposure time of 2 ms, peaks associated with both layers blur and merge. Note that the central peak from the 10 km blurs with one of the secondary peaks from the 5 km layer. Although the position of the central peak from each layer can still be identified, the altitude of the layers cannot be determined with certainty as the secondary peak positions cannot be clearly identified.

Figure 5.34 shows the effects of increasing exposure times on the 2D spatio-temporal covariances obtained for the same set that was used in Figure 4.29 (page 86). High altitude winds were originating from a Westerly direction, hence the covariances peaks seen in pupil-plane images are located on the left-hand side (Figures 5.34(a), 5.34(b) and 5.34(c)). With increasing exposure time the peaks associated with high altitude layers become excessively blurred making it extremely difficult to identify them amongst the noise. For generalised data, the triplet patterns seen is associated with dome turbulence and hence will be subject to minimal blurring (Figures 5.34(d), 5.34(e) and 5.34(f)).

The blurring seen in temporal analysis reinforces the limitations set on exposure time for trending purposes, i.e. 3.5 ms or less. However it should be noted that altitude determination using exposures of 3.5 ms would be highly dependent on the binary star system separation used at the time. For stellar systems with larger separations the altitude sampling is smaller and hence the secondary peaks are more likely to be separated from the central peak.

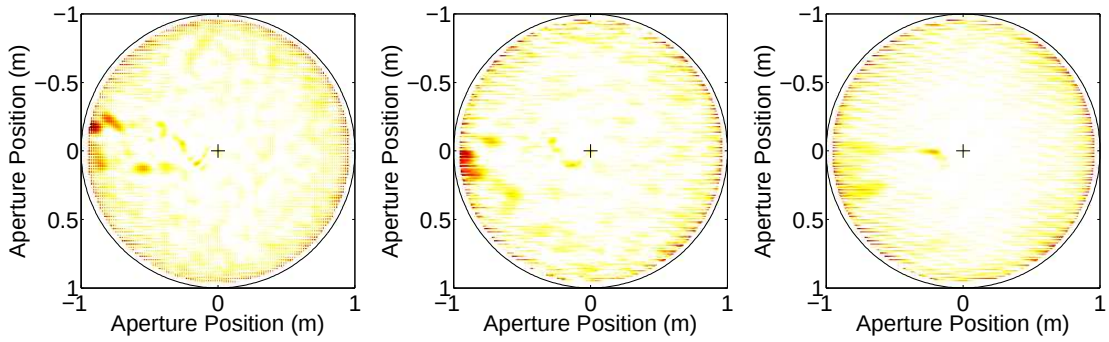

(a) Exposure 1 ms: pupil-plane (run #66)

(b) Exposure 4 ms: pupil-plane (run #67)

(c) Exposure 10 ms: pupil-plane (run #69)

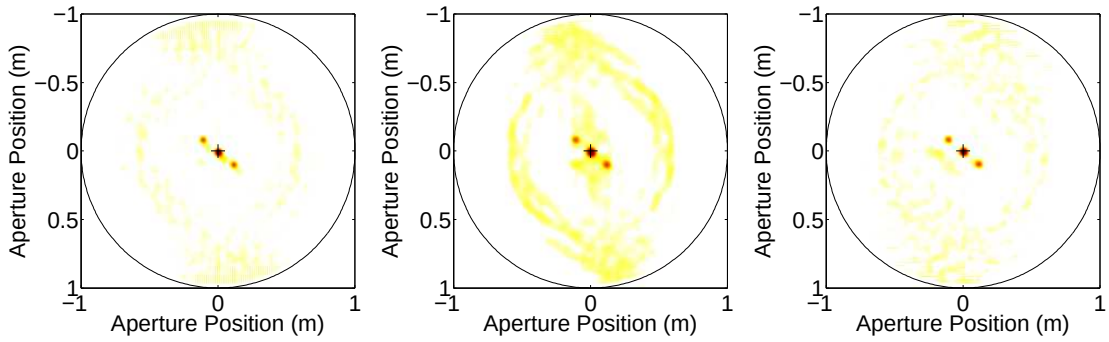

(d) Exposure 1 ms: generalised (run #66)

(e) Exposure 4 ms: generalised (run #67)

(f) Exposure 10 ms: generalised (run #69)

Figure 5.34: The effects of increasing exposure time on 2D spatio-temporal covariances for $\Delta t = 16.7$ ms. Runs shown were taken on 22 July 2004 using α Cen. High altitude winds were originating from a Westerly direction, hence the covariance peaks are located on the left-hand side of pupil-plane image. Generalised profiles are dominated by dome turbulence.

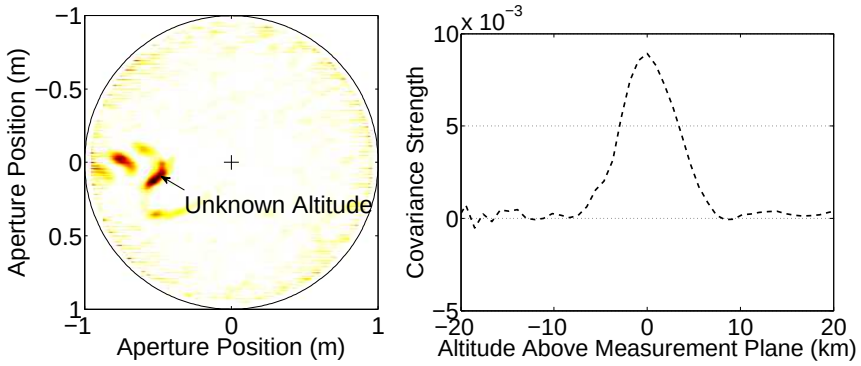

(a) 2D covariance (b) Extracted slice for unknown altitude layer

Figure 5.35: Temporal analysis for pupil-plane data from run #26 taken in July 2005. (a) The 2D covariance determined for $\Delta t = 16.7$ ms reveals a strong layer where secondary peaks are merged with the central peak. The altitude for this layer cannot be determined as no indication of the location of the secondary peak can be seen in the extracted sliced.

5.8 Velocity Measurements in the Presence of Strong NGT

As mentioned in Chapter 4, when exceptionally strong NGT is present, scintillation resulting from low altitudes is detectable in pupil-plane measurements. During temporal analysis, strong NGT will be seen as a strong covariance peak with no identifiable secondary peaks, as the secondary peaks from the low altitude turbulence would merge with the central peak. Figure 5.35(a) shows the 2D covariance determined for the pupil-plane data from run #26 taken in July 2005. The data set uses an altitude sampling, Δh, of approximately 400 m. Multiple layers are seen, however one layer in particular is exceptionally strong, and the secondary peaks associated merge with the central peak. Examination of the extracted slice through the layer (Figure 5.35) suggests that the layer could be located anywhere up to 5 km above the measurement plane. As a result the altitude of the layer cannot be verified. For generalised data (Figure 5.36), the strength associated with NGT means that no layer velocities can be ascertained from this data with any certainty.

For data that layer altitudes could not be verified, the wind velocities were recorded, but not used in trending profiles.

5.9 The Measured Profiles

Full $V(h)$ analysis for individual runs can be found in Appendix I. Site trending of $V(h)$ profiles is found in Chapters 6 and 7, along with the $C_N^2(h)$ profiles obtained using the techniques discussed in Chapter 4.

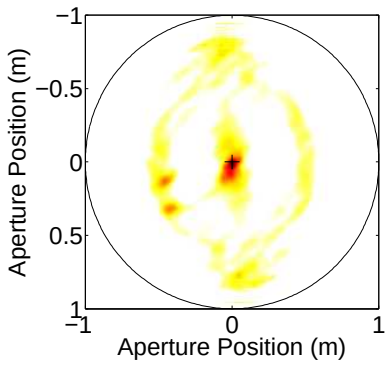

Figure 5.36: Temporal analysis for the generalised data from run #26 taken in July 2005. Due to the strength of NGT, nothing with any certainty can be ascertained from this data.

Chapter 6

Atmospheric Turbulence at MJUO

The first SCIDAR measurements were taken at Mount John University Observatory (MJUO) in April 1999 using the system designed by Imperial College (*Johnston et al.*, 2002). It measured strong near ground turbulence (NGT) and weak high altitude turbulence. For the development of adaptive optics (AO) at MJUO a more complete picture of variations in turbulence profiles is required, and development began on a low-cost system, dubbed UC-SCIDAR, for long term observations in 2003. This chapter discusses measurements taken using the UC-SCIDAR V2005 and V2007 systems.

Measurements of atmospheric turbulence were typically collected using the 1-m telescope at a focal ratio of $F/13.5$. The standard field lenses for UC-SCIDAR (a pupil-plane lens with focal length 12.7 mm and a generalised lens with focal length 10 mm) provided a nominal defocus of 3.9 km below the telescope. Due to the performance characteristics os the CCD cameras used in UC-SCIDAR only a handful of binary star systems were suitable. Stellar parameters of the binary star systems successfully used during the profiling of MJUO are listed in Table 3.3 (page 51).

Not all of the data taken during 2005 and 2007 was suitable for use in profiling the turbulence at MJUO. Only data with exposure times of ≤ 3.5 ms were included in the trending analysis, to ensure that turbulence was not subject to excessive blurring (refer to Chapter 4, section 4.7, page 85 and Chapter 5, section 5.7, page 127). Measurement taken at zenith angles, ζ, greater than 35° were excluded from site profiling. Measurements with $30° < \zeta \leq 35°$ were included only if supporting data taken at $\zeta < 30°$ was acquired within ~ 30 minutes of the run in question. This was to ensure that a suitable altitude range was sampled and that NGT was not subject to vertical air flows located near ground (refer to Chapter 4, section 4.6, page 82). Table 6.1 summarises the usable data collected with the V2005 and V2007 systems. Also indicated is the telescope and the focal ratio configuration used at the time.

Each observation period usually consisted of three to four consecutive nights. Data runs typically consisted of 5000 frames from each camera, which was recorded in file blocks of 500 frames. The V2005 system interleaved 250 frames from each camera per file. The

Table 6.1: Summary of observation runs used in atmospheric turbulence profiling of MJUO.

Month	Dates	# Nights	Telescope	# Collected	# Used	
					$C_N^2(h)$	$V(h)$
June 2007	31/5 – 3/6	4	1-m, F/13.5	P:39, G:30	P:35, G:29	P:35, G:28
May 2007	3–6	4	1-m, F/13.5	P:40, G:25	P:40, G:23	P:38, G:23
January 2007	24–26	3	1-m, F/13.5	P:24, G:10	P: 8, G: 5	P: 5, G: 4
January 2007	27–28	2	1-m, F/7.8	P:12, G:13	P: 6, G: 7	—
January 2007	29–30	2	1-m, F/13.5	P:15, G:15	P: 4, G: 3	P: 4, G: 3
August 2006	10–12	3	B&C, F/13.5	P:38, G:38	P:20, G:16	—
April 2006	20–23	4	B&C, F/13.5	P:30, G:28	P:15, G:13	—
August 2005	12–13	2	1-m, F/13.5	P:37, G:37	P:33, G:33	—
July 2005	6–9	4	1-m, F/13.5	P:72, G:72	P:53, G:50	P:30, G:32
June 2005	11–13	3	1-m, F/13.5	P:35, G:35	P:28, G:29	P:22, G:22
May 2005	12–14	3	1-m, F/13.5	P:55, G:55	P:30, G:47	—
April 2005	22–25	4	1-m, F/13.5	P:30, G:30	P:18, G:25	—
March 2005	10–12	3	1-m, F/13.5	P:39, G:39	P:34, G:35	—

V2007 system files contained 500 frames from a single camera. To decrease processing time 2D spatio-temporal covariances for each camera were calculated using 2500 frames with time delays between consecutive frames of $\Delta t = 0, dt, 2dt \ldots 6dt$, where dt represents the frame rate of the CCD camera used. This ensured that at least 1000 cross-correlations were used in the longer Δt ensembles.

The data presented in this chapter and its analysis is presented from the most recent to earliest measurements taken, starting from 2007 in section 6.1, then 2006 in section 6.2 and 2005 in section 6.3. Data is outlined for each year with a general discussion, followed by a detailed breakdown of each month, again from most recent to earliest results (i.e. December to January). Pertinent features in the refractive index structure constant, $C_N^2(h)$, and the effects on the coherence length, r_0, and isoplanatic angle, θ_0, are discussed for each month. Where relevant, wind velocity profiles, $V(h)$, and the implications on Greenwood frequency, f_G, are also discussed. For full analysis of individual runs see Appendices E and I for $C_N^2(h)$ and $V(h)$ analysis respectively. All r_0, θ_0 and f_G values presented in this chapter have been calculated for a wavelength of 589 nm.

Chapter 7 discusses the seasonal and weather related effects on $C_N^2(h)$ and $V(h)$ profiles. In particular autumn and winter trends are examined. Insufficient number of usable runs were collected during spring and summer months to make any conclusions, and hence these seasons were not examined. Chapter 7 also discusses the models developed to describe the $C_N^2(h)$ and $V(h)$ profiles.

6.1 Measurements from 2007

In 2007, data was collected during the months of January, May and June on the 1-m telescope using UC-SCIDAR V2007 (refer Chapter 3). The majority of the measurements used a focal ratio of $F/13.5$, with the exception being 27–28 January, when a small number of measurements used a focal ratio of $F/7.8$. Figures 6.1 and 6.2 show the overall $C_N^2(h)$ profiles obtained during 2007 for pupil-plane and generalised measurements respectively.

The NGT measurements at MJUO tend to dominate and typically mask any activity present in the upper layers, as seen in Figure 6.1(a). To reveal possible features in these upper layers the $C_N^2(h)$ profiles are scaled so that the colour range is limited to $C_N^2(h)\Delta h$ values between 10^{-14} and 10^{-13} $\mathrm{m}^{1/3}$. Values below 10^{-14} $\mathrm{m}^{1/3}$ are likely to result in images that are diffraction-limited rather than turbulence-limited on a 1-m telescope. r_0 is 1.55 m for a layer with $C_N^2(h)\Delta h = 10^{-14}$ $\mathrm{m}^{1/3}$ and a wavelength of 589 nm. Values greater than 10^{-13} $\mathrm{m}^{1/3}$ are approaching levels that are classified as strong turbulence (*Andrews*, 2004). Figures 6.1(b) and 6.2(b) show the colour scaled images for pupil-plane and generalised measurements from 2007 respectively.

Examination of the overall pupil-plane $C_N^2(h)$ measurements (Figure 6.1) indicate that there was significant turbulence located at low altitudes (i.e. below 5 km above sea level) with an additional layer that could be seen in some measurements at 12 – 14 km above sea level. Where low altitude turbulence was strong (i.e. all of January, the latter half of May and the majority of June) the upper altitude layers were masked. In the generalised data (Figure 6.2) little to no upper altitude activity was detected. The only exception occurred in the first half of May where little NGT was detected in the pupil-plane data.

Table 6.2 summarises the monthly averages and standard deviations for r_0 and θ_0. January exhibited similar r_0 and θ_0 values for both pupil-plane and generalised data, which indicates a significant low-altitude layer. In summer the longer, warmer days heats the surrounding ground and buildings which can lead to greater NGT effects. The pupil-plane θ_0 values obtained for May are smaller than those obtained for June although the r_0 values are similar for the two months. The difference in θ_0 can be attributed to the high altitude layers found in May, which were slightly stronger and higher than those found in June (Figure 6.2(b)).

Figure 6.3 shows the average wind speed, $|V(h)|$, measured as a function of height, h, for the 2007 data. There is some scatter, due to errors associated with height estimation, but the measurements do indicate the presence of a turbulent layer at 11 – 14 km above sea level with an average speed of 18 m/s. In some cases a mid-altitude layer at 6 – 7 km above sea level can be seen moving at approximately 7 m/s. On nights with significant

Table 6.2: Monthly averages and standard deviations for r_0 and θ_0 from 2007, for both pupil-plane and generalised data.

Month	Pupil-plane				Generalised			
	$\overline{r_0}$ (m)	σ_{r_0} (m)	$\overline{\theta_0}$ (arcsec)	σ_{θ_0} (arcsec)	$\overline{r_0}$ (m)	σ_{r_0} (m)	$\overline{\theta_0}$ (arcsec)	σ_{θ_0} (arcsec)
June 2007	0.12	0.03	1.8	0.7	0.05	0.00	1.1	0.3
May 2007	0.11	0.07	1.3	0.9	0.06	0.01	1.0	0.3
January 2007	0.06	0.03	0.8	0.2	0.05	0.02	0.9	0.1

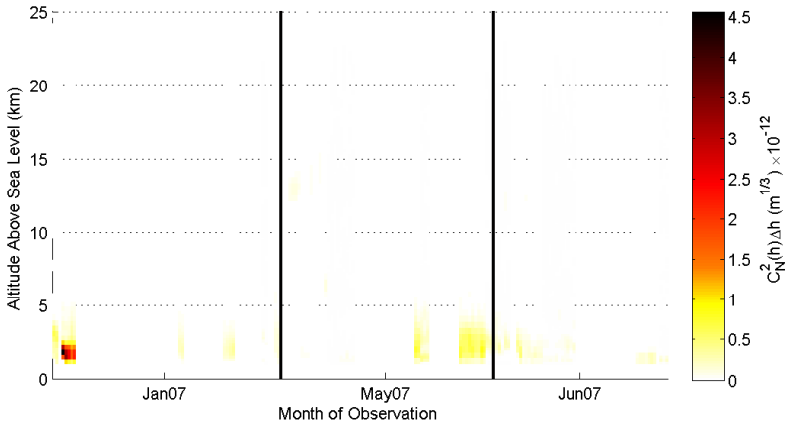

(a) Pupil-plane

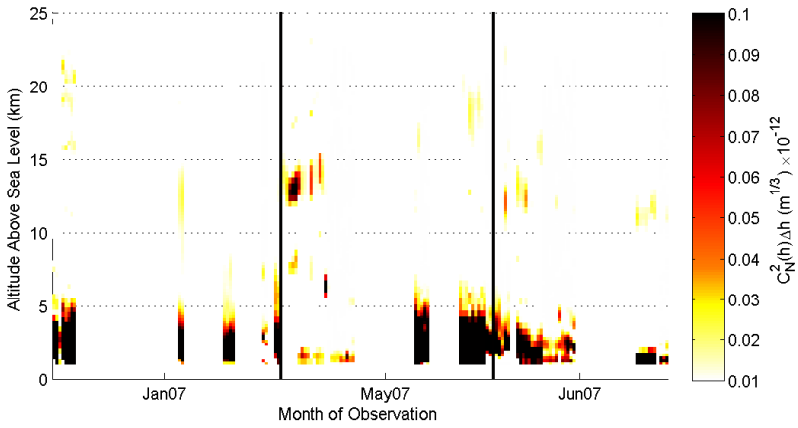

(b) Scaled Pupil-plane

Figure 6.1: Pupil-plane $C_N^2(h)$ profile trends observed over 2007. Gaps have been added where no data is present for more than two hours. Data from the individual months is separated by solid black lines. The image in (b) has been scaled such that any $C_N^2(h)\Delta h$ value above $10^{-13}\mathrm{m}^{1/3}$ is set to the maximum colour range and any $C_N^2(h)\Delta h$ value below $10^{-14}\mathrm{m}^{1/3}$ is set to the minimum colour range.

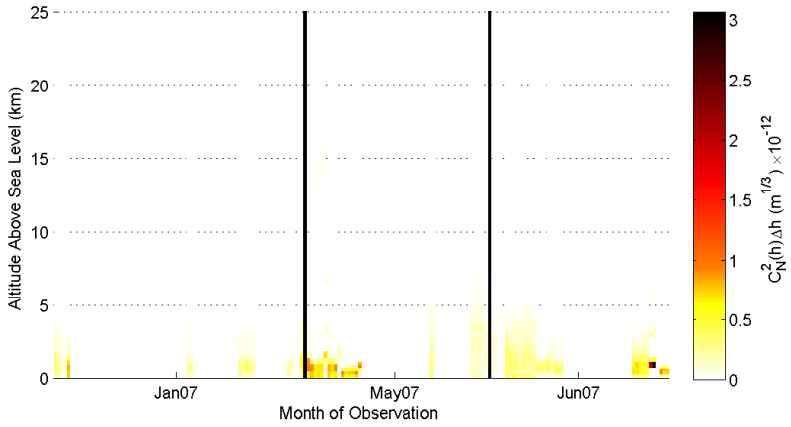

(a) Generalised

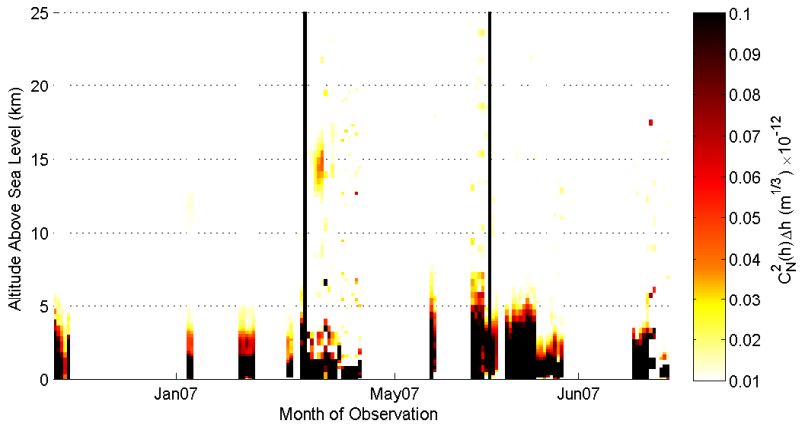

(b) Scaled Generalised

Figure 6.2: Generalised $C_N^2(h)$ profile trends observed over 2007. Time and $C_N^2(h)$ scaling used is as per Figure 6.1.

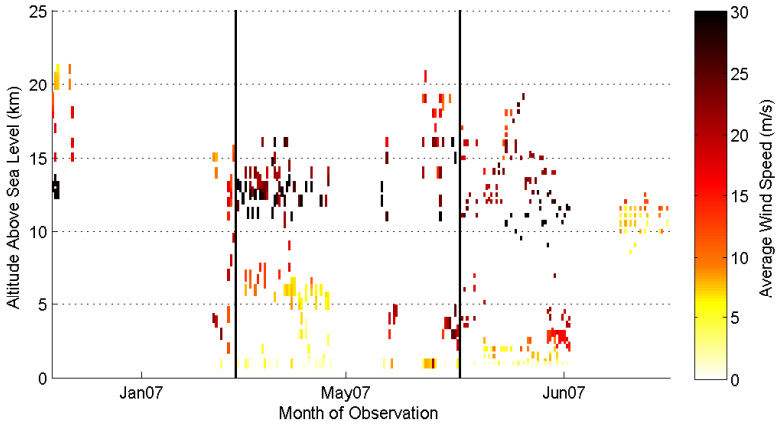

Figure 6.3: Average wind speeds detected, $|V(h)|$, for observations taken during 2007. Time scaling used is as per Figure 6.1.

NGT, a low-altitude layer was seen with wind speeds ranging between 10 to 24 m/s.

The average calculated Greenwood frequency, $\overline{f_G}$, for 2007 was found to be approximately 30 Hz. For a wavelength of 589 nm, the estimate for f_G will typically range between 30 – 90 Hz depending on the models used for $C_N^2(h)$ and $V(h)$ profiles (*Tyson and Frazier*, 2004). The f_G obtained from the data collected at MJUO is at the bottom end of this range. It is most likely that the f_G has been underestimated due to the gaps that exist in the $V(h)$ profiles.

6.1.1 June 2007

During June 2007 the majority of the data sets used α Cen and α Cru, with optimal zenith angles. The SNR on all data sets was sufficient for slice extraction. Figure 6.4 shows the scaled $C_N^2(h)$ profiles for pupil-plane and generalised data and the average wind speed, $|V(h)|$. Although NGT is strong and readily detectable in the pupil-plane data, a weak high-altitude layer can be seen at $\sim$ 12 km above sea level.

Tables 6.3 and 6.4 show the nightly and full run averages for pupil-plane and generalised measurements respectively, for both α Cen and α Cru. The error on the $C_N^2(h)$ estimation fit, ε_C, improves significantly when using α Cru. The shorter exposures used for α Cen had a significant impact on ε_C because the background noise was not smoothed and blurred as would normally occur with longer exposures. This is not considered to be a cause for concern as the r_0 and θ_0 estimates are similar for the two stars.

Observation logs indicate that on 31 May the ground wind speeds reached $\sim$ 20 kph ($\sim$ 6 m/s) with thickening low-altitude cloud. This is reflected in the low $\overline{r_0}$ and $\overline{\theta_0}$ estimates for the pupil-plane data. These values are similar to the measured generalised values indicating that the NGT structure was exceptionally strong on this night.

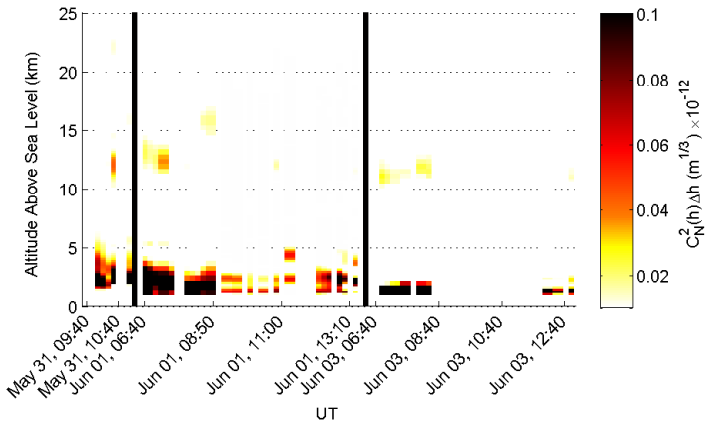

(a) Scaled pupil-plane $C_N^2(h)$ profiles

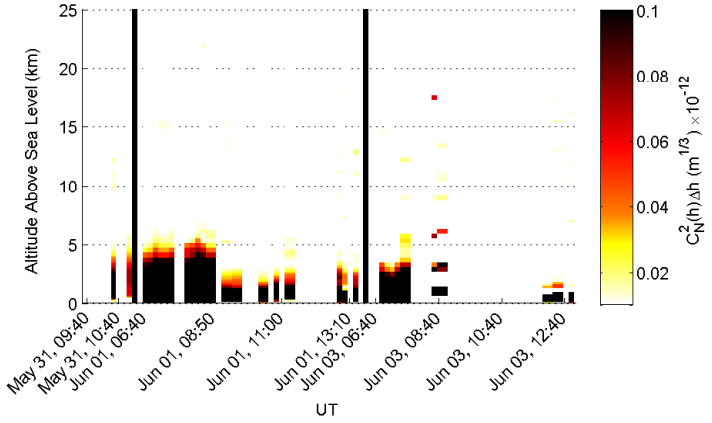

(b) Scaled generalised $C_N^2(h)$ profiles

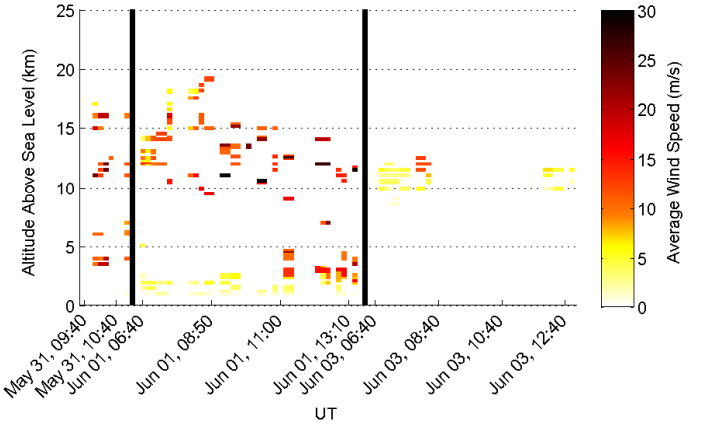

(c) Average wind speeds $|V(h)|$

Figure 6.4: Scaled $C_N^2(h)$ profiles and average wind speeds, $|V(h)|$, for observations taken during June 2007. Time and $C_N^2(h)$ scaling used is as per Figure 6.1.

Table 6.3: Summary of spatial results from June 2007 pupil-plane SCIDAR data.

Date	Star	mean SNR	$\int C_N^2(h)dh$ ($m^{1/3}$)	ε_C (%)	$\overline{r_0}$ (m)	σ_{r_0} (m)	$\overline{\theta_0}$ (arcsec)	σ_{θ_0} (arcsec)
31/05/07	α Cen	39	2.0×10^{-12}	20	0.07	0.02	0.9	0.3
01/06/07	α Cru	22	1.0×10^{-12}	5	0.10	0.11	1.3	1.4
01/06/07	α Cen	37	0.7×10^{-12}	43	0.12	0.03	1.6	0.2
03/06/07	α Cru	23	0.5×10^{-12}	10	0.15	0.02	2.3	0.3
03/06/07	α Cen	25	0.5×10^{-12}	36	0.15	0.04	2.6	0.7
Average	α Cru	23	0.8×10^{-12}	7	0.13	0.03	1.8	0.7
Average	α Cen	34	1.0×10^{-12}	33	0.11	0.04	1.7	0.9
Average	All	29	0.9×10^{-12}	23	0.12	0.03	1.8	0.7

Table 6.4: Summary of spatial results from June 2007 generalised SCIDAR data.

Date	Star	mean SNR	$\int C_N^2(h)dh$ ($m^{1/3}$)	ε_C (%)	$\overline{r_0}$ (m)	σ_{r_0} (m)	$\overline{\theta_0}$ (arcsec)	σ_{θ_0} (arcsec)
31/05/07	α Cen	33	2.1×10^{-12}	3.7	0.06	0.01	0.8	0.0
01/06/07	α Cru	20	2.9×10^{-12}	1.9	0.05	0.00	0.9	0.1
01/06/07	α Cen	29	2.6×10^{-12}	4.6	0.05	0.01	1.1	0.1
03/06/07	α Cru	20	2.5×10^{-12}	3.3	0.05	0.01	1.3	0.1
03/06/07	α Cen	31	2.7×10^{-12}	5.7	0.05	0.00	1.5	0.1
Average	α Cru	20	2.7×10^{-12}	2.6	0.05	0.00	1.1	0.2
Average	α Cen	31	2.5×10^{-12}	4.7	0.06	0.01	1.1	0.3
Average	All	26	2.6×10^{-12}	3.8	0.05	0.00	1.1	0.3

Figures 6.5(a) and 6.5(b) detail the instantaneous measured wind speed, $|V(h)|$, and wind direction, β, as a function of altitude respectively. Each night of observation is represented by a different colour range and corresponding symbol. The size of the symbol used is indicative of the wind speed where:

- a small symbol represents $|V(h)| \leq 10$ m/s,
- a medium sized symbol represents $10 < |V(h)| \leq 20$ m/s, and
- a large sized symbol represents $|V(h)| > 20$ m/s.

Both Figures 6.5(a) and 6.5(b) make no attempt to compensate for the projection error due to telescope orientation on velocity magnitude, $(1 - \varepsilon_{|\vec{v}|})$. Hence $|V(h)|$ profiles are underestimated by up to 10% of the measured value. In Figure 6.5(b) the velocity direction has been corrected for any telescope orientation error. (Chapter 5 , section 5.6 (page 119) provides further discussion on projection errors.) Comparison of the layer heights found during temporal analysis (Figure 6.5(a)) with those found in the pupil-plane $C_N^2(h)$ profiles (Figure 6.5(c)) provide an additional level of validation on the measured $V(h)$ profile.

On 31 May, indicated by the blue squares in Figure 6.5, a layer at ~ 5 km above sea level was found to have a velocity of ~ 20 m/s. At this altitude altocumulus and altostatus clouds are known to form in New Zealand (*Sturman and Tapper*, 1996) and it is likely that this corresponded to the thickening cloud layer observed. Also measured was a high altitude layer at approximately 12 km moving at 24 m/s. This would correspond to a layer located at the tropopause region. A much weaker layer was also detected at approximately 15 km. Velocities of this layer were found to be 12 – 18 m/s.

On 1 June, indicated by the purple circles in Figure 6.5, observations started with a thin cloud layer over the site with ground wind speeds ranging from 10 – 30 kph (2.8 – 8.3 m/s). The cloud layer remained thin and measurements could be taken using exposure times of 0.5 – 2 ms while operating in dual camera mode for the majority of the night. A layer at 2 – 5 km above sea level was found to have $|V(h)|$ ranging from 10 – 20 m/s with NGT moving at 2 – 10 m/s. This is consistent with the observation logs.

The 3rd of June was a calm clear night with little to no ground winds. Examination of pupil-plane $C_N^2(h)$ profiles revealed that the high altitude layer was weaker than seen on earlier nights. This is reflected in the pupil-plane θ_0 values which increase from 1.3 – 1.6 arcseconds to 2.3 – 2.6 arcseconds (Table 6.3). Pupil-plane r_0 estimates also increased from 10 – 12 cm to approximately 15 cm. Generalised θ_0 increased slightly and generalised r_0 remained unchanged (Table 6.4).

The measured $|V(h)|$ for 3 June, indicated by the red stars in Figure 6.5, decreases significantly for the layer located at approximately 10 – 12 km. This corresponds to the decreased $C_N^2(h)\Delta h$ strength that occurs on the same night. Velocity measurements

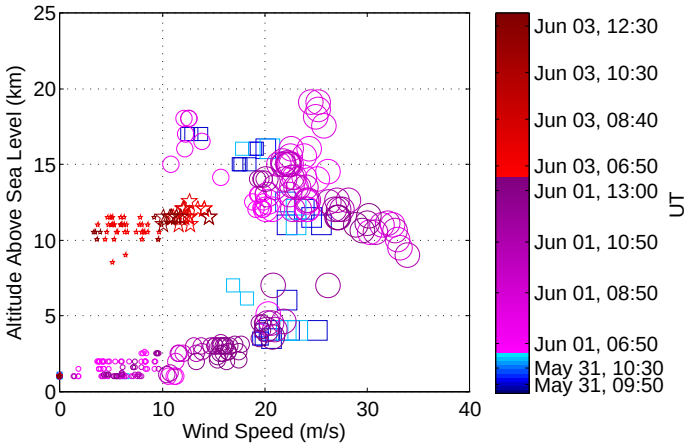

(a) Instantaneous wind speed $|V(h)|$

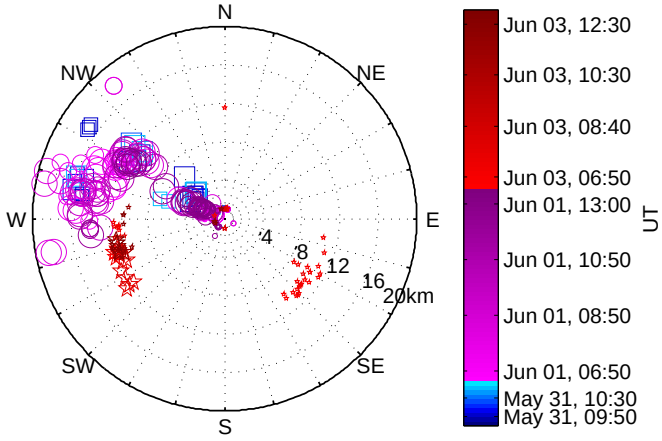

(b) Instantaneous wind direction β

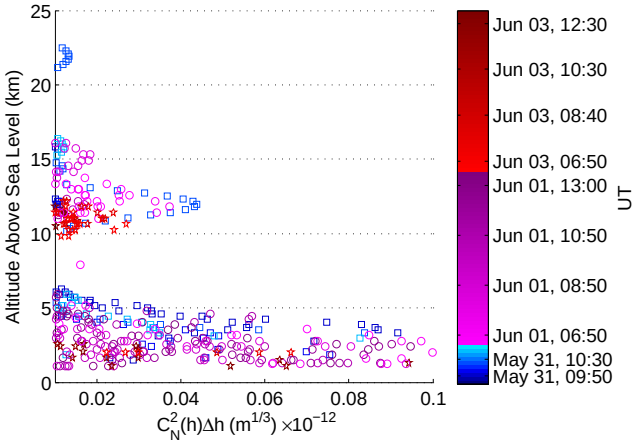

(c) Scaled pupil-plane $C_N^2(h)$ profiles

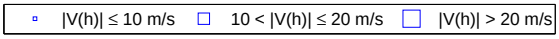

Figure 6.5: Wind velocity analysis for observations made during June 2007. Each night of observation is indicated by a different colour range and symbol (□ – 31 May, ◯ – 1 June and ★ – 3 June). The size of the symbols used in (a) and (b) is indicative of the measured wind speed and corresponds to text on page 141. Layer heights found in (a) should match those detected in the pupil-plane $C_N^2(h)$ profiles shown in (c) for the different nights.

Table 6.5: Nightly averages and standard deviations for f_G during June 2007.

Date	Pupil-plane		Generalised	
	$\overline{f_G}$ (Hz)	σ_{f_G} (Hz)	$\overline{f_G}$ (Hz)	σ_{f_G} (Hz)
31/05/07	27	8	20	29
01/06/07	26	13	30	32
03/06/07	6.7	2.7	–	–
31/05 - 1/06	26	12	29	31

indicate that multiple layers were present for this altitude range. A layer at $\sim$ 10 km above sea level had a velocity of 5 – 10 m/s with a slightly higher layer moving between 10 – 15 m/s. The higher layer originated from a south-west to westerly direction consistently throughout the night. The lower layer originated initially from a south-east to easterly direction (UT 06:45 – 08:00) then shifted to a Westerly wind (UT 12:00 – 12:40).

Figure 6.6 shows the aperture normalised 2D spatio-temporal covariances for multiple time delay between successive frames, Δt, and the extracted layer slices from two pupil-plane runs taken on 3 June: run #400 (UT06:44) and #456 (UT12:40). For both runs there are two dominant layers that are both located at an altitude of approximately 10 km above the measurement plane. The 2D covariance images are oriented to match the primary mirror, but do not compensate for telescope orientation. These images show that at least two turbulent layers exist at this altitude moving with different speeds and in different directions.

Optical turbulence results primarily from temperature differentials (*Andrews*, 2004). Although variations are recognised to exist with location and time, turbulence is usually greatest near ground and decreases exponentially with increasing altitude, except for a peak that is often found at the tropopause region. *Hardy* (1998) suggests that the spike in the $C_N^2(h)$ profiles at the tropopause is due to wind shear. In this case wind shear is considered to be the most probable explanation for the characteristics seen in the $V(h)$ profiles for 3 June.

Table 6.5 shows the nightly average and standard deviation for Greenwood frequency, f_G, based on the profiles shown in Figures 6.4 and 6.5. $\overline{f_G}$ was found to be in the order of 25 – 30 Hz for the nights of 31 May and 1 June. $\overline{f_G}$ for 3 June was extremely low. This is due to the lack of velocity points obtained for this night and the dramatic decrease in high altitude wind speeds. If this night is excluded from calculations the monthly average for June 2007 is in the order of 30 Hz.

f_G calculated from SCIDAR can be underestimated because wind velocity measurements are reliant on covariance strengths in the measurement plane being sufficiently strong enough to be above the noise level. As discussed in Chapter 5, aperture normal-

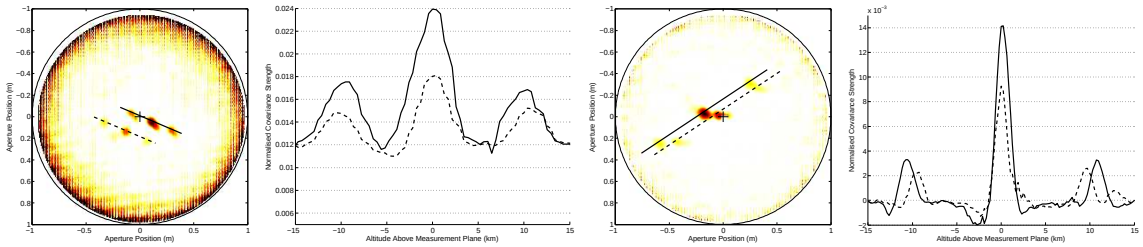

(a) June 2007: #400 $\Delta t = 16.7$ ms (b) Extracted slices indicated in (a) (c) June 2007: #456 $\Delta t = 16.7$ ms (d) Extracted slices indicated in (c)

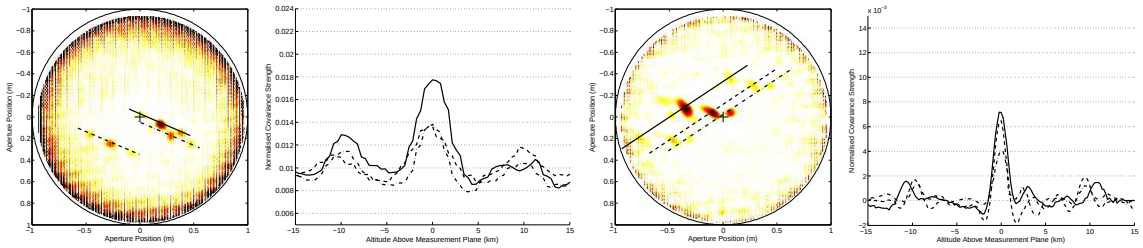

(e) June 2007: #400 $\Delta t = 33.3$ ms (f) Extracted slices indicated in (e) (g) June 2007: #456 $\Delta t = 33.3$ ms (h) Extracted slices indicated in (g)

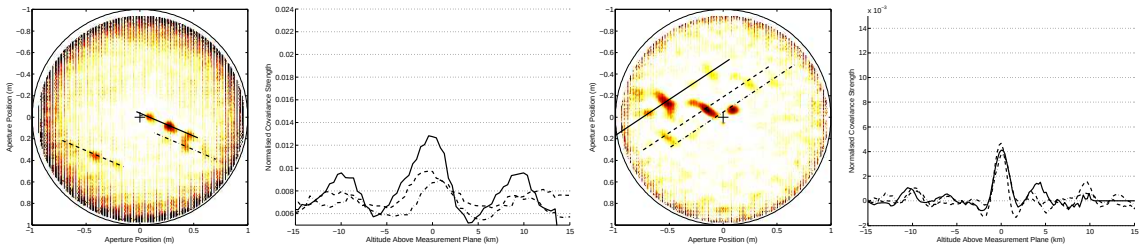

(i) June 2007: #400 $\Delta t = 50.0$ ms (j) Extracted slices indicated in (i) (k) June 2007: #456 $\Delta t = 50.0$ ms (l) Extracted slices indicated in (k)

Figure 6.6: 2D spatio-temporal covariances and extracted slices from selected runs from June 2007. The 2D covariances from run #400 (taken at UT06:44) for increasing time delay between consecutive frames, Δt, are shown in (a), (e) and (i). The lines indicate the location of the corresponding extracted slices shown in (b), (f) and (j). (c), (g) and (k) show the 2D covariances from run #456 (taken at UT12:40), where the extracted slices are in shown (d), (h) and (l).

isation amplifies noise, and peaks approaching the aperture edge can be hidden by the noise. Partial triplet analysis does allow for more layer velocities to be found. Although all layers seen in $V(h)$ will have an associated $C_N^2(h)$ strength, even if extremely weak. Not all $C_N^2(h)$ layers will have a measurable $V(h)$ due to the aperture position and the resulting covariance strength. This is reflected in the large σ_{f_G} values.

6.1.2 May 2007

During May 2007, all pupil-plane measurements were collected using α Cen and α Cru, as were all but two generalised runs. The remaining runs were not suitable for profiling turbulence extending into the tropopause region. Figure 6.7 shows the scaled $C_N^2(h)$ profiles for pupil-plane and generalised data, as well as $|V(h)|$ measured during this period.

On 3 May there were low wispy clouds present, and ground wind speed was recorded at $<$ 2 kph ($<$ 0.5 m/s). $C_N^2(h)$ profiles detected strong NGT with a layer of moderate strength at 12 km and a weaker layer at 6 – 7 km, which was visible only in pupil plane analysis. r_0 for pupil-plane measurements, indicated in Table 6.6, is consistent with observed weather conditions, where $\overline{r_0}$ was 17 cm for α Cru and 23 cm for α Cen.

On 5 May the ground wind speeds averaged 20 – 30 kph (5.6 – 8.3 m/s) with cloud moving across the site from a westerly direction at low- to mid-altitudes. The increased ground wind speed is reflected in r_0 estimates where $\overline{r_0}$ dramatically decreased from the previous night to 4 – 6 cm.

On 6 May there was a thin layer of cloud and ground wind speeds measured 8 kph ($\sim$ 2 m/s) at the start of the evening. Observations were discontinued at UT 12:00 due to ground winds increasing to above 40 kph ($>$ 11 m/s) from the West. $\overline{r_0}$ for this night remained at 4 – 6 cm.

r_0 for generalised measurements on 3 May, indicated in Table 6.7, was 5 – 6 cm, but for later nights r_0 is greater than that seen for pupil-plane data, which was 4 – 5 cm. As discussed in Chapter 4, central peak removal during slice extraction is problematic when a significant amount of turbulence is located near ground, as in the case of 6 May, and usually results in low r_0 estimates for pupil-plane data. In the calculation of the pupil-plane r_0 monthly average, the generalised r_0 estimates were used. The replaced value are indicated by the brackets in Table 6.6.

Figure 6.8 shows the measured velocity and corresponding scaled pupil-plane $C_N^2(h)$ profiles for May 2007. The coding used in Figure 6.8 is similar to that used in Figure 6.5. For 3 May, indicated by the blue squares, the velocity of the layer detected at 12 km above sea level was found to have an average wind speed of 25 m/s and originated from the south-west to west. The 6 – 7 km layer had a velocity ranging from 6 – 14 m/s, whereas the ground winds were found to be below 5 m/s. On 5 May and 6 May, indicated

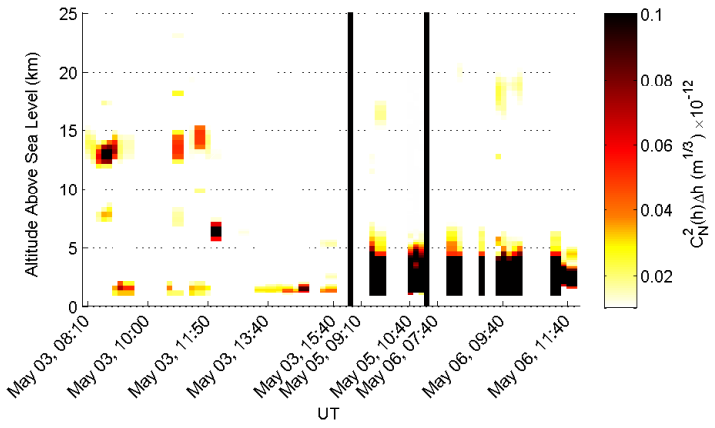

(a) Scaled pupil-plane $C_N^2(h)$ profiles

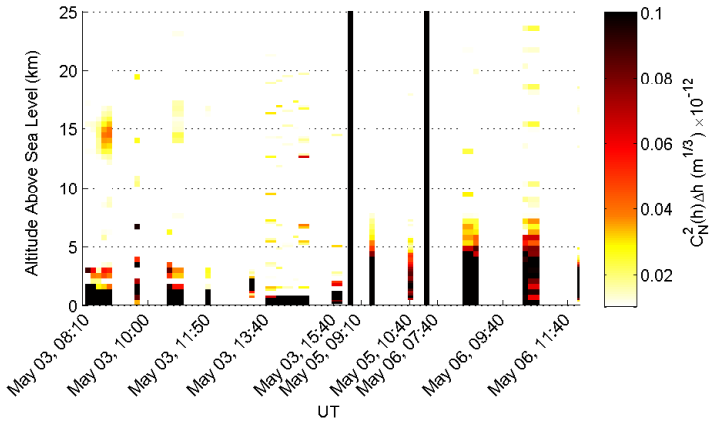

(b) Scaled generalised $C_N^2(h)$ profiles

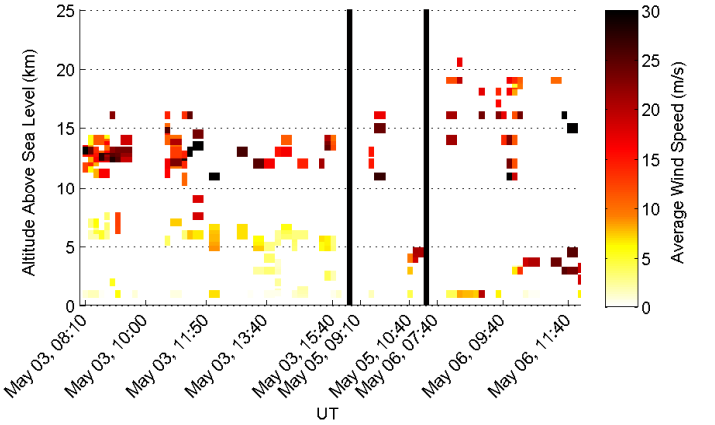

(c) Average wind speed $|V(h)|$

Figure 6.7: Scaled $C_N^2(h)$ profiles and average wind speeds, $|V(h)|$, for observations taken during May 2007. Time and $C_N^2(h)$ scaling used is as per Figure 6.1.

Table 6.6: Summary of spatial results from May 2007 pupil-plane SCIDAR data. For the determination of the averages, some values were replaced by the generalised estimates. These values are indicated by the brackets.

Date	Star	mean SNR	$\int C_N^2(h)dh$ ($m^{1/3}$)	ε_C (%)	$\overline{r_0}$ (m)	σ_{r_0} (m)	$\overline{\theta_0}$ (arcsec)	σ_{θ_0} (arcsec)
03/05/07	α Cru	44	0.5×10^{-12}	10	0.17	0.05	1.2	0.4
03/05/07	α Cen	72	0.2×10^{-12}	45	0.23	0.04	3.1	0.6
05/05/07	α Cru	37	3.5×10^{-12}	3	(0.05)	(–)	0.9	0.0
05/05/07	α Cen	35	4.1×10^{-12}	39	(0.06)	(–)	0.9	0.1
06/05/07	α Cru	37	3.4×10^{-12}	3	(0.07)	(0.01)	0.8	0.1
06/05/07	α Cen	56	2.2×10^{-12}	17	0.06	0.00	1.0	0.0
Average	α Cru	39	2.5×10^{-12}	5	0.10	0.07	1.0	0.2
Average	α Cen	54	2.2×10^{-12}	33	0.11	0.10	1.7	1.2
Average	All	47	2.3×10^{-12}	19	0.11	0.07	1.3	0.9

Table 6.7: Summary of spatial results from May 2007 generalised SCIDAR data.

Date	Star	mean SNR	$\int C_N^2(h)dh$ ($m^{1/3}$)	ε_C (%)	$\overline{r_0}$ (m)	σ_{r_0} (m)	$\overline{\theta_0}$ (arcsec)	σ_{θ_0} (arcsec)
03/05/07	α Cru	32	2.3×10^{-12}	3	0.06	0.01	1.0	0.2
03/05/07	α Cen	52	3.0×10^{-12}	6	0.05	0.02	1.5	0.3
05/05/07	α Cru	31	3.1×10^{-12}	2	0.05	–	0.9	–
05/05/07	α Cen	31	2.1×10^{-12}	3	0.06	–	0.8	–
06/05/07	α Cru	41	1.8×10^{-12}	1	0.07	0.01	0.9	0.0
06/05/07	α Cen	32	2.1×10^{-12}	3	0.06	–	0.8	–
Average	α Cru	34	2.4×10^{-12}	2	0.06	0.01	0.9	0.1
Average	α Cen	38	2.4×10^{-12}	4	0.06	0.01	1.0	0.4
Average	All	36	2.4×10^{-12}	3	0.06	0.01	1.0	0.3

Table 6.8: Nightly averages and standard deviations for f_G during May 2007.

	Pupil-plane		Generalised	
Date	$\overline{f_G}$ (Hz)	σ_{f_G} (Hz)	$\overline{f_G}$ (Hz)	σ_{f_G} (Hz)
03/05/07	24	22	6.6	7.8
05/05/07	41	25	0.5	0.7
06/05/07	36	31	21	20
All	30	23	8	13

by purple circles and red stars respectively, turbulence located below 5 km was found to have wind speeds as high as 25 m/s, with ground wind speeds measuring as high as 21 m/s. These low altitude winds were found to be originating from a westerly direction which was consistent with the observation logs.

Table 6.8 shows the nightly f_G estimates for May 2007. The $\overline{f_G}$ on 3 May was 24 Hz for pupil-plane measurements. This increased to approximately 35 – 40 Hz for 5 May and 6 May, which can be related to the significant increase in wind speeds for the low- to mid-altitude region. This increase in $\overline{f_G}$ is also seen in the generalised measurements for 3 and 6 May, and can be attributed to the dramatic increase in ground wind speeds and resulting turbulent strengths toward the end of the evening. The apparent decrease in generalised $\overline{f_G}$ for 5 May will be related to small number of runs collected on this night. The monthly average $\overline{f_G}$ was ~ 30 Hz for pupil-plane measurements.

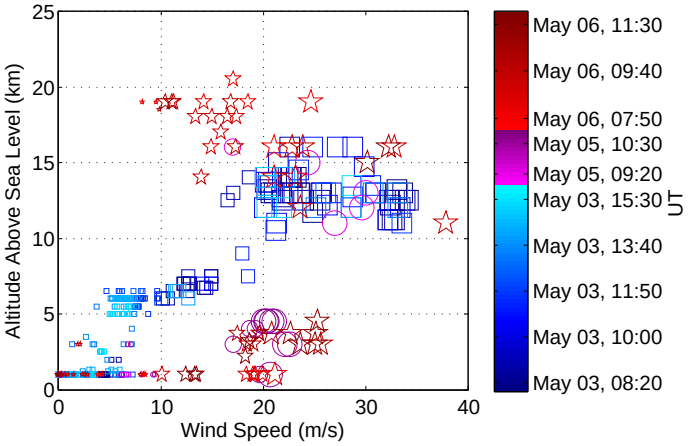

(a) Instantaneous wind speed $|V(h)|$

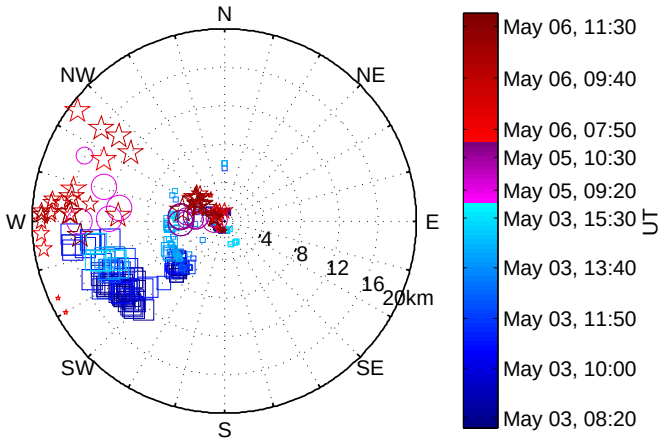

(b) Instantaneous wind direction β

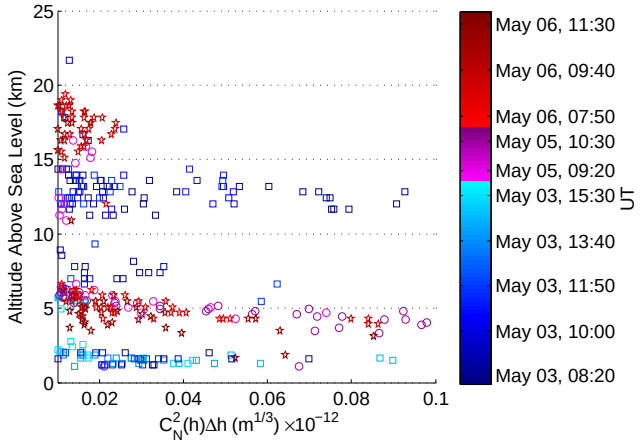

(c) Scaled pupil-plane $C_N^2(h)$ profiles

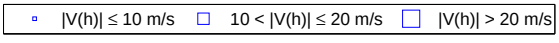

Figure 6.8: Wind velocity analysis for observations made during May 2007. Colour and symbol sizes conventions used are as per Figure 6.5.

6.1.3 January 2007

The majority of the measurements collected during January 2007 used a focal ratio of $F/13.5$. On 27 – 28 January a small number of measurements were obtained using a focal ratio of $F/7.8$. The use of the standard V2007 field lenses resulted in a nominal defocus distance of 1.25 km for $F/7.8$ rather than 3.9 km for $F/13.5$. All measurements taken during January 2007 were collected using the single camera mode on the UC-SCIDAR V2007.

From autumn to early spring, measurements can be readily obtained using α Cen and α Cru because these star systems are ideally positioned in the Southern night sky. During summer months, these star systems are too low in the sky to be used continually throughout the night. The CCD performance characteristics of the V2007 system enabled measurements to be taken using θ Eri and υ Car while operating in single camera mode, which was used during January 2007. When using $F/7.8$, the available light is spread across more pixels such that each pixel represents a smaller area of the primary mirror. This meant that θ Eri and υ Car were unsuitable to use for trending with the $F/7.8$ measurements as the exposure times required to adequately capture the scintillation images would be in the order of 10 ms.

Figure 6.9 shows the scaled $C_N^2(h)$ profile for pupil-plane and generalised measurements, as well as $|V(h)|$, for January 2007. Few velocity measurements are shown in Figure 6.19(c). Strong NGT can blur any covariance peaks detected during temporal analysis, particularly when using star systems with a narrow angular separation. It may not be possible to determine the height of a layer using temporal analysis as the primary and secondary peaks blur together. The spatial sampling in the $F/7.8$ measurements compounded this issue, where both of the secondary peaks from high altitude layers could be located near to, or even off, the aperture edge. Although a full listing of velocity measurements for January 2007 can be found in Appendix I, only a handful of measurement have altitudes that could be determined, as indicated in Figure 6.10.

On 24 January the observation log noted ground winds gusting up to 40 kph (11 m/s) coming from a North-West direction. In contrast, 25 January was calm with slight cloud cover at the start of the evening, which thickened to fog. Unfortunately data collected on 25 January utilised exposure times of 5 – 10 ms and could not be used for trending purposes. On 29 January ground wind speeds ranged from 10 – 20 kph (2.8 – 5.6 m/s) at the start of the evening. Measurements were halted as the winds died down and thick cloud settled over the site.

Tables 6.9 and 6.10 show the nightly averages and standard deviations determined for the spatial analysis of pupil-plane and generalised data respectively. The low pupil-plane r_0 values correspond with the observation logs detailing cloud and high ground

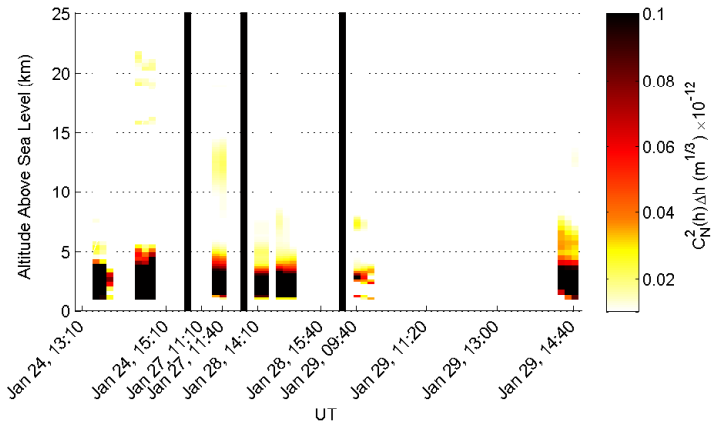

(a) Scaled pupil-plane $C_N^2(h)$ profiles

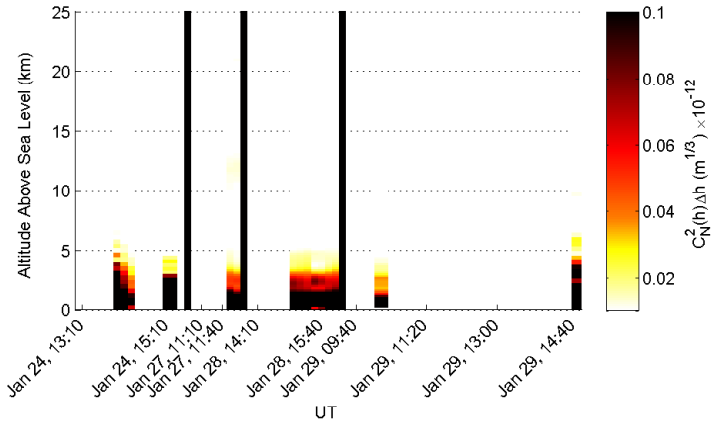

(b) Scaled generalised $C_N^2(h)$ profiles

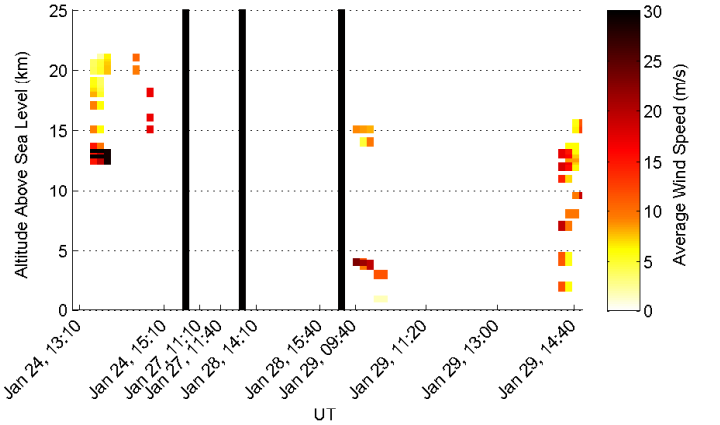

(c) Average wind speed $|V(h)|$

Figure 6.9: Scaled $C_N^2(h)$ profiles and average wind speeds, $|V(h)|$, for observations taken during January 2007. Time and $C_N^2(h)$ scaling used is as per Figure 6.1.

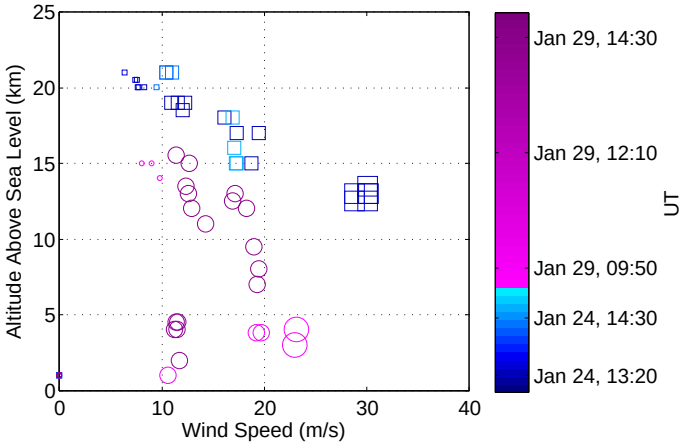

(a) Instantaneous wind speed $|V(h)|$

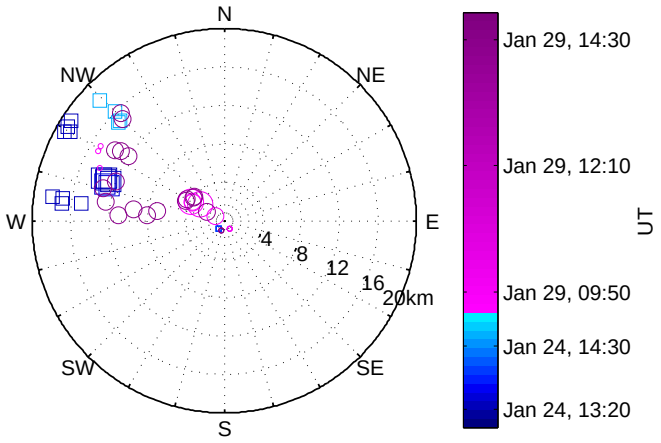

(b) Instantaneous wind direction β

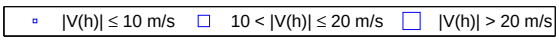

Figure 6.10: Wind velocity analysis for observations made during January 2007. Colour and symbol sizes conventions used are as per Figure 6.5.

Table 6.9: Summary of spatial results from January 2007 pupil-plane SCIDAR data.

Date	Star	mean SNR	$\int C_N^2(h)dh$ ($m^{1/3}$)	ε_C (%)	$\overline{r_0}$ (m)	σ_{r_0} (m)	$\overline{\theta_0}$ (arcsec)	σ_{θ_0} (arcsec)
24/01/07	α Cru	26	2.2×10^{-12}	5	0.09	0.07	1.2	0.8
24/01/07	υ Car	13	9.3×10^{-12}	14	0.02	0.00	0.7	0.1
27/01/07	α Cru	25	3.2×10^{-12}	12	0.05	0.00	0.6	0.0
28/01/07	α Cru	24	2.8×10^{-12}	12	0.05	0.01	0.8	0.1
29/01/07	θ Eri	–	–	–	–	–	–	–
29/01/07	α Cru	31	1.3×10^{-12}	5	0.08	0.00	0.9	0.0
Average	α Cru	27	2.4×10^{-12}	9	0.07	0.02	0.9	0.2
Average	All	24	3.8×10^{-12}	10	0.06	0.03	0.8	0.2

Table 6.10: Summary of spatial results from January 2007 generalised SCIDAR data.

Date	Star	mean SNR	$\int C_N^2(h)dh$ ($m^{1/3}$)	ε_C (%)	$\overline{r_0}$ (m)	σ_{r_0} (m)	$\overline{\theta_0}$ (arcsec)	σ_{θ_0} (arcsec)
24/01/07	α Cru	21	1.9×10^{-12}	4	0.07	0.04	1.0	0.3
24/01/07	υ Car	16	9.8×10^{-12}	5	0.02	–	0.8	–
27/01/07	α Cru	22	2.8×10^{-12}	4	0.05	0.00	0.7	0.0
28/01/07	α Cru	23	2.9×10^{-12}	4	0.05	0.00	1.0	0.1
29/01/07	θ Eri	18	2.0×10^{-12}	16	0.06	0.00	1.0	0.0
29/01/07	α Cru	19	3.6×10^{-12}	3	0.04	–	0.8	–
Average	α Cru	21	2.8×10^{-12}	4	0.05	0.01	0.8	0.2
Average	All	20	3.8×10^{-12}	6	0.05	0.02	0.9	0.1

wind speeds. It should be noted that the pupil-plane $\overline{r_0}$ measurement from υ Car on 24 January was 2 cm compared to the 9 cm measured for α Cru from the same night. This will be related to the increasing ground level turbulence that is seen in the data collected on the night and noted in the observation logs, with gusting ground wind speeds up to 11 m/s. No σ values are provided for generalised measurements of υ Car on 24 January and α Cru on 29 January because only one generalised measurement was taken.

Very few $V(h)$ profiles could be obtained, but using the profiles shown in Figures 6.9 and 6.10, a monthly average $\overline{f_G}$ of approximately 20 Hz ($\sigma_{f_g} \approx 15$ Hz) was calculated.

6.2 Measurements from 2006

Data collection on the 1-m telescope during 2006 utilised the UC-SCIDAR V2006 system. Due to the unreliable nature of the CCD readout of the V2006 system, none of this data could be used for trending.

In April and August of 2006, UC-SCIDAR V2005 was mounted on the 60-cm Boller & Chivens telescope (B & C). When operating at a focal ratio of $F/13.5$, the standard

Table 6.11: Summary of spatial results from August 2006 generalised SCIDAR data.

Date	Star	mean SNR	$\int C_N^2(h)dh$ ($m^{1/3}$)	ε_C (%)	$\overline{r_0}$ (m)	σ_{r_0} (m)	$\overline{\theta_0}$ (arcsec)	σ_{θ_0} (arcsec)
10/08/06	α Cen	25	1.4×10^{-12}	37	0.09	0.04	2.2	0.5
11/08/06	α Cen	24	1.4×10^{-12}	35	0.08	0.00	2.2	0.3
Average	α Cen	24	1.4×10^{-12}	36	0.09	0.03	2.2	0.4

V2005 field lenses resulted in a nominal defocus distance of $\sim$ 1.5 km below the telescope.

Figures 6.11 and 6.12 show the $C_N^2(h)$ profiles for pupil-plane and generalised data respectively for the B & C data. High altitude activity was not detectable when using α Cen as a maximum height of approximately 11 km above the telescope could be sampled. The separation of α Cen at the time was approximately 9 arcseconds. This is evident in the pupil-plane analysis for August 2006, where all useable runs were collected using α Cen.

Generalised analysis for August 2006 suggests that the $\overline{r_0}$ was 8.5 cm (σ_{r_0} = 3.1 cm). The $\overline{\theta_0}$ calculated was 2.2 arcseconds (σ_{θ_0} = 0.4 arcseconds), shown in Table 6.11, however this is most likely high based on the fact that high altitude activity above 11 km, including activity near the tropopause, was not detectable.

In April 2006 some data was collected using α Cru, which permitted measurements up to approximately 18 km above the telescope. On 20 April observation logs noted steady ground winds, but no record of the speed is made as the wind meter readout for the B & C was not operational at the time. A strong high altitude layer was found at 16 – 17 km above sea level with additional layers found near ground, at approximately 6 km and at 12 – 13 km seen weakly in pupil-plane data. The $\overline{r_0}$ for the pupil-plane data was found to be 6.5 cm (σ_{r_0} = 0.4 cm) and $\overline{\theta_0}$ was 0.72 arcseconds (σ_{θ_0} = 0.10 arcseconds). Table 6.12 shows the averages calculated for the generalised analysis. Although the $\overline{r_0}$ values were similar for both stars ($\sim$ 5 cm), the $\overline{\theta_0}$ increased significantly from 0.7 arcseconds for the α Cru data to 1.4 arcseconds for the α Cen data. As with the August 2006 data, the estimate calculated from α Cen data is most likely too high as activity that occurs at altitudes greater than 11 km was not detectable.

Temporal analysis on data collected on the B & C is unlikely to provide useful $V(h)$ profiles. Given a telescope diameter of 0.6 m and a sampling frame rate of 30 Hz, the maximum velocity detectable would be 18 m/s. Based on the $V(h)$ profiles obtained using data collected on the 1-m telescope, this is unlikely to be sufficient.

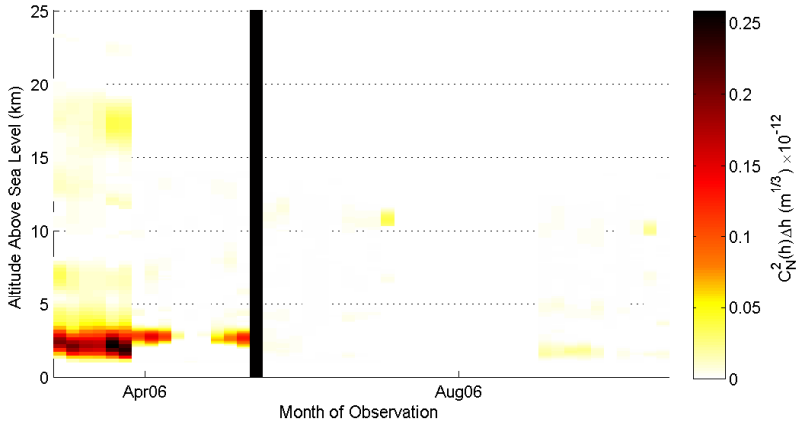

(a) Pupil-plane

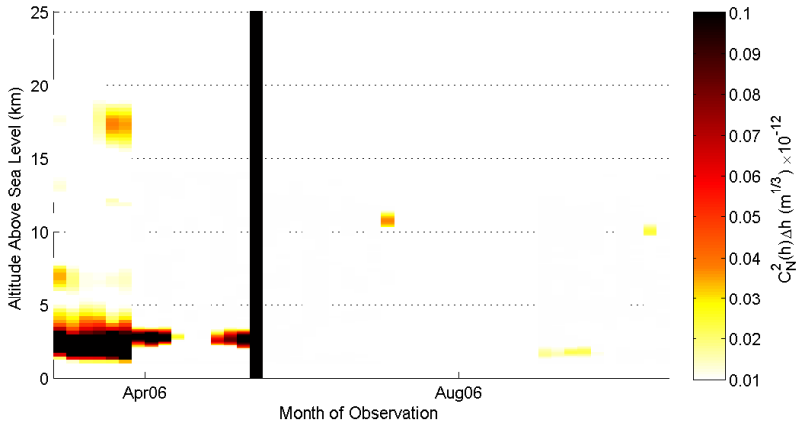

(b) Scaled Pupil-plane

Figure 6.11: Pupil-plane $C_N^2(h)$ profile trends observed over 2006. Time and $C_N^2(h)$ scaling used is as per Figure 6.1.

Table 6.12: Summary of spatial results from April 2006 generalised SCIDAR data.

Date	Star	mean SNR	$\int C_N^2(h)dh$ ($m^{1/3}$)	ε_C (%)	$\overline{r_0}$ (m)	σ_{r_0} (m)	$\overline{\theta_0}$ (arcsec)	σ_{θ_0} (arcsec)
20/04/06	α Cru	21	3.1×10^{-12}	6	0.05	0.00	0.7	0.1
20/04/06	α Cen	24	2.6×10^{-12}	22	0.06	0.01	1.4	0.1
Average	All	23	2.9×10^{-12}	14	0.05	0.01	1.0	0.4

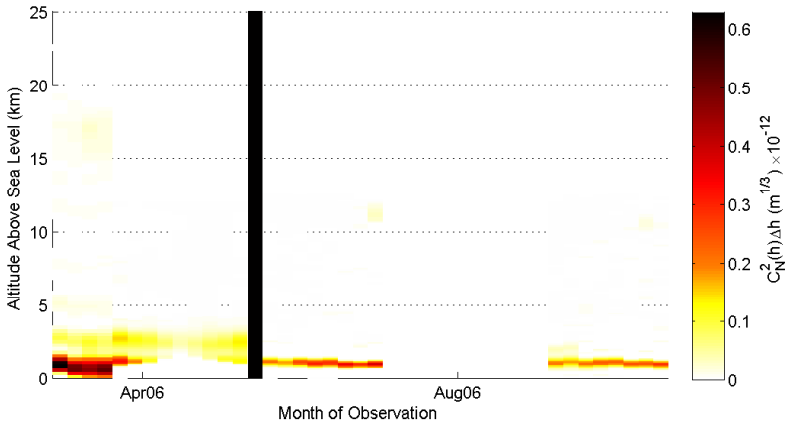

(a) Generalised

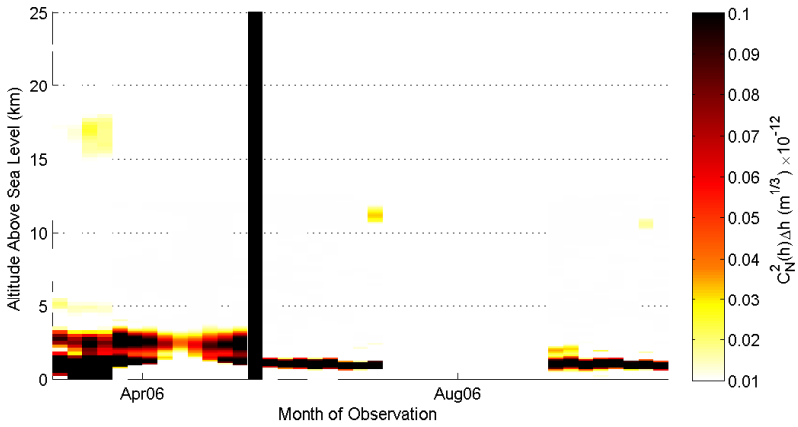

(b) Scaled Generalised

Figure 6.12: Generalised $C_N^2(h)$ profile trends observed over 2006. Time and $C_N^2(h)$ scaling used is as per Figure 6.1.

6.3 Measurements from 2005

In 2005, measurements were collected using the UC-SCIDAR V2005 system on the 1-m telescope operating at a focal ratio of $F/13.5$. An observation campaign was conducted by Clare Worley as part of her ASTR480 project (*Worley*, 2005), where measurements were taken between February to September over three to four consecutive nights during each month. February and March used a pupil-plane field lens with a focal length of 15 mm and a generalised field lens with a focal length of 12.7 mm. This provided a nominal spatial sampling, Δr, of 0.007 m/pix, and a nominal defocus of 2.2 km below the telescope. Some profiles could be used in profiling from data collected in March, but still contain significant amounts of noise. The profiles from February contained too much background noise due to the low SNR. To improve the SNR, Δr was increased to 0.008 m/pix by using different field lenses. They had focal lengths of 12.7 mm and 10 mm for pupil-plane and generalised paths respectively. This provided $C_N^2(h)$ profiles that could be used for profiling during April to August using α Cen and α Cru (*Johnston et al.*, 2005). The change in lenses resulted in an increase in the nominal defocus to 3.9 km below the telescope. During September both α Cen and α Cru were too low in the sky to be captured at the zenith angles required for useful trending. Unfortunately the CCDs used in the V2005 system did not have sufficient quantum efficiency to collect data using fainter binary star systems with short enough exposure times. Figures 6.13 and 6.14 show the $C_N^2(h)$ profiles obtained for pupil-plane and generalised data taken from March to August respectively.

A strong low altitude layer located at less than 5 km above sea level is visible. Also present is a weaker high altitude layer that ranges between 10 – 14 km above sea level. In some months an additional layer can be seen at 6 – 7 km above sea level.

Table 6.13 gives the calculated monthly averages and standard deviations for pupil-plane r_0 and θ_0 during 2005. The winter months (i.e. June and July) have an $\overline{r_0}$ in the order of 20 cm, whereas autumn (i.e. March, April and May) and spring (i.e. August) have an $\overline{r_0}$ ranging from approximately 10 cm to 15 cm.

$\overline{\theta_0}$ follows a similar trend to that of $\overline{r_0}$, with the winter months having a value of approximately 2 arcseconds compared to 1.3 – 1.7 arcseconds for autumn and spring. $\overline{\theta_0}$ for March 2005 was 1.6 arcseconds with a large standard deviation σ_{θ_0} of 0.7, which is associated with the noise present in a significant portion of the runs during March 2005. This is discussed further in section 6.3.6. The monthly r_0 and θ_0 values for generalised analysis are reasonably consistent throughout the year.

UC-SCIDAR V2005 captured data at a frame rate of 30 Hz, which limits the maximum detectable velocity on a 1-m telescope to 30 m/s using partial triplet analysis under

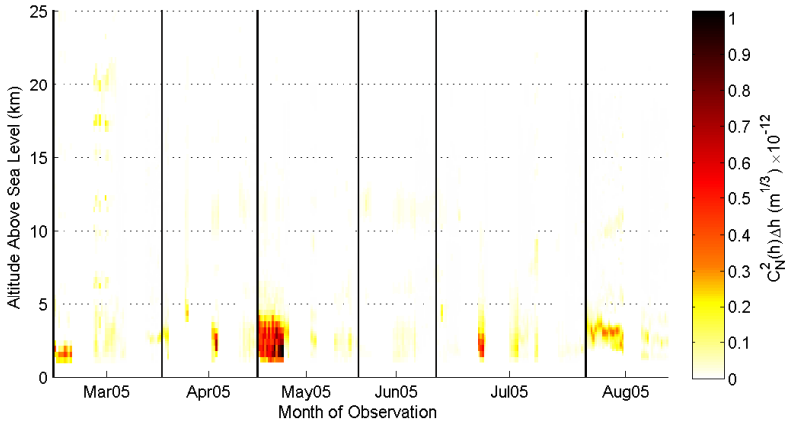

(a) Pupil-plane

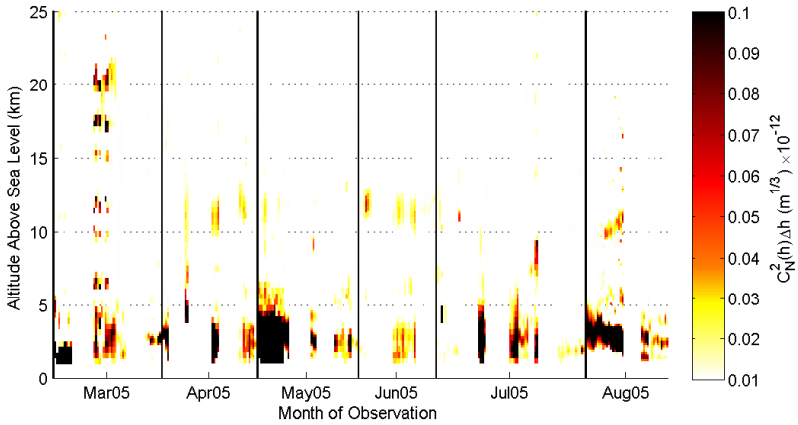

(b) Scaled pupil-plane

Figure 6.13: Pupil-plane $C_N^2(h)$ profile trends observed over 2005. Time and $C_N^2(h)$ scaling used is as per Figure 6.1.

Table 6.13: Monthly averages and standard deviations for r_0 and θ_0 from 2005, for both pupil-plane and generalised data.

Month	Pupil-plane				Generalised			
	$\overline{r_0}$ (m)	σ_{r_0} (m)	$\overline{\theta_0}$ (arcsec)	σ_{θ_0} (arcsec)	$\overline{r_0}$ (m)	σ_{r_0} (m)	$\overline{\theta_0}$ (arcsec)	σ_{θ_0} (arcsec)
August 2005	0.10	0.02	1.7	0.4	0.08	0.01	1.1	0.1
July 2005	0.18	0.04	2.2	0.4	0.07	0.01	1.2	0.2
June 2005	0.22	0.03	1.8	0.3	0.06	0.01	1.1	0.1
May 2005	0.12	0.01	1.7	0.2	0.07	0.01	1.0	0.2
April 2005	0.11	0.03	1.3	0.3	0.07	0.01	0.9	0.1
March 2005	0.15	0.03	1.6	0.7	0.08	0.02	1.1	0.3

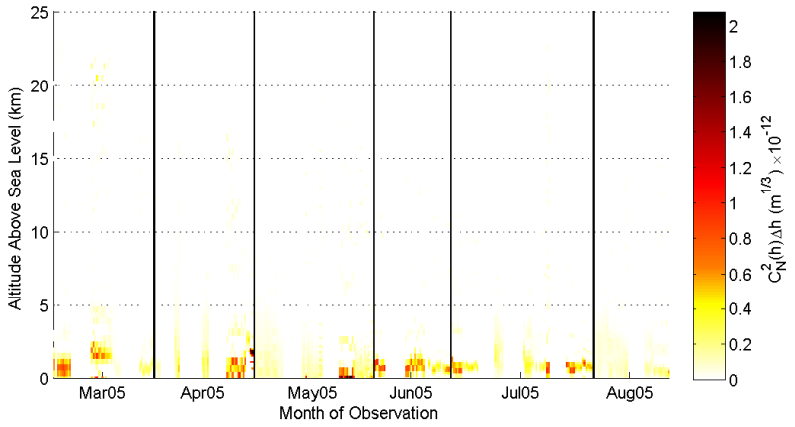

(a) Generalised

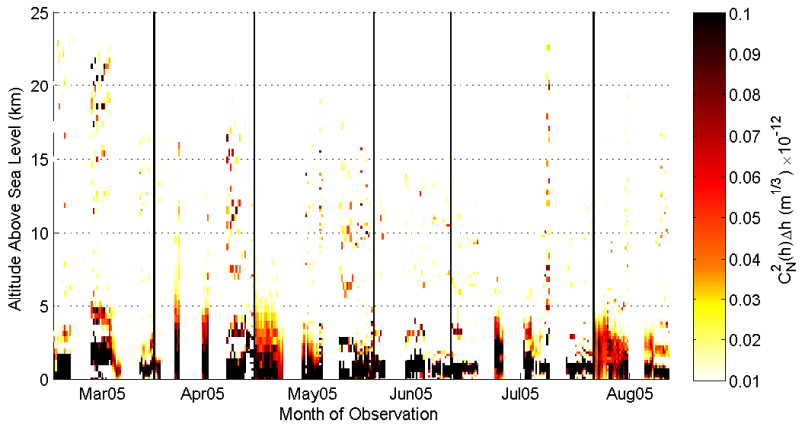

(b) Scaled Generalised

Figure 6.14: Generalised $C_N^2(h)$ profile trends observed over 2005. Time and $C_N^2(h)$ scaling used is as per Figure 6.1.

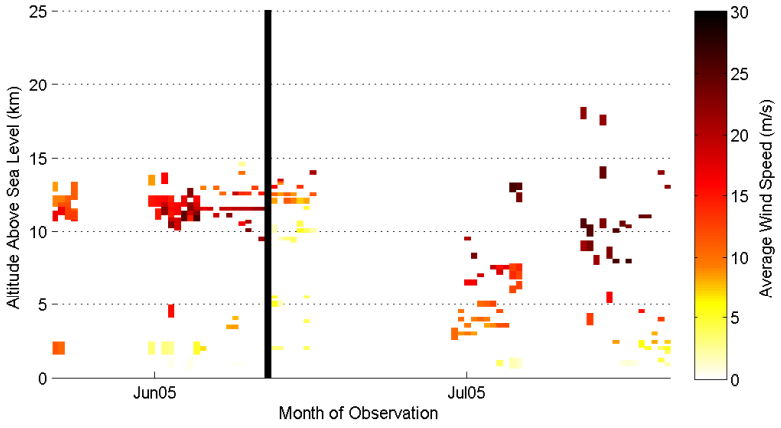

Figure 6.15: Average wind speeds detected, $|V(h)|$, for observations taken during 2005. Data from the individual months is separated by solid black lines.

ideal conditions. Given the $V(h)$ profiles from the V2007 system this should provide a reasonable $V(h)$ profile for low- to mid-altitude layers. As such temporal analysis was performed on data from June and July only. These months provided the most consistent data set with a large number of runs utilising exposures of 1 – 2 ms and covariances containing sufficient signal.

Figure 6.15 shows the average wind speeds detected, $|V(h)|$, for June and July 2005. In June a layer at approximately 12 km above sea level was moving consistently at 12 – 15 m/s. In July there was much more scatter in the average velocity. The $V(h)$ profiles from July and June are discussed in more detail in sections 6.3.2 and 6.3.3 respectively.

Using the $V(h)$ profiles obtained for June and July, the average Greenwood frequency, $\overline{f_G}$, was found to range between 10 and 20 Hz. There are significant gaps present in the $V(h)$ profiles, as indicated by the standard deviation in f_G, σ_{f_G}, ranging between 5 and 15 Hz. As such $\overline{f_G}$ is likely to be underestimated.

6.3.1 August 2005

During August 2005 all usable data was collected with α Cen using an exposure time of 1 ms. Figure 6.16 shows the scaled $C_N^2(h)$ profiles for August 2005.

On 13 August the observation logs note high wispy clouds with ground wind speeds gradually increasing as the night progresses. By the end of observations ground wind speeds were over 40 kph (11 m/s). In the pupil-plane analysis (Figure 6.16(a)) the strength of the layer found at $\sim$ 10 km above sea level gradually increases as the night progresses. An additional layer at 5 km above sea level is also detectable at the end of the evening. *Sturman and Tapper* (1996) and *Hardy* (1998) suggest a connection between near ground wind activity and activity elsewhere in the troposphere. As such an increase in ground

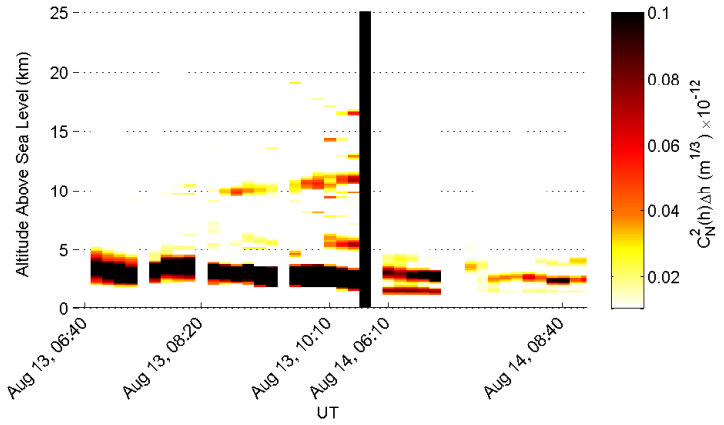

(a) Scaled pupil-plane $C_N^2(h)$ profiles

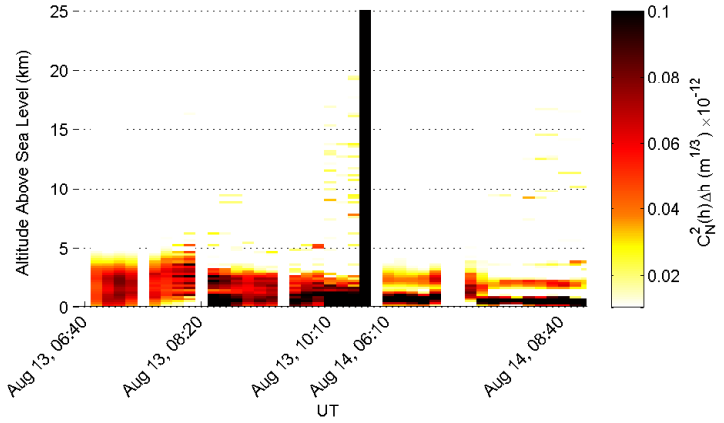

(b) Scaled generalised $C_N^2(h)$ profiles

Figure 6.16: Scaled $C_N^2(h)$ profiles for observations taken during August 2005. Time and $C_N^2(h)$ scaling used is as per Figure 6.1.

wind speeds (as noted in the logs) could result in an increase in the turbulent activity in the tropopause turbulent layer.

On 14 August the observation logs noted calm, clear skies, which is reflected in the measurements made.

Table 6.14 indicates the nightly averages and standard deviations of r_0 and θ_0 for pupil-plane analysis. For 13 August, the generalised estimate for r_0 replaced the pupil-plane estimate in the determination of the monthly average, as indicated by the brackets. As expected, $\overline{r_0}$ and $\overline{\theta_0}$ increased significantly with the calmer weather seen on 14 August. This increase is also seen in the analysis of the generalised data (Table 6.15), where NGT is connected to the turbulence associated with the dome.

Table 6.14: Summary of spatial results from August 2005 pupil-plane SCIDAR data. For the determination of the averages, some values were replaced by the generalised estimates. These values are indicated by the brackets.

Date	Star	mean SNR	$\int C_N^2(h)dh$ ($m^{1/3}$)	ε_C (%)	$\overline{r_0}$ (m)	σ_{r_0} (m)	$\overline{\theta_0}$ (arcsec)	σ_{θ_0} (arcsec)
13/08/05	α Cen	26	2.4×10^{-12}	33	(0.06)	(0.01)	1.1	0.1
14/08/05	α Cen	26	0.6×10^{-12}	57	0.14	0.04	2.2	0.6
Average	All	26	1.5×10^{-12}	45	0.10	0.02	1.7	0.4

Table 6.15: Summary of spatial results from August 2005 generalised SCIDAR data.

Date	Star	mean SNR	$\int C_N^2(h)dh$ ($m^{1/3}$)	ε_C (%)	$\overline{r_0}$ (m)	σ_{r_0} (m)	$\overline{\theta_0}$ (arcsec)	σ_{θ_0} (arcsec)
13/08/05	α Cen	35	1.9×10^{-12}	11	0.06	0.01	0.9	0.1
14/08/05	α Cen	36	1.1×10^{-12}	8	0.09	0.01	1.3	0.2
Average	All	35	1.5×10^{-12}	9	0.08	0.01	1.1	0.1

6.3.2 July 2005

Measurements in July 2005 were taken using α Cen and α Cru at exposure time ranging from 0.5 to 2 ms. Figure 6.17 shows the scaled $C_N^2(h)$ profiles and the average wind speeds obtained. Tables 6.16 and 6.17 show the nightly averages and standard deviations of r_0 and θ_0.

For the V2005 system, there was no reference frame to indicate how the two CCD cameras were mounted with respect to the telescope or with respect to each other. A comparison of 2D covariance images taken using V2005 and V2007 for the same star at similar positions in the sky suggests that the cameras had similar CCD orientations with respect to the primary mirror or were shifted by 180°. Using the orientation corrections for the V2007 system results in the calculated wind direction originating from an easterly direction for the high altitude layers. Geophysical studies of wind over New Zealand indicate Westerly wind at high altitudes and hence a CCD orientation correction that was 180° out with respect to the V2007 system was used to find wind directions.*

On 6 July the observation log noted a calm evening. This can be seen in the $\overline{r_0}$ calculated for the pupil-plane data which was approximately 20 cm. In addition little NGT is detected in the pupil-plane data. Temporal analysis from 6 July (indicated by the blue squares in Figure 6.18) showed a similar characteristic to that seen on 3 June 2007, where a layer at approximately 10 – 12 km above sea level was found to have a wind speed of < 10 m/s and a higher layer was moving at approximately 15 m/s. As with the 3 June 2007 data, the lower high altitude layer was originating from an Easterly direction

*The V2005 cameras no longer work. No other calibration for CCD orientation can be used.

whereas the higher layer was originating from a Westerly direction (Figure 6.18).

On 7 July there was thickening cloud. This impacted on the pupil-plane $C_N^2(h)$ analysis, lowering the $\overline{r_0}$ value to ~ 6 cm. Although temporal analysis was conducted on data from 7 July, the turbulence was such that the layer heights could not be ascertained.

On 8 July ground wind speeds were above 30 kph (8.3 m/s) for most of the night with periods up to 40 kph (11 m/s). Low-altitude turbulence existed at less than 5 km above sea level with wind speeds between 8 – 13 m/s (indicated by the purple circles in Figure 6.18). Also detected was a strong layer at ~ 8 km above sea level in the pupil-plane data, moving with a velocity of approximately 15 m/s. The pupil-plane $\overline{r_0}$ was ~ 10 cm and ~ 14 cm for the α Cru and α Cen measurements respectively.

On 9 July the observation logs note clear skies at the start of the evening, but make no mention of ground wind speed. The $C_N^2(h)$ profiles show little detectable NGT in the pupil-plane analysis. This is reflected in the $\overline{r_0}$ of greater than 20 cm. In addition the dramatic increase in $\overline{\theta_0}$ to over 2.5 arcseconds suggests that little turbulence exists in the upper layers. The $V(h)$ profile for this night (indicated by the red stars in Figure 6.18) suggest differently. A high altitude layer between 8 – 12 km above sea level had a velocity of approximately 23 m/s. NGT was found to have wind speeds as high as 7 m/s with a layer also being detected at approximately 5 km. This suggests that although skies were clear and less turbulent than on previous nights that wind speeds were still high.

Little merit can be given to the f_G values calculated for July 2005, shown in Table 6.18. There is a large variation of the calculated values for the pupil-plane and generalised data, as a significant number of verified velocities where slightly mismatched with altitudes seen in the $C_N^2(h)$ profiles and hence skewed the calculations of f_G.

Table 6.16: Summary of spatial results from July 2005 pupil-plane SCIDAR data.

Date	Star	mean SNR	$\int C_N^2(h)dh$ ($m^{1/3}$)	ε_C (%)	$\overline{r_0}$ (m)	σ_{r_0} (m)	$\overline{\theta_0}$ (arcsec)	σ_{θ_0} (arcsec)
06/07/05	α Cru	17	0.3×10^{-12}	22	0.20	0.04	1.7	0.3
06/07/05	α Cen	25	0.3×10^{-12}	64	0.20	0.02	1.9	0.3
07/07/05	α Cru	23	2.3×10^{-12}	7	0.06	0.01	1.3	0.2
07/07/05	α Cen	18	1.6×10^{-12}	43	0.07	0.00	1.4	0.1
08/07/05	α Cru	23	1.0×10^{-12}	6	0.10	0.03	1.6	0.5
08/07/05	α Cen	26	0.6×10^{-12}	45	0.14	0.04	2.0	0.3
09/07/05	α Cru	23	0.2×10^{-12}	12	0.27	0.04	2.5	0.4
09/07/05	α Cen	25	0.3×10^{-12}	71	0.22	0.04	2.8	0.5
Average	α Cru	21	0.9×10^{-12}	11	0.16	0.03	1.8	0.3
Average	α Cen	23	0.7×10^{-12}	56	0.16	0.02	2.0	0.3
Average	All	24	0.5×10^{-12}	33	0.18	0.04	2.2	0.4

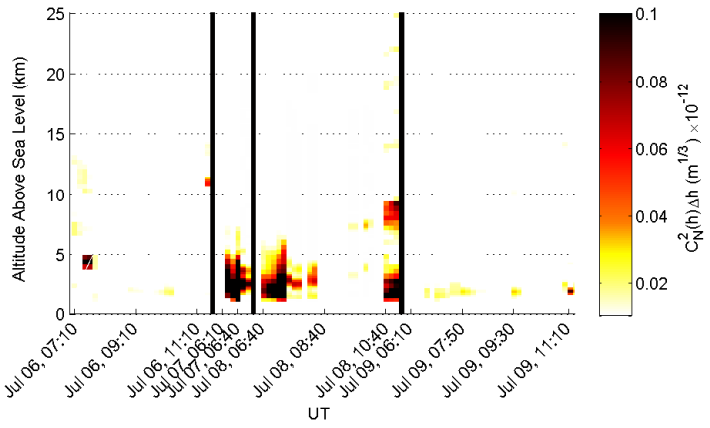

(a) Scaled pupil-plane $C_N^2(h)$ profiles

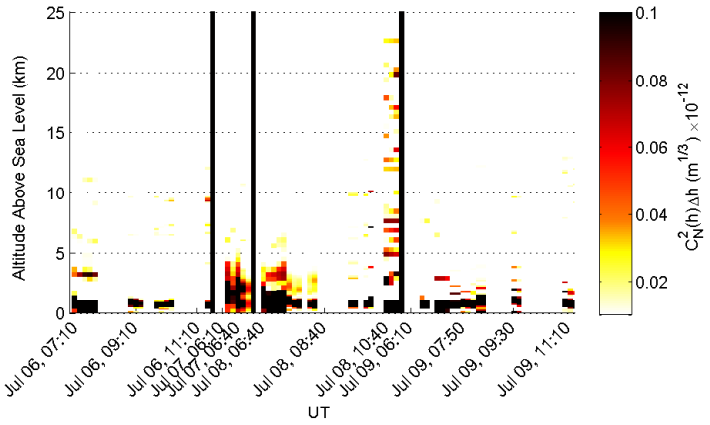

(b) Scaled generalised profiles

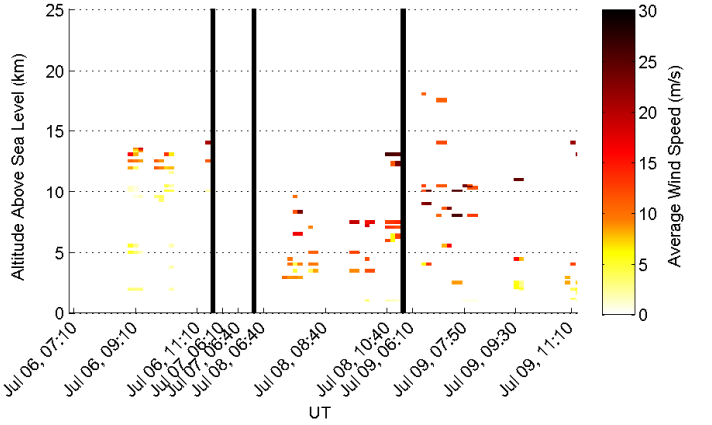

(c) Average wind speed $|V(h)|$

Figure 6.17: Scaled $C_N^2(h)$ profiles and average wind speed for observations taken during July 2005. Time and $C_N^2(h)$ scaling used is as per Figure 6.1.

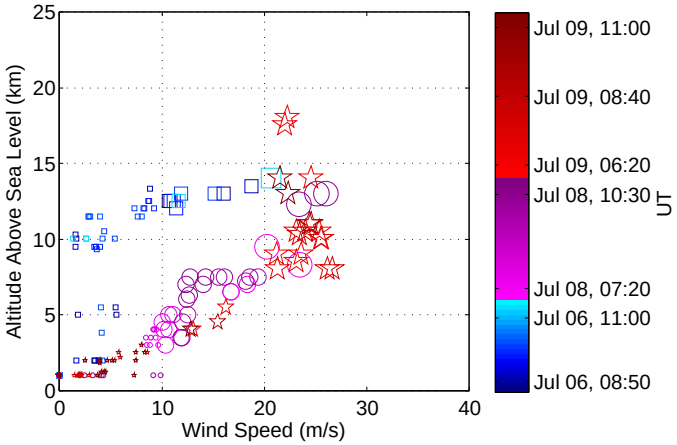

(a) Instantaneous wind speed $|V(h)|$

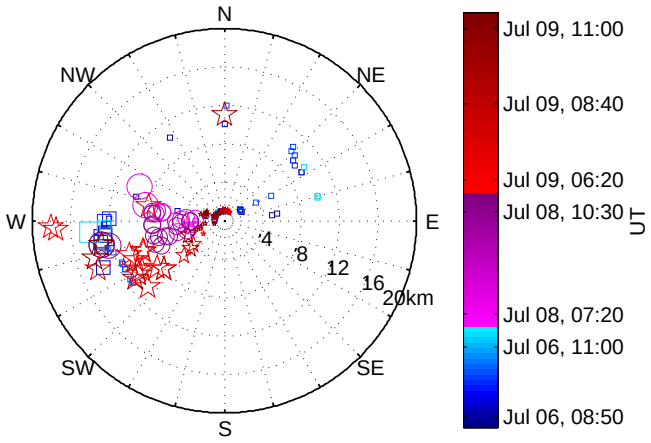

(b) Instantaneous wind direction β

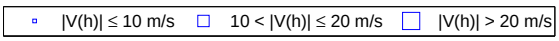

Figure 6.18: Wind velocity analysis for observations made during July 2005. Colour and symbol sizes conventions used are as per Figure 6.5.

Table 6.17: Summary of spatial results from July 2005 generalised SCIDAR data.

Date	Star	mean SNR	$\int C_N^2(h)dh$ ($m^{1/3}$)	ε_C (%)	$\overline{r_0}$ (m)	σ_{r_0} (m)	$\overline{\theta_0}$ (arcsec)	σ_{θ_0} (arcsec)
06/07/05	α Cru	21	1.7×10^{-12}	8	0.07	0.00	1.2	0.1
06/07/05	α Cen	28	1.4×10^{-12}	14	0.08	0.01	1.3	0.1
07/07/05	α Cru	28	2.0×10^{-12}	3	0.06	0.00	1.1	0.1
07/07/05	α Cen	22	1.9×10^{-12}	6	0.06	0.00	0.9	0.0
08/07/05	α Cru	29	2.8×10^{-12}	3	0.05	0.02	1.1	0.3
08/07/05	α Cen	31	1.3×10^{-12}	13	0.08	0.02	1.2	0.2
09/07/05	α Cru	28	1.5×10^{-12}	11	0.08	0.01	1.4	0.1
09/07/05	α Cen	30	2.5×10^{-12}	17	0.05	0.01	1.2	0.1
Average	α Cru	27	2.0×10^{-12}	6	0.07	0.01	1.2	0.1
Average	α Cen	28	1.8×10^{-12}	13	0.07	0.01	1.1	0.1
Average	All	29	2.0×10^{-12}	11	0.07	0.01	1.2	0.2

Table 6.18: Nightly averages and standard deviations for f_G during July 2005.

	Pupil-plane		Generalised	
Date	$\overline{f_G}$ (Hz)	σ_{f_G} (Hz)	$\overline{f_G}$ (Hz)	σ_{f_G} (Hz)
06/07/05	4.9	1.6	5.8	2.5
07/07/05	—	—	—	—
08/07/05	16	8	18	12
09/07/05	7.9	3.6	8	16
All	10	7	11	14

6.3.3 June 2005

No observations were taken on 11 June due to complete cloud cover. On 12 June the start of the night was clear with light ground wind speeds. However cloud formed quickly resulting in just one hour of observation time. On 13 June a layer of fog sat over Lake Tekapo for most of the night, and there was little to no air movement.

Figure 6.19 shows the scaled $C_N^2(h)$ profiles for the pupil-plane and generalised data, and the average wind speed. Figure 6.20 shows the measured instantaneous wind speeds. In both the $C_N^2(h)$ and $V(h)$ analysis there are just two layers present: NGT and the tropopause layer at 11 – 13 km above sea level. Very little scatter exists in the $V(h)$ profile obtained which suggests a stable turbulence structure. r_0 and θ_0 analysis (Tables 6.19 and 6.20 for pupil-plane and generalised measurements respectively) show a consistent pupil-plane $\overline{r_0}$ of $\sim$ 22 cm, a pupil-plane $\overline{\theta_0}$ of $\sim$ 1.8 arcseconds, a generalised $\overline{r_0}$ of $\sim$ 6 cm and generalised $\overline{\theta_0}$ of $\sim$ 1 arcseconds throughout the run. $\overline{f_G}$ for the pupil-plane analysis (Table 6.21) was $\sim$ 13 Hz, with more variation present in the data for 13 June due to the measurements taken using α Cen. Generalised $\overline{f_G}$ was slightly lower at $\sim$ 10 Hz with σ_{f_G}

of nearly 18 Hz. This variation will be due to the fact that not all runs in the generalised data resulted in a measurement of the high altitude layer for the $C_N^2(h)$ strength, as the high altitude layer was masked by the strong NGT.

Table 6.19: Summary of spatial results from June 2005 pupil-plane SCIDAR data.

Date	Star	mean SNR	$\int C_N^2(h)dh$ ($m^{1/3}$)	ε_C (%)	$\overline{r_0}$ (m)	σ_{r_0} (m)	$\overline{\theta_0}$ (arcsec)	σ_{θ_0} (arcsec)
12/06/05	α Cru	18	0.2×10^{-12}	14	0.26	0.05	1.8	0.5
13/06/05	α Cru	18	0.4×10^{-12}	10	0.18	0.03	1.8	0.3
13/06/05	α Cen	28	0.2×10^{-12}	43	0.23	0.02	1.7	0.1
Average	α Cru	18	0.3×10^{-12}	12	0.22	0.04	1.8	0.4
Average	α Cen	28	0.2×10^{-12}	43	0.23	0.02	1.7	0.1
Average	All	21	0.3×10^{-12}	22	0.22	0.03	1.8	0.3

Table 6.20: Summary of spatial results from June 2005 generalised SCIDAR data.

Date	Star	mean SNR	$\int C_N^2(h)dh$ ($m^{1/3}$)	ε_C (%)	$\overline{r_0}$ (m)	σ_{r_0} (m)	$\overline{\theta_0}$ (arcsec)	σ_{θ_0} (arcsec)
12/06/05	α Cru	22	2.0×10^{-12}	8	0.06	0.01	1.1	0.1
13/06/05	α Cru	21	2.2×10^{-12}	7	0.06	0.01	1.0	0.1
13/06/05	α Cen	24	2.5×10^{-12}	14	0.06	0.01	1.1	0.1
Average	α Cru	22	2.1×10^{-12}	7	0.06	0.01	1.1	0.1
Average	α Cen	24	2.5×10^{-12}	14	0.06	0.01	1.1	0.1
Average	All	23	2.2×10^{-12}	10	0.06	0.01	1.1	0.1

Table 6.21: Nightly averages and standard deviations for f_G during June 2005.

	Pupil-plane		Generalised	
Date	$\overline{f_G}$ (Hz)	σ_{f_G} (Hz)	$\overline{f_G}$ (Hz)	σ_{f_G} (Hz)
12/06/05	13	1	14	17
13/06/05	14	6	9	18
All	13	5	10	17

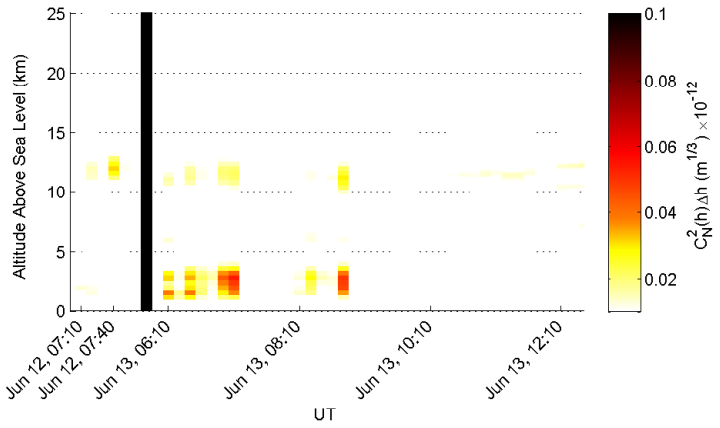

(a) Scaled pupil-plane $C_N^2(h)$ profiles

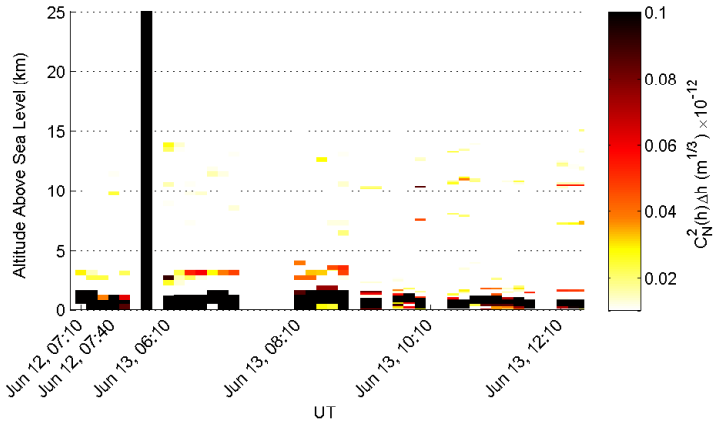

(b) Scaled generalised $C_N^2(h)$ profiles

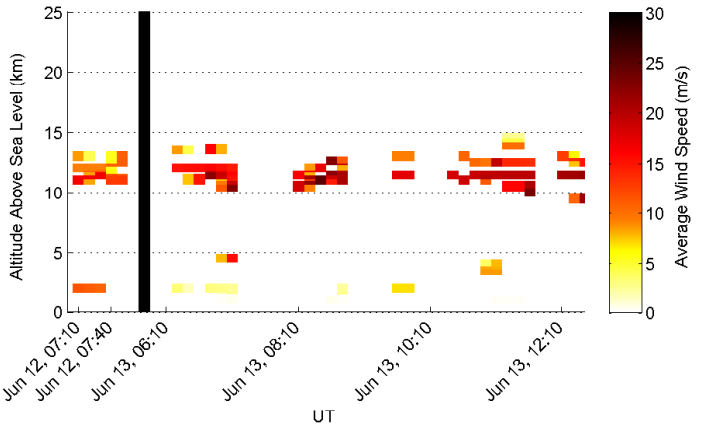

(c) Average wind speed $|V(h)|$

Figure 6.19: Scaled $C_N^2(h)$ profiles and average wind speed for observations taken during June 2005. Time and $C_N^2(h)$ scaling used is as per Figure 6.1.

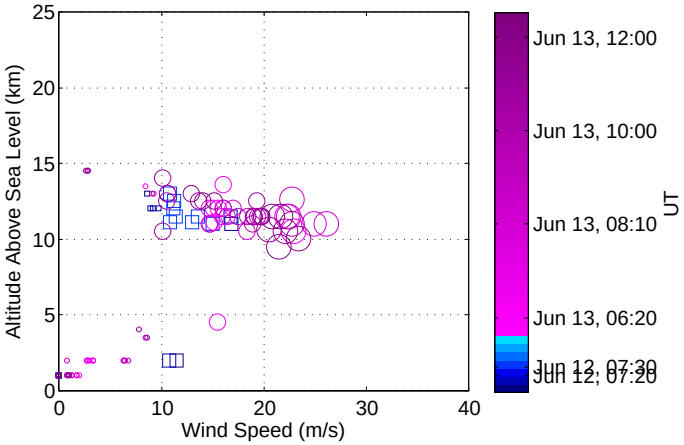

(a) Instantaneous wind speed $|V(h)|$

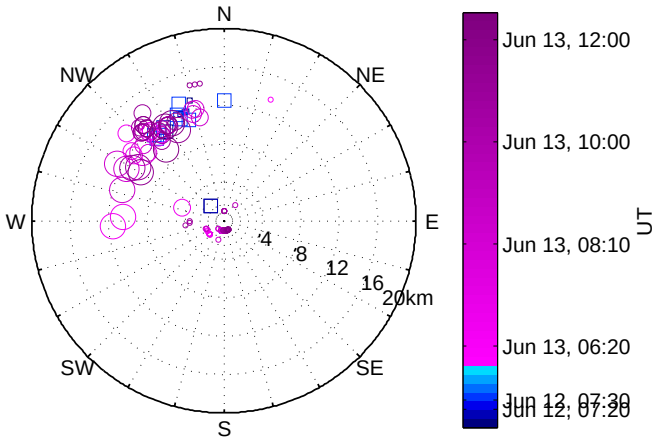

(b) Instantaneous wind direction β

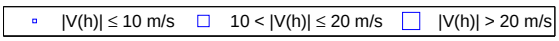

Figure 6.20: Wind velocity analysis for observations made during June 2005. Colour and symbol sizes conventions used are as per Figure 6.5.

6.3.4 May 2005

On 13 May the observation logs noted ground wind speeds of 10 kph (2.8 m/s) with rapid gusts to 50+ kph (13.9+ m/s). In pupil-plane data $\overline{r_0}$ measurements (Table 6.22) were indicative of significant NGT where secondary peaks of turbulence located below 1 km will merge with the central peak, and hence were replaced by the generalised r_0 estimates. Increasing wind strength eventually ended observations.

Observations on 14 May began with ground wind speeds of approximately 20 kph (5.6 m/s) with hazy cloud cover. As the night progressed the cloud cover lifted and wind speeds dropped. Exposure times ranged from 0.25 – 1 ms. Unfortunately this resulted in insufficient signal for slice extraction in pupil-plane data and an increased level of noise present in the generalised data (Figure 6.21). The strength of the NGT in the generalised data also masked any measurements high altitude layers.

On 15 May there were clear skies with low ground wind speeds. Exposure times ranged between 1 – 2 ms for α Cru and 0.25 – 0.5 ms for α Cen. The exposures for α Cru were adequate for slice extraction, however the short exposure times used for α Cen resulted in insufficient signal for slice extraction in pupil-plane measurements and increased the amount of noise present in the generalised data. The pupil-plane $\overline{r_0}$ and $\overline{\theta_0}$ increased significantly, consistent with observation logs indicating significantly improved seeing. Generalised $\overline{r_0}$ (Table 6.23) also increased for 15 May compared to that of previous nights, albeit slightly.

Table 6.22: Summary of spatial results from May 2005 pupil-plane SCIDAR data. For the determination of the averages, some values were replaced by the generalised estimates. These values are indicated by the brackets.

Date	Star	mean SNR	$\int C_N^2(h)dh$ ($m^{1/3}$)	ε_C (%)	$\overline{r_0}$ (m)	σ_{r_0} (m)	$\overline{\theta_0}$ (arcsec)	σ_{θ_0} (arcsec)
13/05/05	α Cru	16	4.0×10^{-12}	7	(0.07)	(0.01)	0.9	0.2
13/05/05	α Cen	25	2.4×10^{-12}	41	(0.07)	(0.00)	1.3	0.2
14/05/05	α Cen	12	1.3×10^{-12}	52	0.08	0.00	1.2	0.2
15/05/05	α Cru	16	0.4×10^{-12}	13	0.19	0.04	2.2	0.4
15/05/05	α Cen	13	0.3×10^{-12}	65	0.21	0.00	2.7	0.0
Average	α Cru	16	2.2×10^{-12}	10	0.13	0.03	1.6	0.3
Average	α Cen	17	1.3×10^{-12}	52	0.12	0.00	1.7	0.1
Average	All	16	1.7×10^{-12}	35	0.12	0.01	1.7	0.2

Table 6.23: Summary of spatial results from May 2005 generalised SCIDAR data.

Date	Star	mean SNR	$\int C_N^2(h)dh$ ($m^{1/3}$)	ε_C (%)	$\overline{r_0}$ (m)	σ_{r_0} (m)	$\overline{\theta_0}$ (arcsec)	σ_{θ_0} (arcsec)
13/05/05	α Cru	22	1.5×10^{-12}	4	0.07	0.01	0.9	0.1
13/05/05	α Cen	31	1.7×10^{-12}	3	0.07	0.00	1.0	0.2
14/05/05	α Cen	16	2.3×10^{-12}	17	0.06	0.01	0.7	0.1
15/05/05	α Cru	29	1.4×10^{-12}	4	0.08	0.01	1.2	0.1
15/05/05	α Cen	21	1.7×10^{-12}	5	0.07	0.01	0.9	0.6
Average	α Cru	25	1.4×10^{-12}	4	0.08	0.01	1.1	0.1
Average	α Cen	23	1.9×10^{-12}	9	0.07	0.01	0.9	0.3
Average	All	24	1.7×10^{-12}	7	0.07	0.01	1.0	0.2

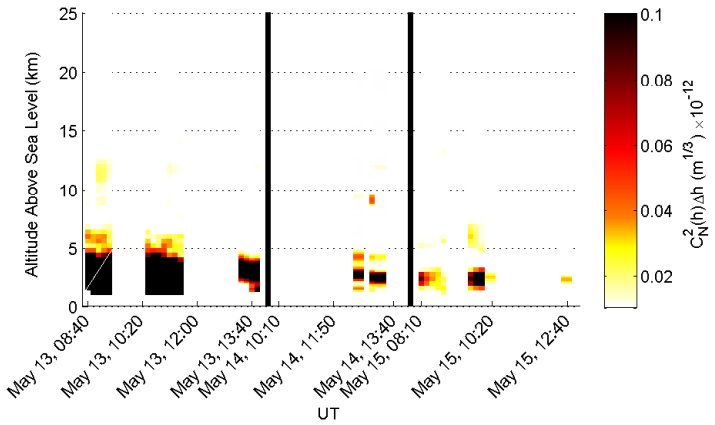

(a) Scaled pupil-plane $C_N^2(h)$ profiles

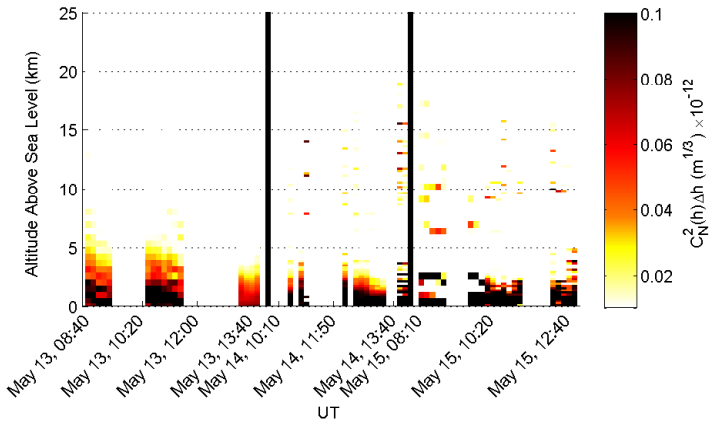

(b) Scaled generalised $C_N^2(h)$ profiles

Figure 6.21: Scaled $C_N^2(h)$ profiles for observations taken during May 2005. Time and $C_N^2(h)$ scaling used is as per Figure 6.1.

6.3.5 April 2005

Measurements taken in April 2005 utilised primarily α Cen and α Cru data. Figure 6.22 shows the scaled the $C_N^2(h)$ profiles for the pupil-plane and generalised measurements. The nightly averages and standard deviations for r_0 and θ_0 are shown in Tables 6.24 and 6.25 for the pupil-plane and generalised measurements respectively.

Observation time on 22 April was limited due to rapidly thickening cloud cover. As seen in other months this resulted in a pupil-plane $\overline{r_0}$ that was low, hence it was replaced with with the generalised r_0.

23 April had wispy clouds with ground wind speeds of 25 – 35 kph (7 – 10 m/s). On 24 April the observation logs noted high winds with no clouds at first, then the winds dying down and the clouds rolling in. Although a slight increase is seen in the pupil-plane $\overline{r_0}$ for 23 April and 24 April the increased strength in the layer at 10 – 11 km above sea level resulted in a decrease of the pupil-plane $\overline{\theta_0}$. This decrease in $\overline{\theta_0}$ is also seen in the generalised measurements.

On 25 April there were clear skies with low ground wind speeds. Exposure times ranged from 0.5 – 2 ms. The data using an exposure time of 0.5 ms provided insufficient signal for slice extraction in pupil-plane measurements. In the corresponding generalised measurements there was noise present in the data. However the strength of the NGT layer meant that it could be included in profiling. The layer at 10 – 11 km was slightly weaker than that detected on the previous night and the strength of the NGT layer detected in the pupil-plane data decreases significantly, resulting in the increase of the pupil-plane $\overline{r_0}$ and $\overline{\theta_0}$. Generalised $\overline{r_0}$ is reasonably constant for the nights of 23 – 25 April.

Table 6.24: Summary of spatial results from April 2005 pupil-plane SCIDAR data. For the determination of the averages, some values were replaced by the generalised estimates. These values are indicated by the brackets.

Date	Star	mean SNR	$\int C_N^2(h)dh$ ($m^{1/3}$)	ε_C (%)	$\overline{r_0}$ (m)	σ_{r_0} (m)	$\overline{\theta_0}$ (arcsec)	σ_{θ_0} (arcsec)
22/04/05	α Cen	24	1.8×10^{-12}	51	(0.09)	(0.03)	1.1	0.6
23/04/05	α Cru	20	1.2×10^{-12}	15	0.08	0.00	0.7	0.0
24/04/05	α Cru	16	1.6×10^{-12}	13	0.08	0.02	1.1	0.2
25/04/05	α Cru	13	0.4×10^{-12}	30	0.16	0.03	1.4	0.2
25/04/05	α Cen	18	0.7×10^{-12}	57	0.13	0.04	2.3	0.3
Average	α Cru	16	1.1×10^{-12}	19	0.11	0.02	1.1	0.1
Average	α Cen	21	1.2×10^{-12}	54	0.11	0.04	1.7	0.4
Average	All	18	1.1×10^{-12}	33	0.11	0.03	1.3	0.3

Table 6.25: Summary of spatial results from April 2005 generalised SCIDAR data.

Date	Star	mean SNR	$\int C_N^2(h)dh$ ($m^{1/3}$)	ε_C (%)	$\overline{r_0}$ (m)	σ_{r_0} (m)	$\overline{\theta_0}$ (arcsec)	σ_{θ_0} (arcsec)
22/04/05	α Cen	25	1.3×10^{-12}	18	0.09	0.03	1.0	0.3
23/04/05	α Cru	23	2.5×10^{-12}	9	0.06	0.01	0.7	0.2
24/04/05	α Cru	19	1.9×10^{-12}	3	0.07	0.01	0.8	0.1
25/04/05	α Cru	16	2.1×10^{-12}	5	0.06	0.00	0.9	0.1
25/04/05	α Cen	22	1.8×10^{-12}	7	0.07	0.01	1.0	0.1
Average	α Cru	19	2.2×10^{-12}	6	0.06	0.01	0.8	0.1
Average	α Cen	24	1.6×10^{-12}	13	0.08	0.02	1.0	0.2
Average	All	21	1.9×10^{-12}	8	0.07	0.01	0.9	0.1

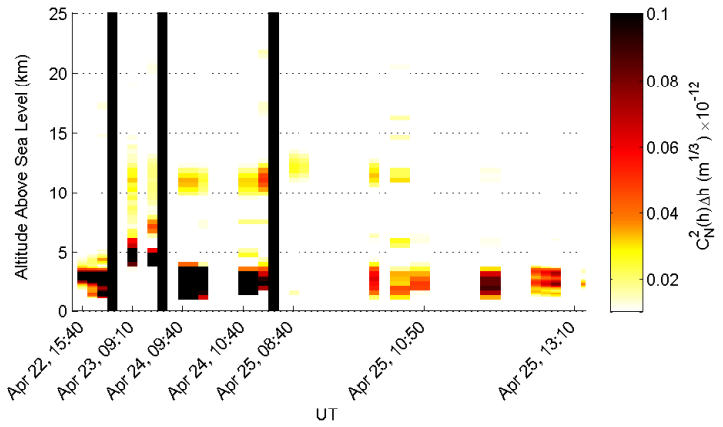

(a) Scaled pupil-plane $C_N^2(h)$ profiles

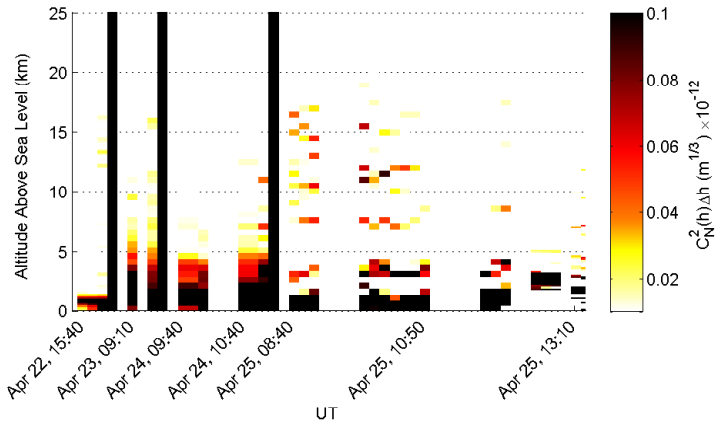

(b) Scaled generalised $C_N^2(h)$ profiles

Figure 6.22: Scaled $C_N^2(h)$ profiles for observations taken during April 2005. Time and $C_N^2(h)$ scaling used is as per Figure 6.1.

6.3.6 March 2005

During March 2005, the V2005 system was still experimental. The field lenses used had a focal length of 15 mm and 12.7 mm for the pupil-plane and generalised measurements respectively. Although some $C_N^2(h)$ profiles could be extracted for trending purposes there was still significant amounts of noise. Figure 6.23 shows the scaled $C_N^2(h)$ profiles for the pupil-plane and generalised data. Tables 6.26 and 6.27 show the nightly averages and standard deviations for r_0 and θ_0 for the pupil-plane and generalised data respectively.

The observation logs indicate the presence of thin wispy clouds during the observation period, but there was no other details.

On 10 March there was strong NGT and a layer at approximately 5 km above sea level. High altitude layers were masked by low altitude activity. Profiles obtained for 11 March were noisy and little was concluded. The noise resulted in a large σ_{θ_0}, and hence were not included in the monthly averages for θ_0. Profiles obtained for 12 March had little NGT detected in the pupil-plane data, with a corresponding increase in $\overline{r_0}$ and $\overline{\theta_0}$.

Table 6.26: Summary of spatial results from March 2005 pupil-plane SCIDAR data. Due to the high σ_{θ_0} obtained on 11 March, this data was not included in the monthly averages for θ_0.

Date	Star	mean SNR	$\int C_N^2(h)dh$ ($m^{1/3}$)	ε_C (%)	$\overline{r_0}$ (m)	σ_{r_0} (m)	$\overline{\theta_0}$ (arcsec)	σ_{θ_0} (arcsec)
10/03/05	α Cru	14	0.9×10^{-12}	21	0.10	0.02	1.5	0.6
10/03/05	α Cru	15	0.6×10^{-12}	21	0.14	0.03	1.0	0.2
11/03/05	α Cen	36	0.4×10^{-12}	64	0.17	0.03	2.8	1.6
12/03/05	α Cen	25	0.4×10^{-12}	48	0.17	0.05	2.3	0.6
Average	α Cru	14	0.7×10^{-12}	21	0.12	0.02	1.3	0.4
Average	α Cen	30	0.4×10^{-12}	56	0.17	0.04	2.3	0.6
Average	All	22	0.6×10^{-12}	38	0.15	0.03	1.6	0.7

Table 6.27: Summary of spatial results from March 2005 generalised SCIDAR data.

Date	Star	mean SNR	$\int C_N^2(h)dh$ ($m^{1/3}$)	ε_C (%)	$\overline{r_0}$ (m)	σ_{r_0} (m)	$\overline{\theta_0}$ (arcsec)	σ_{θ_0} (arcsec)
10/03/05	α Cru	23	2.5×10^{-12}	4.6	0.06	0.01	1.2	0.2
10/03/05	α Cru	22	1.6×10^{-12}	5.5	0.08	0.03	0.8	0.1
11/03/05	α Cen	16	1.0×10^{-12}	8.0	0.10	0.02	1.4	0.6
12/03/05	α Cen	15	1.7×10^{-12}	7.1	0.07	0.01	0.9	0.1
Average	α Cru	22	2.1×10^{-12}	5.1	0.07	0.02	1.0	0.2
Average	α Cen	16	1.3×10^{-12}	7.5	0.08	0.01	1.1	0.4
Average	All	19	1.7×10^{-12}	6.3	0.08	0.02	1.1	0.3

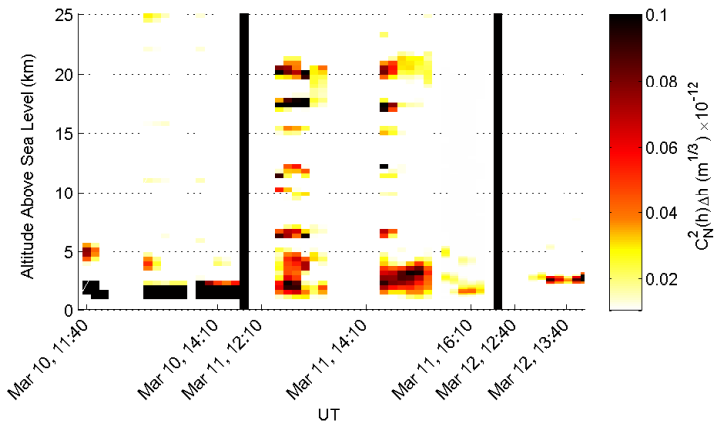

(a) Scaled pupil-plane $C_N^2(h)$ profiles

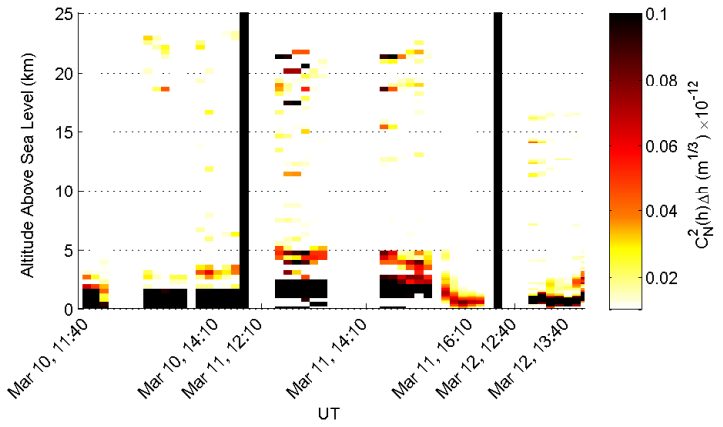

(b) Scaled generalised $C_N^2(h)$ profiles

Figure 6.23: Scaled $C_N^2(h)$ profiles for observations taken during March 2005. Time and $C_N^2(h)$ scaling used is as per Figure 6.1.

6.4 Summary of Profiles Detected at MJUO

UC-SCIDAR measurements taken between 2005 and 2007 indicated the presence of at least two turbulent layers.

The high altitude turbulent layer was located at 10 – 14 km above sea level and can be attributed to the tropopause region. This layer was found to have a velocity ranging from 12 – 30 m/s dependent on the weather experienced at MJUO.

A strong low altitude layer was detected extending from ground up to altitudes of 5 km above sea level. The strength of this layer was such that it was seen in a significant number of pupil-plane measurements and in the generalised measurements it masked any and all activity that occurred at higher altitudes. On nights where the low altitude turbulence was weaker, i.e. not as detectable in pupil-plane measurements, the pupil-plane r_0 estimate was in the order of 20 cm and θ_0 was approximately 2 arcseconds. However on nights where the strong low altitude turbulence was detected the pupil-plane r_0 decreased significantly and in some cases matched the generalised r_0 estimates. Generalised r_0 estimates ranged from 5 – 9 cm, whereas generalised θ_0 estimates were approximately 1 arcsecond. The measured wind speed of the low altitude turbulence ranged from 2 – 20 m/s. This range was consistent with the measurements recorded in the observation logs as measured by a meter attached to the outside of the domes located at MJUO.

An additional layer was detected at 6 – 7 km above sea level in some months. However it was significantly weaker than the tropopause and the low altitude layers. Detection of this layer during velocity analysis was only possible on nights where the low altitude turbulent layer was weak. The measured $V(h)$ for this layer ranged from 6 – 15 m/s.

Turbulence can also be associated with the dome and/or telescope. The exact contribution of dome seeing to the overall profile was not examined as any adaptive optics system installed at MJUO would also need to compensate for dome seeing. Hence an understanding of the full profile, from the dome up, is required.

Greenwood frequency, f_G, estimates from UC-SCIDAR data ranged from 10 – 30 Hz, with a large error on f_G that can be attributed to the gaps in the $V(h)$ profile in terms of altitude. The measured f_G most likely severely underestimates f_G for the site.

Seasonal trends detected during 2005 and 2007 are examined in Chapter 7. Models to describe the $C_N^2(h)$ and $V(h)$ profiles, based on the measured profiles, are also discussed.

Chapter 7

Turbulence Trending at MJUO

The understanding of how atmospheric turbulence changes above a site over a period of months, or even years, is required for the development of models to describe the turbulence structure. In addition, long-term site testing can provide an insight into seasonal and weather-related effects on $C_N^2(h)$ and $V(h)$ profiles.

Chapter 6 examined the monthly analysis of data collected at MJUO using UC-SCIDAR during 2005 – 2007. This chapter examines the seasonal trends detected during this time period, in particular during autumn and winter months. Insufficient number of usable runs were collected during the spring and summer months to make any conclusions and hence these seasons were not investigated. Models developed to describe the $C_N^2(h)$ and $V(h)$ profiles, based on the conclusions drawn here, are discussed in section 7.2.

7.1 Trending over the Years

The variable weather at MJUO (ranging from calm, clear nights to gusting winds and thickening clouds) resulted in a variety of profiles being detected. During cloud cover, with moderate to high winds, the NGT present was exceptionally strong, such that pupil-plane analysis was subject to large amounts of residual central peak. This resulted in a pupil-plane $\overline{r_0}$ values that were similar, and in some cases less than, that found for the generalised data. Table 7.1 lists $\overline{r_0}$ and σ_{r_0} values obtained for various dates throughout 2005 and 2007 with poor weather conditions. With the exception of January 2007, the weather on most nights had some level of cloud cover with moderate to high winds. Although January 2007 experienced a variety of weather conditions the longer and warmer days would heat the surrounding ground and buildings more than in other months. In the cases where pupil-plane r_0 estimates were less than generalised r_0 estimates, the generalised r_0 estimate was used in the determination of the pupil-plane monthly averages.

SCIDAR measurements were first collected in April 1999. The system used at the time was that designed by Imperial College (*Johnston et al.*, 2002). Figure 7.1 shows sample $C_N^2(h)$ profiles obtained during this observation period that were published in

Table 7.1: Summary of nights with poor pupil-plane results related to weather conditions.

			Pupil-plane		Generalised	
Date	Star	Weather Notes	$\overline{r_0}$ (m)	σ_{r_0} (m)	$\overline{r_0}$ (m)	σ_{r_0} (m)
31/05/07	α Cen	Thickening cloud with ground winds at 6 m/s	0.069	0.022	0.062	0.011
06/05/07	α Cru	Thin cloud cover with winds increasing to over 11 m/s	0.045	0.003	0.068	0.006
	α Cen		0.059	0.004	0.061	–
05/05/07	α Cru	Thin cloud cover with ground winds at 5.6 – 8.3 m/s	0.044	0.003	0.048	–
	α Cen		0.040	0.004	0.060	–
00/01/07	All	Variable conditions	0.057	0.025	0.050	0.016
13/08/05	α Cen	High wispy clouds with ground winds increasing to over 11 m/s	0.053	0.007	0.064	0.012
07/07/05	α Cru	Thickening cloud cover	0.058	0.006	0.062	0.002
	α Cen		0.070	0.001	0.063	0.001
13/05/05	α Cru	Gusting winds ranging from 2.8 m/sto over 14 m/s	0.041	0.003	0.072	0.009
	α Cen		0.056	0.006	0.068	0.005
22/04/05	α Cen	Rapidly thickening cloud	0.069	0.022	0.087	0.027

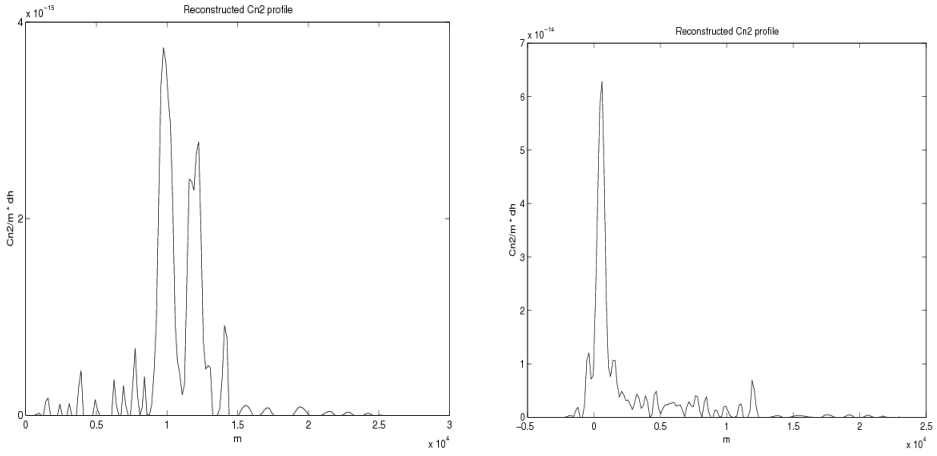

(a) Pupil-plane (b) Generalised

Figure 7.1: $C_N^2(h)$ profile estimates obtained during April 1999 using the system designed by Imperial College. Reprint of Figure 6 from *Johnston and Lane* (1999).

Johnston and Lane (1999). The pupil-plane profile shown in Figure 7.1(a) shows the presence of two different high altitude layers located at approximately 10 and 12 km above the telescope. Temporal analysis indicated that the velocities of the 10 and 12 km layers was 6.45 m/s and 11.63 m/s respectively, whereas the NGT layer seen in Figure 7.1(b) was attributed to the dome. The two high altitude layers were found to have peak strengths of 3.7×10^{-15} $m^{-2/3}$ and 2.7×10^{-15} $m^{-2/3}$ respectively. The resulting pupil-plane r_0 calculated was 50 cm. The resulting r_0 for the generalised profile was found to be 14 cm. *Johnston and Lane* (1999) noted that these r_0 values were higher than expected given the observation conditions at the time. Since *Johnston and Lane* (1999) was published, the determination of aperture normalisation matrices used in $C_N^2(h)$ determination has been improved. Figure 7.2 shows revised generalised $C_N^2(h)$ profiles from April 1999 (*Johnston et al.*, 2002). The average generalised $\overline{r_0}$ for the profiles shown was 12.3 cm.

Table 7.2 shows the monthly averages and standard deviations of r_0 and θ_0 for all available data. For the 2007 data, little variation exists in generalised $\overline{r_0}$ values suggesting that the strength of the NGT layer was relatively constant. However significant variation is seen for generalised $\overline{\theta_0}$ suggesting that the strength of the high altitude layers fluctuates. For the 2005 data, there is little variation in the generalised $\overline{r_0}$ and $\overline{\theta_0}$ measurements. The average r_0 for all UC-SCIDAR data was 12 ± 5 cm and 7 ± 1 cm for the pupil-plane and generalised measurements respectively. θ_0 was 1.5 ± 0.5 arcseconds and 1.1 ± 0.4 arcseconds for the pupil-plane and generalised measurements respectively.

UC-SCIDAR measurements are smaller than those obtained in April 1999 using the Imperial College system, with the strength of the NGT layer in the order of 6 – 10 times stronger for UC-SCIDAR data. Although some variation can be expected due

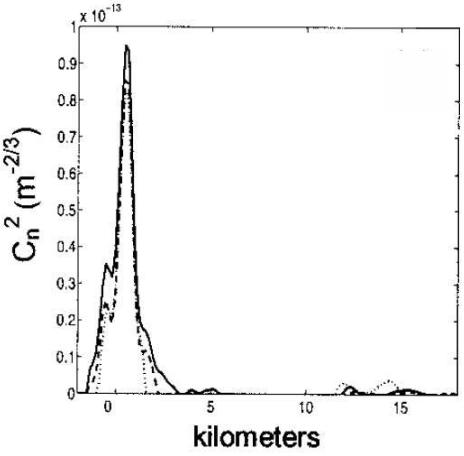

Figure 7.2: Consecutive $C_N^2(h)$ profiles from MJUO during April 1999. Reprint of Fig. 7(a) from *Johnston et al.* (2002). Note the label on the y-axis should have read $C_N^2(h)\Delta h$ or $\int C_N^2(h)dh$.

to the amount of time that had passed between the two instruments being used, this variation is more likely to be due to the poor SNR in the UC-SCIDAR system. However the low r_0 values do match the observation conditions typically seen by observers, which has a nominal angular resolution, $\theta_{\rm res}$, of ~ 2 arcseconds.* $\theta_{\rm res}$ from UC-SCIDAR was 2.5 arcseconds for the full profile, calculated at a wavelength of 589 nm. $\theta_{\rm res}$ for data taken in April 1999 was 1.2 arcseconds.

The large variation in the pupil-plane measurements suggests not only that there is a possible relationship with seasonal changes, but also with the weather at the site. March, June and July of 2005 saw high pupil-plane $\overline{r_0}$ and $\overline{\theta_0}$ values which can be attributed to the calmer weather seen during these observational periods. However most other months show similar $\overline{r_0}$ and $\overline{\theta_0}$ estimates within the margin of error. This suggests that weather conditions have a greater influence on the profiles obtained.

Figure 7.3 shows the true and scaled pupil-plane $C_N^2(h)$ profiles obtained for the autumn months (i.e. April and May) for UC-SCIDAR data. During 2005 a weak high altitude layer was found at approximately 11 – 12 km above sea level with a $C_N^2(h)\Delta h$ strength of approximately 3×10^{-14} m$^{1/3}$. Comparing this to the profiles in Figure 7.1(a) the high altitude layer is approximately at the same altitude given that results from April 1999 show altitudes above the telescope and the elevation of the observatory is 1024 m above sea level. However the strength of the layer is approximately 10 times that seen in April 1999. This is most likely related to the spatial sampling and exposure times used with the UC-SCIDAR system. In May 2007 the height of this high altitude layer increased by approximately 2 km. The height of the tropopause is known to fluctuate up

*Pers. comm. Alan Gilmore (Mount John University Observatory).

Table 7.2: Monthly averages and standard deviations for r_0 and θ_0 for all months.

Month	Pupil-plane				Generalised			
	$\overline{r_0}$ (m)	σ_{r_0} (m)	$\overline{\theta_0}$ (arcsec)	σ_{θ_0} (arcsec)	$\overline{r_0}$ (m)	σ_{r_0} (m)	$\overline{\theta_0}$ (arcsec)	σ_{θ_0} (arcsec)
June 2007	0.12	0.03	1.8	0.7	0.05	0.00	1.1	0.3
May 2007	0.11	0.07	1.3	0.9	0.06	0.01	1.0	0.3
January 2007	0.06	0.03	0.8	0.2	0.05	0.02	0.9	0.1
August 2006	–	–	–	–	0.09	0.03	2.2	0.4
April 2006	0.07	0.04	0.7	0.1	0.05	0.01	1.0	0.4
August 2005	0.10	0.02	1.7	0.4	0.08	0.01	1.1	0.1
July 2005	0.18	0.04	2.2	0.4	0.07	0.01	1.2	0.2
June 2005	0.22	0.03	1.8	0.3	0.06	0.01	1.1	0.1
May 2005	0.12	0.01	1.7	0.2	0.07	0.01	1.0	0.2
April 2005	0.11	0.03	1.3	0.3	0.07	0.01	0.9	0.1
March 2005	0.15	0.03	1.6	0.7	0.08	0.02	1.1	0.3
April 1999	–	–	–	–	0.123	0.014	–	–

to 4 km throughout the year (*Sturman and Tapper*, 1996). As such it is not unreasonable to assume that this is the same layer.

NGT and boundary layer turbulence is seen to extend up to 5 km above sea level. This is seen in both the pupil-plane and generalised data (Figure 7.4). Little can be ascertained from the generalised data as to the height and strength of the high altitude layer. This is due to the strength of the NGT and the noise present in the data.

Figure 7.5 shows the true and scale pupil-plane $C_N^2(h)$ profiles obtained for the winter months (i.e. June and July) with UC-SCIDAR. A high altitude layer is seen consistently at approximately 12 km above sea level with an average $C_N^2(h)\Delta h$ strength of approximately 3×10^{-14} m$^{1/3}$. This is a similar strength to that seen in the autumn months, suggesting little to no difference in the high altitude layer. However, an additional mid-altitude layer is seen in some data, with heights ranging from 6 – 9 km above sea level and with varying strength. This layer is most likely to be a function of weather patterns seen at the time. As seen with the autumn data, NGT and boundary layer turbulence can be seen to extend up to 5 km above sea level. Again little be can ascertained from the generalised data (Figure 7.6) as to heights and strengths of the high altitude layers.

Sturman and Tapper (1996) suggest that in New Zealand, the tropopause may lie 2 – 4 km higher during summer months than during winder. Unfortunately due to the insufficient number of runs from summer months available, this statement cannot be confirmed or denied using UC-SCIDAR data.

Figure 7.7 shows the average wind speed for the winter months, whereas Figure 7.8

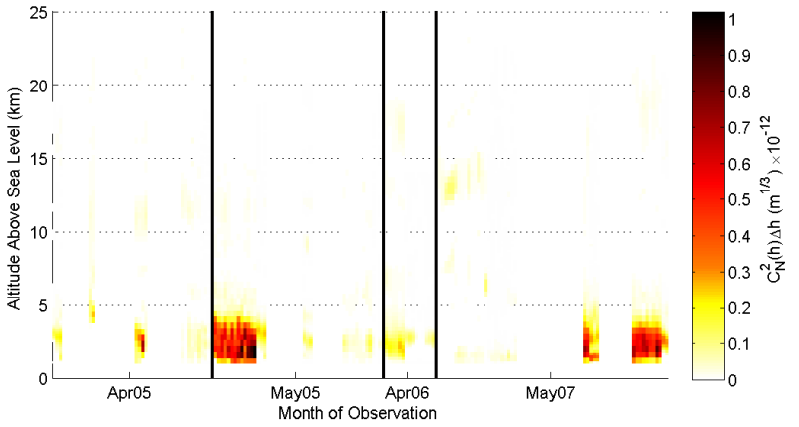

(a) Pupil-plane

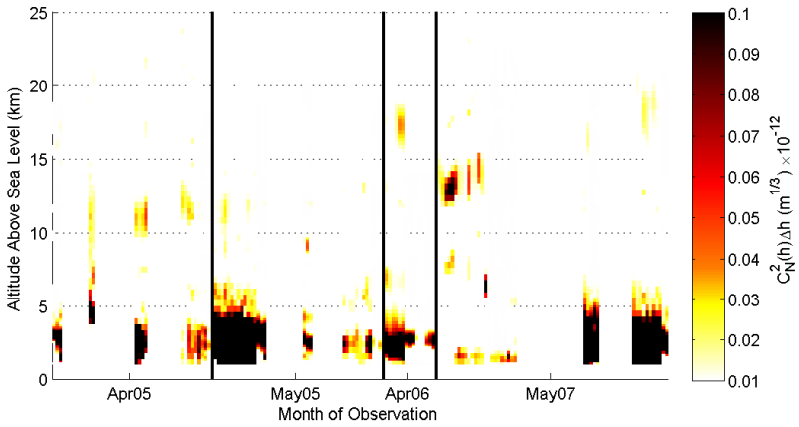

(b) Scaled pupil-plane

Figure 7.3: Pupil-plane $C_N^2(h)$ profile trends observed during autumn from 2005 to 2007. Time and $C_N^2(h)$ scaling used is as per Figure 6.1.

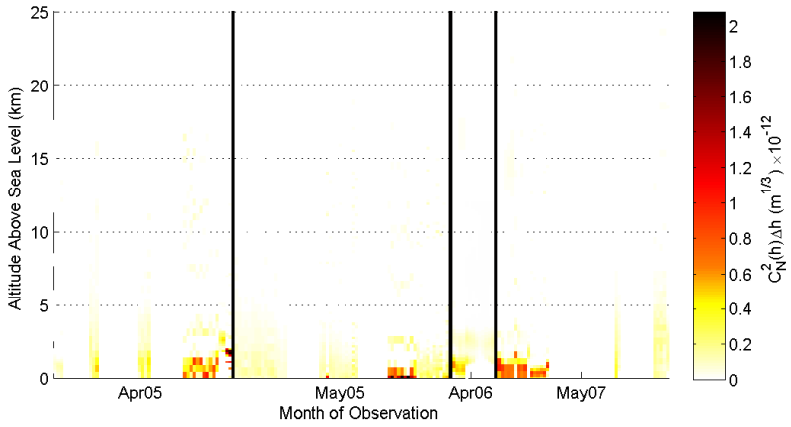

(a) Generalised

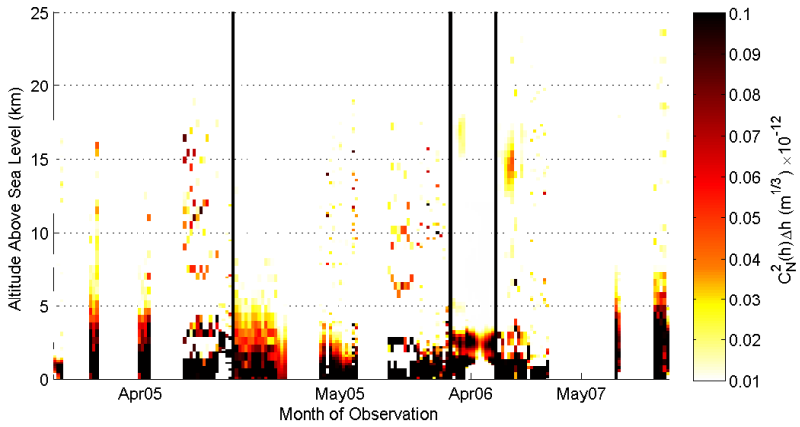

(b) Scaled generalised

Figure 7.4: Generalised $C_N^2(h)$ profile trends observed during autumn from 2005 to 2007. Time and $C_N^2(h)$ scaling used is as per Figure 6.1.

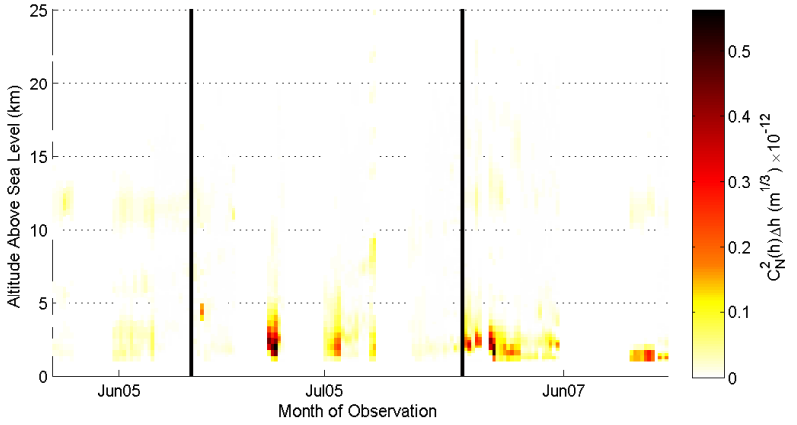

(a) Pupil-plane

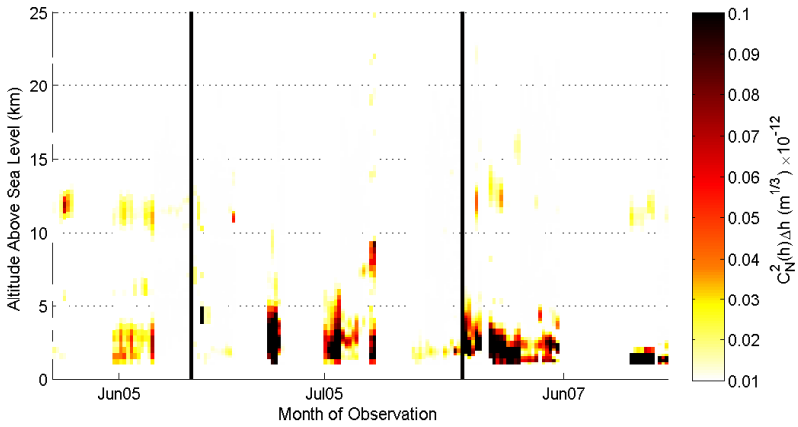

(b) Scaled pupil-plane

Figure 7.5: Pupil-plane $C_N^2(h)$ profile trends observed during autumn from 2005 to 2007. Time and $C_N^2(h)$ scaling used is as per Figure 6.1.

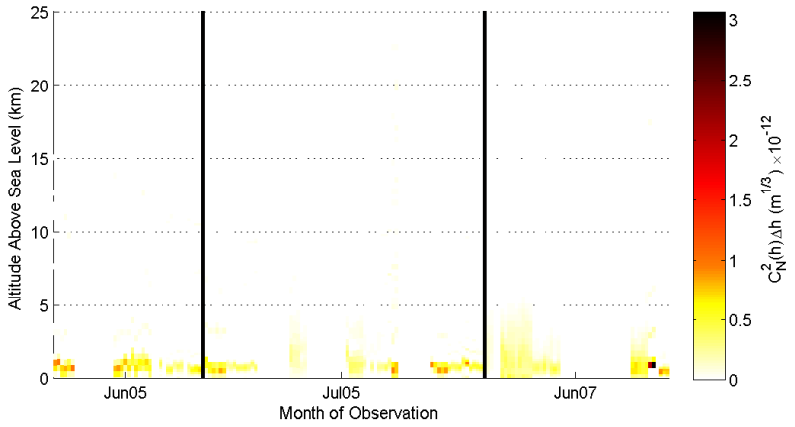

(a) Generalised

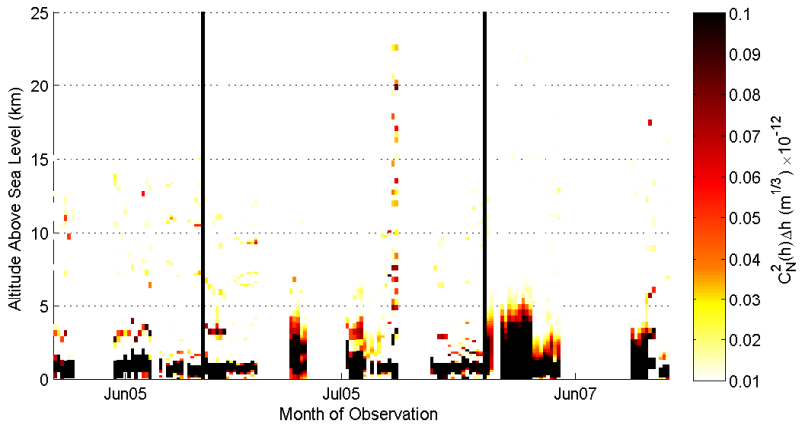

(b) Scaled generalised

Figure 7.6: Generalised $C_N^2(h)$ profile trends observed during autumn from 2005 to 2007. Time and $C_N^2(h)$ scaling used is as per Figure 6.1.

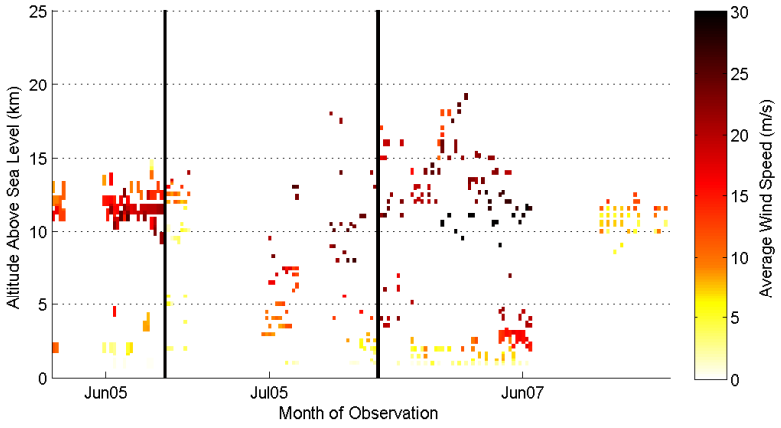

Figure 7.7: Average wind speeds detected, $|V(h)|$, for observations taken during winter from 2005 to 2007. Time scaling used is as per Figure 6.1.

Table 7.3: Nightly averages for f_G for all months where available.

Month	Pupil-plane		Generalised	
	$\overline{f_G}$ (Hz)	σ_{f_G} (Hz)	$\overline{f_G}$ (Hz)	σ_{f_G} (Hz)
June 2007	26	12	29	31
May 2007	30	23	8	13
January 2007	20	15	–	–
July 2005	10	7	11	14
June 2005	13	5	10	18

shows the instantaneous wind velocity. Although a significant amount of scatter exists for the data from July 2005 and June 2007 the layer heights found are similar. The high altitude layer has an average speed of 10 – 15 m/s in calmer weather, but speeds in excess of 25 m/s at other times. In all cases the weather was found to originate from a westerly direction as expected.

Table 7.3 shows the monthly averages and standard deviations for f_G for all the months that were available. Note that the values shown for January 2007 are averaged across both the pupil-plane and generalised data. The values for June 2007 reflect the averages for 31 May and 1 June only. Unfortunately no trend can be properly assessed due to the gaps in the $V(h)$ profiles obtained.

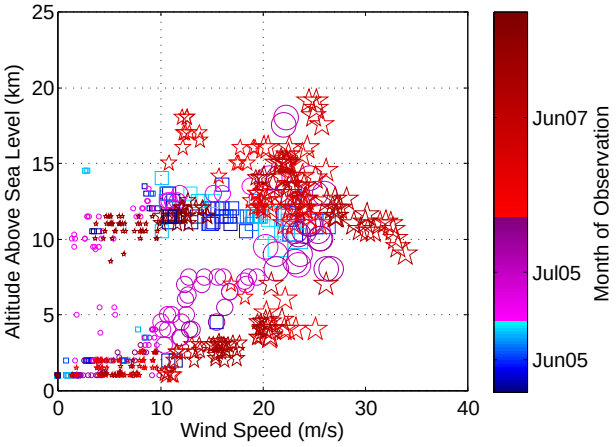

(a) Instantaneous wind speed $|V(h)|$

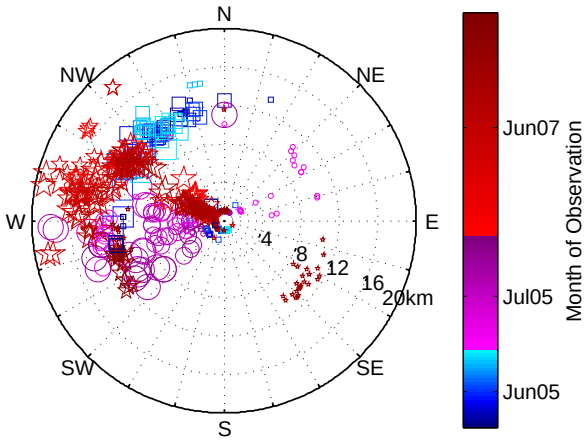

(b) Instantaneous wind direction β

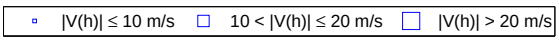

Figure 7.8: Wind velocity analysis for observations made during winter from 2005 to 2007. Colour and symbol sizes conventions used are as per Figure 6.5.

7.2 Finding a Model that Fits

There are many different $C_N^2(h)$ profile models that can be used. A commonly used model is the *Hufnagel-Valley* (HV) model and was described in Chapter 2, but for convenience the generic form is restated here. The generic HV model is a sum of exponential terms such that $C_N^2(h)$ is given by (*Hardy*, 1998)

$$C_N^2(h) = A\exp\left(-\frac{h}{H_A}\right) + B\exp\left(-\frac{h}{H_B}\right) + Ch^{10}\exp\left(-\frac{h}{H_C}\right) + D\exp\left(-\frac{(h-H_D)^2}{2d^2}\right), \tag{2-17}$$

where A is the turbulence coefficient for NGT (i.e. $\propto C_N^2(0)$) and H_A is the height for its $1/e$ decay, B and H_B are similarly defined for turbulence in the troposphere, and C and H_C are related to the turbulence peak located at the tropopause. The fourth term in equation (2-17) can be used to define one or more isolated layers where D and H_D define the strength and height of the layer and d specifies the layer thickness.

The HV model is an average model such that the resulting peak present at the tropopause region is not a spike but rather a broad peak, which accounts for variations in layer heights and fluctuations in the turbulence strength seen over time. Instantaneous spikes and variations in the heights of the turbulent layers are smoothed out. As such the HV model, using equation (2-17), can be fine tuned for turbulence at MJUO.

Figure 7.9 shows selected $C_N^2(h)$ profiles obtained from various months in 2005 and 2007. Also shown are three different models all based on the HV model. The HV 5-7 model (described in section 2.3, page 22) has parameters such that the resulting r_0 and θ_0 are 5 cm and 7 μradians (1.44 arcseconds) when using $\lambda = 500$ nm. Through trial and error, modifications to the parameters were determined to best match the profiles typically seen at MJUO. Table 7.4 lists the parameters for the various models shown in Figure 7.9.

The HV 5-7 model, while producing r_0 and θ_0 values appropriate for the site, results in a tropopause layer that is slightly too low, residing at 10 km above the site (i.e. 11 km above sea level) and too weak. By increasing the altitude of the tropopause peak by 500 m and increasing the coefficient C to 5.94×10^{-53} (MJUO1 model) then the θ_0 decreases to 0.96 arcseconds which is more in line with the measured values from the generalised $C_N^2(h)$ profiles. The near-ground and low-altitude turbulence is seen to regularly extend up to 4 km above sea level (Figure 7.10). An isolated layer was added where the peak was at 1.5 km above the site (i.e. 2.5 km above sea level) that was 1 km thick. The peak strength of this layer has been set to 2×10^{-16} m$^{-2/3}$. The modified HV model with the addition of this low-altitude layer has been dubbed MJUO2. In some profiles an additional layer was found at height ranging from 6 – 9 km above sea level. MJUO3 incorporates an

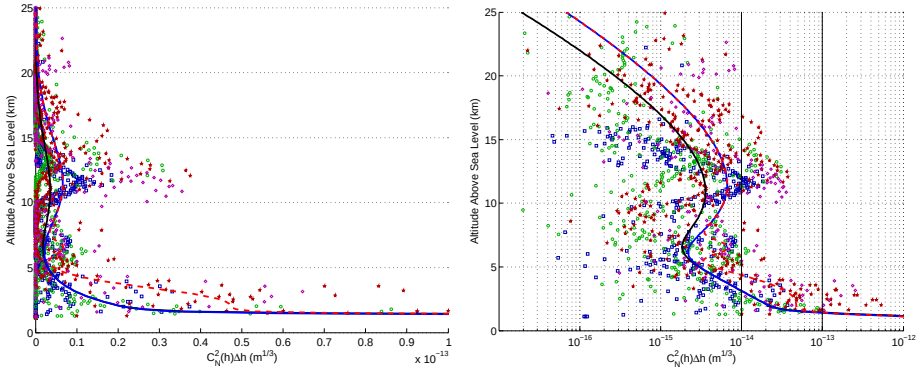

(a) Selected pupil-plane data (b) Selected pupil-plane data

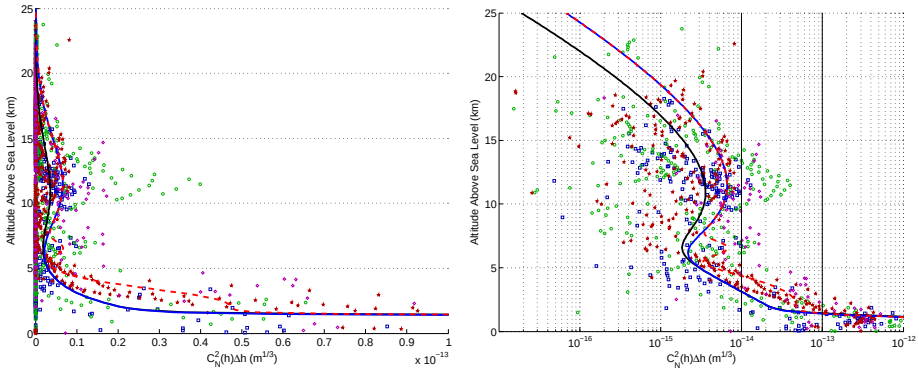

(c) Selected generalised data (d) Selected generalised data

Figure 7.9: $C_N^2(h)$ model fitting. Selected data shown is from (★) June 2007, (◯) May 2007, (□) June 2005 and (◊) April 2005. Models shown are (—) the HV 5-7 model, (—) MJUO1: a modified HV model and (- -) MJUO3: a modified HV model that incorporates two additional layers.

additional layer at 6.5 km above sea level, and is the recommended model for use in the AO design for MJUO. The profiles of the HV 5-7 model, MJUO1 and MJUO3 are shown in Figure 7.11.

It should be reiterated that a model based on the HV model is an average model. In some cases the tropopause layer at MJUO was found to have a peak $C_N^2(h)\Delta h$ strength greater than 10^{-14} $m^{1/3}$, the majority of the measurements were below this value. As such MJUO3 is also below this threshold explaining why the tropopause layer is not visible in Figure 7.10. It would be ideal to refine the model such that the breadth of the tropopause region is not so wide, as a model for AO design MJUO3 is the recommended model. Using a wavelength of 589 nm, r_0 is estimated to be 6 cm for MJUO3. θ_0 is estimated to be 0.9 arcseconds. The low θ_0 estimate will be associated with the broad tropopause layer peak in the modified HV model.

To describe the wind velocity with increasing altitude a Greenwood wind model is commonly used. This model was described in Chapter 2, and for convenience is restated

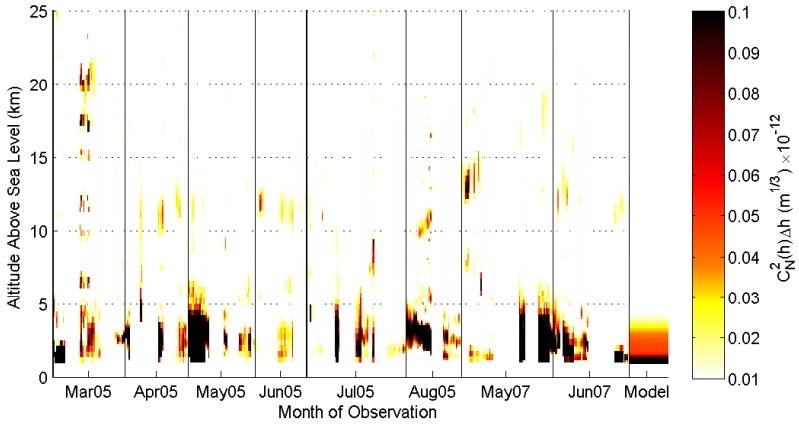

(a) Pupil-plane $C_N^2(h)$ profiles

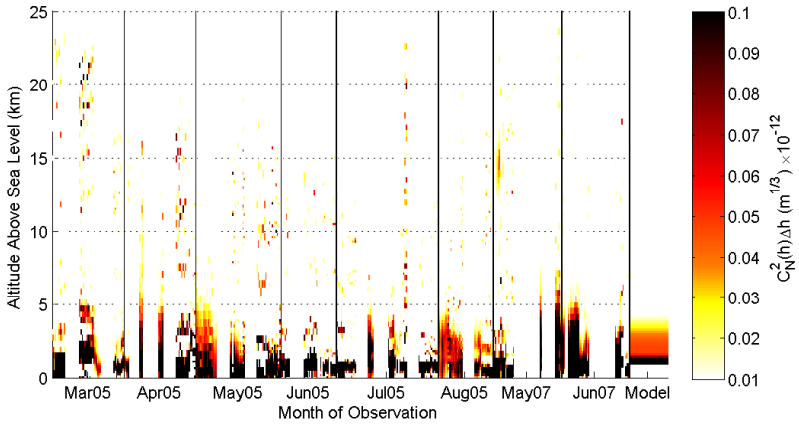

(b) Generalised $C_N^2(h)$ Profiles

Figure 7.10: $C_N^2(h)$ profiles taken with UC-SCIDAR. Model shown is MJUO3. Time and $C_N^2(h)$ scaling used is as per Figure 6.1.

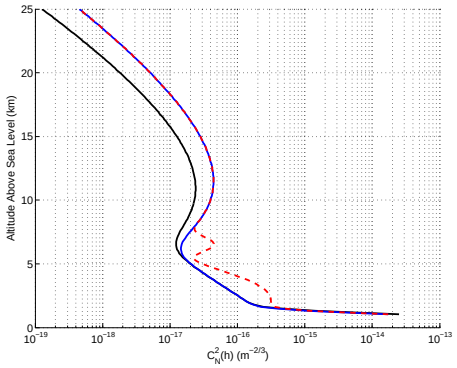

Figure 7.11: Recommended $C_N^2(h)$ turbulence model for MJUO. (—) HV 5-7 model (—) MJUO1: Modified HV model. (- -) MJUO3: Modified HV model incorporating two additional layers.

Table 7.4: Parameters for $C_N^2(h)$ turbulence models. r_0 and θ_0 values are specified for $\lambda = 589$ nm for the full profile and for $h > 3$ km above the telescope in brackets. MJUO 2 includes a strong low-altitude. MJUO 3 incorporates an additional mid-altitude layer for which the parameters are indicated in brackets.

Model	A ($\times 10^{-15}$)	H_A (m)	B ($\times 10^{-17}$)	H_B (m)	C ($\times 10^{-53}$)	H_C (m)	D ($\times 10^{-16}$)	H_D (m)	d (m)	r_0 (m)	θ_0 (arcseconds)
Hufnagel	0		27	1500	5.94	1000	0			0.06 (0.21)	1.33 (1.36)
HV 5-7	17	100	27	1500	3.59	1000	0			0.06 (0.27)	1.74 (1.81)
MJUO1	17	100	27	1500	5.94	1050	0			0.06 (0.16)	0.94 (0.96)
MJUO2	17	100	27	1500	5.94	1050	2	1500	1000	0.05 (0.16)	0.92 (0.95)
MJUO3	17	100	27	1500	5.94	1050	2 (0.3)	1500 (5500)	1000 (500)	0.05 (0.15)	0.90 (0.94)

here. This Greenwood wind model is (*Tyson and Frazier*, 2004)

$$V(h) = V(0) + V(H_T) \exp\left[-\left(\frac{h\cos\zeta - H_T}{L_T}\right)^2\right] \times \left[\sin^2\beta + \cos^2\beta\cos^2\zeta\right]^{1/2}, \quad \text{(2-18)}$$

where $V(0)$ is the wind velocity at ground level, $V(H_T)$ is the velocity at the tropopause located at an altitude H_T, L_T is the thickness of the tropopause layer and β is the wind direction relative to the telescope azimuth. Note that the direction corrections used in the Greenwood wind model are for a telescope that uses a horizontal coordinate system and strictly speaking should not be applied to telescopes at MJUO. However for AO design it is the wind speed that is important. As such for the purpose of further discussion it will be assumed that $\beta = 0°$ and hence equation (2-18) becomes

$$V(h) = V(0) + V(H_T) \exp\left[-\left(\frac{h\cos\zeta - H_T}{L_T}\right)^2\right] \times \cos\zeta. \quad \text{(7-1)}$$

The Bufton model is a specific Greenwood model where $V(0) = 5$ m/s and $V(H_T) = 30$ m/s with $H_T = 9.4$ km and $L_T = 4.8$ km for $\zeta = 0°$.

The $V(h)$ profile for 3 May, 2007, has an ideal profile that can be modelled by a modified Bufton wind model. Figure 7.12 shows the $V(h)$ measurements from 3 May with the Bufton and modified Bufton wind models indicated. The standard Bufton wind model (indicated by the dashed green line) assumes that the tropopause layer is at 9.4 km above the telescope with a wind speed of 30 m/s. This is clearly too low for the $V(h)$ profile for 3 May. Moving the model tropopause height to 12 km above sea level (indicated by the solid black line) allows the model to encompass the lower turbulent layers detected, as well as the activity detected in the tropopause region. If a zenith angle was incorporated into the model (red dashed line) then the effective wind speed in the tropopause region decreases to a value that is better suited to the data. The modified Bufton model used incorporated a zenith angle of 20°, as this was the angle used by most of the measurements made on 3 May.

Regardless of the model parameters used, a Gaussian based model will not adequately describe the $V(h)$ profiles detected when low altitude layers at 2 and 5 km have velocity between 15 – 20 m/s. A large portion of the data collected for velocity had the presence of some low-altitude wind. It was decided to add a second Gaussian peak, such

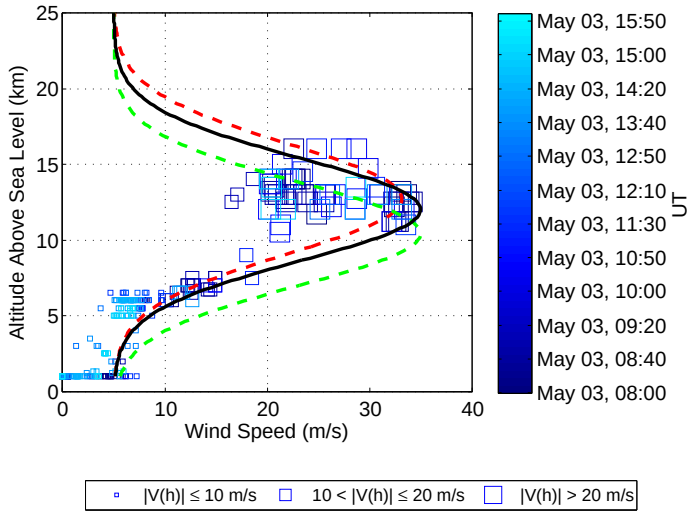

Figure 7.12: Wind speed analysis for observations made on May 3, 2007. Models shown are (- -) the standard Bufton model, (—) a modified Bufton model with $H_T = 11$ km, and (- -) a modified Bufton model with $H_T = 11$ km and $\zeta = 20°$. Elevation for MJUO is 1024 m above sea level.

that

$$V(h) = V(0) + V(H_T)\exp\left[-\left(\frac{h\cos\zeta - H_T}{L_T}\right)^2\right] \times \cos\zeta + V(H_1)\exp\left[-\left(\frac{h\cos\zeta - H_1}{L_1}\right)^2\right] \times \cos\zeta, \quad (7\text{-}2)$$

where $V(H_1)$ is the velocity of a low-altitude layer located at H_1 above the telescope with a thickness of L_1.

Unlike the modelling of $C_N^2(h)$, it is difficult to employ a generic model that would encompass the majority of conditions, as the velocity seen in the upper layers is dependent on the velocity detected near-ground. Figure 7.13(a) shows the instantaneous wind speeds obtained during June and July of 2005 and May and June of 2007. Overlaid are four different $V(h)$ models developed to encompass the range of velocity characteristics detected. The parameters for the four models for MJUO are listed in Table 7.5. Figure 7.14 shows all four models compared to the average wind speed, $|V(h)|$, detected using UC-SCIDAR data.

MJUO1V (indicated by the solid purple line in Figures 7.13(a) and 7.13(b)) is designed for very calm and clear nights where little NGT is present and the high altitude turbulence has low wind speeds, such as those seen on 3 June, 2007, and on 6 July, 2005. MJUO2V (indicated by dashed black line) was developed for nights such as 3 May, 2007,

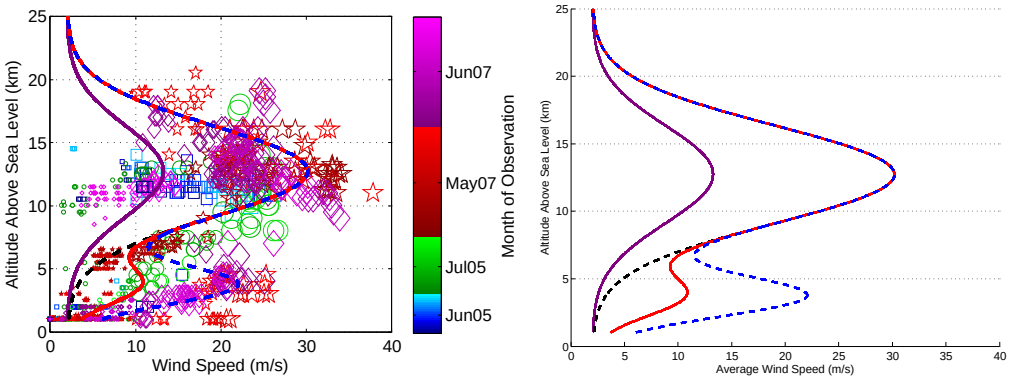

(a) Fit of $V(h)$ models to UC-SCIDAR data (b) MJUO $V(h)$ models

Figure 7.13: Fit of $V(h)$ models to measured profiles. Models shown are (—) MJUO1V, (- -) MJUO2V, (—) MJUO3V and (- -) MJUO4V.

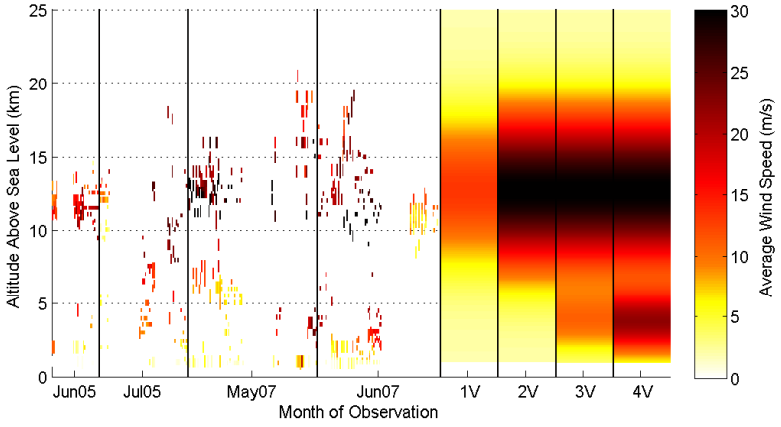

Figure 7.14: $V(h)$ profiles taken with UC-SCIDAR. Models shown are MJUO1V, MJUO2V, MJUO3V and MJUO4V.

Table 7.5: Parameters for wind velocity $V(h)$ models. f_G values are specified for $\lambda = 589$ nm.

Model	Usage	$V(0)$ (m/s)	$V(H_T)$ (m/s)	H_T (km)	L_T (km)	$V(H_1)$ (m/s)	H_1 (km)	L_1 (km)	$f_G(C_N^2(h)$: HV 5-7) (Hz)	$f_G(C_N^2(h)$: MJUO3) (Hz)
Bufton	—	5	30	9.8	4.8	0			29.5	40.6
MJUO1V	Very calm & clear	2	12	11	4.8	0			19.9	32.0
MJUO2V	Low ground winds	2	30	11	4.8	0			36.5	63.6
MJUO3V	Moderate ground winds	2	30	11	4.8	8	2.5	2	46.4	76.9
MJUO4V	High ground winds	2	30	11	4.8	20	2.5	2	65.9	105.0

where high altitude turbulence is strong, but ground wind speeds are very low. Both MJUO1V and MJUO2V are based on the traditional Greenwood wind model. MJUO3V (indicated by the solid red line) and MJUO4V (indicated by the dashed blue line) employ a second Gaussian peak described in equation (7-2). MJUO3V is intended for moderate ground wind speeds measuring 10 – 20 kph (2.8 – 5.6 m/s). Based on UC-SCIDAR measurements obtained this is the most likely situation to be encountered and hence should be the preferred model for AO design. MJUO4V was developed for situations where high ground wind speeds are present.

Using the MJUO3 $C_N^2(h)$ model and the MJUO3V $V(h)$ model for moderate ground wind speeds, f_G is estimated to be 79 Hz for a wavelength of 589 nm.

The $C_N^2(h)$ and $V(h)$ models developed have been used for the discussion on an AO system design in Chapter 8.

Chapter 8

Adaptive Optics for Mount John

Any AO system designed for MJUO must be retrofitted to the existing equipment and it is desirable to avoid any modifications. Therefore the output beam from the AO system should have the same focal point and F-number as the existing uncorrected beam.

The system should be modular with the flexibility to be used for both the $F/13.5$ and $F/7.8$ configurations available for the 1-m telescope. Priority will initially be given to the $F/13.5$ arrangement for use with the HERCULES spectrograph, as imaging is typically performed on a single object. Photometric imaging can be over stellar fields which are arcminutes across. Wavefront sensing associated with wide-field imaging requires more sophisticated sensing and aberration estimation because objects are not limited to an isoplanatic region.

This chapter outlines the issues surrounding AO system design within the context of the 1-m telescope at MJUO. Compensation wavelengths are assessed in section 8.1. Sources of errors within an AO system are discussed in sections 8.2 through 8.7. A summary of AO parameters is given in section 8.8.

8.1 AO Design and Sensor Operational Wavelengths

As presented in Chapter 2, a diffraction-limited system observing at wavelength λ has an the angular resolution, θ_{res}, corresponding to

$$\theta_{\text{res}} = 1.22\frac{\lambda}{D_{\text{T}}}, \tag{2-8}$$

where D_{T} is the diameter of the telescope. In the presence of atmospheric turbulence a telescope with a large aperture is turbulence-limited such that θ_{res} is specified by

$$\theta_{\text{res}} = 1.22\frac{\lambda}{r_0}, \tag{2-14}$$

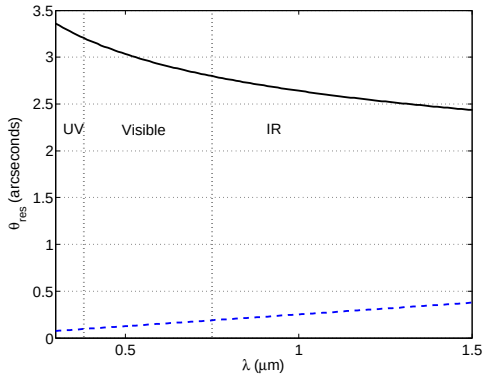

Figure 8.1: The effects of observational wavelength, λ, on angular resolution, θ_{res} on the 1-m telescope at MJUO. (—) Uncompensated resolution calculated using the MJUO3 model. (- -) Diffraction-limited resolution based on a telescope diameter of 1 m.

where r_0 is the turbulence coherence length (*Fried*, 1966). r_0 was defined in Chapter 1, but is restated here for convenience

$$r_0 = \left[0.423k^2 \sec(\zeta) \int C_N^2(h)dh\right]^{-3/5}, \tag{1-3}$$

where $k = 2\pi/\lambda$ is the wavenumber for a given wavelength λ and ζ is the zenith angle.

Figure 8.1 shows the θ_{res} for a given observational wavelength, λ, for uncompensated and diffraction-limited imaging for the 1-m telescope at MJUO. The uncompensated resolution was calculated using the MJUO3 model for $C_N^2(h)$ profile estimation (refer to Chapter 6). The idea of AO is to move the uncompensated line (indicated by the solid black line) towards the diffraction-limited line (indicated by the dashed blue line). The potential for improvement in imaging is greatest at shorter wavelengths. Although ultraviolet (UV) and visible wavelengths have greater potential for improvement, AO systems tend to be designed to operate at infrared (IR) wavelengths. This is because the resulting image size for longer wavelengths is smaller and so provides a finer spatial sampling for the wavefront sensing and hence a better estimate and fit to the aberrated wavefront (*Hardy*, 1998). In addition the isoplanatic angle increases with wavelength (refer to equation (1-4), page 6) reducing isoplanatic errors. (Angular anisoplanatic errors are discussed further in section 8.6.)

Different projects at MJUO utilise different wavelengths. Some projects involving the HERCULES spectrograph pass the incident light through an iodine cell resulting in a spectrum from iodine that is superimposed over the stellar spectrum and is used as a reference.* This functionality of HERCULES operates at wavelengths between 480 – 656 nm. An AO system at MJUO would ideally compensate for atmospheric turbulence at

*Pers. comm. John Hearnshaw, Department of Physics & Astronomy, University of Canterbury

these wavelengths.

Commercially available CCDs exist with a peak quantum efficiency at 550 nm.* This wavelength will be used for calculations performed in this chapter. At this wavelength the coherence length, r_0, is estimated to be 0.055 m. This corresponds to a θ_{res} of 2.1 arcseconds.

8.2 Optimising System Performance

In assessing the performance of an AO system it becomes essential to have a measure that compares the quality of the image obtained to that of the aberration-free (or diffraction-limited) image. The *Strehl intensity ratio* (normally abbreviated to Strehl) is commonly used for this purpose and is defined as the ratio of the peak intensity of the actual image, $(I_{\max})_{\text{actual}}$, to the peak intensity of the diffraction-limited image, $(I_{\max})_{\text{diffraction-limited}}$, and is defined mathematically as

$$S = \frac{(I_{\max})_{\text{actual}}}{(I_{\max})_{\text{diffraction-limited}}}. \tag{8-1}$$

The values of S can lie only in the interval 0 to 1. It is not possible to achieve a true diffraction-limited system. A system is treated as diffraction-limited if S does not fall below 0.8 (*Longhurst*, 1973).

If wavefront distortions induced by aberrations are smaller than one wavelength then the Strehl S can be found to decrease exponentially according to (*Tyson*, 1991)

$$S \approx exp\left(-\sigma_{\Phi}^2\right), \tag{8-2}$$

where σ_{Φ}^2 is the mean-square residual phase error of the system resulting from all error sources.

If each error source was statistically independent then the overall error for the system, σ_{Φ}^2, would be the summation of the individual effects, $\langle\sigma_i^2\rangle$, such that (*Tyson*, 1991)

$$\sigma_{\Phi}^2 = \sum_i \langle\sigma_i^2\rangle. \tag{8-3}$$

In practice, correlations do exist between some errors. Hence equation (8-3) can lead to an overestimation of the total system error. This is not considered a disadvantage in AO system design as this allows for the compensation of unforeseen errors. However, to optimise a system's performance it is necessary to minimise the total error in the system.

The error associated with an AO system can be divided into six main components:

*Dalsa Website: http://www.dalsa.com/

- *fitting errors* associated with the inability of a compensation device to exactly match an aberrated wavefront, σ^2_{fit};
- *temporal errors* associated with the finite system bandwidth, $\sigma^2_{\text{temporal}}$;
- *measurement errors*, σ^2_{sensor}, associated with the magnitude m_v of a reference star, noise characteristics of the CCD and the type of sensor employed;
- *angular anisoplanatic errors* related to the angular difference between the guide star and the science object, $\sigma^2_{\Delta\theta}$;
- *tilt errors* resulting from a tip/tilt compensation system, σ^2_{tilt}; and
- residual error resulting from uncompensated aberrations.

Systems that use a laser guide star for measuring wavefront aberrations will also have errors associated with the laser guide system. It is unlikely that MJUO will utilise a laser guide star due to the costs associated with such a system.

Sections 8.3 through 8.7 focus on the above error sources and the implications of these error sources on the design for any AO system at MJUO.

8.3 Fitting Errors from a Deformable Mirror

The finite sampling of the wavefront and finite degrees of freedom of a deformable mirror (DM) will limit the ability to compensate for high-order aberrations. The inability of a DM to exactly match an aberrated wavefront is known as the *fitting error*. If a DM was able to compensated for n_{Zern} modes of aberration then, from Chapter 2, the residual fitting error associated would be (*Noll*, 1976)

$$\sigma^2_{(\text{fit}=n_{\text{Zern}})} = 0.2944 n_{\text{Zern}}^{-\sqrt{3}/2} \left(D_{\text{T}}/r_0\right)^{5/3} . \tag{8-4}$$

The number of actuators used represents the degrees of freedom of a DM and is roughly equal to the number of Zernike modes that can be corrected for by the mirror (*Tyson and Frazier*, 2004). If actuators were spaced such that a distance s_{act} existed between each actuator then the total number of actuators required would be (*Tyson and Frazier*, 2004)

$$n_{\text{act}} = \frac{\pi}{4} \left(\frac{D_{\text{T}}}{s_{\text{act}}}\right)^2 , \tag{8-5}$$

where s_{act} is measured in the same plane as r_0. For MJUO, n_{act} would be 256 if $s_{\text{act}}/r_0 = 1$ for r_0 calculated at 550 nm. This provides the potential to correct for 256 Zernike modes.

In practice not all modes are compensated for. Hence the fitting error for a DM can

be related to the r_0 for the site such that (*Tyson*, 1991)

$$\left(\sigma^2_{\text{fit}}\right)_{\text{DM}} = \kappa \left(\frac{s_{\text{act}}}{r_0}\right)^{5/3}, \tag{8-6}$$

where κ is the fitting parameter which is dependent on the actuator influence function. The influence function describes how much influence an actuator has on the overall shape of a DM based on the type of mirror and the distance of an actuator from the mirror centre. For a continuous faceplate mirror where there is one actuator used per sub-aperture region, κ ranges between 0.28 – 0.34 rad^2(*Hardy*, 1998).

The amount of movement required in a deformable mirror (DM) will depend on the strength of the turbulence present. If tip and tilt were fully compensated for the residual error is

$$\sigma_{(n_{\text{Zern}}=3)} = \sqrt{0.134 \left(\frac{D_{\text{T}}}{r_0}\right)^{5/3}}, \tag{8-7}$$

in radians (refer to Table 2.2, page 21). Due to the nature of reflection, one unit of motion of the DM will result in two units of wavefront correction. If one assumes that the majority of the aberrations lie within $\pm\sigma_{n_{\text{Zern}=3}}$, then the required linear stroke of the deformable mirror actuators will be (*Hardy*, 1998)

$$\text{Stroke}_{\text{DM}} = \frac{1}{2}\left(2.5\lambda \frac{\sigma_{(n_{\text{Zern}}=3)}}{2\pi}\right), \tag{8-8}$$

where λ is the wavelength for which r_0 is determined. As r_0 is proportional to $\lambda^{6/5}$ then $\text{Stroke}_{\text{DM}}$ is independent of λ. For MJUO, the linear stroke $\text{Stroke}_{\text{DM}}$ would be ~ 0.52 μm.

8.4 Temporal Effects

An AO system's inability to respond to instantaneous changes in the atmospheric turbulence will result in *temporal errors*. Any time delay between sampling the wavefront to the subsequent correction contributes to this error. Temporal errors can be divided into two main categories: errors associated with the system bandwidth which is specified by atmospheric conditions and exposure times of the wavefront sensor; and pure time delays resulting from CCD readout time, processing time and the response time of the compensation device. Each category will be assessed in turn.

8.4.1 Correction Bandwidth

Due to the wind speed and strength of optical turbulence an AO system will be required to respond at a rate to adequately compensate for turbulence induced aberrations. The Greenwood frequency, f_G, is often used to described the rate of atmospheric turbulence change. f_G was first introduced in Chapter 1 and its definition is restated here for convenience

$$f_G = 0.255 \left[k^2 \sec\zeta \int C_N^2(h) V(h)^{5/3} dh \right]^{3/5}, \tag{1-5}$$

where $V(h)$ is the average wind velocity as a function of altitude h.

The temporal error associated with system bandwidth can be found by (*Tyson and Frazier*, 2004)

$$\sigma_{\mathrm{BW}}^2 = \left(\frac{f_G}{f_{\mathrm{system}}} \right)^{5/3}, \tag{8-9}$$

where f_{system} is the system bandwidth. f_{system} is set to be four to ten times than that of f_G to ensure that an AO system adequately samples temporal variations in the incident wavefront (**?**). f_{system} determines the effective exposure time for any wavefront sensing.

8.4.2 Pure Time Delays

Equation (8-9) does not account for errors caused by time delays in the feedback control loop or any averaging effects that may arise due to the exposure time used in wavefront sensing. The error associated with the time delay between time of measurement and time of correction can be expressed as (*Hardy*, 1998)

$$\sigma_{\Delta t}^2 = \left(\frac{\Delta t}{\tau_0} \right)^{5/3}, \tag{8-10}$$

where Δt is the measured time delay and τ_0 is the coherence time constant. $\sigma_{\Delta t}^2$ is added to σ_{BW}^2 to obtain the total temporal error.

τ_0, from Chapter 1, can be defined as (*Klückers et al.*, 1998)

$$\tau_0 = \left[2.91 k^2 \sec\zeta \int C_N^2(h) V(h)^{5/3} dh \right]^{-3/5}. \tag{1-6}$$

From equation (1-5), τ_0 can be related to f_G by

$$\tau_0 = \frac{0.134}{f_G}. \tag{8-11}$$

Table 8.1 shows the estimated f_G and τ_0 for the various $C_N^2(h)$ and $V(h)$ models presented in Chapter 6. An AO system that aims to compensate for high-order aberra-

Table 8.1: Greenwood frequency, f_G, and coherence time, τ_0, for various models for $C_N^2(h)$ and $V(h)$ profiles. Values shown have been calculated for $\lambda = 550$ nm and $D_\mathrm{T} = 1$ m.

Model	f_G (Hz)	τ_0 (ms)
HV 5-7; Bufton	30	4.4
MJUO3; MJUO1V	33	4.1
MJUO3; MJUO2V	68	2.0
MJUO3; MJUO3V	81	1.7
MJUO3; MJUO4V	108	1.2

tions should have a system bandwidth, f_system, in the order of 1000 Hz to encompass all conditions at MJUO.

8.5 Wavefront Sensing

The *wavefront sensing measurement error* consists of two main components: the sensor noise and the photon noise. *Photon noise* is related to the number of photons counted from the reference source and the surrounding background. *Sensor noise* is due to random signal fluctuations generated by the transfer of photons through the sensor array and the off-chip pre-amplifiers and digitizers (*Parenti and Sasiela*, 1994). Because the error associated with a wavefront sensor is dependent on the type of sensor and detector used, an expression for wavefront measurement error cannot be extended into a generalised case, and so specific designs must be considered.

The noise characteristics of the SH are reasonably well understood and described (*Parenti and Sasiela*, 1994), and so subsequent discussion will be limited to this sensor type.

In a SH sensor, a lenslet array images a plane conjugate to the telescope pupil. Traditionally the number of sub-apertures used is equal to the number of actuators on the DM. If the size of each lenslet represents d_sub of the aperture, and a circular aperture was filled with square sub-apertures, then the number of sub-apertures used would be (*Hardy*, 1998)

$$n_\mathrm{sub} = \frac{\pi}{4}\left(\frac{D_\mathrm{T}}{d_\mathrm{sub}}\right)^2, \tag{8-12}$$

where D_T was the diameter of the telescope. If $d_\mathrm{sub}/r_0 \approx 1$ then each sub-aperture would form a diffraction-limited image, where the sub-image centroid is shifted from the position associated with abberation-free imaging. The detected centroid shift is directly proportional to the local wavefront tilt.

Parenti and Sasiela (1994) determined that the photon noise of a SH sensor could be expressed as

$$\left(\sigma^2_{\mathrm{SH}}\right)_{\mathrm{PN}} \approx \frac{2\pi^2}{n_{pe}}\left[1+\left(\frac{d_{\mathrm{sub}}}{r_0}\right)^2\right], \tag{8-13}$$

where n_{pe} is the number of photons collected by the lenslet and PN denotes photon noise. *Parenti and Sasiela* (1994) went on to state that the sensor noise could be expressed as

$$\left(\sigma^2_{\mathrm{SH}}\right)_{\mathrm{SN}} \approx \frac{4\pi^2 n_{\mathrm{pix}}\left(n_{\mathrm{pix}}-1\right)\left(n_{\mathrm{pix}}+1\right)}{3\left(G_e n_{pe}\right)^2}\left[1+\left(\frac{d_{\mathrm{sub}}}{r_0}\right)^2\right] N^2_{\mathrm{rms}}, \tag{8-14}$$

where a $n_{\mathrm{pix}} \times n_{\mathrm{pix}}$ pixel array is used for each sub-aperture and N^2_{rms} is the variance of the noise generated by the transfer of photons through the sensor array and the off-chip pre-amplifiers and digitizers, and G_e is the gain of the CCD intensifier. For a non-intensified CCD, $G_e = 1$. If e represents the mean-square transfer detected in electrons per pixel then

$$N^2_{\mathrm{rms}} = n^2_{\mathrm{pix}} e^2. \tag{8-15}$$

The total number of photons collected over a square sub-aperture, n_{pe}, can be expressed as (*Parenti and Sasiela*, 1994)

$$n_{pe} = \left(\frac{\lambda}{hc}\right)\eta\tau_d d^2_{\mathrm{sub}} I_s, \tag{8-16}$$

where η is the sensor quantum efficiency, τ_d is the effective exposure time (known as the sensor dwell time), c is the velocity of light (3×10^8 m/s) and h is Planck's constant (6.626×10^{-34} J.s). I_s is the light intensity at the entrance of the wavefront sensor (W/m^2) and is related to the reference source magnitude and the optical transmission function through the atmosphere and the optics of the telescope. For a NGS, $I_s \propto 10^{-0.4 m_v}$ where m_v is the visual magnitude of the star (*Hardy*, 1998).

In astronomical AO systems, the wavefront sensor operates in low-light levels resulting in large wavefront measurement errors. In general the wavefront measurement error can be reduced by increasing the exposure times, resulting in an increase in the light intensity seen at the entrance to the wavefront sensor. However an increased exposure time will increase the temporal errors. An increase in the sub-aperture size, d_{sub}, will increase the number of photons collected per sub-aperture for a constant reference star magnitude, while decreasing the number of sub-apertures needed to sample the telescope aperture. The number of actuators used in a system on the DM is typically equal to the number of sub-apertures in the wavefront sensor. As such an increase in d_{sub} results in a decrease in the number of actuators on the DM, resulting in an increase in the fitting

Table 8.2: Sensor operational conditions used for simulations in Figure 8.2.

Sensing wavelength	λ	550 nm
Sensor spectral band	$\Delta\lambda$	200 nm
Overall quantum efficiency of CCD	η	0.4
Read noise per pixel	e	5 electrons per pixel
Number of pixels per sub-aperture	$n_{\text{pix}} \times n_{\text{pix}}$	2×2
Gain of CCD	G_e	1
Atmospheric optical transmission		0.8
Optical transmission of telescope and AO optics		0.1
DM fitting parameter	κ	0.3

error for a DM. A trade-off is required for the optimum performance.

Figure 8.2 shows the effects of changing the exposure time and the sub-aperture size on the overall wavefront error from a SH sensor, σ^2_{SH}, combined with the fitting error for a deformable mirror, $(\sigma^2_{\text{fit}})_{\text{DM}}$, and the temporal error resulting from time delay, $\sigma^2_{\Delta t}$. Table 8.2 lists the parameters used during simulations. r_0 and τ_0 values were calculated using the MJUO3 $C_N^2(h)$ model and the MJUO3V $V(h)$ model described in Chapter 6. In the determination of $\sigma^2_{\Delta t}$ it was assumed that the time an AO system takes to apply a correction to a wavefront after the initial exposure time is negligible. In reality this will not be the case and hence $\sigma^2_{\Delta t}$ is underestimated. In the determination of $(\sigma^2_{\text{fit}})_{\text{DM}}$ it was assumed that the spacing between actuators on the DM was $s_{\text{act}} \approx d_{\text{sub}}$ in the aperture plane.

From equation (8-6), $(\sigma^2_{\text{fit}})_{\text{DM}}$ is constant for a given d_{sub}. This has the effect of imposing a minimum error that can be obtained for $\tau_d \approx 1$ ms. After $\tau_d \approx 4$ ms the temporal error becomes the dominant factor.

The examples shown in Figure 8.2 are for a non-intensified CCD and for 10% transmission through the telescope and AO optics to the wavefront sensor, which allows for the majority of the light to be sent to the science instrument. To achieve a Strehl, S, of 0.1 then the overall error σ^2_Φ needs to be less 2.3 rad^2. Given the conditions listed in Table 8.2 this is not possible. If natural star guiding at MJUO is to be employed an intensified CCD must be used in the compensation for high-order aberrations.

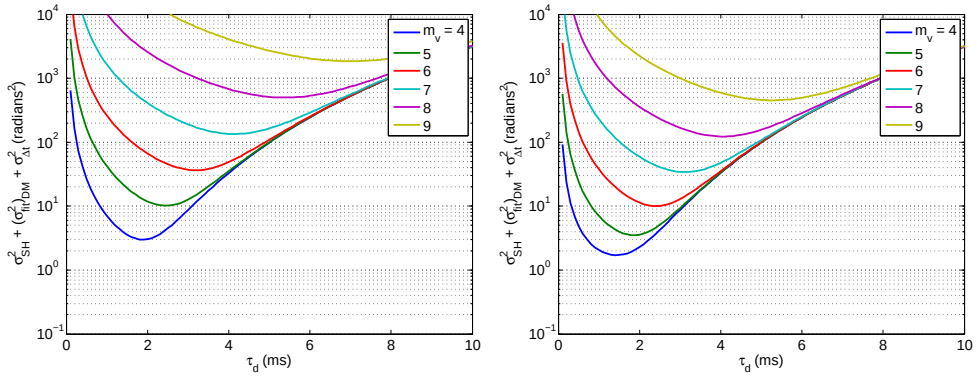

(a) $d_{\text{sub}} = 5.3$ mm (b) $d_{\text{sub}} = 11.1$ mm

(c) $d_{\text{sub}} = 14.2$ mm (d) $d_{\text{sub}} = 20.0$ mm

Figure 8.2: Optimisation of exposure time, τ_0, and reference star magnitude, m_v based on sub-aperture size, d_{sub}. Sensor operational conditions used as per Table 8.2. Models used for $C_N^2(h)$ and $V(h)$ profiles were MJUO3 and MJUO3V respectively.

8.6 Angular Anisoplanatism

When the object used to measure the wavefront is angularly displaced from the science object, the sampled turbulence will differ from the light seen originating from the science object. Wavefronts from the two light sources pass through slightly different portions of the atmosphere and hence the resulting aberrated wavefronts are not identical. Any measurement made using one source to infer information about the aberrations present in the wavefront from the other source will have an error known as *tilt anisoplanatism* or *angular anisoplanatism*.

The *isoplanatic angle*, θ_0, first described in Chapter 1, describes the maximum angle between the two objects where the two aberrated wavefronts can be considered identical*, and is found by

$$\theta_0 = \left[2.91k^2 \sec^{8/3}(\zeta) \int C_N^2(h) h^{5/3} dh\right]^{-3/5}. \tag{1-4}$$

The error variance associated with the isoplanatic angle when correcting for high-order modes of aberrations can be expressed as (*Tyson*, 1991)

$$\sigma^2_{\Delta\theta} = \left(\frac{\Delta\theta}{\theta_0}\right)^{5/3}, \tag{8-17}$$

where $\Delta\theta$ is the angular separation between the reference star and the science object. When $\Delta\theta$ is much smaller than θ_0 the correction that an AO system applies can be very good. However when the opposite is true the AO system will not apply an appropriate correction to the wavefront.

For MJUO, θ_0 is estimated as 0.83 arcseconds for an observing wavelength of 550 nm. This means that any natural guide star (NGS) is required to be within 0.83 arcseconds of the science object for wavefront sensing of high-order aberrations performed at 550 nm. Based on the value of θ_0 it is recommended to use a self guiding system where the science object itself is used for wavefront sensing of high-order aberrations.

8.7 Correcting for Tip/Tilt

Astronomical images consist of a speckled pattern where the image centroid moves randomly. This image motion is due to the overall wavefront tilt, which produces *angle-of-arrival* fluctuations. The angle-of-arrival has a Gaussian distribution and has a variance

*θ_0 is not to be confused with the angular resolution, θ_{res}, which describes the minimum angular distance between two resolvable objects.

of (*Hardy*, 1998)

$$\sigma_\alpha^2 = 0.184 \left(\frac{\lambda}{D_\mathrm{T}}\right)^2 \left(\frac{D_\mathrm{T}}{r_0}\right)^{5/3}, \tag{8-18}$$

where λ is the wavelength for which r_0 is determined. Note equation (8-18) is for the random tilt error in one direction. In some cases the image motion is different in the x and y directions. When the difference is small, then (*Hardy*, 1998)

$$\sigma_\alpha^2 = \frac{1}{2}\left[\sigma_{\alpha_x}^2 + \sigma_{\alpha_y}^2\right]. \tag{8-19}$$

Correction of overall image motion for long exposure astronomical images is typically performed using a fast steering mirror (FSM), also known as a tip/tilt mirror, that is controlled separately to the DM used for high-order corrections. There are three varieties of tip/tilt correction systems (*Olivier et al.*, 1993):

- a simple system that senses only the centroid of the uncorrected stellar image,
- a system that measures coma aberrations to eliminate the effects of *centroid anisoplanatism*, and
- a system incorporates a laser guide star to correct for high-order aberrations forming a short-exposure diffraction-limited image of the NGS before centroid position is estimated.

The third system type will not be discussed further.

The error associated with a tip/tilt correction system can be divided into four main components:

- temporal errors related to the finite bandwidth of the tip/tilt system, $(\sigma_\mathrm{BW}^2)_\mathrm{tilt}$;
- measurement error associated with the magnitude m_v of the reference star, $(\sigma_\mathrm{SNR}^2)_\mathrm{tilt}$;
- angular anisoplanatic errors related to the angular difference between the guide star and the science objects, $(\sigma_{\Delta\theta}^2)_\mathrm{tilt}$; and
- an error associated with uncompensated high-order aberrations containing a tilt component, σ_CA^2, termed the *centroid anisoplanatism* error.

The requirements for a FSM are based on the characteristics of the angle-of-arrival. A FSM is typically positioned such that the diameter of the aperture image is scaled by a factor

$$\frac{D_\mathrm{T}}{D_\mathrm{FSM}}, \tag{8-20}$$

where D_{T} is the diameter of the telescope and D_{FSM} is the diameter of the fast steering mirror. The required angular stroke of the FSM is (*Tyson and Frazier*, 2004)

$$\mathrm{Stroke}_{\mathrm{FSM}} = \frac{1}{2}\left(2.5\sigma_{\alpha}\right)\left(\frac{D_{\mathrm{T}}}{D_{\mathrm{FSM}}}\right), \tag{8-21}$$

assuming that the majority of the distribution lies within $\pm\sigma_{\alpha}$. As r_0 is proportional to $\lambda^{6/5}$ then $\mathrm{Stroke}_{\mathrm{FSM}}$ is independent of λ.

If a FSM with diameter 50 mm was used at MJUO then $\mathrm{Stroke}_{\mathrm{FSM}}$ would be 76 μrad. The linear stoke would depend on the distance of the actuators from the centre of the mirror. Typically three actuators are placed on a concentric circle on the back of a FSM. If the actuators resided on a pitch circle diameter of 30 mm then the linear stroke would be ~ 1.1 μm.

8.7.1 Temporal Errors in a Tip/Tilt System

The Greenwood frequency, f_G, defined by equation (1-5), describes the rate at which turbulence is changing, in particular the rate at which both tilt and high-order wavefront deformations are changing. Tilt changes at a slower rate compared to high-order aberrations (*Tyler*, 1994). As such a lower bandwidth is required to compensate for tip and tilt.

When considering mean tilt, *Tyler* (1994) found that the single-axis tilt variance due to a finite closed-loop bandwidth could be expressed as

$$\left(\sigma^2_{\mathrm{BW}}\right)_{\mathrm{tilt}} = \left(\frac{f_T}{f_{\mathrm{system}}}\right)^2 \left(\frac{\lambda}{D_{\mathrm{T}}}\right)^2, \tag{8-22}$$

where D_{T} is the telescope aperture, λ is the measurement wavelength, f_{system} is the bandwidth of the control system, and f_T is the Tyler frequency given by (*Tyler*, 1994)

$$f_T = 0.368 D_{\mathrm{T}}^{-1/6} \lambda^{-1} \left[\sec(\zeta) \int C_N^2(h) V(h)^2 dh\right]^{1/2}, \tag{8-23}$$

where ζ is the zenith angle and $V(h)$ is the wind velocity profile. Tracking control in the order of

$$\frac{1}{4}\frac{\lambda}{D_{\mathrm{T}}} \tag{8-24}$$

is adequate for most astronomical applications (*Tyler*, 1994), hence f_{system} can be set to four times f_T.

Table 8.3 indicates the f_G and f_T values calculated using various models for $C_N^2(h)$ and $V(h)$ profiles for the 1-m telescope at MJUO, as presented in Chapter 6. In all cases

Table 8.3: Greenwood frequency, f_G, and Tyler frequency, f_T, for various models for $C_N^2(h)$ and $V(h)$ profiles. Values shown have been calculated for $\lambda = 550$ nm and $D_{\mathrm{T}} = 1$ m.

Model	f_G (Hz)	f_T (Hz)
HV 5-7; Bufton	30	4.5
MJUO3; MJUO1V	33	4.9
MJUO3; MJUO2V	68	10
MJUO3; MJUO3V	81	12
MJUO3; MJUO4V	108	15

$f_T \approx 0.15 f_G$. To encompass the majority of observation conditions at MJUO a tip/tilt system would need to operate at approximately 60 Hz, which is four times the f_T when using the MJUO4V $V(h)$ model. This is significantly smaller than the required bandwidth for high-order aberration correction which was ~ 1000 Hz. The lower system bandwidth allows exposure times of up to ~ 16 ms during wavefront sensing assuming minimal time delay between wavefront sensing and tip/tilt correction.

8.7.2 Angular Anisoplanatism in a Tip/Tilt System

As a tip/tilt system can employ longer exposure times in wavefront sensing the effects of turbulence become blurred. This results in an increase in the isoplanatic angle. When considering tilt only the isoplanatic angle can be defined as (*Hardy*, 1998)

$$(\theta_0)_{\mathrm{tilt}} = \left[0.668 k^2 \sec^3(\zeta) \int C_n^2(h) h^2 dh D_{\mathrm{T}}^{-1/3}\right]^{-1/2}, \tag{8-25}$$

Like θ_0 (defined in equation (1-4)), $(\theta_0)_{\mathrm{tilt}}$ is significantly influenced by weak high-altitude layers. For MJUO, $(\theta_0)_{\mathrm{tilt}}$ is 2.6 arcseconds for the MJUO3 $C_N^2(h)$ model when $\lambda = 550$ nm.

The error associated with angular anisoplanatism for a tip/tilt system is (*Hardy*, 1998)

$$\left(\sigma^2_{\Delta\theta}\right)_{\mathrm{tilt}} = \left(\frac{\Delta\theta}{(\theta_0)_{\mathrm{tilt}}}\right)^2. \tag{8-26}$$

Although $(\theta_0)_{\mathrm{tilt}}$ is larger than θ_0, the sky coverage attainable is very small. Based on the estimate for $(\theta_0)_{\mathrm{tilt}}$ for MJUO it is recommended to look at the option of a self guiding system where the science object itself is used for tip/tilt estimation.

8.7.3 Measurements Errors in a Tip/Tilt System

When tilt estimation consists of a simple image centroid measurement, then the single-axis tilt error due to SNR for a quad-cell detector (i.e. 2×2 pixel array) is given by (*Tyler and Fried*, 1982)

$$\left(\sigma^2_{\text{SNR}}\right)_{\text{tilt}} = \frac{9\pi^2}{256}\left(\frac{1}{\text{SNR}}\right)^2\left(\frac{\lambda}{D_{\text{T}}}\right)^2, \tag{8-27}$$

where SNR is the signal-to-noise ratio of a quad-cell detector based on the number of photons collected. For $D_{\text{T}} > r_0$ it can be shown that (*Hardy*, 1998)

$$\left(\sigma^2_{\text{SNR}}\right)_{\text{tilt}} = \frac{9\pi^2}{256}\left(\frac{1}{\text{SNR}}\right)^2\left(\frac{\lambda}{r_0}\right)^2 K^2, \tag{8-28}$$

where K is a loss factor due to the gap between quad-cell detector elements and is normally between 1.3 – 1.5.

For a conventional CCD detector the SNR can be expressed as (*Tyson and Frazier*, 2004)

$$\text{SNR} = \frac{n_{pe}}{\sqrt{n_{pe} + n_{\text{pix}}\left[n_B + \left(\frac{e}{G_e}\right)^2\right]}}, \tag{8-29}$$

where n_{pe} is the number of photons collected per sub-aperture, n_{pix} is the number of pixels per sub-aperture, n_B is the number of background photons detected per sub-aperture from the surrounding sky, e is the electron read-noise in electrons per pixel and G_e is the gain of the CCD. $n_{\text{pix}} = 4$ for a quad-cell and $G_e = 1$ for a non-intensified CCD.

For a circular aperture sampled using a quad-cell detector, following a similar form to equation (8-16), it can be shown that

$$\left(n_{pe}\right)_{\text{quad-cell}} = \left(\frac{\lambda}{hc}\right)\eta\left(\frac{1}{f_s}\right)\frac{\pi}{4}D^2_{\text{T}}I_s, \tag{8-30}$$

where η is the quad-cell quantum efficiency, f_s is the sampling frequency, c is the velocity of light, h is Planck's constant and I_s is the light intensity at the entrance of the sensor arrangement (W/m^2).

Figure 8.3 shows the effect of exposure time on $\left(\sigma^2_{\text{SNR}}\right)_{\text{tilt}}$ for various stellar magnitude, m_v. The parameters use are those listed in Table 8.2 and the MJUO3 $C^2_N(h)$ model is used to estimate r_0 for $\lambda = 550$ nm. With increasing m_v the number of detectable photons over the aperture decreases resulting in an increase in $\left(\sigma^2_{\text{SNR}}\right)_{\text{tilt}}$.

The error values shown in Figure 8.3 are underestimated as it was assumed no background radiation is detected by quad-cell detector. However the approximations shown indicate that tilt centroid estimation should be possible in a self guiding system

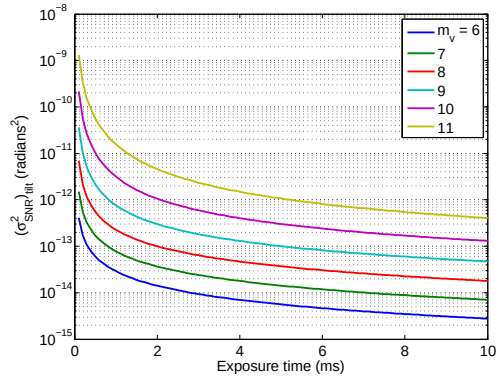

Figure 8.3: The effect of exposure time on measurement error of a quad-cell during simple centroid estimation. Sensor operational conditions used as per Table 8.2. Model used for $C_N^2(h)$ profile is MJUO3.

regardless of the magnitude of the science object used.

Figure 8.4(a) shows the expected uncorrected image of a single star at MJUO where the source of aberrations are limited to purely the effects of turbulence. Due to the level of turbulence present, the uncompensated image has an angular resolution, θ_{res}, of ~ 2.1 arcseconds with a resulting Strehl, S, of 0.0053. If tip/tilt corrections were applied based purely on centroid estimation (Figure 8.4(b)) θ_{res} could be expected to decrease to 1.54 arcseconds with an improved S of 0.0085.

8.7.4 Centroid Anisoplanatism

Centroid anisoplanatism results from uncompensated high-order aberrations containing a tilt component. Assuming that tilt estimation consists of a simple image centroid measurement, then the single-axis tilt error due to centroid anisoplanatism is (*Olivier and Gavel*, 1994)

$$\sigma_{\text{CA}}^2 = 0.00303 \left(\frac{\lambda}{D_{\text{T}}}\right)^2 \left(\frac{D_{\text{T}}}{r_0}\right)^{5/3}. \tag{8-31}$$

σ_{CA} can be related to the variance of angle-of-arrival, σ_α^2 (defined by equation (8-18), by

$$\sigma_{\text{CA}}^2 = 0.0165\sigma_\alpha^2. \tag{8-32}$$

Although the second and third modes of aberration are the tip and tilt modes (refer to Z_2 and Z_3 in Table 2.2) any Zernike aberration mode with a azimuthal order $m = 1$ and an odd radial order n will correspond to tilt with an order of pure-coma. Pure centroid measurements misinterpret the orders of coma as tilt (*Olivier and Gavel*, 1994). If a more detailed measurement was made of the tilt reference wavefront then the error associated

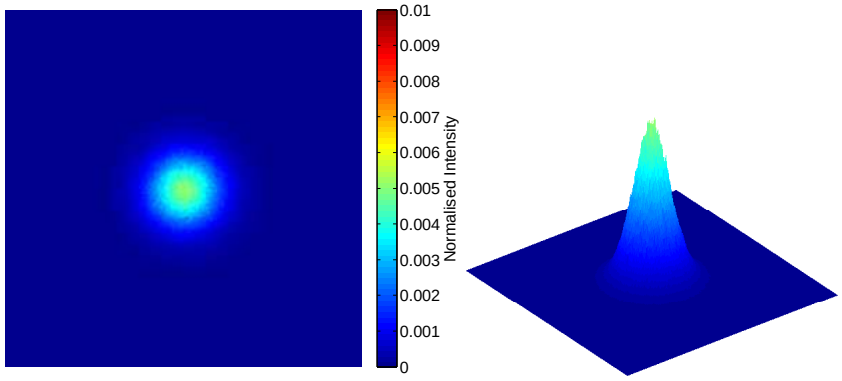

(a) Uncorrected

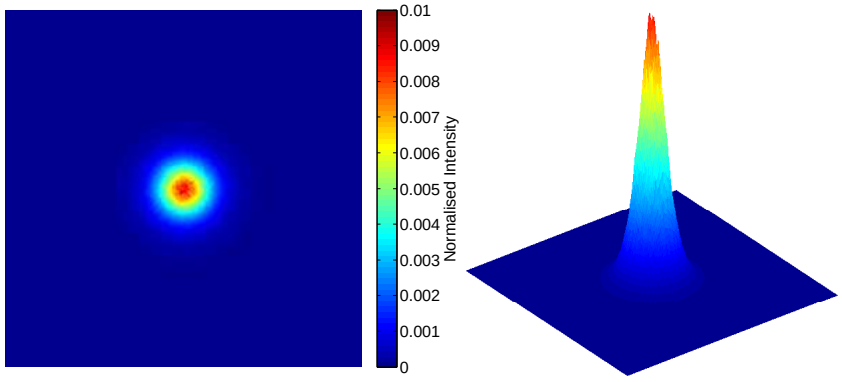

(b) Centroid estimated only

Figure 8.4: The effect of compensation of tip/tilt aberrations using simple centroid estimation for imaging at MJUO.

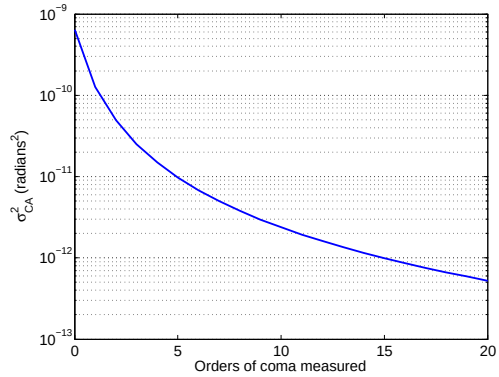

Figure 8.5: The effect of number of orders of coma incorporated into the tilt measurement on centroid anisoplanatism. Plot shown is for the MJUO3 $C_N^2(h)$ model at $\lambda = 550$ nm.

with centroid anisoplanatism can be reduced. If n_{coma} orders of pure coma are measured and used in the tilt estimation then the single-axis tilt error is given by (*Olivier and Gavel*, 1994)

$$\sigma^2_{\text{CA}} = 0.0165\,(n_{\text{coma}} + 1)^{-7/3}\,\sigma^2_{\alpha}. \tag{8-33}$$

Figure 8.5 shows the error variance associated with centroid anisoplanatism for MJUO at a wavelength of 550 nm. Note σ^2_{CA} is small for MJUO.

8.8 Summary of AO Parameters

Current uncompensated Strehl for the McLellan 1-m telescope at MJUO is approximated to be 0.0053. This is due to the significant level of turbulence located near ground level (refer Chapter 6). The key parameters for AO design for MJUO are listed in Table 8.4. The values shown have been calculated for the MJUO3 $C_N^2(h)$ model for a wavelength $\lambda = 550$ nm. Both the MJUO2V and MJUO3V $V(h)$ models have been used for temporal parameters to encompass light to moderate ground wind speeds.

Ideally any AO system designed for the McLellan 1-m telescope at MJUO should be modular. It is recommended that initially the AO system be designed to be used with science instruments that operate with the $F/13.5$ configuration of the telescope. However design should remain flexible such that the system could be extended for using with the $F/7.8$ science instruments at a later date.

Some measurements made with the HERCULES spectrograph superimpose a spectrum from an iodine cell over the measured stellar spectrum. As this functionality operates primarily with wavelengths between 480 – 656 nm it is suggested that initially wavefront sensing and corrections are applied over this range.

Table 8.4: AO design parameters for the McLellan 1-m MJUO. Values shown have been calculated using the MJUO3 $C_N^2(h)$ model for a wavelength $\lambda = 550$ nm. For temporal parameters estimates using both the MJUO2V and MJUO3V $V(h)$ models have been provided.

Telescope focal ratio	$F/13.5$
Coherence length r_0 (m)	0.06
Uncompensated angular resolution θ_{res} (arcseconds)	2.1
Isoplanatic angle θ_0 (arcseconds)	0.8
Isoplanatic angle for tilt $(\theta_0)_{\text{tilt}}$ (arcseconds)	2.6
Greenwood frequency $f_G\,(V(h) = \text{MJUO2V})$ (Hz)	68
Coherence time constant $\tau_0\,(V(h) = \text{MJUO2V})$ (ms)	2.0
Tyler frequency $f_T\,(V(h) = \text{MJUO2V})$ (Hz)	10
Greenwood frequency $f_G\,(V(h) = \text{MJUO3V})$ (Hz)	81
Coherence time constant $\tau_0\,(V(h) = \text{MJUO3V})$ (ms)	1.7
Tyler frequency $f_T\,(V(h) = \text{MJUO3V})$ (Hz)	12

Initial design should focus on tip/tilt correction. To correct for high-order aberrations using a NGS an intensified CCD is required. In addition, due to the size of θ_0, it is unlikely that a suitable guide star would be found.

It is suggested that the estimate of centroid position incorporate measurements of coma. An investigation as to the number of orders of coma needed to be measured is required.

Wavefront sensing in a tip/tilt system is only required to determine image centroid. As such light can be focused into a smaller region. Due to the size of $(\theta_0)_{\text{tilt}}$ it is suggested that self-guiding be employed which uses light from the science object itself to estimate tip/tilt aberrations.

To encompass all weather conditions at MJUO it is recommended that a tip/tilt system has a system bandwidth in the order of 60 Hz. If high ground wind speed conditions are to be excluded then this can be lowered to 45 Hz.

Based on the values indicated in Table 8.4, the required angular stroke of a 50 mm FSM is 76 μrad. For a FSM with actuators located on a pitch diameter of 30 mm this equates to ~ 1.1 μm.

Chapter 9

Conclusions and Future Work

This chapter summarises the key results and makes suggestions for the direction of future research.

Section 9.1 highlights the advantages and disadvantages of the purpose-built system, UC-SCIDAR, as described in Chapter 3, and draws together the main conclusions from the analysis methods presented in Chapters 4 and 5. Also discussed are the key results from Chapters 6 and 7 from the $C_N^2(h)$ and $V(h)$ profiles and models for MJUO, and the implications for an AO system design at the site, as presented in Chapter 8.

Section 9.2 suggests possible improvements for the UC-SCIDAR system and areas of further research to improve the analysis of the spatio-temporal covariance profiles.

9.1 Conclusions

As part of a collaboration project between the Department of Physics & Astronomy and the Department of Electrical & Computer Engineering, a purpose built system was constructed to measure the optical turbulence present above MJUO. The UC-SCIDAR system was developed from primarily off-the-shelf components at low cost. The system employs a dual channel configuration which provides the ability to collect simultaneous pupil-plane and generalised SCIDAR measurements, and uses a bread-board mounting system which allows for easy component changes as required.

UC-SCIDAR saw first light at MJUO in 2003, and since then has undergone several revisions to improve the spatial sampling of the primary mirror, the noise characteristics of the CCDs, and temporal sampling between successive frames. The V2007 system utilises cameras that can readily capture images at a frame rate of 60 Hz, providing a sufficiently high frame rate for $V(h)$ profiling. The V2007 system also includes the use of a removable beamsplitter, which allows for a simple change between single and dual camera capture modes. This feature proved useful in the presence of thin cloud cover and for data collection using fainter stars. The current system is highly portable and could easily be mounted onto a different telescope through the use of a different mounting plate.

$V(h)$ profiling using SCIDAR data is commonly performed on a 2-m class telescope. This allows the use of full triplets (i.e. central peak with two secondary peaks) to locate high altitude layers. For a 1-m telescope, the maximum detectable velocity, $V_{\max}(h)$, is significantly less for the same frame rate, $1/\Delta t$, and binary star angular separation, ϕ. For $\phi = 14$ arcseconds and using a CCD frame rate of 30 Hz, as used in the V2005 system, $V_{\max}(h)$ for a 10 km layer is 9.6 m/s using full triplet analysis. This increases to 19 m/s for a frame rate of 60 Hz, as used in the V2007 system. When $\phi = 4$, $V_{\max}(h)$ is 24 m/s and 48 m/s for a frame rate of 30 Hz and 60 Hz respectively.

The use of partial triplet analysis (i.e. detection of the central peak and one secondary peak) removes the dependence of $V_{\max}(h)$ on ϕ, and instead the limiting factor becomes the diameter of the telescope aperture. For a 1-m telescope $V_{\max}(h)$ increases to 30 m/s and 60 m/s for 30 Hz and 60 Hz respectively.

9.1.1 MJUO Profiling

UC-SCIDAR measurements taken between 2005 – 2007 detected strong NGT with a weaker layer located at 12 – 14 km above sea level. On calm nights, a third mid-altitude layer was detected at ~ 6 km above sea level. In a significant amount of data the strong low altitude turbulence extended up to 4 km above sea level. Monthly averages for the coherence length, r_0, and the isoplanatic angle, θ_0, calculated for a wavelength of 589 nm, are presented in Table 9.1. The results suggest an average r_0 of 12 ± 5 cm and 7 ± 1 cm for pupil-plane and generalised profiles respectively. This corresponds to an angular resolution, θ_{res}, of 2.1 arcseconds for the full profile. The average θ_0 values were 1.5 ± 0.5 arcseconds and 1.1 ± 0.4 arcseconds for pupil-plane and generalised profiles respectively.

Temporal analysis detected layers located at similar altitudes, with tropopause layer velocities of 12 – 30 m/s, dependent on weather conditions. Low altitude turbulence layers had velocities ranging from 2 m/s to well in excess of 24 m/s. The monthly averages for Greenwood frequency, f_G, are shown in Table 9.2. Unfortunately no seasonal trends could be established due to the gaps in the $V(h)$ profiles obtained.

Little seasonal variation was detected in the $C_N^2(h)$ profiles obtained. Both $C_N^2(h)$ and $V(h)$ profiles were highly dependent on the weather conditions.

A modified Hufnagel-Valley (HV) model was developed to describe the $C_N^2(h)$ profile, incorporating a strong NGT layer, a layer at 11 km above the telescope (i.e. 12 km above sea level) and two additional layers: one at 5.5 km above the telescope and the other at 1.5 km above the telescope extending up to 4 km. The resulting model estimates an r_0 of 6 cm for a wavelength of 589 nm, which corresponds to a θ_{res} of 2.5 arcseconds. θ_0 is estimated at 0.9 arcseconds.

A series of $V(h)$ models were developed, based on the Greenwood wind model with

Table 9.1: Monthly averages and standard deviations for r_0 and θ_0. This table is an abbreviated form of Table 7.2 (page 181).

Month	Pupil-plane				Generalised			
	$\overline{r_0}$ (m)	σ_{r_0} (m)	$\overline{\theta_0}$ (arcsec)	σ_{θ_0} (arcsec)	$\overline{r_0}$ (m)	σ_{r_0} (m)	$\overline{\theta_0}$ (arcsec)	σ_{θ_0} (arcsec)
June 2007	0.12	0.03	1.8	0.7	0.05	0.00	1.1	0.3
May 2007	0.11	0.07	1.3	0.9	0.06	0.01	1.0	0.3
January 2007	0.06	0.03	0.8	0.2	0.05	0.02	0.9	0.1
August 2006	–	–	–	–	0.09	0.03	2.2	0.4
April 2006	0.07	0.04	0.7	0.1	0.05	0.01	1.0	0.4
August 2005	0.10	0.02	1.7	0.4	0.08	0.01	1.1	0.1
July 2005	0.18	0.04	2.2	0.4	0.07	0.01	1.2	0.2
June 2005	0.22	0.03	1.8	0.3	0.06	0.01	1.1	0.1
May 2005	0.12	0.01	1.7	0.2	0.07	0.01	1.0	0.2
April 2005	0.11	0.03	1.3	0.3	0.07	0.01	0.9	0.1
March 2005	0.15	0.03	1.6	0.7	0.08	0.02	1.1	0.3

Table 9.2: Nightly average for f_G for all months where available. This table is a repeat of Table 7.3 (page 186).

Month	Pupil-plane		Generalised	
	$\overline{f_G}$ (Hz)	σ_{f_G} (Hz)	$\overline{f_G}$ (Hz)	σ_{f_G} (Hz)
June 2007	26	12	29	31
May 2007	30	23	8	13
January 2007	20	15	–	–
July 2005	10	7	11	14
June 2005	13	5	10	18

an additional Gaussian peak located at low altitudes to model the $V(h)$ profiles seen at MJUO. The models correspond to calm, light, moderate and strong ground wind speed conditions seen at the site. Using the modified HV model for $C_N^2(h)$ profiles and the suggested model for $V(h)$ profiles in the presence of moderate ground wind speeds, f_G was estimated at 79 Hz for a wavelength of 589 nm. The Tyler frequency, f_T, was estimated at 12 Hz for a wavelength of 550 nm, and 11 Hz at 589 nm.

The implications of the $C_N^2(h)$ and $V(h)$ profiles at MJUO on an AO system design were discussed and summarised in Chapter 8. Due to financial considerations, it is recommended that the initial AO design for the 1-m McLellan telescope focus on the correction of tip/tilt only. Due to the small θ_0, the system should be self-guiding, as it is unlikely any star located in close proximity to the science object would be suitable as a guide star. The low f_T obtained suggests that an AO system bandwidth in the order of 60 Hz is adequate to correct for tip/tilt aberrations.

9.2 Future Work

The CCD cameras used in the UC-SCIDAR system were acquired at low cost and had poor noise characteristics. Although changes made to the spatial sampling across the primary mirror improved the signal-to-noise characteristics of the data, the background noise level was still high, limiting the observable objects for SCIDAR data. The V2005 system provided useful profiles from α Cen and α Cru, and the changes in the cameras meant that θ Eri and υ Car could also be used. However the number of observable star systems was still limited. The use of cameras with much improved noise characteristics and quantum efficiency would be beneficial. Ideally SCIDAR measurements using stars of magnitude $m_v = 4$ would be required, as this would increase the number of usable SCIDAR objects to 10 – 20 star systems. The advancements in technology over the past few years have seen significant performance improvements in low cost CCD cameras. The same money spent today to acquire CCDs used in the V2005 system will provide a CCD camera with significantly improved characteristics.

Analysis of the measurements taken for use in $C_N^2(h)$ profiling utilised standard techniques. Secondary peak slice extraction is typically performed by taking the difference between a slice taken in the direction of the binary and a slice taken perpendicular to the binary. In practice a residual central peak results due to pixelisation, which can lead to false low altitude layers or the true strengths of low altitude turbulent layers being overestimated. This is particularly true for narrow binary star systems that result in poor altitude resolution, and strong near ground turbulence (NGT). In the presence of strong NGT the central peak elongates in the direction of the binary, adding to the issues

associated with the identification of secondary peaks. In some cases the pupil-plane r_0 estimate would be less than the generalised r_0 estimate. In these cases the generalised r_0 estimate was used, because the pupil-plane result was deemed to be unreliable. Attempts were made to correct for this issue by means of truncation, but with no success. Further investigation is required to devise a method that would improve the extraction of secondary peak information.

The velocity detection algorithm employed was based on a modification of CLEAN. Current covariance models do not adequately match profiles seen, so the algorithm utilises a rectangular mask. To improve the data mask used, further investigation is required into the shape of the spatio-temporal covariance profile as it approaches the edge of the aperture under the presence of noise. It would be desirable to identify a mathematical relationship for the partial triplet profile to aid in the automatic detection of partial triplets.

Exposure times for the analysis of $C_N^2(h)$ and $V(h)$ profiles were limited to ≤ 3.5 ms to limit excessive blurring of scintillation from fast moving layers. Even with this restriction some blurring of the 2D triplet profile occurred for fast moving layers. A full investigation of the effects of exposure time on the triplet profile is suggested, with the aim of refining the mask used in a CLEAN algorithm for velocity detection. Other factors that result in the blurring of triplet peaks include the partial failure of Taylor's hypothesis and velocity fluctuations.

Analysis models used during this research assumed that turbulence could be described using Kolmogorov statistics. It has been suggested that in the presence of strong turbulence Kolmogorov theory should be modified (*Toselli et al.*, 2007). The NGT present at MJUO is exceptionally strong and hence Kolmogorov turbulence may be inappropriate for the analysis of data from MJUO. In the $C_N^2(h)$ analysis the kernel used for the inversion would require modification. For the $V(h)$ analysis, the measured $V(h)$ will not change, however an investigation into the effects of non-Kolmogorov turbulence may help to refine the triplet mask.

Variations detected in the $C_N^2(h)$ and $V(h)$ profiles above MJUO, as measured by UC-SCIDAR, suggested a connection between the weather conditions noted by observers and the profiles measured. It is suggested that data obtained from UC-SCIDAR be correlated to meteorological data to investigate whether SCIDAR data could predict weather-related seeing over the site.

The modified HV model used to describe the $C_N^2(h)$ profile above MJUO has a broad peak associated with the tropopause region. This results in a decrease seen in the θ_0 estimate based on the model. The suggested model could be further refined by narrowing the peak of the tropopause, increasing the θ_0 estimate from the model. Although adequate

models for $V(h)$ profiles were determined, it is recommended that more temporal data be collected to refine the models. An investigation into the correlation between low and high altitude velocities should also be conducted.

9.2.1 Increasing NGT Strength

During the full analysis of all data an issue was highlighted with respect to the different detected strengths for a given layer in simultaneous pupil-plane and generalised data.

Consider a simulated profile with three layers located at near-ground, 5 and 10 km above the telescope, where the NGT layer is of variable strength. Table 9.3 shows the strengths of the 5 and 10 km layer.

Table 9.3: The altitude and turbulence strength of the mid- to high-altitude layers present in a simulated profile.

Layer Altitude (km)	$\int C_N^2(h)dh$ ($m^{1/3}$)	$r_0(\lambda = 589\text{nm})$ (cm)
5	1×10^{-13}	38.95
10	3×10^{-13}	20.15

Figure 9.1 shows the resulting $C_N^2(h)$ profiles that are obtained from ideal covariances with no noise for a binary star system using the system of equations discussed in Chapter 2 on scintillation and covariances. Consider that case where no regularisation is used in the estimation of the $C_N^2(h)$ profile, i.e. $\gamma = 0$ (Figure 9.1(a)). As expected, the calculated $C_N^2(h)$ strength seen for the 5 and 10 km layers are constant within margin of error, both in the peak strength and width, for increasing strength of NGT ranging from no NGT, as is assumed to be the case during pupil-plane analysis, to strong NGT of $C_N^2(h)\Delta h = 3 \times 10^{-12}$ $m^{1/3}$. With increasing levels of regularisation, γ (Figures 9.1(b) and 9.1(c)), the peak strengths decrease. However the area under the curve is constant resulting in a constant r_0 estimate of 38 – 39 cm and $\sim$ 20 cm for the 5 and 10 km layers respectively. However the ideal covariance assumes that there are an infinite number of frames used in its determination. In reality only a small number of frames are used.

Figure 9.2 shows the resulting $C_N^2(h)$ profiles obtained from an ensemble of 1000 simulated scintillation frames with no noise and increasing NGT strength. For the simulation shown, a binary star system with an angular separation of 10 arcseconds and magnitude difference of 1.36 was used, assuming measurements taken at zenith. In each case the spatial sampling across the aperture was 0.0031 m/pix, the regularisation parameter was set to 0.1, and the width of the Gaussian used had a $\sigma = 0.003$. (See Appendix F for the significance of σ during the simulation of scintillation frames.) A defocus distance of 3 km was used for generalised SCIDAR simulations. Table 9.4 shows the values of the

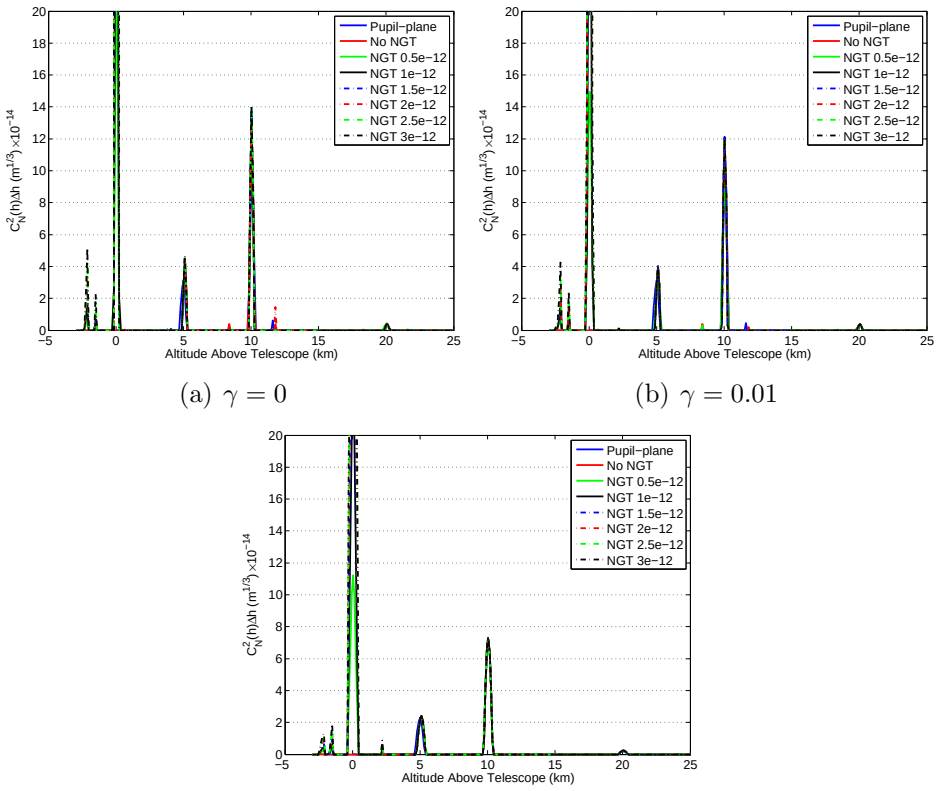

(a) $\gamma = 0$ (b) $\gamma = 0.01$

(c) $\gamma = 0.1$

Figure 9.1: $C_N^2(h)$ profiles obtained from ideal covariances with no noise for increasing strength of NGT. (a) As expected, the calculated $C_N^2(h)$ strength of the 5 and 10 km layers from an ideal profile is constant in peak strength and width. (b) and (c) With increasing regularisation, γ, the peak strength of the 5 and 10 km layers decreases. However the area under the curve remains constant within margin of error.

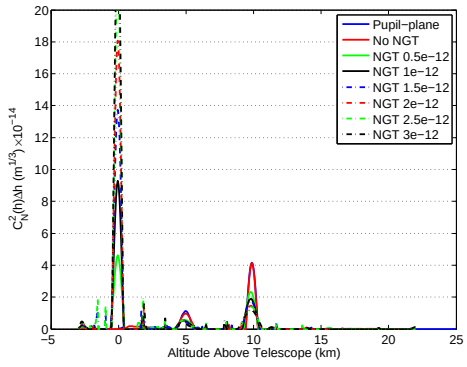

Figure 9.2: $C_N^2(h)$ profiles obtained from simulated scintillation frames with no noise for increasing strength of NGT. As NGT strength increases the detected peak strengths of the 5 and 10 km layers decrease significantly. The area under the curve also decreases resulting in an increase in the estimated r_0 values. 1000 frames were used in the sample, with $\sigma = 0.003$ and $\gamma = 0.1$. All other parameters for the simulation match those used for Figure 9.1.

peak strengths and the corresponding r_0 estimates for the 5 and 10 km layers using a wavelength of 589 nm.

The peak strengths of the higher altitude layers is significantly less than the ideal case for the same regularisation value. For the 10 km layer this did not make a significant impact on the estimate for r_0 for the layer, but for the 5 km layer there is a notable difference between both the ideal and the pupil-plane simulation indicated. Little to no difference can be seen between the pupil-plane and generalised profile with no NGT as expected, as the only difference between the two simulations is the defocus distance associated with the measurement plane being located in a different location. However what is surprising is the significant drop in layer strength with an increase in NGT for both high altitude layers in terms of peak value and area under the curve, and the resulting increase in the r_0 estimate for each layer.

In the estimated r_0 for the 10 km layer the difference seen between the estimate for no NGT strength ($r_0 = 0.18 \pm 0.03$ m) and a NGT strength of $C_N^2(h)\Delta h = 3 \times 10^{-12}$ m$^{1/3}$ ($r_0 = 0.26 \pm 0.05$ m) for $\gamma = 0.1$ is approximately 50%. The estimated r_0 for the 5 km layer also sees the same 50% difference where $r_0 = 0.34 \pm 0.06$ increases to 0.51 ± 0.09 m between no NGT and NGT of 3×10^{-12} m$^{1/3}$.

The issue of weaker upper layer strengths in generalised data compared to that detected in pupil-plane data was particularly noticeable in data taken on 3 May, 2007 (Figure 9.3). Both the pupil-plane and generalised data has been scaled to the same colour scale. If an ideal profile was found then the layer seen at 12 – 15 km above sea level would show similar colour range in both Figures 9.3(a) and 9.3(b). Examination of the near-ground layer detected in the generalised data shows the $C_N^2(h)\Delta h$ NGT strength is approximately 2.4×10^{-12} m$^{1/3}$. Based on the values indicated in Table 9.4, this can lead to a peak strength of the tropopause region that is 33% less for generalised data than that detected for pupil-plane data. If a constant correction factor of 0.33 was applied to the layer detected in the tropopause region (Figure 9.3(c)) then the colour ranges match that detected in the pupil-plane data. It should be noted that this correction has little effect on the estimated r_0 for the profiles, due to the strength of the NGT layer dominating the profiles.

Further investigation is required to ascertain the true effects on the number of scintillation frames used in the estimation on the resulting layer strengths. From a thorough investigation one should be able to devise a relationship between the number of frames used and the strength of the NGT layer to interpolate a correction factor that can be applied to the higher altitude layers. Using a constant correction factor for a given altitude range is not appropriate as the width of the layer is also effected by the increase in NGT.

Table 9.4: Peak strengths and estimated r_0 for mid- to high-altitude layers in a profile with increasing NGT strength calculated from simulated scintillation frames. Table refers to profiles depicted in Figure 9.2 where a regularisation parameter of 0.1 was used. r_0 values are calculated for a wavelength of 589 nm.

NGT Strength $C_N^2(h)\Delta h$ $\times 10^{-12}$ ($m^{1/3}$)	Ideal r_0 (m)	Simulated r_0 (m)	10 km Layer Peak $C_N^2(h)\Delta h$ $\times 10^{-14}$ ($m^{1/3}$)	10 km Layer Area $C_N^2(h)\Delta h$ $\times 10^{-14}$ ($m^{1/3}$)	10 km Layer r_0 (m)	5 km Layer Peak $C_N^2(h)\Delta h$ $\times 10^{-14}$ ($m^{1/3}$)	5 km Layer Area $C_N^2(h)\Delta h$ $\times 10^{-14}$ ($m^{1/3}$)	5 km Layer r_0 (m)
Ideal pupil-plane	0.165 ± 0.003	—	7.19	30.34	0.200 ± 0.003	2.31	10.3	0.38 ± 0.01
pupil-plane	0.165 ± 0.003	0.14 ± 0.02	4.17	37.94	0.18 ± 0.03	1.13	1.26	0.34 ± 0.06
0	0.166 ± 0.003	0.14 ± 0.02	4.14	35.34	0.18 ± 0.03	0.97	1.26	0.34 ± 0.06
0.5	0.102 ± 0.002	0.11 ± 0.01	2.34	24.79	0.23 ± 0.03	0.57	0.87	0.42 ± 0.05
1	0.078 ± 0.001	0.09 ± 0.01	1.89	23.24	0.23 ± 0.03	0.54	0.79	0.45 ± 0.06
1.5	0.065 ± 0.001	0.07 ± 0.01	1.75	22.15	0.24 ± 0.04	0.54	0.74	0.47 ± 0.07
2	0.057 ± 0.001	0.07 ± 0.01	1.45	21.31	0.25 ± 0.04	0.5	0.72	0.47 ± 0.07
2.5	0.050 ± 0.001	0.06 ± 0.01	1.37	20.37	0.25 ± 0.04	0.54	0.67	0.49 ± 0.08
3	0.046 ± 0.001	0.06 ± 0.01	1.19	19.59	0.26 ± 0.05	0.53	0.65	0.51 ± 0.09

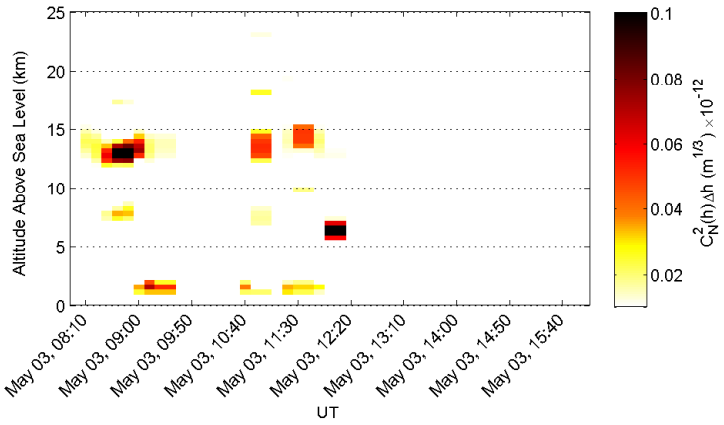

(a) Pupil-plane

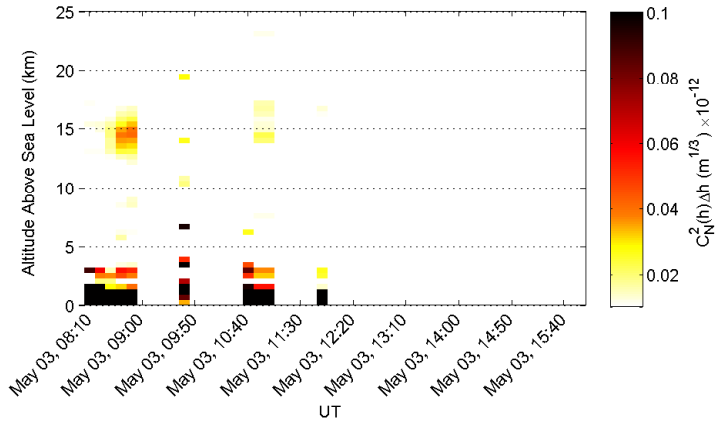

(b) Generalised

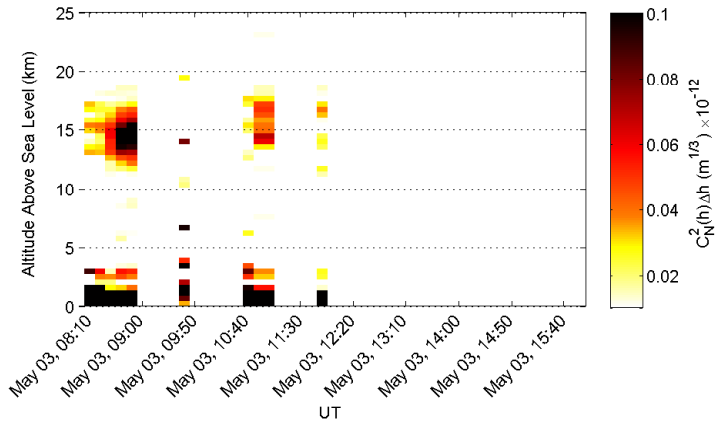

(c) Corrected Generalised

Figure 9.3: $C_N^2(h)$ profiles collected on 3 May, 2007. Ideally the colour range used for the layer detected at 12 – 15 km above sea level should be the same for the (a) pupil-plane and (b) generalised measurements as the colour scale on the plots is identical. (c) Applying a constant correction factor of 0.33 to the data detected in the tropopause region brings the peak strength of the layer up to similar strengths detected in the pupil-plane data.

Appendix A

Sign Conventions Used for Optics

To aid in the understanding of optical diagrams and formulas throughout this thesis, a standard sign convention is utilised. The sign conventions used are the same as those defined in *Greivenkamp* (2004) and are show graphically in Figure A.1.

- The *optical axis* is in the z-axis.
- All distances are measured relative to a reference point, line or plane. Within a Cartesian coordinate system distances above or to the right are positive; distances below or to the left are negative.
- All angles are measured relative to a reference line or plane: counter-clockwise angles are positive; clockwise angles are negative.
- Light travels from left to right (from $-z$ to z) in a medium with a positive refractive index.

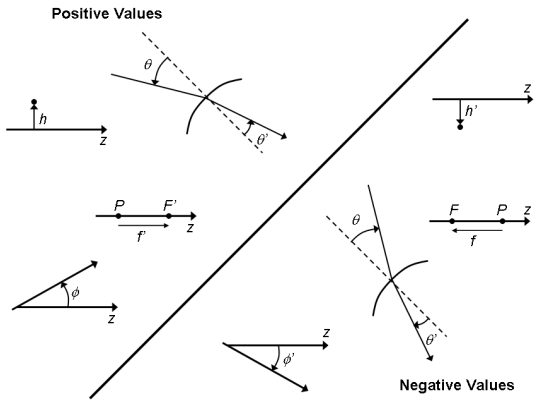

Figure A.1: Sign conventions for optical diagrams used in this thesis. Based on sign conventions in *Greivenkamp* (2004).

Appendix B

Determination of the Defocus Distance from Data

For the design of a SCIDAR system the lenses used are selected to provide adequate spatial sampling across the aperture of the telescope and appropriate generalised plane measurements for an ideal case. Figure B.1 shows the lens configurations for both pupil-plane and generalised SCIDAR.

B.1 Ideal Defocus

For pupil-plane SCIDAR (Figure B.1(a)), the telescope aperture is imaged onto a CCD by a field lens L_p. The focal length of L_p is chosen to give the correct sampling across the telescope aperture. Using the thin lens formula, the focal length of L_p, f_p, is given by

$$\frac{1}{f_\mathrm{p}} = \frac{1}{i_\mathrm{p}} - \frac{1}{p_\mathrm{p}}, \tag{B-1}$$

where i_p is the distance from L_p to the CCD and p_p is the distance between L_p and the telescope primary mirror, L_T, assuming that the aperture plane coincides with the primary mirror. Based on the sign conventions defined in Appendix A (page 227), p_p is negative measured from L_p. The magnification of L_p, m_p, is given by

$$m_\mathrm{p} = \frac{i_\mathrm{p}}{p_\mathrm{p}} = -\frac{h_\mathrm{p}}{h_\mathrm{T}}, \tag{B-2}$$

where h_p is the size of the aperture image at the CCD and h_T is the size of the aperture.

Similar equations can be found for the generalised SCIDAR lens configuration (Figure B.1(b)) such that

$$\frac{1}{f_\mathrm{g}} = \frac{1}{i_\mathrm{g}} - \frac{1}{p_\mathrm{g}}, \tag{B-3}$$

where f_g is the focal length of L_g, i_g is the distance from L_g to the CCD and p_g is the

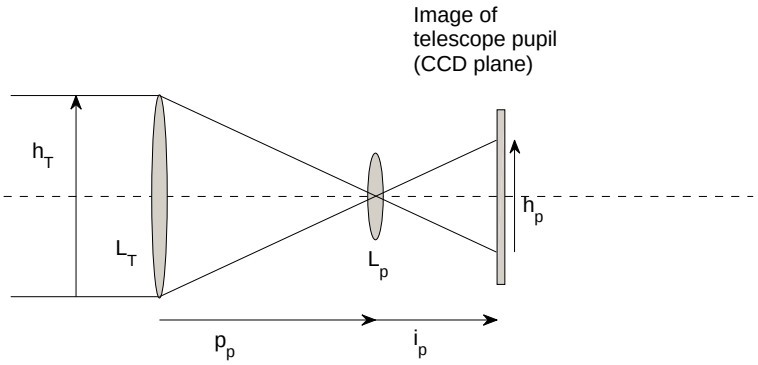

(a) Pupil-plane Lens Placement

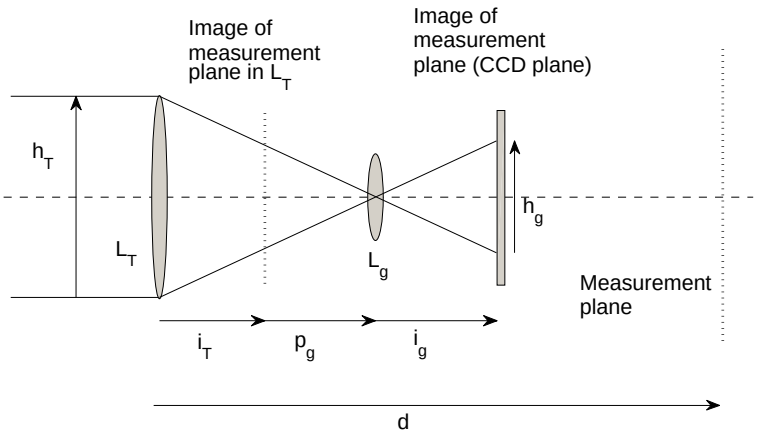

(b) Generalised Lens Placement

Figure B.1: Optical layout for pupil-plane and generalised SCIDAR. In pupil-plane SCIDAR, the telescope mirror, $L_{\rm T}$, is imaged by the field lens, $L_{\rm p}$, onto the CCD plane. For generalised SCIDAR, $L_{\rm p}$ is replace by $L_{\rm g}$. In this case $L_{\rm T}$ acts like another lens. The combination of $L_{\rm T}$ and $L_{\rm g}$ image a measurement plane located at d below the telescope onto the CCD plane. (Image is based on Fig. 2 in *Klückers et al.* (1998).)

distance between L_g to the image of L_T, and

$$\frac{1}{f_T} = \frac{1}{i_T} - \frac{1}{d}, \tag{B-4}$$

where f_T is the focal length of L_T, i_T is the distance from L_T to the image and d is the distance to the measurement plane (defocus distance).

If p_p is sufficiently large then the lens L_p is placed at approximately f_T away from L_T, hence

$$f_T \approx -p_p = i_T - p_g, \tag{B-5}$$

where p_p and p_g are negative measured from L_p and L_g respectively.

From equations (B-4) and (B-5),

$$d = -\left(\frac{f_T^2 + f_T p_g}{p_g}\right). \tag{B-6}$$

Using equation (B-3),

$$d \approx \frac{-f_T^2\,(f_g - i_g) - f_T f_g i_g}{f_g i_g}. \tag{B-7}$$

If L_p and L_g are placed such that $i_p \approx i_g$ and p_p is sufficiently large such that

$$i_p \approx f_p. \tag{B-8}$$

then equation B-7 becomes

$$d \approx \frac{-f_T^2\,(f_g - f_p) - f_T f_g f_p}{f_g f_p}. \tag{B-9}$$

SCIDAR measurements at MJUO taken with the 1-m McLellan telescope operating at a $F/13.5$ focal ratio. A pupil-plane SCIDAR lens of focal length 12.7 mm and a generalised SCIDAR lens of focal length 10 mm results in a defocus distance, d, of 3.89 km below the telescope.

B.2 Defocus from Pupil-plane Image Size

The above calculations assumes thin lenses. In practice the lenses used in the UC-SCIDAR system are achromat doublets, which are *fat* lenses. As such the precise location of each field lens with respect to the image plane differs slightly. In addition, there exists a depth of focus that will produce an acceptable pupil-plane SCIDAR image. Hence the telescope pupil will not coincide with the primary mirror (or aperture), but rather be located

somewhere between the primary and secondary mirrors. The exact distance between the pupil-plane field lens and the image plane cannot be measured and the precise location of the telescope pupil cannot be determined.

Through practical experimentation, it was found that the distance between the pupil-plane field lens and the primary mirror, p_{p}, that results in an acceptable pupil-plane SCIDAR image was $f_{\mathrm{T}} \pm 2f_{\mathrm{p}}$. For any given SCIDAR measurement, it is impossible to know the exactly distance of p_{p}. However the size of the SCIDAR image varies as the telescope is moved through this range. One can interpolate the necessary measurements for defocus calculations based on the size of the image collected.

To simplify calculations it is assumed that the distance between the aperture plane and the primary mirror L_{T}, is small compared to f_{T}.

Using the measured image magnification assuming that the size of the aperture is the size of the primary mirror diameter, then, from equations (B-1) and (B-2), the position of L_{p} with respect to the CCD is

$$i_{\mathrm{p}} = (1 - m_{\mathrm{p}}) f_{\mathrm{p}}. \tag{B-10}$$

If the size of generalised SCIDAR image at the CCD, $h_{\mathrm{g}} \approx h_{\mathrm{p}}$, then equation (B-7) becomes

$$d \approx \frac{-f_{\mathrm{T}}^2 \left(f_{\mathrm{g}} - (1 - m_{\mathrm{p}}) f_{\mathrm{p}}\right) - (1 - m_{\mathrm{p}}) f_{\mathrm{T}} f_{\mathrm{g}} f_{\mathrm{p}}}{(1 - m_{\mathrm{p}}) f_{\mathrm{g}} f_{\mathrm{p}}}. \tag{B-11}$$

For the same system described above, producing a pupil-plane and generalised SCIDAR image of 127 pixels in diameter on a CCD with 7.4 μm square pixels, d would be 3.87 km below the telescope.

B.3 Defocus from Generalised Image Size

During the alignment of the capture system, the telescope focal position is moved in the attempt to make the generalised images the same size as the pupil-plane images. Due to the blurred nature of the generalised image edges, this is difficult to achieve. More often then not, the generalised image captured is larger than the pupil-plane image. This was due to the slight variations in the lens placements for the pupil-plane and generalised measurements.

If the magnification resulting from $L_{\mathrm{g}}$was given by

$$m_{\mathrm{g}} = -\frac{h_{\mathrm{g}}}{h_{\mathrm{T}}}, \tag{B-12}$$

where h_{g} is the size of the generalised SCIDAR image at the CCD, then

$$(i_{\mathrm{p}})_{\mathrm{eff}} = -m_{\mathrm{g}} f_{\mathrm{T}}, \tag{B-13}$$

where $(i_{\mathrm{p}})_{\mathrm{eff}}$ is the effective pupil-plane lens placement of L_{p} that will result in an image of size h_{g}. Note that due to the concept of depth of focus are there two possible values for $(i_{\mathrm{p}})_{\mathrm{eff}}$, located Δi on either side of i_{p}, such that

$$(i_{\mathrm{p}})_{\mathrm{eff}} = i_{\mathrm{p}} \pm \Delta i. \tag{B-14}$$

Assuming the L_{p} and L_{g} lenses are placed such that $i_{\mathrm{g}} = i_{\mathrm{p}} + \Delta i = i_{\mathrm{p}} + |i_{\mathrm{p}} - (i_{\mathrm{p}})_{\mathrm{eff}}|$ then

$$i_{\mathrm{g}} = f_{\mathrm{T}} \left(-m_{\mathrm{p}} + |m_{\mathrm{g}} - m_{\mathrm{p}}|\right). \tag{B-15}$$

generalised SCIDAR measurements with UC-SCIDAR typically resulted in $h_{\mathrm{g}} > h_{\mathrm{p}}$, hence

$$i_{\mathrm{g}} = f_{\mathrm{T}} \left(m_{\mathrm{g}} - 2m_{\mathrm{p}}\right). \tag{B-16}$$

and equation (B-7) becomes

$$d \approx \frac{-f_{\mathrm{T}}^2 \left(f_{\mathrm{g}} - f_{\mathrm{T}} \left(m_{\mathrm{g}} - 2m_{\mathrm{p}}\right)\right) - f_{\mathrm{T}} f_{\mathrm{g}} f_{\mathrm{T}} \left(m_{\mathrm{g}} - 2m_{\mathrm{p}}\right)}{f_{\mathrm{g}} f_{\mathrm{T}} \left(m_{\mathrm{g}} - 2m_{\mathrm{p}}\right)}. \tag{B-17}$$

To correct for large zenith angles, ζ, d can be multiplied by $\cos\zeta$.

Appendix C

Mounting Plate Drawings for UC-SCIDAR

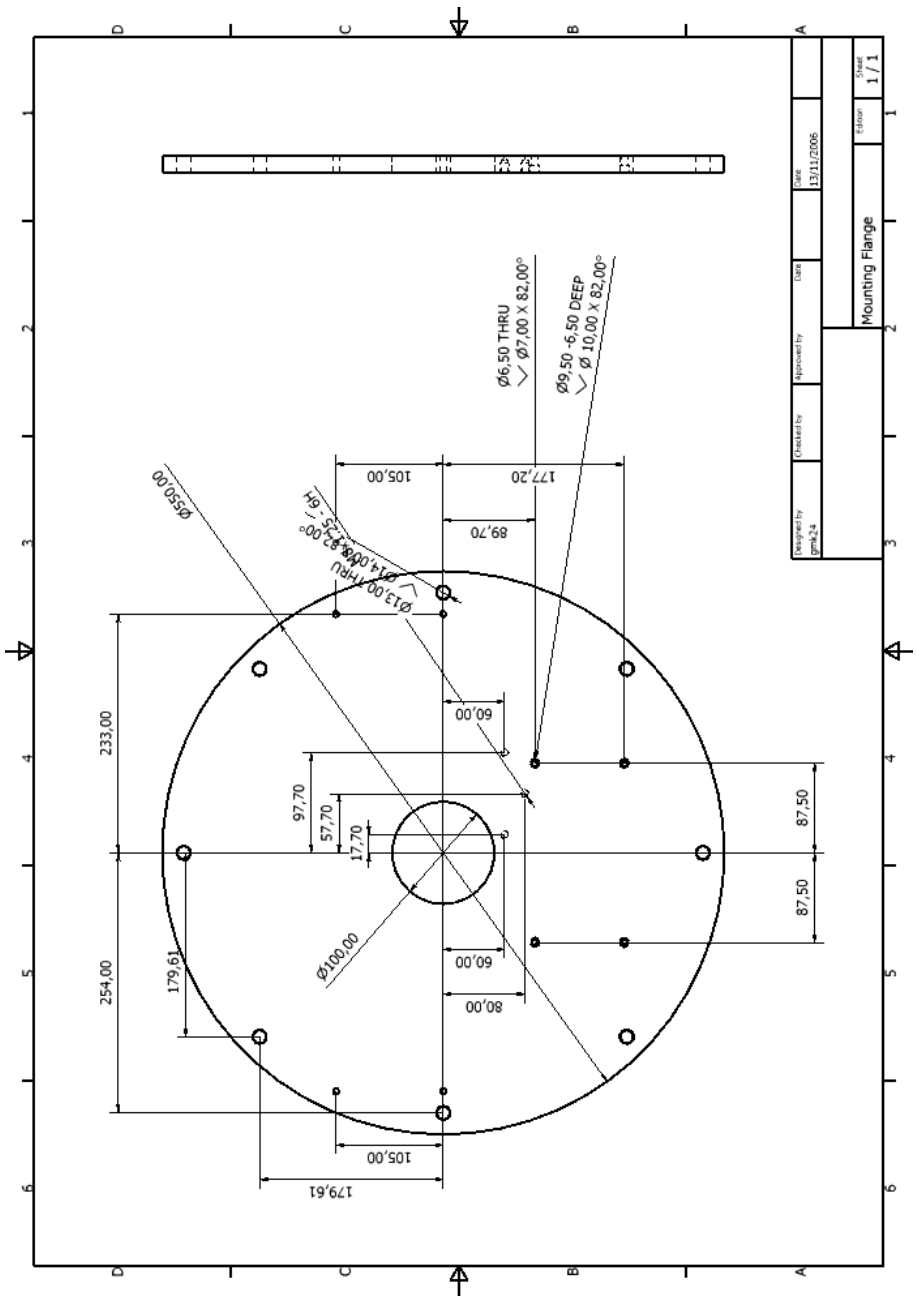

Appendix D

Noise Removal

Analysis of SCIDAR data requires averaged covariance functions. However data frames contain scintillation information as well as measurement noise. Although the averaging process reduces the random effects of measurement noise it is desirable to perform additional noise removal prior to analysis. This is done by one of two different regimes: the removal of noise covariance from data covariances, or the removal of the mean noise from individual data frames.

Removal of Noise Covariance: Let $m(\rho, \phi, t)$ denote the observed data taken at time t at coordinates $\rho = (x, y)$ using a binary star system with separation ϕ. Hence

$$m(\rho, \phi, t) = (s(\rho, \phi, t) + \bar{s}(\rho, \phi, t)) + (n(\rho, \phi, t) + \bar{n}(\rho, \phi, t)), \tag{D-1}$$

where $s(\rho, \phi, t)$ denotes the zero-mean scintillation data, $\bar{s}(\rho, \phi, t)$ is the mean scintillation data and $(n(\rho, \phi, t) + \bar{n}(\rho, \phi, t))$ denotes the noise present. The SCIDAR spatio-temporal covariance used in analysis can be found using

$$\begin{aligned} C_B^{\otimes}(\rho, \phi, \Delta t) &= [(s(\rho, \phi, t) + \bar{s}(\rho, \phi, t)) - \bar{s}(\rho, \phi, t)] \\ &\quad \otimes [(s(\rho, \phi, t + \Delta t) + \bar{s}(\rho, \phi, t + \Delta t)) - \bar{s}(\rho, \phi, t + \Delta t)] \\ &= s(\rho, \phi, t) \otimes s(\rho, \phi, t + \Delta t) \end{aligned} \tag{D-2}$$

where Δt is the time difference between successive frames and the $\otimes$ operator denotes convolution. Let the correlation of the measured data be defined as

$$\begin{aligned} C_m^{\otimes}(\rho, \phi, \Delta t) &= m(\rho, \phi, t) \otimes m(\rho, \phi, t + \Delta t) \\ &= (s(\rho, \phi, t) \otimes s(\rho, \phi, t + \Delta t)) + (\bar{s}(\rho, \phi, t) \otimes \bar{s}(\rho, \phi, t + \Delta t)) \\ &\quad + (n(\rho, \phi, t) \otimes n(\rho, \phi, t + \Delta t)) + (\bar{n}(\rho, \phi, t) \otimes \bar{n}(\rho, \phi, t + \Delta t)) \\ &\quad + (\bar{s}(\rho, \phi, t) \otimes \bar{n}(\rho, \phi, t + \Delta t)) + (\bar{n}(\rho, \phi, t) \otimes \bar{s}(\rho, \phi, t + \Delta t)), \end{aligned} \tag{D-3}$$

and the correlation of the mean data, $\bar{m} = \bar{s} + \bar{n}$, be

$$\begin{aligned} C^{\otimes}_{\bar{m}}(\rho,\phi,\Delta t) &= \bar{m}(\rho,\phi,t) \otimes \bar{m}(\rho,\phi,t+\Delta t) \\ &= (\bar{s}(\rho,\phi,t) \otimes \bar{s}(\rho,\phi,t+\Delta t)) + (\bar{n}(\rho,\phi,t) \otimes \bar{n}(\rho,\phi,t+\Delta t)) \\ &\quad +(\bar{s}(\rho,\phi,t) \otimes \bar{n}(\rho,\phi,t+\Delta t)) + (\bar{n}(\rho,\phi,t) \otimes \bar{s}(\rho,\phi,t+\Delta t)), \end{aligned} \tag{D-4}$$

Let the correlation of the noise be defined as

$$\begin{aligned} C^{\otimes}_{n}(\rho,\phi,\Delta t) &= (n(\rho,\phi,t) + \bar{n}(\rho,\phi,t)) \otimes (n(\rho,\phi,t+\Delta t) + \bar{n}(\rho,\phi,t+\Delta t)) \\ &= (n(\rho,\phi,t) \otimes n(\rho,\phi,t+\Delta t)) + (\bar{n}(\rho,\phi,t) \otimes \bar{n}(\rho,\phi,t+\Delta t)), \end{aligned} \tag{D-5}$$

$$C^{\otimes}_{\bar{n}}(\rho,\phi,\Delta t) = \bar{n}(\rho,\phi,t) \otimes \bar{n}(\rho,\phi,t+\Delta t). \tag{D-6}$$

Thus,

$$C^{\otimes}_{B}(\rho,\phi,\Delta t) = C^{\otimes}_{m}(\rho,\phi,\Delta t) - C^{\otimes}_{\bar{m}}(\rho,\phi,\Delta t) - C^{\otimes}_{n}(\rho,\phi,\Delta t) + C^{\otimes}_{\bar{n}}(\rho,\phi,\Delta t). \tag{D-7}$$

Removal of Mean Noise: The removal of mean noise is much more straight forward. The mean noise frame, calculated from dark frame noise, is subtracted from $m(\rho,\phi,t)$ prior to the calculation of the frame correlation, such that

$$\begin{aligned} C^{\otimes}_{(m-\bar{n})}(\rho,\phi,\Delta t) &= (s(\rho,\phi,t) \otimes s(\rho,\phi,t+\Delta t)) + (\bar{s}(\rho,\phi,t) \otimes \bar{s}(\rho,\phi,t+\Delta t)) \\ &\quad +(n(\rho,\phi,t) \otimes n(\rho,\phi,t+\Delta t)). \end{aligned} \tag{D-8}$$

If one assumes that the noise is not correlated then

$$(n(\rho,\phi,t) \otimes n(\rho,\phi,t+\Delta t)) = 0. \tag{D-9}$$

In addition, as the average measurement contains only mean scintillation then

$$C^{\otimes}_{\bar{m}}(\rho,\phi,\Delta t) = (\bar{s}(\rho,\phi,t) \otimes \bar{s}(\rho,\phi,t+\Delta t)). \tag{D-10}$$

Hence for the removal of mean noise the SCIDAR spatio-temporal covariance is found by

$$C^{\otimes}_{B}(\rho,\phi,\Delta t) = C^{\otimes}_{(m-\bar{n})}(\rho,\phi,\Delta t) - C^{\otimes}_{\bar{m}}(\rho,\phi,\Delta t). \tag{D-11}$$

Figure D.1 indicates the algorithm steps used to calculate noise removed covariance data using both methods.

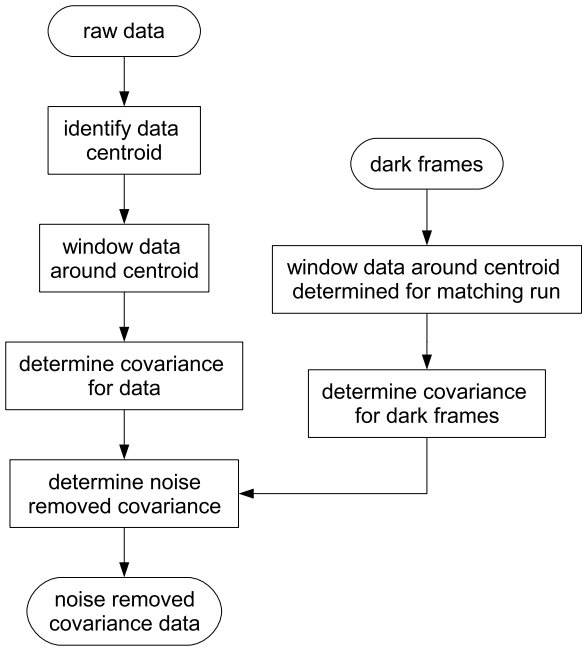

(a) Removal of noise covariance

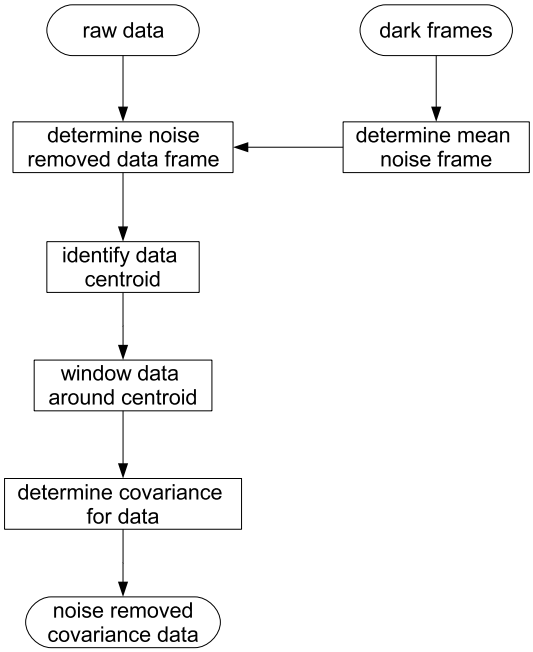

(b) Removal of mean noise

Figure D.1: The main steps taken to determine noise removed covariance data. Two different regimes are used: (a) the removal of noise covariance from data covariances, and (b) the removal of mean noise from individual data frames.

Figure D.2 shows the effect of noise removal using the two different regimes presented. When no noise removal is employed, shown in Figures D.2(a) and D.2(b), the 2D covariance and extracted 1D slice contain background noise which impacts on the data. When removing noise by way of subtracting the noise covariance, shown in Figures D.2(c) and D.2(d), the background noise is minimised. However removing noise by way of subtracting the average noise, shown in Figures D.2(e) and D.2(f), the strengths of the covariance peaks are affected and background noise is not removed properly. This suggests that the assumption that noise is not correlated is incorrect for this data and hence noise removal by way of subtracting noise covariance should be employed.

The majority of data collected during the course of this research was analysed using subtracted noise covariances. However some data collected during January 2007 used noise removal by way of subtracting average noise due to the noise characteristics of the CCD employed at the time. This was discussed in section 3.4.1 (page 46).

D.1 Aperture Normalisation

All data measured is subject to an aperture. As a result $C_B^{\otimes}(\rho, \phi, \Delta t)$ should be normalised for aperture effects to remove any bias toward the aperture. This can by done by dividing $C_B^{\otimes}(\rho, \phi, \Delta t)$ by the correlation of the mean signal, $\bar{s} = \bar{m} - \bar{n}$, such that

$$C_B(\rho, \phi, \Delta t) = \frac{C_B^{\otimes}(\rho, \phi, \Delta t)}{C_{(\bar{m}-\bar{n})}^{\otimes}(\rho, \phi, \Delta t)}, \tag{D-12}$$

where

$$C_{(\bar{m}-\bar{n})}^{\otimes}(\rho, \phi, \Delta t) = (\bar{m}(\rho, \phi, t) - \bar{n}(\rho, \phi, t)) \otimes (\bar{m}(\rho, \phi, t + \Delta t) - \bar{n}(\rho, \phi, t + \Delta t)). \tag{D-13}$$

If sufficient number of samples are taken then $C_{(\bar{m}-\bar{n})}^{\otimes}(\rho, \phi, \Delta t)$ approaches $C_{(\bar{m}-\bar{n})}^{\otimes}(\rho, \phi, 0)$ as $\bar{s}(\rho, \phi, t) \approx \bar{s}(\rho, \phi, t + \Delta t)$.

The specifics of aperture normalisation as it applies to $C_N^2(h)$ and $V(h)$ determination are discussed further in Chapters 4 and 5 respectively.

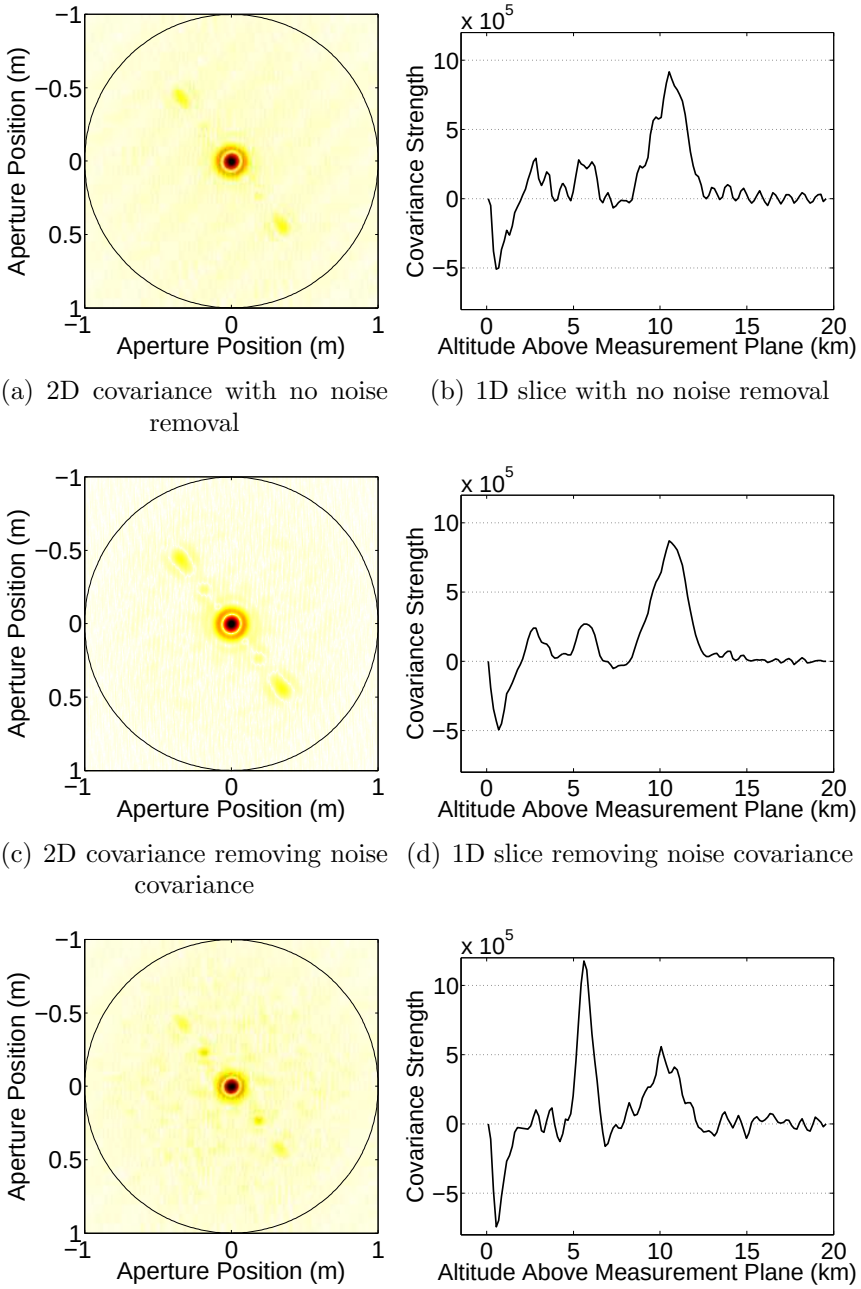

(a) 2D covariance with no noise removal

(b) 1D slice with no noise removal

(c) 2D covariance removing noise covariance

(d) 1D slice removing noise covariance

(e) 2D covariance removing average noise

(f) 1D slice removing average noise

Figure D.2: Effect of noise removal on covariance data using different regimes. ((a) and (b)) If no noise is removed the extracted data contains noisy spikes. ((c) and (d)) The removal of noise covariance reduces the spikes and background noise detected. ((e) and (f)) Noise removal using average noise does not properly remove background noise and affects the strength of the covariance peaks detected considerably. This suggests that the assumption that noise is not correlated is incorrect for this data.

Appendix E

$C_N^2(h)$ Analysis for Individual Runs

This appendix is an electronic appendix where the $C_N^2(h)$ analysis for individual runs are found within files separated into individual observational months. Each observational month file contains all the runs associated with that month. A sample page has been included here.

List of Files:

Filename	Observational Month
`200407.pdf`	July 2004
`200502.pdf`	February 2005
`200503.pdf`	March 2005
`200504.pdf`	April 2005
`200505.pdf`	May 2005
`200506.pdf`	June 2005
`200507.pdf`	July 2005
`200508.pdf`	August 2005
`200509.pdf`	September 2005
`200604.pdf`	April 2006
`200608.pdf`	August 2006
`200701.pdf`	January 2007
`200705.pdf`	May 2007
`200706.pdf`	June 2007

All files are located in the root directory of the attached CD.

jun05:run30

Run ID	run30
Time (UT)	13-Jun-2005 10:59:00
No. Frames	Captured:4750 (19 blocks); Used:2500 (10 blocks)
Rig	V2005: C0:f12.7mm Micropix M640 Straight, C1:f10mm Thorlabs DC111 Side
Filtering	Pre-filtering
Exposure/Gain	1 ms / max gain
Star	α Cen: ϕ:10.2 arcseconds, m_1:-0.01, Δm:1.36, Epoch:2005.5
Stellar Coords	Dec: -60:51:20; HA: 01:08:00
Zenith Angle	19.73° (Air Mass: 1.06)
Air Temp	3.2°C
Comments	computer froze on block 20

Camera ID: C0

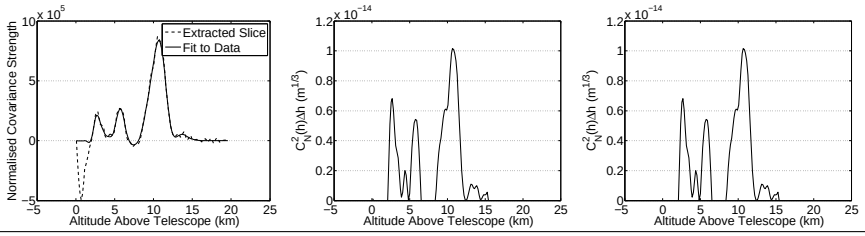

SNR	26.7	Altitude Limits (km)	0 - 20	2 - 20
% Satuation	0.0	$\int C_N^2(h)dh$ ($m^{1/3}$)	0.239×10^{-12}	0.000×10^{-12}
mean max pixel	224.51	ε_C (%)	36.2	36.2
Process Inputs	[9 66 25 2]	r_0 (m)	0.223	0.223
γ	0.15	ε_{r_0} (m)	0.048	0.048
defocus (km)	-0.00	θ_0 (arcseconds)	1.653	1.653
dr (m.pix^{-1})	1/124	ε_{θ_0} (arcseconds)	0.368	0.368
dh (m.pix^{-1})	154			
$h_{\max}$ (km)	19.6			

Camera ID: C1

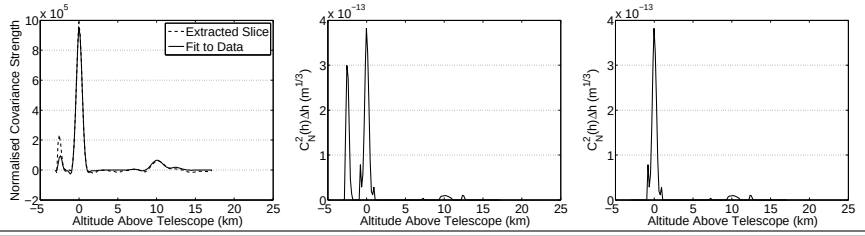

SNR	27.3	Altitude Limits (km)	-3 - 17	-1 - 17
% Satuation	1.0	$\int C_N^2(h)dh$ ($m^{1/3}$)	2.740×10^{-12}	0.000×10^{-12}
mean max pixel	255.00	ε_C (%)	22.8	22.8
Process Inputs	[8 21 20 -1]	r_0 (m)	0.052	0.066
γ	0.05	ε_{r_0} (m)	0.007	0.009
defocus (km)	-3.10	θ_0 (arcseconds)	1.021	1.036
dr (m.pix^{-1})	1/120	ε_{θ_0} (arcseconds)	0.154	0.155
dh (m.pix^{-1})	159			
$h_{\max}$ (km)	17.1			

Appendix F

Simulation of Scintillation Covariance

Simulations used in this thesis used one of two different methods depending on what was being examined at the time. Ideal covariances are easily generated by determining the spatio-temporal covariance of a single star and creating the triplet pattern seen for a binary star accordingly. (The spatio-temporal covariance function for a binary star is discussed in detail in Chapter 2, section 2.4, page 26.) However in most cases it was necessary to start with scintillation images. The technique employed for the simulation of scintillation images assumed Kolmogorov turbulence and is discussed in detail in *Johnston and Lane* (2000) and *Johnston* (2000), including full mathematical treatment. The key aspects to understanding the extension to the simulations employed in this thesis for the simulation of SCIDAR images and the resulting spatio-temporal covariances as discussed.

In SCIDAR, the spatio-temporal covariance function resulting from the scintillation frames for multiple layers can be approximated by the summation of the covariances due to the individual layers. As such, during simulation each layer is treated separately. The following discussion is for the single layer case.

F.1 Scintillation Frames from Binary Star Systems

Simulations of atmospheric turbulence is achieved by generating a series of phase screens, where each phase screen is a snap-shot of the phase distortions induced by a given layer structure. Scintillation frames are estimated by propagating the phase distortions induced by the phase screens over the distance z which describes the height of a given layer above the measurement plane. The algorithm for generating a scintillation frame resulting from a single star is outlined in *Johnston and Lane* (2000).

The accuracy of the simulated single star scintillation frame is determined by a user-defined parameter σ which defines the width of a Gaussian that is used during simulation to ensure computable solutions. The Gaussian is convolved with the computed incident wavefront during propagation calculations. This allows assumptions regarding stationary phase to be applied to the solution (*Johnston and Lane*, 2000). As the convolution during

simulation introduces an error, it is desirable to use $\sigma \to 0$. A small σ will mean that the simulation is more accurate but requires more computation time. For simulations used throughout this thesis, $\sigma = 0.003$.

Simulation of binary star system SCIDAR scintillation covariances is an extension of the simulation of single star scintillation frames. A scintillation matrix for a single star is calculated for a given layer strength $C_N^2(h)\Delta h$ located at $z = |h - d|$ above the measurement plane, where h is the height of the layer above the telescope and d is the negative distance to the measurement plane below the aperture. This frame is then scaled by

$$\alpha = 10^{-0.4\Delta m}, \tag{F-1}$$

where Δm is the magnitude difference between the binary star system components, and is shifted by

$$s_{|h-d|} = |h - d| \sec(\zeta)\phi, \tag{F-2}$$

where ϕ is the angular separation of the binary star system and ζ is the zenith angle. An aperture is applied to the shifted and scaled scintillation matrix along with the original scintillation matrix. Both resulting matrices are then overlapped with a separation between aperture centres of

$$s_d = d \sec(\zeta)\phi \tag{F-3}$$

and then used in the determination of the covariance data. Simulations used in this thesis typically assume that ζ is zero.

The main steps of the algorithm used are outlined in Figure F.1.

Figure F.2 shows how the above method for simulated binary star system scintillation covariances compares with the ideal covariance profiles as computed from ideal single star covariances determined using equation 8.13 in *Roddier* (1981). To compare ideal profiles it is necessary to convolve the ideal profile with a Gaussian with width σ, where σ is the same value used in the simulation of scintillation frames.

F.2 Simulations for $\Delta t > 0$

Using the algorithms described in *Johnston and Lane* (2000), each scintillation frame is temporally independent. To simulate temporal motion of a layer it is therefore necessary to use the same scintillation frame. Consider a layer with a given wind velocity, $V(h)$, sampled such that the time delay between successive scintillation frames is Δt. As above, the single star scintillation matrix is scaled and shifted to approximate the binary companion aperture, however the single star scintillation matrix is now generated with an aperture dimension of $3D$ where D is the telescope diameter. This does not change

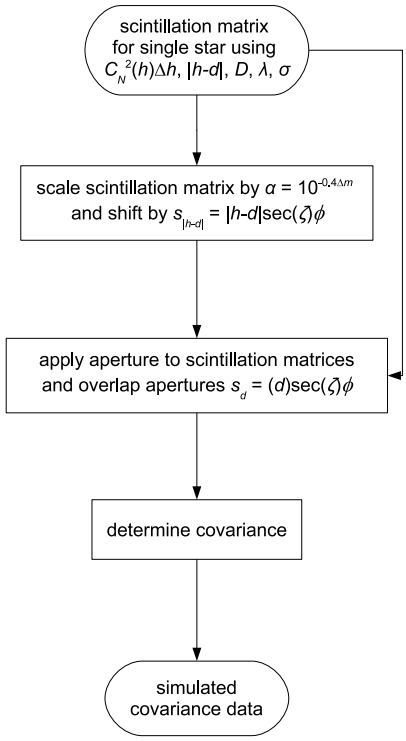

Figure F.1: Flowchart depicting the key steps in simulating binary star SCIDAR scintillation covariance.

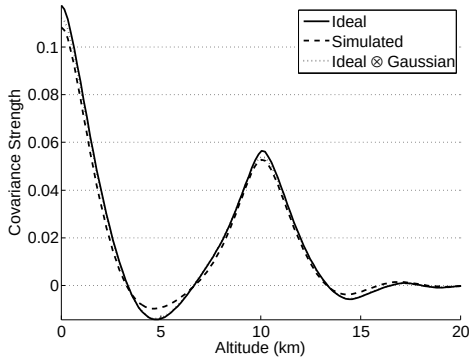

Figure F.2: Extracted slice from simulated covariances using different simulation methods. Common simulation parameters are as follows: $\phi = 4$ arcseconds, $\Delta m = 0.3$, $z = 10$ km, $\lambda = 589$ nm, $r_0(\lambda) = 20.15$ cm, $D = 1$ m.

the spatial sampling that is applied to the simulation, but rather ensures that sufficient number of pixels are available to simulate a maximum detectable velocity. If one assumes that Taylor's hypothesis holds true, then both the original scintillation matrix and the scaled, shifted companion matrix can be shifted by

$$s_v = V(h)\Delta t \tag{F-4}$$

prior to the application of the aperture. This velocity shifted binary star scintillation image is cross-correlated with the binary star scintillation image prior to velocity shift to obtain spatio-temporal covariance data. Figure F.3 outlines the main steps in simulating spatio-temporal covariances and Figure F.4 shows an ideal 2D spatio-temporal covariance, a shifted ideal covariance using equation 8.13 in *Roddier* (1981), and a 2D spatio-temporal covariance calculated from simulated scintillation frames using the above suggested algorithm.

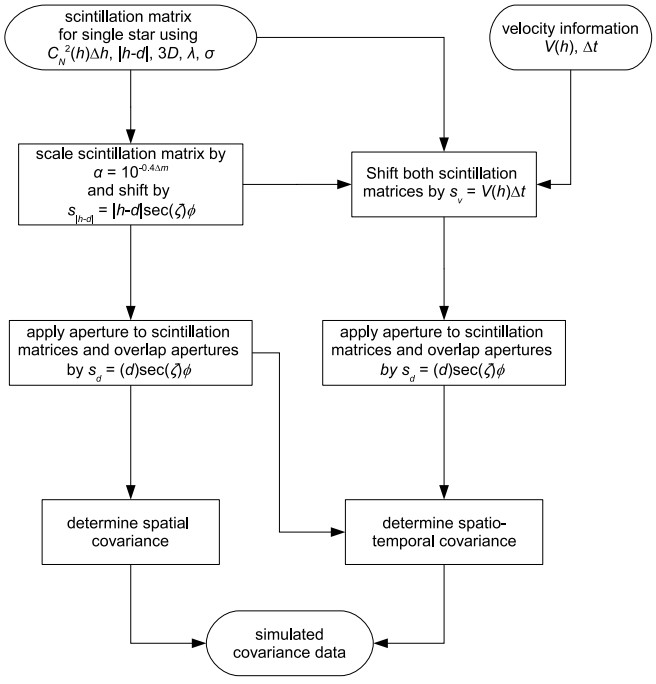

Figure F.3: Flowchart depicting the key steps in simulating temporal movement in SCIDAR scintillation frames.

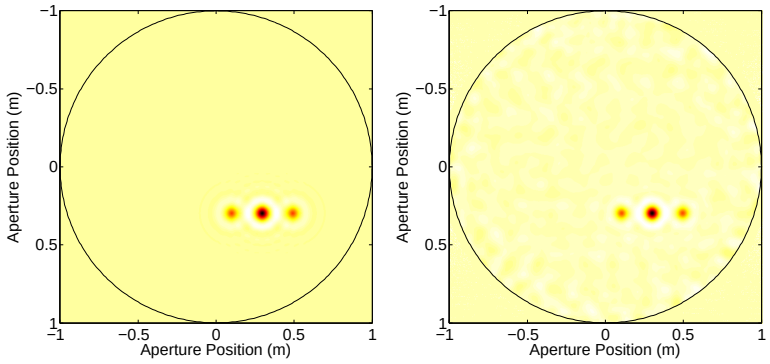

(a) Ideal simulation (b) Simulation scintillation frames

Figure F.4: Simulated 2D covariances using (a) the ideal covariances and (b) simulated scintillation frames.

F.3 Simulating Long Exposure Covariances

Simulating long exposure spatio-temporal covariances requires the use of simulated scintillation frames. However it is not just a simple matter of taking two successive simulated frames and averaging them as each simulated scintillation frame is temporally independent. Instead is is necessary to apply an incremental shift. Let a simulated scintillation matrix represent an exposure time of 1 ms. If p_v is the number of pixels that a covariance peak will shift given a velocity shift, s_v, and a spatial sampling, Δr, then the simulated scintillation matrix needs to be shifted and averaged over p_v iterations. This incremental shift simulates the blurring seen with increase exposure time. The main steps of the simulation algorithm used are depicted in Figure F.5.

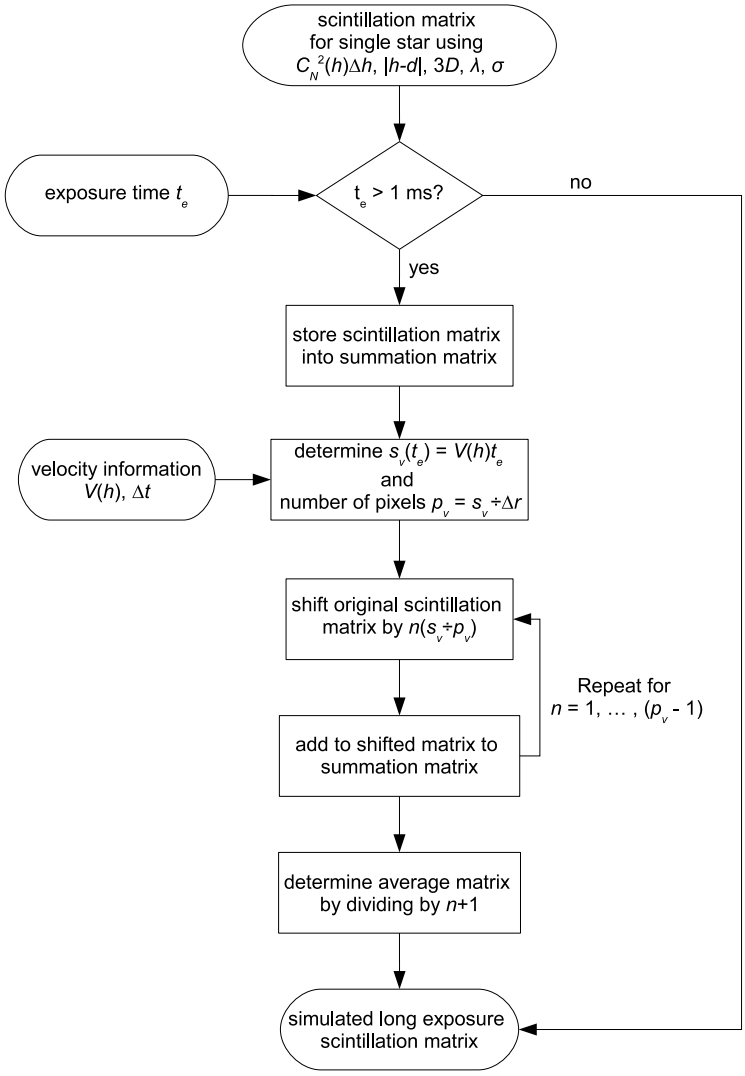

Figure F.5: Flowchart depicting the key steps in generating long exposure scintillation frames for use within SCIDAR simulations.

Appendix G

Finding Error on $V(h)$

The 1-m McLellan and 60-cm Boller & Chivens telescopes at MJUO employ a RA-Dec coordinate system to describe their position. When tracking a star the orientation of the primary mirror changes relative to compass directions. However if a star's instantaneous position is known then corrections can be made. This appendix details the error on $V(h)$ (both magnitude and direction) resulting from the motion of a RA-Dec telescope.

G.1 Rotation of the Primary Mirror on an RA-Dec Telescope

Meaningful wind velocity measurements are expressed relative to the ground. Hence it is necessary to understand how the primary mirror is rotated with respect to the ground as the telescope moves.

Let a cartesian coordinate system be defined such that X is aligned with West, Y with North and Z with the observer's zenith (Figure G.1). The orientation of the right ascension drives is rotated about the X-axis so that right ascension rotational axis is aligned with the celestial polar axis. This rotation is equal to the surface latitude position φ from the equator (Figure G.2). For MJUO, $\varphi = -43°59.2'$.

If $X_{\rm CA}Y_{\rm CA}Z_{\rm CA}$ define the rotated coordinate system such that $Y_{\rm CA}$ is align with the North celestial pole and $Z_{\rm CA}$ is aligned with the celestial equator, then

$$\begin{aligned} x_{\rm CA} &= x; \\ y_{\rm CA} &= y\cos\varphi + z\sin\varphi; \\ z_{\rm CA} &= -y\sin\varphi + z\cos\varphi. \end{aligned} \tag{G-1}$$

Consider rotation in declination only (Figure G.3(a)). The declination, δ, is measured from the celestial equator toward the North celestial pole such that objects at the pole have $\delta = +90°$. To observe a star at a given declination the telescope needs to rotate δ, from the celestial equator. Rotation to $X_{\rm D}Y_{\rm D}Z_{\rm D}$, the new rotated coordinate system,

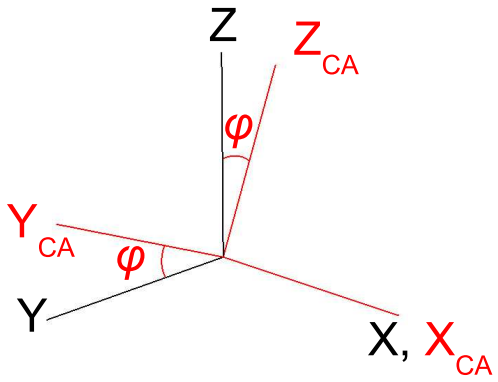

Figure G.1: Rotation of telescope reference frame to the celestial pole. The X-, Y- and Z-axes are aligned with West, North and the observer's zenith respectively. Rotation to the celestial axes is about the X-axis through an angle equal to the surface latitude position, φ, from the equator.

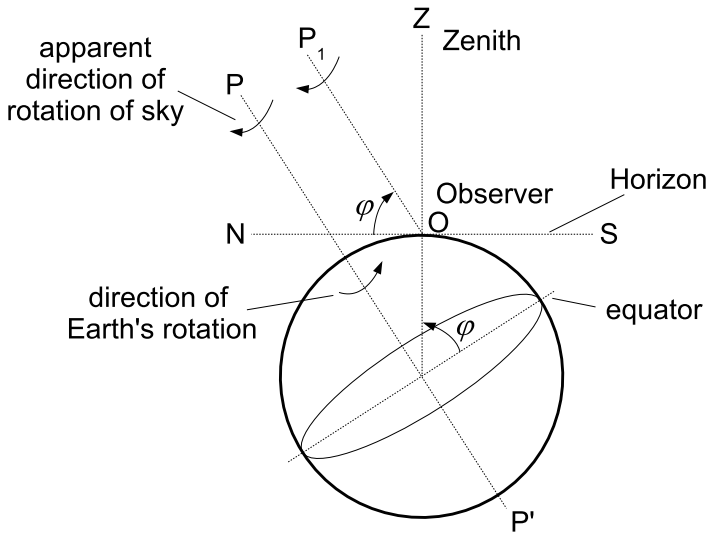

Figure G.2: The celestial polar axis. The axis of rotation for the heavens is aligned with the Earth's rotational axis. The angle that the celestial polar axis forms with the horizon is equal to the latitude, φ, from the equator. (Based on Fig. 7.1 from *Roy and Clarke* (1988).)

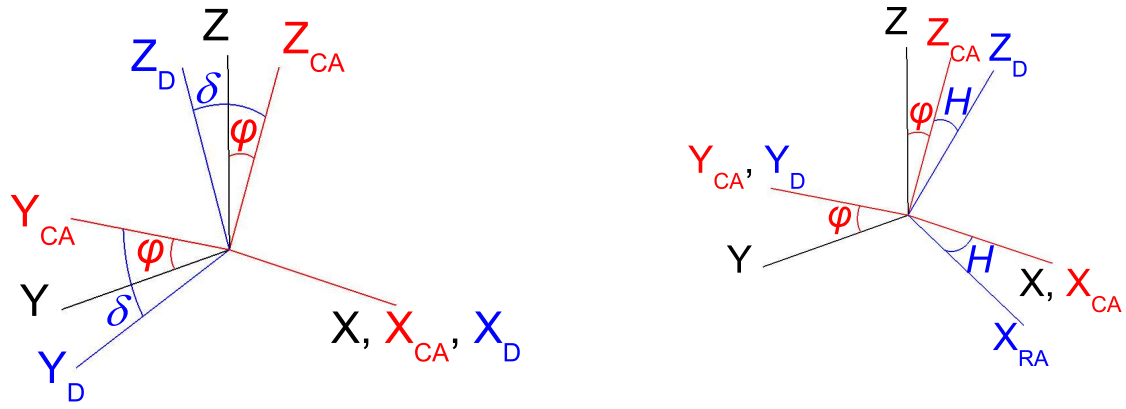

(a) Pure declination rotation

(b) Pure right ascension rotation

Figure G.3: Rotation of telescope reference frame through (a) declination, δ, and (b) right ascension, H.

from $X_{\rm CA}Y_{\rm CA}Z_{\rm CA}$, is through an angle δ about $X_{\rm CA}$ such that

$$\begin{aligned} x_{\rm D} &= x_{\rm CA}; \\ y_{\rm D} &= y_{\rm CA}\cos\delta - z_{\rm CA}\sin\delta; \\ z_{\rm D} &= y_{\rm CA}\sin\delta + z_{\rm CA}\cos\delta. \end{aligned} \tag{G-2}$$

Rotation in right ascension is about the $Y_{\rm CA}$-axis. Pure right ascension rotation through an angle H (Figure G.3(b)) is

$$\begin{aligned} x_{\rm RA} &= x_{\rm CA}\cos H - z_{\rm CA}\sin H; \\ y_{\rm RA} &= y_{\rm CA}; \\ z_{\rm RA} &= x_{\rm CA}\sin H + z_{\rm CA}\cos H, \end{aligned} \tag{G-3}$$

where $X_{\rm RA}Y_{\rm RA}Z_{\rm RA}$ describes the coordinate system after rotation and H is the hour angle measured from the meridian in a westerly direction.

Applying rotations in right ascension then declination result in translations of (written in matrix form)

$$\begin{bmatrix} x_{\rm m} \\ y_{\rm m} \\ z_{\rm m} \end{bmatrix} = \begin{bmatrix} l_{\rm x} & m_{\rm x} & n_{\rm x} \\ l_{\rm y} & m_{\rm y} & n_{\rm y} \\ l_{\rm z} & m_{\rm z} & n_{\rm z} \end{bmatrix} \times \begin{bmatrix} x \\ y \\ z \end{bmatrix}, \tag{G-4}$$

where $X_{\rm m}Y_{\rm m}Z_{\rm m}$ describes the coordinate system on the mirror surface and

$$\begin{aligned} l_{\rm x} &= \cos H, \\ m_{\rm x} &= \sin\varphi \sin H, \\ n_{\rm x} &= -\cos\varphi \sin H; \end{aligned} \tag{G-5}$$

$$\begin{aligned} l_{\rm y} &= -\sin H \sin\delta, \\ m_{\rm y} &= \cos\varphi\cos\delta + \sin\varphi\cos H\sin\delta, \\ n_{\rm y} &= \sin\varphi\cos\delta - \cos\varphi\cos H\sin\delta; \end{aligned} \tag{G-6}$$

$$\begin{aligned} l_{\rm z} &= \sin H\cos\delta, \\ m_{\rm z} &= \cos\varphi\sin\delta - \sin\varphi\cos H\cos\delta, \\ n_{\rm z} &= \sin\varphi\sin\delta + \cos\varphi\cos H\cos\delta. \end{aligned} \tag{G-7}$$

G.2 Error in $V(h)$

Let $\vec{v}$ define a vector in space determined by the direction cosines $(\cos\alpha, \cos\beta, \cos\gamma)$ in XYZ and $(\cos\alpha_{\rm m}, \cos\beta_{\rm m}, \cos\gamma_{\rm m})$ in $X_{\rm m}Y_{\rm m}Z_{\rm m}$ (Figure G.4). Then

$$x = |\vec{v}|\cos\alpha; \quad y = |\vec{v}|\cos\beta; \quad z = |\vec{v}|\cos\gamma, \tag{G-8}$$

$$x_{\rm m} = |\vec{v}|\cos\alpha_{\rm m}; \quad y_{\rm m} = |\vec{v}|\cos\beta_{\rm m}; \quad z_{\rm m} = |\vec{v}|\cos\gamma_{\rm m}. \tag{G-9}$$

If $\vec{v_{\rm m}}$ was the projection of $\vec{v}$ onto the $X_{\rm m}Y_{\rm m}$ plane and formed an angle $b_{\rm m}$ with the $Y_{\rm m}$-axis, then

$$x_{\rm m} = |\vec{v_{\rm m}}|\sin b_{\rm m}; y_{\rm m} = |\vec{v_{\rm m}}|\cos b_{\rm m}. \tag{G-10}$$

The length of $\vec{v_{\rm m}}$ is

$$|\vec{v_{\rm m}}| = |\vec{v}|\sin\gamma_{\rm m}. \tag{G-11}$$

Given the above relations then

$$\begin{aligned} \sin\gamma_{\rm m}\sin b_{\rm m} &= l_{\rm x}\cos\alpha + m_{\rm x}\cos\beta + n_{\rm x}\cos\gamma, \\ \sin\gamma_{\rm m}\cos b_{\rm m} &= l_{\rm y}\cos\alpha + m_{\rm y}\cos\beta + n_{\rm y}\cos\gamma, \\ \cos\gamma_{\rm m} &= l_{\rm z}\cos\alpha + m_{\rm z}\cos\beta + n_{\rm z}\cos\gamma. \end{aligned} \tag{G-12}$$

The motion of all turbulent layers is assumed to be confined to the XY plane and hence has no component in Z (i.e. $\cos\alpha = \sin\beta$ and $\cos\gamma = 0$). The relations in equation

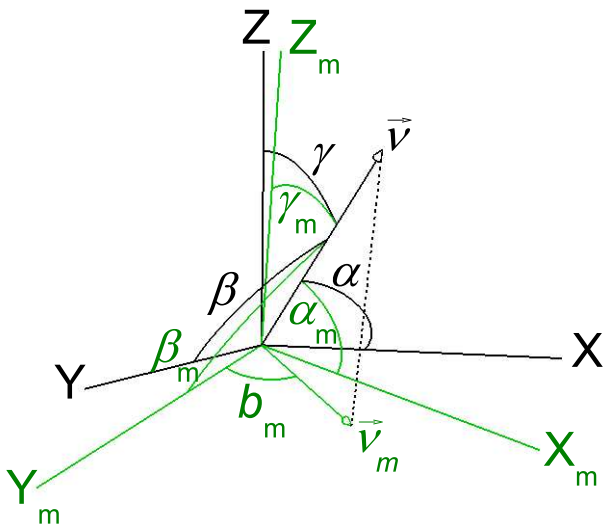

Figure G.4: Rotation of mirror coordinate system $X_\mathrm{m}Y_\mathrm{m}Z_\mathrm{m}$ in 3D space. The vector $\vec{v}$ forms an angle α, β and γ with the X-, Y- and Z-axes respectively. The projection of $\vec{v}$ on the $X_\mathrm{m}Y_\mathrm{m}$ plane, $\vec{v}_\mathrm{m}$, forms an angle b_m with the Y_m-axis.

(G-12) simplify to

$$\begin{aligned} \sin\gamma_\mathrm{m}\sin b_\mathrm{m} &= l_\mathrm{x}\sin\beta + m_\mathrm{x}\cos\beta, \\ \sin\gamma_\mathrm{m}\cos b_\mathrm{m} &= l_\mathrm{y}\sin\beta + m_\mathrm{y}\cos\beta, \\ \cos\gamma_\mathrm{m} &= l_\mathrm{z}\sin\beta + m_\mathrm{z}\cos\beta. \end{aligned} \tag{G-13}$$

Note β is measured in a westerly direction from Y (i.e. negative bearing measurement) and b_m is measured westerly from Y_m.

The error in measurement direction, $\varepsilon_{\angle\mathrm{v}}$, has two components. One is related to the direction found in $X_\mathrm{m}Y_\mathrm{m}$ as measured by the CCD and the other is related to the telescope motion from Z, such that

$$\begin{aligned} \varepsilon_{\angle\mathrm{v}} &= \varepsilon_\beta + \varepsilon_\gamma \\ &= (\beta - b_\mathrm{m}) + (\gamma - \gamma_\mathrm{m})\,. \end{aligned} \tag{G-14}$$

As γ_m cannot be measured empirically from the CCD, focus is given to ε_β. Using the relations in equation (G-13),

$$\varepsilon_\beta = (\beta - b_\mathrm{m})_\mathrm{radians} = \beta - \arctan\left(\frac{l_\mathrm{x}\sin\beta + m_\mathrm{x}\cos\beta}{l_\mathrm{y}\sin\beta + m_\mathrm{y}\cos\beta}\right). \tag{G-15}$$

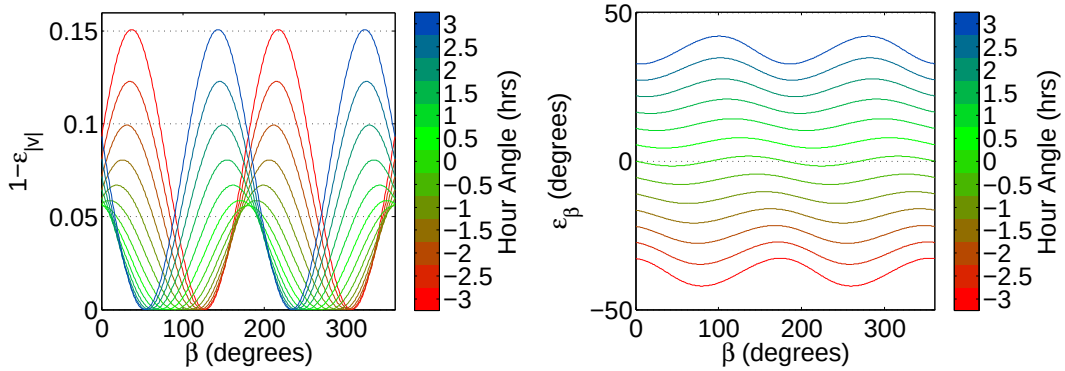

(a) Error in Wind Speed $\varepsilon_{|\vec{v}|}$ (b) Error in Wind Direction ε_{β}

Figure G.5: The effect of actual wind direction, β, on the (a) error in wind speed and (b) wind direction. Values shown are for telescope tracking of stellar object at $\delta = -63°15'$ through an hour angle of -3:00 to 3:00.

Using equations (G-13) and (G-11), the error in the velocity magnitude, $\varepsilon_{|\vec{v}|}$, is defined as

$$\varepsilon_{|\vec{v}|} = \frac{|\vec{v_{\rm m}}|}{|\vec{v}|} = \sqrt{1 - (l_{\rm z} \sin\beta + m_{\rm z} \cos\beta)^2}. \tag{G-16}$$

The direction of maximum error on velocity magnitude (i.e. $\varepsilon_{|\vec{v}|} = 1$) for an RA-Dec telescope will not be at 90° to the azimuth angle (i.e. the bearing location of where the telescope is looking) as one would think due to the additional rotation experienced by the primary mirror. Rather this will occur when

$$(l_{\rm z} \sin\beta + m_{\rm z} \cos\beta)^2 = 0, \tag{G-17}$$

such that

$$\beta = \arccos\left(sqrt\frac{l_{\rm z}^2}{l_{\rm z}^2 + m_{\rm z}^2}\right) + \frac{n\pi}{2}, \tag{G-18}$$

where n is an odd integer.

The significance of $\varepsilon_{|\vec{v}|}$ and ε_{β} depend greatly on the location of the SCIDAR object in the night sky. Consider a telescope at MJUO tracking an object at $\delta = -63°15'$, such as α Cru. Figure G.5 shows the effect of actual wind direction, β, on the error in wind direction, ε_{β}, and wind speed, $\varepsilon_{|\vec{v}|}$, for an hour angle, H, of -3:00 to 3:00 hrs. For $H = 3$ hrs, the mean ε_{β} is 37.16°(standard deviation is 3.43°). The maximum $1 - \varepsilon_{|\vec{v}|}$ is 0.15. As the telescope approaches the meridian (i.e. $H = 0$ hrs) the mean ε_{β} decreases to 0° (standard deviation is 1.15°). The maximum $1 - \varepsilon_{|\vec{v}|}$ decreases to 0.056.

Appendix H

Velocity Direction Look-up Tables

The following pages contain look-up tables that can be used to determine wind direction, β and error on wind velocity, $\varepsilon_{|\vec{v}|}$, based on the instantaneous orientation of the 1-m McLellan telescope at MJUO and the measure velocity direction from the CCD, b_{m}. The tables presented are specific to the stars used in trending.

List of Symbols:

β	corrected wind direction (degrees)
b_{m}	measured wind direction (degrees)
$\varepsilon_{\vert\vec{v}\vert}$	estimate error in $\vert V(h)\vert$ resulting from telescope motion

Notes:

- β and b_{m} defy the standard sign conventions used in this thesis. Instead they follow standard navigational conventions, which is measured in a clockwise direction from North.
- A negative hour angle will be in the east portion of the sky.

List of Tables:

Table H.1: Direction corrections based on stars at a declination of -43.99°.

Declination: -43.99°
Angle from zenith along meridian: 0.00°

Hour Angle (hours)		-3.00		-2.50		-2.00		-1.50		-1.00		-0.50		0.00	
Hour Angle (degrees)		-45.00		-37.50		-30.00		-22.50		-15.00		-7.50		0.00	
Wind Direction	β	$\varepsilon_{\lvert\vec{v}\rvert}$	b_m	$\varepsilon_{\lvert\vec{v}\rvert}$	b_m	$\varepsilon_{\lvert\vec{v}\rvert}$	b_m	$\varepsilon_{\lvert\vec{v}\rvert}$	b_m	$\varepsilon_{\lvert\vec{v}\rvert}$	b_m	$\varepsilon_{\lvert\vec{v}\rvert}$	b_m	$\varepsilon_{\lvert\vec{v}\rvert}$	b_m
N	0.00	0.99	-29.76	0.99	-25.15	1.00	-20.37	1.00	-15.42	1.00	-10.36	1.00	-5.20	1.00	0.00
	22.50	1.00	-10.57	1.00	-5.00	1.00	0.61	1.00	6.22	1.00	11.76	1.00	17.21	1.00	22.50
NE	45.00	0.97	9.09	0.97	15.65	0.98	22.02	0.99	28.17	0.99	34.05	1.00	39.66	1.00	45.00
	67.50	0.91	30.75	0.93	37.84	0.95	44.51	0.97	50.75	0.99	56.63	1.00	62.19	1.00	67.50
E	90.00	0.86	55.22	0.90	61.95	0.93	68.15	0.96	73.95	0.98	79.46	1.00	84.78	1.00	90.00
	112.50	0.85	81.54	0.90	87.05	0.93	92.28	0.96	97.34	0.98	102.34	1.00	107.37	1.00	112.50
SE	135.00	0.89	107.06	0.92	111.44	0.95	115.86	0.98	120.38	0.99	125.05	1.00	129.91	1.00	135.00
	157.50	0.94	129.89	0.96	133.98	0.98	138.27	0.99	142.76	1.00	147.47	1.00	152.39	1.00	157.50
S	180.00	0.99	150.24	0.99	154.85	1.00	159.63	1.00	164.58	1.00	169.64	1.00	174.80	1.00	180.00
	202.50	1.00	169.43	1.00	175.00	1.00	-179.39	1.00	-173.78	1.00	-168.24	1.00	-162.79	1.00	-157.50
SW	225.00	0.97	-170.91	0.97	-164.35	0.98	-157.98	0.99	-151.83	0.99	-145.95	1.00	-140.34	1.00	-135.00
	247.50	0.91	-149.26	0.93	-142.16	0.95	-135.49	0.97	-129.25	0.99	-123.37	1.00	-117.81	1.00	-112.50
W	270.00	0.86	-124.78	0.90	-118.05	0.93	-111.85	0.96	-106.05	0.98	-100.54	1.00	-95.22	1.00	-90.00
	292.50	0.85	-98.46	0.90	-92.95	0.93	-87.72	0.96	-82.66	0.98	-77.66	1.00	-72.63	1.00	-67.50
NW	315.00	0.89	-72.94	0.92	-68.56	0.95	-64.14	0.98	-59.62	0.99	-54.95	1.00	-50.09	1.00	-45.00
	337.50	0.94	-50.11	0.96	-46.02	0.98	-41.73	0.99	-37.24	1.00	-32.53	1.00	-27.62	1.00	-22.50

Hour Angle (hours)		0.50		1.00		1.50		2.00		2.50		3.00	
Hour Angle (degrees)		7.50		15.00		22.50		30.00		37.50		45.00	
Wind Direction	β	$\varepsilon_{\lvert\vec{v}\rvert}$	b_m	$\varepsilon_{\lvert\vec{v}\rvert}$	b_m	$\varepsilon_{\lvert\vec{v}\rvert}$	b_m	$\varepsilon_{\lvert\vec{v}\rvert}$	b_m	$\varepsilon_{\lvert\vec{v}\rvert}$	b_m	$\varepsilon_{\lvert\vec{v}\rvert}$	b_m
N	0.00	1.00	5.20	1.00	10.36	1.00	15.42	1.00	20.37	0.99	25.15	0.99	29.76
	22.50	1.00	27.62	1.00	32.53	0.99	37.24	0.98	41.73	0.96	46.02	0.94	50.11
NE	45.00	1.00	50.09	0.99	54.95	0.98	59.62	0.95	64.14	0.92	68.56	0.89	72.94
	67.50	1.00	72.63	0.98	77.66	0.96	82.66	0.93	87.72	0.90	92.95	0.85	98.46
E	90.00	1.00	95.22	0.98	100.54	0.96	106.05	0.93	111.85	0.90	118.05	0.86	124.78
	112.50	1.00	117.81	0.99	123.37	0.97	129.25	0.95	135.49	0.93	142.16	0.91	149.26
SE	135.00	1.00	140.34	0.99	145.95	0.99	151.83	0.98	157.98	0.97	164.35	0.97	170.91
	157.50	1.00	162.79	1.00	168.24	1.00	173.78	1.00	179.39	1.00	-175.00	1.00	-169.43
S	180.00	1.00	-174.80	1.00	-169.64	1.00	-164.58	1.00	-159.63	0.99	-154.85	0.99	-150.24
	202.50	1.00	-152.39	1.00	-147.47	0.99	-142.76	0.98	-138.27	0.96	-133.98	0.94	-129.89
SW	225.00	1.00	-129.91	0.99	-125.05	0.98	-120.38	0.95	-115.86	0.92	-111.44	0.89	-107.06
	247.50	1.00	-107.37	0.98	-102.34	0.96	-97.34	0.93	-92.28	0.90	-87.05	0.85	-81.54
W	270.00	1.00	-84.78	0.98	-79.46	0.96	-73.95	0.93	-68.15	0.90	-61.95	0.86	-55.22
	292.50	1.00	-62.19	0.99	-56.63	0.97	-50.75	0.95	-44.51	0.93	-37.84	0.91	-30.75
NW	315.00	1.00	-39.66	0.99	-34.05	0.99	-28.17	0.98	-22.02	0.97	-15.65	0.97	-9.09
	337.50	1.00	-17.21	1.00	-11.76	1.00	-6.22	1.00	-0.61	1.00	5.00	1.00	10.57

Table H.2: Direction corrections based on stars at a declination of -63.12° (e.g. α Cru).

α Cru
Declination: -63.12°
Angle from zenith along meridian: -19.13°

Hour Angle (hours)		-3.00		-2.50		-2.00		-1.50		-1.00		-0.50		0.00	
Hour Angle (degrees)		-45.00		-37.50		-30.00		-22.50		-15.00		-7.50		0.00	
Wind Direction	β	$\varepsilon_{\lvert\vec{v}\rvert}$	b_{m}	$\varepsilon_{\lvert\vec{v}\rvert}$	b_{m}	$\varepsilon_{\lvert\vec{v}\rvert}$	b_{m}	$\varepsilon_{\lvert\vec{v}\rvert}$	b_{m}	$\varepsilon_{\lvert\vec{v}\rvert}$	b_{m}	$\varepsilon_{\lvert\vec{v}\rvert}$	b_{m}	$\varepsilon_{\lvert\vec{v}\rvert}$	b_{m}
N	0.00	0.91	-32.75	0.92	-27.37	0.93	-21.95	0.94	-16.49	0.94	-11.01	0.94	-5.51	0.94	0.00
	22.50	0.96	-10.95	0.97	-5.17	0.97	0.63	0.97	6.42	0.96	12.20	0.96	17.95	0.95	23.67
NE	45.00	1.00	8.81	1.00	15.24	0.99	21.64	0.99	27.98	0.99	34.25	0.98	40.47	0.97	46.63
	67.50	0.99	28.01	0.99	35.05	1.00	41.97	1.00	48.77	1.00	55.47	1.00	62.08	0.99	68.63
E	90.00	0.95	48.27	0.96	55.61	0.97	62.75	0.98	69.72	0.99	76.56	1.00	83.30	1.00	90.00
	112.50	0.89	70.94	0.91	78.07	0.94	84.96	0.96	91.69	0.97	98.30	0.98	104.84	0.99	111.37
SE	135.00	0.85	96.32	0.88	102.69	0.91	108.92	0.93	115.06	0.95	121.16	0.96	127.26	0.97	133.37
	157.50	0.86	122.64	0.88	128.23	0.90	133.80	0.92	139.39	0.93	145.00	0.94	150.64	0.95	156.33
S	180.00	0.91	147.25	0.92	152.63	0.93	158.05	0.94	163.51	0.94	168.99	0.94	174.49	0.94	180.00
	202.50	0.96	169.05	0.97	174.83	0.97	-179.37	0.97	-173.58	0.96	-167.80	0.96	-162.05	0.95	-156.33
SW	225.00	1.00	-171.19	1.00	-164.76	0.99	-158.36	0.99	-152.02	0.99	-145.75	0.98	-139.53	0.97	-133.37
	247.50	0.99	-151.99	0.99	-144.95	1.00	-138.03	1.00	-131.23	1.00	-124.53	1.00	-117.92	0.99	-111.37
W	270.00	0.95	-131.73	0.96	-124.39	0.97	-117.25	0.98	-110.28	0.99	-103.44	1.00	-96.70	1.00	-90.00
	292.50	0.89	-109.06	0.91	-101.93	0.94	-95.04	0.96	-88.31	0.97	-81.70	0.98	-75.16	0.99	-68.63
NW	315.00	0.85	-83.68	0.88	-77.31	0.91	-71.08	0.93	-64.94	0.95	-58.84	0.96	-52.74	0.97	-46.63
	337.50	0.86	-57.36	0.88	-51.77	0.90	-46.20	0.92	-40.61	0.93	-35.00	0.94	-29.36	0.95	-23.67

Hour Angle (hours)		0.50		1.00		1.50		2.00		2.50		3.00	
Hour Angle (degrees)		7.50		15.00		22.50		30.00		37.50		45.00	
Wind Direction	β	$\varepsilon_{\lvert\vec{v}\rvert}$	b_{m}	$\varepsilon_{\lvert\vec{v}\rvert}$	b_{m}	$\varepsilon_{\lvert\vec{v}\rvert}$	b_{m}	$\varepsilon_{\lvert\vec{v}\rvert}$	b_{m}	$\varepsilon_{\lvert\vec{v}\rvert}$	b_{m}	$\varepsilon_{\lvert\vec{v}\rvert}$	b_{m}
N	0.00	0.94	5.51	0.94	11.01	0.94	16.49	0.93	21.95	0.92	27.37	0.91	32.75
	22.50	0.94	29.36	0.93	35.00	0.92	40.61	0.90	46.20	0.88	51.77	0.86	57.36
NE	45.00	0.96	52.74	0.95	58.84	0.93	64.94	0.91	71.08	0.88	77.31	0.85	83.68
	67.50	0.98	75.16	0.97	81.70	0.96	88.31	0.94	95.04	0.91	101.93	0.89	109.06
E	90.00	1.00	96.70	0.99	103.44	0.98	110.28	0.97	117.25	0.96	124.39	0.95	131.73
	112.50	1.00	117.92	1.00	124.53	1.00	131.23	1.00	138.03	0.99	144.95	0.99	151.99
SE	135.00	0.98	139.53	0.99	145.75	0.99	152.02	0.99	158.36	1.00	164.76	1.00	171.19
	157.50	0.96	162.05	0.96	167.80	0.97	173.58	0.97	179.37	0.97	-174.83	0.96	-169.05
S	180.00	0.94	-174.49	0.94	-168.99	0.94	-163.51	0.93	-158.05	0.92	-152.63	0.91	-147.25
	202.50	0.94	-150.64	0.93	-145.00	0.92	-139.39	0.90	-133.80	0.88	-128.23	0.86	-122.64
SW	225.00	0.96	-127.26	0.95	-121.16	0.93	-115.06	0.91	-108.92	0.88	-102.69	0.85	-96.32
	247.50	0.98	-104.84	0.97	-98.30	0.96	-91.69	0.94	-84.96	0.91	-78.07	0.89	-70.94
W	270.00	1.00	-83.30	0.99	-76.56	0.98	-69.72	0.97	-62.75	0.96	-55.61	0.95	-48.27
	292.50	1.00	-62.08	1.00	-55.47	1.00	-48.77	1.00	-41.97	0.99	-35.05	0.99	-28.01
NW	315.00	0.98	-40.47	0.99	-34.25	0.99	-27.98	0.99	-21.64	1.00	-15.24	1.00	-8.81
	337.50	0.96	-17.95	0.96	-12.20	0.97	-6.42	0.97	-0.63	0.97	5.17	0.96	10.95

Table H.3: Direction corrections based on stars at a declination of -60.85° (e.g. α Cen).

α Cen
Declination: -60.85°
Angle from zenith along meridian: -16.86°

Hour Angle (hours)		-3.00		-2.50		-2.00		-1.50		-1.00		-0.50		0.00	
Hour Angle (degrees)		-45.00		-37.50		-30.00		-22.50		-15.00		-7.50		0.00	
Wind Direction	β	$\varepsilon_{\lvert\vec{v}\rvert}$	b_m	$\varepsilon_{\lvert\vec{v}\rvert}$	b_m	$\varepsilon_{\lvert\vec{v}\rvert}$	b_m	$\varepsilon_{\lvert\vec{v}\rvert}$	b_m	$\varepsilon_{\lvert\vec{v}\rvert}$	b_m	$\varepsilon_{\lvert\vec{v}\rvert}$	b_m	$\varepsilon_{\lvert\vec{v}\rvert}$	b_m
N	0.00	0.92	-32.22	0.93	-26.95	0.94	-21.63	0.95	-16.27	0.95	-10.87	0.96	-5.44	0.96	0.00
	22.50	0.97	-10.84	0.98	-5.12	0.98	0.62	0.98	6.36	0.97	12.08	0.97	17.76	0.96	23.40
NE	45.00	1.00	8.79	1.00	15.21	1.00	21.57	1.00	27.86	0.99	34.07	0.99	40.20	0.98	46.26
	67.50	0.99	28.18	0.99	35.21	1.00	42.09	1.00	48.84	1.00	55.45	1.00	61.95	0.99	68.38
E	90.00	0.94	48.87	0.96	56.17	0.97	63.24	0.98	70.11	0.99	76.83	1.00	83.44	1.00	90.00
	112.50	0.88	72.06	0.91	79.06	0.94	85.81	0.96	92.38	0.97	98.84	0.99	105.24	0.99	111.62
SE	135.00	0.85	97.69	0.89	103.86	0.91	109.89	0.93	115.86	0.95	121.80	0.97	127.75	0.98	133.74
	157.50	0.87	123.74	0.90	129.14	0.92	134.55	0.93	139.99	0.95	145.47	0.96	151.01	0.96	156.60
S	180.00	0.92	147.78	0.93	153.05	0.94	158.37	0.95	163.73	0.95	169.13	0.96	174.56	0.96	180.00
	202.50	0.97	169.16	0.98	174.88	0.98	-179.38	0.98	-173.64	0.97	-167.92	0.97	-162.24	0.96	-156.60
SW	225.00	1.00	-171.21	1.00	-164.79	1.00	-158.43	1.00	-152.14	0.99	-145.93	0.99	-139.80	0.98	-133.74
	247.50	0.99	-151.82	0.99	-144.79	1.00	-137.91	1.00	-131.16	1.00	-124.55	1.00	-118.05	0.99	-111.62
W	270.00	0.94	-131.13	0.96	-123.83	0.97	-116.76	0.98	-109.89	0.99	-103.17	1.00	-96.56	1.00	-90.00
	292.50	0.88	-107.94	0.91	-100.94	0.94	-94.19	0.96	-87.62	0.97	-81.16	0.99	-74.76	0.99	-68.38
NW	315.00	0.85	-82.31	0.89	-76.14	0.91	-70.11	0.93	-64.14	0.95	-58.20	0.97	-52.25	0.98	-46.26
	337.50	0.87	-56.26	0.90	-50.86	0.92	-45.45	0.93	-40.01	0.95	-34.53	0.96	-28.99	0.96	-23.40

Hour Angle (hours)		0.50		1.00		1.50		2.00		2.50		3.00	
Hour Angle (degrees)		7.50		15.00		22.50		30.00		37.50		45.00	
Wind Direction	β	$\varepsilon_{\lvert\vec{v}\rvert}$	b_m	$\varepsilon_{\lvert\vec{v}\rvert}$	b_m	$\varepsilon_{\lvert\vec{v}\rvert}$	b_m	$\varepsilon_{\lvert\vec{v}\rvert}$	b_m	$\varepsilon_{\lvert\vec{v}\rvert}$	b_m	$\varepsilon_{\lvert\vec{v}\rvert}$	b_m
N	0.00	0.96	5.44	0.95	10.87	0.95	16.27	0.94	21.63	0.93	26.95	0.92	32.22
	22.50	0.96	28.99	0.95	34.53	0.93	40.01	0.92	45.45	0.90	50.86	0.87	56.26
NE	45.00	0.97	52.25	0.95	58.20	0.93	64.14	0.91	70.11	0.89	76.14	0.85	82.31
	67.50	0.99	74.76	0.97	81.16	0.96	87.62	0.94	94.19	0.91	100.94	0.88	107.94
E	90.00	1.00	96.56	0.99	103.17	0.98	109.89	0.97	116.76	0.96	123.83	0.94	131.13
	112.50	1.00	118.05	1.00	124.55	1.00	131.16	1.00	137.91	0.99	144.79	0.99	151.82
SE	135.00	0.99	139.80	0.99	145.93	1.00	152.14	1.00	158.43	1.00	164.79	1.00	171.21
	157.50	0.97	162.24	0.97	167.92	0.98	173.64	0.98	179.38	0.98	-174.88	0.97	-169.16
S	180.00	0.96	-174.56	0.95	-169.13	0.95	-163.73	0.94	-158.37	0.93	-153.05	0.92	-147.78
	202.50	0.96	-151.01	0.95	-145.47	0.93	-139.99	0.92	-134.55	0.90	-129.14	0.87	-123.74
SW	225.00	0.97	-127.75	0.95	-121.80	0.93	-115.86	0.91	-109.89	0.89	-103.86	0.85	-97.69
	247.50	0.99	-105.24	0.97	-98.84	0.96	-92.38	0.94	-85.81	0.91	-79.06	0.88	-72.06
W	270.00	1.00	-83.44	0.99	-76.83	0.98	-70.11	0.97	-63.24	0.96	-56.17	0.94	-48.87
	292.50	1.00	-61.95	1.00	-55.45	1.00	-48.84	1.00	-42.09	0.99	-35.21	0.99	-28.18
NW	315.00	0.99	-40.20	0.99	-34.07	1.00	-27.86	1.00	-21.57	1.00	-15.21	1.00	-8.79
	337.50	0.97	-17.76	0.97	-12.08	0.98	-6.36	0.98	-0.62	0.98	5.12	0.97	10.84

Table H.4: Direction corrections based on stars at a declination of -40.28° (e.g. θ Eri).

θ Eri
Declination: -40.28°
Angle from zenith along meridian: 3.71°

Hour Angle (hours)		-3.00		-2.50		-2.00		-1.50		-1.00		-0.50		0.00	
Hour Angle (degrees)		-45.00		-37.50		-30.00		-22.50		-15.00		-7.50		0.00	
Wind Direction	β	$\varepsilon_{\lvert\vec{v}\rvert}$	b_{m}	$\varepsilon_{\lvert\vec{v}\rvert}$	b_{m}	$\varepsilon_{\lvert\vec{v}\rvert}$	b_{m}	$\varepsilon_{\lvert\vec{v}\rvert}$	b_{m}	$\varepsilon_{\lvert\vec{v}\rvert}$	b_{m}	$\varepsilon_{\lvert\vec{v}\rvert}$	b_{m}	$\varepsilon_{\lvert\vec{v}\rvert}$	b_{m}
N	0.00	1.00	-29.54	1.00	-25.04	1.00	-20.32	1.00	-15.42	1.00	-10.37	1.00	-5.21	1.00	0.00
	22.50	0.99	-10.63	0.99	-5.04	0.99	0.61	0.99	6.26	0.99	11.83	1.00	17.28	1.00	22.54
NE	45.00	0.95	9.27	0.96	15.93	0.96	22.36	0.97	28.52	0.99	34.36	0.99	39.87	1.00	45.06
	67.50	0.89	31.68	0.91	38.82	0.94	45.42	0.96	51.53	0.98	57.21	0.99	62.52	1.00	67.54
E	90.00	0.84	57.12	0.89	63.61	0.92	69.53	0.96	75.01	0.98	80.17	1.00	85.13	1.00	90.00
	112.50	0.85	83.84	0.89	88.90	0.93	93.69	0.97	98.35	0.99	102.97	1.00	107.65	1.00	112.46
SE	135.00	0.90	108.86	0.93	112.81	0.96	116.86	0.98	121.05	0.99	125.44	1.00	130.05	1.00	134.94
	157.50	0.96	130.81	0.98	134.64	0.99	138.71	1.00	143.02	1.00	147.59	1.00	152.40	1.00	157.46
S	180.00	1.00	150.46	1.00	154.96	1.00	159.68	1.00	164.58	1.00	169.63	1.00	174.79	1.00	180.00
	202.50	0.99	169.37	0.99	174.96	0.99	-179.39	0.99	-173.74	0.99	-168.17	1.00	-162.72	1.00	-157.46
SW	225.00	0.95	-170.73	0.96	-164.07	0.96	-157.64	0.97	-151.48	0.99	-145.64	0.99	-140.13	1.00	-134.94
	247.50	0.89	-148.32	0.91	-141.18	0.94	-134.58	0.96	-128.47	0.98	-122.79	0.99	-117.48	1.00	-112.46
W	270.00	0.84	-122.88	0.89	-116.39	0.92	-110.47	0.96	-104.99	0.98	-99.83	1.00	-94.87	1.00	-90.00
	292.50	0.85	-96.16	0.89	-91.10	0.93	-86.31	0.97	-81.65	0.99	-77.03	1.00	-72.35	1.00	-67.54
NW	315.00	0.90	-71.14	0.93	-67.19	0.96	-63.14	0.98	-58.95	0.99	-54.56	1.00	-49.95	1.00	-45.06
	337.50	0.96	-49.19	0.98	-45.36	0.99	-41.29	1.00	-36.98	1.00	-32.41	1.00	-27.60	1.00	-22.54

Hour Angle (hours)		0.50		1.00		1.50		2.00		2.50		3.00	
Hour Angle (degrees)		7.50		15.00		22.50		30.00		37.50		45.00	
Wind Direction	β	$\varepsilon_{\lvert\vec{v}\rvert}$	b_{m}	$\varepsilon_{\lvert\vec{v}\rvert}$	b_{m}	$\varepsilon_{\lvert\vec{v}\rvert}$	b_{m}	$\varepsilon_{\lvert\vec{v}\rvert}$	b_{m}	$\varepsilon_{\lvert\vec{v}\rvert}$	b_{m}	$\varepsilon_{\lvert\vec{v}\rvert}$	b_{m}
N	0.00	1.00	5.21	1.00	10.37	1.00	15.42	1.00	20.32	1.00	25.04	1.00	29.54
	22.50	1.00	27.60	1.00	32.41	1.00	36.98	0.99	41.29	0.98	45.36	0.96	49.19
NE	45.00	1.00	49.95	0.99	54.56	0.98	58.95	0.96	63.14	0.93	67.19	0.90	71.14
	67.50	1.00	72.35	0.99	77.03	0.97	81.65	0.93	86.31	0.89	91.10	0.85	96.16
E	90.00	1.00	94.87	0.98	99.83	0.96	104.99	0.92	110.47	0.89	116.39	0.84	122.88
	112.50	0.99	117.48	0.98	122.79	0.96	128.47	0.94	134.58	0.91	141.18	0.89	148.32
SE	135.00	0.99	140.13	0.99	145.64	0.97	151.48	0.96	157.64	0.96	164.07	0.95	170.73
	157.50	1.00	162.72	0.99	168.17	0.99	173.74	0.99	179.39	0.99	-174.96	0.99	-169.37
S	180.00	1.00	-174.79	1.00	-169.63	1.00	-164.58	1.00	-159.68	1.00	-154.96	1.00	-150.46
	202.50	1.00	-152.40	1.00	-147.59	1.00	-143.02	0.99	-138.71	0.98	-134.64	0.96	-130.81
SW	225.00	1.00	-130.05	0.99	-125.44	0.98	-121.05	0.96	-116.86	0.93	-112.81	0.90	-108.86
	247.50	1.00	-107.65	0.99	-102.97	0.97	-98.35	0.93	-93.69	0.89	-88.90	0.85	-83.84
W	270.00	1.00	-85.13	0.98	-80.17	0.96	-75.01	0.92	-69.53	0.89	-63.61	0.84	-57.12
	292.50	0.99	-62.52	0.98	-57.21	0.96	-51.53	0.94	-45.42	0.91	-38.82	0.89	-31.68
NW	315.00	0.99	-39.87	0.99	-34.36	0.97	-28.52	0.96	-22.36	0.96	-15.93	0.95	-9.27
	337.50	1.00	-17.28	0.99	-11.83	0.99	-6.26	0.99	-0.61	0.99	5.04	0.99	10.63

Table H.5: Direction corrections based on stars at a declination of -65.09° (e.g. υ Car).

υ Car
Declination: -65.09°
Angle from zenith along meridian: -21.10°

Hour Angle (hours)		-3.00		-2.50		-2.00		-1.50		-1.00		-0.50		0.00	
Hour Angle (degrees)		-45.00		-37.50		-30.00		-22.50		-15.00		-7.50		0.00	
Wind Direction	β	$\varepsilon_{\lvert\vec{v}\rvert}$	b_{m}	$\varepsilon_{\lvert\vec{v}\rvert}$	b_{m}	$\varepsilon_{\lvert\vec{v}\rvert}$	b_{m}	$\varepsilon_{\lvert\vec{v}\rvert}$	b_{m}	$\varepsilon_{\lvert\vec{v}\rvert}$	b_{m}	$\varepsilon_{\lvert\vec{v}\rvert}$	b_{m}	$\varepsilon_{\lvert\vec{v}\rvert}$	b_{m}
N	0.00	0.90	-33.27	0.91	-27.77	0.92	-22.26	0.92	-16.72	0.93	-11.16	0.93	-5.58	0.93	0.00
	22.50	0.95	-11.06	0.96	-5.22	0.96	0.63	0.96	6.48	0.95	12.32	0.95	18.14	0.94	23.94
NE	45.00	0.99	8.84	0.99	15.30	0.99	21.72	0.99	28.11	0.98	34.45	0.98	40.74	0.97	46.99
	67.50	0.99	27.90	1.00	34.95	1.00	41.90	1.00	48.75	1.00	55.52	1.00	62.22	0.99	68.87
E	90.00	0.95	47.79	0.97	55.16	0.98	62.36	0.99	69.41	0.99	76.34	1.00	83.19	1.00	90.00
	112.50	0.90	70.01	0.92	77.22	0.94	84.23	0.96	91.08	0.97	97.82	0.98	104.48	0.99	111.13
SE	135.00	0.85	95.11	0.88	101.65	0.90	108.04	0.92	114.33	0.94	120.57	0.96	126.79	0.97	133.01
	157.50	0.85	121.63	0.87	127.38	0.89	133.10	0.91	138.82	0.92	144.54	0.93	150.29	0.94	156.06
S	180.00	0.90	146.73	0.91	152.23	0.92	157.74	0.92	163.28	0.93	168.84	0.93	174.42	0.93	180.00
	202.50	0.95	168.94	0.96	174.78	0.96	-179.37	0.96	-173.52	0.95	-167.68	0.95	-161.86	0.94	-156.06
SW	225.00	0.99	-171.16	0.99	-164.70	0.99	-158.28	0.99	-151.89	0.98	-145.55	0.98	-139.26	0.97	-133.01
	247.50	0.99	-152.10	1.00	-145.05	1.00	-138.10	1.00	-131.25	1.00	-124.48	1.00	-117.78	0.99	-111.13
W	270.00	0.95	-132.21	0.97	-124.84	0.98	-117.64	0.99	-110.59	0.99	-103.66	1.00	-96.81	1.00	-90.00
	292.50	0.90	-109.99	0.92	-102.78	0.94	-95.77	0.96	-88.92	0.97	-82.18	0.98	-75.52	0.99	-68.87
NW	315.00	0.85	-84.89	0.88	-78.35	0.90	-71.96	0.92	-65.67	0.94	-59.43	0.96	-53.21	0.97	-46.99
	337.50	0.85	-58.37	0.87	-52.62	0.89	-46.90	0.91	-41.18	0.92	-35.46	0.93	-29.71	0.94	-23.94

Hour Angle (hours)		0.50		1.00		1.50		2.00		2.50		3.00	
Hour Angle (degrees)		7.50		15.00		22.50		30.00		37.50		45.00	
Wind Direction	β	$\varepsilon_{\lvert\vec{v}\rvert}$	b_{m}	$\varepsilon_{\lvert\vec{v}\rvert}$	b_{m}	$\varepsilon_{\lvert\vec{v}\rvert}$	b_{m}	$\varepsilon_{\lvert\vec{v}\rvert}$	b_{m}	$\varepsilon_{\lvert\vec{v}\rvert}$	b_{m}	$\varepsilon_{\lvert\vec{v}\rvert}$	b_{m}
N	0.00	0.93	5.58	0.93	11.16	0.92	16.72	0.92	22.26	0.91	27.77	0.90	33.27
	22.50	0.93	29.71	0.92	35.46	0.91	41.18	0.89	46.90	0.87	52.62	0.85	58.37
NE	45.00	0.96	53.21	0.94	59.43	0.92	65.67	0.90	71.96	0.88	78.35	0.85	84.89
	67.50	0.98	75.52	0.97	82.18	0.96	88.92	0.94	95.77	0.92	102.78	0.90	109.99
E	90.00	1.00	96.81	0.99	103.66	0.99	110.59	0.98	117.64	0.97	124.84	0.95	132.21
	112.50	1.00	117.78	1.00	124.48	1.00	131.25	1.00	138.10	1.00	145.05	0.99	152.10
SE	135.00	0.98	139.26	0.98	145.55	0.99	151.89	0.99	158.28	0.99	164.70	0.99	171.16
	157.50	0.95	161.86	0.95	167.68	0.96	173.52	0.96	179.37	0.96	-174.78	0.95	-168.94
S	180.00	0.93	-174.42	0.93	-168.84	0.92	-163.28	0.92	-157.74	0.91	-152.23	0.90	-146.73
	202.50	0.93	-150.29	0.92	-144.54	0.91	-138.82	0.89	-133.10	0.87	-127.38	0.85	-121.63
SW	225.00	0.96	-126.79	0.94	-120.57	0.92	-114.33	0.90	-108.04	0.88	-101.65	0.85	-95.11
	247.50	0.98	-104.48	0.97	-97.82	0.96	-91.08	0.94	-84.23	0.92	-77.22	0.90	-70.01
W	270.00	1.00	-83.19	0.99	-76.34	0.99	-69.41	0.98	-62.36	0.97	-55.16	0.95	-47.79
	292.50	1.00	-62.22	1.00	-55.52	1.00	-48.75	1.00	-41.90	1.00	-34.95	0.99	-27.90
NW	315.00	0.98	-40.74	0.98	-34.45	0.99	-28.11	0.99	-21.72	0.99	-15.30	0.99	-8.84
	337.50	0.95	-18.14	0.95	-12.32	0.96	-6.48	0.96	-0.63	0.96	5.22	0.95	11.06

Appendix I

$V(h)$ Analysis for Individual Runs

The following pages contain the $V(h)$ analysis for individual runs collected during the course of this research.

List of Symbols:

β	corrected wind direction (degrees)
b_{m}	measured wind direction (degrees)
$\lvert d\rvert$	defocus distance (km)
Δm	binary star system magnitude difference
Δr	spatial sampling across the aperture (m/pix)
$\varepsilon_{\lvert\vec{v}\rvert}$	estimate error in $\lvert V(h)\rvert$ resulting from telescope motion
h	measured altitude (km) (NaN = altitude not measurable)
HA	hour angle
ϕ	binary star system angular separation (arcseconds)
Skip #	time between successive frames Δt = (Skip #)(System Framerate)
UT	Universal Time
$\lvert V(h)\rvert$	measured wind speed (m/s)
ζ	zenith angle (degrees)

Notes:

- β and b_{m} defy the standard sign conventions used in this thesis. Instead they follow standard navigational conventions, which is measured in a clockwise direction from North.

- A negative hour angle will be in the east portion of the sky.

List of Tables:

Table I.1: Verified velocity for June 2005.

Run #:Camera	UT	HA	Star	$[\zeta, \phi, \Delta m, \Delta r, \lvert d \rvert]$	Skip #	h	$\lvert V(h) \rvert$	b_{m}	β	$\varepsilon_{\lvert \vec{v} \rvert}$
2:0	12-Jun-05 07:08	-00:33:00	α Cru	[19.73, 4, 0.3, 1/124, 0]	1	10	16.85	138.17	327	0.95
2:0	12-Jun-05 07:08	-00:33:00	α Cru	[19.73, 4, 0.3, 1/124, 0]	1	12	8.63	-23.49	344	0.94
2:0	12-Jun-05 07:08	-00:33:00	α Cru	[19.73, 4, 0.3, 1/124, 0]	1	1	11.5	129.01	318	0.96
2:0	12-Jun-05 07:08	-00:33:00	α Cru	[19.73, 4, 0.3, 1/124, 0]	2	11	9.15	-27.5	340	0.94
2:1	12-Jun-05 07:08	-00:33:00	α Cru	[19.73, 4, 0.3, 1/120, 3.4]	1	0	0	0	186	0.95
2:1	12-Jun-05 07:08	-00:33:00	α Cru	[19.73, 4, 0.3, 1/120, 3.4]	2	0	0	180	186	0.95
3:0	12-Jun-05 07:15	-00:26:00	α Cru	[19.53, 4, 0.3, 1/124, 0]	1	11	9.74	154.22	341	0.94
3:0	12-Jun-05 07:15	-00:26:00	α Cru	[19.53, 4, 0.3, 1/124, 0]	1	1	10.78	-49.27	318	0.96
3:0	12-Jun-05 07:15	-00:26:00	α Cru	[19.53, 4, 0.3, 1/124, 0]	1	10.5	16.78	139.89	327	0.95
3:0	12-Jun-05 07:15	-00:26:00	α Cru	[19.53, 4, 0.3, 1/124, 0]	2	11	8.93	-28.07	338	0.95
3:1	12-Jun-05 07:15	-00:26:00	α Cru	[19.53, 4, 0.3, 1/120, 3.4]	1	0	0	0	185	0.95
3:1	12-Jun-05 07:15	-00:26:00	α Cru	[19.53, 4, 0.3, 1/120, 3.4]	2	0	0	180	185	0.95
5:0	12-Jun-05 07:30	-00:11:00	α Cru	[19.24, 4, 0.3, 1/124, 0]	1	11	11.14	152.5	336	0.95
5:0	12-Jun-05 07:30	-00:11:00	α Cru	[19.24, 4, 0.3, 1/124, 0]	1	10.5	13.55	-42.97	321	0.96
5:0	12-Jun-05 07:30	-00:11:00	α Cru	[19.24, 4, 0.3, 1/124, 0]	2	10.5	11.41	153.07	337	0.95
5:1	12-Jun-05 07:30	-00:11:00	α Cru	[19.24, 4, 0.3, 1/120, 3.4]	1	0	0	180	182	0.95
5:1	12-Jun-05 07:30	-00:11:00	α Cru	[19.24, 4, 0.3, 1/120, 3.4]	1	10.1	13.01	139.23	323	0.96
5:1	12-Jun-05 07:30	-00:11:00	α Cru	[19.24, 4, 0.3, 1/120, 3.4]	2	0	0	180	182	0.95
6:0	12-Jun-05 07:36	-00:05:00	α Cru	[19.18, 4, 0.3, 1/124, 0]	1	12	10.84	156.51	339	0.95
6:0	12-Jun-05 07:36	-00:05:00	α Cru	[19.18, 4, 0.3, 1/124, 0]	1	10	15.02	-42.4	321	0.97
6:0	12-Jun-05 07:36	-00:05:00	α Cru	[19.18, 4, 0.3, 1/124, 0]	2	11.5	11.22	155.94	0	0.94
6:1	12-Jun-05 07:36	-00:05:00	α Cru	[19.18, 4, 0.3, 1/120, 3.4]	1	0	0	180	181	0.94
6:1	12-Jun-05 07:36	-00:05:00	α Cru	[19.18, 4, 0.3, 1/120, 3.4]	1	10.1	10.86	158.14	341	0.95
6:1	12-Jun-05 07:36	-00:05:00	α Cru	[19.18, 4, 0.3, 1/120, 3.4]	2	0	0	180	181	0.94
12:0	13-Jun-05 06:18	-01:20:00	α Cru	[22.35, 4, 0.3, 1/124, 0]	1	11	15.09	121.56	320	0.93
12:0	13-Jun-05 06:18	-01:20:00	α Cru	[22.35, 4, 0.3, 1/124, 0]	1	12.5	8.44	6.3	21	0.96
12:0	13-Jun-05 06:18	-01:20:00	α Cru	[22.35, 4, 0.3, 1/124, 0]	1	1	3.31	40.77	237	1

Continued on next page

Table I.1: Verified velocity for June 2005. (continued)

Run #:Camera	UT	HA	Star	$[\zeta, \phi, \Delta m, \Delta r, \lvert d \rvert]$	Skip #	h	$\lvert V(h) \rvert$	b_{m}	β	$\varepsilon_{\lvert \vec{v} \rvert}$
12:0	13-Jun-05 06:18	-01:20:00	α Cru	[22.35, 4, 0.3, 1/124, 0]	2	1	3.35	-136.94	239	1
12:1	13-Jun-05 06:18	-01:20:00	α Cru	[22.35, 4, 0.3, 1/120, 3.4]	1	0	0	0	195	0.96
12:1	13-Jun-05 06:18	-01:20:00	α Cru	[22.35, 4, 0.3, 1/120, 3.4]	2	0	0	180	195	0.96
12:1	13-Jun-05 06:18	-01:20:00	α Cru	[22.35, 4, 0.3, 1/120, 3.4]	3	0	0	0	195	0.96
13:0	13-Jun-05 06:26	-01:11:00	α Cru	[21.75, 4, 0.3, 1/124, 0]	1	11	15.55	-55	321	0.94
13:1	13-Jun-05 06:26	-01:11:00	α Cru	[21.75, 4, 0.3, 1/120, 3.4]	1	0	0	0	193	0.95
13:1	13-Jun-05 06:26	-01:11:00	α Cru	[21.75, 4, 0.3, 1/120, 3.4]	1	10.1	15.17	-51.66	324	0.93
13:1	13-Jun-05 06:26	-01:11:00	α Cru	[21.75, 4, 0.3, 1/120, 3.4]	2	0	0	0	193	0.95
13:1	13-Jun-05 06:26	-01:11:00	α Cru	[21.75, 4, 0.3, 1/120, 3.4]	3	0	0	180	193	0.95
15:0	13-Jun-05 06:44	00:55:00	α Cru	[20.69, 4, 0.3, 1/124, 0]	1	11	16.04	136.46	307	0.99
15:0	13-Jun-05 06:44	00:55:00	α Cru	[20.69, 4, 0.3, 1/124, 0]	1	10.5	22.27	-80.79	267	0.99
15:0	13-Jun-05 06:44	00:55:00	α Cru	[20.69, 4, 0.3, 1/124, 0]	1	1	3.35	60.82	228	0.95
15:0	13-Jun-05 06:44	00:55:00	α Cru	[20.69, 4, 0.3, 1/124, 0]	2	1	2.98	-119.75	228	0.95
15:1	13-Jun-05 06:44	00:55:00	α Cru	[20.69, 4, 0.3, 1/120, 3.4]	1	0	0	0	171	0.95
15:1	13-Jun-05 06:44	00:55:00	α Cru	[20.69, 4, 0.3, 1/120, 3.4]	1	12.6	16.04	-39.05	312	0.99
15:1	13-Jun-05 06:44	00:55:00	α Cru	[20.69, 4, 0.3, 1/120, 3.4]	2	0	0	0	171	0.95
15:1	13-Jun-05 06:44	00:55:00	α Cru	[20.69, 4, 0.3, 1/120, 3.4]	3	0	0	180	171	0.95
16:0	13-Jun-05 06:57	00:46:00	α Cru	[20.28, 4, 0.3, 1/124, 0]	1	10	14.75	149.63	322	0.98
16:0	13-Jun-05 06:57	00:46:00	α Cru	[20.28, 4, 0.3, 1/124, 0]	1	10.5	15.98	-46.41	306	0.99
16:0	13-Jun-05 06:57	00:46:00	α Cru	[20.28, 4, 0.3, 1/124, 0]	1	1	2.83	56.24	226	0.95
16:0	13-Jun-05 06:57	00:46:00	α Cru	[20.28, 4, 0.3, 1/124, 0]	1	9.5	22.88	-77.92	272	1
16:0	13-Jun-05 06:57	00:46:00	α Cru	[20.28, 4, 0.3, 1/124, 0]	1	3.5	15.47	116.4	288	1
16:0	13-Jun-05 06:57	00:46:00	α Cru	[20.28, 4, 0.3, 1/124, 0]	2	1	2.72	-122.61	227	0.96
16:0	13-Jun-05 06:57	00:46:00	α Cru	[20.28, 4, 0.3, 1/124, 0]	3	1	2.76	56.81	226	0.95
16:1	13-Jun-05 06:57	00:46:00	α Cru	[20.28, 4, 0.3, 1/120, 3.4]	1	0	0	180	172	0.95
16:1	13-Jun-05 06:57	00:46:00	α Cru	[20.28, 4, 0.3, 1/120, 3.4]	1	11	14.66	147.82	321	0.98
16:1	13-Jun-05 06:57	00:46:00	α Cru	[20.28, 4, 0.3, 1/120, 3.4]	2	0	0	180	172	0.95

Continued on next page

Table I.1: Verified velocity for June 2005. (continued)

Run #:Camera	UT	HA	Star	$[\zeta, \phi, \Delta m, \Delta r, \lvert d \rvert]$	Skip #	h	$\lvert V(h) \rvert$	b_{m}	β	$\varepsilon_{\lvert \vec{v} \rvert}$
16:1	13-Jun-05 06:57	00:46:00	α Cru	[20.28, 4, 0.3, 1/120, 3.4]	3	0	0	0	172	0.95
16:1	13-Jun-05 06:57	00:46:00	α Cru	[20.28, 4, 0.3, 1/120, 3.4]	3	0	1.73	-166.82	185	0.94
16:1	13-Jun-05 06:57	00:46:00	α Cru	[20.28, 4, 0.3, 1/120, 3.4]	4	0	0	0	172	0.95
16:1	13-Jun-05 06:57	00:46:00	α Cru	[20.28, 4, 0.3, 1/120, 3.4]	4	0	1.98	-167.97	184	0.94
16:1	13-Jun-05 06:57	00:46:00	α Cru	[20.28, 4, 0.3, 1/120, 3.4]	5	0	0	0	172	0.95
16:1	13-Jun-05 06:57	00:46:00	α Cru	[20.28, 4, 0.3, 1/120, 3.4]	5	0	1.75	-166.82	185	0.94
18:0	13-Jun-05 08:09	00:31:00	α Cru	[19.7, 4, 0.3, 1/124, 0]	1	10.5	16.4	168.54	344	0.95
18:0	13-Jun-05 08:09	00:31:00	α Cru	[19.7, 4, 0.3, 1/124, 0]	1	9.5	18.38	-43.54	312	0.98
18:1	13-Jun-05 08:09	00:31:00	α Cru	[19.7, 4, 0.3, 1/120, 3.4]	1	0	0	0	175	0.95
18:1	13-Jun-05 08:09	00:31:00	α Cru	[19.7, 4, 0.3, 1/120, 3.4]	2	0	0	180	175	0.95
18:1	13-Jun-05 08:09	00:31:00	α Cru	[19.7, 4, 0.3, 1/120, 3.4]	3	0	0	0	175	0.95
19:0	13-Jun-05 08:17	00:39:00	α Cru	[19.99, 4, 0.3, 1/124, 0]	1	11	17	-8.02	346	0.95
19:0	13-Jun-05 08:17	00:39:00	α Cru	[19.99, 4, 0.3, 1/124, 0]	1	10	24.94	136.46	310	0.99
19:1	13-Jun-05 08:17	00:39:00	α Cru	[19.99, 4, 0.3, 1/120, 3.4]	1	0	0	180	174	0.95
19:1	13-Jun-05 08:17	00:39:00	α Cru	[19.99, 4, 0.3, 1/120, 3.4]	2	0	0	0	174	0.95
19:1	13-Jun-05 08:17	00:39:00	α Cru	[19.99, 4, 0.3, 1/120, 3.4]	3	0	0	180	174	0.95
21:0	13-Jun-05 08:34	00:56:00	α Cru	[20.93, 4, 0.3, 1/124, 0]	1	10.5	22.44	128.43	298	1
21:0	13-Jun-05 08:34	00:56:00	α Cru	[20.93, 4, 0.3, 1/124, 0]	1	10	14.71	-4.01	347	0.95
21:1	13-Jun-05 08:34	00:56:00	α Cru	[20.93, 4, 0.3, 1/120, 3.4]	1	0	0	0	171	0.95
21:1	13-Jun-05 08:34	00:56:00	α Cru	[20.93, 4, 0.3, 1/120, 3.4]	1	11.6	22.76	-51.66	298	1
21:1	13-Jun-05 08:34	00:56:00	α Cru	[20.93, 4, 0.3, 1/120, 3.4]	2	0	0	0	171	0.95
21:1	13-Jun-05 08:34	00:56:00	α Cru	[20.93, 4, 0.3, 1/120, 3.4]	3	0	0	180	171	0.95
21:1	13-Jun-05 08:34	00:56:00	α Cru	[20.93, 4, 0.3, 1/120, 3.4]	4	0	1.24	44.12	212	0.94
21:1	13-Jun-05 08:34	00:56:00	α Cru	[20.93, 4, 0.3, 1/120, 3.4]	5	0	1.21	-137.03	211	0.94
22:0	13-Jun-05 08:43	01:06:00	α Cru	[21.41, 4, 0.3, 1/124, 0]	1	10	26.15	120.41	287	1
22:0	13-Jun-05 08:43	01:06:00	α Cru	[21.41, 4, 0.3, 1/124, 0]	1	10.5	19.37	-35.52	313	0.99
22:0	13-Jun-05 08:43	01:06:00	α Cru	[21.41, 4, 0.3, 1/124, 0]	1	11	16.02	175.42	344	0.96

Continued on next page

Table I.1: Verified velocity for June 2005. (continued)

Run #:Camera	UT	HA	Star	$[\zeta, \phi, \Delta m, \Delta r, \lvert d \rvert]$	Skip #	h	$\lvert V(h) \rvert$	b_{m}	β	$\varepsilon_{\lvert \vec{v} \rvert}$
22:0	13-Jun-05 08:43	01:06:00	α Cru	[21.41, 4, 0.3, 1/124, 0]	1	1	6.32	-99.12	246	0.97
22:0	13-Jun-05 08:43	01:06:00	α Cru	[21.41, 4, 0.3, 1/124, 0]	2	1	6.4	80.31	245	0.97
22:0	13-Jun-05 08:43	01:06:00	α Cru	[21.41, 4, 0.3, 1/124, 0]	3	1	6.42	-100.27	245	0.97
22:1	13-Jun-05 08:43	01:06:00	α Cru	[21.41, 4, 0.3, 1/120, 3.4]	1	0	0	0	169	0.95
22:1	13-Jun-05 08:43	01:06:00	α Cru	[21.41, 4, 0.3, 1/120, 3.4]	2	0	0	180	169	0.95
22:1	13-Jun-05 08:43	01:06:00	α Cru	[21.41, 4, 0.3, 1/120, 3.4]	3	0	0	0	169	0.95
22:1	13-Jun-05 08:43	01:06:00	α Cru	[21.41, 4, 0.3, 1/120, 3.4]	4	0	0	180	169	0.95
22:1	13-Jun-05 08:43	01:06:00	α Cru	[21.41, 4, 0.3, 1/120, 3.4]	4	0	0.75	32.09	199	0.93
22:1	13-Jun-05 08:43	01:06:00	α Cru	[21.41, 4, 0.3, 1/120, 3.4]	5	0	0	180	169	0.95
22:1	13-Jun-05 08:43	01:06:00	α Cru	[21.41, 4, 0.3, 1/120, 3.4]	5	1	0.76	29.79	197	0.93
24:0	13-Jun-05 09:38	-00:12:00	α Cen	[17, 10.2, 1.36, 1/124, 0]	1	10.5	17.51	-33.8	330	0.96
24:0	13-Jun-05 09:38	-00:12:00	α Cen	[17, 10.2, 1.36, 1/124, 0]	1	12	9.08	135.31	319	0.97
24:0	13-Jun-05 09:38	-00:12:00	α Cen	[17, 10.2, 1.36, 1/124, 0]	1	1	6.8	34.95	37	0.98
24:0	13-Jun-05 09:38	-00:12:00	α Cen	[17, 10.2, 1.36, 1/124, 0]	2	12	9.25	134.16	318	0.97
24:1	13-Jun-05 09:38	-00:12:00	α Cen	[17, 10.2, 1.36, 1/120, 3.3]	1	0	0	180	183	0.96
24:1	13-Jun-05 09:38	-00:12:00	α Cen	[17, 10.2, 1.36, 1/120, 3.3]	2	0	0	0	183	0.96
24:1	13-Jun-05 09:38	-00:12:00	α Cen	[17, 10.2, 1.36, 1/120, 3.3]	3	0	0	180	183	0.96
26:0	13-Jun-05 10:23	00:32:00	α Cen	[17.57, 10.2, 1.36, 1/124, 0]	1	10.5	18.47	150.21	326	0.98
26:1	13-Jun-05 10:23	00:32:00	α Cen	[17.57, 10.2, 1.36, 1/120, 3.4]	1	0	0	180	175	0.96
26:1	13-Jun-05 10:23	00:32:00	α Cen	[17.57, 10.2, 1.36, 1/120, 3.4]	2	0	0	0	175	0.96
26:1	13-Jun-05 10:23	00:32:00	α Cen	[17.57, 10.2, 1.36, 1/120, 3.4]	3	0	0	180	175	0.96
27:0	13-Jun-05 10:32	00:41:00	α Cen	[17.99, 10.2, 1.36, 1/124, 0]	1	10	18.94	150.21	324	0.98
27:0	13-Jun-05 10:32	00:41:00	α Cen	[17.99, 10.2, 1.36, 1/124, 0]	1	12	10.63	-33.8	320	0.99
27:0	13-Jun-05 10:32	00:41:00	α Cen	[17.99, 10.2, 1.36, 1/124, 0]	2	12	10.61	144.48	318	0.99
27:1	13-Jun-05 10:32	00:41:00	α Cen	[17.99, 10.2, 1.36, 1/120, 3.4]	1	0	0	180	173	0.96
27:1	13-Jun-05 10:32	00:41:00	α Cen	[17.99, 10.2, 1.36, 1/120, 3.4]	2	0	0	0	173	0.96
27:1	13-Jun-05 10:32	00:41:00	α Cen	[17.99, 10.2, 1.36, 1/120, 3.4]	3	0	0	180	173	0.96

Continued on next page

Table I.1: Verified velocity for June 2005. (continued)

Run #:Camera	UT	HA	Star	$[\zeta, \phi, \Delta m, \Delta r, \lvert d \rvert]$	Skip #	h	$\lvert V(h) \rvert$	b_{m}	β	$\varepsilon_{\lvert \vec{v} \rvert}$
27:1	13-Jun-05 10:32	00:41:00	α Cen	[17.99, 10.2, 1.36, 1/120, 3.4]	4	0	0	0	173	0.96
28:0	13-Jun-05 10:40	00:50:00	α Cen	[18.46, 10.2, 1.36, 1/124, 0]	1	10.5	19.06	-28.07	324	0.98
28:0	13-Jun-05 10:40	00:50:00	α Cen	[18.46, 10.2, 1.36, 1/124, 0]	1	11.5	10.53	148.49	320	0.99
28:1	13-Jun-05 10:40	00:50:00	α Cen	[18.46, 10.2, 1.36, 1/120, 3.4]	1	0	0	180	172	0.96
28:1	13-Jun-05 10:40	00:50:00	α Cen	[18.46, 10.2, 1.36, 1/120, 3.4]	2	0	0	0	172	0.96
28:1	13-Jun-05 10:40	00:50:00	α Cen	[18.46, 10.2, 1.36, 1/120, 3.4]	3	0	0	180	172	0.96
28:1	13-Jun-05 10:40	00:50:00	α Cen	[18.46, 10.2, 1.36, 1/120, 3.4]	4	0	0	0	172	0.96
29:0	13-Jun-05 10:50	00:59:00	α Cen	[19.07, 10.2, 1.36, 1/124, 0]	1	10.5	19.01	-20.63	330	0.98
29:0	13-Jun-05 10:50	00:59:00	α Cen	[19.07, 10.2, 1.36, 1/124, 0]	1	10	22.73	131.3	300	1
29:0	13-Jun-05 10:50	00:59:00	α Cen	[19.07, 10.2, 1.36, 1/124, 0]	1	2.5	8.4	-77.92	270	0.99
29:1	13-Jun-05 10:50	00:59:00	α Cen	[19.07, 10.2, 1.36, 1/120, 3.4]	1	0	0	0	170	0.96
29:1	13-Jun-05 10:50	00:59:00	α Cen	[19.07, 10.2, 1.36, 1/120, 3.4]	2	0	0	180	170	0.96
29:1	13-Jun-05 10:50	00:59:00	α Cen	[19.07, 10.2, 1.36, 1/120, 3.4]	3	0	0	0	170	0.96
29:1	13-Jun-05 10:50	00:59:00	α Cen	[19.07, 10.2, 1.36, 1/120, 3.4]	4	0	0	180	170	0.96
30:0	13-Jun-05 10:59	01:08:00	α Cen	[19.73, 10.2, 1.36, 1/124, 0]	1	11.5	19.34	149.06	317	0.99
30:0	13-Jun-05 10:59	01:08:00	α Cen	[19.73, 10.2, 1.36, 1/124, 0]	1	10.5	19.67	-19.48	329	0.98
30:0	13-Jun-05 10:59	01:08:00	α Cen	[19.73, 10.2, 1.36, 1/124, 0]	1	2.5	8.56	100.93	266	0.99
30:0	13-Jun-05 10:59	01:08:00	α Cen	[19.73, 10.2, 1.36, 1/124, 0]	2	3	7.77	-82.51	263	0.98
30:1	13-Jun-05 10:59	01:08:00	α Cen	[19.73, 10.2, 1.36, 1/120, 3.1]	1	0	0	0	0	0.95
30:1	13-Jun-05 10:59	01:08:00	α Cen	[19.73, 10.2, 1.36, 1/120, 3.1]	2	0	0	180	0	0.95
30:1	13-Jun-05 10:59	01:08:00	α Cen	[19.73, 10.2, 1.36, 1/120, 3.1]	3	0	0	0	0	0.95
30:1	13-Jun-05 10:59	01:08:00	α Cen	[19.73, 10.2, 1.36, 1/120, 3.1]	3	0	0.96	-176.56	172	0.96
30:1	13-Jun-05 10:59	01:08:00	α Cen	[19.73, 10.2, 1.36, 1/120, 3.1]	4	0	0	0	0	0.95
30:1	13-Jun-05 10:59	01:08:00	α Cen	[19.73, 10.2, 1.36, 1/120, 3.1]	4	0	1	-178.28	170	0.96
30:1	13-Jun-05 10:59	01:08:00	α Cen	[19.73, 10.2, 1.36, 1/120, 3.1]	5	0	0	0	0	0.95
30:1	13-Jun-05 10:59	01:08:00	α Cen	[19.73, 10.2, 1.36, 1/120, 3.1]	5	0	0.8	-178.28	170	0.96
32:0	13-Jun-05 11:19	01:29:00	α Cen	[21.52, 10.2, 1.36, 1/124, 0]	1	10.5	19.79	165.1	329	0.98

Continued on next page

Table I.1: Verified velocity for June 2005. (continued)

Run #:Camera	UT	HA	Star	$[\zeta, \phi, \Delta m, \Delta r, \lvert d \rvert]$	Skip #	h	$\lvert V(h) \rvert$	b_{m}	β	$\varepsilon_{\lvert \vec{v} \rvert}$
32:0	13-Jun-05 11:19	01:29:00	α Cen	[21.52, 10.2, 1.36, 1/124, 0]	1	11.5	14.05	-26.36	317	0.99
32:0	13-Jun-05 11:19	01:29:00	α Cen	[21.52, 10.2, 1.36, 1/124, 0]	1	9.5	22.12	139.32	302	1
32:0	13-Jun-05 11:19	01:29:00	α Cen	[21.52, 10.2, 1.36, 1/124, 0]	1	13.5	2.64	5.73	350	0.96
32:0	13-Jun-05 11:19	01:29:00	α Cen	[21.52, 10.2, 1.36, 1/124, 0]	1	13	10.14	158.8	323	0.99
32:0	13-Jun-05 11:19	01:29:00	α Cen	[21.52, 10.2, 1.36, 1/124, 0]	2	13.5	2.75	3.44	348	0.96
32:0	13-Jun-05 11:19	01:29:00	α Cen	[21.52, 10.2, 1.36, 1/124, 0]	2	9.5	10.1	158.23	322	0.99
32:0	13-Jun-05 11:19	01:29:00	α Cen	[21.52, 10.2, 1.36, 1/124, 0]	3	13.5	2.87	1.72	346	0.97
32:1	13-Jun-05 11:19	01:29:00	α Cen	[21.52, 10.2, 1.36, 1/120, 3.4]	1	0	0	0	165	0.97
32:1	13-Jun-05 11:19	01:29:00	α Cen	[21.52, 10.2, 1.36, 1/120, 3.4]	2	0	0	180	165	0.97
32:1	13-Jun-05 11:19	01:29:00	α Cen	[21.52, 10.2, 1.36, 1/120, 3.4]	3	0	0	0	165	0.97
32:1	13-Jun-05 11:19	01:29:00	α Cen	[21.52, 10.2, 1.36, 1/120, 3.4]	4	0	0	180	165	0.97
32:1	13-Jun-05 11:19	01:29:00	α Cen	[21.52, 10.2, 1.36, 1/120, 3.4]	4	0	0.95	18.33	183	0.95
32:1	13-Jun-05 11:19	01:29:00	α Cen	[21.52, 10.2, 1.36, 1/120, 3.4]	5	0	0	180	165	0.97
32:1	13-Jun-05 11:19	01:29:00	α Cen	[21.52, 10.2, 1.36, 1/120, 3.4]	5	0	0.94	16.62	181	0.95
33:0	13-Jun-05 11:32	01:41:00	α Cen	[22.65, 10.2, 1.36, 1/124, 0]	1	10.5	19.82	-8.59	334	0.98
33:0	13-Jun-05 11:32	01:41:00	α Cen	[22.65, 10.2, 1.36, 1/124, 0]	1	11.5	13.6	157.08	318	0.99
33:0	13-Jun-05 11:32	01:41:00	α Cen	[22.65, 10.2, 1.36, 1/124, 0]	1	9	23.36	-39.53	300	1
33:1	13-Jun-05 11:32	01:41:00	α Cen	[22.65, 10.2, 1.36, 1/120, 3.4]	1	0	0	0	162	0.97
33:1	13-Jun-05 11:32	01:41:00	α Cen	[22.65, 10.2, 1.36, 1/120, 3.4]	1	9.6	20.53	-8.69	333	0.98
33:1	13-Jun-05 11:32	01:41:00	α Cen	[22.65, 10.2, 1.36, 1/120, 3.4]	2	0	0	0	162	0.97
33:1	13-Jun-05 11:32	01:41:00	α Cen	[22.65, 10.2, 1.36, 1/120, 3.4]	3	0	0	180	162	0.97
33:1	13-Jun-05 11:32	01:41:00	α Cen	[22.65, 10.2, 1.36, 1/120, 3.4]	4	0	0	0	162	0.97
34:0	13-Jun-05 12:06	02:16:00	α Cen	[26.32, 10.2, 1.36, 1/124, 0]	1	10.5	20.87	-3.44	332	0.98
34:0	13-Jun-05 12:06	02:16:00	α Cen	[26.32, 10.2, 1.36, 1/124, 0]	1	12	12.89	166.25	320	1
34:1	13-Jun-05 12:06	02:16:00	α Cen	[26.32, 10.2, 1.36, 1/120, 3.4]	1	0	0	180	155	0.98
34:1	13-Jun-05 12:06	02:16:00	α Cen	[26.32, 10.2, 1.36, 1/120, 3.4]	2	0	0	0	155	0.98
34:1	13-Jun-05 12:06	02:16:00	α Cen	[26.32, 10.2, 1.36, 1/120, 3.4]	3	0	0	180	155	0.98

Continued on next page

Table I.1: Verified velocity for June 2005. (continued)

Run #:Camera	UT	HA	Star	$[\zeta, \phi, \Delta m, \Delta r, \lvert d \rvert]$	Skip #	h	$\lvert V(h) \rvert$	b_{m}	β	$\varepsilon_{\lvert \vec{v} \rvert}$
34:1	13-Jun-05 12:06	02:16:00	α Cen	[26.32, 10.2, 1.36, 1/120, 3.4]	4	0	0	0	155	0.98
35:0	13-Jun-05 12:14	02:24:00	α Cen	[27.25, 10.2, 1.36, 1/124, 0]	1	10.5	21.65	-5.16	328	0.99
35:0	13-Jun-05 12:14	02:24:00	α Cen	[27.25, 10.2, 1.36, 1/124, 0]	1	11.5	15.14	167.39	320	1
35:1	13-Jun-05 12:14	02:24:00	α Cen	[27.25, 10.2, 1.36, 1/120, 3.4]	1	0	0	180	154	0.98
35:1	13-Jun-05 12:14	02:24:00	α Cen	[27.25, 10.2, 1.36, 1/120, 3.4]	1	8.5	21.47	168.45	321	1
35:1	13-Jun-05 12:14	02:24:00	α Cen	[27.25, 10.2, 1.36, 1/120, 3.4]	2	0	0	180	154	0.98
35:1	13-Jun-05 12:14	02:24:00	α Cen	[27.25, 10.2, 1.36, 1/120, 3.4]	3	0	0	0	154	0.98
35:1	13-Jun-05 12:14	02:24:00	α Cen	[27.25, 10.2, 1.36, 1/120, 3.4]	4	0	0	180	154	0.98

Table I.2: Verified velocity for July 2005.

Run #:Camera	UT	HA	Star	$[\zeta, \phi, \Delta m, \Delta r, \lvert d \rvert]$	Skip #	h	$\lvert V(h) \rvert$	b_{m}	β	$\varepsilon_{\lvert \vec{v} \rvert}$
8:0	06-Jul-05 08:57	00:37:00	α Cen	[17.8, 10.1, 1.36, 1/124, 0]	1	11.5	10.71	-88.9	263	0.99
8:0	06-Jul-05 08:57	00:37:00	α Cen	[17.8, 10.1, 1.36, 1/124, 0]	1	12	16.05	-91.76	260	0.99
8:0	06-Jul-05 08:57	00:37:00	α Cen	[17.8, 10.1, 1.36, 1/124, 0]	1	1	3.51	67.13	59	0.98
8:0	06-Jul-05 08:57	00:37:00	α Cen	[17.8, 10.1, 1.36, 1/124, 0]	1	9.3	1.57	-27.02	327	0.98
8:0	06-Jul-05 08:57	00:37:00	α Cen	[17.8, 10.1, 1.36, 1/124, 0]	1	4.5	5.48	90.05	82	0.99
8:0	06-Jul-05 08:57	00:37:00	α Cen	[17.8, 10.1, 1.36, 1/124, 0]	2	11.5	10.81	-88.33	264	0.99
8:0	06-Jul-05 08:57	00:37:00	α Cen	[17.8, 10.1, 1.36, 1/124, 0]	2	11	8.27	-81.45	271	1
8:0	06-Jul-05 08:57	00:37:00	α Cen	[17.8, 10.1, 1.36, 1/124, 0]	2	1	3.4	70.57	62	0.98
8:0	06-Jul-05 08:57	00:37:00	α Cen	[17.8, 10.1, 1.36, 1/124, 0]	2	9	1.66	-4.67	0	0.96
8:0	06-Jul-05 08:57	00:37:00	α Cen	[17.8, 10.1, 1.36, 1/124, 0]	2	4	5.58	91.19	83	0.99
8:1	06-Jul-05 08:57	00:37:00	α Cen	[17.8, 10.1, 1.36, 1/126, 3]	1	0	0	0	354	0.96
8:1	06-Jul-05 08:57	00:37:00	α Cen	[17.8, 10.1, 1.36, 1/126, 3]	2	0	0	0	354	0.96
8:1	06-Jul-05 08:57	00:37:00	α Cen	[17.8, 10.1, 1.36, 1/126, 3]	3	0	0	0	354	0.96
9:0	06-Jul-05 09:05	00:45:00	α Cen	[18.2, 10.1, 1.36, 1/124, 0]	1	11.5	8.64	-82.6	268	0.99
9:0	06-Jul-05 09:05	00:45:00	α Cen	[18.2, 10.1, 1.36, 1/124, 0]	1	12.5	18.72	-101.5	249	0.98
9:0	06-Jul-05 09:05	00:45:00	α Cen	[18.2, 10.1, 1.36, 1/124, 0]	1	4	1.78	-68.85	282	1
9:0	06-Jul-05 09:05	00:45:00	α Cen	[18.2, 10.1, 1.36, 1/124, 0]	1	1	3.78	66.55	57	0.97
9:0	06-Jul-05 09:05	00:45:00	α Cen	[18.2, 10.1, 1.36, 1/124, 0]	2	12.3	8.87	-85.46	265	0.99
9:0	06-Jul-05 09:05	00:45:00	α Cen	[18.2, 10.1, 1.36, 1/124, 0]	2	8.5	1.57	-66.55	285	1
9:0	06-Jul-05 09:05	00:45:00	α Cen	[18.2, 10.1, 1.36, 1/124, 0]	2	1	3.9	63.69	54	0.97
9:0	06-Jul-05 09:05	00:45:00	α Cen	[18.2, 10.1, 1.36, 1/124, 0]	3	1	1.64	-67.13	284	1
9:1	06-Jul-05 09:05	00:45:00	α Cen	[18.2, 10.1, 1.36, 1/126, 3]	1	0	0	0	353	0.96
9:1	06-Jul-05 09:05	00:45:00	α Cen	[18.2, 10.1, 1.36, 1/126, 3]	2	0	0	0	353	0.96
9:1	06-Jul-05 09:05	00:45:00	α Cen	[18.2, 10.1, 1.36, 1/126, 3]	3	0	0	0	353	0.96
12:0	06-Jul-05 09:42	01:22:00	α Cen	[20.8, 10.1, 1.36, 1/124, 0]	1	8.5	3.53	66.55	49	0.94
12:0	06-Jul-05 09:42	01:22:00	α Cen	[20.8, 10.1, 1.36, 1/124, 0]	1	11.5	11.16	-72.28	270	0.99
12:0	06-Jul-05 09:42	01:22:00	α Cen	[20.8, 10.1, 1.36, 1/124, 0]	2	8.5	3.39	75.72	58	0.95

Continued on next page

Table I.2: Verified velocity for July 2005. (continued)

Run #:Camera	UT	HA	Star	$[\zeta, \phi, \Delta m, \Delta r, \lvert d \rvert]$	Skip #	h	$\lvert V(h) \rvert$	b_{m}	β	$\varepsilon_{\lvert \vec{v} \rvert}$
12:0	06-Jul-05 09:42	01:22:00	α Cen	[20.8, 10.1, 1.36, 1/124, 0]	2	11	11.41	-71.14	271	0.99
12:1	06-Jul-05 09:42	01:22:00	α Cen	[20.8, 10.1, 1.36, 1/126, 3]	1	0	0	0	346	0.97
12:1	06-Jul-05 09:42	01:22:00	α Cen	[20.8, 10.1, 1.36, 1/126, 3]	2	0	0	0	346	0.97
12:1	06-Jul-05 09:42	01:22:00	α Cen	[20.8, 10.1, 1.36, 1/126, 3]	3	0	0	0	346	0.97
13:0	06-Jul-05 09:50	01:30:00	α Cen	[21.5, 10.1, 1.36, 1/124, 0]	1	8.3	3.62	71.14	52	0.94
13:0	06-Jul-05 09:50	01:30:00	α Cen	[21.5, 10.1, 1.36, 1/124, 0]	1	11	9.2	-80.88	259	0.97
13:0	06-Jul-05 09:50	01:30:00	α Cen	[21.5, 10.1, 1.36, 1/124, 0]	2	8.5	3.94	76.87	58	0.95
13:0	06-Jul-05 09:50	01:30:00	α Cen	[21.5, 10.1, 1.36, 1/124, 0]	2	11.5	8.75	-83.74	257	0.97
13:1	06-Jul-05 09:50	01:30:00	α Cen	[21.5, 10.1, 1.36, 1/126, 3]	1	0	0	0	344	0.97
13:1	06-Jul-05 09:50	01:30:00	α Cen	[21.5, 10.1, 1.36, 1/126, 3]	2	0	0	0	344	0.97
13:1	06-Jul-05 09:50	01:30:00	α Cen	[21.5, 10.1, 1.36, 1/126, 3]	3	0	0	0	344	0.97
15:0	06-Jul-05 10:05	01:45:00	α Cen	[23.1, 10.1, 1.36, 1/124, 0]	1	9.5	4.38	64.26	43	0.92
15:0	06-Jul-05 10:05	01:45:00	α Cen	[23.1, 10.1, 1.36, 1/124, 0]	1	12	15.15	-79.16	258	0.96
15:0	06-Jul-05 10:05	01:45:00	α Cen	[23.1, 10.1, 1.36, 1/124, 0]	1	11	7.29	19.57	1	0.94
15:0	06-Jul-05 10:05	01:45:00	α Cen	[23.1, 10.1, 1.36, 1/124, 0]	2	9	5.42	68.85	47	0.93
15:0	06-Jul-05 10:05	01:45:00	α Cen	[23.1, 10.1, 1.36, 1/124, 0]	2	12	11.86	-75.72	261	0.96
15:1	06-Jul-05 10:05	01:45:00	α Cen	[23.1, 10.1, 1.36, 1/126, 3]	1	0	0	0	342	0.97
15:1	06-Jul-05 10:05	01:45:00	α Cen	[23.1, 10.1, 1.36, 1/126, 3]	2	0	0	0	342	0.97
15:1	06-Jul-05 10:05	01:45:00	α Cen	[23.1, 10.1, 1.36, 1/126, 3]	3	0	0	0	342	0.97
16:0	06-Jul-05 10:13	01:58:00	α Cen	[23.9, 10.1, 1.36, 1/124, 0]	1	10.5	3.96	-90.05	244	0.93
16:0	06-Jul-05 10:13	01:58:00	α Cen	[23.9, 10.1, 1.36, 1/124, 0]	1	9	4.21	68.27	44	0.91
16:0	06-Jul-05 10:13	01:58:00	α Cen	[23.9, 10.1, 1.36, 1/124, 0]	1	10.5	7.64	-96.92	238	0.92
16:0	06-Jul-05 10:13	01:58:00	α Cen	[23.9, 10.1, 1.36, 1/124, 0]	2	10.5	2.97	-90.05	244	0.93
16:0	06-Jul-05 10:13	01:58:00	α Cen	[23.9, 10.1, 1.36, 1/124, 0]	2	10.5	8.04	-98.64	236	0.92
16:0	06-Jul-05 10:13	01:58:00	α Cen	[23.9, 10.1, 1.36, 1/124, 0]	2	11	8.22	-79.73	254	0.95
16:0	06-Jul-05 10:13	01:58:00	α Cen	[23.9, 10.1, 1.36, 1/124, 0]	2	2.8	4.12	85.46	60	0.93
16:0	06-Jul-05 10:13	01:58:00	α Cen	[23.9, 10.1, 1.36, 1/124, 0]	3	10.5	2.85	-87.75	247	0.94

Continued on next page

Table I.2: Verified velocity for July 2005. (continued)

Run #:Camera	UT	HA	Star	$[\zeta, \phi, \Delta m, \Delta r, \lvert d \rvert]$	Skip #	h	$\lvert V(h) \rvert$	b_{m}	β	$\varepsilon_{\lvert \vec{v} \rvert}$
16:0	06-Jul-05 10:13	01:58:00	α Cen	[23.9, 10.1, 1.36, 1/124, 0]	3	4.5	4.06	87.18	62	0.93
16:0	06-Jul-05 10:13	01:58:00	α Cen	[23.9, 10.1, 1.36, 1/124, 0]	4	10.5	2.85	-86.03	248	0.94
16:0	06-Jul-05 10:13	01:58:00	α Cen	[23.9, 10.1, 1.36, 1/124, 0]	4	1	4.18	84.89	60	0.93
16:1	06-Jul-05 10:13	01:58:00	α Cen	[23.9, 10.1, 1.36, 1/126, 3]	1	0	0	0	339	0.97
16:1	06-Jul-05 10:13	01:58:00	α Cen	[23.9, 10.1, 1.36, 1/126, 3]	2	0	0	0	339	0.97
16:1	06-Jul-05 10:13	01:58:00	α Cen	[23.9, 10.1, 1.36, 1/126, 3]	3	0	0	0	339	0.97
17:0	06-Jul-05 11:29	03:10:00	α Cen	[32.5, 10.1, 1.36, 1/124, 0]	1	11.5	11.65	-49.37	267	0.93
17:0	06-Jul-05 11:29	03:10:00	α Cen	[32.5, 10.1, 1.36, 1/124, 0]	1	13	20.71	-52.23	265	0.92
17:0	06-Jul-05 11:29	03:10:00	α Cen	[32.5, 10.1, 1.36, 1/124, 0]	2	NaN	11.14	-48.22	269	0.93
17:0	06-Jul-05 11:29	03:10:00	α Cen	[32.5, 10.1, 1.36, 1/124, 0]	2	9	1.31	96.35	56	0.85
17:0	06-Jul-05 11:29	03:10:00	α Cen	[32.5, 10.1, 1.36, 1/124, 0]	3	9	2.59	118.12	75	0.89
17:0	06-Jul-05 11:29	03:10:00	α Cen	[32.5, 10.1, 1.36, 1/124, 0]	4	9	2.6	118.69	76	0.9
17:1	06-Jul-05 11:29	03:10:00	α Cen	[32.5, 10.1, 1.36, 1/126, 2.7]	1	0	0	0	323	0.99
17:1	06-Jul-05 11:29	03:10:00	α Cen	[32.5, 10.1, 1.36, 1/126, 2.7]	2	0	0	0	323	0.99
17:1	06-Jul-05 11:29	03:10:00	α Cen	[32.5, 10.1, 1.36, 1/126, 2.7]	3	0	0	0	323	0.99
25:0	07-Jul-05 06:13	00:09:00	α Cru	[19.2, 4, 0.3, 1/124, 0]	1	NaN	15.72	-81.45	277	1
25:0	07-Jul-05 06:13	00:09:00	α Cru	[19.2, 4, 0.3, 1/124, 0]	1	NaN	18.14	-70.57	289	1
25:0	07-Jul-05 06:13	00:09:00	α Cru	[19.2, 4, 0.3, 1/124, 0]	1	NaN	18.64	-57.39	303	0.99
25:1	07-Jul-05 06:13	00:09:00	α Cru	[19.2, 4, 0.3, 1/126, 3]	1	NaN	0	0	359	0.94
25:1	07-Jul-05 06:13	00:09:00	α Cru	[19.2, 4, 0.3, 1/126, 3]	2	NaN	0	0	359	0.94
25:1	07-Jul-05 06:13	00:09:00	α Cru	[19.2, 4, 0.3, 1/126, 3]	3	NaN	0	0	359	0.94
26:0	07-Jul-05 06:21	00:17:00	α Cru	[19.3, 4, 0.3, 1/124, 0]	1	NaN	16.17	-77.44	280	1
26:0	07-Jul-05 06:21	00:17:00	α Cru	[19.3, 4, 0.3, 1/124, 0]	1	NaN	22.57	-91.76	265	1
26:0	07-Jul-05 06:21	00:17:00	α Cru	[19.3, 4, 0.3, 1/124, 0]	1	NaN	18.6	-55.1	303	0.99
26:1	07-Jul-05 06:21	00:17:00	α Cru	[19.3, 4, 0.3, 1/126, 3]	1	NaN	0	0	0	0.94
26:1	07-Jul-05 06:21	00:17:00	α Cru	[19.3, 4, 0.3, 1/126, 3]	2	NaN	0	0	0	0.94
26:1	07-Jul-05 06:21	00:17:00	α Cru	[19.3, 4, 0.3, 1/126, 3]	3	NaN	0	0	0	0.94

Continued on next page

Table I.2: Verified velocity for July 2005. (continued)

Run #:Camera	UT	HA	Star	$[\zeta, \phi, \Delta m, \Delta r, \lvert d \rvert]$	Skip #	h	$\lvert V(h) \rvert$	b_{m}	β	$\varepsilon_{\lvert \vec{v} \rvert}$
28:0	07-Jul-05 06:45	-01:31:00	α Cen	[21.7, 10.1, 1.36, 1/124, 0]	1	NaN	15.81	-91.19	290	0.96
28:1	07-Jul-05 06:45	-01:31:00	α Cen	[21.7, 10.1, 1.36, 1/126, 3]	1	NaN	0	0	17	0.97
33:0	08-Jul-05 07:02	01:02:00	α Cru	[21.2, 4, 0.3, 1/124, 0]	1	NaN	11.55	-79.73	267	0.99
33:0	08-Jul-05 07:02	01:02:00	α Cru	[21.2, 4, 0.3, 1/124, 0]	2	NaN	11.45	-80.31	266	0.99
33:1	08-Jul-05 07:02	01:02:00	α Cru	[21.2, 4, 0.3, 1/126, 3]	1	0	0	0	350	0.95
33:1	08-Jul-05 07:02	01:02:00	α Cru	[21.2, 4, 0.3, 1/126, 3]	2	0	0	0	350	0.95
33:1	08-Jul-05 07:02	01:02:00	α Cru	[21.2, 4, 0.3, 1/126, 3]	3	0	0	0	350	0.95
34:0	08-Jul-05 07:10	01:11:00	α Cru	[21.7, 4, 0.3, 1/124, 0]	1	NaN	12.68	-72.86	272	0.99
34:1	08-Jul-05 07:10	01:11:00	α Cru	[21.7, 4, 0.3, 1/126, 3]	1	0	0	0	348	0.95
34:1	08-Jul-05 07:10	01:11:00	α Cru	[21.7, 4, 0.3, 1/126, 3]	1	2	10.36	-70.47	274	0.99
34:1	08-Jul-05 07:10	01:11:00	α Cru	[21.7, 4, 0.3, 1/126, 3]	1	NaN	12.95	-53.29	293	1
34:1	08-Jul-05 07:10	01:11:00	α Cru	[21.7, 4, 0.3, 1/126, 3]	2	0	0	0	348	0.95
34:1	08-Jul-05 07:10	01:11:00	α Cru	[21.7, 4, 0.3, 1/126, 3]	3	0	0	0	348	0.95
35:0	08-Jul-05 07:22	-00:50:00	α Cen	[18.5, 10.1, 1.36, 1/124, 0]	1	3.5	10.01	-99.21	272	0.99
35:0	08-Jul-05 07:22	-00:50:00	α Cen	[18.5, 10.1, 1.36, 1/124, 0]	2	3	10.22	-96.92	275	0.99
35:1	08-Jul-05 07:22	-00:50:00	α Cen	[18.5, 10.1, 1.36, 1/126, 3]	1	0	0	0	9	0.96
35:1	08-Jul-05 07:22	-00:50:00	α Cen	[18.5, 10.1, 1.36, 1/126, 3]	1	2	8.81	-100.27	271	0.99
35:1	08-Jul-05 07:22	-00:50:00	α Cen	[18.5, 10.1, 1.36, 1/126, 3]	1	NaN	13.09	-81.93	290	0.98
35:1	08-Jul-05 07:22	-00:50:00	α Cen	[18.5, 10.1, 1.36, 1/126, 3]	2	0	0	0	9	0.96
35:1	08-Jul-05 07:22	-00:50:00	α Cen	[18.5, 10.1, 1.36, 1/126, 3]	3	0	0	0	9	0.96
36:0	08-Jul-05 07:31	-00:42:00	α Cen	[18, 10.1, 1.36, 1/124, 0]	1	2	9.65	-105.52	264	1
36:0	08-Jul-05 07:31	-00:42:00	α Cen	[18, 10.1, 1.36, 1/124, 0]	1	5.5	16.73	-92.34	278	0.99
36:0	08-Jul-05 07:31	-00:42:00	α Cen	[18, 10.1, 1.36, 1/124, 0]	1	8.5	20.28	-78.59	292	0.98
36:0	08-Jul-05 07:31	-00:42:00	α Cen	[18, 10.1, 1.36, 1/124, 0]	2	2.5	9.43	-106.66	263	1
36:1	08-Jul-05 07:31	-00:42:00	α Cen	[18, 10.1, 1.36, 1/126, 3]	1	0	0	0	8	0.96
36:1	08-Jul-05 07:31	-00:42:00	α Cen	[18, 10.1, 1.36, 1/126, 3]	2	0	0	0	8	0.96
36:1	08-Jul-05 07:31	-00:42:00	α Cen	[18, 10.1, 1.36, 1/126, 3]	3	0	0	0	8	0.96

Continued on next page

Table I.2: Verified velocity for July 2005. (continued)

Run #:Camera	UT	HA	Star	$[\zeta, \phi, \Delta m, \Delta r, \lvert d \rvert]$	Skip #	h	$\lvert V(h) \rvert$	b_{m}	β	$\varepsilon_{\lvert \vec{v} \rvert}$
37:0	08-Jul-05 07:39	-00:33:00	α Cen	[17.6, 10.1, 1.36, 1/124, 0]	1	3	9.14	-104.37	263	1
37:0	08-Jul-05 07:39	-00:33:00	α Cen	[17.6, 10.1, 1.36, 1/124, 0]	1	7.3	23.46	-87.18	281	0.99
37:0	08-Jul-05 07:39	-00:33:00	α Cen	[17.6, 10.1, 1.36, 1/124, 0]	1	5.5	16.77	-91.19	277	0.99
37:0	08-Jul-05 07:39	-00:33:00	α Cen	[17.6, 10.1, 1.36, 1/124, 0]	2	3	9.2	-104.94	262	1
37:1	08-Jul-05 07:39	-00:33:00	α Cen	[17.6, 10.1, 1.36, 1/126, 3]	1	0	0	0	6	0.96
37:1	08-Jul-05 07:39	-00:33:00	α Cen	[17.6, 10.1, 1.36, 1/126, 3]	1	2	8.54	-107.72	260	1
37:1	08-Jul-05 07:39	-00:33:00	α Cen	[17.6, 10.1, 1.36, 1/126, 3]	2	0	0	0	6	0.96
37:1	08-Jul-05 07:39	-00:33:00	α Cen	[17.6, 10.1, 1.36, 1/126, 3]	2	NaN	8.45	-106.57	261	1
37:1	08-Jul-05 07:39	-00:33:00	α Cen	[17.6, 10.1, 1.36, 1/126, 3]	3	0	0	0	6	0.96
38:0	08-Jul-05 08:01	-00:11:00	α Cen	[17, 10.1, 1.36, 1/124, 0]	1	3	10.69	-106.66	256	1
38:0	08-Jul-05 08:01	-00:11:00	α Cen	[17, 10.1, 1.36, 1/124, 0]	1	6	18.38	-84.89	278	1
38:0	08-Jul-05 08:01	-00:11:00	α Cen	[17, 10.1, 1.36, 1/124, 0]	2	4	10.67	-106.66	256	1
38:1	08-Jul-05 08:01	-00:11:00	α Cen	[17, 10.1, 1.36, 1/126, 3]	1	0	0	0	2	0.96
38:1	08-Jul-05 08:01	-00:11:00	α Cen	[17, 10.1, 1.36, 1/126, 3]	2	0	0	0	2	0.96
38:1	08-Jul-05 08:01	-00:11:00	α Cen	[17, 10.1, 1.36, 1/126, 3]	3	0	0	0	2	0.96
39:0	08-Jul-05 08:10	-00:02:00	α Cen	[16.9, 10.1, 1.36, 1/124, 0]	1	3	9.49	-106.09	254	1
39:0	08-Jul-05 08:10	-00:02:00	α Cen	[16.9, 10.1, 1.36, 1/124, 0]	1	4	11.09	-90.62	270	1
39:0	08-Jul-05 08:10	-00:02:00	α Cen	[16.9, 10.1, 1.36, 1/124, 0]	2	3	9.27	-104.37	256	1
39:1	08-Jul-05 08:10	-00:02:00	α Cen	[16.9, 10.1, 1.36, 1/126, 3]	1	0	0	0	1	0.96
39:1	08-Jul-05 08:10	-00:02:00	α Cen	[16.9, 10.1, 1.36, 1/126, 3]	1	2.5	8.4	-110.01	250	1
39:1	08-Jul-05 08:10	-00:02:00	α Cen	[16.9, 10.1, 1.36, 1/126, 3]	2	0	0	0	1	0.96
39:1	08-Jul-05 08:10	-00:02:00	α Cen	[16.9, 10.1, 1.36, 1/126, 3]	3	0	0	0	1	0.96
45:0	08-Jul-05 09:28	01:15:00	α Cen	[20.3, 10.1, 1.36, 1/124, 0]	1	6.5	19.39	-67.13	277	0.99
45:0	08-Jul-05 09:28	01:15:00	α Cen	[20.3, 10.1, 1.36, 1/124, 0]	1	4	12.49	-80.31	263	0.98
45:0	08-Jul-05 09:28	01:15:00	α Cen	[20.3, 10.1, 1.36, 1/124, 0]	1	2.5	8.93	-94.63	249	0.97
45:1	08-Jul-05 09:28	01:15:00	α Cen	[20.3, 10.1, 1.36, 1/126, 3]	1	0	0	0	347	0.96
45:1	08-Jul-05 09:28	01:15:00	α Cen	[20.3, 10.1, 1.36, 1/126, 3]	2	0	0	0	347	0.96

Continued on next page

Table I.2: Verified velocity for July 2005. (continued)

Run #:Camera	UT	HA	Star	$[\zeta, \phi, \Delta m, \Delta r, \lvert d \rvert]$	Skip #	h	$\lvert V(h) \rvert$	b_{m}	β	$\varepsilon_{\lvert \vec{v} \rvert}$
45:1	08-Jul-05 09:28	01:15:00	α Cen	[20.3, 10.1, 1.36, 1/126, 3]	3	0	0	0	347	0.96
47:0	08-Jul-05 09:53	01:41:00	α Cen	[22.5, 10.1, 1.36, 1/124, 0]	1	6.2	18.17	-61.97	276	0.98
47:0	08-Jul-05 09:53	01:41:00	α Cen	[22.5, 10.1, 1.36, 1/124, 0]	1	6.5	15.52	-71.71	266	0.97
47:0	08-Jul-05 09:53	01:41:00	α Cen	[22.5, 10.1, 1.36, 1/124, 0]	1	3.5	12.03	-70.57	267	0.97
47:0	08-Jul-05 09:53	01:41:00	α Cen	[22.5, 10.1, 1.36, 1/124, 0]	2	2.5	11.87	-69.42	269	0.98
47:1	08-Jul-05 09:53	01:41:00	α Cen	[22.5, 10.1, 1.36, 1/126, 3]	1	0	0	0	342	0.97
47:1	08-Jul-05 09:53	01:41:00	α Cen	[22.5, 10.1, 1.36, 1/126, 3]	1	0	9.89	-46.41	293	1
47:1	08-Jul-05 09:53	01:41:00	α Cen	[22.5, 10.1, 1.36, 1/126, 3]	2	0	0	0	342	0.97
47:1	08-Jul-05 09:53	01:41:00	α Cen	[22.5, 10.1, 1.36, 1/126, 3]	2	0	9.13	-46.98	292	1
47:1	08-Jul-05 09:53	01:41:00	α Cen	[22.5, 10.1, 1.36, 1/126, 3]	3	0	0	0	342	0.97
48:0	08-Jul-05 10:02	01:50:00	α Cen	[23.4, 10.1, 1.36, 1/124, 0]	1	6.5	16.14	-68.85	267	0.97
48:0	08-Jul-05 10:02	01:50:00	α Cen	[23.4, 10.1, 1.36, 1/124, 0]	1	6.5	18.61	-60.25	276	0.98
48:0	08-Jul-05 10:02	01:50:00	α Cen	[23.4, 10.1, 1.36, 1/124, 0]	1	2.5	11.98	-67.13	269	0.97
48:1	08-Jul-05 10:02	01:50:00	α Cen	[23.4, 10.1, 1.36, 1/126, 3]	1	0	0	0	341	0.97
48:1	08-Jul-05 10:02	01:50:00	α Cen	[23.4, 10.1, 1.36, 1/126, 3]	2	0	0	0	341	0.97
48:1	08-Jul-05 10:02	01:50:00	α Cen	[23.4, 10.1, 1.36, 1/126, 3]	3	0	0	0	341	0.97
49:0	08-Jul-05 10:39	04:40:00	α Cru	[43.1, 4, 0.3, 1/124, 0]	1	6	14.01	-36.19	256	0.84
49:0	08-Jul-05 10:39	04:40:00	α Cru	[43.1, 4, 0.3, 1/124, 0]	1	12	26.03	-32.75	259	0.85
49:0	08-Jul-05 10:39	04:40:00	α Cru	[43.1, 4, 0.3, 1/124, 0]	2	6.5	12.76	-41.92	251	0.82
49:1	08-Jul-05 10:39	04:40:00	α Cru	[43.1, 4, 0.3, 1/126, 2.7]	1	0	0	0	298	0.99
49:1	08-Jul-05 10:39	04:40:00	α Cru	[43.1, 4, 0.3, 1/126, 2.7]	1	0	3.89	-17.76	276	0.93
49:1	08-Jul-05 10:39	04:40:00	α Cru	[43.1, 4, 0.3, 1/126, 2.7]	1	5	12.41	-37.82	254	0.83
49:1	08-Jul-05 10:39	04:40:00	α Cru	[43.1, 4, 0.3, 1/126, 2.7]	2	0	0	0	298	0.99
49:1	08-Jul-05 10:39	04:40:00	α Cru	[43.1, 4, 0.3, 1/126, 2.7]	2	0	4.09	-15.47	278	0.94
49:1	08-Jul-05 10:39	04:40:00	α Cru	[43.1, 4, 0.3, 1/126, 2.7]	3	0	0	0	298	0.99
49:1	08-Jul-05 10:39	04:40:00	α Cru	[43.1, 4, 0.3, 1/126, 2.7]	3	0	4.26	-17.76	276	0.93
50:0	08-Jul-05 10:49	04:50:00	α Cru	[44.2, 4, 0.3, 1/124, 0]	1	6.5	14.28	-31.03	258	0.84

Continued on next page

Table I.2: Verified velocity for July 2005. (continued)

Run #:Camera	UT	HA	Star	$[\zeta, \phi, \Delta m, \Delta r, \lvert d \rvert]$	Skip #	h	$\lvert V(h) \rvert$	b_{m}	β	$\varepsilon_{\lvert \vec{v} \rvert}$
50:0	08-Jul-05 10:49	04:50:00	α Cru	[44.2, 4, 0.3, 1/124, 0]	1	12	25.14	-30.46	259	0.85
50:0	08-Jul-05 10:49	04:50:00	α Cru	[44.2, 4, 0.3, 1/124, 0]	2	6	12.33	-41.92	248	0.8
50:1	08-Jul-05 10:49	04:50:00	α Cru	[44.2, 4, 0.3, 1/126, 2.7]	1	0	0	0	295	0.99
50:1	08-Jul-05 10:49	04:50:00	α Cru	[44.2, 4, 0.3, 1/126, 2.7]	1	0	3.28	-22.92	267	0.89
50:1	08-Jul-05 10:49	04:50:00	α Cru	[44.2, 4, 0.3, 1/126, 2.7]	1	5.3	12.64	-34.38	255	0.83
50:1	08-Jul-05 10:49	04:50:00	α Cru	[44.2, 4, 0.3, 1/126, 2.7]	1	11.3	23.37	-30.94	258	0.84
50:1	08-Jul-05 10:49	04:50:00	α Cru	[44.2, 4, 0.3, 1/126, 2.7]	2	0	0	0	295	0.99
50:1	08-Jul-05 10:49	04:50:00	α Cru	[44.2, 4, 0.3, 1/126, 2.7]	2	0	2.47	-16.62	274	0.92
50:1	08-Jul-05 10:49	04:50:00	α Cru	[44.2, 4, 0.3, 1/126, 2.7]	3	0	0	0	295	0.99
50:1	08-Jul-05 10:49	04:50:00	α Cru	[44.2, 4, 0.3, 1/126, 2.7]	3	0	1.96	-15.47	275	0.92
51:0	09-Jul-05 06:20	00:02:00	α Cru	[19.6, 4, 0.3, 1/124, 0]	1	9.5	25.41	-108.95	250	0.99
51:0	09-Jul-05 06:20	00:02:00	α Cru	[19.6, 4, 0.3, 1/124, 0]	1	8	21.26	-110.1	249	0.99
51:0	09-Jul-05 06:20	00:02:00	α Cru	[19.6, 4, 0.3, 1/124, 0]	1	17	22.25	-91.76	268	1
51:1	09-Jul-05 06:20	00:02:00	α Cru	[19.6, 4, 0.3, 1/126, 3]	1	0	0	0	0	0.94
51:1	09-Jul-05 06:20	00:02:00	α Cru	[19.6, 4, 0.3, 1/126, 3]	2	0	0	0	0	0.94
51:1	09-Jul-05 06:20	00:02:00	α Cru	[19.6, 4, 0.3, 1/126, 3]	3	0	0	0	0	0.94
51:1	09-Jul-05 06:20	00:02:00	α Cru	[19.6, 4, 0.3, 1/126, 3]	4	0	0	0	0	0.94
52:0	09-Jul-05 06:28	00:32:00	α Cru	[19.8, 4, 0.3, 1/124, 0]	1	9	25.53	-112.96	239	0.97
52:0	09-Jul-05 06:28	00:32:00	α Cru	[19.8, 4, 0.3, 1/124, 0]	1	8	23.61	-102.65	250	0.99
52:0	09-Jul-05 06:28	00:32:00	α Cru	[19.8, 4, 0.3, 1/124, 0]	1	3	13.04	-119.84	232	0.97
52:1	09-Jul-05 06:28	00:32:00	α Cru	[19.8, 4, 0.3, 1/126, 3]	1	0	0	0	355	0.95
52:1	09-Jul-05 06:28	00:32:00	α Cru	[19.8, 4, 0.3, 1/126, 3]	2	0	0	0	355	0.95
52:1	09-Jul-05 06:28	00:32:00	α Cru	[19.8, 4, 0.3, 1/126, 3]	3	0	0	0	355	0.95
52:1	09-Jul-05 06:28	00:32:00	α Cru	[19.8, 4, 0.3, 1/126, 3]	4	0	0	0	355	0.95
53:0	09-Jul-05 06:50	00:55:00	α Cru	[21, 4, 0.3, 1/124, 0]	1	7	21.34	-67.7	281	1
53:1	09-Jul-05 06:50	00:55:00	α Cru	[21, 4, 0.3, 1/126, 3]	1	0	0	0	351	0.95
53:1	09-Jul-05 06:50	00:55:00	α Cru	[21, 4, 0.3, 1/126, 3]	2	0	0	0	351	0.95

Continued on next page

Table I.2: Verified velocity for July 2005. (continued)

Run #:Camera	UT	HA	Star	$[\zeta, \phi, \Delta m, \Delta r, \lvert d \rvert]$	Skip #	h	$\lvert V(h) \rvert$	b_{m}	β	$\varepsilon_{\lvert \vec{v} \rvert}$
53:1	09-Jul-05 06:50	00:55:00	α Cru	[21, 4, 0.3, 1/126, 3]	3	0	0	0	351	0.95
53:1	09-Jul-05 06:50	00:55:00	α Cru	[21, 4, 0.3, 1/126, 3]	4	0	0	0	351	0.95
54:0	09-Jul-05 06:59	01:04:00	α Cru	[21.3, 4, 0.3, 1/124, 0]	1	13	24.6	-96.92	249	0.97
54:0	09-Jul-05 06:59	01:04:00	α Cru	[21.3, 4, 0.3, 1/124, 0]	1	9.5	23.19	-116.4	229	0.95
54:0	09-Jul-05 06:59	01:04:00	α Cru	[21.3, 4, 0.3, 1/124, 0]	1	16.5	22.02	-79.16	267	0.99
54:1	09-Jul-05 06:59	01:04:00	α Cru	[21.3, 4, 0.3, 1/126, 3]	1	0	0	0	349	0.95
54:1	09-Jul-05 06:59	01:04:00	α Cru	[21.3, 4, 0.3, 1/126, 3]	2	0	0	0	349	0.95
54:1	09-Jul-05 06:59	01:04:00	α Cru	[21.3, 4, 0.3, 1/126, 3]	3	0	0	0	349	0.95
54:1	09-Jul-05 06:59	01:04:00	α Cru	[21.3, 4, 0.3, 1/126, 3]	4	0	0	0	349	0.95
55:0	09-Jul-05 07:07	01:11:00	α Cru	[21.8, 4, 0.3, 1/124, 0]	1	4.5	16.29	-115.26	229	0.94
55:0	09-Jul-05 07:07	01:11:00	α Cru	[21.8, 4, 0.3, 1/124, 0]	1	7.5	23.16	-109.53	235	0.95
55:1	09-Jul-05 07:07	01:11:00	α Cru	[21.8, 4, 0.3, 1/126, 3]	1	0	0	0	348	0.95
55:1	09-Jul-05 07:07	01:11:00	α Cru	[21.8, 4, 0.3, 1/126, 3]	2	0	0	0	348	0.95
55:1	09-Jul-05 07:07	01:11:00	α Cru	[21.8, 4, 0.3, 1/126, 3]	3	0	0	0	348	0.95
55:1	09-Jul-05 07:07	01:11:00	α Cru	[21.8, 4, 0.3, 1/126, 3]	4	0	0	0	348	0.95
57:0	09-Jul-05 07:28	-00:41:00	α Cen	[19.9, 10.1, 1.36, 1/124, 0]	1	7	26.19	-136.46	231	0.99
57:0	09-Jul-05 07:28	-00:41:00	α Cen	[19.9, 10.1, 1.36, 1/124, 0]	1	9	25.64	-122.7	246	1
57:0	09-Jul-05 07:28	-00:41:00	α Cen	[19.9, 10.1, 1.36, 1/124, 0]	1	1.5	8.57	-130.15	238	1
57:1	09-Jul-05 07:28	-00:41:00	α Cen	[19.9, 10.1, 1.36, 1/126, 3]	1	0	0	0	8	0.96
58:0	09-Jul-05 07:47	-00:22:00	α Cen	[17.2, 10.1, 1.36, 1/124, 0]	1	9.5	24.03	-126.14	238	0.99
58:1	09-Jul-05 07:47	-00:22:00	α Cen	[17.2, 10.1, 1.36, 1/126, 3]	1	0	0	0	4	0.96
58:1	09-Jul-05 07:47	-00:22:00	α Cen	[17.2, 10.1, 1.36, 1/126, 3]	2	0	0	0	4	0.96
58:1	09-Jul-05 07:47	-00:22:00	α Cen	[17.2, 10.1, 1.36, 1/126, 3]	2	0	2.08	14.9	19	0.97
58:1	09-Jul-05 07:47	-00:22:00	α Cen	[17.2, 10.1, 1.36, 1/126, 3]	3	0	0	0	4	0.96
58:1	09-Jul-05 07:47	-00:22:00	α Cen	[17.2, 10.1, 1.36, 1/126, 3]	3	0	1.9	14.9	19	0.97
58:1	09-Jul-05 07:47	-00:22:00	α Cen	[17.2, 10.1, 1.36, 1/126, 3]	4	0	0	0	4	0.96
58:1	09-Jul-05 07:47	-00:22:00	α Cen	[17.2, 10.1, 1.36, 1/126, 3]	4	0	1.96	12.03	16	0.96

Continued on next page

Table I.2: Verified velocity for July 2005. (continued)

Run #:Camera	UT	HA	Star	$[\zeta, \phi, \Delta m, \Delta r, \lvert d \rvert]$	Skip #	h	$\lvert V(h) \rvert$	b_{m}	β	$\varepsilon_{\lvert \vec{v} \rvert}$
59:0	09-Jul-05 07:54	-00:14:00	α Cen	[17, 10.1, 1.36, 1/124, 0]	1	7	26.67	-131.3	231	0.99
59:0	09-Jul-05 07:54	-00:14:00	α Cen	[17, 10.1, 1.36, 1/124, 0]	1	9.3	23.49	-120.99	241	0.99
59:1	09-Jul-05 07:54	-00:14:00	α Cen	[17, 10.1, 1.36, 1/126, 3]	1	0	0	0	3	0.96
59:1	09-Jul-05 07:54	-00:14:00	α Cen	[17, 10.1, 1.36, 1/126, 3]	2	0	0	0	3	0.96
59:1	09-Jul-05 07:54	-00:14:00	α Cen	[17, 10.1, 1.36, 1/126, 3]	2	0	2.91	32.66	35	0.98
59:1	09-Jul-05 07:54	-00:14:00	α Cen	[17, 10.1, 1.36, 1/126, 3]	3	0	0	0	3	0.96
59:1	09-Jul-05 07:54	-00:14:00	α Cen	[17, 10.1, 1.36, 1/126, 3]	3	0	2.2	29.22	31	0.97
59:1	09-Jul-05 07:54	-00:14:00	α Cen	[17, 10.1, 1.36, 1/126, 3]	4	0	0	0	3	0.96
59:1	09-Jul-05 07:54	-00:14:00	α Cen	[17, 10.1, 1.36, 1/126, 3]	4	0	1.92	27.5	30	0.97
60:1	09-Jul-05 08:02	-00:07:00	α Cen	[16.9, 10.1, 1.36, 1/126, 3]	1	0	0	0	2	0.96
60:1	09-Jul-05 08:02	-00:07:00	α Cen	[16.9, 10.1, 1.36, 1/126, 3]	2	0	0	0	2	0.96
60:1	09-Jul-05 08:02	-00:07:00	α Cen	[16.9, 10.1, 1.36, 1/126, 3]	2	0	2.13	20.63	22	0.96
60:1	09-Jul-05 08:02	-00:07:00	α Cen	[16.9, 10.1, 1.36, 1/126, 3]	3	0	0	0	2	0.96
60:1	09-Jul-05 08:02	-00:07:00	α Cen	[16.9, 10.1, 1.36, 1/126, 3]	3	0	1.79	20.05	21	0.96
60:1	09-Jul-05 08:02	-00:07:00	α Cen	[16.9, 10.1, 1.36, 1/126, 3]	4	0	0	0	2	0.96
60:1	09-Jul-05 08:02	-00:07:00	α Cen	[16.9, 10.1, 1.36, 1/126, 3]	4	0	1.49	16.04	17	0.96
65:0	09-Jul-05 09:29	01:16:00	α Cen	[20.3, 10.1, 1.36, 1/124, 0]	1	10	24.44	-106.09	0	0.95
65:0	09-Jul-05 09:29	01:16:00	α Cen	[20.3, 10.1, 1.36, 1/124, 0]	1	1.2	6	-58.53	286	1
65:0	09-Jul-05 09:29	01:16:00	α Cen	[20.3, 10.1, 1.36, 1/124, 0]	1	3.5	15.47	-113.54	230	0.95
65:0	09-Jul-05 09:29	01:16:00	α Cen	[20.3, 10.1, 1.36, 1/124, 0]	2	1.5	5.84	-59.11	285	1
65:1	09-Jul-05 09:29	01:16:00	α Cen	[20.3, 10.1, 1.36, 1/126, 2.5]	1	0	0	0	347	0.96
65:1	09-Jul-05 09:29	01:16:00	α Cen	[20.3, 10.1, 1.36, 1/126, 2.5]	2	0	0	0	347	0.96
65:1	09-Jul-05 09:29	01:16:00	α Cen	[20.3, 10.1, 1.36, 1/126, 2.5]	3	0	0	0	347	0.96
65:1	09-Jul-05 09:29	01:16:00	α Cen	[20.3, 10.1, 1.36, 1/126, 2.5]	4	0	0	0	347	0.96
66:0	09-Jul-05 09:31	01:23:00	α Cen	[21, 10.1, 1.36, 1/124, 0]	1	10	24.57	-105.52	237	0.95
66:0	09-Jul-05 09:31	01:23:00	α Cen	[21, 10.1, 1.36, 1/124, 0]	1	1	5.39	-60.25	283	1
66:1	09-Jul-05 09:31	01:23:00	α Cen	[21, 10.1, 1.36, 1/126, 3]	1	0	0	0	346	0.97

Continued on next page

Table I.2: Verified velocity for July 2005. (continued)

Run #:Camera	UT	HA	Star	$[\zeta, \phi, \Delta m, \Delta r, \lvert d \rvert]$	Skip #	h	$\lvert V(h) \rvert$	b_{m}	β	$\varepsilon_{\lvert \vec{v} \rvert}$
66:1	09-Jul-05 09:31	01:23:00	α Cen	[21, 10.1, 1.36, 1/126, 3]	2	0	0	0	346	0.97
66:1	09-Jul-05 09:31	01:23:00	α Cen	[21, 10.1, 1.36, 1/126, 3]	3	0	0	0	346	0.97
66:1	09-Jul-05 09:31	01:23:00	α Cen	[21, 10.1, 1.36, 1/126, 3]	4	0	0	0	346	0.97
71:0	09-Jul-05 11:03	02:56:00	α Cen	[30.9, 10.1, 1.36, 1/124, 0]	1	1.5	8.38	-70.57	250	0.89
71:0	09-Jul-05 11:03	02:56:00	α Cen	[30.9, 10.1, 1.36, 1/124, 0]	2	2	8.02	-68.27	252	0.9
71:1	09-Jul-05 11:03	02:56:00	α Cen	[30.9, 10.1, 1.36, 1/126, 2.7]	1	0	0	0	327	0.99
71:1	09-Jul-05 11:03	02:56:00	α Cen	[30.9, 10.1, 1.36, 1/126, 2.7]	2	0	0	0	327	0.99
71:1	09-Jul-05 11:03	02:56:00	α Cen	[30.9, 10.1, 1.36, 1/126, 2.7]	3	0	0	0	327	0.99
71:1	09-Jul-05 11:03	02:56:00	α Cen	[30.9, 10.1, 1.36, 1/126, 2.7]	4	0	0	0	327	0.99
72:0	09-Jul-05 11:13	03:05:00	α Cen	[31.9, 10.1, 1.36, 1/124, 0]	1	1	4.67	-26.45	294	0.99
72:0	09-Jul-05 11:13	03:05:00	α Cen	[31.9, 10.1, 1.36, 1/124, 0]	1	13	21.59	-64.84	254	0.89
72:0	09-Jul-05 11:13	03:05:00	α Cen	[31.9, 10.1, 1.36, 1/124, 0]	1	3	12.8	-71.14	248	0.88
72:0	09-Jul-05 11:13	03:05:00	α Cen	[31.9, 10.1, 1.36, 1/124, 0]	1	1	2.52	-23.58	297	0.99
72:0	09-Jul-05 11:13	03:05:00	α Cen	[31.9, 10.1, 1.36, 1/124, 0]	2	1	5.15	-25.87	294	0.99
72:1	09-Jul-05 11:13	03:05:00	α Cen	[31.9, 10.1, 1.36, 1/126, 2.7]	1	0	0	0	325	0.99
72:1	09-Jul-05 11:13	03:05:00	α Cen	[31.9, 10.1, 1.36, 1/126, 2.7]	1	0.2	4.4	-26.93	293	0.99
72:1	09-Jul-05 11:13	03:05:00	α Cen	[31.9, 10.1, 1.36, 1/126, 2.7]	2	0	0	0	325	0.99
72:1	09-Jul-05 11:13	03:05:00	α Cen	[31.9, 10.1, 1.36, 1/126, 2.7]	2	0.2	4.13	-24.06	296	0.99
72:1	09-Jul-05 11:13	03:05:00	α Cen	[31.9, 10.1, 1.36, 1/126, 2.7]	3	0	0	0	325	0.99
72:1	09-Jul-05 11:13	03:05:00	α Cen	[31.9, 10.1, 1.36, 1/126, 2.7]	3	0.2	4.51	-25.78	294	0.99
72:1	09-Jul-05 11:13	03:05:00	α Cen	[31.9, 10.1, 1.36, 1/126, 2.7]	4	0	0	0	325	0.99
73:0	09-Jul-05 11:20	03:12:00	α Cen	[32.7, 10.1, 1.36, 1/124, 0]	1	12	22.36	-57.39	259	0.9
73:0	09-Jul-05 11:20	03:12:00	α Cen	[32.7, 10.1, 1.36, 1/124, 0]	1	1.5	7.48	-60.82	256	0.89
73:0	09-Jul-05 11:20	03:12:00	α Cen	[32.7, 10.1, 1.36, 1/124, 0]	1	0.8	3.95	-27.02	291	0.98
73:0	09-Jul-05 11:20	03:12:00	α Cen	[32.7, 10.1, 1.36, 1/124, 0]	2	1	7.45	-55.67	261	0.91
73:0	09-Jul-05 11:20	03:12:00	α Cen	[32.7, 10.1, 1.36, 1/124, 0]	2	1	3.95	-27.02	291	0.98
73:1	09-Jul-05 11:20	03:12:00	α Cen	[32.7, 10.1, 1.36, 1/126, 2.7]	1	0	0	0	323	0.99

Continued on next page

Table I.2: Verified velocity for July 2005. (continued)

Run #:Camera	UT	HA	Star	$[\zeta, \phi, \Delta m, \Delta r, \lvert d \rvert]$	Skip #	h	$\lvert V(h) \rvert$	b_{m}	β	$\varepsilon_{\lvert \vec{v} \rvert}$
73:1	09-Jul-05 11:20	03:12:00	α Cen	[32.7, 10.1, 1.36, 1/126, 2.7]	1	0	7.29	-61.31	255	0.89
73:1	09-Jul-05 11:20	03:12:00	α Cen	[32.7, 10.1, 1.36, 1/126, 2.7]	2	0	0	0	323	0.99
73:1	09-Jul-05 11:20	03:12:00	α Cen	[32.7, 10.1, 1.36, 1/126, 2.7]	2	0	3.74	-27.5	291	0.98
73:1	09-Jul-05 11:20	03:12:00	α Cen	[32.7, 10.1, 1.36, 1/126, 2.7]	3	0	0	0	323	0.99

Table I.3: Verified velocity for January 2007.

Run #:Camera	UT	HA	Star	$[\zeta, \phi, \Delta m, \Delta r, \lvert d \rvert]$	Skip #	h	$\lvert V(h) \rvert$	b_{m}	β	$\varepsilon_{\lvert \vec{v} \rvert}$
12:0	24-Jan-07 13:25	-03:26:00	α Cru	[34.72, 3.9, 0.3, 1/120, 0]	1	17	16.12	-131.3	278	0.91
12:0	24-Jan-07 13:25	-03:26:00	α Cru	[34.72, 3.9, 0.3, 1/120, 0]	3	18	11.59	-104.37	303	0.84
12:0	24-Jan-07 13:25	-03:26:00	α Cru	[34.72, 3.9, 0.3, 1/120, 0]	4	17.5	12	-107.23	300	0.85
12:0	24-Jan-07 13:25	-03:26:00	α Cru	[34.72, 3.9, 0.3, 1/120, 0]	5	18	12.26	-108.95	299	0.85
12:0	24-Jan-07 13:25	-03:26:00	α Cru	[34.72, 3.9, 0.3, 1/120, 0]	1	12	30.11	-118.69	290	0.87
12:0	24-Jan-07 13:25	-03:26:00	α Cru	[34.72, 3.9, 0.3, 1/120, 0]	2	18	10.91	-106.09	301	0.85
12:0	24-Jan-07 13:25	-03:26:00	α Cru	[34.72, 3.9, 0.3, 1/120, 0]	2	12	30.19	-119.84	289	0.88
13:0	24-Jan-07 13:29	-03:21:00	α Cru	[34.24, 3.9, 0.3, 1/120, 0]	2	11.5	30.11	-118.69	289	0.88
13:0	24-Jan-07 13:29	-03:21:00	α Cru	[34.24, 3.9, 0.3, 1/120, 0]	3	16	19.48	-131.3	276	0.92
13:0	24-Jan-07 13:29	-03:21:00	α Cru	[34.24, 3.9, 0.3, 1/120, 0]	3	19.5	7.56	-74.58	327	0.83
13:0	24-Jan-07 13:29	-03:21:00	α Cru	[34.24, 3.9, 0.3, 1/120, 0]	4	19	8.31	-80.31	322	0.83
13:0	24-Jan-07 13:29	-03:21:00	α Cru	[34.24, 3.9, 0.3, 1/120, 0]	1	16	17.33	-129.58	278	0.91
13:0	24-Jan-07 13:29	-03:21:00	α Cru	[34.24, 3.9, 0.3, 1/120, 0]	1	12.5	30.11	-118.69	289	0.88
13:0	24-Jan-07 13:29	-03:21:00	α Cru	[34.24, 3.9, 0.3, 1/120, 0]	2	19	7.67	-71.14	330	0.83
13:0	24-Jan-07 13:29	-03:21:00	α Cru	[34.24, 3.9, 0.3, 1/120, 0]	2	14	18.74	-130.73	277	0.92
14:0	24-Jan-07 13:36	-03:15:00	α Cru	[33.51, 3.9, 0.3, 1/120, 0]	3	20	6.37	-75.72	325	0.83
14:0	24-Jan-07 13:36	-03:15:00	α Cru	[33.51, 3.9, 0.3, 1/120, 0]	3	NaN	15.99	-129.58	277	0.92
14:0	24-Jan-07 13:36	-03:15:00	α Cru	[33.51, 3.9, 0.3, 1/120, 0]	2	NaN	18.55	-128.43	278	0.92
14:0	24-Jan-07 13:36	-03:15:00	α Cru	[33.51, 3.9, 0.3, 1/120, 0]	1	NaN	12.99	-123.85	282	0.91
14:0	24-Jan-07 13:36	-03:15:00	α Cru	[33.51, 3.9, 0.3, 1/120, 0]	4	NaN	13.81	-123.85	282	0.91
14:0	24-Jan-07 13:36	-03:15:00	α Cru	[33.51, 3.9, 0.3, 1/120, 0]	4	NaN	19.08	-127.29	279	0.91
14:0	24-Jan-07 13:36	-03:15:00	α Cru	[33.51, 3.9, 0.3, 1/120, 0]	2	NaN	13.37	-125	281	0.91
14:0	24-Jan-07 13:36	-03:15:00	α Cru	[33.51, 3.9, 0.3, 1/120, 0]	1	12	28.85	-119.27	287	0.89
14:0	24-Jan-07 13:36	-03:15:00	α Cru	[33.51, 3.9, 0.3, 1/120, 0]	3	NaN	19.26	-126.71	280	0.91
14:0	24-Jan-07 13:36	-03:15:00	α Cru	[33.51, 3.9, 0.3, 1/120, 0]	2	11.5	28.85	-119.27	287	0.89
14:0	24-Jan-07 13:36	-03:15:00	α Cru	[33.51, 3.9, 0.3, 1/120, 0]	2	19.5	7.43	-81.45	320	0.83
14:0	24-Jan-07 13:36	-03:15:00	α Cru	[33.51, 3.9, 0.3, 1/120, 0]	1	19	7.7	-88.33	314	0.84

Continued on next page

Table I.3: Verified velocity for January 2007. (continued)

Run #:Camera	UT	HA	Star	$[\zeta, \phi, \Delta m, \Delta r, \lvert d\rvert]$	Skip #	h	$\lvert V(h)\rvert$	b_{m}	β	$\varepsilon_{\lvert\vec{v}\rvert}$
15:0	24-Jan-07 13:57	-02:53:00	α Cru	[31.14, 3.9, 0.3, 1/126, 2.5]	1	NaN	11.58	-108.95	0	0.91
15:0	24-Jan-07 13:57	-02:53:00	α Cru	[31.14, 3.9, 0.3, 1/126, 2.5]	2	NaN	11.58	-108.95	0	0.91
15:0	24-Jan-07 13:57	-02:53:00	α Cru	[31.14, 3.9, 0.3, 1/126, 2.5]	2	0	0	180	214	0.99
16:0	24-Jan-07 14:01	-02:50:00	α Cru	[30.85, 3.9, 0.3, 1/126, 2.5]	3	0	0	180	213	0.98
16:0	24-Jan-07 14:01	-02:50:00	α Cru	[30.85, 3.9, 0.3, 1/126, 2.5]	1	NaN	11.58	-115.26	285	0.92
16:0	24-Jan-07 14:01	-02:50:00	α Cru	[30.85, 3.9, 0.3, 1/126, 2.5]	2	0	0	180	213	0.98
16:0	24-Jan-07 14:01	-02:50:00	α Cru	[30.85, 3.9, 0.3, 1/126, 2.5]	2	NaN	10.69	-116.97	283	0.92
16:0	24-Jan-07 14:01	-02:50:00	α Cru	[30.85, 3.9, 0.3, 1/126, 2.5]	3	NaN	10.8	-117.55	282	0.92
17:0	24-Jan-07 14:05	-02:46:00	α Cru	[30.5, 3.9, 0.3, 1/126, 2.5]	3	0	0	180	212	0.98
17:0	24-Jan-07 14:05	-02:46:00	α Cru	[30.5, 3.9, 0.3, 1/126, 2.5]	3	NaN	11.59	-105.52	293	0.9
17:0	24-Jan-07 14:05	-02:46:00	α Cru	[30.5, 3.9, 0.3, 1/126, 2.5]	1	NaN	9.15	-108.38	290	0.91
17:0	24-Jan-07 14:05	-02:46:00	α Cru	[30.5, 3.9, 0.3, 1/126, 2.5]	2	NaN	11.35	-107.23	0	0.91
18:0	24-Jan-07 14:08	-02:42:00	α Cru	[30.1, 3.9, 0.3, 1/126, 2.5]	3	NaN	7.19	-95.2	302	0.89
18:0	24-Jan-07 14:08	-02:42:00	α Cru	[30.1, 3.9, 0.3, 1/126, 2.5]	4	0	0	180	211	0.98
18:0	24-Jan-07 14:08	-02:42:00	α Cru	[30.1, 3.9, 0.3, 1/126, 2.5]	1	NaN	7.04	-95.2	302	0.89
18:0	24-Jan-07 14:08	-02:42:00	α Cru	[30.1, 3.9, 0.3, 1/126, 2.5]	4	NaN	7.61	-97.49	300	0.89
18:0	24-Jan-07 14:08	-02:42:00	α Cru	[30.1, 3.9, 0.3, 1/126, 2.5]	2	NaN	7.04	-95.2	302	0.89
20:0	24-Jan-07 14:24	00:12:00	υ Car	[21.27, 5, 2.98, 1/120, 0]	4	20	10.99	-53.95	306	0.98
20:0	24-Jan-07 14:24	00:12:00	υ Car	[21.27, 5, 2.98, 1/120, 0]	3	NaN	18.28	-76.29	282	1
20:0	24-Jan-07 14:24	00:12:00	υ Car	[21.27, 5, 2.98, 1/120, 0]	4	NaN	18.97	-77.44	281	1
20:0	24-Jan-07 14:24	00:12:00	υ Car	[21.27, 5, 2.98, 1/120, 0]	5	NaN	10.89	-53.95	306	0.98
20:0	24-Jan-07 14:24	00:12:00	υ Car	[21.27, 5, 2.98, 1/120, 0]	6	NaN	11.17	-54.52	305	0.98
20:0	24-Jan-07 14:24	00:12:00	υ Car	[21.27, 5, 2.98, 1/120, 0]	1	19	9.48	-52.23	308	0.98
20:0	24-Jan-07 14:24	00:12:00	υ Car	[21.27, 5, 2.98, 1/120, 0]	2	20	10.47	-52.8	307	0.98
20:0	24-Jan-07 14:24	00:12:00	υ Car	[21.27, 5, 2.98, 1/120, 0]	3	20	10.47	-52.8	307	0.98
20:0	24-Jan-07 14:24	00:12:00	υ Car	[21.27, 5, 2.98, 1/120, 0]	2	NaN	18.76	-75.72	283	1
21:0	24-Jan-07 14:30	00:18:00	υ Car	[21.34, 5, 2.98, 1/120, 0]	1	NaN	6.4	-43.06	316	0.97

Continued on next page

Table I.3: Verified velocity for January 2007. (continued)

Run #:Camera	UT	HA	Star	$[\zeta, \phi, \Delta m, \Delta r, \lvert d \rvert]$	Skip #	h	$\lvert V(h) \rvert$	b_{m}	β	$\varepsilon_{\lvert \vec{v} \rvert}$
21:0	24-Jan-07 14:30	00:18:00	υ Car	[21.34, 5, 2.98, 1/120, 0]	3	NaN	9.8	-54.52	304	0.98
21:0	24-Jan-07 14:30	00:18:00	υ Car	[21.34, 5, 2.98, 1/120, 0]	4	NaN	2.94	27.59	23	0.94
21:0	24-Jan-07 14:30	00:18:00	υ Car	[21.34, 5, 2.98, 1/120, 0]	2	NaN	8.42	-52.23	306	0.98
21:0	24-Jan-07 14:30	00:18:00	υ Car	[21.34, 5, 2.98, 1/120, 0]	2	NaN	17.99	-72.86	285	1
21:0	24-Jan-07 14:30	00:18:00	υ Car	[21.34, 5, 2.98, 1/120, 0]	4	NaN	10.27	-53.95	304	0.98
21:0	24-Jan-07 14:30	00:18:00	υ Car	[21.34, 5, 2.98, 1/120, 0]	3	NaN	2.05	6.97	4	0.93
21:0	24-Jan-07 14:30	00:18:00	υ Car	[21.34, 5, 2.98, 1/120, 0]	3	NaN	18.32	-72.28	285	1
22:0	24-Jan-07 14:35	00:23:00	υ Car	[21.45, 5, 2.98, 1/120, 0]	2	NaN	20.36	-78.59	277	1
22:0	24-Jan-07 14:35	00:23:00	υ Car	[21.45, 5, 2.98, 1/120, 0]	3	NaN	7.28	-36.19	322	0.97
22:0	24-Jan-07 14:35	00:23:00	υ Car	[21.45, 5, 2.98, 1/120, 0]	4	NaN	6.75	-31.6	326	0.96
22:0	24-Jan-07 14:35	00:23:00	υ Car	[21.45, 5, 2.98, 1/120, 0]	1	NaN	5.34	-41.34	316	0.97
22:0	24-Jan-07 14:35	00:23:00	υ Car	[21.45, 5, 2.98, 1/120, 0]	2	NaN	7.12	-35.61	322	0.97
22:0	24-Jan-07 14:35	00:23:00	υ Car	[21.45, 5, 2.98, 1/120, 0]	2	NaN	18.34	-56.24	301	0.99
22:0	24-Jan-07 14:35	00:23:00	υ Car	[21.45, 5, 2.98, 1/120, 0]	5	NaN	6.93	-32.75	325	0.96
22:0	24-Jan-07 14:35	00:23:00	υ Car	[21.45, 5, 2.98, 1/120, 0]	3	NaN	18.61	-59.11	298	0.99
22:0	24-Jan-07 14:35	00:23:00	υ Car	[21.45, 5, 2.98, 1/120, 0]	6	NaN	7.05	-33.32	324	0.96
22:0	24-Jan-07 14:35	00:23:00	υ Car	[21.45, 5, 2.98, 1/120, 0]	3	NaN	19.66	-78.01	278	1
23:0	24-Jan-07 14:40	00:28:00	υ Car	[21.55, 5, 2.98, 1/120, 0]	2	NaN	17.91	-45.93	311	0.98
23:0	24-Jan-07 14:40	00:28:00	υ Car	[21.55, 5, 2.98, 1/120, 0]	4	NaN	17.62	-47.07	309	0.98
23:0	24-Jan-07 14:40	00:28:00	υ Car	[21.55, 5, 2.98, 1/120, 0]	2	NaN	7.4	-44.78	312	0.98
23:0	24-Jan-07 14:40	00:28:00	υ Car	[21.55, 5, 2.98, 1/120, 0]	1	NaN	6.37	-43.06	314	0.98
23:0	24-Jan-07 14:40	00:28:00	υ Car	[21.55, 5, 2.98, 1/120, 0]	4	NaN	7.92	-45.35	311	0.98
23:0	24-Jan-07 14:40	00:28:00	υ Car	[21.55, 5, 2.98, 1/120, 0]	3	NaN	17.61	-44.78	312	0.98
23:0	24-Jan-07 14:40	00:28:00	υ Car	[21.55, 5, 2.98, 1/120, 0]	3	NaN	7.75	-44.78	312	0.98
23:0	24-Jan-07 14:40	00:28:00	υ Car	[21.55, 5, 2.98, 1/120, 0]	6	NaN	7.43	-43.06	314	0.98
23:0	24-Jan-07 14:40	00:28:00	υ Car	[21.55, 5, 2.98, 1/120, 0]	5	NaN	7.27	-41.34	315	0.98
24:0	24-Jan-07 14:44	00:32:00	υ Car	[21.7, 5, 2.98, 1/120, 0]	3	NaN	3.7	-34.47	321	0.97

Continued on next page

Table I.3: Verified velocity for January 2007. (continued)

Run #:Camera	UT	HA	Star	$[\zeta, \phi, \Delta m, \Delta r, \lvert d\rvert]$	Skip #	h	$\lvert V(h)\rvert$	b_{m}	β	$\varepsilon_{\lvert\vec{v}\rvert}$
24:0	24-Jan-07 14:44	00:32:00	υ Car	[21.7, 5, 2.98, 1/120, 0]	2	14	17.26	-42.49	313	0.98
24:0	24-Jan-07 14:44	00:32:00	υ Car	[21.7, 5, 2.98, 1/120, 0]	6	NaN	3.32	-35.61	320	0.97
24:0	24-Jan-07 14:44	00:32:00	υ Car	[21.7, 5, 2.98, 1/120, 0]	6	NaN	7.48	-47.07	309	0.98
24:0	24-Jan-07 14:44	00:32:00	υ Car	[21.7, 5, 2.98, 1/120, 0]	3	NaN	7.83	-48.79	307	0.99
24:0	24-Jan-07 14:44	00:32:00	υ Car	[21.7, 5, 2.98, 1/120, 0]	1	NaN	4.4	-37.33	319	0.97
24:0	24-Jan-07 14:44	00:32:00	υ Car	[21.7, 5, 2.98, 1/120, 0]	2	NaN	4.4	-37.33	319	0.97
24:0	24-Jan-07 14:44	00:32:00	υ Car	[21.7, 5, 2.98, 1/120, 0]	4	15	17.09	-40.77	315	0.98
24:0	24-Jan-07 14:44	00:32:00	υ Car	[21.7, 5, 2.98, 1/120, 0]	4	NaN	3.63	-34.47	321	0.97
24:0	24-Jan-07 14:44	00:32:00	υ Car	[21.7, 5, 2.98, 1/120, 0]	4	NaN	8.01	-47.65	308	0.98
24:0	24-Jan-07 14:44	00:32:00	υ Car	[21.7, 5, 2.98, 1/120, 0]	5	17	16.9	-41.34	314	0.98
24:0	24-Jan-07 14:44	00:32:00	υ Car	[21.7, 5, 2.98, 1/120, 0]	5	NaN	3.57	-33.9	322	0.97
24:0	24-Jan-07 14:44	00:32:00	υ Car	[21.7, 5, 2.98, 1/120, 0]	3	14	17.29	-41.92	314	0.98
24:0	24-Jan-07 14:44	00:32:00	υ Car	[21.7, 5, 2.98, 1/120, 0]	5	NaN	7.7	-46.5	309	0.98
30:0	24-Jan-07 15:09	00:58:00	υ Car	[22.7, 5, 2.98, 1/126, 2.5]	1	NaN	0	180	170	0.94
50:0	27-Jan-07 11:28	-00:58:00	α Cru	[20.93, 3.9, 0.3, 1/250, 0]	1	NaN	23.92	-43.64	0	0.94
51:0	27-Jan-07 11:33	-00:53:00	α Cru	[20.62, 3.9, 0.3, 1/250, 0]	1	NaN	24.76	-40.77	331	0.94
52:0	27-Jan-07 11:41	-00:44:00	α Cru	[22.22, 3.9, 0.3, 1/262, 1.5]	1	NaN	19.78	-41.92	329	0.94
52:0	27-Jan-07 11:41	-00:44:00	α Cru	[22.22, 3.9, 0.3, 1/262, 1.5]	1	NaN	0	-90.05	281	0.99
52:0	27-Jan-07 11:41	-00:44:00	α Cru	[22.22, 3.9, 0.3, 1/262, 1.5]	2	NaN	0	180	188	0.95
54:0	27-Jan-07 11:50	-00:36:00	α Cru	[19.87, 3.9, 0.3, 1/262, 1.5]	1	NaN	14.93	-33.32	335	0.94
54:0	27-Jan-07 11:50	-00:36:00	α Cru	[19.87, 3.9, 0.3, 1/262, 1.5]	1	NaN	0	-90.05	279	0.99
54:0	27-Jan-07 11:50	-00:36:00	α Cru	[19.87, 3.9, 0.3, 1/262, 1.5]	2	NaN	15.56	-35.04	334	0.94
54:0	27-Jan-07 11:50	-00:36:00	α Cru	[19.87, 3.9, 0.3, 1/262, 1.5]	2	NaN	0	-90.05	279	0.99
54:0	27-Jan-07 11:50	-00:36:00	α Cru	[19.87, 3.9, 0.3, 1/262, 1.5]	3	NaN	0	-90.05	279	0.99
120:0	28-Jan-07 14:00	-02:34:00	α Cru	[29.13, 3.9, 0.3, 1/250, 0]	1	NaN	15.6	-70.57	322	0.87
120:0	28-Jan-07 14:00	-02:34:00	α Cru	[29.13, 3.9, 0.3, 1/250, 0]	1	NaN	36.07	-68.27	324	0.87
120:0	28-Jan-07 14:00	-02:34:00	α Cru	[29.13, 3.9, 0.3, 1/250, 0]	1	NaN	24.37	-94.06	301	0.9

Continued on next page

Table I.3: Verified velocity for January 2007. (continued)

Run #:Camera	UT	HA	Star	$[\zeta, \phi, \Delta m, \Delta r, \lvert d \rvert]$	Skip #	h	$\lvert V(h) \rvert$	b_{m}	β	$\varepsilon_{\lvert \vec{v} \rvert}$
121:0	28-Jan-07 14:08	-02:26:00	α Cru	[28.26, 3.9, 0.3, 1/250, 0]	1	NaN	18.64	-76.29	316	0.88
127:0	28-Jan-07 14:48	-01:46:00	α Cru	[24.53, 3.9, 0.3, 1/250, 0]	1	NaN	41.2	-90.05	295	0.94
127:0	28-Jan-07 14:48	-01:46:00	α Cru	[24.53, 3.9, 0.3, 1/250, 0]	1	NaN	23.56	-84.32	300	0.93
128:0	28-Jan-07 14:57	-01:37:00	α Cru	[23.75, 3.9, 0.3, 1/262, 1.5]	1	NaN	19.24	-73.43	309	0.93
128:0	28-Jan-07 14:57	-01:37:00	α Cru	[23.75, 3.9, 0.3, 1/262, 1.5]	2	NaN	20.83	-72.28	310	0.93
128:0	28-Jan-07 14:57	-01:37:00	α Cru	[23.75, 3.9, 0.3, 1/262, 1.5]	2	NaN	0	-122.7	259	0.99
128:0	28-Jan-07 14:57	-01:37:00	α Cru	[23.75, 3.9, 0.3, 1/262, 1.5]	3	NaN	0	180	198	0.96
128:0	28-Jan-07 14:57	-01:37:00	α Cru	[23.75, 3.9, 0.3, 1/262, 1.5]	1	NaN	0	180	198	0.96
129:0	28-Jan-07 15:05	-01:29:00	α Cru	[23.08, 3.9, 0.3, 1/262, 1.5]	1	NaN	0	180	196	0.96
129:0	28-Jan-07 15:05	-01:29:00	α Cru	[23.08, 3.9, 0.3, 1/262, 1.5]	1	NaN	27.05	-80.31	301	0.94
129:0	28-Jan-07 15:05	-01:29:00	α Cru	[23.08, 3.9, 0.3, 1/262, 1.5]	1	NaN	24.51	-67.13	313	0.93
129:0	28-Jan-07 15:05	-01:29:00	α Cru	[23.08, 3.9, 0.3, 1/262, 1.5]	2	NaN	0	180	196	0.96
134:0	28-Jan-07 15:28	-01:05:00	α Cru	[21.37, 3.9, 0.3, 1/262, 1.5]	1	NaN	0	180	192	0.95
134:0	28-Jan-07 15:28	-01:05:00	α Cru	[21.37, 3.9, 0.3, 1/262, 1.5]	1	NaN	29.66	-65.98	310	0.95
134:0	28-Jan-07 15:28	-01:05:00	α Cru	[21.37, 3.9, 0.3, 1/262, 1.5]	2	NaN	0	180	192	0.95
140:0	28-Jan-07 15:36	-00:58:00	α Cru	[20.9, 3.9, 0.3, 1/262, 1.5]	1	NaN	0	180	191	0.95
140:0	28-Jan-07 15:36	-00:58:00	α Cru	[20.9, 3.9, 0.3, 1/262, 1.5]	2	NaN	0	180	191	0.95
140:0	28-Jan-07 15:36	-00:58:00	α Cru	[20.9, 3.9, 0.3, 1/262, 1.5]	1	NaN	30.37	-65.41	309	0.95
141:0	28-Jan-07 15:45	-00:58:00	α Cru	[20.49, 3.9, 0.3, 1/262, 1.5]	1	NaN	0	180	191	0.95
141:0	28-Jan-07 15:45	-00:58:00	α Cru	[20.49, 3.9, 0.3, 1/262, 1.5]	1	NaN	27.2	-60.82	313	0.95
141:0	28-Jan-07 15:45	-00:58:00	α Cru	[20.49, 3.9, 0.3, 1/262, 1.5]	2	NaN	24.26	-62.54	0	0.94
141:0	28-Jan-07 15:45	-00:58:00	α Cru	[20.49, 3.9, 0.3, 1/262, 1.5]	2	NaN	0	180	191	0.95
200:0	29-Jan-07 09:37	02:33:00	θ Eri	[28.41, 8.3, 0.92, 1/120, 0]	1	3	23.18	-30.46	300	0.92
200:0	29-Jan-07 09:37	02:33:00	θ Eri	[28.41, 8.3, 0.92, 1/120, 0]	1	14	9.02	-31.6	299	0.92
201:0	29-Jan-07 09:45	02:42:00	θ Eri	[29.95, 8.3, 0.92, 1/120, 0]	1	2.8	19.74	-28.17	300	0.92
201:0	29-Jan-07 09:45	02:42:00	θ Eri	[29.95, 8.3, 0.92, 1/120, 0]	2	2.8	19.27	-27.59	301	0.92
201:0	29-Jan-07 09:45	02:42:00	θ Eri	[29.95, 8.3, 0.92, 1/120, 0]	1	14	8.07	-27.59	301	0.92

Continued on next page

Table I.3: Verified velocity for January 2007. (continued)

Run #:Camera	UT	HA	Star	$[\zeta, \phi, \Delta m, \Delta r, \lvert d\rvert]$	Skip #	h	$\lvert V(h)\rvert$	b_{m}	β	$\varepsilon_{\lvert\vec{v}\rvert}$
201:0	29-Jan-07 09:45	02:42:00	θ Eri	[29.95, 8.3, 0.92, 1/120, 0]	2	13	9.81	-35.61	293	0.9
204:0	29-Jan-07 10:04	03:01:00	θ Eri	[33.33, 8.3, 0.92, 1/127, 2.5]	2	0	0	180	145	0.97
204:0	29-Jan-07 10:04	03:01:00	θ Eri	[33.33, 8.3, 0.92, 1/127, 2.5]	1	0	0	180	145	0.97
205:0	29-Jan-07 10:09	03:06:00	θ Eri	[34.28, 8.3, 0.92, 1/127, 2.5]	1	0	0	180	144	0.97
205:0	29-Jan-07 10:09	03:06:00	θ Eri	[34.28, 8.3, 0.92, 1/127, 2.5]	2	0	0	180	144	0.97
205:0	29-Jan-07 10:09	03:06:00	θ Eri	[34.28, 8.3, 0.92, 1/127, 2.5]	1	2	23	-19	304	0.92
205:0	29-Jan-07 10:09	03:06:00	θ Eri	[34.28, 8.3, 0.92, 1/127, 2.5]	1	0	10.62	-25.3	298	0.9
230:0	29-Jan-07 14:29	-02:01:00	α Cru	[25.89, 3.9, 0.3, 1/120, 0]	2	NaN	1.47	1.81	24	0.97
230:0	29-Jan-07 14:29	-02:01:00	α Cru	[25.89, 3.9, 0.3, 1/120, 0]	1	NaN	1.54	-21.29	1	0.93
230:0	29-Jan-07 14:29	-02:01:00	α Cru	[25.89, 3.9, 0.3, 1/120, 0]	3	NaN	1.39	0.66	23	0.97
230:0	29-Jan-07 14:29	-02:01:00	α Cru	[25.89, 3.9, 0.3, 1/120, 0]	2	3	11.46	-78.59	309	0.91
230:0	29-Jan-07 14:29	-02:01:00	α Cru	[25.89, 3.9, 0.3, 1/120, 0]	2	6	19.31	-110.1	278	0.96
230:0	29-Jan-07 14:29	-02:01:00	α Cru	[25.89, 3.9, 0.3, 1/120, 0]	3	3.5	11.57	-90.62	297	0.93
230:0	29-Jan-07 14:29	-02:01:00	α Cru	[25.89, 3.9, 0.3, 1/120, 0]	4	NaN	2.49	33.32	59	1
230:0	29-Jan-07 14:29	-02:01:00	α Cru	[25.89, 3.9, 0.3, 1/120, 0]	2	11	18.26	-98.07	290	0.94
230:0	29-Jan-07 14:29	-02:01:00	α Cru	[25.89, 3.9, 0.3, 1/120, 0]	2	1	11.73	-91.19	297	0.93
230:0	29-Jan-07 14:29	-02:01:00	α Cru	[25.89, 3.9, 0.3, 1/120, 0]	2	10	14.31	-114.68	273	0.97
230:0	29-Jan-07 14:29	-02:01:00	α Cru	[25.89, 3.9, 0.3, 1/120, 0]	1	12	17.15	-103.8	285	0.95
230:0	29-Jan-07 14:29	-02:01:00	α Cru	[25.89, 3.9, 0.3, 1/120, 0]	1	3	11.26	-80.31	307	0.91
230:0	29-Jan-07 14:29	-02:01:00	α Cru	[25.89, 3.9, 0.3, 1/120, 0]	3	3.5	11.4	-88.33	300	0.92
231:0	29-Jan-07 14:39	-01:52:00	α Cru	[25.07, 3.9, 0.3, 1/120, 0]	3	NaN	5.2	-53.38	330	0.91
231:0	29-Jan-07 14:39	-01:52:00	α Cru	[25.07, 3.9, 0.3, 1/120, 0]	3	11	12.89	-82.02	304	0.93
231:0	29-Jan-07 14:39	-01:52:00	α Cru	[25.07, 3.9, 0.3, 1/120, 0]	1	NaN	5.13	-49.37	334	0.91
231:0	29-Jan-07 14:39	-01:52:00	α Cru	[25.07, 3.9, 0.3, 1/120, 0]	2	NaN	5.49	-47.07	336	0.91
231:0	29-Jan-07 14:39	-01:52:00	α Cru	[25.07, 3.9, 0.3, 1/120, 0]	2	12	12.63	-82.02	304	0.93
231:0	29-Jan-07 14:39	-01:52:00	α Cru	[25.07, 3.9, 0.3, 1/120, 0]	1	12.5	12.33	-83.17	303	0.93
231:0	29-Jan-07 14:39	-01:52:00	α Cru	[25.07, 3.9, 0.3, 1/120, 0]	1	11.5	16.89	-107.23	279	0.96

Continued on next page

Table I.3: Verified velocity for January 2007. (continued)

Run #:Camera	UT	HA	Star	$[\zeta, \phi, \Delta m, \Delta r, \lvert d \rvert]$	Skip #	h	$\lvert V(h) \rvert$	b_{m}	β	$\varepsilon_{\lvert \vec{v} \rvert}$
231:0	29-Jan-07 14:39	-01:52:00	α Cru	[25.07, 3.9, 0.3, 1/120, 0]	1	7	19.5	-111.82	274	0.97
232:0	29-Jan-07 14:46	-01:45:00	α Cru	[24.43, 3.9, 0.3, 1/127, 2.5]	1	8.5	19.02	-107.23	277	0.97
232:0	29-Jan-07 14:46	-01:45:00	α Cru	[24.43, 3.9, 0.3, 1/127, 2.5]	1	0	0	180	199	0.96
232:0	29-Jan-07 14:46	-01:45:00	α Cru	[24.43, 3.9, 0.3, 1/127, 2.5]	2	14.5	11.37	-67.7	316	0.92
232:0	29-Jan-07 14:46	-01:45:00	α Cru	[24.43, 3.9, 0.3, 1/127, 2.5]	2	0	0	180	199	0.96
232:0	29-Jan-07 14:46	-01:45:00	α Cru	[24.43, 3.9, 0.3, 1/127, 2.5]	1	14	12.7	-68.27	315	0.92
232:0	29-Jan-07 14:46	-01:45:00	α Cru	[24.43, 3.9, 0.3, 1/127, 2.5]	3	0	0	180	199	0.96

Table I.4: Verified velocity for May 2007.

Run #:Camera	UT	HA	Star	$[\zeta, \phi, \Delta m, \Delta r, \lvert d \rvert]$	Skip #	h	$\lvert V(h) \rvert$	b_{m}	β	$\varepsilon_{\lvert \vec{v} \rvert}$
210:0	03-May-07 08:06	-02:13:00	α Cru	[26.99, 3.9, 0.3, 1/130, 2.3]	1	0	0	-155.27	232	1
210:0	03-May-07 08:06	-02:13:00	α Cru	[26.99, 3.9, 0.3, 1/130, 2.3]	1	10.7	24.87	-155.27	232	1
210:0	03-May-07 08:06	-02:13:00	α Cru	[26.99, 3.9, 0.3, 1/130, 2.3]	1	12.2	33.06	-151.83	236	1
210:0	03-May-07 08:06	-02:13:00	α Cru	[26.99, 3.9, 0.3, 1/130, 2.3]	1	0	4.19	-7.45	17	0.96
210:0	03-May-07 08:06	-02:13:00	α Cru	[26.99, 3.9, 0.3, 1/130, 2.3]	2	0	0.51	-155.27	232	1
210:0	03-May-07 08:06	-02:13:00	α Cru	[26.99, 3.9, 0.3, 1/130, 2.3]	2	0	3.7	-2.29	23	0.97
210:0	03-May-07 08:06	-02:13:00	α Cru	[26.99, 3.9, 0.3, 1/130, 2.3]	2	0	4.15	-131.78	258	0.99
210:0	03-May-07 08:06	-02:13:00	α Cru	[26.99, 3.9, 0.3, 1/130, 2.3]	3	0	0.5	-28.65	356	0.92
211:0	03-May-07 08:06	-02:13:00	α Cru	[26.99, 3.9, 0.3, 1/122, 0]	1	12	25.61	-157.08	230	1
211:0	03-May-07 08:06	-02:13:00	α Cru	[26.99, 3.9, 0.3, 1/122, 0]	1	12	33.6	-154.79	233	1
212:0	03-May-07 08:14	-02:07:00	α Cru	[26.46, 3.9, 0.3, 1/130, 2.3]	1	0	0	0	24	0.97
212:0	03-May-07 08:14	-02:07:00	α Cru	[26.46, 3.9, 0.3, 1/130, 2.3]	1	11.2	32.45	-151.83	234	1
212:0	03-May-07 08:14	-02:07:00	α Cru	[26.46, 3.9, 0.3, 1/130, 2.3]	2	0	0	0	24	0.97
212:0	03-May-07 08:14	-02:07:00	α Cru	[26.46, 3.9, 0.3, 1/130, 2.3]	3	0	0	0	24	0.97
213:0	03-May-07 08:14	-02:07:00	α Cru	[26.46, 3.9, 0.3, 1/122, 0]	1	12	33.07	-153.07	233	1
213:0	03-May-07 08:14	-02:07:00	α Cru	[26.46, 3.9, 0.3, 1/122, 0]	1	13	23.25	-141.61	246	1
213:0	03-May-07 08:14	-02:07:00	α Cru	[26.46, 3.9, 0.3, 1/122, 0]	1	6	12.3	-163.96	221	0.99
213:0	03-May-07 08:14	-02:07:00	α Cru	[26.46, 3.9, 0.3, 1/122, 0]	1	5	8.08	-148.49	238	1
213:0	03-May-07 08:14	-02:07:00	α Cru	[26.46, 3.9, 0.3, 1/122, 0]	1	0	4.71	-102.08	288	0.94
213:0	03-May-07 08:14	-02:07:00	α Cru	[26.46, 3.9, 0.3, 1/122, 0]	1	0	4.53	-12.7	11	0.95
213:0	03-May-07 08:14	-02:07:00	α Cru	[26.46, 3.9, 0.3, 1/122, 0]	2	5	8.27	-153.07	233	1
213:0	03-May-07 08:14	-02:07:00	α Cru	[26.46, 3.9, 0.3, 1/122, 0]	2	0	4.71	-102.08	288	0.94
213:0	03-May-07 08:14	-02:07:00	α Cru	[26.46, 3.9, 0.3, 1/122, 0]	2	6	12.83	-163.38	222	0.99
213:0	03-May-07 08:14	-02:07:00	α Cru	[26.46, 3.9, 0.3, 1/122, 0]	2	13	22.66	-144.48	243	1
213:0	03-May-07 08:14	-02:07:00	α Cru	[26.46, 3.9, 0.3, 1/122, 0]	2	0	4.75	-10.4	13	0.95
213:0	03-May-07 08:14	-02:07:00	α Cru	[26.46, 3.9, 0.3, 1/122, 0]	3	5	8.16	-154.79	231	1
213:0	03-May-07 08:14	-02:07:00	α Cru	[26.46, 3.9, 0.3, 1/122, 0]	3	0	4.71	-102.08	288	0.94

Continued on next page

Table I.4: Verified velocity for May 2007. (continued)

Run #:Camera	UT	HA	Star	$[\zeta, \phi, \Delta m, \Delta r, \lvert d \rvert]$	Skip #	h	$\lvert V(h) \rvert$	b_{m}	β	$\varepsilon_{\lvert \vec{v} \rvert}$
213:0	03-May-07 08:14	-02:07:00	α Cru	[26.46, 3.9, 0.3, 1/122, 0]	3	0	3.56	-14.99	0	0.93
213:0	03-May-07 08:14	-02:07:00	α Cru	[26.46, 3.9, 0.3, 1/122, 0]	4	0	4.44	-104.37	285	0.95
214:0	03-May-07 08:24	-01:57:00	α Cru	[25.54, 3.9, 0.3, 1/130, 2.3]	1	0	0.51	-155.84	228	1
214:0	03-May-07 08:24	-01:57:00	α Cru	[25.54, 3.9, 0.3, 1/130, 2.3]	1	10.2	32.18	-147.82	236	1
214:0	03-May-07 08:24	-01:57:00	α Cru	[25.54, 3.9, 0.3, 1/130, 2.3]	1	0	5.54	-179.91	202	0.97
214:0	03-May-07 08:24	-01:57:00	α Cru	[25.54, 3.9, 0.3, 1/130, 2.3]	2	0	0.25	-155.84	228	1
214:0	03-May-07 08:24	-01:57:00	α Cru	[25.54, 3.9, 0.3, 1/130, 2.3]	2	0	5.08	-2.29	19	0.96
214:0	03-May-07 08:24	-01:57:00	α Cru	[25.54, 3.9, 0.3, 1/130, 2.3]	3	0	0.17	-155.84	228	1
214:0	03-May-07 08:24	-01:57:00	α Cru	[25.54, 3.9, 0.3, 1/130, 2.3]	3	0	4.78	-178.76	203	0.97
214:0	03-May-07 08:24	-01:57:00	α Cru	[25.54, 3.9, 0.3, 1/130, 2.3]	4	0	0.13	-155.84	228	1
214:0	03-May-07 08:24	-01:57:00	α Cru	[25.54, 3.9, 0.3, 1/130, 2.3]	4	0	4.09	-9.17	12	0.95
215:0	03-May-07 08:24	-01:57:00	α Cru	[25.54, 3.9, 0.3, 1/122, 0]	1	11.5	32.84	-148.49	236	1
215:0	03-May-07 08:24	-01:57:00	α Cru	[25.54, 3.9, 0.3, 1/122, 0]	1	13	22.41	-144.48	240	1
215:0	03-May-07 08:24	-01:57:00	α Cru	[25.54, 3.9, 0.3, 1/122, 0]	1	6	12.23	-157.65	226	1
215:0	03-May-07 08:24	-01:57:00	α Cru	[25.54, 3.9, 0.3, 1/122, 0]	2	12	22.83	-149.63	234	1
215:0	03-May-07 08:24	-01:57:00	α Cru	[25.54, 3.9, 0.3, 1/122, 0]	2	5.5	11.18	-161.09	222	0.99
216:0	03-May-07 08:34	-01:47:00	α Cru	[24.66, 3.9, 0.3, 1/130, 2.3]	1	0	0.51	-155.84	225	0.99
216:0	03-May-07 08:34	-01:47:00	α Cru	[24.66, 3.9, 0.3, 1/130, 2.3]	1	10.2	32.57	-143.81	238	1
216:0	03-May-07 08:34	-01:47:00	α Cru	[24.66, 3.9, 0.3, 1/130, 2.3]	1	11.7	21.81	-137.51	245	1
216:0	03-May-07 08:34	-01:47:00	α Cru	[24.66, 3.9, 0.3, 1/130, 2.3]	2	0	0.51	-155.84	225	0.99
216:0	03-May-07 08:34	-01:47:00	α Cru	[24.66, 3.9, 0.3, 1/130, 2.3]	3	0	0.51	-155.84	225	0.99
216:0	03-May-07 08:34	-01:47:00	α Cru	[24.66, 3.9, 0.3, 1/130, 2.3]	4	0	0.51	-155.84	225	0.99
217:0	03-May-07 08:34	-01:47:00	α Cru	[24.66, 3.9, 0.3, 1/122, 0]	1	11.5	33.87	-144.48	238	1
217:0	03-May-07 08:34	-01:47:00	α Cru	[24.66, 3.9, 0.3, 1/122, 0]	1	13	22.74	-141.04	241	1
217:0	03-May-07 08:34	-01:47:00	α Cru	[24.66, 3.9, 0.3, 1/122, 0]	1	5	10.18	-150.21	231	1
217:0	03-May-07 08:34	-01:47:00	α Cru	[24.66, 3.9, 0.3, 1/122, 0]	2	5	10.71	-150.78	231	1
218:0	03-May-07 08:42	-01:39:00	α Cru	[23.97, 3.9, 0.3, 1/130, 2.3]	1	0	0.51	-155.84	223	0.99

Continued on next page

Table I.4: Verified velocity for May 2007. (continued)

Run #:Camera	UT	HA	Star	$[\zeta, \phi, \Delta m, \Delta r, \lvert d \rvert]$	Skip #	h	$\lvert V(h) \rvert$	b_{m}	β	$\varepsilon_{\lvert \vec{v} \rvert}$
218:0	03-May-07 08:42	-01:39:00	α Cru	[23.97, 3.9, 0.3, 1/130, 2.3]	1	10.2	32.83	-142.09	238	1
218:0	03-May-07 08:42	-01:39:00	α Cru	[23.97, 3.9, 0.3, 1/130, 2.3]	1	12.7	20.52	-139.8	241	1
218:0	03-May-07 08:42	-01:39:00	α Cru	[23.97, 3.9, 0.3, 1/130, 2.3]	1	5.7	14.16	-155.84	223	0.99
218:0	03-May-07 08:42	-01:39:00	α Cru	[23.97, 3.9, 0.3, 1/130, 2.3]	2	0	0.51	-155.84	223	0.99
218:0	03-May-07 08:42	-01:39:00	α Cru	[23.97, 3.9, 0.3, 1/130, 2.3]	2	12.2	20.34	-141.52	239	1
218:0	03-May-07 08:42	-01:39:00	α Cru	[23.97, 3.9, 0.3, 1/130, 2.3]	2	5.7	14.41	-155.84	223	0.99
218:0	03-May-07 08:42	-01:39:00	α Cru	[23.97, 3.9, 0.3, 1/130, 2.3]	3	0	0.34	-155.84	223	0.99
218:0	03-May-07 08:42	-01:39:00	α Cru	[23.97, 3.9, 0.3, 1/130, 2.3]	4	0	0.25	-155.84	223	0.99
219:0	03-May-07 08:42	-01:39:00	α Cru	[23.97, 3.9, 0.3, 1/122, 0]	1	11.5	34.19	-142.18	238	1
219:0	03-May-07 08:42	-01:39:00	α Cru	[23.97, 3.9, 0.3, 1/122, 0]	1	6.5	14.89	-157.65	221	0.99
219:0	03-May-07 08:42	-01:39:00	α Cru	[23.97, 3.9, 0.3, 1/122, 0]	1	12.5	20.71	-139.32	241	1
219:0	03-May-07 08:42	-01:39:00	α Cru	[23.97, 3.9, 0.3, 1/122, 0]	2	6.5	14.89	-157.65	221	0.99
219:0	03-May-07 08:42	-01:39:00	α Cru	[23.97, 3.9, 0.3, 1/122, 0]	2	12	21.11	-143.33	237	1
220:0	03-May-07 08:53	-01:28:00	α Cru	[23.07, 3.9, 0.3, 1/122, 0]	1	11.5	32.32	-143.9	234	1
220:0	03-May-07 08:53	-01:28:00	α Cru	[23.07, 3.9, 0.3, 1/122, 0]	1	15	22.59	-118.69	261	0.99
220:0	03-May-07 08:53	-01:28:00	α Cru	[23.07, 3.9, 0.3, 1/122, 0]	1	12	23.54	-151.35	226	0.99
220:0	03-May-07 08:53	-01:28:00	α Cru	[23.07, 3.9, 0.3, 1/122, 0]	1	1	5.2	-73.43	307	0.94
220:0	03-May-07 08:53	-01:28:00	α Cru	[23.07, 3.9, 0.3, 1/122, 0]	2	11.5	23.96	-154.79	222	0.99
220:0	03-May-07 08:53	-01:28:00	α Cru	[23.07, 3.9, 0.3, 1/122, 0]	2	12	20.77	-141.61	236	1
220:0	03-May-07 08:53	-01:28:00	α Cru	[23.07, 3.9, 0.3, 1/122, 0]	2	1	5.88	-75.72	305	0.94
221:0	03-May-07 09:04	-01:17:00	α Cru	[22.26, 3.9, 0.3, 1/122, 0]	1	11.5	25.52	-146.2	229	0.99
221:0	03-May-07 09:04	-01:17:00	α Cru	[22.26, 3.9, 0.3, 1/122, 0]	1	6	12.83	-151.93	223	0.99
221:0	03-May-07 09:04	-01:17:00	α Cru	[22.26, 3.9, 0.3, 1/122, 0]	2	0	5.88	-75.72	303	0.95
221:0	03-May-07 09:04	-01:17:00	α Cru	[22.26, 3.9, 0.3, 1/122, 0]	2	5.5	12.56	-151.93	223	0.99
221:0	03-May-07 09:04	-01:17:00	α Cru	[22.26, 3.9, 0.3, 1/122, 0]	2	12	23.57	-146.77	228	0.99
221:0	03-May-07 09:04	-01:17:00	α Cru	[22.26, 3.9, 0.3, 1/122, 0]	3	6.5	12.7	-150.21	225	0.99
221:0	03-May-07 09:04	-01:17:00	α Cru	[22.26, 3.9, 0.3, 1/122, 0]	4	0	6.22	-76.29	302	0.95

Continued on next page

Table I.4: Verified velocity for May 2007. (continued)

Run #:Camera	UT	HA	Star	$[\zeta, \phi, \Delta m, \Delta r, \lvert d \rvert]$	Skip #	h	$\lvert V(h) \rvert$	b_{m}	β	$\varepsilon_{\lvert \vec{v} \rvert}$
221:0	03-May-07 09:04	-01:17:00	α Cru	[22.26, 3.9, 0.3, 1/122, 0]	4	6	12.64	-149.06	226	0.99
222:0	03-May-07 09:18	-01:03:00	α Cru	[21.3, 3.9, 0.3, 1/122, 0]	1	11.5	21.89	-143.9	228	0.99
222:0	03-May-07 09:18	-01:03:00	α Cru	[21.3, 3.9, 0.3, 1/122, 0]	1	12	31.02	-138.17	234	1
222:0	03-May-07 09:18	-01:03:00	α Cru	[21.3, 3.9, 0.3, 1/122, 0]	1	13	18.57	-123.85	249	1
222:0	03-May-07 09:18	-01:03:00	α Cru	[21.3, 3.9, 0.3, 1/122, 0]	2	12	22.41	-144.48	227	0.99
222:0	03-May-07 09:18	-01:03:00	α Cru	[21.3, 3.9, 0.3, 1/122, 0]	2	12	17.09	-142.18	230	0.99
222:0	03-May-07 09:18	-01:03:00	α Cru	[21.3, 3.9, 0.3, 1/122, 0]	3	11.5	16.52	-142.76	229	0.99
223:0	03-May-07 09:33	-00:48:00	α Cru	[20.48, 3.9, 0.3, 1/110, 2.3]	1	0	0	-89.47	282	0.99
223:0	03-May-07 09:33	-00:48:00	α Cru	[20.48, 3.9, 0.3, 1/110, 2.3]	2	0	0	-89.47	282	0.99
223:0	03-May-07 09:33	-00:48:00	α Cru	[20.48, 3.9, 0.3, 1/110, 2.3]	3	0	0	-90.05	282	0.99
223:0	03-May-07 09:33	-00:48:00	α Cru	[20.48, 3.9, 0.3, 1/110, 2.3]	3	0	2.94	-8.69	1	0.94
223:0	03-May-07 09:33	-00:48:00	α Cru	[20.48, 3.9, 0.3, 1/110, 2.3]	4	0	0	-90.05	282	0.99
223:0	03-May-07 09:33	-00:48:00	α Cru	[20.48, 3.9, 0.3, 1/110, 2.3]	4	0	2.88	-6.97	2	0.94
230:0	03-May-07 10:32	00:11:00	α Cru	[19.38, 3.9, 0.3, 1/130, 2.3]	1	0	0	-89.95	268	1
230:0	03-May-07 10:32	00:11:00	α Cru	[19.38, 3.9, 0.3, 1/130, 2.3]	1	13.7	29.89	-98.55	259	1
230:0	03-May-07 10:32	00:11:00	α Cru	[19.38, 3.9, 0.3, 1/130, 2.3]	1	10.2	32.22	-112.87	244	0.99
230:0	03-May-07 10:32	00:11:00	α Cru	[19.38, 3.9, 0.3, 1/130, 2.3]	2	0	0.26	-154.7	203	0.95
230:0	03-May-07 10:32	00:11:00	α Cru	[19.38, 3.9, 0.3, 1/130, 2.3]	3	0	0.49	-108.29	249	0.99
230:0	03-May-07 10:32	00:11:00	α Cru	[19.38, 3.9, 0.3, 1/130, 2.3]	4	0	0.37	-108.29	249	0.99
231:0	03-May-07 10:32	00:11:00	α Cru	[19.38, 3.9, 0.3, 1/122, 0]	1	11	33.39	-112.96	244	0.99
231:0	03-May-07 10:32	00:11:00	α Cru	[19.38, 3.9, 0.3, 1/122, 0]	1	15	28.74	-98.64	259	1
231:0	03-May-07 10:32	00:11:00	α Cru	[19.38, 3.9, 0.3, 1/122, 0]	1	13	21.88	-95.2	262	1
231:0	03-May-07 10:32	00:11:00	α Cru	[19.38, 3.9, 0.3, 1/122, 0]	1	4.5	7.47	-126.14	230	0.97
231:0	03-May-07 10:32	00:11:00	α Cru	[19.38, 3.9, 0.3, 1/122, 0]	2	4.5	7.82	-122.13	235	0.98
231:0	03-May-07 10:32	00:11:00	α Cru	[19.38, 3.9, 0.3, 1/122, 0]	2	14	21.51	-111.25	246	0.99
231:0	03-May-07 10:32	00:11:00	α Cru	[19.38, 3.9, 0.3, 1/122, 0]	3	4.5	7.62	-127.29	229	0.97
231:0	03-May-07 10:32	00:11:00	α Cru	[19.38, 3.9, 0.3, 1/122, 0]	4	4.5	7.81	-127.86	229	0.97

Continued on next page

Table I.4: Verified velocity for May 2007. (continued)

Run #:Camera	UT	HA	Star	$[\zeta, \phi, \Delta m, \Delta r, \lvert d \rvert]$	Skip #	h	$\lvert V(h) \rvert$	b_{m}	β	$\varepsilon_{\lvert \vec{v} \rvert}$
232:0	03-May-07 10:46	00:25:00	α Cru	[19.66, 3.9, 0.3, 1/130, 2.3]	1	0	0.51	-155.27	0	0.94
232:0	03-May-07 10:46	00:25:00	α Cru	[19.66, 3.9, 0.3, 1/130, 2.3]	1	11.2	26.25	-115.74	238	0.98
232:0	03-May-07 10:46	00:25:00	α Cru	[19.66, 3.9, 0.3, 1/130, 2.3]	1	12.7	20.21	-93.97	260	0.99
232:0	03-May-07 10:46	00:25:00	α Cru	[19.66, 3.9, 0.3, 1/130, 2.3]	1	0	6.09	-155.27	0	0.94
232:0	03-May-07 10:46	00:25:00	α Cru	[19.66, 3.9, 0.3, 1/130, 2.3]	2	0	0.25	-155.27	0	0.94
232:0	03-May-07 10:46	00:25:00	α Cru	[19.66, 3.9, 0.3, 1/130, 2.3]	3	0	0.17	-155.27	0	0.94
233:0	03-May-07 10:46	00:25:00	α Cru	[19.66, 3.9, 0.3, 1/122, 0]	1	12	26.7	-118.69	235	0.97
233:0	03-May-07 10:46	00:25:00	α Cru	[19.66, 3.9, 0.3, 1/122, 0]	1	6	14.94	-126.14	228	0.97
233:0	03-May-07 10:46	00:25:00	α Cru	[19.66, 3.9, 0.3, 1/122, 0]	1	13	20.25	-94.06	260	0.99
233:0	03-May-07 10:46	00:25:00	α Cru	[19.66, 3.9, 0.3, 1/122, 0]	2	6	14.94	-126.14	228	0.97
233:0	03-May-07 10:46	00:25:00	α Cru	[19.66, 3.9, 0.3, 1/122, 0]	2	12	25.68	-118.69	235	0.97
233:0	03-May-07 10:46	00:25:00	α Cru	[19.66, 3.9, 0.3, 1/122, 0]	2	11	20.13	-93.48	261	1
233:0	03-May-07 10:46	00:25:00	α Cru	[19.66, 3.9, 0.3, 1/122, 0]	3	6	14.04	-123.85	230	0.97
234:0	03-May-07 11:00	00:39:00	α Cru	[20.12, 3.9, 0.3, 1/130, 2.3]	1	0	0	-89.95	261	0.99
234:0	03-May-07 11:00	00:39:00	α Cru	[20.12, 3.9, 0.3, 1/130, 2.3]	1	11.7	28.75	-104.85	246	0.98
234:0	03-May-07 11:00	00:39:00	α Cru	[20.12, 3.9, 0.3, 1/130, 2.3]	2	0	0.25	-155.27	197	0.94
234:0	03-May-07 11:00	00:39:00	α Cru	[20.12, 3.9, 0.3, 1/130, 2.3]	3	0	0.17	-155.27	197	0.94
235:0	03-May-07 11:00	00:39:00	α Cru	[20.2, 3.9, 0.3, 1/122, 0]	1	11	28.56	-111.25	240	0.97
235:0	03-May-07 11:00	00:39:00	α Cru	[20.2, 3.9, 0.3, 1/122, 0]	1	10	21.34	-120.41	230	0.96
235:0	03-May-07 11:00	00:39:00	α Cru	[20.2, 3.9, 0.3, 1/122, 0]	1	15	27.24	-86.03	265	0.99
235:0	03-May-07 11:00	00:39:00	α Cru	[20.2, 3.9, 0.3, 1/122, 0]	2	9.5	21.21	-122.13	229	0.96
235:0	03-May-07 11:00	00:39:00	α Cru	[20.2, 3.9, 0.3, 1/122, 0]	2	5	6.89	-135.31	216	0.95
240:0	03-May-07 11:13	00:52:00	α Cru	[20.71, 3.9, 0.3, 1/122, 0]	1	12	30.97	-100.93	247	0.97
240:0	03-May-07 11:13	00:52:00	α Cru	[20.71, 3.9, 0.3, 1/122, 0]	1	5	7.81	-116.4	232	0.96
240:0	03-May-07 11:13	00:52:00	α Cru	[20.71, 3.9, 0.3, 1/122, 0]	1	15	24.8	-87.75	261	0.99
240:0	03-May-07 11:13	00:52:00	α Cru	[20.71, 3.9, 0.3, 1/122, 0]	2	5	7.61	-120.99	227	0.95
240:0	03-May-07 11:13	00:52:00	α Cru	[20.71, 3.9, 0.3, 1/122, 0]	3	5	7.41	-122.13	226	0.95

Continued on next page

Table I.4: Verified velocity for May 2007. (continued)

Run #:Camera	UT	HA	Star	$[\zeta, \phi, \Delta m, \Delta r, \lvert d \rvert]$	Skip #	h	$\lvert V(h) \rvert$	b_{m}	β	$\varepsilon_{\lvert \vec{v} \rvert}$
241:0	03-May-07 11:27	01:05:00	α Cru	[21.49, 3.9, 0.3, 1/122, 0]	1	12.5	30.49	-94.63	251	0.97
241:0	03-May-07 11:27	01:05:00	α Cru	[21.49, 3.9, 0.3, 1/122, 0]	1	6.5	18.49	-118.69	227	0.95
241:0	03-May-07 11:27	01:05:00	α Cru	[21.49, 3.9, 0.3, 1/122, 0]	1	5	6.7	-107.23	238	0.96
241:0	03-May-07 11:27	01:05:00	α Cru	[21.49, 3.9, 0.3, 1/122, 0]	2	13.5	23.47	-104.37	241	0.96
241:0	03-May-07 11:27	01:05:00	α Cru	[21.49, 3.9, 0.3, 1/122, 0]	2	8	17.92	-122.13	224	0.94
246:0	03-May-07 11:57	01:36:00	α Cru	[23.68, 3.9, 0.3, 1/122, 0]	1	5.5	8.22	-118.69	221	0.92
246:0	03-May-07 11:57	01:36:00	α Cru	[23.68, 3.9, 0.3, 1/122, 0]	1	10	33.58	-89.47	249	0.95
246:0	03-May-07 11:57	01:36:00	α Cru	[23.68, 3.9, 0.3, 1/122, 0]	1	5.5	4.71	-102.08	237	0.94
246:0	03-May-07 11:57	01:36:00	α Cru	[23.68, 3.9, 0.3, 1/122, 0]	1	0	6.61	-93.48	245	0.95
246:0	03-May-07 11:57	01:36:00	α Cru	[23.68, 3.9, 0.3, 1/122, 0]	2	5.5	5.96	-116.4	223	0.92
246:0	03-May-07 11:57	01:36:00	α Cru	[23.68, 3.9, 0.3, 1/122, 0]	2	5.5	9.67	-120.41	219	0.92
246:0	03-May-07 11:57	01:36:00	α Cru	[23.68, 3.9, 0.3, 1/122, 0]	2	0	7.24	-78.59	260	0.97
246:0	03-May-07 11:57	01:36:00	α Cru	[23.68, 3.9, 0.3, 1/122, 0]	3	5.5	5.89	-116.4	223	0.92
246:0	03-May-07 11:57	01:36:00	α Cru	[23.68, 3.9, 0.3, 1/122, 0]	3	5	9.7	-122.7	217	0.92
246:0	03-May-07 11:57	01:36:00	α Cru	[23.68, 3.9, 0.3, 1/122, 0]	4	5	6.06	-117.55	222	0.92
246:0	03-May-07 11:57	01:36:00	α Cru	[23.68, 3.9, 0.3, 1/122, 0]	4	5	9.67	-123.28	217	0.92
246:0	03-May-07 11:57	01:36:00	α Cru	[23.68, 3.9, 0.3, 1/122, 0]	4	4.5	7.81	-127.86	0	0.93
246:0	03-May-07 11:57	01:36:00	α Cru	[23.68, 3.9, 0.3, 1/122, 0]	5	5	6	-117.55	222	0.92
246:0	03-May-07 11:57	01:36:00	α Cru	[23.68, 3.9, 0.3, 1/122, 0]	5	4	8.72	-120.99	219	0.92
246:0	03-May-07 11:57	01:36:00	α Cru	[23.68, 3.9, 0.3, 1/122, 0]	5	5	10.04	-121.56	218	0.92
246:0	03-May-07 11:57	01:36:00	α Cru	[23.68, 3.9, 0.3, 1/122, 0]	6	5	5.82	-118.69	221	0.92
246:0	03-May-07 11:57	01:36:00	α Cru	[23.68, 3.9, 0.3, 1/122, 0]	6	5	8.46	-123.28	217	0.92
250:0	03-May-07 12:47	00:12:00	α Cen	[17.07, 8.8, 1.36, 1/122, 0]	1	5.5	6.18	-118.69	238	0.98
250:0	03-May-07 12:47	00:12:00	α Cen	[17.07, 8.8, 1.36, 1/122, 0]	1	12	26.15	-110.67	246	0.99
250:0	03-May-07 12:47	00:12:00	α Cen	[17.07, 8.8, 1.36, 1/122, 0]	2	5.5	6.21	-115.83	241	0.99
250:0	03-May-07 12:47	00:12:00	α Cen	[17.07, 8.8, 1.36, 1/122, 0]	2	5.5	8.04	-134.74	222	0.97
250:0	03-May-07 12:47	00:12:00	α Cen	[17.07, 8.8, 1.36, 1/122, 0]	3	5	5.95	-114.68	242	0.99

Continued on next page

Table I.4: Verified velocity for May 2007. (continued)

Run #:Camera	UT	HA	Star	$[\zeta, \phi, \Delta m, \Delta r, \lvert d \rvert]$	Skip #	h	$\lvert V(h) \rvert$	b_{m}	β	$\varepsilon_{\lvert \vec{v} \rvert}$
250:0	03-May-07 12:47	00:12:00	α Cen	[17.07, 8.8, 1.36, 1/122, 0]	3	5.5	7.36	-130.15	227	0.98
250:0	03-May-07 12:47	00:12:00	α Cen	[17.07, 8.8, 1.36, 1/122, 0]	4	5	6.68	-114.11	243	0.99
250:0	03-May-07 12:47	00:12:00	α Cen	[17.07, 8.8, 1.36, 1/122, 0]	4	5	8.42	-126.71	230	0.98
251:0	03-May-07 13:03	00:29:00	α Cen	[17.52, 8.8, 1.36, 1/118, 2.3]	1	0	0.62	-35.61	320	0.98
251:0	03-May-07 13:03	00:29:00	α Cen	[17.52, 8.8, 1.36, 1/118, 2.3]	2	0	0.54	-161.09	0	0.96
251:0	03-May-07 13:03	00:29:00	α Cen	[17.52, 8.8, 1.36, 1/118, 2.3]	3	0	0.36	-161.09	0	0.96
251:0	03-May-07 13:03	00:29:00	α Cen	[17.52, 8.8, 1.36, 1/118, 2.3]	4	0	0.27	-161.09	0	0.96
251:0	03-May-07 13:03	00:29:00	α Cen	[17.52, 8.8, 1.36, 1/118, 2.3]	5	0	0.22	-161.09	0	0.96
252:0	03-May-07 13:17	00:43:00	α Cen	[18.15, 8.8, 1.36, 1/122, 0]	1	4	7.42	-90.05	261	0.99
252:0	03-May-07 13:17	00:43:00	α Cen	[18.15, 8.8, 1.36, 1/122, 0]	1	11	25.13	-104.94	246	0.98
252:0	03-May-07 13:17	00:43:00	α Cen	[18.15, 8.8, 1.36, 1/122, 0]	1	2	3.45	-64.84	287	1
252:0	03-May-07 13:17	00:43:00	α Cen	[18.15, 8.8, 1.36, 1/122, 0]	2	4.5	3.71	-57.96	294	1
252:0	03-May-07 13:17	00:43:00	α Cen	[18.15, 8.8, 1.36, 1/122, 0]	2	4.5	7.42	-90.05	261	0.99
252:0	03-May-07 13:17	00:43:00	α Cen	[18.15, 8.8, 1.36, 1/122, 0]	3	4.5	7.66	-91.19	260	0.99
252:0	03-May-07 13:17	00:43:00	α Cen	[18.15, 8.8, 1.36, 1/122, 0]	3	2	1.32	-60.25	292	1
260:0	03-May-07 13:39	01:05:00	α Cen	[19.57, 8.8, 1.36, 1/122, 0]	1	11	33.13	-94.06	252	0.97
260:0	03-May-07 13:39	01:05:00	α Cen	[19.57, 8.8, 1.36, 1/122, 0]	1	2	6.4	-117.55	229	0.95
260:0	03-May-07 13:39	01:05:00	α Cen	[19.57, 8.8, 1.36, 1/122, 0]	1	3	7.19	-82.02	264	0.99
260:0	03-May-07 13:39	01:05:00	α Cen	[19.57, 8.8, 1.36, 1/122, 0]	2	4	6.38	-119.84	226	0.95
260:0	03-May-07 13:39	01:05:00	α Cen	[19.57, 8.8, 1.36, 1/122, 0]	2	2	7.19	-82.02	264	0.99
261:0	03-May-07 13:39	01:05:00	α Cen	[19.57, 8.8, 1.36, 1/130, 2.3]	1	0	0	0	349	0.96
261:0	03-May-07 13:39	01:05:00	α Cen	[19.57, 8.8, 1.36, 1/130, 2.3]	2	0	0.28	-33.23	315	0.99
261:0	03-May-07 13:39	01:05:00	α Cen	[19.57, 8.8, 1.36, 1/130, 2.3]	2	0	2.36	-12.03	337	0.97
261:0	03-May-07 13:39	01:05:00	α Cen	[19.57, 8.8, 1.36, 1/130, 2.3]	3	0	0.18	-33.23	315	0.99
261:0	03-May-07 13:39	01:05:00	α Cen	[19.57, 8.8, 1.36, 1/130, 2.3]	3	0	2.41	-26.36	322	0.99
261:0	03-May-07 13:39	01:05:00	α Cen	[19.57, 8.8, 1.36, 1/130, 2.3]	4	0	0.14	-33.23	315	0.99
261:0	03-May-07 13:39	01:05:00	α Cen	[19.57, 8.8, 1.36, 1/130, 2.3]	4	0	2.65	-179.34	170	0.96

Continued on next page

Table I.4: Verified velocity for May 2007. (continued)

Run #:Camera	UT	HA	Star	$[\zeta, \phi, \Delta m, \Delta r, \lvert d \rvert]$	Skip #	h	$\lvert V(h) \rvert$	b_{m}	β	$\varepsilon_{\lvert \vec{v} \rvert}$
262:0	03-May-07 13:53	01:18:00	α Cen	[20.64, 8.8, 1.36, 1/122, 0]	1	4.5	6.36	-90.05	253	0.97
262:0	03-May-07 13:53	01:18:00	α Cen	[20.64, 8.8, 1.36, 1/122, 0]	1	12	30.73	-96.35	247	0.96
262:0	03-May-07 13:53	01:18:00	α Cen	[20.64, 8.8, 1.36, 1/122, 0]	2	4.5	5.47	-108.38	235	0.95
262:0	03-May-07 13:53	01:18:00	α Cen	[20.64, 8.8, 1.36, 1/122, 0]	2	2.5	2.72	-74.58	269	0.99
262:0	03-May-07 13:53	01:18:00	α Cen	[20.64, 8.8, 1.36, 1/122, 0]	2	5	6.04	-80.88	262	0.98
262:0	03-May-07 13:53	01:18:00	α Cen	[20.64, 8.8, 1.36, 1/122, 0]	2	5	5.21	-48.79	296	1
262:0	03-May-07 13:53	01:18:00	α Cen	[20.64, 8.8, 1.36, 1/122, 0]	3	5	5.22	-106.66	237	0.95
262:0	03-May-07 13:53	01:18:00	α Cen	[20.64, 8.8, 1.36, 1/122, 0]	3	2	3.29	-49.94	295	1
262:0	03-May-07 13:53	01:18:00	α Cen	[20.64, 8.8, 1.36, 1/122, 0]	4	5	5.05	-107.23	236	0.95
262:0	03-May-07 13:53	01:18:00	α Cen	[20.64, 8.8, 1.36, 1/122, 0]	4	5	5.84	-76.87	266	0.98
263:0	03-May-07 13:53	01:18:00	α Cen	[20.64, 8.8, 1.36, 1/130, 2.3]	1	0	0	0	347	0.96
263:0	03-May-07 13:53	01:18:00	α Cen	[20.64, 8.8, 1.36, 1/130, 2.3]	2	0	0.28	-33.23	312	1
263:0	03-May-07 13:53	01:18:00	α Cen	[20.64, 8.8, 1.36, 1/130, 2.3]	2	0.2	4.85	-48.13	297	1
263:0	03-May-07 13:53	01:18:00	α Cen	[20.64, 8.8, 1.36, 1/130, 2.3]	3	0	0.18	-33.23	312	1
263:0	03-May-07 13:53	01:18:00	α Cen	[20.64, 8.8, 1.36, 1/130, 2.3]	3	0.2	2.36	-78.5	265	0.98
263:0	03-May-07 13:53	01:18:00	α Cen	[20.64, 8.8, 1.36, 1/130, 2.3]	3	1	4.8	-50.42	294	1
263:0	03-May-07 13:53	01:18:00	α Cen	[20.64, 8.8, 1.36, 1/130, 2.3]	4	0	0	0	347	0.96
263:0	03-May-07 13:53	01:18:00	α Cen	[20.64, 8.8, 1.36, 1/130, 2.3]	5	0	0	0	347	0.96
263:0	03-May-07 13:53	01:18:00	α Cen	[20.64, 8.8, 1.36, 1/130, 2.3]	6	0	0	0	347	0.96
264:0	03-May-07 14:08	01:34:00	α Cen	[22.05, 8.8, 1.36, 1/122, 0]	1	5.5	11.82	-96.92	243	0.95
264:0	03-May-07 14:08	01:34:00	α Cen	[22.05, 8.8, 1.36, 1/122, 0]	1	13	22.09	-79.73	260	0.97
264:0	03-May-07 14:08	01:34:00	α Cen	[22.05, 8.8, 1.36, 1/122, 0]	1	12	33.19	-86.61	253	0.96
264:0	03-May-07 14:08	01:34:00	α Cen	[22.05, 8.8, 1.36, 1/122, 0]	2	5	7.42	-105.52	0	0.95
264:0	03-May-07 14:08	01:34:00	α Cen	[22.05, 8.8, 1.36, 1/122, 0]	2	5	6.47	-76.87	263	0.97
264:0	03-May-07 14:08	01:34:00	α Cen	[22.05, 8.8, 1.36, 1/122, 0]	2	5.5	11.56	-99.79	240	0.94
264:0	03-May-07 14:08	01:34:00	α Cen	[22.05, 8.8, 1.36, 1/122, 0]	3	5	6.8	-105.52	0	0.95
264:0	03-May-07 14:08	01:34:00	α Cen	[22.05, 8.8, 1.36, 1/122, 0]	3	5	6.67	-78.59	261	0.97

Continued on next page

Table I.4: Verified velocity for May 2007. (continued)

Run #:Camera	UT	HA	Star	$[\zeta, \phi, \Delta m, \Delta r, \lvert d \rvert]$	Skip #	h	$\lvert V(h) \rvert$	b_{m}	β	$\varepsilon_{\lvert \vec{v} \rvert}$
264:0	03-May-07 14:08	01:34:00	α Cen	[22.05, 8.8, 1.36, 1/122, 0]	3	5.5	11.4	-101.5	238	0.94
264:0	03-May-07 14:08	01:34:00	α Cen	[22.05, 8.8, 1.36, 1/122, 0]	3	5	12.65	-92.91	247	0.95
264:0	03-May-07 14:08	01:34:00	α Cen	[22.05, 8.8, 1.36, 1/122, 0]	4	5	6.7	-106.09	234	0.94
264:0	03-May-07 14:08	01:34:00	α Cen	[22.05, 8.8, 1.36, 1/122, 0]	4	5	6.62	-78.59	261	0.97
264:0	03-May-07 14:08	01:34:00	α Cen	[22.05, 8.8, 1.36, 1/122, 0]	5	5	6.64	-106.09	234	0.94
264:0	03-May-07 14:08	01:34:00	α Cen	[22.05, 8.8, 1.36, 1/122, 0]	5	5	6.68	-77.44	262	0.97
265:0	03-May-07 14:08	01:34:00	α Cen	[22.05, 8.8, 1.36, 1/130, 2.3]	1	0	0	0	344	0.97
265:0	03-May-07 14:08	01:34:00	α Cen	[22.05, 8.8, 1.36, 1/130, 2.3]	2	0	0.28	-33.23	309	1
265:0	03-May-07 14:08	01:34:00	α Cen	[22.05, 8.8, 1.36, 1/130, 2.3]	3	0	0	0	344	0.97
265:0	03-May-07 14:08	01:34:00	α Cen	[22.05, 8.8, 1.36, 1/130, 2.3]	3	0	1.08	-64.74	275	0.99
265:0	03-May-07 14:08	01:34:00	α Cen	[22.05, 8.8, 1.36, 1/130, 2.3]	4	0	0	0	344	0.97
265:0	03-May-07 14:08	01:34:00	α Cen	[22.05, 8.8, 1.36, 1/130, 2.3]	4	0	1.09	-83.65	256	0.96
265:0	03-May-07 14:08	01:34:00	α Cen	[22.05, 8.8, 1.36, 1/130, 2.3]	5	0	0	0	344	0.97
265:0	03-May-07 14:08	01:34:00	α Cen	[22.05, 8.8, 1.36, 1/130, 2.3]	5	0	0.87	-83.65	256	0.96
266:0	03-May-07 14:22	01:48:00	α Cen	[23.41, 8.8, 1.36, 1/122, 0]	1	5	5.83	-99.79	237	0.93
266:0	03-May-07 14:22	01:48:00	α Cen	[23.41, 8.8, 1.36, 1/122, 0]	1	4	6.89	-64.84	272	0.98
266:0	03-May-07 14:22	01:48:00	α Cen	[23.41, 8.8, 1.36, 1/122, 0]	2	5	6.08	-103.8	233	0.93
266:0	03-May-07 14:22	01:48:00	α Cen	[23.41, 8.8, 1.36, 1/122, 0]	2	5	6.65	-70.57	266	0.97
266:0	03-May-07 14:22	01:48:00	α Cen	[23.41, 8.8, 1.36, 1/122, 0]	3	5	5.9	-106.09	231	0.93
266:0	03-May-07 14:22	01:48:00	α Cen	[23.41, 8.8, 1.36, 1/122, 0]	3	4.5	7.61	-75.15	261	0.96
266:0	03-May-07 14:22	01:48:00	α Cen	[23.41, 8.8, 1.36, 1/122, 0]	4	0	1.25	-168.54	173	0.95
266:0	03-May-07 14:22	01:48:00	α Cen	[23.41, 8.8, 1.36, 1/122, 0]	4	5	6.04	-106.66	231	0.93
266:0	03-May-07 14:22	01:48:00	α Cen	[23.41, 8.8, 1.36, 1/122, 0]	4	5	7.7	-75.15	261	0.96
266:0	03-May-07 14:22	01:48:00	α Cen	[23.41, 8.8, 1.36, 1/122, 0]	5	0	1.3	-170.26	171	0.96
266:0	03-May-07 14:22	01:48:00	α Cen	[23.41, 8.8, 1.36, 1/122, 0]	5	5	5.92	-107.23	230	0.93
267:0	03-May-07 14:22	01:48:00	α Cen	[23.41, 8.8, 1.36, 1/130, 2.3]	1	0	0	0	341	0.97
267:0	03-May-07 14:22	01:48:00	α Cen	[23.41, 8.8, 1.36, 1/130, 2.3]	2	0	0	0	341	0.97

Continued on next page

Table I.4: Verified velocity for May 2007. (continued)

Run #:Camera	UT	HA	Star	$[\zeta, \phi, \Delta m, \Delta r, \lvert d \rvert]$	Skip #	h	$\lvert V(h) \rvert$	b_{m}	β	$\varepsilon_{\lvert \vec{v} \rvert}$
267:0	03-May-07 14:22	01:48:00	α Cen	[23.41, 8.8, 1.36, 1/130, 2.3]	2	0	3.33	-25.78	314	1
267:0	03-May-07 14:22	01:48:00	α Cen	[23.41, 8.8, 1.36, 1/130, 2.3]	3	0	0	0	341	0.97
267:0	03-May-07 14:22	01:48:00	α Cen	[23.41, 8.8, 1.36, 1/130, 2.3]	3	0	3.24	-18.33	322	0.99
267:0	03-May-07 14:22	01:48:00	α Cen	[23.41, 8.8, 1.36, 1/130, 2.3]	4	0	0	0	341	0.97
267:0	03-May-07 14:22	01:48:00	α Cen	[23.41, 8.8, 1.36, 1/130, 2.3]	4	0	1.53	-169.6	172	0.96
267:0	03-May-07 14:22	01:48:00	α Cen	[23.41, 8.8, 1.36, 1/130, 2.3]	4	0	2.16	-16.04	324	0.99
267:0	03-May-07 14:22	01:48:00	α Cen	[23.41, 8.8, 1.36, 1/130, 2.3]	5	0	0	0	341	0.97
267:0	03-May-07 14:22	01:48:00	α Cen	[23.41, 8.8, 1.36, 1/130, 2.3]	5	0	1.39	-175.9	165	0.97
267:0	03-May-07 14:22	01:48:00	α Cen	[23.41, 8.8, 1.36, 1/130, 2.3]	6	0	0	0	341	0.97
267:0	03-May-07 14:22	01:48:00	α Cen	[23.41, 8.8, 1.36, 1/130, 2.3]	6	0	1.39	-175.9	165	0.97
268:0	03-May-07 14:37	02:03:00	α Cen	[25, 8.8, 1.36, 1/122, 0]	1	5	6.05	-80.88	252	0.94
268:0	03-May-07 14:37	02:03:00	α Cen	[25, 8.8, 1.36, 1/122, 0]	1	11	28.6	-87.18	246	0.93
268:0	03-May-07 14:37	02:03:00	α Cen	[25, 8.8, 1.36, 1/122, 0]	1	5	7.12	-33.9	301	1
268:0	03-May-07 14:37	02:03:00	α Cen	[25, 8.8, 1.36, 1/122, 0]	2	5	6	-87.75	0	0.94
268:0	03-May-07 14:37	02:03:00	α Cen	[25, 8.8, 1.36, 1/122, 0]	2	5	6.9	-64.84	268	0.97
268:0	03-May-07 14:37	02:03:00	α Cen	[25, 8.8, 1.36, 1/122, 0]	3	5	5.88	-87.18	246	0.93
268:0	03-May-07 14:37	02:03:00	α Cen	[25, 8.8, 1.36, 1/122, 0]	3	5	6.9	-64.84	268	0.97
268:0	03-May-07 14:37	02:03:00	α Cen	[25, 8.8, 1.36, 1/122, 0]	4	5	5.83	-86.61	247	0.93
268:0	03-May-07 14:37	02:03:00	α Cen	[25, 8.8, 1.36, 1/122, 0]	4	5	6.9	-64.84	268	0.97
268:0	03-May-07 14:37	02:03:00	α Cen	[25, 8.8, 1.36, 1/122, 0]	4	0	1.49	-8.11	329	0.99
268:0	03-May-07 14:37	02:03:00	α Cen	[25, 8.8, 1.36, 1/122, 0]	5	5	5.72	-87.18	246	0.93
268:0	03-May-07 14:37	02:03:00	α Cen	[25, 8.8, 1.36, 1/122, 0]	5	5	6.86	-59.68	273	0.97
268:0	03-May-07 14:37	02:03:00	α Cen	[25, 8.8, 1.36, 1/122, 0]	5	5	6.49	-68.85	264	0.96
268:0	03-May-07 14:37	02:03:00	α Cen	[25, 8.8, 1.36, 1/122, 0]	5	0	1.48	-70.57	262	0.96
268:0	03-May-07 14:37	02:03:00	α Cen	[25, 8.8, 1.36, 1/122, 0]	6	5	5.59	-86.03	247	0.93
268:0	03-May-07 14:37	02:03:00	α Cen	[25, 8.8, 1.36, 1/122, 0]	6	5	7.08	-62.54	270	0.97
269:0	03-May-07 14:37	02:03:00	α Cen	[25, 8.8, 1.36, 1/130, 2.3]	1	0	0	0	338	0.98

Continued on next page

Table I.4: Verified velocity for May 2007. (continued)

Run #:Camera	UT	HA	Star	$[\zeta, \phi, \Delta m, \Delta r, \lvert d \rvert]$	Skip #	h	$\lvert V(h) \rvert$	b_{m}	β	$\varepsilon_{\lvert \vec{v} \rvert}$
269:0	03-May-07 14:37	02:03:00	α Cen	[25, 8.8, 1.36, 1/130, 2.3]	1	0	5.58	-41.83	293	1
269:0	03-May-07 14:37	02:03:00	α Cen	[25, 8.8, 1.36, 1/130, 2.3]	2	0	0	0	338	0.98
269:0	03-May-07 14:37	02:03:00	α Cen	[25, 8.8, 1.36, 1/130, 2.3]	2	0.2	5.53	-37.82	297	1
269:0	03-May-07 14:37	02:03:00	α Cen	[25, 8.8, 1.36, 1/130, 2.3]	2	0	1.44	-16.04	321	0.99
269:0	03-May-07 14:37	02:03:00	α Cen	[25, 8.8, 1.36, 1/130, 2.3]	2	0.3	3.33	-25.78	310	1
269:0	03-May-07 14:37	02:03:00	α Cen	[25, 8.8, 1.36, 1/130, 2.3]	3	0	0	0	338	0.98
269:0	03-May-07 14:37	02:03:00	α Cen	[25, 8.8, 1.36, 1/130, 2.3]	3	0	1.75	-14.32	323	0.99
269:0	03-May-07 14:37	02:03:00	α Cen	[25, 8.8, 1.36, 1/130, 2.3]	3	0	3.32	-13.18	324	0.99
269:0	03-May-07 14:37	02:03:00	α Cen	[25, 8.8, 1.36, 1/130, 2.3]	3	0.3	5.18	-39.53	295	1
269:0	03-May-07 14:37	02:03:00	α Cen	[25, 8.8, 1.36, 1/130, 2.3]	4	0	0	0	338	0.98
269:0	03-May-07 14:37	02:03:00	α Cen	[25, 8.8, 1.36, 1/130, 2.3]	4	0	1.52	-8.59	329	0.99
269:0	03-May-07 14:37	02:03:00	α Cen	[25, 8.8, 1.36, 1/130, 2.3]	4	0.3	3.03	-8.59	329	0.99
269:0	03-May-07 14:37	02:03:00	α Cen	[25, 8.8, 1.36, 1/130, 2.3]	4	0.3	5.93	-34.95	300	1
269:0	03-May-07 14:37	02:03:00	α Cen	[25, 8.8, 1.36, 1/130, 2.3]	5	0	0	0	338	0.98
269:0	03-May-07 14:37	02:03:00	α Cen	[25, 8.8, 1.36, 1/130, 2.3]	5	0	1.47	-20.05	316	1
269:0	03-May-07 14:37	02:03:00	α Cen	[25, 8.8, 1.36, 1/130, 2.3]	5	0	3.1	-10.89	326	0.99
270:0	03-May-07 15:12	02:38:00	α Cen	[28.87, 8.8, 1.36, 1/122, 0]	1	4	6.17	-50.51	274	0.96
270:0	03-May-07 15:12	02:38:00	α Cen	[28.87, 8.8, 1.36, 1/122, 0]	1	11	20.33	-74.58	250	0.91
270:0	03-May-07 15:12	02:38:00	α Cen	[28.87, 8.8, 1.36, 1/122, 0]	1	11	21.81	-74.58	250	0.91
270:0	03-May-07 15:12	02:38:00	α Cen	[28.87, 8.8, 1.36, 1/122, 0]	2	4	5.48	-47.65	277	0.96
270:0	03-May-07 15:12	02:38:00	α Cen	[28.87, 8.8, 1.36, 1/122, 0]	3	4	5.25	-46.5	279	0.97
270:0	03-May-07 15:12	02:38:00	α Cen	[28.87, 8.8, 1.36, 1/122, 0]	3	4	6.7	-62.54	262	0.93
270:0	03-May-07 15:12	02:38:00	α Cen	[28.87, 8.8, 1.36, 1/122, 0]	4	4	5.34	-48.22	277	0.96
270:0	03-May-07 15:12	02:38:00	α Cen	[28.87, 8.8, 1.36, 1/122, 0]	4	4.5	6.91	-62.54	262	0.93
270:0	03-May-07 15:12	02:38:00	α Cen	[28.87, 8.8, 1.36, 1/122, 0]	5	4	5	-48.22	277	0.96
270:0	03-May-07 15:12	02:38:00	α Cen	[28.87, 8.8, 1.36, 1/122, 0]	5	4	5.84	-47.65	277	0.96
270:0	03-May-07 15:12	02:38:00	α Cen	[28.87, 8.8, 1.36, 1/122, 0]	6	4	5.06	-47.07	278	0.97

Continued on next page

Table I.4: Verified velocity for May 2007. (continued)

Run #:Camera	UT	HA	Star	$[\zeta, \phi, \Delta m, \Delta r, \lvert d \rvert]$	Skip #	h	$\lvert V(h) \rvert$	b_{m}	β	$\varepsilon_{\lvert \vec{v} \rvert}$
270:0	03-May-07 15:12	02:38:00	α Cen	[28.87, 8.8, 1.36, 1/122, 0]	6	4	5.8	-48.22	277	0.96
271:0	03-May-07 15:25	02:51:00	α Cen	[30.34, 8.8, 1.36, 1/122, 0]	1	1.5	4.43	-176.56	152	0.98
271:0	03-May-07 15:25	02:51:00	α Cen	[30.34, 8.8, 1.36, 1/122, 0]	1	4	6.73	-48.79	273	0.95
271:0	03-May-07 15:25	02:51:00	α Cen	[30.34, 8.8, 1.36, 1/122, 0]	1	13	20.17	-68.85	253	0.9
271:0	03-May-07 15:25	02:51:00	α Cen	[30.34, 8.8, 1.36, 1/122, 0]	1	12.5	28.68	-61.4	260	0.92
271:0	03-May-07 15:25	02:51:00	α Cen	[30.34, 8.8, 1.36, 1/122, 0]	2	1.5	4.2	-174.27	154	0.98
271:0	03-May-07 15:25	02:51:00	α Cen	[30.34, 8.8, 1.36, 1/122, 0]	2	4.3	6.63	-45.35	276	0.96
271:0	03-May-07 15:25	02:51:00	α Cen	[30.34, 8.8, 1.36, 1/122, 0]	2	12.5	20.43	-69.42	252	0.9
271:0	03-May-07 15:25	02:51:00	α Cen	[30.34, 8.8, 1.36, 1/122, 0]	3	1.5	4.05	-166.25	163	0.96
271:0	03-May-07 15:25	02:51:00	α Cen	[30.34, 8.8, 1.36, 1/122, 0]	3	1.5	4.1	-178.28	150	0.99
271:0	03-May-07 15:25	02:51:00	α Cen	[30.34, 8.8, 1.36, 1/122, 0]	3	4.5	6.6	-44.21	278	0.96
271:0	03-May-07 15:25	02:51:00	α Cen	[30.34, 8.8, 1.36, 1/122, 0]	4	1.5	4.19	-165.68	164	0.96
271:0	03-May-07 15:25	02:51:00	α Cen	[30.34, 8.8, 1.36, 1/122, 0]	4	1.5	4.18	-177.71	150	0.99
271:0	03-May-07 15:25	02:51:00	α Cen	[30.34, 8.8, 1.36, 1/122, 0]	4	4.5	5.72	-44.78	277	0.96
271:0	03-May-07 15:25	02:51:00	α Cen	[30.34, 8.8, 1.36, 1/122, 0]	4	4.5	6.92	-44.78	277	0.96
271:0	03-May-07 15:25	02:51:00	α Cen	[30.34, 8.8, 1.36, 1/122, 0]	5	4.5	5.69	-46.5	275	0.96
271:0	03-May-07 15:25	02:51:00	α Cen	[30.34, 8.8, 1.36, 1/122, 0]	5	4.5	6.85	-44.21	278	0.96
272:0	03-May-07 15:39	03:05:00	α Cen	[32.07, 8.8, 1.36, 1/110, 2.3]	1	0	0	180	145	0.99
272:0	03-May-07 15:39	03:05:00	α Cen	[32.07, 8.8, 1.36, 1/110, 2.3]	1	0	3.41	-16.13	306	1
272:0	03-May-07 15:39	03:05:00	α Cen	[32.07, 8.8, 1.36, 1/110, 2.3]	2	0	0	180	145	0.99
272:0	03-May-07 15:39	03:05:00	α Cen	[32.07, 8.8, 1.36, 1/110, 2.3]	2	0	3.58	-33.32	286	0.97
272:0	03-May-07 15:39	03:05:00	α Cen	[32.07, 8.8, 1.36, 1/110, 2.3]	3	0	0	180	145	0.99
301:0	05-May-07 09:21	-00:52:00	α Cru	[20.64, 3.9, 0.3, 1/122, 0]	1	11	29.6	-101.5	271	0.99
301:0	05-May-07 09:21	-00:52:00	α Cru	[20.64, 3.9, 0.3, 1/122, 0]	1	12	30.04	-86.61	286	0.98
302:0	05-May-07 09:21	-00:52:00	α Cru	[20.64, 3.9, 0.3, 1/130, 2.3]	1	0	6.1	-40.68	331	0.94
302:0	05-May-07 09:21	-00:52:00	α Cru	[20.64, 3.9, 0.3, 1/130, 2.3]	2	0	6.61	-42.97	329	0.94
302:0	05-May-07 09:21	-00:52:00	α Cru	[20.64, 3.9, 0.3, 1/130, 2.3]	2	0	0.25	-155.27	214	0.98

Continued on next page

Table I.4: Verified velocity for May 2007. (continued)

Run #:Camera	UT	HA	Star	$[\zeta, \phi, \Delta m, \Delta r, \lvert d \rvert]$	Skip #	h	$\lvert V(h) \rvert$	b_{m}	β	$\varepsilon_{\lvert \vec{v} \rvert}$
302:0	05-May-07 09:21	-00:52:00	α Cru	[20.64, 3.9, 0.3, 1/130, 2.3]	3	0	0.17	-155.27	214	0.98
302:0	05-May-07 09:21	-00:52:00	α Cru	[20.64, 3.9, 0.3, 1/130, 2.3]	3	0	6.85	-42.4	330	0.94
302:0	05-May-07 09:21	-00:52:00	α Cru	[20.64, 3.9, 0.3, 1/130, 2.3]	4	0	0.13	-40.68	331	0.94
303:0	05-May-07 09:34	-00:39:00	α Cru	[20.04, 3.9, 0.3, 1/122, 0]	1	10	27	-92.34	277	0.99
303:0	05-May-07 09:34	-00:39:00	α Cru	[20.04, 3.9, 0.3, 1/122, 0]	1	14	24.32	-99.21	270	1
303:0	05-May-07 09:34	-00:39:00	α Cru	[20.04, 3.9, 0.3, 1/122, 0]	1	15	16.96	-75.15	295	0.98
310:0	05-May-07 10:30	-01:56:00	α Cen	[24.11, 8.7, 1.36, 1/122, 0]	1	2	22.63	-106.66	280	0.96
310:0	05-May-07 10:30	-01:56:00	α Cen	[24.11, 8.7, 1.36, 1/122, 0]	1	3	19.22	-114.11	272	0.97
310:0	05-May-07 10:30	-01:56:00	α Cen	[24.11, 8.7, 1.36, 1/122, 0]	2	2	22.13	-106.66	280	0.96
310:0	05-May-07 10:30	-01:56:00	α Cen	[24.11, 8.7, 1.36, 1/122, 0]	2	2	17.06	-113.54	273	0.97
310:0	05-May-07 10:30	-01:56:00	α Cen	[24.11, 8.7, 1.36, 1/122, 0]	2	2	7.1	-99.79	287	0.95
310:0	05-May-07 10:30	-01:56:00	α Cen	[24.11, 8.7, 1.36, 1/122, 0]	3	2	6.76	-92.91	293	0.94
311:0	05-May-07 10:30	-01:56:00	α Cen	[24.11, 8.7, 1.36, 1/130, 2.3]	1	0	20.64	-108.29	278	0.96
311:0	05-May-07 10:30	-01:56:00	α Cen	[24.11, 8.7, 1.36, 1/130, 2.3]	1	0	9.25	-78.5	307	0.92
311:0	05-May-07 10:30	-01:56:00	α Cen	[24.11, 8.7, 1.36, 1/130, 2.3]	2	0	19.6	-104.85	282	0.95
311:0	05-May-07 10:30	-01:56:00	α Cen	[24.11, 8.7, 1.36, 1/130, 2.3]	2	0	8.13	-75.06	310	0.92
311:0	05-May-07 10:30	-01:56:00	α Cen	[24.11, 8.7, 1.36, 1/130, 2.3]	2	0	0	0	22	0.98
311:0	05-May-07 10:30	-01:56:00	α Cen	[24.11, 8.7, 1.36, 1/130, 2.3]	3	0	0.24	-130.63	255	0.99
311:0	05-May-07 10:30	-01:56:00	α Cen	[24.11, 8.7, 1.36, 1/130, 2.3]	3	0	9.43	-75.63	310	0.92
311:0	05-May-07 10:30	-01:56:00	α Cen	[24.11, 8.7, 1.36, 1/130, 2.3]	4	0	0.23	-89.95	296	0.93
312:0	05-May-07 10:43	-01:43:00	α Cen	[22.78, 8.7, 1.36, 1/122, 0]	1	3.5	20.26	-108.38	275	0.97
312:0	05-May-07 10:43	-01:43:00	α Cen	[22.78, 8.7, 1.36, 1/122, 0]	2	3.5	21.05	-116.4	267	0.98
312:0	05-May-07 10:43	-01:43:00	α Cen	[22.78, 8.7, 1.36, 1/122, 0]	2	3	18.64	-106.09	277	0.97
313:0	05-May-07 10:55	-01:31:00	α Cen	[21.69, 8.7, 1.36, 1/122, 0]	1	3.5	20.82	-104.94	276	0.98
313:0	05-May-07 10:55	-01:31:00	α Cen	[21.69, 8.7, 1.36, 1/122, 0]	2	3.5	20.39	-113.54	267	0.99
313:0	05-May-07 10:55	-01:31:00	α Cen	[21.69, 8.7, 1.36, 1/122, 0]	2	3.5	20.03	-104.37	276	0.98
401:0	06-May-07 07:58	-02:11:00	α Cru	[26.82, 3.9, 0.3, 1/122, 0]	1	13	21.1	-92.91	297	0.92

Continued on next page

Table I.4: Verified velocity for May 2007. (continued)

Run #:Camera	UT	HA	Star	$[\zeta, \phi, \Delta m, \Delta r, \lvert d \rvert]$	Skip #	h	$\lvert V(h) \rvert$	b_{m}	β	$\varepsilon_{\lvert \vec{v} \rvert}$
401:0	06-May-07 07:58	-02:11:00	α Cru	[26.82, 3.9, 0.3, 1/122, 0]	1	18	18.51	-123.85	266	0.98
401:0	06-May-07 07:58	-02:11:00	α Cru	[26.82, 3.9, 0.3, 1/122, 0]	2	18	8.23	-143.33	245	1
401:0	06-May-07 07:58	-02:11:00	α Cru	[26.82, 3.9, 0.3, 1/122, 0]	2	15	21.09	-108.38	282	0.95
401:0	06-May-07 07:58	-02:11:00	α Cru	[26.82, 3.9, 0.3, 1/122, 0]	3	0	3.91	-157.08	230	1
401:0	06-May-07 07:58	-02:11:00	α Cru	[26.82, 3.9, 0.3, 1/122, 0]	3	18	9.57	-147.34	240	1
401:0	06-May-07 07:58	-02:11:00	α Cru	[26.82, 3.9, 0.3, 1/122, 0]	4	0	4.27	-157.08	230	1
402:0	06-May-07 08:12	-01:57:00	α Cru	[25.52, 3.9, 0.3, 1/122, 0]	1	19.5	17.04	-119.27	268	0.98
402:0	06-May-07 08:12	-01:57:00	α Cru	[25.52, 3.9, 0.3, 1/122, 0]	1	18	24.69	-79.73	307	0.92
402:0	06-May-07 08:12	-01:57:00	α Cru	[25.52, 3.9, 0.3, 1/122, 0]	1	0	8.5	-50.51	0	0.93
402:0	06-May-07 08:12	-01:57:00	α Cru	[25.52, 3.9, 0.3, 1/122, 0]	2	0	8.26	-44.78	339	0.91
402:0	06-May-07 08:12	-01:57:00	α Cru	[25.52, 3.9, 0.3, 1/122, 0]	2	18	14.22	-125	261	0.99
402:0	06-May-07 08:12	-01:57:00	α Cru	[25.52, 3.9, 0.3, 1/122, 0]	3	0	8.33	-43.64	340	0.91
403:0	06-May-07 08:28	-01:41:00	α Cru	[24.07, 3.9, 0.3, 1/110, 2.3]	1	0	0	180	199	0.96
403:0	06-May-07 08:28	-01:41:00	α Cru	[24.07, 3.9, 0.3, 1/110, 2.3]	1	0	19.94	-75.72	0	0.93
403:0	06-May-07 08:28	-01:41:00	α Cru	[24.07, 3.9, 0.3, 1/110, 2.3]	2	0	19.2	-75.15	308	0.93
403:0	06-May-07 08:28	-01:41:00	α Cru	[24.07, 3.9, 0.3, 1/110, 2.3]	2	0	0	180	199	0.96
403:0	06-May-07 08:28	-01:41:00	α Cru	[24.07, 3.9, 0.3, 1/110, 2.3]	3	0	0	180	199	0.96
404:0	06-May-07 08:40	-01:29:00	α Cru	[23.11, 3.9, 0.3, 1/110, 2.3]	1	0	0	180	196	0.96
404:0	06-May-07 08:40	-01:29:00	α Cru	[23.11, 3.9, 0.3, 1/110, 2.3]	1	0	18.32	-69.42	311	0.93
404:0	06-May-07 08:40	-01:29:00	α Cru	[23.11, 3.9, 0.3, 1/110, 2.3]	2	0	0	180	196	0.96
404:0	06-May-07 08:40	-01:29:00	α Cru	[23.11, 3.9, 0.3, 1/110, 2.3]	2	0	19.01	-66.55	314	0.93
404:0	06-May-07 08:40	-01:29:00	α Cru	[23.11, 3.9, 0.3, 1/110, 2.3]	3	0	0	180	196	0.96
405:0	06-May-07 08:52	-01:17:00	α Cru	[22.22, 3.9, 0.3, 1/122, 0]	1	0	21.16	-72.28	306	0.95
405:0	06-May-07 08:52	-01:17:00	α Cru	[22.22, 3.9, 0.3, 1/122, 0]	1	17	17.36	-101.5	277	0.98
405:0	06-May-07 08:52	-01:17:00	α Cru	[22.22, 3.9, 0.3, 1/122, 0]	1	15	32.87	-104.94	273	0.99
405:0	06-May-07 08:52	-01:17:00	α Cru	[22.22, 3.9, 0.3, 1/122, 0]	2	0	19.15	-65.98	312	0.94
405:0	06-May-07 08:52	-01:17:00	α Cru	[22.22, 3.9, 0.3, 1/122, 0]	2	15	14.91	-105.52	272	0.99

Continued on next page

Table I.4: Verified velocity for May 2007. (continued)

Run #:Camera	UT	HA	Star	$[\zeta, \phi, \Delta m, \Delta r, \lvert d \rvert]$	Skip #	h	$\lvert V(h) \rvert$	b_{m}	β	$\varepsilon_{\lvert \vec{v} \rvert}$
406:0	06-May-07 09:21	-00:48:00	α Cru	[20.47, 3.9, 0.3, 1/122, 0]	1	0	10.1	-39.05	332	0.94
406:0	06-May-07 09:21	-00:48:00	α Cru	[20.47, 3.9, 0.3, 1/122, 0]	1	15	22.8	-64.84	307	0.96
406:0	06-May-07 09:21	-00:48:00	α Cru	[20.47, 3.9, 0.3, 1/122, 0]	1	16	15.89	-95.2	276	0.99
406:0	06-May-07 09:21	-00:48:00	α Cru	[20.47, 3.9, 0.3, 1/122, 0]	2	17	15.01	-99.21	272	0.99
406:0	06-May-07 09:21	-00:48:00	α Cru	[20.47, 3.9, 0.3, 1/122, 0]	2	0	8.05	-37.33	334	0.94
406:0	06-May-07 09:21	-00:48:00	α Cru	[20.47, 3.9, 0.3, 1/122, 0]	3	17	13.37	-98.64	273	0.99
406:0	06-May-07 09:21	-00:48:00	α Cru	[20.47, 3.9, 0.3, 1/122, 0]	3	0	0.89	-157.08	211	0.97
407:0	06-May-07 09:33	-00:36:00	α Cru	[19.96, 3.9, 0.3, 1/122, 0]	1	13	13.99	-91.76	277	0.99
407:0	06-May-07 09:33	-00:36:00	α Cru	[19.96, 3.9, 0.3, 1/122, 0]	2	15	17.32	-90.62	278	0.99
408:0	06-May-07 09:47	-00:23:00	α Cru	[19.56, 3.9, 0.3, 1/122, 0]	1	17	16.53	-90.05	276	1
408:0	06-May-07 09:47	-00:23:00	α Cru	[19.56, 3.9, 0.3, 1/122, 0]	1	13	23.16	-57.96	309	0.97
408:0	06-May-07 09:47	-00:23:00	α Cru	[19.56, 3.9, 0.3, 1/122, 0]	1	10	37.84	-92.34	273	1
408:0	06-May-07 09:47	-00:23:00	α Cru	[19.56, 3.9, 0.3, 1/122, 0]	2	18	16.85	-92.34	273	1
408:0	06-May-07 09:47	-00:23:00	α Cru	[19.56, 3.9, 0.3, 1/122, 0]	2	11	23.64	-60.82	306	0.97
409:0	06-May-07 09:59	-00:10:00	α Cru	[19.34, 3.9, 0.3, 1/122, 0]	2	2	18.41	-68.27	296	0.99
409:0	06-May-07 09:59	-00:10:00	α Cru	[19.34, 3.9, 0.3, 1/122, 0]	1	18	11.24	-92.34	270	1
409:0	06-May-07 09:59	-00:10:00	α Cru	[19.34, 3.9, 0.3, 1/122, 0]	1	15	23.89	-84.32	279	1
409:0	06-May-07 09:59	-00:10:00	α Cru	[19.34, 3.9, 0.3, 1/122, 0]	1	2	19.05	-67.13	297	0.99
409:0	06-May-07 09:59	-00:10:00	α Cru	[19.34, 3.9, 0.3, 1/122, 0]	1	2	25.67	-59.11	305	0.98
409:0	06-May-07 09:59	-00:10:00	α Cru	[19.34, 3.9, 0.3, 1/122, 0]	2	17.5	9.86	-92.91	270	1
409:0	06-May-07 09:59	-00:10:00	α Cru	[19.34, 3.9, 0.3, 1/122, 0]	3	18	11.09	-90.62	272	1
409:0	06-May-07 09:59	-00:10:00	α Cru	[19.34, 3.9, 0.3, 1/122, 0]	3	2	2.1	-31.03	333	0.95
409:0	06-May-07 09:59	-00:10:00	α Cru	[19.34, 3.9, 0.3, 1/122, 0]	4	2	1.91	-33.32	331	0.96
410:0	06-May-07 10:12	00:01:00	α Cru	[19.28, 3.9, 0.3, 1/110, 2.3]	1	0	0	180	180	0.94
410:0	06-May-07 10:12	00:01:00	α Cru	[19.28, 3.9, 0.3, 1/110, 2.3]	1	2.7	19.61	-50.51	311	0.98
410:0	06-May-07 10:12	00:01:00	α Cru	[19.28, 3.9, 0.3, 1/110, 2.3]	2	0	0.63	-64.84	297	0.99
410:0	06-May-07 10:12	00:01:00	α Cru	[19.28, 3.9, 0.3, 1/110, 2.3]	2	2.7	17.44	-45.35	317	0.97

Continued on next page

Table I.4: Verified velocity for May 2007. (continued)

Run #:Camera	UT	HA	Star	$[\zeta, \phi, \Delta m, \Delta r, \lvert d \rvert]$	Skip #	h	$\lvert V(h) \rvert$	b_{m}	β	$\varepsilon_{\lvert \vec{v} \rvert}$
410:0	06-May-07 10:12	00:01:00	α Cru	[19.28, 3.9, 0.3, 1/110, 2.3]	3	0	0	180	180	0.94
410:0	06-May-07 10:12	00:01:00	α Cru	[19.28, 3.9, 0.3, 1/110, 2.3]	4	0	0	180	180	0.94
410:0	06-May-07 10:12	00:01:00	α Cru	[19.28, 3.9, 0.3, 1/110, 2.3]	4	0	2.6	-51.08	311	0.98
410:0	06-May-07 10:12	00:01:00	α Cru	[19.28, 3.9, 0.3, 1/110, 2.3]	5	0	0	180	180	0.94
410:0	06-May-07 10:12	00:01:00	α Cru	[19.28, 3.9, 0.3, 1/110, 2.3]	5	0	2.88	-49.94	312	0.98
410:0	06-May-07 10:12	00:01:00	α Cru	[19.28, 3.9, 0.3, 1/110, 2.3]	6	0	0	180	180	0.94
410:0	06-May-07 10:12	00:01:00	α Cru	[19.28, 3.9, 0.3, 1/110, 2.3]	6	0	2.38	-36.76	325	0.96
411:0	06-May-07 10:24	00:14:00	α Cru	[19.39, 3.9, 0.3, 1/110, 2.3]	1	2.7	20.87	-49.37	310	0.98
411:0	06-May-07 10:24	00:14:00	α Cru	[19.39, 3.9, 0.3, 1/110, 2.3]	1	0	1.46	-41.92	317	0.98
411:0	06-May-07 10:24	00:14:00	α Cru	[19.39, 3.9, 0.3, 1/110, 2.3]	2	2.7	19.6	-48.22	311	0.98
411:0	06-May-07 10:24	00:14:00	α Cru	[19.39, 3.9, 0.3, 1/110, 2.3]	2	0	0.3	-155.94	201	0.95
411:0	06-May-07 10:24	00:14:00	α Cru	[19.39, 3.9, 0.3, 1/110, 2.3]	3	0	0.2	-155.94	201	0.95
411:0	06-May-07 10:24	00:14:00	α Cru	[19.39, 3.9, 0.3, 1/110, 2.3]	4	0	0	180	178	0.95
411:0	06-May-07 10:24	00:14:00	α Cru	[19.39, 3.9, 0.3, 1/110, 2.3]	5	0	0	180	178	0.95
415:0	06-May-07 11:06	00:54:00	α Cru	[20.87, 3.9, 0.3, 1/122, 0]	1	2.7	25.18	-45.35	305	0.99
415:0	06-May-07 11:06	00:54:00	α Cru	[20.87, 3.9, 0.3, 1/122, 0]	1	18	10.47	-76.29	272	1
415:0	06-May-07 11:06	00:54:00	α Cru	[20.87, 3.9, 0.3, 1/122, 0]	2	2.7	22.69	-43.64	307	0.99
420:0	06-May-07 11:23	-00:59:00	α Cen	[19.08, 8.7, 1.36, 1/122, 0]	1	2	25.09	-70.57	303	0.96
420:0	06-May-07 11:23	-00:59:00	α Cen	[19.08, 8.7, 1.36, 1/122, 0]	1	15	32.3	-100.36	273	0.99
422:0	06-May-07 11:36	-00:46:00	α Cen	[18.3, 8.7, 1.36, 1/122, 0]	1	2	23.61	-68.27	303	0.97
422:0	06-May-07 11:36	-00:46:00	α Cen	[18.3, 8.7, 1.36, 1/122, 0]	1	3.5	25.29	-86.61	284	0.99
422:0	06-May-07 11:36	-00:46:00	α Cen	[18.3, 8.7, 1.36, 1/122, 0]	1	14	30.2	-106.09	264	1
430:0	06-May-07 11:56	-00:27:00	α Cen	[17.4, 8.7, 1.36, 1/110, 2.3]	1	0	0	180	185	0.96
430:0	06-May-07 11:56	-00:27:00	α Cen	[17.4, 8.7, 1.36, 1/110, 2.3]	1	0	13.32	-80.31	287	0.99
430:0	06-May-07 11:56	-00:27:00	α Cen	[17.4, 8.7, 1.36, 1/110, 2.3]	1	2.2	18.71	-61.97	305	0.98
430:0	06-May-07 11:56	-00:27:00	α Cen	[17.4, 8.7, 1.36, 1/110, 2.3]	2	0	13.44	-83.17	284	0.99
430:0	06-May-07 11:56	-00:27:00	α Cen	[17.4, 8.7, 1.36, 1/110, 2.3]	2	1.2	18.3	-59.68	308	0.97

Continued on next page

Table I.4: Verified velocity for May 2007. (continued)

Run #:Camera	UT	HA	Star	$[\zeta, \phi, \Delta m, \Delta r, \lvert d \rvert]$	Skip #	h	$\lvert V(h) \rvert$	b_{m}	β	$\varepsilon_{\lvert \vec{v} \rvert}$
430:0	06-May-07 11:56	-00:27:00	α Cen	[17.4, 8.7, 1.36, 1/110, 2.3]	2	0	0	180	185	0.96
430:0	06-May-07 11:56	-00:27:00	α Cen	[17.4, 8.7, 1.36, 1/110, 2.3]	3	0	0	180	185	0.96
430:0	06-May-07 11:56	-00:27:00	α Cen	[17.4, 8.7, 1.36, 1/110, 2.3]	3	0	12.4	-80.88	286	0.99

Table I.5: Verified velocity for June 2007.

Run #:Camera	UT	HA	Star	$[\zeta, \phi, \Delta m, \Delta r, \lvert d \rvert]$	Skip #	h	$\lvert V(h) \rvert$	b_{m}	β	$\varepsilon_{\lvert \vec{v} \rvert}$
1:0	31-May-07 09:51	-00:52:00	α Cen	[18.69, 8.7, 1.36, 1/122, 0]	1	10	22.21	-65.41	307	0.96
1:0	31-May-07 09:51	-00:52:00	α Cen	[18.69, 8.7, 1.36, 1/122, 0]	1	3	25.19	-75.15	297	0.97
1:0	31-May-07 09:51	-00:52:00	α Cen	[18.69, 8.7, 1.36, 1/122, 0]	1	16	13.77	-69.42	303	0.97
1:0	31-May-07 09:51	-00:52:00	α Cen	[18.69, 8.7, 1.36, 1/122, 0]	1	14	17.47	-91.76	280	0.99
1:0	31-May-07 09:51	-00:52:00	α Cen	[18.69, 8.7, 1.36, 1/122, 0]	2	3	20.4	-61.4	311	0.96
1:0	31-May-07 09:51	-00:52:00	α Cen	[18.69, 8.7, 1.36, 1/122, 0]	2	3	22.4	-67.7	305	0.97
1:0	31-May-07 09:51	-00:52:00	α Cen	[18.69, 8.7, 1.36, 1/122, 0]	2	16	12.8	-67.7	305	0.97
1:0	31-May-07 09:51	-00:52:00	α Cen	[18.69, 8.7, 1.36, 1/122, 0]	2	14	17.67	-93.48	279	0.99
1:0	31-May-07 09:51	-00:52:00	α Cen	[18.69, 8.7, 1.36, 1/122, 0]	3	16	12.46	-68.27	304	0.97
2:0	31-May-07 09:58	-00:46:00	α Cen	[18.33, 8.7, 1.36, 1/122, 0]	1	2.5	20.68	-64.84	306	0.97
2:0	31-May-07 09:58	-00:46:00	α Cen	[18.33, 8.7, 1.36, 1/122, 0]	1	10	25.57	-67.7	303	0.97
2:0	31-May-07 09:58	-00:46:00	α Cen	[18.33, 8.7, 1.36, 1/122, 0]	1	14	18.48	-83.74	287	0.98
2:0	31-May-07 09:58	-00:46:00	α Cen	[18.33, 8.7, 1.36, 1/122, 0]	2	5	22.16	-55.1	316	0.96
2:0	31-May-07 09:58	-00:46:00	α Cen	[18.33, 8.7, 1.36, 1/122, 0]	2	2.5	19.69	-64.84	306	0.97
2:0	31-May-07 09:58	-00:46:00	α Cen	[18.33, 8.7, 1.36, 1/122, 0]	2	15	19.2	-83.74	287	0.98
3:0	31-May-07 10:05	-00:38:00	α Cen	[17.97, 8.7, 1.36, 1/122, 0]	1	10.5	24.59	-68.85	301	0.98
3:0	31-May-07 10:05	-00:38:00	α Cen	[17.97, 8.7, 1.36, 1/122, 0]	1	2.5	19.48	-57.96	311	0.97
3:0	31-May-07 10:05	-00:38:00	α Cen	[17.97, 8.7, 1.36, 1/122, 0]	1	15	19.08	-85.46	284	0.99
3:0	31-May-07 10:05	-00:38:00	α Cen	[17.97, 8.7, 1.36, 1/122, 0]	2	11	23.89	-71.71	298	0.98
3:0	31-May-07 10:05	-00:38:00	α Cen	[17.97, 8.7, 1.36, 1/122, 0]	2	3	19.75	-57.96	311	0.97
3:0	31-May-07 10:05	-00:38:00	α Cen	[17.97, 8.7, 1.36, 1/122, 0]	2	15	20.12	-87.75	281	0.99
10:0	31-May-07 10:21	-00:22:00	α Cen	[17.36, 8.7, 1.36, 1/122, 0]	1	11.5	22.01	-57.39	309	0.98
11:0	31-May-07 10:21	-00:22:00	α Cen	[17.36, 8.7, 1.36, 1/132, 1.9]	1	0.1	0	0	4	0.96
20:0	31-May-07 10:50	00:05:00	α Cen	[17.06, 8.7, 1.36, 1/132, 1.9]	1	0	0	0	0	0.96
20:0	31-May-07 10:50	00:05:00	α Cen	[17.06, 8.7, 1.36, 1/132, 1.9]	1	3	23.24	-48.13	313	0.98
20:0	31-May-07 10:50	00:05:00	α Cen	[17.06, 8.7, 1.36, 1/132, 1.9]	1	0	5.93	-46.41	314	0.98
20:0	31-May-07 10:50	00:05:00	α Cen	[17.06, 8.7, 1.36, 1/132, 1.9]	1	6	16.92	-72.77	287	1

Continued on next page

Table I.5: Verified velocity for June 2007. (continued)

Run #:Camera	UT	HA	Star	$[\zeta, \phi, \Delta m, \Delta r, \lvert d \rvert]$	Skip #	h	$\lvert V(h) \rvert$	b_{m}	β	$\varepsilon_{\lvert \vec{v} \rvert}$
20:0	31-May-07 10:50	00:05:00	α Cen	[17.06, 8.7, 1.36, 1/132, 1.9]	2	0	0	0	0	0.96
20:0	31-May-07 10:50	00:05:00	α Cen	[17.06, 8.7, 1.36, 1/132, 1.9]	2	0	6.52	-45.84	315	0.98
20:0	31-May-07 10:50	00:05:00	α Cen	[17.06, 8.7, 1.36, 1/132, 1.9]	2	5.11	18.29	-72.77	287	1
20:0	31-May-07 10:50	00:05:00	α Cen	[17.06, 8.7, 1.36, 1/132, 1.9]	2	3	22.14	-49.85	311	0.98
20:0	31-May-07 10:50	00:05:00	α Cen	[17.06, 8.7, 1.36, 1/132, 1.9]	3	0	0	0	0	0.96
20:0	31-May-07 10:50	00:05:00	α Cen	[17.06, 8.7, 1.36, 1/132, 1.9]	4	0	0	0	0	0.96
21:0	31-May-07 10:50	00:05:00	α Cen	[17.06, 8.7, 1.36, 1/122, 0]	1	11	23.06	-51.66	309	0.98
21:0	31-May-07 10:50	00:05:00	α Cen	[17.06, 8.7, 1.36, 1/122, 0]	1	15	17.8	-74	286	1
21:0	31-May-07 10:50	00:05:00	α Cen	[17.06, 8.7, 1.36, 1/122, 0]	2	10	23.06	-51.66	309	0.98
21:0	31-May-07 10:50	00:05:00	α Cen	[17.06, 8.7, 1.36, 1/122, 0]	2	15	20.52	-74	286	1
100:0	01-Jun-07 06:31	-01:56:00	α Cru	[25.38, 3.9, 0.3, 1/132, 1.9]	1	11.5	19.88	-91.1	296	0.93
100:0	01-Jun-07 06:31	-01:56:00	α Cru	[25.38, 3.9, 0.3, 1/132, 1.9]	1	1.5	8.09	-89.95	297	0.93
100:0	01-Jun-07 06:31	-01:56:00	α Cru	[25.38, 3.9, 0.3, 1/132, 1.9]	2	0	0	-89.95	297	0.93
100:0	01-Jun-07 06:31	-01:56:00	α Cru	[25.38, 3.9, 0.3, 1/132, 1.9]	2	0.5	3.81	-111.15	276	0.97
100:0	01-Jun-07 06:31	-01:56:00	α Cru	[25.38, 3.9, 0.3, 1/132, 1.9]	2	1	7.98	-88.24	299	0.93
100:0	01-Jun-07 06:31	-01:56:00	α Cru	[25.38, 3.9, 0.3, 1/132, 1.9]	2	11.5	18.85	-85.94	301	0.93
100:0	01-Jun-07 06:31	-01:56:00	α Cru	[25.38, 3.9, 0.3, 1/132, 1.9]	2	4.1	20.36	-93.97	293	0.94
100:0	01-Jun-07 06:31	-01:56:00	α Cru	[25.38, 3.9, 0.3, 1/132, 1.9]	2	13.1	15.72	-117.46	269	0.98
100:0	01-Jun-07 06:31	-01:56:00	α Cru	[25.38, 3.9, 0.3, 1/132, 1.9]	3	0	0	-89.95	297	0.93
100:0	01-Jun-07 06:31	-01:56:00	α Cru	[25.38, 3.9, 0.3, 1/132, 1.9]	3	1	3.75	-113.45	274	0.97
100:0	01-Jun-07 06:31	-01:56:00	α Cru	[25.38, 3.9, 0.3, 1/132, 1.9]	3	1.5	8.4	-88.81	298	0.93
100:0	01-Jun-07 06:31	-01:56:00	α Cru	[25.38, 3.9, 0.3, 1/132, 1.9]	4	0	0	-89.95	297	0.93
100:0	01-Jun-07 06:31	-01:56:00	α Cru	[25.38, 3.9, 0.3, 1/132, 1.9]	4	1	3.63	-114.02	273	0.97
100:0	01-Jun-07 06:31	-01:56:00	α Cru	[25.38, 3.9, 0.3, 1/132, 1.9]	4	1.6	8.27	-88.24	299	0.93
100:0	01-Jun-07 06:31	-01:56:00	α Cru	[25.38, 3.9, 0.3, 1/132, 1.9]	4	0.5	1.81	-108.29	279	0.96
100:0	01-Jun-07 06:31	-01:56:00	α Cru	[25.38, 3.9, 0.3, 1/132, 1.9]	5	0	0	-89.95	297	0.93
100:0	01-Jun-07 06:31	-01:56:00	α Cru	[25.38, 3.9, 0.3, 1/132, 1.9]	5	0	1.83	-101.41	286	0.95

Continued on next page

Table I.5: Verified velocity for June 2007. (continued)

Run #:Camera	UT	HA	Star	$[\zeta, \phi, \Delta m, \Delta r, \lvert d \rvert]$	Skip #	h	$\lvert V(h) \rvert$	b_{m}	β	$\varepsilon_{\lvert \vec{v} \rvert}$
100:0	01-Jun-07 06:31	-01:56:00	α Cru	[25.38, 3.9, 0.3, 1/132, 1.9]	5	0.5	3.77	-112.3	275	0.97
100:0	01-Jun-07 06:31	-01:56:00	α Cru	[25.38, 3.9, 0.3, 1/132, 1.9]	5	1.5	8	-88.81	298	0.93
100:0	01-Jun-07 06:31	-01:56:00	α Cru	[25.38, 3.9, 0.3, 1/132, 1.9]	6	0	0	-89.95	297	0.93
100:0	01-Jun-07 06:31	-01:56:00	α Cru	[25.38, 3.9, 0.3, 1/132, 1.9]	6	0	1.81	-111.73	275	0.97
100:0	01-Jun-07 06:31	-01:56:00	α Cru	[25.38, 3.9, 0.3, 1/132, 1.9]	6	0.5	3.93	-112.3	275	0.97
101:0	01-Jun-07 06:31	-01:56:00	α Cru	[25.38, 3.9, 0.3, 1/122, 0]	1	1	4.11	-118.69	268	0.98
101:0	01-Jun-07 06:31	-01:56:00	α Cru	[25.38, 3.9, 0.3, 1/122, 0]	1	1	8.39	-90.05	297	0.93
101:0	01-Jun-07 06:31	-01:56:00	α Cru	[25.38, 3.9, 0.3, 1/122, 0]	1	11	19.8	-91.19	296	0.93
101:0	01-Jun-07 06:31	-01:56:00	α Cru	[25.38, 3.9, 0.3, 1/122, 0]	2	1	3.91	-116.4	270	0.98
101:0	01-Jun-07 06:31	-01:56:00	α Cru	[25.38, 3.9, 0.3, 1/122, 0]	2	1	8.3	-88.33	299	0.93
101:0	01-Jun-07 06:31	-01:56:00	α Cru	[25.38, 3.9, 0.3, 1/122, 0]	2	12	19.3	-87.75	299	0.93
101:0	01-Jun-07 06:31	-01:56:00	α Cru	[25.38, 3.9, 0.3, 1/122, 0]	3	1	3.84	-115.26	272	0.97
101:0	01-Jun-07 06:31	-01:56:00	α Cru	[25.38, 3.9, 0.3, 1/122, 0]	3	1	8.39	-90.05	297	0.93
101:0	01-Jun-07 06:31	-01:56:00	α Cru	[25.38, 3.9, 0.3, 1/122, 0]	4	1	3.81	-114.68	272	0.97
101:0	01-Jun-07 06:31	-01:56:00	α Cru	[25.38, 3.9, 0.3, 1/122, 0]	4	1	8.34	-88.33	299	0.93
102:0	01-Jun-07 06:37	-01:50:00	α Cru	[24.88, 3.9, 0.3, 1/132, 1.9]	1	11.1	19.64	-91.1	295	0.94
102:0	01-Jun-07 06:37	-01:50:00	α Cru	[24.88, 3.9, 0.3, 1/132, 1.9]	1	0	5.34	-80.21	305	0.93
102:0	01-Jun-07 06:37	-01:50:00	α Cru	[24.88, 3.9, 0.3, 1/132, 1.9]	2	0	0	0	20	0.96
102:0	01-Jun-07 06:37	-01:50:00	α Cru	[24.88, 3.9, 0.3, 1/132, 1.9]	2	0.5	4.78	-81.93	303	0.93
102:0	01-Jun-07 06:37	-01:50:00	α Cru	[24.88, 3.9, 0.3, 1/132, 1.9]	2	12.1	19.87	-87.66	298	0.93
102:0	01-Jun-07 06:37	-01:50:00	α Cru	[24.88, 3.9, 0.3, 1/132, 1.9]	3	0	0	0	20	0.96
102:0	01-Jun-07 06:37	-01:50:00	α Cru	[24.88, 3.9, 0.3, 1/132, 1.9]	3	0.5	4.25	-81.93	303	0.93
102:0	01-Jun-07 06:37	-01:50:00	α Cru	[24.88, 3.9, 0.3, 1/132, 1.9]	4	0	0	0	20	0.96
102:0	01-Jun-07 06:37	-01:50:00	α Cru	[24.88, 3.9, 0.3, 1/132, 1.9]	4	0.5	4.26	-82.51	303	0.93
103:0	01-Jun-07 06:37	-01:50:00	α Cru	[24.88, 3.9, 0.3, 1/122, 0]	1	1	4.2	-90.05	296	0.94
103:0	01-Jun-07 06:37	-01:50:00	α Cru	[24.88, 3.9, 0.3, 1/122, 0]	1	11	20.79	-88.9	297	0.94
103:0	01-Jun-07 06:37	-01:50:00	α Cru	[24.88, 3.9, 0.3, 1/122, 0]	2	1	4.1	-86.61	299	0.93

Continued on next page

Table I.5: Verified velocity for June 2007. (continued)

Run #:Camera	UT	HA	Star	$[\zeta, \phi, \Delta m, \Delta r, \lvert d \rvert]$	Skip #	h	$\lvert V(h) \rvert$	b_{m}	β	$\varepsilon_{\lvert \vec{v} \rvert}$
103:0	01-Jun-07 06:37	-01:50:00	α Cru	[24.88, 3.9, 0.3, 1/122, 0]	2	11.5	20.39	-90.62	295	0.94
103:0	01-Jun-07 06:37	-01:50:00	α Cru	[24.88, 3.9, 0.3, 1/122, 0]	3	1	4.2	-90.05	296	0.94
103:0	01-Jun-07 06:37	-01:50:00	α Cru	[24.88, 3.9, 0.3, 1/122, 0]	4	1	4.25	-91.76	294	0.94
104:0	01-Jun-07 06:45	-01:42:00	α Cru	[24.14, 3.9, 0.3, 1/132, 1.9]	1	0	0	0	19	0.96
104:0	01-Jun-07 06:45	-01:42:00	α Cru	[24.14, 3.9, 0.3, 1/132, 1.9]	1	0.5	8.34	-87.09	297	0.94
104:0	01-Jun-07 06:45	-01:42:00	α Cru	[24.14, 3.9, 0.3, 1/132, 1.9]	1	13.1	22.95	-88.81	295	0.94
104:0	01-Jun-07 06:45	-01:42:00	α Cru	[24.14, 3.9, 0.3, 1/132, 1.9]	2	0	0	0	19	0.96
104:0	01-Jun-07 06:45	-01:42:00	α Cru	[24.14, 3.9, 0.3, 1/132, 1.9]	2	0.5	8.53	-89.95	294	0.95
104:0	01-Jun-07 06:45	-01:42:00	α Cru	[24.14, 3.9, 0.3, 1/132, 1.9]	3	0	0	0	19	0.96
104:0	01-Jun-07 06:45	-01:42:00	α Cru	[24.14, 3.9, 0.3, 1/132, 1.9]	3	0	4.69	-84.22	300	0.94
104:0	01-Jun-07 06:45	-01:42:00	α Cru	[24.14, 3.9, 0.3, 1/132, 1.9]	3	0.5	9.27	-88.81	295	0.94
104:0	01-Jun-07 06:45	-01:42:00	α Cru	[24.14, 3.9, 0.3, 1/132, 1.9]	4	0	0	0	19	0.96
104:0	01-Jun-07 06:45	-01:42:00	α Cru	[24.14, 3.9, 0.3, 1/132, 1.9]	4	0	4.17	-87.09	297	0.94
104:0	01-Jun-07 06:45	-01:42:00	α Cru	[24.14, 3.9, 0.3, 1/132, 1.9]	4	1	9.34	-88.81	295	0.94
104:0	01-Jun-07 06:45	-01:42:00	α Cru	[24.14, 3.9, 0.3, 1/132, 1.9]	5	0	0	0	19	0.96
105:0	01-Jun-07 06:54	-01:33:00	α Cru	[23.43, 3.9, 0.3, 1/122, 0]	1	11	20.13	-83.17	299	0.94
105:0	01-Jun-07 06:54	-01:33:00	α Cru	[23.43, 3.9, 0.3, 1/122, 0]	2	12	19.37	-82.02	300	0.94
105:0	01-Jun-07 06:54	-01:33:00	α Cru	[23.43, 3.9, 0.3, 1/122, 0]	2	11.5	24.14	-98.07	284	0.97
106:0	01-Jun-07 07:09	-01:18:00	α Cru	[22.24, 3.9, 0.3, 1/132, 1.9]	1	0	0	0	14	0.95
106:0	01-Jun-07 07:09	-01:18:00	α Cru	[22.24, 3.9, 0.3, 1/132, 1.9]	1	0	10.6	-84.8	294	0.96
106:0	01-Jun-07 07:09	-01:18:00	α Cru	[22.24, 3.9, 0.3, 1/132, 1.9]	1	13	25.19	-87.66	291	0.96
106:0	01-Jun-07 07:09	-01:18:00	α Cru	[22.24, 3.9, 0.3, 1/132, 1.9]	2	0	0	0	14	0.95
106:0	01-Jun-07 07:09	-01:18:00	α Cru	[22.24, 3.9, 0.3, 1/132, 1.9]	2	0	5.91	-85.37	293	0.96
106:0	01-Jun-07 07:09	-01:18:00	α Cru	[22.24, 3.9, 0.3, 1/132, 1.9]	2	0	11.12	-84.22	294	0.96
106:0	01-Jun-07 07:09	-01:18:00	α Cru	[22.24, 3.9, 0.3, 1/132, 1.9]	2	13.5	26.2	-87.66	291	0.96
106:0	01-Jun-07 07:09	-01:18:00	α Cru	[22.24, 3.9, 0.3, 1/132, 1.9]	3	0	0	0	14	0.95
106:0	01-Jun-07 07:09	-01:18:00	α Cru	[22.24, 3.9, 0.3, 1/132, 1.9]	3	0	5.91	-85.37	293	0.96

Continued on next page

Table I.5: Verified velocity for June 2007. (continued)

Run #:Camera	UT	HA	Star	$[\zeta, \phi, \Delta m, \Delta r, \lvert d \rvert]$	Skip #	h	$\lvert V(h) \rvert$	b_{m}	β	$\varepsilon_{\lvert \vec{v} \rvert}$
106:0	01-Jun-07 07:09	-01:18:00	α Cru	[22.24, 3.9, 0.3, 1/132, 1.9]	3	0	11.3	-83.65	295	0.96
106:0	01-Jun-07 07:09	-01:18:00	α Cru	[22.24, 3.9, 0.3, 1/132, 1.9]	4	0	0	0	14	0.95
107:0	01-Jun-07 07:09	-01:18:00	α Cru	[22.24, 3.9, 0.3, 1/122, 0]	1	1	5.41	-84.89	294	0.96
107:0	01-Jun-07 07:09	-01:18:00	α Cru	[22.24, 3.9, 0.3, 1/122, 0]	1	11	19.87	-80.31	298	0.96
107:0	01-Jun-07 07:09	-01:18:00	α Cru	[22.24, 3.9, 0.3, 1/122, 0]	1	11	24.21	-92.34	286	0.97
107:0	01-Jun-07 07:09	-01:18:00	α Cru	[22.24, 3.9, 0.3, 1/122, 0]	2	1	5.97	-80.88	298	0.96
107:0	01-Jun-07 07:09	-01:18:00	α Cru	[22.24, 3.9, 0.3, 1/122, 0]	2	11	19.13	-79.16	299	0.95
107:0	01-Jun-07 07:09	-01:18:00	α Cru	[22.24, 3.9, 0.3, 1/122, 0]	2	11	24.1	-91.76	287	0.97
108:0	01-Jun-07 07:22	-01:05:00	α Cru	[21.38, 3.9, 0.3, 1/132, 1.9]	1	0	0	-89.95	286	0.98
108:0	01-Jun-07 07:22	-01:05:00	α Cru	[21.38, 3.9, 0.3, 1/132, 1.9]	1	14	10.83	-80.21	296	0.96
108:0	01-Jun-07 07:22	-01:05:00	α Cru	[21.38, 3.9, 0.3, 1/132, 1.9]	1	13.1	23.85	-87.66	288	0.97
108:0	01-Jun-07 07:22	-01:05:00	α Cru	[21.38, 3.9, 0.3, 1/132, 1.9]	2	0	0	-89.95	286	0.98
108:0	01-Jun-07 07:22	-01:05:00	α Cru	[21.38, 3.9, 0.3, 1/132, 1.9]	2	15	12.22	-84.8	291	0.97
108:0	01-Jun-07 07:22	-01:05:00	α Cru	[21.38, 3.9, 0.3, 1/132, 1.9]	3	0	0	-89.95	286	0.98
108:0	01-Jun-07 07:22	-01:05:00	α Cru	[21.38, 3.9, 0.3, 1/132, 1.9]	3	1	4.88	-69.9	306	0.95
108:0	01-Jun-07 07:22	-01:05:00	α Cru	[21.38, 3.9, 0.3, 1/132, 1.9]	4	0	0	-89.95	286	0.98
108:0	01-Jun-07 07:22	-01:05:00	α Cru	[21.38, 3.9, 0.3, 1/132, 1.9]	4	0	4.71	-70.47	305	0.95
109:0	01-Jun-07 07:22	-01:05:00	α Cru	[21.38, 3.9, 0.3, 1/122, 0]	1	9.5	30.26	-69.99	306	0.95
109:0	01-Jun-07 07:22	-01:05:00	α Cru	[21.38, 3.9, 0.3, 1/122, 0]	1	16	12.31	-88.9	287	0.98
109:0	01-Jun-07 07:22	-01:05:00	α Cru	[21.38, 3.9, 0.3, 1/122, 0]	1	15	24.37	-100.93	274	0.99
109:0	01-Jun-07 07:22	-01:05:00	α Cru	[21.38, 3.9, 0.3, 1/122, 0]	2	15.5	13.91	-97.49	278	0.99
109:0	01-Jun-07 07:22	-01:05:00	α Cru	[21.38, 3.9, 0.3, 1/122, 0]	2	14.5	23.88	-102.65	273	0.99
109:0	01-Jun-07 07:22	-01:05:00	α Cru	[21.38, 3.9, 0.3, 1/122, 0]	3	17	12.11	-86.61	289	0.97
109:0	01-Jun-07 07:22	-01:05:00	α Cru	[21.38, 3.9, 0.3, 1/122, 0]	3	1	4.7	-72.28	303	0.96
111:0	01-Jun-07 07:58	-00:29:00	α Cru	[19.71, 3.9, 0.3, 1/132, 1.9]	1	0	0	0	0	0.94
111:0	01-Jun-07 07:58	-00:29:00	α Cru	[19.71, 3.9, 0.3, 1/132, 1.9]	2	0	0	0	0	0.94
112:0	01-Jun-07 08:10	-00:17:00	α Cru	[19.41, 3.9, 0.3, 1/122, 0]	1	1	6.01	-55.1	311	0.97

Continued on next page

Table I.5: Verified velocity for June 2007. (continued)

Run #:Camera	UT	HA	Star	$[\zeta, \phi, \Delta m, \Delta r, \lvert d\rvert]$	Skip #	h	$\lvert V(h)\rvert$	b_{m}	β	$\varepsilon_{\lvert\vec{v}\rvert}$
112:0	01-Jun-07 08:10	-00:17:00	α Cru	[19.41, 3.9, 0.3, 1/122, 0]	1	14	22.58	-84.89	280	1
112:0	01-Jun-07 08:10	-00:17:00	α Cru	[19.41, 3.9, 0.3, 1/122, 0]	1	10	32.54	-56.81	309	0.97
112:0	01-Jun-07 08:10	-00:17:00	α Cru	[19.41, 3.9, 0.3, 1/122, 0]	1	17	12.59	-45.35	320	0.96
112:0	01-Jun-07 08:10	-00:17:00	α Cru	[19.41, 3.9, 0.3, 1/122, 0]	2	17	12.59	-45.35	320	0.96
112:0	01-Jun-07 08:10	-00:17:00	α Cru	[19.41, 3.9, 0.3, 1/122, 0]	2	14	22.4	-83.74	281	1
112:0	01-Jun-07 08:10	-00:17:00	α Cru	[19.41, 3.9, 0.3, 1/122, 0]	2	1	6.77	-82.02	283	0.99
113:0	01-Jun-07 08:10	-00:17:00	α Cru	[19.41, 3.9, 0.3, 1/132, 1.9]	1	0	0	0	3	0.95
113:0	01-Jun-07 08:10	-00:17:00	α Cru	[19.41, 3.9, 0.3, 1/132, 1.9]	1	16.5	25.83	-81.93	283	0.99
113:0	01-Jun-07 08:10	-00:17:00	α Cru	[19.41, 3.9, 0.3, 1/132, 1.9]	2	0	0	0	3	0.95
113:0	01-Jun-07 08:10	-00:17:00	α Cru	[19.41, 3.9, 0.3, 1/132, 1.9]	2	0	5.83	-99.12	265	1
113:0	01-Jun-07 08:10	-00:17:00	α Cru	[19.41, 3.9, 0.3, 1/132, 1.9]	3	0	4.06	-50.42	315	0.97
113:0	01-Jun-07 08:10	-00:17:00	α Cru	[19.41, 3.9, 0.3, 1/132, 1.9]	3	0	0	0	3	0.95
113:0	01-Jun-07 08:10	-00:17:00	α Cru	[19.41, 3.9, 0.3, 1/132, 1.9]	3	0	5.85	-95.68	268	1
113:0	01-Jun-07 08:10	-00:17:00	α Cru	[19.41, 3.9, 0.3, 1/132, 1.9]	4	0	0	0	3	0.95
113:0	01-Jun-07 08:10	-00:17:00	α Cru	[19.41, 3.9, 0.3, 1/132, 1.9]	4	0	4.15	-50.99	315	0.97
113:0	01-Jun-07 08:10	-00:17:00	α Cru	[19.41, 3.9, 0.3, 1/132, 1.9]	4	0	6.1	-93.39	271	1
114:0	01-Jun-07 08:24	-00:03:00	α Cru	[19.27, 3.9, 0.3, 1/122, 0]	1	14.5	22.51	-80.31	281	1
114:0	01-Jun-07 08:24	-00:03:00	α Cru	[19.27, 3.9, 0.3, 1/122, 0]	1	9	32.98	-56.81	306	0.98
114:0	01-Jun-07 08:24	-00:03:00	α Cru	[19.27, 3.9, 0.3, 1/122, 0]	2	15	22.63	-81.45	280	1
115:0	01-Jun-07 08:24	-00:03:00	α Cru	[19.27, 3.9, 0.3, 1/132, 1.9]	1	0	0	-90.05	271	1
115:0	01-Jun-07 08:24	-00:03:00	α Cru	[19.27, 3.9, 0.3, 1/132, 1.9]	1	0	7.13	115.83	118	0.99
115:0	01-Jun-07 08:24	-00:03:00	α Cru	[19.27, 3.9, 0.3, 1/132, 1.9]	1	17.6	25.27	-101.5	259	1
115:0	01-Jun-07 08:24	-00:03:00	α Cru	[19.27, 3.9, 0.3, 1/132, 1.9]	2	0	0	-90.05	271	1
115:0	01-Jun-07 08:24	-00:03:00	α Cru	[19.27, 3.9, 0.3, 1/132, 1.9]	2	17.1	25.01	-101.5	259	1
115:0	01-Jun-07 08:24	-00:03:00	α Cru	[19.27, 3.9, 0.3, 1/132, 1.9]	2	0	6.26	-118.12	242	0.99
115:0	01-Jun-07 08:24	-00:03:00	α Cru	[19.27, 3.9, 0.3, 1/132, 1.9]	2	0	6.97	114.11	117	0.99
116:0	01-Jun-07 08:38	00:10:00	α Cru	[19.33, 3.9, 0.3, 1/122, 0]	1	14	21.43	-75.72	283	1

Continued on next page

Table I.5: Verified velocity for June 2007. (continued)

Run #:Camera	UT	HA	Star	$[\zeta, \phi, \Delta m, \Delta r, \lvert d \rvert]$	Skip #	h	$\lvert V(h) \rvert$	b_{m}	β	$\varepsilon_{\lvert \vec{v} \rvert}$
116:0	01-Jun-07 08:38	00:10:00	α Cru	[19.33, 3.9, 0.3, 1/122, 0]	1	8.5	33.25	-53.95	306	0.98
116:0	01-Jun-07 08:38	00:10:00	α Cru	[19.33, 3.9, 0.3, 1/122, 0]	1	1	11.31	-38.48	322	0.97
116:0	01-Jun-07 08:38	00:10:00	α Cru	[19.33, 3.9, 0.3, 1/122, 0]	2	14	22.28	-78.59	280	1
117:0	01-Jun-07 08:38	00:10:00	α Cru	[19.33, 3.9, 0.3, 1/132, 1.9]	1	0	0	-89.95	268	1
117:0	01-Jun-07 08:38	00:10:00	α Cru	[19.33, 3.9, 0.3, 1/132, 1.9]	1	18.1	24.52	-73.91	285	1
117:0	01-Jun-07 08:38	00:10:00	α Cru	[19.33, 3.9, 0.3, 1/132, 1.9]	2	0	0	-89.95	268	1
117:0	01-Jun-07 08:38	00:10:00	α Cru	[19.33, 3.9, 0.3, 1/132, 1.9]	2	0	6.45	-62.45	297	0.99
117:0	01-Jun-07 08:38	00:10:00	α Cru	[19.33, 3.9, 0.3, 1/132, 1.9]	2	18.1	25.22	-77.92	281	1
120:0	01-Jun-07 09:06	-01:34:00	α Cen	[21.99, 8.7, 1.36, 1/122, 0]	1	12	22.45	-103.8	278	0.97
120:0	01-Jun-07 09:06	-01:34:00	α Cen	[21.99, 8.7, 1.36, 1/122, 0]	1	10	31.48	-78.59	303	0.94
120:0	01-Jun-07 09:06	-01:34:00	α Cen	[21.99, 8.7, 1.36, 1/122, 0]	2	12.5	23.06	-104.94	277	0.97
120:0	01-Jun-07 09:06	-01:34:00	α Cen	[21.99, 8.7, 1.36, 1/122, 0]	2	12	20.29	-115.26	266	0.99
121:0	01-Jun-07 09:06	-01:34:00	α Cen	[21.99, 8.7, 1.36, 1/132, 1.9]	1	0	0	0	17	0.97
121:0	01-Jun-07 09:06	-01:34:00	α Cen	[21.99, 8.7, 1.36, 1/132, 1.9]	1	0.1	6.19	-77.35	304	0.94
121:0	01-Jun-07 09:06	-01:34:00	α Cen	[21.99, 8.7, 1.36, 1/132, 1.9]	1	12.6	22.71	-103.71	278	0.97
121:0	01-Jun-07 09:06	-01:34:00	α Cen	[21.99, 8.7, 1.36, 1/132, 1.9]	1	10.1	32.03	-75.06	306	0.94
121:0	01-Jun-07 09:06	-01:34:00	α Cen	[21.99, 8.7, 1.36, 1/132, 1.9]	2	0	0	0	17	0.97
121:0	01-Jun-07 09:06	-01:34:00	α Cen	[21.99, 8.7, 1.36, 1/132, 1.9]	2	0.1	6.01	-79.07	302	0.94
121:0	01-Jun-07 09:06	-01:34:00	α Cen	[21.99, 8.7, 1.36, 1/132, 1.9]	2	1	9.2	-92.82	289	0.96
121:0	01-Jun-07 09:06	-01:34:00	α Cen	[21.99, 8.7, 1.36, 1/132, 1.9]	3	0	0	0	17	0.97
121:0	01-Jun-07 09:06	-01:34:00	α Cen	[21.99, 8.7, 1.36, 1/132, 1.9]	3	0	4.38	-85.94	295	0.95
121:0	01-Jun-07 09:06	-01:34:00	α Cen	[21.99, 8.7, 1.36, 1/132, 1.9]	3	1.5	9.47	-93.39	288	0.96
121:0	01-Jun-07 09:06	-01:34:00	α Cen	[21.99, 8.7, 1.36, 1/132, 1.9]	4	0	0	0	17	0.97
122:0	01-Jun-07 09:28	-01:12:00	α Cen	[20.06, 8.7, 1.36, 1/122, 0]	1	1.5	12	-87.75	289	0.97
122:0	01-Jun-07 09:28	-01:12:00	α Cen	[20.06, 8.7, 1.36, 1/122, 0]	1	14.2	21.8	-96.35	280	0.98
122:0	01-Jun-07 09:28	-01:12:00	α Cen	[20.06, 8.7, 1.36, 1/122, 0]	1	11	23.37	-76.87	300	0.96
122:0	01-Jun-07 09:28	-01:12:00	α Cen	[20.06, 8.7, 1.36, 1/122, 0]	2	1.5	11.66	-90.05	287	0.97

Continued on next page

Table I.5: Verified velocity for June 2007. (continued)

Run #:Camera	UT	HA	Star	$[\zeta, \phi, \Delta m, \Delta r, \lvert d \rvert]$	Skip #	h	$\lvert V(h) \rvert$	b_{m}	β	$\varepsilon_{\lvert \vec{v} \rvert}$
122:0	01-Jun-07 09:28	-01:12:00	α Cen	[20.06, 8.7, 1.36, 1/122, 0]	2	11	22.72	-78.01	299	0.96
122:0	01-Jun-07 09:28	-01:12:00	α Cen	[20.06, 8.7, 1.36, 1/122, 0]	2	12.5	21.03	-95.2	281	0.98
122:0	01-Jun-07 09:28	-01:12:00	α Cen	[20.06, 8.7, 1.36, 1/122, 0]	3	1.5	11.55	-90.62	286	0.97
123:0	01-Jun-07 09:28	-01:12:00	α Cen	[20.06, 8.7, 1.36, 1/132, 1.9]	1	0	0	-89.95	287	0.97
123:0	01-Jun-07 09:28	-01:12:00	α Cen	[20.06, 8.7, 1.36, 1/132, 1.9]	1	0	7.93	-80.21	296	0.96
123:0	01-Jun-07 09:28	-01:12:00	α Cen	[20.06, 8.7, 1.36, 1/132, 1.9]	1	14.1	22.3	-100.27	276	0.98
123:0	01-Jun-07 09:28	-01:12:00	α Cen	[20.06, 8.7, 1.36, 1/132, 1.9]	1	11.6	24.24	-73.91	303	0.96
123:0	01-Jun-07 09:28	-01:12:00	α Cen	[20.06, 8.7, 1.36, 1/132, 1.9]	2	0	0	-89.95	287	0.97
123:0	01-Jun-07 09:28	-01:12:00	α Cen	[20.06, 8.7, 1.36, 1/132, 1.9]	2	0.6	7.93	-80.21	296	0.96
123:0	01-Jun-07 09:28	-01:12:00	α Cen	[20.06, 8.7, 1.36, 1/132, 1.9]	2	11.6	24.1	-75.06	302	0.96
123:0	01-Jun-07 09:28	-01:12:00	α Cen	[20.06, 8.7, 1.36, 1/132, 1.9]	3	0	0	-89.95	287	0.97
123:0	01-Jun-07 09:28	-01:12:00	α Cen	[20.06, 8.7, 1.36, 1/132, 1.9]	4	0	0	-89.95	287	0.97
123:0	01-Jun-07 09:28	-01:12:00	α Cen	[20.06, 8.7, 1.36, 1/132, 1.9]	5	0	0	-89.95	287	0.97
130:0	01-Jun-07 09:53	-00:47:00	α Cen	[18.35, 8.7, 1.36, 1/122, 0]	1	12.5	24.01	-87.75	283	0.99
130:0	01-Jun-07 09:53	-00:47:00	α Cen	[18.35, 8.7, 1.36, 1/122, 0]	2	12.5	23.3	-90.05	281	0.99
135:0	01-Jun-07 10:42	00:02:00	α Cen	[16.97, 8.7, 1.36, 1/132, 1.9]	1	0	0	-89.95	270	1
135:0	01-Jun-07 10:42	00:02:00	α Cen	[16.97, 8.7, 1.36, 1/132, 1.9]	1	0.6	7.35	-75.63	285	1
135:0	01-Jun-07 10:42	00:02:00	α Cen	[16.97, 8.7, 1.36, 1/132, 1.9]	1	11.6	28.2	-65.32	296	0.99
135:0	01-Jun-07 10:42	00:02:00	α Cen	[16.97, 8.7, 1.36, 1/132, 1.9]	2	0	0	-89.95	270	1
135:0	01-Jun-07 10:42	00:02:00	α Cen	[16.97, 8.7, 1.36, 1/132, 1.9]	2	0	7.56	-74.48	286	1
135:0	01-Jun-07 10:42	00:02:00	α Cen	[16.97, 8.7, 1.36, 1/132, 1.9]	3	0	0	-89.95	270	1
135:0	01-Jun-07 10:42	00:02:00	α Cen	[16.97, 8.7, 1.36, 1/132, 1.9]	3	0.1	7.63	-73.91	287	1
135:0	01-Jun-07 10:42	00:02:00	α Cen	[16.97, 8.7, 1.36, 1/132, 1.9]	4	0	0	-89.95	270	1
135:0	01-Jun-07 10:42	00:02:00	α Cen	[16.97, 8.7, 1.36, 1/132, 1.9]	4	0	1.43	-50.42	311	0.98
135:0	01-Jun-07 10:42	00:02:00	α Cen	[16.97, 8.7, 1.36, 1/132, 1.9]	4	0	7.79	-75.06	286	1
135:0	01-Jun-07 10:42	00:02:00	α Cen	[16.97, 8.7, 1.36, 1/132, 1.9]	5	0	0	-89.95	270	1
135:0	01-Jun-07 10:42	00:02:00	α Cen	[16.97, 8.7, 1.36, 1/132, 1.9]	5	0	1.32	-40.68	321	0.97

Continued on next page

Table I.5: Verified velocity for June 2007. (continued)

Run #:Camera	UT	HA	Star	$[\zeta, \phi, \Delta m, \Delta r, \lvert d \rvert]$	Skip #	h	$\lvert V(h) \rvert$	b_{m}	β	$\varepsilon_{\lvert \vec{v} \rvert}$
136:0	01-Jun-07 10:42	00:02:00	α Cen	[16.97, 8.7, 1.36, 1/122, 0]	1	11	27.55	-69.42	291	1
136:0	01-Jun-07 10:42	00:02:00	α Cen	[16.97, 8.7, 1.36, 1/122, 0]	1	14	21.89	-87.75	272	1
136:0	01-Jun-07 10:42	00:02:00	α Cen	[16.97, 8.7, 1.36, 1/122, 0]	2	14	22.39	-89.47	271	1
136:0	01-Jun-07 10:42	00:02:00	α Cen	[16.97, 8.7, 1.36, 1/122, 0]	2	10.5	27.19	-69.99	291	1
140:0	01-Jun-07 10:14	-00:26:00	α Cen	[17.4, 8.7, 1.36, 1/122, 0]	1	13	21.97	-86.03	281	0.99
140:0	01-Jun-07 10:14	-00:26:00	α Cen	[17.4, 8.7, 1.36, 1/122, 0]	1	9.5	30.8	-61.4	306	0.98
140:0	01-Jun-07 10:14	-00:26:00	α Cen	[17.4, 8.7, 1.36, 1/122, 0]	2	14	21.8	-85.46	281	0.99
141:0	01-Jun-07 10:14	-00:26:00	α Cen	[17.4, 8.7, 1.36, 1/132, 1.9]	1	0	0	-89.95	276	1
141:0	01-Jun-07 10:14	-00:26:00	α Cen	[17.4, 8.7, 1.36, 1/132, 1.9]	1	0.1	7.72	-65.89	301	0.98
141:0	01-Jun-07 10:14	-00:26:00	α Cen	[17.4, 8.7, 1.36, 1/132, 1.9]	1	13.1	22.68	-83.08	284	0.99
141:0	01-Jun-07 10:14	-00:26:00	α Cen	[17.4, 8.7, 1.36, 1/132, 1.9]	1	9.6	32.77	-57.3	310	0.97
141:0	01-Jun-07 10:14	-00:26:00	α Cen	[17.4, 8.7, 1.36, 1/132, 1.9]	2	0	0	-89.95	276	1
141:0	01-Jun-07 10:14	-00:26:00	α Cen	[17.4, 8.7, 1.36, 1/132, 1.9]	2	0.1	7.33	-60.16	307	0.98
141:0	01-Jun-07 10:14	-00:26:00	α Cen	[17.4, 8.7, 1.36, 1/132, 1.9]	3	0	0	-89.95	276	1
141:0	01-Jun-07 10:14	-00:26:00	α Cen	[17.4, 8.7, 1.36, 1/132, 1.9]	4	0	0	-89.95	276	1
150:0	01-Jun-07 11:05	00:25:00	α Cen	[17.39, 8.7, 1.36, 1/122, 0]	1	3.5	20.71	-64.84	291	1
150:0	01-Jun-07 11:05	00:25:00	α Cen	[17.39, 8.7, 1.36, 1/122, 0]	1	11.5	26.26	-51.66	305	0.99
150:0	01-Jun-07 11:05	00:25:00	α Cen	[17.39, 8.7, 1.36, 1/122, 0]	1	1.5	13.3	-65.98	290	1
150:0	01-Jun-07 11:05	00:25:00	α Cen	[17.39, 8.7, 1.36, 1/122, 0]	1	8	33.95	-49.37	307	0.99
150:0	01-Jun-07 11:05	00:25:00	α Cen	[17.39, 8.7, 1.36, 1/122, 0]	2	3.5	20.24	-64.26	292	1
150:0	01-Jun-07 11:05	00:25:00	α Cen	[17.39, 8.7, 1.36, 1/122, 0]	2	2	13.04	-66.55	289	1
151:0	01-Jun-07 11:05	00:25:00	α Cen	[17.39, 8.7, 1.36, 1/132, 1.9]	1	0	0	0	356	0.96
151:0	01-Jun-07 11:05	00:25:00	α Cen	[17.39, 8.7, 1.36, 1/132, 1.9]	1	0.5	9.67	-59.01	297	1
151:0	01-Jun-07 11:05	00:25:00	α Cen	[17.39, 8.7, 1.36, 1/132, 1.9]	1	3.6	21.91	-63.03	293	1
151:0	01-Jun-07 11:05	00:25:00	α Cen	[17.39, 8.7, 1.36, 1/132, 1.9]	1	11.6	27.04	-51.57	305	0.99
151:0	01-Jun-07 11:05	00:25:00	α Cen	[17.39, 8.7, 1.36, 1/132, 1.9]	2	0	0	0	356	0.96
151:0	01-Jun-07 11:05	00:25:00	α Cen	[17.39, 8.7, 1.36, 1/132, 1.9]	2	0.6	6.14	-70.47	285	1

Continued on next page

Table I.5: Verified velocity for June 2007. (continued)

Run #:Camera	UT	HA	Star	$[\zeta, \phi, \Delta m, \Delta r, \lvert d \rvert]$	Skip #	h	$\lvert V(h) \rvert$	b_{m}	β	$\varepsilon_{\lvert \vec{v} \rvert}$
151:0	01-Jun-07 11:05	00:25:00	α Cen	[17.39, 8.7, 1.36, 1/132, 1.9]	2	0.1	10.42	-56.72	300	1
151:0	01-Jun-07 11:05	00:25:00	α Cen	[17.39, 8.7, 1.36, 1/132, 1.9]	2	1.6	13.88	-65.89	290	1
151:0	01-Jun-07 11:05	00:25:00	α Cen	[17.39, 8.7, 1.36, 1/132, 1.9]	2	3.1	21	-63.03	293	1
151:0	01-Jun-07 11:05	00:25:00	α Cen	[17.39, 8.7, 1.36, 1/132, 1.9]	3	0	0	0	356	0.96
151:0	01-Jun-07 11:05	00:25:00	α Cen	[17.39, 8.7, 1.36, 1/132, 1.9]	3	0.2	6.06	-69.33	286	1
151:0	01-Jun-07 11:05	00:25:00	α Cen	[17.39, 8.7, 1.36, 1/132, 1.9]	3	0.2	10.78	-57.87	298	1
151:0	01-Jun-07 11:05	00:25:00	α Cen	[17.39, 8.7, 1.36, 1/132, 1.9]	3	2	13.81	-64.74	291	1
151:0	01-Jun-07 11:05	00:25:00	α Cen	[17.39, 8.7, 1.36, 1/132, 1.9]	4	0	0	0	356	0.96
151:0	01-Jun-07 11:05	00:25:00	α Cen	[17.39, 8.7, 1.36, 1/132, 1.9]	4	0.2	6.02	-68.75	287	1
160:0	01-Jun-07 12:05	01:25:00	α Cen	[21.16, 8.7, 1.36, 1/122, 0]	1	11	26.81	-43.06	300	1
160:0	01-Jun-07 12:05	01:25:00	α Cen	[21.16, 8.7, 1.36, 1/122, 0]	1	2	15.69	-46.5	297	1
160:0	01-Jun-07 12:05	01:25:00	α Cen	[21.16, 8.7, 1.36, 1/122, 0]	1	13	19.94	-75.72	266	0.98
160:0	01-Jun-07 12:05	01:25:00	α Cen	[21.16, 8.7, 1.36, 1/122, 0]	2	2.2	15.69	-46.5	297	1
160:0	01-Jun-07 12:05	01:25:00	α Cen	[21.16, 8.7, 1.36, 1/122, 0]	2	13	20.15	-78.59	263	0.98
161:0	01-Jun-07 12:14	01:34:00	α Cen	[22.02, 8.7, 1.36, 1/122, 0]	1	2	15.12	-47.07	294	1
161:0	01-Jun-07 12:14	01:34:00	α Cen	[22.02, 8.7, 1.36, 1/122, 0]	1	1.5	9.44	-38.48	303	1
161:0	01-Jun-07 12:14	01:34:00	α Cen	[22.02, 8.7, 1.36, 1/122, 0]	1	11	27.26	-40.77	301	1
161:0	01-Jun-07 12:14	01:34:00	α Cen	[22.02, 8.7, 1.36, 1/122, 0]	1	13	19.34	-74	266	0.98
161:0	01-Jun-07 12:14	01:34:00	α Cen	[22.02, 8.7, 1.36, 1/122, 0]	1	1	7.29	-132.44	209	0.93
161:0	01-Jun-07 12:14	01:34:00	α Cen	[22.02, 8.7, 1.36, 1/122, 0]	2	2	15.12	-47.07	294	1
161:0	01-Jun-07 12:14	01:34:00	α Cen	[22.02, 8.7, 1.36, 1/122, 0]	2	13	19.64	-74.58	265	0.98
161:0	01-Jun-07 12:14	01:34:00	α Cen	[22.02, 8.7, 1.36, 1/122, 0]	2	1.5	9.41	-36.19	306	1
161:0	01-Jun-07 12:14	01:34:00	α Cen	[22.02, 8.7, 1.36, 1/122, 0]	2	6	20.86	-47.07	294	1
161:0	01-Jun-07 12:14	01:34:00	α Cen	[22.02, 8.7, 1.36, 1/122, 0]	2	6	26.16	-41.92	299	1
161:0	01-Jun-07 12:14	01:34:00	α Cen	[22.02, 8.7, 1.36, 1/122, 0]	3	2	14.74	-47.65	293	1
161:0	01-Jun-07 12:14	01:34:00	α Cen	[22.02, 8.7, 1.36, 1/122, 0]	3	1.5	9.61	-36.76	305	1
161:0	01-Jun-07 12:14	01:34:00	α Cen	[22.02, 8.7, 1.36, 1/122, 0]	4	1.5	9.57	-37.33	304	1

Continued on next page

Table I.5: Verified velocity for June 2007. (continued)

Run #:Camera	UT	HA	Star	$[\zeta, \phi, \Delta m, \Delta r, \lvert d \rvert]$	Skip #	h	$\lvert V(h) \rvert$	b_{m}	β	$\varepsilon_{\lvert \vec{v} \rvert}$
165:0	01-Jun-07 12:43	02:02:00	α Cen	[24.87, 8.7, 1.36, 1/132, 1.9]	1	0	0	-89.95	244	0.93
165:0	01-Jun-07 12:43	02:02:00	α Cen	[24.87, 8.7, 1.36, 1/132, 1.9]	1	2.1	17.1	-41.83	293	1
165:0	01-Jun-07 12:43	02:02:00	α Cen	[24.87, 8.7, 1.36, 1/132, 1.9]	1	0.6	7.14	-26.93	309	1
165:0	01-Jun-07 12:43	02:02:00	α Cen	[24.87, 8.7, 1.36, 1/132, 1.9]	1	10.1	30.03	-33.8	302	1
165:0	01-Jun-07 12:43	02:02:00	α Cen	[24.87, 8.7, 1.36, 1/132, 1.9]	2	0	0	-89.95	244	0.93
165:0	01-Jun-07 12:43	02:02:00	α Cen	[24.87, 8.7, 1.36, 1/132, 1.9]	2	0.1	4.8	-18.91	318	1
165:0	01-Jun-07 12:43	02:02:00	α Cen	[24.87, 8.7, 1.36, 1/132, 1.9]	2	0.6	7.2	-24.06	312	1
165:0	01-Jun-07 12:43	02:02:00	α Cen	[24.87, 8.7, 1.36, 1/132, 1.9]	2	1.1	15.42	-41.25	293	1
165:0	01-Jun-07 12:43	02:02:00	α Cen	[24.87, 8.7, 1.36, 1/132, 1.9]	2	2.1	17.7	-42.97	292	0.99
165:0	01-Jun-07 12:43	02:02:00	α Cen	[24.87, 8.7, 1.36, 1/132, 1.9]	3	0	0	-89.95	244	0.93
165:0	01-Jun-07 12:43	02:02:00	α Cen	[24.87, 8.7, 1.36, 1/132, 1.9]	3	0.1	6.06	-116.88	219	0.91
165:0	01-Jun-07 12:43	02:02:00	α Cen	[24.87, 8.7, 1.36, 1/132, 1.9]	3	0.1	4.68	-20.05	317	1
165:0	01-Jun-07 12:43	02:02:00	α Cen	[24.87, 8.7, 1.36, 1/132, 1.9]	4	0	0	-89.95	244	0.93
165:0	01-Jun-07 12:43	02:02:00	α Cen	[24.87, 8.7, 1.36, 1/132, 1.9]	4	0.1	4.31	-121.47	215	0.91
165:0	01-Jun-07 12:43	02:02:00	α Cen	[24.87, 8.7, 1.36, 1/132, 1.9]	4	0.1	4.49	-20.63	316	1
166:0	01-Jun-07 12:43	02:02:00	α Cen	[24.87, 8.7, 1.36, 1/122, 0]	1	2	16.09	-43.06	291	0.99
166:0	01-Jun-07 12:43	02:02:00	α Cen	[24.87, 8.7, 1.36, 1/122, 0]	1	10.5	27.04	-35.04	300	1
166:0	01-Jun-07 12:43	02:02:00	α Cen	[24.87, 8.7, 1.36, 1/122, 0]	2	2	16.17	-44.21	290	0.99
166:0	01-Jun-07 12:43	02:02:00	α Cen	[24.87, 8.7, 1.36, 1/122, 0]	3	1.5	15.95	-44.21	290	0.99
167:0	01-Jun-07 12:52	02:12:00	α Cen	[25.93, 8.7, 1.36, 1/132, 1.9]	1	0	0	-89.95	242	0.92
167:0	01-Jun-07 12:52	02:12:00	α Cen	[25.93, 8.7, 1.36, 1/132, 1.9]	1	1.6	16.46	-39.53	293	0.99
167:0	01-Jun-07 12:52	02:12:00	α Cen	[25.93, 8.7, 1.36, 1/132, 1.9]	1	9.6	29.52	-30.37	303	1
167:0	01-Jun-07 12:52	02:12:00	α Cen	[25.93, 8.7, 1.36, 1/132, 1.9]	2	0	0	-89.95	242	0.92
167:0	01-Jun-07 12:52	02:12:00	α Cen	[25.93, 8.7, 1.36, 1/132, 1.9]	2	1.6	16.4	-36.67	296	1
167:0	01-Jun-07 12:52	02:12:00	α Cen	[25.93, 8.7, 1.36, 1/132, 1.9]	2	3.1	20.2	-34.95	298	1
167:0	01-Jun-07 12:52	02:12:00	α Cen	[25.93, 8.7, 1.36, 1/132, 1.9]	3	0	0	-89.95	242	0.92
167:0	01-Jun-07 12:52	02:12:00	α Cen	[25.93, 8.7, 1.36, 1/132, 1.9]	3	0	5.5	-118.03	216	0.9

Continued on next page

Table I.5: Verified velocity for June 2007. (continued)

Run #:Camera	UT	HA	Star	$[\zeta, \phi, \Delta m, \Delta r, \lvert d \rvert]$	Skip #	h	$\lvert V(h) \rvert$	b_{m}	β	$\varepsilon_{\lvert \vec{v} \rvert}$
167:0	01-Jun-07 12:52	02:12:00	α Cen	[25.93, 8.7, 1.36, 1/132, 1.9]	3	2	16.58	-36.67	296	1
167:0	01-Jun-07 12:52	02:12:00	α Cen	[25.93, 8.7, 1.36, 1/132, 1.9]	4	0	0	-89.95	242	0.92
167:0	01-Jun-07 12:52	02:12:00	α Cen	[25.93, 8.7, 1.36, 1/132, 1.9]	4	0	5.57	-118.03	216	0.9
167:0	01-Jun-07 12:52	02:12:00	α Cen	[25.93, 8.7, 1.36, 1/132, 1.9]	5	0	0	-89.95	242	0.92
167:0	01-Jun-07 12:52	02:12:00	α Cen	[25.93, 8.7, 1.36, 1/132, 1.9]	5	0	5.6	-119.18	215	0.9
168:0	01-Jun-07 12:52	02:12:00	α Cen	[25.93, 8.7, 1.36, 1/122, 0]	1	2	15.97	-36.76	296	1
168:0	01-Jun-07 12:52	02:12:00	α Cen	[25.93, 8.7, 1.36, 1/122, 0]	1	3.5	19.51	-36.19	296	1
168:0	01-Jun-07 12:52	02:12:00	α Cen	[25.93, 8.7, 1.36, 1/122, 0]	1	10	28.95	-32.18	301	1
168:0	01-Jun-07 12:52	02:12:00	α Cen	[25.93, 8.7, 1.36, 1/122, 0]	2	1.5	15.66	-36.76	296	1
168:0	01-Jun-07 12:52	02:12:00	α Cen	[25.93, 8.7, 1.36, 1/122, 0]	2	3.5	19.78	-35.04	298	1
168:0	01-Jun-07 12:52	02:12:00	α Cen	[25.93, 8.7, 1.36, 1/122, 0]	3	2	15.56	-35.61	297	1
169:0	01-Jun-07 13:12	02:32:00	α Cen	[28.14, 8.7, 1.36, 1/132, 1.9]	1	0	0	-89.95	0	0.93
169:0	01-Jun-07 13:12	02:32:00	α Cen	[28.14, 8.7, 1.36, 1/132, 1.9]	1	1.6	17.49	-30.94	297	0.99
169:0	01-Jun-07 13:12	02:32:00	α Cen	[28.14, 8.7, 1.36, 1/132, 1.9]	1	10.6	30.2	-27.5	301	1
169:0	01-Jun-07 13:12	02:32:00	α Cen	[28.14, 8.7, 1.36, 1/132, 1.9]	2	0	0	-89.95	0	0.93
169:0	01-Jun-07 13:12	02:32:00	α Cen	[28.14, 8.7, 1.36, 1/132, 1.9]	2	0	5.28	-102.56	226	0.88
169:0	01-Jun-07 13:12	02:32:00	α Cen	[28.14, 8.7, 1.36, 1/132, 1.9]	2	1.1	17.47	-32.09	296	0.99
169:0	01-Jun-07 13:12	02:32:00	α Cen	[28.14, 8.7, 1.36, 1/132, 1.9]	2	2.6	20.75	-34.95	293	0.99
169:0	01-Jun-07 13:12	02:32:00	α Cen	[28.14, 8.7, 1.36, 1/132, 1.9]	3	0	0	-89.95	0	0.93
170:0	01-Jun-07 13:12	02:32:00	α Cen	[28.14, 8.7, 1.36, 1/122, 0]	1	10.5	27.22	-29.89	298	1
170:0	01-Jun-07 13:12	02:32:00	α Cen	[28.14, 8.7, 1.36, 1/122, 0]	1	2.5	19.51	-36.19	291	0.99
170:0	01-Jun-07 13:12	02:32:00	α Cen	[28.14, 8.7, 1.36, 1/122, 0]	1	1.3	15.36	-31.6	297	0.99
170:0	01-Jun-07 13:12	02:32:00	α Cen	[28.14, 8.7, 1.36, 1/122, 0]	2	3	19.8	-36.19	291	0.99
170:0	01-Jun-07 13:12	02:32:00	α Cen	[28.14, 8.7, 1.36, 1/122, 0]	2	1	16.24	-32.18	296	0.99
170:0	01-Jun-07 13:12	02:32:00	α Cen	[28.14, 8.7, 1.36, 1/122, 0]	3	1	13.28	-49.37	277	0.97
400:0	03-Jun-07 06:44	-01:36:00	α Cru	[23.62, 3.9, 0.3, 1/122, 0]	1	9.5	6.4	107.81	130	0.93
400:0	03-Jun-07 06:44	-01:36:00	α Cru	[23.62, 3.9, 0.3, 1/122, 0]	1	10.5	11.42	-130.15	251	1

Continued on next page

Table I.5: Verified velocity for June 2007. (continued)

Run #:Camera	UT	HA	Star	$[\zeta, \phi, \Delta m, \Delta r, \lvert d \rvert]$	Skip #	h	$\lvert V(h) \rvert$	b_{m}	β	$\varepsilon_{\lvert \vec{v} \rvert}$
400:0	03-Jun-07 06:44	-01:36:00	α Cru	[23.62, 3.9, 0.3, 1/122, 0]	2	10.5	11.08	-127.29	254	1
400:0	03-Jun-07 06:44	-01:36:00	α Cru	[23.62, 3.9, 0.3, 1/122, 0]	2	9	9.66	120.41	142	0.92
400:0	03-Jun-07 06:44	-01:36:00	α Cru	[23.62, 3.9, 0.3, 1/122, 0]	2	9.5	5.64	104.37	127	0.93
400:0	03-Jun-07 06:44	-01:36:00	α Cru	[23.62, 3.9, 0.3, 1/122, 0]	3	10	5.19	104.37	127	0.93
400:0	03-Jun-07 06:44	-01:36:00	α Cru	[23.62, 3.9, 0.3, 1/122, 0]	3	9.5	9.68	120.99	142	0.92
400:0	03-Jun-07 06:44	-01:36:00	α Cru	[23.62, 3.9, 0.3, 1/122, 0]	3	10.5	10.95	-128.43	253	1
401:0	03-Jun-07 06:44	-01:36:00	α Cru	[23.62, 3.9, 0.3, 1/132, 1.9]	1	0	0	0	18	0.96
402:0	03-Jun-07 06:55	-01:24:00	α Cru	[22.74, 3.9, 0.3, 1/122, 0]	1	11	13.46	-127.86	250	1
402:0	03-Jun-07 06:55	-01:24:00	α Cru	[22.74, 3.9, 0.3, 1/122, 0]	1	9.5	8.07	117.55	137	0.93
402:0	03-Jun-07 06:55	-01:24:00	α Cru	[22.74, 3.9, 0.3, 1/122, 0]	2	9	4.42	99.79	120	0.95
402:0	03-Jun-07 06:55	-01:24:00	α Cru	[22.74, 3.9, 0.3, 1/122, 0]	2	10	8.07	117.55	137	0.93
402:0	03-Jun-07 06:55	-01:24:00	α Cru	[22.74, 3.9, 0.3, 1/122, 0]	2	11	14.14	-125	253	1
402:0	03-Jun-07 06:55	-01:24:00	α Cru	[22.74, 3.9, 0.3, 1/122, 0]	3	10	4.78	97.49	117	0.95
402:0	03-Jun-07 06:55	-01:24:00	α Cru	[22.74, 3.9, 0.3, 1/122, 0]	3	10.5	7.88	115.26	0	0.94
402:0	03-Jun-07 06:55	-01:24:00	α Cru	[22.74, 3.9, 0.3, 1/122, 0]	3	11	14.12	-125.57	253	1
402:0	03-Jun-07 06:55	-01:24:00	α Cru	[22.74, 3.9, 0.3, 1/122, 0]	4	10.5	4.69	100.36	120	0.95
402:0	03-Jun-07 06:55	-01:24:00	α Cru	[22.74, 3.9, 0.3, 1/122, 0]	4	10	7.8	116.4	136	0.93
403:0	03-Jun-07 06:55	-01:24:00	α Cru	[22.74, 3.9, 0.3, 1/132, 1.9]	1	0	0	0	15	0.96
404:0	03-Jun-07 07:04	-01:15:00	α Cru	[22.07, 3.9, 0.3, 1/122, 0]	1	10.5	4.93	-116.4	260	1
404:0	03-Jun-07 07:04	-01:15:00	α Cru	[22.07, 3.9, 0.3, 1/122, 0]	1	9.5	8.03	112.96	131	0.94
404:0	03-Jun-07 07:04	-01:15:00	α Cru	[22.07, 3.9, 0.3, 1/122, 0]	1	10.5	12.69	-129.01	247	1
404:0	03-Jun-07 07:04	-01:15:00	α Cru	[22.07, 3.9, 0.3, 1/122, 0]	2	10	5.29	-111.25	266	0.99
404:0	03-Jun-07 07:04	-01:15:00	α Cru	[22.07, 3.9, 0.3, 1/122, 0]	2	7.5	5.15	104.37	122	0.95
404:0	03-Jun-07 07:04	-01:15:00	α Cru	[22.07, 3.9, 0.3, 1/122, 0]	2	9.5	8.59	116.97	134	0.94
404:0	03-Jun-07 07:04	-01:15:00	α Cru	[22.07, 3.9, 0.3, 1/122, 0]	3	10	5.17	-112.96	264	0.99
404:0	03-Jun-07 07:04	-01:15:00	α Cru	[22.07, 3.9, 0.3, 1/122, 0]	3	9.5	5.6	103.8	122	0.95
404:0	03-Jun-07 07:04	-01:15:00	α Cru	[22.07, 3.9, 0.3, 1/122, 0]	4	10	5.29	-111.82	265	0.99

Continued on next page

Table I.5: Verified velocity for June 2007. (continued)

Run #:Camera	UT	HA	Star	$[\zeta, \phi, \Delta m, \Delta r, \lvert d \rvert]$	Skip #	h	$\lvert V(h) \rvert$	b_{m}	β	$\varepsilon_{\lvert \vec{v} \rvert}$
404:0	03-Jun-07 07:04	-01:15:00	α Cru	[22.07, 3.9, 0.3, 1/122, 0]	4	10.5	5.99	104.37	122	0.95
405:0	03-Jun-07 07:04	-01:15:00	α Cru	[22.07, 3.9, 0.3, 1/132, 1.9]	1	0	0	-89.95	288	0.97
406:0	03-Jun-07 07:11	-01:08:00	α Cru	[21.62, 3.9, 0.3, 1/122, 0]	1	9.5	7.48	84.32	101	0.98
406:0	03-Jun-07 07:11	-01:08:00	α Cru	[21.62, 3.9, 0.3, 1/122, 0]	1	10	12.77	-123.85	251	1
406:0	03-Jun-07 07:11	-01:08:00	α Cru	[21.62, 3.9, 0.3, 1/122, 0]	2	10	3.72	92.34	109	0.97
406:0	03-Jun-07 07:11	-01:08:00	α Cru	[21.62, 3.9, 0.3, 1/122, 0]	2	9.5	8.3	115.26	131	0.95
406:0	03-Jun-07 07:11	-01:08:00	α Cru	[21.62, 3.9, 0.3, 1/122, 0]	2	10	5.11	-109.53	266	0.99
406:0	03-Jun-07 07:11	-01:08:00	α Cru	[21.62, 3.9, 0.3, 1/122, 0]	2	10.5	12.17	-123.28	251	1
406:0	03-Jun-07 07:11	-01:08:00	α Cru	[21.62, 3.9, 0.3, 1/122, 0]	3	8	6.48	105.52	122	0.96
406:0	03-Jun-07 07:11	-01:08:00	α Cru	[21.62, 3.9, 0.3, 1/122, 0]	3	9.5	8.22	115.83	132	0.95
406:0	03-Jun-07 07:11	-01:08:00	α Cru	[21.62, 3.9, 0.3, 1/122, 0]	3	10.5	5.19	-107.81	268	0.99
406:0	03-Jun-07 07:11	-01:08:00	α Cru	[21.62, 3.9, 0.3, 1/122, 0]	4	9.5	6.61	106.09	122	0.96
406:0	03-Jun-07 07:11	-01:08:00	α Cru	[21.62, 3.9, 0.3, 1/122, 0]	4	10	8.6	118.69	135	0.94
406:0	03-Jun-07 07:11	-01:08:00	α Cru	[21.62, 3.9, 0.3, 1/122, 0]	4	10.5	5.11	-109.53	266	0.99
407:0	03-Jun-07 07:11	-01:08:00	α Cru	[21.62, 3.9, 0.3, 1/132, 1.9]	1	0	0	0	12	0.95
407:0	03-Jun-07 07:11	-01:08:00	α Cru	[21.62, 3.9, 0.3, 1/132, 1.9]	2	0	0	0	12	0.95
408:0	03-Jun-07 07:25	-00:54:00	α Cru	[20.77, 3.9, 0.3, 1/122, 0]	1	10	6.07	-111.82	260	1
408:0	03-Jun-07 07:25	-00:54:00	α Cru	[20.77, 3.9, 0.3, 1/122, 0]	1	9	8.07	117.55	131	0.95
408:0	03-Jun-07 07:25	-00:54:00	α Cru	[20.77, 3.9, 0.3, 1/122, 0]	1	10.5	12.62	-120.41	251	1
408:0	03-Jun-07 07:25	-00:54:00	α Cru	[20.77, 3.9, 0.3, 1/122, 0]	2	10	6.29	-116.4	255	1
408:0	03-Jun-07 07:25	-00:54:00	α Cru	[20.77, 3.9, 0.3, 1/122, 0]	3	10.5	6.27	-119.27	252	1
408:0	03-Jun-07 07:25	-00:54:00	α Cru	[20.77, 3.9, 0.3, 1/122, 0]	4	10	6.53	-119.84	252	1
409:0	03-Jun-07 07:25	-00:54:00	α Cru	[20.77, 3.9, 0.3, 1/132, 1.9]	1	0	0	0	10	0.95
409:0	03-Jun-07 07:25	-00:54:00	α Cru	[20.77, 3.9, 0.3, 1/132, 1.9]	2	0	0	0	10	0.95
409:0	03-Jun-07 07:25	-00:54:00	α Cru	[20.77, 3.9, 0.3, 1/132, 1.9]	3	0	0	0	10	0.95
410:0	03-Jun-07 07:56	-00:23:00	α Cru	[19.56, 3.9, 0.3, 1/122, 0]	1	10.5	12.14	-129.01	235	0.99
410:0	03-Jun-07 07:56	-00:23:00	α Cru	[19.56, 3.9, 0.3, 1/122, 0]	1	9	5.34	118.12	125	0.97

Continued on next page

Table I.5: Verified velocity for June 2007. (continued)

Run #:Camera	UT	HA	Star	$[\zeta, \phi, \Delta m, \Delta r, \lvert d \rvert]$	Skip #	h	$\lvert V(h) \rvert$	b_{m}	β	$\varepsilon_{\lvert \vec{v} \rvert}$
410:0	03-Jun-07 07:56	-00:23:00	α Cru	[19.56, 3.9, 0.3, 1/122, 0]	2	11	12.13	-129.01	235	0.99
410:0	03-Jun-07 07:56	-00:23:00	α Cru	[19.56, 3.9, 0.3, 1/122, 0]	3	11.5	12.66	-129.58	234	0.99
411:0	03-Jun-07 08:11	-00:10:00	α Cru	[19.33, 3.9, 0.3, 1/122, 0]	1	11	12.2	-118.69	243	0.99
411:0	03-Jun-07 08:11	-00:10:00	α Cru	[19.33, 3.9, 0.3, 1/122, 0]	1	9.5	4.6	-102.08	260	1
411:0	03-Jun-07 08:11	-00:10:00	α Cru	[19.33, 3.9, 0.3, 1/122, 0]	2	11	12.04	-122.13	239	0.99
411:0	03-Jun-07 08:11	-00:10:00	α Cru	[19.33, 3.9, 0.3, 1/122, 0]	2	10	5.93	-109.53	252	1
411:0	03-Jun-07 08:11	-00:10:00	α Cru	[19.33, 3.9, 0.3, 1/122, 0]	3	10	6.02	-107.23	255	1
411:0	03-Jun-07 08:11	-00:10:00	α Cru	[19.33, 3.9, 0.3, 1/122, 0]	3	10	11.65	-114.11	247	0.99
412:0	03-Jun-07 08:24	00:04:00	α Cru	[19.29, 3.9, 0.3, 1/126, 2.8]	1	0	0	180	180	0.94
412:0	03-Jun-07 08:24	00:04:00	α Cru	[19.29, 3.9, 0.3, 1/126, 2.8]	2	0	0	180	180	0.94
412:0	03-Jun-07 08:24	00:04:00	α Cru	[19.29, 3.9, 0.3, 1/126, 2.8]	3	0	0	180	180	0.94
413:0	03-Jun-07 08:37	00:17:00	α Cru	[19.44, 3.9, 0.3, 1/126, 2.8]	1	0	0	180	0	0.94
413:0	03-Jun-07 08:37	00:17:00	α Cru	[19.44, 3.9, 0.3, 1/126, 2.8]	2	0	0	180	0	0.94
450:0	03-Jun-07 11:58	01:26:00	α Cen	[21.26, 8.7, 1.36, 1/130, 2.2]	1	0	0	-89.95	251	0.96
450:0	03-Jun-07 11:58	01:26:00	α Cen	[21.26, 8.7, 1.36, 1/130, 2.2]	2	0	0	-89.95	251	0.96
450:0	03-Jun-07 11:58	01:26:00	α Cen	[21.26, 8.7, 1.36, 1/130, 2.2]	3	0	0	-89.95	251	0.96
451:0	03-Jun-07 11:58	01:26:00	α Cen	[21.26, 8.7, 1.36, 1/122, 0]	1	10.5	11.81	-86.61	255	0.97
451:0	03-Jun-07 11:58	01:26:00	α Cen	[21.26, 8.7, 1.36, 1/122, 0]	2	9	3.65	-64.84	277	0.99
451:0	03-Jun-07 11:58	01:26:00	α Cen	[21.26, 8.7, 1.36, 1/122, 0]	2	10	10.14	-90.05	251	0.96
451:0	03-Jun-07 11:58	01:26:00	α Cen	[21.26, 8.7, 1.36, 1/122, 0]	2	10.5	14.57	-88.9	252	0.96
451:0	03-Jun-07 11:58	01:26:00	α Cen	[21.26, 8.7, 1.36, 1/122, 0]	3	10	9.96	-90.05	251	0.96
451:0	03-Jun-07 11:58	01:26:00	α Cen	[21.26, 8.7, 1.36, 1/122, 0]	3	10.5	14.57	-88.33	253	0.97
452:0	03-Jun-07 12:19	01:46:00	α Cen	[23.22, 8.7, 1.36, 1/122, 0]	1	10.5	9.22	-83.74	253	0.95
452:0	03-Jun-07 12:19	01:46:00	α Cen	[23.22, 8.7, 1.36, 1/122, 0]	2	9	9.64	-83.74	253	0.95
452:0	03-Jun-07 12:19	01:46:00	α Cen	[23.22, 8.7, 1.36, 1/122, 0]	3	10.5	10.08	-84.89	252	0.95
453:0	03-Jun-07 12:19	01:46:00	α Cen	[23.22, 8.7, 1.36, 1/130, 2.2]	1	0	0	0	341	0.97
453:0	03-Jun-07 12:19	01:46:00	α Cen	[23.22, 8.7, 1.36, 1/130, 2.2]	2	0	0	0	341	0.97

Continued on next page

Table I.5: Verified velocity for June 2007. (continued)

Run #:Camera	UT	HA	Star	$[\zeta, \phi, \Delta m, \Delta r, \lvert d \rvert]$	Skip #	h	$\lvert V(h) \rvert$	b_{m}	β	$\varepsilon_{\lvert \vec{v} \rvert}$
456:0	03-Jun-07 12:40	02:08:00	α Cen	[25.53, 8.7, 1.36, 1/122, 0]	1	10.5	11.36	-72.28	259	0.95
456:0	03-Jun-07 12:40	02:08:00	α Cen	[25.53, 8.7, 1.36, 1/122, 0]	1	9.5	3.96	-60.25	272	0.97
456:0	03-Jun-07 12:40	02:08:00	α Cen	[25.53, 8.7, 1.36, 1/122, 0]	2	10.5	10.9	-74.58	257	0.94
456:0	03-Jun-07 12:40	02:08:00	α Cen	[25.53, 8.7, 1.36, 1/122, 0]	2	9.5	3.45	-64.84	267	0.96
456:0	03-Jun-07 12:40	02:08:00	α Cen	[25.53, 8.7, 1.36, 1/122, 0]	3	10.5	10.75	-75.15	257	0.94
456:0	03-Jun-07 12:40	02:08:00	α Cen	[25.53, 8.7, 1.36, 1/122, 0]	3	9.5	3.3	-60.25	272	0.97
457:0	03-Jun-07 12:40	02:08:00	α Cen	[25.53, 8.7, 1.36, 1/130, 2.2]	1	0	0	-89.95	242	0.92

References

Andrews, L. C., *Field Guide to Atmospheric Optics*, vol. FG03 of *SPIE Field Guides*. SPIE Press, Bellingham, WA, 2004.

Avila, R., Oberservational methods for the study of optical turbulence, in *Astronomical Site Evaluation in the Visible and Radio Range. IAU Technical Workshop. 13-17 Nov 2000.*, edited by J. Vernin, Z. Benkhaldoun, and C. Muñoz-Tuñón, vol. 266, pp. 48–63. 2002.

Avila, R., J. Vernin, and L. J. Sánchez, Whole atmospheric-turbulence profiling with generalized scidar, *Appl. Opt.*, *36*(30), 7898–7905, 1997.

Avila, R., J. Vernin, and L. J. Sánchez, Atmospheric turbulence and wind profiles monitoring with generalized scidar, *A&A*, *369*, 364–372, 2001.

Avila, R., E. Masciadri, J. Vernin, and L. J. Sánchez, Generalised SCIDAR Measurements at San Pedro Mártir. I. Turbulence Profile Statistics, *PASP*, *116*, 682–692, 2004.

Avila, R., E. Carrasco, F. Ibañez, J. Vernin, J.-L. Prieur, and D. X. Cruz, Generalised SCIDAR Measurements at San Pedro Mártir. II. Wind Profile Statistics, *PASP*, *118*, 503–515, 2006.

Avila, R., J. L. Avilés, R. W. Wilson, M. Chun, T. Butterley, and E. Carrasco, LOLAS: an optical turbulence profiler in the atmospheric boundary layer with extreme altitude resolution, *MNRAS*, *387*, 1511–1516, 2008.

Azouit, M., and J. Vernin, Remote investigation of tropospheric turbulence by two-dimensional analysis of stellar scintillation, *J. Atmo. Sci.*, *37*, 1550–1557, 1980.

Beckers, J. M., Adaptive Optics for Astronomy: Principles, Performance, and Applications, *Annu. Rev. Astron. Astrophys.*, *31*, 13–62, 1993.

Beckers, J. M., A Seeing Monitor for Solar and Other Extended Object Observations, *Experimental Astronomy*, *12*, 1–20, 2001.

Caccia, J.-L., M. Azouit, and J. Vernin, Wind and C_n^2 profiling by single-star scintillation analysis, *Appl. Opt.*, *26*(7), 1288–1294, 1987.

Coburn, D., D. Garnier, and J. C. Dainty, A Single Star SCIDAR system for Profiling Atmospheric Turbulence, in *Optics in Atmospheric Propagation and Adaptive Systems VIII*, edited by K. Stein, and A. Kohnle, vol. 5981 of *Proc. SPIE*, pp. 105–114. 2005.

Eaton, F. D., Recent developments of optical turbulence measurement techniques (invited paper), in *Atmospheric Propagation II*, edited by C. Y. Young, and G. C. Gilbreath, vol. 5793 of *Proc. SPIE*, pp. 68–77. 2005.

Fried, D. L., Optical resolution through a randomly inhomogeneous medium for very long and very short exposures, *J. Opt. Soc. Am.*, *56*(10), 1372–1379, 1966.

Fuchs, A., M. Tallon, and J. Vernin, Focusing on a Turbulent Layer: Principle of the "Generalised SCIDAR", *PASP*, *110*, 86–91, 1998.

Fuensalida, J. J., et al., Vertical Structure of the Turbulence above the Observatories of the Canary Islands: Parameters and Statistics for Adaptive Optics, in *Advancements in Adaptive Optics*, edited by D. B. Calia, B. L. Ellerbroek, and R. Ragazzoni, vol. 5490 of *Proc. SPIE*, pp. 749–757. 2004.

García-Lorenzo, B., and J. J. Fuensalida, Automatic determination of atmospheric turbulence wind profiles using wavelets, in *Ground-based and Airborne Telescopes*, edited by L. M. Stepp, vol. 6267 of *Proc. SPIE*, p. 62671W. 2006a.

García-Lorenzo, B., and J. J. Fuensalida, Processing of Turbulent-Layer Wind Speed with Generalized SCIDAR Through Wavelet Analysis, *MNRAS*, *372*(4), 1483–1495, 2006b.

Gimmestad, G., D. Roberts, J. Stewart, and J. Wood, LIDAR System for Monitoring Atmospheric Turbulence Profiles, in *Advanced Maui Optical and Space Surveillance Technologies Conference*, edited by S. Ryan, p. E26. 2007.

Goodman, J., *Introduction to Fourier Optics*. Roberts & Company Publishers, Englewood, CA, 3rd edn., 2005.

Greivenkamp, J. E., *Field Guide to Geometrical Optics*, vol. FG01 of *SPIE Field Guides*. SPIE Press, Bellingham, WA, 2004.

Habib, H., J. Vernin, Z. Benkhaldoun, and H. Lanteri, Single star scidar: atmospheric parameters profiling using the simulated annealing algorithm, *MNRAS*, *368*, 1456–1462, 2006.

Halliday, D., and R. Resnick, *Fundamentals of Physics*. John Wiley and Sons, Inc., New York, 3rd extended edn., 1988.

Hardy, J. W., *Adaptive Optics for Astronomical Telescopes*, no. 16 in Oxford Series in Optical and Imaging Sciences. Oxford University Press, New York, 1998.

Hickson, P., and K. Lanzetta, Measuring atmospheric turbulence with a lunar scintillometer array, *Publications of the Astronomical Society of the Pacific*, *116*(826), 1143–1152, 2004.

Hoegemann, C. K., S. Chueca, J. M. Delgado, J. J. Fuensalida, B. García-Lorenzo, E. G. Mendizábal, M. Reyes, M. Verde, and J. Vernin, Cute SCIDAR: Presentation of the new Canarian instrument and first observational results, in *Advancements in Adaptive Optics*, edited by D. B. Calia, B. L. Ellerbroek, and R. Ragazzoni, vol. 5490 of *Proc. SPIE*, pp. 774–784. 2004.

Hoinka, K. P., The tropopause: discovery, definition and demarcation, *Meteorol. Zeitschrift, N. F.*, *6*, 281–303, 1997.

Howison, P., *Form 7 Physics Revision*. ESA Publications, Auckland, 1992.

Johnston, R. A., Inverse Problems in Astronomical Imaging, Ph.D. thesis, University of Canterbury, 2000.

Johnston, R. A., and R. G. Lane, Results from Mount John SCIDAR experiments, in *Proceedings of Image and Vision Computing NZ 1999 (IVCNZ'99)*, edited by D. Pairman, and H. North, pp. 271–276, Christchurch. 1999.

Johnston, R. A., and R. G. Lane, Modeling scintillation from an aperiodic Kolmogorov phase screen, *Appl. Opt.*, *39*(26), 4761–4769, 2000.

Johnston, R. A., T. J. Connolly, and R. G. Lane, An improved method for deconvolving a positive image, *Opt. Commun.*, *181*, 267–278, 2000.

Johnston, R. A., C. Dainty, N. J. Wooder, and R. G. Lane, Generalized scintillation detection and ranging results obtained by use of a modified inversion technique., *Appl. Opt.*, *41*(32), 6768–6773, 2002.

Johnston, R. A., J. L. Mohr, P. L. Cottrell, and R. G. Lane, A bread-board SCIDAR system at Mount John, in *Proceedings of Image and Vision Computing New Zealand 2004*, edited by D. Pairman, H. North, and S. McNeill, pp. 209–214, Akaroa, New Zealand. 2004.

Johnston, R. A., C. C. Worley, J. L. Mohr, R. G. Lane, and P. L. Cottrell, Turbulence Monitoring at Mount John, in *Proceedings of Image and Vision Computing New Zealand 2005*, edited by B. McCane, pp. 487–492, Dunedin, New Zealand. 2005.

Jumper, G. Y., E. A. Murphy, F. H. Ruggiero, J. R. Roadcap, A. J. Ratkowski, J. Vernin, and H. Trinquet, OHP-APT 2002 Gravity Wave Campaign: Waves, Turbulence and Forecasts, *Environ. Fluid Mech.*, *7*, 351–370, 2007.

Klückers, V. A., N. J. Wooder, T. W. Nicholls, M. J. Adcock, I. H. Munro, and J. C. Dainty, Profiling of atmospheric turbulence strength and velocity using a generalised SCIDAR technique, *Astron. Astrophys. Suppl. Ser.*, *130*, 141–155, 1998.

Kornilov, V., A. A. Tokovinin, O. Vozyakova, A. Zaitsev, N. Shatsky, S. F. Potanin, and M. S. Sarazin, MASS: a monitor of the vertical turbulence distribution, in *Society of Photo-Optical Instrumentation Engineers (SPIE) Conference Series*, edited by P. L. Wizinowich, and D. Bonaccini, vol. 4839 of *Proc. SPIE*, pp. 837–845. 2003.

Longhurst, R. S., *Geometrical and Physical Optics*. Longman Group Ltd., London, 3rd edn., 1973.

Mohr, J. L., R. A. Johnston, C. C. Worley, and P. L. Cottrell, Determination of Average Wind Velocity using Generalised SCIDAR, in *Proceedings of Image and Vision Computing New Zealand 2006*, edited by P. Delmas, J. James, and J. Morris, pp. 523–528, Great Barrier Island, New Zealand. 2006.

Mohr, J. L., R. A. Johnston, and P. L. Cottrell, Detection of wind velocities from scintillation images, in *2008 23rd International Conference Image and Vision Computing New Zealand*, edited by K. Irie, and D. Pairman, Lincoln University, Christchurch, New Zealand. IEEE, 2008.

Mohr, J. L., R. A. Johnston, C. C. Worley, and P. L. Cottrell, Optical turbulence profiling at mount john university observatory, in *Optics in Atmospheric Propagation and Adaptive Systems XI*, edited by A. Kohnle, K. Stein, and J. D. Gonglewski, vol. 7108 of *Proc. SPIE*, p. 710809. 2008.

Noll, R. J., Zernike polynomials and atmospheric turbulence, *J. Opt. Soc. Am.*, *66*(3), 207–211, 1976.

Northcott, M. J., Performance Estimation and System Modelling, in *Adaptive Optics in Astronomy*, edited by F. Roddier, pp. 155–168. Cambridge University Press, Cambridge, 1999.

Olivier, S. S., and D. T. Gavel, Tip-tilt compensation for astronomical imaging, *J. Opt. Soc. Am. A*, *11*(1), 368–378, 1994.

Olivier, S. S., C. E. Max, D. T. Gavel, and J. M. Brase, Tip-tilt Compensation: Resolution limits for ground-based telescopes using laser guide star adaptive optics, *ApJ*, *407*, 428–439, 1993.

Parenti, R. R., and R. J. Sasiela, Laser-guide-star systems for astronomical applications, *J. Opt. Soc. Am. A*, *11*(1), 288–309, 1994.

Prieur, J.-L., G. Daigne, and R. Avila, SCIDAR measurements at Pic du Midi, *A&A*, *371*, 366–377, 2001.

Prieur, J.-L., R. Avila, G. Daigne, and J. Vernin, Automatic Determination of Wind Profiles with Generalized SCIDAR, *PASP*, *116*, 778–789, 2004.

Roddier, F., The Effects of Atmospheric Turbulence In Optical Astronomy, in *Progress in Optics*, edited by E. Wolf, vol. 19, pp. 281–376. North-Holland Publishing Company, Amsterdam, Netherlands, 1981.

Roggemann, M. C., B. M. Welsh, and R. Q. Fugate, Improving the resolution of ground-based telescopes, *Review of Modern Physics*, *69*, 437–505, 1997.

Roy, A. E., and D. Clarke, *Astronomy: Princlples and Practice*. Institute of Physics Publishing, Bristol, UK, third edn., 1988.

Sturman, A., and N. Tapper, *The Weather and Climate of Australia and New Zealand*. Oxford University Press, Melbourne, Australia, 1996.

Thomas-Osip, J., E. Bustos, M. Goodwin, C. Jenkins, A. Lambert, G. Prieto, and A. Tokovinin, Two campaigns to compare three turbulence profiling techniques at Las Campanas Observatory, in *Ground-based and Airborne Instrumentation for Astronomy II*, edited by I. McLean, and M. Casali, vol. 7014 of *Proc. SPIE*, p. 70145I. 2008.

Tokovinin, A., From differential image motion to seeing, *PASP*, *114*, 1156 – 1166, 2002.

Tokovinin, A., Turbulence profiles from the scintillation of Stars, Planets, and Moon, *RevMexAA (Serie de Conferencias)*, *31*, 61–70, 2007.

Tokovinin, A., J. Vernin, A. Ziad, and M. R. Chun, Optical Turbulence Profiles at Mauna Kea Measured by MASS and SCIDAR, *PASP*, *117*, 395–400, 2005.

Tokovinin, A., A. Kellerer, and V. Coudé Du Foresto, FADE, an instrument to measure the atmospheric coherence time, *A&A*, *477*, 671–680, 2008.

Toselli, I., L. C. Andrews, R. L. Phillips, and V. Ferrero, Scintillation index of optical plane wave propagating through non-kolmogorov moderate-strong turbulence, in *Optics in Atmospheric Propagation and Adaptive Systems X*, edited by K. Stein, A. Kohnle, and J. D. Gonglewski, vol. 6747 of *Proc. SPIE*, p. 67470B. 2007.

Tyler, G. A., Bandwidth considerations for tracking through turbulence., *J. Opt. Soc. Am. A*, *11*(1), 358–367, 1994.

Tyler, G. A., and D. L. Fried, Image-position error associated with a quadrant detector, *J. Opt. Soc. Am.*, *72*(6), 804–808, 1982.

Tyson, R. K., *Principles of Adaptive Optics*. Academic Press, Inc., Boston, 1991.

Tyson, R. K., *Introduction to Adaptive Optics*. SPIE, Bellingham, WA, 2000.

Tyson, R. K., and B. W. Frazier, *Field Guide to Adaptive Optics*, vol. FG03 of *SPIE Field Guides*. SPIE Press, Bellingham, WA, 2004.

Vernin, J., M. Crochet, M. Azouit, and O. Ghebrebrhan, SCIDAR/radar simultaneous measurements of atmospheric turbulence, *Radio Science*, *25*(5), 953–959, 1990.

Wang, L., M. Schöck, and G. Chanan, Atmospheric turbulence profiling with SLODAR using multiple adaptive optics wavefront sensors, *Appl. Opt.*, *47*(11), 1880–1892, 2008.

Wilson, R. W., SLODAR: measuring optical turbulence altitude with a Shack-Hartmann wavefront sensor, *MNRAS*, *337*, 103–108, 2002.

Worley, C. C., Atmospheric Turbulence Monitoring at Mt. John, ASTR480 Honours Project, Department of Physics and Astonomy, University of Canterbury, 2005.